12-2021

Creep Behavior and Deformation Mechanisms of Spark Plasma Sintered Oxide Ceramics for Aerospace Systems at 1300˚C - 1400˚C

David D. Swanson

CREEP BEHAVIOR AND DEFORMATION MECHANISMS OF SPARK PLASMA SINTERED OXIDE CERAMICS FOR AEROSPACE SYSTEMS AT 1300°C-1400°C

DISSERTATION

David D. Swanson, Major, USAF
AFIT-ENY-DS-21-D-075

DEPARTMENT OF THE AIR FORCE
AIR UNIVERSITY

AIR FORCE INSTITUTE OF TECHNOLOGY

Wright-Patterson Air Force Base, Ohio

AFIT-ENY-DS-21-D-075

CREEP BEHAVIOR AND DEFORMATION MECHANISMS OF SPARK PLASMA SINTERED OXIDE CERAMICS FOR AEROSPACE SYSTEMS AT 1300°C-1400°C

DISSERTATION

Presented to the Faculty

Department of Aeronautics and Astronautics

Graduate School of Engineering and Management

Air Force Institute of Technology

Air University

Air Education and Training Command

In Partial Fulfillment of the Requirements for the

Degree of Doctor of Philosophy

David D. Swanson, MS

Major, USAF

December 2021

AFIT-ENY-DS-21-D-075

CREEP BEHAVIOR AND DEFORMATION MECHANISMS OF SPARK PLASMA SINTERED OXIDE CERAMICS FOR AEROSPACE SYSTEMS AT 1300°C-1400°C

David D. Swanson, MS

Major, USAF

COMMITTEE MEMBERSHIP

Marina B. Ruggles-Wrenn, PhD
Chairman

Larry W. Burggraf, PhD
Member

Maj Ryan A. Kemnitz, PhD
Member

Adedeji B. Badiru, PhD
Dean, Graduate School of Engineering and Management

AFIT-ENY-DS-21-D-075

Abstract

Oxide ceramic materials are leading candidates for aerospace structural applications due to their high strength and stiffness and their ability to maintain these properties at high temperatures in corrosive and oxidizing environments. A class of oxide ceramics, which has shown excellent potential for use in aerospace structural applications in extreme environments, is garnet ceramics. Specifically, Yttrium Aluminum Garnet (YAG, $Y_3Al_5O_{12}$) has demonstrated superior creep resistance at high temperatures in air and in steam rich environments compared to other oxide ceramics, which suggests it is an ideal material for structures that are required to operate at high temperatures for extended periods of time.

However, investigation into its behavior is limited, and further exploration of its high-temperature capabilities is needed to increase confidence in its widespread use. A related material of interest within the garnet family is Lutetium Aluminum Garnet (LuAG, $Lu_3Al_5O_{12}$). Its stable crystal structure, high density, and high melting temperature exceeding that of YAG, make it an exciting material candidate for structural applications; however, no previous research studies have investigated its mechanical performance at high temperatures.

This research effort examined several aspects of the material characteristics and mechanical behavior of YAG and LuAG at elevated temperatures. The specific materials investigated in this work include high-purity, polycrystalline YAG, high-purity, polycrystalline LuAG, and two doped variants of YAG: 2at% Yb-doped, polycrystalline YAG and 2at% Er-doped, polycrystalline YAG. Several billets of each material were prepared and processed by means of spark plasma sintering (SPS). Many different sintering parameters were utilized in order to

obtain materials with various physical properties and to identify the effects of sintering parameters on the average grain size of the resulting materials.

Basic material properties were determined following SPS processing, including density and hardness. Additionally, the material microstructure was analyzed for each billet by means of scanning electron microscopy in order to understand the quantity and location of porosity and to determine the material grain size.

The compressive creep behavior of these materials was investigated at 1300°C and 1400°C in air and in steam. Several billets of each material variant were tested in order to determine the effects of grain size on the creep behavior. The steady-state creep strain rates were determined from the results of each creep test, which enabled the identification of the stress exponent, grain size exponent, and the activation energy for the steady-state creep of both YAG and LuAG.

These studies of creep performance were accompanied by a thorough investigation into the post-creep microstructure of each material, including changes to the average grain size and grain aspect ratio following creep. This analysis of the post creep microstructure coupled with the creep results of each material contributed to the determination of the primary creep mechanisms responsible for the deformation observed at high temperature.

YAG continues to demonstrate the highest creep resistance of any oxide ceramic currently investigated, displaying steady-state creep rates on the order of 10^{-9} s^{-1} at 1300°C for large grain sizes. LuAG surprisingly demonstrated strain rates between one and two orders of magnitude greater than that of YAG for similar grain sizes, despite the high density and melting temperature of LuAG. Temperature and grain size significantly impact the creep resistance of these materials; however, YAG remains unaffected by the presence of dopants, and both YAG and LuAG are not affected by the presence of steam during creep.

Acknowledgements

I have learned many important things throughout my time as a doctoral student, including countless facts about aerospace materials, techniques to operate lab equipment, and the ability to juggle academics alongside all other areas of life. However, perhaps the most important lesson that I have learned is that no one overcomes obstacles and achieves success alone. I am constantly amazed at the seemingly infinite outpouring of help and support that I have received from my supervisors, coworkers, family, and friends, to whom I will be forever grateful.

I would like to thank my advisor, Dr. Ruggles-Wrenn. You are an outstanding contributor and a role model to many within our field of material science and engineering. I am sincerely grateful for your wisdom and guidance. Your willingness to help has left a lasting impression on me, and I will continue to strive toward your standards of excellence in every area of my life.

I am grateful for all the assistance from fellow scientists and engineers at AFIT and AFRL. I would like to thank Dr. Kemnitz and Dr. Burggraf for dedicating your time as members of my committee. I am grateful to Dr. Hay and Dr. Kim for always offering help and support. Jamie and Mike, this would not have been possible without your constant willingness to keep the labs running. I would also like to express my thanks to Brian, Dean, Dan, Chris, and Joe in the Model Shop for the countless hours spent fabricating materials and equipment to make this possible.

Finally, I would like to thank my family for their never-ending love and support throughout this process. I have the most encouraging parents who are always willing to offer help and support whenever I need it. I am grateful to my patient, supportive, and inspiring kids, Jacob and Emma. You constantly give so much joy and happiness to all of us around you. And Tina, you are my best friend and partner in life. I am humbled and amazed at your willingness to always be there for me. I love you and could not have done any of this without you.

Table of Contents

List of Figures

List of Tables

CREEP BEHAVIOR AND DEFORMATION MECHANISMS OF SPARK PLASMA SINTERED OXIDE CERAMICS FOR AEROSPACE SYSTEMS AT 1300°C-1400°C

1. Introduction

1.1. Ceramics in the Aerospace Industry

The ever-growing need for high-performance structures within the aerospace industry has enabled rapid advancements in the field of material science and engineering throughout the past several decades. The focus of these advancements has been the development of strong and light materials that can continually operate in extreme environments. Such materials find applications in aerospace structures developed for use in aircraft and spacecraft, such as sharp leading edges, nose cones, rocket nozzles, engine components, structures for hypersonic vehicles, and high-speed thermal protection systems (TPS), among others [1]. Material properties of interest for use in these state-of-the-art aerospace structures are high specific strength and stiffness, high thermal stability, resistance to thermal shock, wear resistance, and chemical stability in corrosive and oxidizing environments [1]–[3]. The need for these desirable properties in aerospace structures has led to increased interest and rapid advancements in ceramic materials.

Ceramics make up a vast and important group of materials commonly used throughout science and engineering and in many facets of everyday life in general. They have a wide range of applications, including household goods, construction materials, electronics, refractory materials, and medical devices and implants [4]. However, the most significant advancements in engineering ceramics have been heavily driven by progress in the aerospace industry. The extreme operating conditions often seen by aerospace structures have caused designers to move beyond the use of metals and polymers in these applications. Although metals can often provide high strength, stiffness, and durability, they are heavy and are not typically able to withstand

high temperatures in corrosive environments. And although polymers are light and can often be tailored to meet specific requirements, they typically lack the required strength and high-temperature stability required of aerospace structures.

Ceramic materials are able to fill these requirement gaps and meet the needs of the aerospace industry. They possess the high strength and stiffness characteristics required of critical structural components, and they are lighter than most metals [2], [3]. Furthermore, the most valuable and unique characteristic of ceramic materials is their ability to operate in extreme environments. The TPS material used for previous generation re-entry vehicles has been required to survive temperatures approaching 1600°C [5]. Similarly, in hypersonic flight, sharp leading edges can see temperatures in excess of 2000°C [6]. The use of ceramics has increased the efficiency of jet engines due to their use in critical engine components, such as stator vanes, rotor blades, and combustor liners, among others [7]. The materials used in these applications must be capable of surviving high temperatures while maintaining structural integrity, requiring strong, durable materials with high melting points, low coefficients of thermal expansion, and resistance to corrosion.

These applications require the use of materials that are capable of maintaining their properties in corrosive and oxidizing environments for extended amounts of time. Although they are typically more resistant to corrosion than other materials, many high-performing ceramics will still degrade over time when forced to operate at high temperatures in air [8]. This requirement has led to the increased interest in a specific class of ceramic materials: *oxide ceramics*. Because of their chemical composition, oxide ceramics inherently resist oxidation, even at high temperatures, and are therefore able to operate continually in these extreme environments. However, research into the capabilities and ultimate potential of oxide ceramics is

still a relatively new and ongoing activity. The continued development of materials with these unique properties is critical to the advancement of the aerospace industry; therefore, the investigation into newly developed oxide ceramics with more advanced capabilities, higher temperature limits, higher strength properties, and longer life spans is an important research effort, which continues today.

1.2. Problem Statement

As more ceramic materials are developed for use in aerospace applications, a critical requirement and common limiting factor have become readily apparent. These materials must be capable of maintaining their properties in oxidizing environments. Although a fundamental characteristic of ceramics is increased corrosion resistance over metals, many ceramics are not entirely resistant to corrosion at high temperatures [8]. One form of corrosion, which many common ceramics are still susceptible to is oxidation, which is amplified at high temperatures. Many commonly used non-oxide ceramics, such as carbides, nitrides, and borides, among others, have been shown to quickly oxidize in oxygen rich environments, including air, resulting in degraded mechanical properties [9]–[13].

This problem is intensified even further in combustion environments, where the conditions more readily promote the potential for oxidation. Ceramics in these environments will see elevated temperatures and pressures and will also be exposed to water vapor, which can be a typical by-product of combustion [14]–[17]. Several studies have shown that the presence of water vapor at high temperatures will drastically increase the rate of oxidation, as water molecules are more soluble in SiO_2 than in O_2 gas [14]–[20].

Although oxide ceramics inherently resist oxidation due to their chemical composition, previous research has demonstrated that these resilient properties of oxide ceramics and oxide ceramic composites may still be insufficient for the current needs presented by the aerospace industry. Specifically, the creep resistance and creep-rupture times of oxide ceramic materials have still been observed to decrease in steam environment, due to the many degradation and failure mechanisms present in such conditions [21]–[23]. For several years the highest-performing state-of-the-art materials in the oxide ceramic group have been commercially available polycrystalline alumina and alumina-mullite fibers, fabricated for use in ceramic matrix composites. Although the strength properties of these fibers have significantly surpassed those of other oxide ceramics, they are still inferior to those observed in non-oxide ceramics in inert environments. Additionally, in many applications the use of alumina is limited to 1100°C by the high-temperature strengths and creep rates that have been observed in oxidizing environments [24]. These shortcomings of currently available oxide ceramics have furthered the need for ongoing research into these materials and their properties. Additional materials must be fabricated and thoroughly investigated in order to provide a long-term oxidation-resistant ceramic material solution for the aerospace industry.

1.3. Research Focus

This research is focused on determining the mechanical properties of advanced oxide ceramics, which have not yet been thoroughly tested and analyzed for use in extreme aerospace environments. Materials of interest in this investigation are two potentially high-performing garnet ceramics, which may be capable of demonstrating substantial deformation resistance at high temperatures. This deformation behavior must be studied in order to determine whether

these materials are valuable candidates for further research efforts and future aerospace applications. The specific materials, which will be investigated in this research effort, are Yttrium Aluminum Garnet (YAG, $Y_3Al_5O_{12}$) and Lutetium Aluminum Garnet (LuAG, $Lu_3Al_5O_{12}$). Each of these materials have characteristics and physical properties, which suggest that they may possess superior time-dependent mechanical properties over currently used oxide ceramics, specifically in extreme oxidizing environments. However, a thorough analysis of their behavior under these conditions has yet to be performed.

This research is an exploratory effort, which aims to determine the mechanical behavior of these materials. Specifically, the creep properties of these oxide ceramic materials will be determined through testing and analysis in conditions that have not yet been investigated. Creep experiments will take place in both air and steam in order to evaluate behavior in two different oxidizing environments. YAG has a melting temperature of 1970°C, is stable in oxidizing and reducing environments, and possesses a highly symmetric cubic crystal structure, which suggests a particular resistance to creep [25]. Creep rates (in air or in vacuum), grain growth rates, and corrosion resistance in combustion environments of both single-crystal YAG and polycrystalline YAG have been shown to be superior to those of alumina and mullite [26], [27]. Although some research has been conducted on the creep performance of YAG at high temperatures, investigation of YAG performance in air and steam is limited at 1300°C and has not yet been extended to 1400°C [28]. This research will go further in air and steam, studying doped and undoped, polycrystalline YAG materials with different grain sizes at various temperatures and creep stresses. This research will help determine the dependence of the creep behavior of YAG on temperature, creep stress, environment, grain size, and dopant at temperature approaching the

melting point of YAG. This work will also give insight into the creep mechanisms responsible for the deformation of YAG at these temperatures in air and in steam.

Essentially no research has been conducted on the mechanical properties of LuAG. Up to this point, LuAG has been fabricated primarily for laser applications due to its optical properties and transparency. This exploratory effort will provide the first creep results of LuAG specimens, and will examine the effects of temperature, applied stress, and environment on the deformation behavior of LuAG. Based on the material similarities and physical properties of LuAG and YAG, it is expected that LuAG will demonstrate some of the most creep resistant behavior of any known polycrystalline oxide ceramic.

The steady-state creep strain rates, controlling creep mechanisms, and creep activation energies of these materials at high temperatures remain an ongoing area of research. The absence of extensive microstructural examination casts doubt on what mechanisms are truly active during creep in certain conditions. Yet this information is critical to advancing the use of oxide ceramics and investing in their application as reliable structural materials operating in extreme environments.

Mechanical testing in oxidizing environments at high temperatures is not a trivial matter. Creep experiments planned in this work have been historically difficult to perform. By utilizing lessons and techniques established throughout the past usage of specialized experimental facilities and test procedures previously developed at AFIT [29]–[31], reliable experimental results will be obtained to fill gaps in the current understanding of the creep behavior of these oxide ceramics. Determination of creep mechanisms is critical to ensure models are based on sound physics and valid assumptions. This study aims to add to the body of knowledge pertaining to the creep characteristics and overall behavior of these emerging oxide ceramics.

1.4. Research Objectives

The research objectives laid out in this section are associated with determining the creep behavior of the oxide ceramics of interest in this study, which will result in a valuable contribution towards the continued development of oxidation resistant materials capable of withstanding extreme operating conditions required of aerospace materials. These objectives provide the basis for a detailed research plan, which is focused on initial material characterization, experimental facility installation and setup, creep testing at high temperatures in air and in steam, and post-creep microstructural analysis. The five primary research objectives as well as the various tasks associated with each objective are summarized below:

1. Fabricate polycrystalline YAG and LuAG material billets by Spark Plasma Sintering (SPS) and prepare specimens for microstructural characterization and creep testing.
    a. Prepare ceramic powder for SPS, including undoped, polycrystalline YAG, 2at% Yb-doped, polycrystalline YAG, 2at% Er-doped, polycrystalline YAG, and undoped, polycrystalline LuAG.
    b. Create fully dense material billets with a variety of grain sizes by adjusting temperature and pressure parameters for different SPS runs for each material.
    c. Machine pucks into specimens for creep testing and prepare additional samples for material characterization in the SEM.
    d. Determine dimensions and mass of each creep test specimen.
2. Characterize various physical and microstructural properties of all materials prior to creep testing.
    a. Determine the density of each creep test specimen by means of the Archimedes density measurement technique and a Helium pycnometer.

b. Perform impurity analyses on each material variant and determine the typical pore structure by analysis in the SEM after processing.
c. Determine the average grain size of each SPS billet by analysis in the SEM using quantitative image analysis software.
d. Perform microhardness measurements on each material billet following SPS.
e. Determine the correlation between material grain size and SPS parameters.

3. Validate the capabilities and functionality of the 1500°C Amteco furnace in conjunction with the 5 Kip universal material testing machine and calibrate the associated equipment and instrumentation.
    a. Ensure the furnace and testing machine interface properly, and the load train and equipment fit together, to include the fabrication and installation of the custom furnace-expanding insert.
    b. Test the temperature capabilities of the new furnace prior to creep testing, and perform temperature calibrations for each material, at each target temperature, in air and in steam.
    c. Ensure the steam generator is functional and interfaces properly with the new furnace and susceptor surrounding each specimen.
    d. Ensure furnace, susceptor, and load train are centered with the extensometer and extensometer mounting system. Perform extensometer calibration to ensure proper strain measurement.
4. Perform creep tests on each material variant.

a. Conduct five-hour long creep tests on undoped, polycrystalline YAG specimens of various grain sizes at 1300°C and 1400°C in air and in steam with compressive stress levels between 50 MPa and 200 MPa.
b. Conduct five-hour long creep tests on 2at% Yb-doped, polycrystalline YAG and 2at% Er-doped, polycrystalline YAG specimens of various grain sizes at 1300°C in air with compressive stress levels between 50 MPa and 200 MPa.
c. Conduct five-hour long creep tests on undoped, polycrystalline LuAG specimens of various grain sizes at 1300°C and 1400°C in air and in steam with compressive stress levels between 50 MPa and 200 MPa.

5. Analyze the creep data, and perform microstructural analysis of specimens following creep testing in order to determine the creep mechanisms and deformation characteristics for each material variant.
    a. Determine the steady-state creep strain rates for each material variant under each test condition.
    b. Determine stress exponents and grain size exponents for each material variant in order to quantify the effects of stress and grain size on the resulting creep behavior and to identify the active creep mechanisms.
    c. Determine the activation energy of undoped, polycrystalline YAG and LuAG in order to understand the nature of diffusion during creep.
    d. Prepare post-creep specimens for microstructural analysis by cutting in the axial loading direction through the center and polishing cut surfaces.
    e. Analyze post-creep specimens in the SEM to determine post-creep grain size and overall structure to include any changes in grain aspect ratio.

2. Background and Literature Review

In order to fully understand the context and relevance of the experimental results and analysis presented in this research study, a thorough background and literature review is provided in this section. An overview of ceramic materials is presented, which includes the history of traditional ceramics, the progress made in the field of engineering ceramics, and the advantages and properties of oxide ceramics.

Following this overview of ceramics, a thorough literature review is presented, which will explore the physical attributes, performance properties, and previous research studies surrounding specific types of oxide ceramics, including various garnet ceramics. Within each of these sections, the specific materials of interest (YAG, and LuAG) will be highlighted, to include a detailed description of their crystal structures and material properties.

In order to understand the experimental focus of this research, an explanation of creep theory and the science behind various creep mechanisms are provided. Additionally, a literature review of previous creep studies of various oxide ceramics is presented. This review focuses on the creep properties of garnet ceramics, as well as some other widely-used oxide ceramics, which possess similar performance characteristics, in order to understand the current state-of-the-art and the ongoing need for further creep research of ceramic materials.

The next section in this literature review provides a description of potential environmental failure modes observed in ceramic materials. This research focuses on the deformation and potential failure of ceramics exposed to high temperatures in oxidizing and corrosive environments. Therefore, the environmental effects on these materials must be understood. An overview of fracture mechanics and sub-critical crack growth is provided, followed by a review of previous experimental studies of environmentally-assisted failure of oxide ceramics.

The final section in this literature review summarizes the implications of previous work on this current research effort, and how this study will provide new and relevant information, which will add to the current body of knowledge surrounding oxide ceramic materials. This background and literature review is divided into six main sections, which are outlined below:

2.1. Introduction to Engineering Ceramics

2.2. Garnet Ceramics

2.3. Creep of Ceramics

2.4. Environmental Effects on Oxide Ceramics

2.5. Implications for Current Research

2.1. Introduction to Engineering Ceramics

2.1.1. An Overview of Ceramic Materials

Ceramics make up one of the largest and most important groups of materials used in science and engineering and in everyday life in general. They encompass a broad range of material properties, enabling their applications to span across several industries from household goods to construction to aerospace. Ceramics have a long and progressive history, and their use has been critical to pushing technology further for thousands of years. In the early days of their use ceramics included only simple figurines and sculptures, dating back to the late Paleolithic period. Thousands of years later the technology eventually improved, allowing the creation of clay pottery and weaponry made in small kilns dug into the ground [32], [33]. Throughout the years since, ceramic technology has progressed to include strong, reliable structural material and high-temperature resistant aircraft and spacecraft components. In the following paragraphs ceramic materials are defined as a distinct class of materials, and their properties, advantages, and primary uses are laid out in detail.

The word ceramic originates from the Greek, *keramos* (κέραμος), meaning "pottery" or "potter's clay", and the Greek root can be traced back to the ancient Sanskrit, *çar*, meaning "burnt material". It is clear that the Greek's focused more on the process and not the actual resulting material, as this particular term was only used for products made from a burning or firing process, and was therefore only used to describe clay pottery or other heat treated earthenware of the time [2], [4], [31], [34], [35]. Modern material science has allowed this history and etymology of ceramic materials, focusing on the process of changing the chemical or physical properties of a material with the application of heat, to encompass many different types of materials, including "pottery, porcelain, refractories, structural clay products, abrasives,

porcelain-enamels, cements, and glass, but also nonmetallic magnetic materials, ferroelectrics, manufactured single crystals [and] glass ceramics" [4], [35]. In recent years ceramics also incorporate more modern materials, such as advanced engineering ceramics, which will be discussed in detail in later paragraphs.

Given the variety of ceramic materials and the diversity of their use, it is not surprising that one precise definition is difficult to come by. Several authors of material science texts offer up perhaps the most common and concise description of ceramic materials as non-metallic, inorganic solid materials, which easily includes all of the above examples and successfully distinguishes ceramics from metals and carbon chain-based, organic materials, such as polymers [2]–[4], [31], [36]. Others prefer a more restrictive definition and define ceramics by the nature of their chemical structure, typically compounds between metallic and nonmetallic elements for which the interatomic bonds are either totally ionic or a mix of ionic and covalent [2], [3], [31], [37]. The most common chemical structures of ceramics are oxides, carbides, and nitrides, but also include silicides, borides, phosphides, and sulfides, among others. Elemental Silicon and Boron, as well as Carbon in its graphite or diamond form are also typically grouped into ceramics [2], [36]. The diversity of ceramics extends to their crystal structures as well. Typical ceramics are crystalline solids, which include single crystal materials, polycrystalline materials, and partially crystalline materials. Additionally, certain amorphous materials, such as glasses, are included as well [2], [3], [36].

Often ceramics are defined based on mechanical characteristics and properties. Due to the varied chemical structures, elements present, and types of atomic bonding across all ceramics, there can be a wide range of properties and levels of performance to consider. However, some basic characteristics and properties are generally observed across all ceramics, the most

notorious of which is the brittle nature of ceramics. As is shown in Figure 1, brittle ceramics will generally have a much steeper stress-strain curve than metals and polymers, and they will see little plastic deformation before catastrophic failure. Brittle failure with little plastic deformation means that ceramics generally have very low fracture toughness, and can fail easily due to small cracks and defects present. This is considered one of the greatest weaknesses of ceramic materials, and recent advancements are seeking to improve upon this weakness.

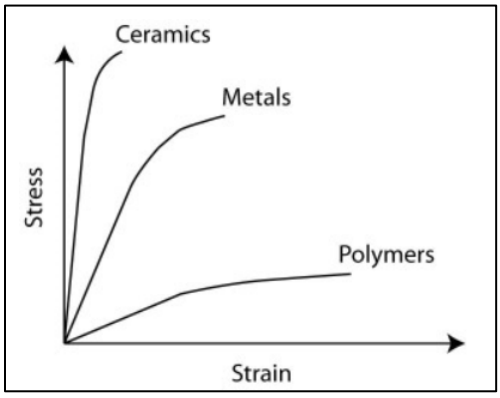

Figure 1: Typical stress-strain behavior of three main classes of materials.

Other characteristics of many ceramic materials include high strength and stiffness, and due to the nature of their processing, they can withstand relatively high temperatures compared to other classes of materials [2], [3], [7], [38]. They typically have fewer free electrons than metals, making them good electrical and thermal insulators, and their strong chemical bonds lead to high melting temperatures and increased chemical stability and corrosion resistance [2], [3], [38]–[40].

Ceramics are generally split into two main categories: traditional (or conventional) ceramics and engineering (or advanced) ceramics. Traditional ceramics are typically made from clay, silica, or feldspar, and include many of the earliest known examples of ceramic materials, including clay pottery, whitewares, cements, refractories, and glasses [40]–[43]. Table 1 below summarizes the types and most common examples of traditional ceramics.

Table 1: Types and examples of traditional ceramics [43]

Traditional Ceramics	
Type	Examples
Structural clay products	Bricks
	Tiles
	Pipes
Whitewares	Stoneware
	China
	Porcelain
Cements	Concrete
	Mortar
Refractories	Silica
	Aluminum Silicate
	Magnesite
Glass	Soda-lime Glass

Traditional ceramics can be thought of as everyday materials, and many are common in an average household. In contrast to engineering ceramics, traditional ceramics are not meant to perform in harsh environments under significant mechanical loads. [2], [3], [37]. Engineering ceramics are manufactured (or engineered) for advanced technological applications, such as electronics, aerospace, and energy, among other industries, typically requiring much more stringent quality control with regards to microstructure, porosity, reproducibility, and fabricated dimensional tolerance [3], [37], [41]–[43]. Typically, engineering ceramics are manufactured by a more sophisticated chemical process, which can result in a much higher purity (>99%) and more desirable properties [37], [41]. Further, their properties can be tailored to suit a specific need and to highlight certain desired material properties, such as improved structural properties, corrosion or oxidation resistance, thermal, electrical, optical, or even magnetic properties [44].

Despite their wide-spread use today, engineering ceramics are a relatively recent technology, going back to the early 20th century, which is primarily due to their difficult and complex processing requirements [41]–[43]. Engineering ceramics can be further subdivided into categories based on the many applications to which they could be tailored, such as structural

ceramics, electrical ceramics, thermal, magnetic, optical, ceramic coatings, and chemical processing/environmental ceramics [44]–[46].

Important examples of engineering ceramics are oxides, nitrides, and carbides, based on silicon, aluminum, titanium, and zirconium, among others [37]. Notable and advantageous properties of engineering ceramics include exceptional strength and stiffness combined with low density, making them a very attractive choice for aerospace applications [2], [3], [37], [47]. Table 2 summarizes the densities and some mechanical properties of several engineering ceramics compared with stainless steel.

Table 2: Flexural strength, elastic modulus and density of engineering materials [2], [37], [47].

Material	Density (g/cm^3)	Flexural Strength (MPa)	Modulus of Elasticity (GPA)
Zirconia (ZrO_2)	6.6	800-1500	205
Alumina (Al_2O_3)	3.96	275-700	393
Silicon Carbide (SiC)*	3.1	100-820	345
Silicon Nitride (Si_3N_4)	3.17	250-1000	304
Mullite ($3Al_2O_3$-$2SiO_2$)	3.12	185	145
Magnesium Oxide (MgO)**	3.58	105	225
Stainless Steel	7.8	300-1400	210

*Sintered SiC
**Sintered MgO with 5% porosity

Engineering ceramics also possess advantageous thermal properties. These include high melting points compared to metals, low thermal expansion coefficients, and low thermal conductivity [3], [4], [7], [37], [38]. A distinct class of ceramics, known as ultra-high temperature ceramics (UHTCs), have melting points above 3000°C, and can be used in the harshest environments required for aerospace applications [1]. These thermal properties lead to improved mechanical performance at higher temperatures for longer periods of time. Figure 2, reproduced with permission from Chawla's book on ceramic matrix composites (CMCs), shows how the service temperature of typical engineering ceramics compares to that of metals and polymers.

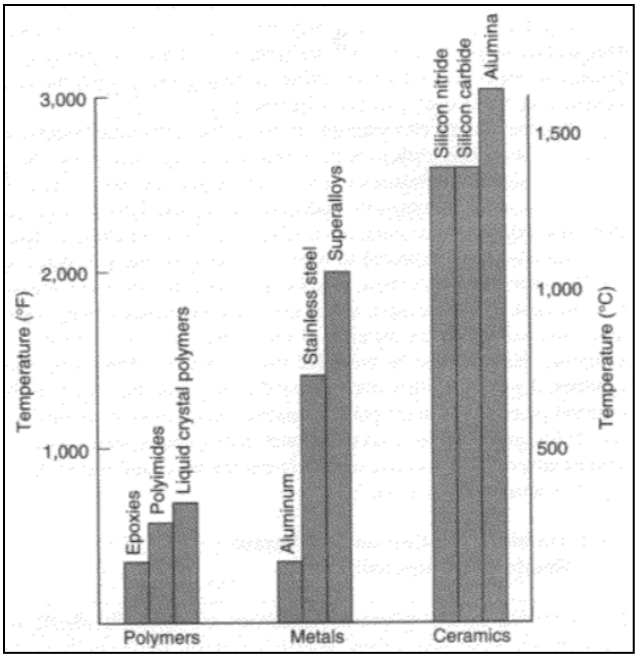

Figure 2: Summary of service temperature limits of commonly used ceramics, metals, and polymers from Chawla [37]. Reproduced with permission from Springer Nature.

While engineering ceramics possess more durability and wear resistance than traditional ceramics, the fracture toughness and propensity to catastrophically fail due to the presence of small flaws remain a great disadvantage [29], [38], [48]–[53]. In order to combat this problem of brittle failure, monolithic ceramics can be reinforced with a secondary phase, creating a composite material. In cases where the material must withstand high temperatures and maintain some amount of toughness and durability, a ceramic matrix is typically reinforced with either ceramic fibers or particulates, forming a ceramic matrix composite (CMC) [29], [37], [49]. This special class of ceramic materials is of particular importance to the aerospace industry and successfully allows for high temperature performance while enabling a more graceful and predictable failure.

This vast group of engineering ceramic materials can also be split into two main categories based on chemical composition: Oxides and Non-Oxides. This separation along with classic examples is visualized by Heimann in *Classic and Advanced Ceramics*, shown in Figure 3.

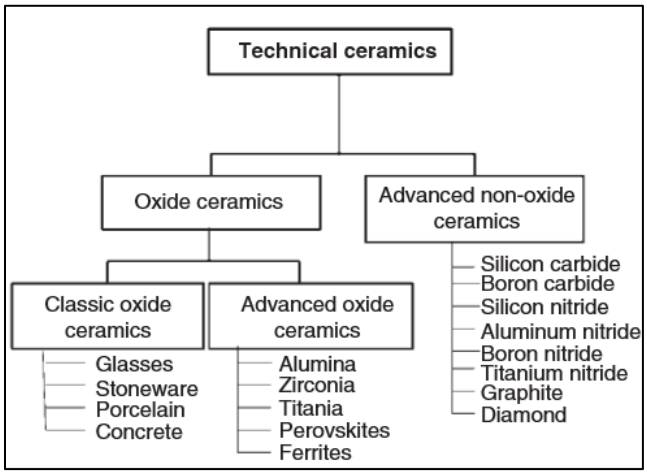

Figure 3: Flow chart of oxide and non-oxide ceramics from Heimann [45]. Reproduced with permission from John Wiley and Sons.

Non-Oxide ceramics are formed by the reaction of a metal with various Oxygen-free elements, which include carbides, nitrides, sulfides and borides, among others [46]. They exhibit some of the highest strength properties and can operate at the highest temperatures. However, they can only achieve such high-performance properties if their use is limited to inert environments due to their tendency to quickly oxidize at high temperatures. Once oxidation begins, the material can quickly degrade, and the mechanical properties will suffer [49]. This phenomenon has resulted in the increased study and use of oxide ceramics, which are chemically stable, will not oxidize at high temperatures, and are capable of achieving maximum performance in Oxygen-rich environments. Oxide ceramics provide a valuable solution to a difficult problem and enable the use of ceramics in more complex applications.

2.1.2. Introduction to Oxide Ceramics

An Overview

Oxides in the most generic sense can be defined as materials made up of chemical compounds with one or more Oxygen atoms combined with another element [54]. These are, of course, present in everyday life as solids, liquids, and gasses in their room-temperature state. Oxides can be formed by the reaction of Oxygen with another substance, sometimes requiring high temperature, and they can also be formed by the thermal decomposition of various chemicals, which already contain Oxygen, resulting in an oxide plus some by products [54]–[56]. One mechanism of forming an oxide, termed oxidation, is often thought of as an undesirable phenomenon, and is categorized as a form of corrosion, often called "dry corrosion" [2], [57]. This will occur when a material, such as a metal, comes into contact with an environment or substance containing Oxygen, resulting in a reaction, which changes the chemical structure of the material [58].

In order for oxidation to occur on the surface of a metal, there must be an adequate supply of Oxygen in contact with the metal, and there must be enough available energy to create mobility of the Oxygen atoms [59]. Atomic bonds are then broken, and a chemical reaction can occur. Oxygen ions must diffuse into the metal, while metal ions diffuse away via various possible transport mechanisms [57]–[59]. This process can create a layer of metal oxide on the surface of the metal as is shown in Figure 4.

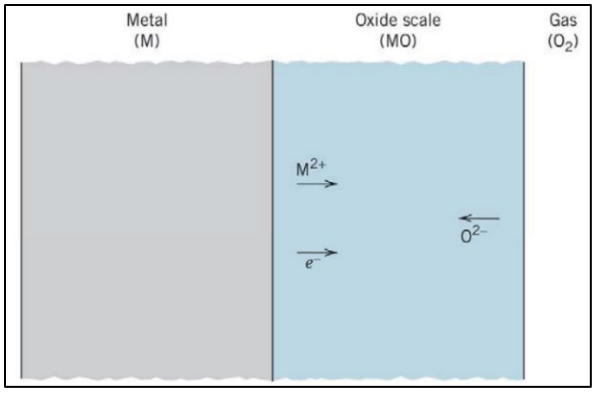

Figure 4: Formation of an oxide scale from contact between O_2 gas and the surface of a metal from Callister [2]. Reproduced with permission from John Wiley and Sons.

For most metal applications, especially structural applications, oxidation often has deleterious effects on the desired performance of the underlying material [57]. Depending on the oxidation environment, the oxide scale can be porous and weak, and in some cases a secondary reaction can cause the scale to volatilize entirely, resulting in an overall loss of mass. This type of oxidation can reduce structural properties, and change electrical and thermal properties as well, ultimately causing the material to be less effective in its intended application [2]. Alternatively, oxidation may form a dense, protective oxide layer, which inhibits deeper oxidation, and protects the underlying material from the harsh environment in which it operates [57]–[61]. This type of oxidation can have a desirable outcome, and it is sometimes integrated into the engineering design of a structural component.

These oxidation processes can occur in ceramic materials as well. A fundamental characteristic of ceramics is increased corrosion resistance over metals; however, one form of corrosion, which ceramics are still susceptible to is oxidation, especially at high temperatures. Many commonly used non-oxide ceramics, such as carbides, nitrides, and borides, among others, have been shown to quickly oxidize in an Oxygen-rich environment [9]–[13]. Additionally, Carbon materials, which can be grouped into ceramic materials, such as structural Carbon fibers,

are susceptible to oxidation and associated degradation of properties at high temperatures [62], [63].

In contrast to non-oxide ceramic materials, oxide ceramics are chemically stable in Oxygen-rich environments, as their chemical structures already include Oxygen. Oxide ceramics are oxides of various elements, which are chemically stable solids at room temperature, and possess properties typical of ceramic materials [64]. They represent the largest category of ceramics produced today, and include many different types used for many applications [65]. Oxides of certain elements are of little interest as ceramics because of their inherent chemical instability, such as CaO, SrO, and BaO [64]. Silicate ceramics are based on silica (Silicon dioxide: SiO_2), and include many of the more traditional ceramics, not typically used in load bearing applications. More advanced oxide ceramics include oxides of metals, such as Aluminum, Titanium, and Zirconium, among others [65]. Recent advancements in the field of oxide ceramics have seen excellent thermal and mechanical property improvements, allowing the widespread use of oxide ceramics in the aerospace industry.

Why Oxide Ceramics?

High performing, non-oxide ceramic materials have demonstrated low density [2], exceptional strength and stiffness at high temperatures [4], low coefficients of thermal expansion [37], and improved resistance to corrosion and wear over most metals [38]. These attributes have given them widespread use in aerospace applications, where they are required to operate at high temperatures in chemically reactive environments.

A significant problem with these materials is that they exhibit poor oxidation resistance at high temperatures in oxidizing environments [10], [11], [29], [62], [66]. Once oxidation occurs,

material performance can become unreliable. In certain environments mechanical properties can quickly degrade, causing the material to fail under its normal operational load. This inherent weakness of non-oxide ceramic materials has led to the widespread investigation of their oxidation rates and mechanisms, and the increased use of more oxidation resistant materials. A commonly used high-performance non-oxide ceramic material, such as Silicon carbide (SiC), will oxidize when used in a dry Oxygen-rich environment (such as air) by one of the following possible chemical reactions [18], [67], [68]:

$$SiC(s) + (3/2)O_2(g) = SiO_2(s) + CO(g)\ [67] \quad \text{(Equ. 1)}$$

$$SiC(s) + O_2(g) = SiO(g) + CO(g)\ [67] \quad \text{(Equ. 2)}$$

Equations 1 and 2 represent passive and active oxidation, respectively. The former represents a non-aggressive type of oxidation, where solid Silicon dioxide (SiO_2) forms a thin, dense film on the surface of the substrate. Once in place, this thin oxide scale can act as a protective barrier, slowing further oxidation, as ionic diffusion will occur at a slower rate through the outer oxide layer [10]. Passive oxidation on the surface of a material, such as a non-oxide ceramic, can be beneficial in preventing deeper oxidation and maintaining mechanical properties [2], [57]. Furthermore, in certain conditions the outer oxide scale can flow, sealing any pores or micro-cracks on the surface of the brittle ceramic. This oxidation mechanism can then toughen and even strengthen the material [9], [60].

In contrast, active oxidation is a much more aggressive form of corrosion, represented by Equation 2. The resultant SiO is vaporized and will not form an outer oxide scale, resulting in an overall loss of mass [9], [10]. This process ultimately results in recession and the formation of pitting on the surface of the material. This form of oxidation can be very harmful to the original ceramic material, drastically decreasing the mechanical properties. The environmental conditions

determine which type of oxidation will occur, based primarily on temperature, pressure, and the Oxygen content in contact with the material. Figure 5 shows these two types of oxidation reactions occurring on the surface of Silicon carbide.

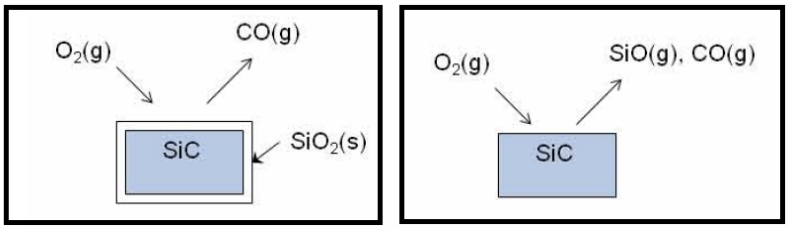

Figure 5: A diagram illustrating two possible oxidation reactions on Silicon Carbide (SiC) from Jacobson and Myers [67]. Reproduced with permission from Springer Nature.

Ceramic materials are also used as structural components in combustion environments due to their increased resistance to corrosion and their ability to operate at high temperatures. Ceramics in these environments will see elevated temperatures and pressures and will also be exposed to water vapor during use, as it is a typical by-product of burning hydrocarbon fuels for combustion [8], [14]–[17]. Several studies have shown that the presence of water vapor at high temperatures will drastically increase the rate of oxidation, as water molecules are more soluble in SiO_2 than in O_2 gas [8], [14]–[20]. For the case of SiC, in addition to the previously discussed chemical reactions, oxidation in water vapor will typically occur according to the following oxidation reaction:

$$SiC(s) + 3H_2O(g) = SiO_2(s) + 3H_2(g) + CO(g)\ [8], [19] \qquad \text{(Equ. 3)}$$

In the presence of water vapor it is more likely that the oxidation mechanism will transition from passive to active, causing any protective oxide coating to simultaneously volatilize, forming a gaseous species [14], [66], [69]–[71]. This mass loss from the removal of the oxide scale will leave the material more vulnerable to further oxidation and will lead to increased surface recessions and more rapid degradation of mechanical properties [8], [15], [17], [70], [72], [73].

Figure 6 shows the potential differences between oxide scales formed in air and in water vapor, reproduced with permission from More et al. [15]. The former is dense and thin, effectively slowing further oxidation. The latter is thick due to the increased oxidation rate, but has partially volatilized, leaving a porous, unprotective scale.

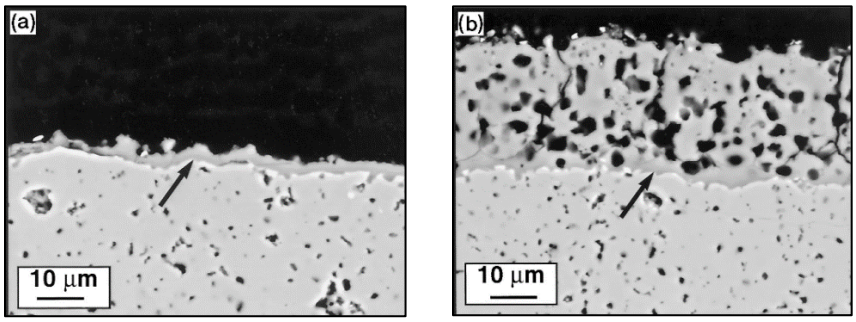

Figure 6: Comparison of dense protective oxide scale after exposure in air (a) and a porous, volatilizing oxide scale after exposure to water vapor (b), from More et al. [15]. Reproduced with permission from John Wiley and Sons.

Oxidation represents an inherent vulnerability of many commonly used ceramic materials, and must be considered when making material selections for extreme operating conditions. Due to this limiting factor of non-oxide ceramics operating in oxidizing environments, specifically combustion environments containing water vapor, there has been an increased interest in the performance of oxide ceramics in recent years. These materials inherently resist oxidation, are thermochemically stable, and are capable of demonstrating excellent mechanical properties at high temperatures. These properties have made oxide ceramics a highly researched topic within the aerospace industry and the state-of-the-art in reliable, oxidation-resistant materials.

2.1.3. Common Oxide Ceramics and Their Properties

There are many different types of oxide ceramic materials, both with simple and more complex chemical structures, and both naturally occurring and those produced by complicated

processing methods. Each has unique properties enabling them to be used in various applications; however, one common attribute among oxide ceramics is their high melting points and associated chemical stability at high temperatures. Table 3 lists the melting points and densities of several common oxide ceramics.

Table 3: Approximate melting temperatures and densities of important oxide ceramics [74].

Oxide Ceramic	**Melting Temperature [°C]**	**Density [g/cm^3]**
Al_2O_3	2050	2.6 - 4.0
ZrO_2	2700	5.6 – 6.1
MgO	2850	3.6
TiO_2	1840	3.8 – 4.3
SiO_2	1720	2.2 (Silica Glass) 2.65 (β-quartz)
Y_2O_3	2450	4.5
HfO_2	2900	9.7 – 10
ThO_2	3200	10.0

The most common and arguably the most important simple ceramic oxide is alumina (Aluminum oxide: Al_2O_3). Although pure alumina, known as corundum, is rarely found on its own in nature, Aluminum is one of the most common elements on earth, and alumina is found as a chemical constituent in rock throughout the earth's crust. This abundance and low cost has led to extensive production and research into the properties and uses of alumina [64], [75]. Naturally occurring single crystal alumina is a rare mineral, commonly used as a gemstone. White and blue sapphire as well as red ruby are examples of single crystal alumina with various impurities present, which account for the various colors. Single-crystal alumina can also be synthesized and used in specialized applications, requiring improved strength and stiffness over polycrystalline alumina [76]. Polycrystalline alumina can be refined and synthesized from abundant raw materials with ease and relatively low cost, which is uncommon for most refractory, ceramic materials used in advanced applications. Polycrystalline alumina can be synthesized by a variety of different methods, although the most common is sintering at high temperatures. This method

of processing can result in high purity alumina (>99.99% Al_2O_3) with high hardness, excellent mechanical and thermal properties, and superior wear and corrosion resistance [75]–[77]. Properties of polycrystalline alumina are summarized in Table 4 for various purity levels.

Table 4: Typically observed property values for various alumina ceramic materials [74], [75].

Property	**Al_2O_3 (>99.7%)**	**Al_2O_3 (99%)**	**Al_2O_3 (80% – 95%)**
Density [g/cm^3]	3.96 – 3.99	3.8 – 3.9	2.6 – 3.8
Vickers Hardness [GPa]	20	15 –16	10 – 15
Fracture Toughness [MPa·m$^{1/2}$]	4-5	6	3-4
Young's Modulus [GPa]	400	380-400	200-300
Poisson's Ratio	0.23	0.23	0.23
Compressive Strength [MPa]	3000-4000	2500	2000
Bend Strength at 20°C [MPa]	400-600	350	200-300
Bend Strength at 1200°C [MPa]	100-150	-	50-100
Thermal Expansion [10^{-6} K^{-1}]	8.5	8.0	7.0
Thermal Conductivity [W/m·K]	33	25-30	15-25

Due to its exceptional thermal and chemical stability, alumina is a common refractory material in furnace components and insulation [75]. It is commonly used for medical and dental implants due to its high strength and hardness [76]. Additionally, alumina is used in high-temperature electronic devices as an electrical insulator [77]. As with all monolithic ceramics, alumina lacks the necessary fracture toughness to be used as a structural material for many aerospace applications. Therefore, alumina fibers have been developed as a reinforcement for ceramic matrix composite materials since the 1970's. Two important commercially available ceramic oxide fibers are the Nextel 610 and the Nextel 720 fibers, developed by 3M in the 1990's [29]. The Nextel 610 oxide ceramic fibers are made up of 99% polycrystalline α-alumina. They have a single filament strength of nearly 3000 MPa at room temperature, and can continuously operate up to 1000°C before losing significant ultimate strength [24].

The Nextel 720 oxide ceramic fibers are composed of α-alumina and mullite, which is a crystalline aluminosilicate with a chemical structure of $3Al_2O_3$ - $2SiO_2$. Mullite has excellent thermal and chemical stability, high creep resistance, and is not easily susceptible to thermal

shock [75]. With the addition of the mullite phase, both the high temperature strength retention and the creep resistance are increased over other oxide ceramic fibers [24]. These two structural alumina fibers have been very significant in creating effective oxidation resistant oxide ceramic matrix composites for many high temperature structural applications.

Another valuable and common oxide ceramic material is zirconia (Zirconium oxide: ZrO_2). Zirconia has a very high melting point, is chemically unreactive, and can be synthesized to exhibit excellent mechanical properties, including improved fracture toughness over other monolithic ceramic oxides [75]. It also possesses very low thermal conductivity in its cubic phase. Zirconia changes from a monoclinic to a tetragonal and then to a cubic crystal structure at high temperatures. Upon cooling, residual stresses can cause the material to break apart. Therefore, in order to take advantage of the desirable properties of cubic zirconia, it must be stabilized by the addition of other oxides, such as Magnesium, Yttrium, or Calcium oxide [74], [78], among others. Resultant properties include improved wear resistance and fracture toughness, improved mechanical properties at higher temperatures, and decreased thermal conductivity [64]. The low thermal conductivity of stabilized cubic zirconia allows it to be used as an effective thermal barrier coating in the aerospace industry [79].

Magnesia (Magnesium oxide: MgO) is commonly used as a refractory material due to its stability at high temperatures and its very high melting point (2850°C) [64]. Fine-grained, high-purity MgO can also exhibit excellent mechanical properties at high temperatures. MgO is known to have high thermal conductivity and low electrical conductivity [80].

Additional oxide ceramics include those used primarily in functional applications, such as Titania (Titanium dioxide: TiO_2), Zinc oxide (ZnO), and Yttria (Yttrium oxide, Y_2O_3). TiO_2 is widely used as a dye or pigment due to its high refractive index and as the active ingredient in

sunscreen due to its ability to absorb ultra-violet (UV) light [81]. It is also used in more specialized applications, such as high frequency capacitors and photocatalytic devices [74]. ZnO is a white powder used in similar industrial applications as TiO_2 due to its high refractive index and UV absorbing qualities. It is also used as a main ingredient in skincare ointments [75]. ZnO is used in combination with other ceramic compounds to improve aesthetic appearance, such as a ceramic glaze for decorative items. Its electrical properties, including a wide band gap and high electron mobility, allow its use in semiconductor applications [82].

Y_2O_3 has many applications as well. It is used as a stabilizer for cubic zirconium, resulting in a very hard and durable ceramic material used primarily in dentistry. It is also used as an optical material for solid-state lasers and infra-red (IR) sensors. Its high melting temperature and thermochemical stability enables its use as an oxidation resistant coating in reactive environments [75]. Yttrium is also used to produce Yttrium Aluminum Garnet ($Y_3Al_5O_{12}$: YAG), which is another transparent ceramic used in solid-state laser applications, and its excellent high temperature resistant structural properties are currently being investigated for potential use in the aerospace industry. YAG will be discussed in more detail in the *Garnet Ceramics* section of this literature review.

2.2. Garnet Ceramics

2.2.1. The Garnet Structure

Another sub-group of materials, which falls under oxide ceramics and is of great interest to the present study, is the garnet ceramic group. This is a diverse set of materials with several different forms found in nature, and even more synthetic types fabricated in laboratory environments. They are all linked by their unique chemical structure, but represent a diverse set of attributes and properties. Most notably, garnet ceramics provide some of the highest structural performance and chemical stability at high temperatures [83], [84]. This has increased overall interest of garnet ceramics within the aerospace industry, and has made them prime candidates for advanced material research and development.

Naturally occurring garnets are a unique group of minerals, which are commonly found throughout the earth's crust, and represent the foundation of this class of ceramics. Garnets are typically classified as a sub-group of oxide ceramics, and all naturally occurring garnets are also silicates, with Silicon and Oxygen being primary constituents within their chemical makeup. They are hard crystalline solids, which exist in many forms, but are all similar in terms of physical properties, crystal structure, and chemical composition [85]–[87]. Historically, naturally occurring garnets have been used as gemstones dating back 5000 years to the ancient Egyptians. They were also commonly used as gemstones and jewelry throughout the Roman Empire. High quality garnet specimens are still used as valuable gemstones today [87], [88]. They have also found popularity as a key component in abrasives for industrial applications, such as sand blasting, water jet additives, and sand paper [86], [87].

Garnets are best defined by their chemical composition. Naturally occurring garnets all possess the general formula: $A_3B_2(SiO_4)_3$, with several possible elements filling in the locations

of the *A* and *B* placeholders [86]. They all contain Oxygen, and, therefore, possess the attributes and general chemical stability of other oxides. They are silicate ceramics, with the $[SiO_4]^{4-}$ tetrahedron making up the backbone of the structure, as has been discussed in the previous section [85]. The first position (*A* in the general formula above) is typically filled by divalent cations, Ca, Mg, Fe, or Mn. Trivalent cations occupy the *B* position, such as Al, Fe, or Cr [85], [86]. Among the different types of naturally occurring garnets, varieties with Aluminum in the *B* position within the chemical structure include Almandine ($Fe_3Al_2(SiO_4)_3$), Pyrope ($Mg_3Al_2(SiO_4)_3$), and Spessartine ($Mn_3Al_2(SiO_4)_3$). These are all considered aluminosilicates, are typically dark red in color, and comprise the majority of the natural garnet gemstones. Another common subgroup of garnets has Calcium in the *A* position within the chemical structure and include Andradite ($Ca_3Fe_2(SiO_4)_3$), Grossular ($Ca_3Al_2(SiO_4)_3$), and Uvarovite ($Ca_3Cr_2(SiO_4)_3$). This group is less common than the Aluminum garnets, and represents most of the green garnet gemstones, commonly used as substitutes for the emerald. These naturally occurring garnets have density values between 3.5 g/cm^3 and 4.3 g/cm^3 [85]–[87].

The garnet crystal structure is body-centered cubic, as first determined by Menzer in 1928 [89]. It belongs to the space group Ia3d with varied point symmetry depending on the specific elements present. All garnets possess three axes of symmetry, with 96 Oxygen atoms per unit cell, each bonded to one tetrahedron, one octahedron, and two dodecahedron sites. This crystal structure is visualized in Figure 7, which is reproduced with permission from Smyth and Mccormick [85].

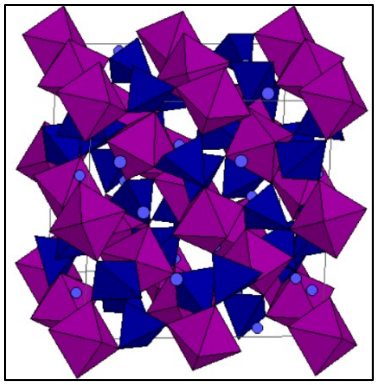

Figure 7: Visualization of the crystal structure of the garnet group from Smyth and Mccormick [85]. Reproduced with permission from American Geophysical Union.

The crystal structure of garnets suggests that this group of ceramics could possess superior structural properties. The highly symmetric cubic structure with a large unit cell and no close packed planes suggests that dislocations must overcome significant crystal lattice friction in order to create plastic deformation [83], [84]. This limited dislocation glide mobility should result in improved mechanical strength and stiffness.

The chemical stability and potentially advantageous structural properties of the garnet group are being exploited through the fabrication of synthetic garnets. Even more elements are being experimented with as valuable constituents within the garnet chemical structure. While the naturally occurring garnets are silicates, synthetic garnets are being created with alternative elements occupying the third position within the chemical structure. Synthetic garnets can be described as conforming to the chemical composition: $A_3B_2(CO_4)_3$, with various elements occupying the *C* site besides Si, including Ge, Ga, Al, V, and Fe [86]. In general there is a wider range of potential elements filling in all three sites within the chemical structure, including rare-earth transition metals with high melting points, yielding desirable high-temperature resistant properties.

Basic physical properties of synthetic garnets are often similar to naturally occurring garnets, including the cubic crystal structure and overall hardness; however, other properties differ and can be tailored to specific needs. Specifically, the high temperature properties of high performing synthetic garnet ceramics tend to be significantly improved, as metals with high melting points are becoming a primary chemical constituent. Some notable synthetic garnets with high temperature properties include Yttrium Iron Garnet (YIG: $Y_3Fe_5O_{12}$), which sees minimal plastic deformation below 1200°C, Gadolinium-Gallium Garnet (GGG: Gd3Ga5O12), which sees minimal plastic deformation below 1450°C, and Yttrium Aluminum Garnet (YAG: $Y_3Al_5O_{12}$), which sees minimal plastic deformation below 1600°C [65]. Another synthetic garnet with interesting high temperature potential is Lutetium Aluminum Garnet (LuAG: $Lu_3Al_5O_{12}$), although there are currently no studies describing its structural deformation behavior.

There are exhaustive lists of combinations of elements used in the fabrication of synthetic garnets found throughout the literature with various physical and structural properties. However, this investigation will focus on two specific synthetic garnet ceramics, which are known or projected to have excellent mechanical and thermal properties beyond their counterparts, and are of particular interest within the aerospace industry: YAG and LuAG.

2.2.2. Yttrium Aluminum Garnet (YAG)

Yttrium Aluminum garnet is a well-known and heavily researched synthetic garnet and oxide ceramic material with several unique properties. As with other oxides, it is stable in oxidizing environments, and it has a high melting temperature of approximately 1950°C, making it desirable for high temperature applications [83]. YAG can be fabricated as a single crystal or a polycrystalline material. YAG single crystals are grown by a typical crystal growth method, such

as the Czochralski method [90], [91] or the float zone method [92]. Polycrystalline YAG can be fabricated by a variety of methods, but most commonly high temperature sintering, hot pressing of YAG powders [28], [93], [94], or from sintering a combination of Yttrium and Alumina powders [95], [96]. The crystal structure of YAG follows the general cubic nature of the garnet group with three different Oxygen-centered polyhedra. The dodecahedral sites are occupied by Y^{3+} ions, while the octahedral and tetrahedral sites are occupied by Al^{3+} ions. The structure is defined by the various radii of the ionic bonds [90]. The unit cell contains eight molecular units, and is visualized in Figure 8, reproduced with permission from Kostic et al. [90].

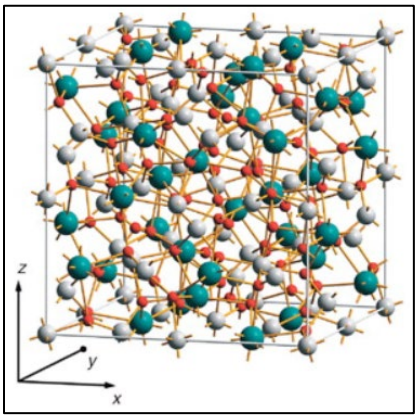

Figure 8: The visual representation of the unit cell of YAG. Green spheres represent Y atoms, white spheres represent Al atoms, and red spheres represent O atoms from Kostic et al. [90]. Reproduced with permission from Elsevier.

YAG can be carefully fabricated to maximize density and minimize porosity, resulting in a highly transparent ceramic with desirable optical properties. YAG specifically has been shown to possess homogenous and isotropic optical properties [97]. These attributes along with its chemical and thermal stability make it one of the most common oxide crystals used as the active medium in solid-state lasers. With proper doping of various elements, such as Neodymium, Erbium, or Cerium, the optical properties of YAG allow its use as a host material for lasers, as a

semiconductor light source, and in cathode ray tubes [90], [97], [98]. Optical properties of YAG include high transmittance for wavelengths between 400 nm to 1100 nm, based on various doping schemes. It has a high thermal conductivity and a high fluorescent lifetime. It has also been shown to have a refractive index of approximately 1.82 for the wavelength range from 800 nm to 1500 nm [99].

In addition to these optical uses, there are potential applications of YAG that take advantage of its mechanical and thermal properties as well. Previous studies of YAG have demonstrated that its mechanical properties and stability at high temperatures make it a perfect candidate for ceramic structural components and reinforcements in ceramic matrix composites within advanced aerospace applications [83], [100]. Early research on YAG and similar synthetic garnets has suggested that garnet materials will show minimal deformation at temperatures very near their melting points [84], [100]. This concept has driven research on YAG forward, and it continues today. General properties of YAG are shown in Table 5, acquired from a variety of sources.

Table 5: Important physical and structural properties of YAG [83], [94], [101], [102].

Chemical Formula	$Y_3Al_5O_{12}$
Hardness	8.0 – 8.5
Melting Point	1950°C
Density	4.55 g/cm^3
Thermal Conductivity*	0.14 W/cm^3·K
Coefficient of Thermal Expansion*	6.9 x10^{-6} – 8.7x10^{-6} °C^{-1}
Refractive Index*	1.823
Dielectric Constant	$\varepsilon_0 = 11.7 \quad \varepsilon_\infty = 3.65$
Flexural Strength	600 – 700 MPa (up to 1200°C)
Young's Modulus (single crystal)	279.9 GPa
Young's Modulus (polycrystalline)**	283.6 GPa
Poisson's Ratio (single crystal)	0.230
Poisson's Ratio (polycrystalline)**	0.226
Fracture Toughness (single crystal)	1.48 – 2.2 MPa·m$^{1/2}$
Fracture Toughness (polycrystalline)**	1.5 – 1.61 MPa·m$^{1/2}$

**Measurements taken from Neodymium doped YAG specimens (concentration: 0.725% Nd^{3+})*
***Polycrystalline YAG with grain size between 1.0 – 1.5 μm*

Polycrystalline and single-crystal YAG have been shown to possess excellent mechanical properties even at high temperatures. Hoshiteru et al. conducted flexural tests on polycrystalline YAG, and determined that the flexural strength of 600-700 MPa was maintained to approximately 1200°C [94]. Keller et al. demonstrated that the strength of YAG can be maintained up to 1400°C [93]. The high flexural strengths (approximately 2 GPa) of alumina-YAG eutectic rods were shown to retain most of their strength up to 1650°C by Pastor et al. in 2005 [92]. The fracture toughness of single-crystal YAG was studied by Mah and Parthasarathy in 1997 [103], which revealed that the fracture toughness measurements significantly increased from room temperature up to 1600°C from 2.2 $MPa \cdot m^{1/2}$ to 4.5 $MPa \cdot m^{1/2}$ in air and to 5.5 $MPa \cdot m^{1/2}$ in a vacuum.

Among the measured properties of YAG, the most notable and heavily researched characteristic is its creep resistance. Creep experiments have been carried out on various YAG specimens over the past 30 years, both single-crystal and polycrystalline, and they have revealed that YAG is among the most creep resistant oxide materials currently studied [25], [104]–[107]. This resistance to plastic deformation at temperatures close to its melting point make YAG a strong candidate for structural components in aerospace vehicles. A more detailed history of creep testing on single-crystal and polycrystalline YAG is given in the next section of this literature review, when discussing creep of oxide ceramics.

2.2.3. Lutetium Aluminum Garnet (LuAG)

Another interesting synthetic oxide ceramic of the garnet structure, also containing a rare-earth metal constituent, is Lutetium Aluminum Garnet (LuAG: $Lu_3Al_5O_{12}$). LuAG has a much shorter and more recent history than YAG, and much of its capabilities and usefulness in

potential applications still remains to be researched. In many ways LuAG is similar to YAG, including its crystal structure and its comparable thermal properties [108], but there are some key differences, which generate serious intrigue and potential value associated with current and future research and development efforts.

LuAG is harder, denser, and potentially more chemically stable than YAG. Additionally, it has a higher melting point, which has generated increased interest in LuAG for various high temperature applications [109]. The melting point of LuAG is typically measured between 1980°C and 2050°C, which is about 100° above that of YAG. Also, its density has been measured at approximately 6.71 g/cm^3, which is significantly higher than YAG at 4.53 g/cm^3 [108], [109]. Several properties of LuAG have been tabulated in Table 6 and presented alongside the properties of YAG. These physical, thermal, and optical properties were measured for single-crystal specimens of LuAG and YAG, published by Kuwano et al. in 2004 [108].

Table 6: Physical, thermal, and optical properties of LuAG and YAG [108].

Property*	**LuAG**	**YAG**
Melting Point (°C)	2010	1930
Density (g/cm^3)	6.71	4.53
Lattice Parameter (Å)	11.9164	12.0075
Refractive Index**	1.811 - 1.869	1.801 - 1.859
Thermal Conductivity (W/m·K)	9.6	12.9
Heat Capacity (J/g·K)	0.411	0.603
Thermal Diffusivity (cm^2/s)	0.0347	0.0473
Coefficient of Thermal Expansion (K^{-1})	6.13 x 10^{-6}	

*Measurements taken for single crystals grown using the Czochralski method.
**Refractive indices corresponding to wavelengths between 410 nm and 1970 nm.

The crystal structure of LuAG is similar to YAG and other garnet ceramics. It has a complex cubic crystal structure, with a unit cell composed of 8 formula units. One unit cell projected onto the [100] plane is shown in Figure 9. Each unit cell contains 24 Lutetium atoms, represented by the black spheres in the dodecahedral positions, and 40 Aluminum atoms, represented by the

yellow and blue spheres filling in the octahedral and tetrahedral positions, respectively. 96 Oxygen atoms are represented by the small red spheres [108]–[111].

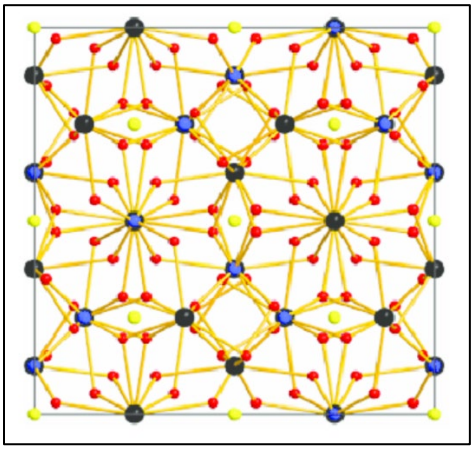

Figure 9: The crystal structure of LuAG represented as one unit cell projected onto the [100] plane, reproduced with permission from John Wiley and Sons [112].

The atomic mass of Lutetium is much greater than that of Yttrium, which is much closer to many of the desirable dopant atoms for laser material applications. This attribute combined with similarities in atomic radii allow the addition of various dopant atoms to the LuAG chemical structure, such as Yb, Tm, Er, Ho, and Ce without significantly altering necessary properties, such as the thermal conductivity and the crystal structure parameters [113]. This has made LuAG more desirable in certain laser material applications over YAG. Its high density, high thermal conductivity even after doping, and high atomic number make LuAG a desirable scintillating crystal. Also with proper doping it becomes an excellent and efficient host material for solid state lasers [111], [113]. LuAG can be grown or fabricated as a colorless, transparent ceramic, but can also be made luminescent in various colors by excitation and proper doping [114].

LuAG single crystals can be grown by the typical crystal growth methods, most commonly the Czochralski method [108], [110]. Polycrystalline LuAG specimens of varied grain size have been fabricated by various high temperature sintering methods, typically requiring high purity

Lu_2O_3 and α-Al_2O_3 powders. Previous studies have successfully produced transparent polycrystalline LuAG specimens by means of pressureless sintering techniques [115], [116], and by means of reactive sintering in a vacuum, followed by hot isostatic pressing [117]–[119]. However, these methods have typically resulted in highly porous samples with large grain sizes, likely leading to poor mechanical properties. A preferred processing method requiring lower temperatures and shorter times is spark plasma sintering (SPS). Experiments by An et al. have shown that finer grains and more optimal physical properties of LuAG specimens can be obtained through SPS [110]. Additionally, Xu et al. have demonstrated benefits of SPS for superior luminescent properties of LuAG for high-power laser lighting [120].

All processing methods, which are used to obtain LuAG specimens, have a high degree of difficulty due to the high temperatures typically required on account of its high melting point. Additionally, quantities of high purity Lu_2O_3 powder are limited and can be very expensive. These limitations have resulted in minimal investigations into the potential applications and advantages of LuAG. Specifically, little work has been done to investigate the benefits of LuAG as a structural ceramic for high temperature applications.

The optical properties of LuAG are well known and have been studied by many authors due to original interest in using transparent LuAG ceramics in solid-state lasers and as a highly efficient scintillator material. Along with the high melting point of LuAG, it has a highly desirable refractive index over a variety of wavelengths, reaching 1.869 (see Table 6). Based on the refractive index, a theoretical maximum optical transmittance has been calculated for LuAG at approximately 83.33% [119]. This value is rarely attained due to processing limitations and imperfect specimens; however, transmittance values have been measured by Kuntz et al. reaching 73% at 550 nm [114] and by An et al. reaching 77.8% at 2000 nm [110]. The highest

in-line transmittance of Yb-doped LuAG was reported to have reached 83% by Ma et al. after fabrication by vacuum sintering [112]. These optical properties along with its high density, atomic number, and thermal stability, make LuAG a valuable scintillator crystal for positron emission tomography (PET), imaging screens, and additional applications in energy, nuclear, and medical fields.

In terms of mechanical performance, little is known about LuAG. Several authors have reported its hardness in order to prove the effectiveness of various processing methods. An et al. reported Vickers hardness numbers for polycrystalline LuAG ranging from 14.2 GPa to 17.2 GPa [110], although the hardness is typically reported on the MOHS scale from 7.5 to 8.4 [111], [121]. Fracture toughness has been reported by Auffray et al. to be 1.1 $MPa \cdot m^{½}$ [121] and by An et al. ranging from 1.2 to 1.6 $MPa \cdot m^{½}$ [110]. Beyond these cases, mechanical properties of LuAG are rarely found in the literature and are not typically the focus of many scientific investigations.

As was discussed earlier in this chapter, the structural properties of YAG, specifically its resistance to creep at high temperatures, have proven to be very impressive, making YAG a very desirably candidate material for use in aerospace components, required to operate at high temperatures for long periods of time. Due to the similarities of LuAG and YAG, there is increased interest in the potential benefits of LuAG for similar applications. This investigation aims to begin an in-depth analysis into the mechanical properties of LuAG by first determining the time-dependent deformation of LuAG at high temperatures, and to determine if LuAG could be superior to the high creep resistance of YAG.

2.3. Creep of Ceramics

2.3.1. An Overview

The experimentation in this study will focus on the creep of oxide ceramic materials subject to constant a load and exposed to high temperatures, simulating the harsh operating conditions seen by aerospace structures. In order to thoroughly review previous creep tests conducted on oxide ceramics and to understand the results and analyses of the experiments in the present study, a thorough review of creep and its mechanisms is provided in the following sections.

Creep is usually defined as the continuous inelastic deformation of a material under constant load [38], [122], [123]. Furthermore, the constant load is usually far below the ultimate strength of the material, and the deformation and eventual failure is brought on by the effects of high temperature or some other destructive environmental factors over time [123]. Therefore, the potential creep properties of a material must be investigated when designing structural components for aerospace systems, which are typically forced to continually operate in extreme environmental conditions.

Several authors attribute the first scientific study of creep to Percy Phillips in 1905, who investigated the slow elongation of certain materials, such as rubber, glass, and metal wires, subject to a constant load [124]. A more in-depth study into the creep behavior of metals came shortly after this with the classic work of Andrade in 1910 [125]. Continuous work throughout the 20^{th} century has resulted in a vast library of creep data for many material systems, primarily metals. The first documented creep studies of modern engineering ceramics came in the 1950s with creep studies of single-crystal and polycrystalline alumina by Wachtman and Maxwell [126], Stavrolakis and Norton [127], and Kingery and Coble [128]. Cannon and Langdon report that the slow development of creep studies of ceramic materials is due to the little interest in

ceramics during these early years of creep investigations. Only in recent years has ceramic processing improved enough to fabricate reliable materials with significant structural potential [129].

Creep is a time-dependent material behavior, and thus is analyzed and interpreted much differently than an instantaneous material property, such as ultimate strength or elastic modulus. The primary goal or key material property when looking at the creep behavior of a material is the creep strain rate and the associated total plastic strain. These material performance metrics are based on a variety of factors, such as the basic material properties, including microstructural considerations, the applied stress, temperature, and potential oxidation or corrosion, among other things [130].

A typical creep curve is shown in Figure 10, which depicts the creep strain of a representative material plotted versus time [30].

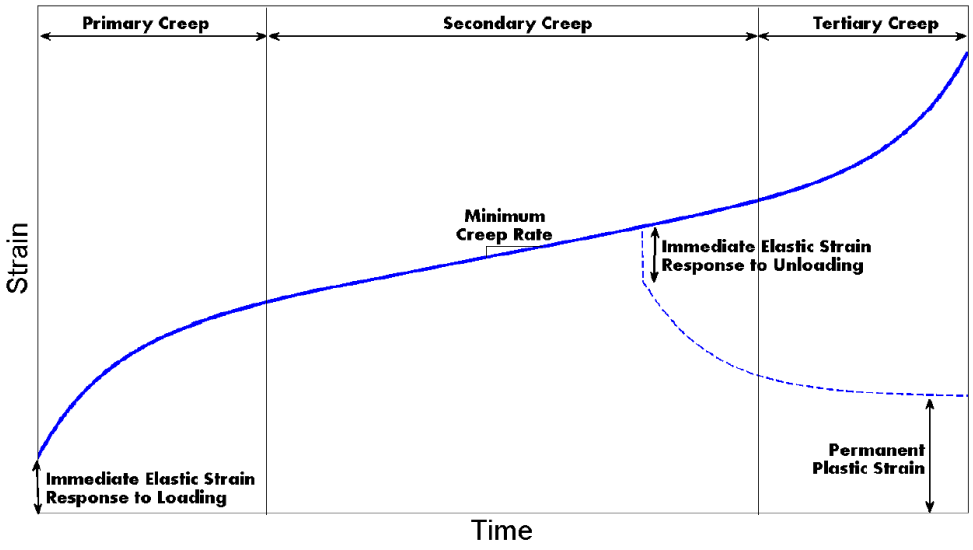

Figure 10: Typical creep curve showing the creep strain plotted vs. time from DeGregoria [30]. Reproduced with permission from the Air Force Institute of Technology.

Figure 10 demonstrates the three creep regimes, which are typically observed for many materials: primary, secondary, and tertiary creep. Primary creep begins with an immediate elastic strain response to initial loading. Then the strain rate decreases as the material response to loading transitions from nearly instantaneous elastic strain to inelastic strain. Primary creep is often a result of grain growth, dislocation motion, or changes in the stress distribution during initial loading [130]. In secondary creep, also known as steady-state creep, the strain rate is nearly constant and represents the minimum strain rate observed during the creep process. Finally, in tertiary creep, the strain rate appears to rapidly increase, often due to the formation of cracks and voids, ending in ultimate failure, also known as creep rupture [130]. The apparent increase in strain rate during tertiary creep can often be misleading, as typical creep experiments observe elongation under constant load, and do not take into account the true stress applied to the specimen or the potential change in cross-sectional area [125].

The resulting creep curve can vary significantly depending on the material and the test conditions, and one or two of the creep regimes are sometimes not observed all together. During tensile creep tests failure can occur rapidly during secondary creep, avoiding tertiary creep entirely [131]. Similarly, primary creep can exist alone given the right conditions [130], and it has also been observed to transition directly into tertiary creep skipping the steady-state regime [123]. Additionally, the primary regime can be observed to be minimal and insignificant, and steady-state creep is observed almost immediately after beginning the test [132]. Typically, the focus of experimental analysis of ceramic materials is on the steady-state creep rate, which will typically appear nearly constant, given enough time, and is predicted by most of the high-temperature ceramic creep models [38], [132].

The general equation for steady-state creep, summarized by Cannon and Langdon [129], which fits most experimental data, is given below:

$$\dot{\varepsilon} = \frac{ADGb}{kT}\left(\frac{b}{d}\right)^m \left(\frac{\sigma}{G}\right)^n \quad \text{(Equ. 4)}$$

This equation defines the creep strain rate as a function of applied normal stress, σ, absolute temperature, T, and grain size, d. Additionally, D is the diffusion coefficient, defined further in Equation 5, G is the shear modulus, b is the magnitude of the Burger's vector, k is Boltzmann's constant, A is a dimensionless constant, which takes into account various constants related to the active creep mechanism, m is the exponent associated with the inverse grain size, and n is the stress exponent. The specific creep mechanisms can typically be identified by determining the constant, A, the exponents, m and n, and by the true activation energy, Q. Although the experimental values of the constant, A, depend on the exponents and the activation energy, and therefore, A is not as important when determining the active creep mechanisms causing deformation [129].

The standard definition of the diffusion coefficient is given by:

$$D = D_0 e^{-\frac{Q}{RT}} \quad \text{(Equ. 5)}$$

where D_0 is a frequency factor, Q is the activation energy associated with diffusion, and R is the gas constant [2], [129]. The diffusion coefficient quantifies the diffusivity of the relevant species through the crystal lattice or through a grain boundary, depending on the specific creep mechanism [30].

According to Cannon and Langdon [129] and Hynes and Doremus [132], the activation energy, Q, can be determined from the slope of a plot of log $\dot{\varepsilon}$ vs. 1/T. To obtain this plot, the creep rate is experimentally determined from several samples with similar grain size and applied stress, but at different temperatures. Unfortunately, this result is only an apparent activation

energy, as the true value must take into account the term, $(1/kT)$, and it also must account for variation in shear modulus with temperature. However, this method of estimation is still used when the stress exponent, *n*, is approximately equal to 1, when the variation in shear modulus is small [132]. Additionally, the true activation energy can be determined from a plot of log $\dot{\varepsilon}G^{n-1}T$ vs. $1/T$. When *n* is large, the true activation energy ends up significantly lower than the apparent activation energy [129].

The shear modulus, *G*, can be estimated for a given temperature based on the following equation:

$$G = G_0 - (\Delta G)T \qquad \text{(Equ. 6)}$$

where ΔG is the variation in shear modulus per degree Kelvin and G_0 represents the estimated shear modulus corresponding to absolute zero temperature, which must be linearly extrapolated from known data at high temperatures [133]. Porosity should also be taken into consideration when determining the actual shear modulus. Although a material is often assumed to be perfectly dense in order to develop creep models, it is also known that the steady state creep rate will increase with increasing porosity, and it will have an effect on several parameters in Equation 4 [134]. Specifically, the shear modulus can be adjusted by the following equation:

$$G = G_0\left[\frac{1+(\beta P)}{1-(\beta+1)P}\right] \qquad \text{(Equ. 7)}$$

where G_0 is the previously described shear modulus value assuming a fully dense body, *P* is the porosity volume fraction, and β is a constant [134], [135]. The applied true stress is also affected by porosity, and can be estimated by Equation 8, known as the McClelland Approximation [134], [136].

$$\sigma_{eff} = \frac{\sigma_{applied}}{1-P^{2/3}} \qquad \text{(Equ. 8)}$$

The final term affected by the presence of porosity is the dimensionless constant, A, if pores affect the movement of dislocations or dislocation sliding [134]. However, this relationship is very complex, and often not worth pursuing. Therefore, A is assumed to be independent of porosity, and only G and σ are modified. Considering these changes to the overall creep equation, a plot has been developed by Langdon [134] to demonstrate the effect of porosity on creep rate. Figure 11 shows creep rate vs. porosity for $n \approx 1$ to 5, up to 10% porosity. The plot shows the drastic increase in creep rate vs. porosity.

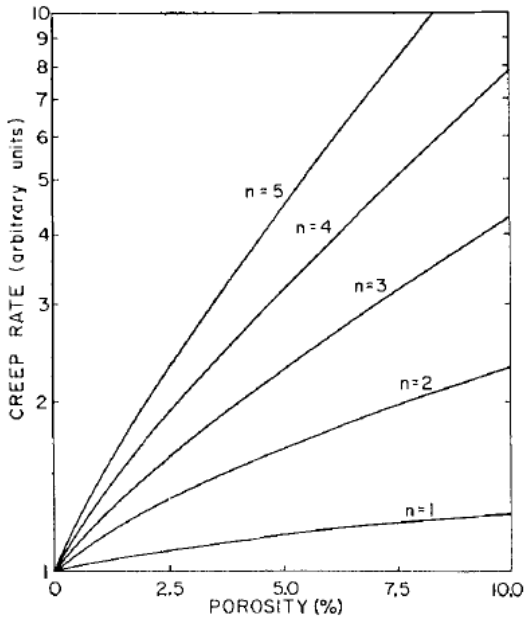

Figure 11: Dependence of creep rate on porosity for $n \approx 1$ to 5, up to 10% porosity from Langdon [134]. Reproduced with permission from John Wiley and Sons.

When modeling steady-state creep, most authors focus on the two exponent terms in Equation 4, the grain size exponent, m, and the stress exponent, n, in order to fit the model to experimental data. Values for m and n are, therefore, used to identify creep mechanisms. A brief summary of possible creep mechanisms is provided here before the more detailed discussion in the next section. Hynes and Doremus summarize 8 primary creep mechanisms, which are elastic

strain, diffusion, dislocation motion, grain boundary sliding, viscous flow, solution-precipitation, twinning, and cracking/cavitation [132]. In creep of high temperature ceramics diffusion, dislocation motion, and grain boundary sliding are considered the most relevant and are discussed in detail here. Additionally, a given creep mechanism could act independently or could act in combination with another. When two or more creep mechanisms occur together, they have been observed to act either in parallel (simultaneously) or sequentially. These possibilities are important to identify as they affect which mechanism is the primary rate-controlling process. If mechanisms occur independently, then the fastest creep rate dominates. Similarly, when two creep mechanisms occur simultaneously, the two creep rates are added together, and the mechanism with the fastest creep rate is of primary concern. However, when two mechanisms occur sequentially, one mechanism can be dependent on the other. Therefore, the mechanism with the slower creep rate is the rate-controlling process [132].

A summary of the various creep mechanisms associated with different values of the grain size exponent, *m*, and the stress exponent, *n* was published by Cannon and Langdon in 1983 [129] and was reproduced by Chokshi and Langdon in 1991 [137]. Their summary divides the primary creep mechanisms into two categories: lattice mechanisms and boundary mechanisms. Lattice mechanisms include intragranular motion of dislocations and requires a value of $m = 0$ in Equation 4. Boundary mechanisms include motion along grain boundaries, resulting in displaced grains with respect to one another, which requires a value of $m \geq 1$ in Equation 7. Frost and Ashby [138] produced an illustration of the difference between lattice and boundary diffusion, shown in Figure 12.

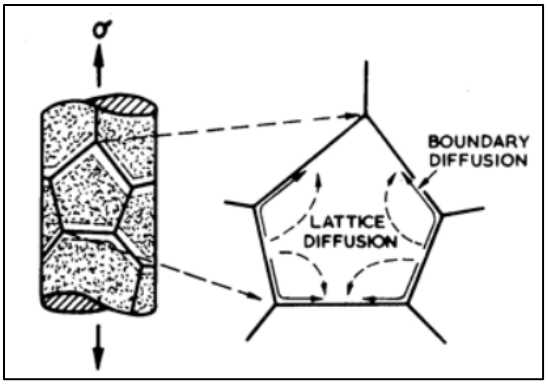

Figure 12: Illustration of boundary diffusion and lattice diffusion from Frost and Ashby [138]. Reproduced with permission from Elsevier Books Limited.

Table 7 summarizes the creep mechanisms associated with lattice motion and Table 8 summarizes the creep mechanisms associated with grain boundary motion. Both of these tables have been populated based on the information presented by Cannon and Langdon [129] and Chokshi and Langdon [137].

Table 7: Primary mechanisms for ceramic creep associated with lattice motion [137].

Creep Mechanism	*n*	*m*
Dislocation glide and climb controlled by climb	4-5	0
Dislocation glide and climb controlled by glide	3	0
Dislocation climb from Bardeen-Herring sources		
Controlled by lattice diffusion	3	0
Controlled by pipe diffusion	5	0
Harper-Dorn creep	1	0

Table 8: Primary mechanisms for ceramic creep associated with boundary motion [137].

Creep Mechanism	*n*	*m*
Lifshitz sliding		
Sliding accommodated by diffusion		
Nabarro-Herring creep	1	2
Coble creep	1	3
Sliding accommodated by flow across grains	1	1
Rachinger sliding		
Without glassy phase		
Sliding accommodated by formation of boundary cavities	2	1
Sliding accommodated by triple point fold formation	3-5	2
With glassy phase	1	1
	1	2
	1	3
Interface reaction control		
Without glassy phase	>1	1
	>1	1
	2	1
	2	2
By solute drag	2	1
With glassy phase	1	1

2.3.2. Creep Mechanisms

In this section the various creep mechanisms listed in Table 7 and Table 8 are described in detail. Although many creep mechanisms have been identified and studied throughout the past century, there are three primary mechanisms, which are the most dominant in ceramic materials. These three mechanisms are diffusion, dislocation motion, and grain boundary sliding.

Diffusion Creep

A primary mechanism of creep in many materials including ceramics is diffusion. Diffusion can be defined as the mass flow process in which atoms change their positions relative to their neighbors, usually associated with a temperature or stress gradient [139], or more simply, the phenomenon of material transport by atomic motion [2]. Diffusion can be thought of as the

movement of atoms in a material, or conversely, as the movement of vacancies, which remain when atoms move away. Atoms are able to move throughout a solid material because they are never really stationary. They will constantly execute rapid, small-amplitude vibrations about an equilibrium position. These vibrations will increase with increasing temperature, and at a given temperature atoms may have sufficient amplitude to move from one atomic position to an adjacent one [139]. Other factors can help initiate diffusion in a solid material as well, such as the presence of vacancies. The extent to which vacancy diffusion will occur is a function of the concentration of these defects [2]. Furthermore, the rate at which atoms will diffuse through a material is quantified by the diffusion coefficient, D, which was defined previously in Equation 5, and it also appears in the steady-state creep equation, shown in Equation 4.

The movement of vacancies has also been linked to the applied stress on a solid material. Nabarro in 1948 first demonstrated that a material under pure shear stress would cause the movement of vacancies [140]. In a state of pure shear stress a material can be in tension in one direction and in compression in the other two orthogonal directions. In this scenario Nabarro showed that vacancies will flow through the material from the face in tension to the faces in compression. In other words, atoms will be pushed away by compression causing plastic deformation in the direction of the compressive stress and will move into space enabled by the tensile stress, causing elongation [140]. This phenomenon is visualized in Figure 13 [141].

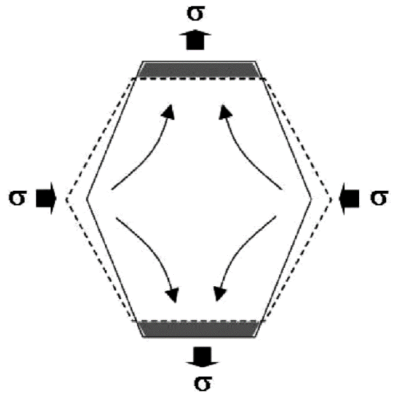

Figure 13: Stress induced diffusion causing plastic deformation from Na and Lee [141]. Reproduced with permission from the Korean Institute of Metals and Materials.

This phenomenon was investigated further by Herring in 1950. He demonstrated that matter transport will occur by means of diffusion through the grains in a polycrystalline material [142]. This type of diffusion creep through the grains has been termed Nabarro-Herring (N-H) creep due to the early work, which demonstrated the concept. N-H creep can be a significant source of creep in ceramics.

As is shown in Table 8, the stress exponent from Equation 4 for N-H creep is $n = 1$, which shows that the strain rate is directly proportional to the applied stress and the inverse of the shear modulus. The grain size exponent from Equation 4 for N-H creep is $m = 2$. Therefore, the strain rate is proportional to the inverse of the square of the grain size, which means that the strain rate will significantly increase as grain size decreases.

Diffusion creep can also occur by the movement of vacancies along the grain boundaries. This phenomenon was first introduced by Coble in 1963. He concluded that diffusion along the grain boundaries is associated with a smaller activation energy when compared to lattice diffusion [143]. Similar to N-H creep, the stress exponent from Equation 4 for Coble creep is $n = 1$. However, the grain size exponent from Equation 4 for Coble creep is $m = 3$. In this case

the strain rate will be dependent on the inverse of the grain size cubed; therefore, Coble creep is the dominant creep mechanism when grain sizes are small [38]. Similarly, at low temperatures Coble creep is typically the primary creep mechanism due to the lower activation energy required for intergranular diffusion [144].

Multiple creep mechanisms often occur simultaneously. Diffusion creep mechanisms are no exception. It is common for N-H and Coble creep to occur in parallel, which means the associated strain rates would be additive. Also, N-H creep and Coble creep are considered diffusional creep mechanisms that help enable grain boundary sliding, which is why diffusion creep mechanisms are categorized as a subset of boundary mechanisms in Table 8. Once diffusion causes individual grain elongation, sliding at the grain boundaries is a necessary result. Therefore, these two creep mechanisms will occur together [133], [144], [145].

Additionally, both N-H and Coble creep assume that grain boundaries are prefect sources and sinks for vacancies and use this classical theory to explain experimental results [137]. However, small diffusion sources and sinks may be controlled by reactions at the grain boundary interfaces. Therefore, for small grains and low stresses, the creep rate may actually be smaller than those predicted by N-H and Coble creep models, as noted by Ashby et al. [138], [146], [147]. The primary creep mechanism in this case is likely to fall under interface-reaction controlled creep with a stress exponent of $n > 1$ and a grain size exponent of $m < 3$ [137].

Grain Boundary Sliding

Grain boundary sliding (GBS) is a creep mechanism that can occur in polycrystalline materials when grains move or “slide” in relation to one another. This motion can include rotation, elongation, or any adjacent movement along a grain boundary [133]. GBS falls into the

category of boundary creep mechanisms, as the definition implies that creep deformation occurs along the grain boundaries, and the various types of grain boundary sliding are listed in Table 8. GBS is often the dominant strain mechanism in many materials, but it typically does not occur alone. In ceramics GBS is usually accommodated by another simultaneous mechanism, primarily diffusion, and in this case, the creep mechanism can be referred to as GBS accommodated by diffusion or diffusion accommodated by GBS [137], [145].

When studying creep, the majority of deformation in a ceramic material is plastic deformation prior to failure. However, the total strain is a combination of both plastic and elastic strain [123]. Grain boundary sliding can be a primary mechanism for both types of strain. Hynes and Doremus point out that elastic strain can occur due to grain boundary sliding, typically at low stresses and low temperatures. If the applied external stress is perfectly matched by internal grain boundary stresses that develop then sliding will stop entirely. However, when the boundary stresses are exceeded by the external applied stresses, then grain boundary sliding will continue [148].

Various phenomena can cause grain boundary sliding to occur in a material. It can simply occur when the bonds at the grain boundaries are weaker than those within the crystal lattice within grains. Also stress concentrations can arise directly at the grain boundaries, which can initiate motion, causing grain boundary sliding [30]. Grain boundaries can have different compositions, such as a glassy phase in some materials, which could soften at high temperatures. If a glassy phase exists, viscous flow could occur at the grain boundaries at high temperatures. This is common in ceramics when sintering aids are added to assist in the densification process and inadvertently add a glassy phase at the grain boundaries [29]. The temperature required to initiate flow of a glassy phase is often lower than temperatures required to initiate other creep

mechanisms within the grains, such as diffusion. Therefore, grain boundary sliding is commonly the first mechanism to initiate creep deformation in a material.

When a glassy phase exists at the grain boundaries, the resulting creep rate is controlled by the viscosity. Grain boundary sliding can occur by flow of a glassy phase in a variety of different ways. Shear stresses can cause the viscous fluid to be redistributed and to flow from boundaries in compression to those in tension, similarly to atomic movement during diffusion [149]. Alternatively, high stresses could force grains to dissolve into the liquid at the boundary, move throughout the material, and precipitate once a region of lower stress is reached. It is also possible for dislocations to pile up at the glassy boundaries and then be annihilated by a similar amount of vacancies left behind from the dislocation motion [150]. These several types of grain boundary sliding accommodated by a glassy phase are shown in Table 8. In each case the strain rate is directly proportional to the stress with a stress exponent of $n = 1$. However, the specific type of grain boundary sliding can see a grain size exponent anywhere from $m = 1$ to 3.

The main types of grain boundary sliding are Lifshitz sliding and Rachinger sliding. Lifshitz sliding refers to the elongation of grains along the longitudinal tensile axis and requires simultaneous vacancy diffusion [151]. Diffusion across grains (N-H creep) or diffusion along the grain boundaries (Coble creep) can accommodate Lifshitz sliding. In addition to diffusion Lifshitz sliding may be accommodated by additional mechanisms, such as intragranular flow across grains due to a glassy boundary phase.

Rachinger sliding occurs when grains maintain their size and shape but move relative to one another, exchanging neighboring locations. Rachinger sliding can be accommodated with or without a glassy phase at the grain boundary [152]. Without a glassy phase sliding is accommodated by the nucleation and growth of cavities at the grain boundary, producing a stress

exponent of $n = 2$ [153]. The larger stress exponent means that cavity nucleation and growth rates are more sensitive to increasing applied stress. Therefore, grain boundary sliding by means of cavity formation is usually associated with higher applied stresses [154]. Similarly, without a glassy phase, sliding may occur due to the formation of a triple point fold, increasing the stress exponent even further from $n = 3$ to 5 [155]. Rachinger sliding can also occur along with diffusion or viscous flow at the boundaries due to a glassy phase, producing a stress exponent of $n = 1$, and a range of grain size exponents of $m = 1$ to 3.

Several boundary mechanisms are not included in Table 8 because they are newly investigated and require more thorough study to create reliable models. These mechanisms include viscous or diffusive growth of intergranular cavities, the solution-precipitation process at the glassy boundary (discussed previously), elastic creep due to cavity formation, and crack growth [129]. Superplasticity is another phenomenon attributed largely to grain boundary sliding. In general, superplasticity occurs when a crystalline solid material plastically deforms beyond its typical point of fracture, often well beyond 100% in ceramics [156]–[158]. Superplasticity has been observed in several ceramic materials, such as Zirconia, Silicon nitride, and Silicon carbide, and is facilitated by very small grain sizes, high temperatures, and very slow strain rates [156]. In order for superplasticity to occur in ceramics, the applied stress must be low enough that grain boundary sliding occurs alone, and additional creep mechanisms are not able to take over, such as dislocation motion or the formation of cavities.

Dislocation Motion

Dislocation motion occurs due to the movement of dislocations, or line defects, in a crystal lattice, which causes plastic deformation. Dislocations are linear crystallographic defects

within a crystalline material, which can move, allowing atoms to shift positions, and ultimately causing plastic deformation to occur [159]. Dislocation motion is considered a lattice mechanism for creep, and is therefore listed in Table 7. Because dislocation motion does not involve the grain boundaries, the grain size exponent, *m*, is zero for all types of dislocation motion. The two main types of dislocations are edge dislocations and screw dislocations, which are illustrated in Figure 14.

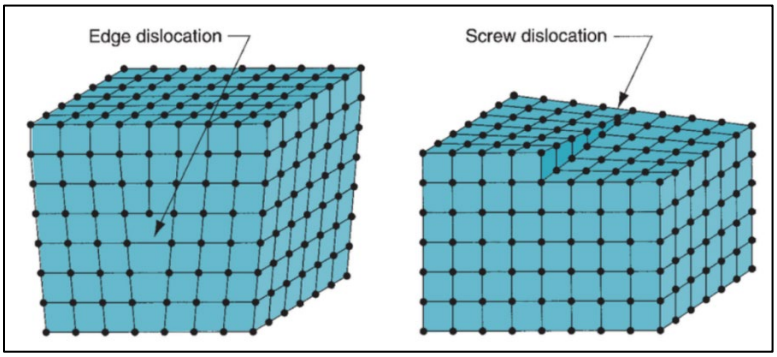

Figure 14: Illustration of edge dislocations (left) and screw dislocations (right), reproduced with permission from Molla [160].

Edge dislocations move parallel to an applied shear stress. The linear vacancy shown on the left side of Figure 14 would move left or right, until it reaches the edge of the material. Screw dislocations move perpendicular to an applied shear stress, as shown by the vertical motion on the right side of Figure 14. The distance and direction of the movement of individual atoms due to dislocation motion are quantified by the Burger's vector, seen in Equation 4. In metals the presence of dislocations dictate many important material properties, such as yield strength, ductility, and hardness, among others [159].

The two primary modes of dislocation motion are dislocation glide and climb [133]. Dislocation glide describes the movement of a dislocation within the slip plane, in the direction of the Burger's vector. Dislocation climb describes the movement of a dislocation out of its slip

plane to another adjacent plane. The crystalline order can be restored on either side of a dislocation; however, the atoms on one side have moved by one lattice position [159]. Plastic deformation of a material will only occur by the creation and movement of many dislocations, and it is possible for dislocation glide and climb to occur simultaneously. However, only one type of dislocation motion is described as the controlling mechanism.

The simultaneous glide and climb of intragranular dislocations, where the rate-controlling mechanism is *climb*, is typically associated with a stress exponent of $n = 5$. In the same slip plane dislocations can pile up, leading to plastic deformation, based on the following strain rate, proposed by Weertman in 1957 [161] and reviewed and summarized by Cannon and Langdon [133]:

$$\dot{\varepsilon} = \frac{B_2 \Omega D_1 \sigma^{4.5}}{G^{3.5} M^{0.5} b^{3.5} kT} \qquad \text{(Equ. 9)}$$

where M is the concentration of active dislocations sources, B_2 is a constant, which describes the piled-up arrays of dislocations, and Ω is the atomic volume. D_1 is the lattice diffusivity, which assumes that the diffusion associated with dislocation climb occurs exclusively through the crystal lattice [133]. This assumption is true at temperatures higher than half the melting temperature (>0.5T_m); however, at low temperatures, this assumption is no longer accurate.

Dislocation glide and climb, where the rate-controlling mechanism is *glide*, is typically associated with a stress exponent of $n = 3$. An example of this behavior is in metallic solid-solution alloys. Models for the steady-state creep rate for this behavior have been developed; however, they are not presented here, as most ceramics contain no solute. In some cases it is more likely that drag is controlled by impurity ion diffusion; however, these models and the associated diffusion coefficients are not fully understood [133].

A second example of steady-state creep associated with a stress exponent of $n = 3$ is dislocation motion controlled by *climb* from Bardeen-Herring Sources. In this case the creep rate is given by:

$$\dot{\varepsilon} = \frac{B_3 \pi \Omega D_1 \sigma^3}{G^2 b^2 kT} \quad \text{(Equ. 10)}$$

where B_3 is a constant with an estimated value of approximately 0.1, according to Weertman [162]. Sources for this type of dislocation multiplication, proposed by Bardeen and Herring, are edge components, which climb due to a concentration of defects out of equilibrium. The formed edge dislocations either absorb or create more point defects to re-establish equilibrium [163].

Harper-Dorn creep is an additional lattice mechanism associated with dislocation motion, which does not follow these other mechanisms with $n = 3$ to 5. First investigated and identified by Harper and Dorn in 1957 [164], this mechanism has primarily been observed in metals, but small amounts of data have been published referencing Harper-Dorn creep in single-crystal $KZnF_3$, NaCl, and CaO, and is assumed to occur in other ceramic systems as well [133]. Harper-Dorn creep is linked primarily to the climb of edge dislocations when the material is saturated with vacancies [165]. Based on the published experimental data, which cite Harper-Dorn creep, the creep rate can be described by the following model equation:

$$\dot{\varepsilon} = B_{HD} \frac{D_1 G b}{kT} \left(\frac{\sigma}{G}\right) \quad \text{(Equ. 11)}$$

where B_{HD} is a constant with a value found from experimental data on the order of 10^{-11} [133]. As with other dislocation mechanisms, Harper-Dorn creep predicts that grain size is irrelevant with $m = 0$, and the stress is directly proportional with $n = 1$. Harper-Dorn creep is associated with grain elongation, similar to diffusion creep, but is observed to result in faster creep rates. Additionally, Harper-Dorn creep can occur alone without the accommodation of grain boundary sliding [165].

2.3.3. Creep Studies of Oxide Ceramics

Early Creep Experiments

When researching the creep performance of oxide ceramic materials, the vast majority of experimental data is on the behavior of alumina (Al_2O_3), and for much of the 20th century alumina represented a baseline for oxide ceramic creep performance. Most of the research on fine-grained (1-15 μm) polycrystalline alumina demonstrates that plastic deformation over time occurs by means of three possible mechanisms: diffusional creep, basal slip, or grain boundary sliding [166].

In alumina diffusional creep can occur as both lattice diffusion or grain boundary diffusion. Generally speaking, this creep mechanism is usually rate-controlled by the diffusion of the aluminum ion since oxygen diffusion is slow through the lattice, yet very rapid along the grain boundaries [166]. Diffusion is typically reported as the dominant creep mechanism in alumina, but this has also been observed to transition and become interface controlled, specifically in very fine-grained specimens, as reported by Cannon et al. [167] and Pysher et al. [168]. Under certain conditions polycrystalline alumina has been observed to be more creep resistant than single-crystal alumina (Sapphire), even in the most favorable directions [169]. Although single-crystal materials are generally not isotropic, and applications are limited due to crystal growth and fabrication limitations, their creep resistance is usually far superior to polycrystalline materials [166]. This anomalous behavior of polycrystalline alumina has led to considerable research on the topic.

Folweiler in 1961 was the first to investigate the creep behavior of fully dense polycrystalline alumina based on temperature and grain size [170]. Specimens were tested over a temperature range of 1400°C to 1800°C. A grain size exponent of $m = 2$ was determined, and Nabarro-

Herring diffusional creep was concluded to be the primary mechanism at work. However, in this work it is important to consider that creep results based on flexure tests are difficult to interpret with confidence as multiple stress states may be occurring simultaneously [166].

Nabarro-Herring creep was also noted as the primary mechanism for polycrystalline alumina up to 1800°C by Warshaw and Norton in 1962 [171]. They also concluded that dislocation mechanisms and grain boundary sliding occurred during creep in compression. Additional creep investigations of polycrystalline alumina were continued by Passmore and Vasilos in 1966 [172], [173], Hewson and Kingery in 1967 [174], Hollenberg and Gordon in 1973 [175], and Lessing and Gordon in 1977 [176], who additionally looked into the effects of environment and various dopants on the creep rates of fine-grained polycrystalline alumina.

Cannon et al. continued the study of creep of fine-grained alumina up to 1800°C [167]. He reported observing diffusional creep as the dominant mechanism. Coble creep was observed for lower applied stresses and N-H creep was observed at higher applied stresses. For very small grain sizes Cannon et al. reported observing a transition to interface reaction-controlled creep with a stress exponent of $n = 2$, which accounts for the often-observed non-Newtonian behavior of fine-grained polycrystalline alumina. Cannon et al. [167] and Heuer et al. [177] discovered that basal slip and grain boundary sliding can occur simultaneously in fine-grained polycrystalline alumina. They referenced observations of dislocation motion, grain boundary sliding, and cavity formation, although diffusion was still concluded to be the primary mechanism.

This wealth of reported creep mechanisms and various conclusions for polycrystalline alumina is possibly a result of performing creep testing in flexure, making the results difficult to interpret. As a result, many authors have chosen to focus more on creep in compression to better

understand the deformation mechanisms at work. Beginning with Rhodes et al. in 1965 [178] and continuing with Sugita et al. in 1970 [179], Becher in 1971 [180], Mocellin and Kingery in 1971 [181], and Hou et al. in 1979 [182], compression creep tests gave evidence of primarily diffusion controlled creep, especially at low stresses. As stresses rise, more observations were made of grain boundary sliding taking over as a significant source of creep. The occurrence of stress exponents greater than one was often attributed to the presence of basal slip as a simultaneous creep mechanism in fine-grained alumina. These authors reported various creep rates for polycrystalline alumina based on stress, temperature, grain size, and other parameters, establishing alumina as a viable deformation-resistant, high temperature structural material.

More recently Armani experimented with the creep of polycrystalline alumina, both SiO_2-doped and undoped at 1100°C and 1300°C in air [29]. Compressive creep tests were conducted with applied stress ranging from 100 MPa to 250 MPa. Excellent creep resistance was reported with strain rates at 1100°C ranging from 4.22×10^{-7} to 1.20×10^{-6} s^{-1} depending on the applied stress. Similarly, at 1300°C, strain rates ranged from 8.13×10^{-7} to 5.76×10^{-6} s^{-1} depending on the applied stress. Results for specimens with silica doping showed decreased strain rates by approximately one order of magnitude, demonstrating very impressive creep resistance for alumina [29].

Among other oxide ceramics to exhibit exceptional resistance to creep are aluminosilicates, specifically Mullite. Penty and Hasselman investigated the creep of high-density, fine-grained, polycrystalline mullite by four point bend at temperatures between 1430°C and 1512°C [183]. The creep tests revealed excellent resistance to plastic deformation at high temperatures. A comparison was made to fine-grained alumina under identical test conditions at 1415°C and 8200 psi, tested by Cannon and Rhodes [184]. Under these conditions alumina exhibited a

steady-state creep rate of approximately 10^{-4} s^{-1} while mullite exhibited a superior steady-state creep rate of 3.2 x 10^{-6} s^{-1}. This low creep rate was attributed primarily to an unusually high activation energy, which was determined to be approximately 167 Kcal, which is in agreement with the activation energy of mullite as measured by other authors [185], [186]. A stress exponent of $n = 1.1$ to $n = 1.4$ was determined and suggests the dominant creep mechanism is N-H diffusional creep as with similar materials. The rise of the stress exponent with increasing temperature above $n = 1$ also suggests that the creep of mullite may become interface reaction controlled, or that there is a simultaneous addition of grain boundary sliding or dislocation glide [183].

Creep of Garnets

A significant number of creep experiments have demonstrated that the most promising creep resistant oxide ceramic materials come from the garnet group. Many properties of garnets help to enable a significant resistance to plastic deformation at high temperatures. Corman explains that the complex body-centered cubic crystal structure has a large unit cell, no close-packed Oxygen planes, a large Burger's vector, and large Peierl's stresses, which all contribute to limited dislocation glide mobility, and overall reduced plastic deformation under stress [83]. Garem et al. explains that dislocations in garnets have to overcome high lattice friction stresses, contributing to a high resistance to plastic deformation [84], [166]. Additionally, garnets, such as YAG, possess high stiffness at room temperature (>300 GPa), are stable in oxidizing environments, exhibit high melting temperatures (>1900°C), and have low coefficients of thermal expansion. These desirable properties have led to the continued study of the deformation of garnets at temperatures close to their melting points.

Rabier et al. [187], [188] and Garem et al. [84] have investigated the plastic deformation of single-crystal Gadolinium-Gallium garnet (GGG) and Yttrium-Iron garnet (YIG). It was determined that relatively high stresses were required (>200 MPa) to induce any plastic deformation at temperatures close to the melting point of each material, and that this behavior should be a general trend within the garnet group of ceramics. Compression creep tests up to 1500°C in air revealed glide anisotropy in different slip planes. An extremely low dislocation density was also observed in these single-crystal garnets [84]. It was also noted that the garnet crystal structure naturally resists plastic deformation due to dislocation glide, and uniquely allows dislocation climb to disassociate and occur alone [188].

Due to the superior mechanical properties and high melting temperature of YAG, there has been significant interest in its creep performance at high temperatures, leading to many studies over the past 30 years. Various creep tests of single-crystal and polycrystalline YAG have determined that YAG is one of the most creep resistant materials at temperatures very close to its melting point in both inert and oxidizing environments [25], [27], [104]–[107], [189], [190]. Early creep experiments by Corman [83], [107] and Parthasarathy et al. [27], [189], [190] in the early 1990s demonstrated the overall creep resistance of YAG in inert environments up to 1850°C. Later the work of Armani and Ruggles-Wrenn [28], [29] further proved the high creep resistance of YAG in air and steam-rich environments at temperatures up to 1300°C. Several important studies on the creep of YAG are detailed in the following paragraphs.

The early investigations on the creep of single-crystal YAG was conducted by Corman in 1993 [83]. He conducted compressive creep tests at 1650°C to 1850°C in Helium at stresses between 50 and 280 MPa. His analysis concluded that single-crystal YAG is highly creep

resistant, with creep rates lower than that of single crystal alumina, as seen in Figure 15. Again, this behavior was attributed to the large lattice parameters of YAG, limiting dislocation motion.

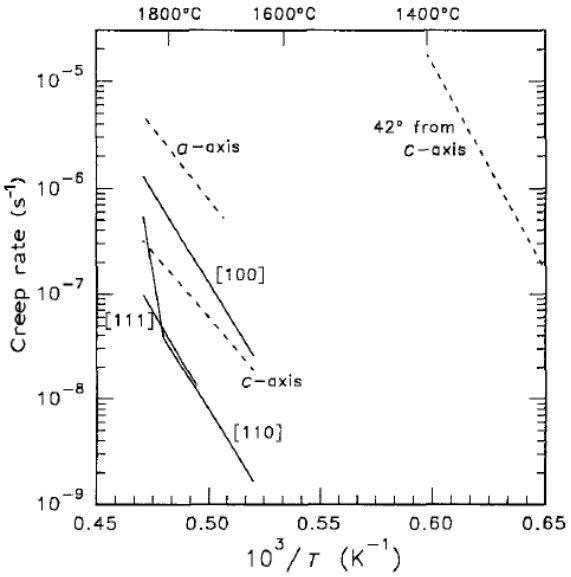

Figure 15: Creep rates of single-crystal YAG compared to previously published creep rates of single-crystal alumina from Corman [83]. Reproduced with permission from Springer Nature.

The creep of single-crystal YAG was also investigated by Armani at 1300°C in a steam rich environment [29]. A specimen was tested under these conditions at slowly increasing stress levels in compression. The applied stress was increased slowly from 50 MPa to 200 MPa. No measurable strain was observed from 50 MPa to 150 MPa. Only at 200 MPa for a duration of 5 hours was a small amount of strain measured (approximately 0.1%). The final steady-state creep rate was calculated to be 1.06×10^{-8} s^{-1}. This test verified that single-crystal YAG is the most creep resistant material currently studied under these conditions [29].

Parthasarathy et al. investigated the creep rates of fine-grained polycrystalline YAG in compression at temperatures from 1400°C to 1610°C in a vacuum [27], [189], [190]. It was

concluded that the primary creep mechanism for polycrystalline YAG is likely N-H or Coble diffusional creep with a stress exponent of $n = 1.24$. Although still highly creep resistant, polycrystalline YAG had higher creep rates than single-crystal YAG, suggesting that the creep of these two materials occurs by two different mechanisms. However, it was also determined that they may possess the same activation energy, suggesting that creep of both single-crystal and polycrystalline YAG are lattice diffusion controlled [27].

Significant creep testing of polycrystalline YAG was also conducted by Armani et al. at the Air Force Institute of Technology (AFIT) [28], [29]. Compressive creep tests of high-purity polycrystalline YAG and silica-doped YAG were conducted between 50 and 200 MPa at 1300°C in air and in steam, in order to understand the creep rates of YAG in combustion environments. Creep results were consistent with the Nabarro-Herring diffusional creep mechanism, with the creep rate limited by lattice diffusion of Yttrium cations (Y^{3+}) and a stress exponent of $n = 1$. Silica-doped YAG specimens had a grain size of approximately 2.41 μm and slightly lower creep rates than undoped YAG with 0.92 μm grain size. The creep rates of polycrystalline YAG in air were found to be superior to the creep rates of both polycrystalline alumina and mullite. It was also concluded from these experiments that the creep rates of polycrystalline YAG are only slightly increased by the presence of steam, still maintaining superior creep performance overall. A summary of the resulting strain rates of YAG specimens are shown in Figure 16.

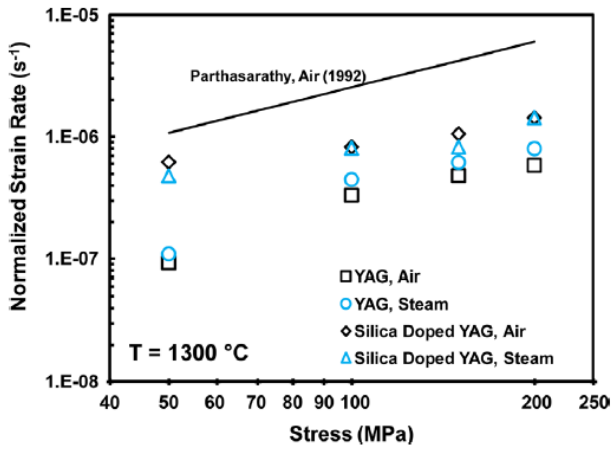

Figure 16: Normalized strain rates of YAG specimens creep tested in compression from Armani et al. [28]. Results are compared to predicted performance presented by Parthasarathy et al. in 1992 [27]. Reproduced with permission from the Air Force Institute of Technology.

Jain et al. from the NEI Corporation investigated YAG as a viable matrix material for ceramic matrix composites by testing its creep performance. This work was documented in a Department of Energy Report by the same author [191]. Polycrystalline YAG with various dopants was synthesized by hot pressing and conventional sintering. Specimens were tested in air in compression from 1300°C to 1400°C and from 75 to 150 MPa. The average grain size was statistically determined to be approximately 9 µm. As in previous studies, the steady-state creep rates of YAG were found to be far superior to alumina, mullite, and even previously tested YAG specimens. However, when comparing creep rates across various studies, it is important to account for the material grain size. In this case, the grain size of YAG was approximately 9 µm, which is larger than most other YAG and alumina materials discussed in this section.

Additionally, there was significant abnormal grain growth reported by Jain et al., which made it difficult to account for grain size variations between specimens. The test method in this study did not allow for mounting of the extensometer on the specimens during testing. As an alternate

deformation measurement method, the final length of the specimen was compared to the initial length, capturing the total change in length during creep. This method successfully captures the change in deformation, but makes it difficult to determine the steady-state creep rate.

The reduction in creep rate due to the presence of various dopant ions was attributed to the segregation of the ions with large ionic radii at the grain boundaries, which likely reduced the grain boundary diffusion rate. Both the stress and grain size exponents were concluded to be in the expected range for either Nabarro-Herring or Coble diffusional creep as the primary creep mechanism. Figure 17 shows the creep rates of doped polycrystalline YAG compared with the creep rates of alumina, mullite, and a combined alumina-YAG material.

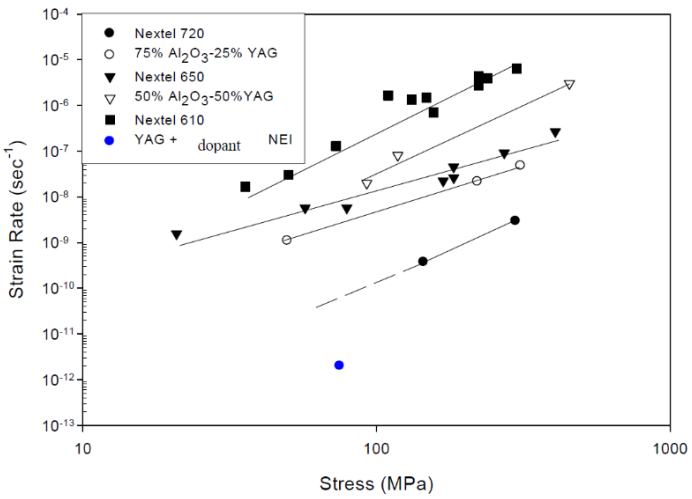

Figure 17: Creep of doped polycrystalline YAG, compared with other ceramic oxide materials from a Department of Energy report by Jain et al. [191].

Another garnet material expected to perform very well in creep is LuAG. As was discussed in the previous section, LuAG is harder, denser, and potentially more chemically stable than YAG. Additionally, it has a higher melting point ($\approx 2050°C$), which suggests that its creep resistance may be superior to YAG at equivalent temperatures. However, the creep of LuAG has not yet been determined. Due to the limited availability and often-inhibitive costs of obtaining Lutetium, the structural performance of LuAG remains unknown. Several authors have investigated the hardness and fracture toughness of LuAG specimens, which revealed promising results; however, to date no studies have investigated the creep rates or active creep mechanisms of LuAG.

2.4. Environmental Effects on the Performance of Oxide Ceramics

The history of engineering ceramic materials has demonstrated their excellent performance at high temperatures compared to other types of structural materials. Despite their shortfalls, such as their brittle nature and their tendency to fail due to small flaws and cracks, ceramics have proven to be valuable structural materials at high temperatures due to their high melting points and the stability of their mechanical properties at high temperatures. However, as with many structural materials, high temperatures can facilitate oxidation and corrosion of ceramics in oxidizing environments. This has limited the use of many standard engineering ceramics whose properties are degraded due to the presence of Oxygen at high temperatures. This has given rise to the development and use of oxide ceramics, whose chemical composition naturally resists further oxidation, even at high temperatures.

However, oxide ceramics are still susceptible to degradation when operating in certain environments. Studies have shown that even the most impressive oxide ceramics, such as alumina and YAG, are not completely resistant to all forms of chemical attack. This section attempts to review the previous experimental work, which demonstrates the extent of the vulnerability of oxide ceramics to the most extreme operating conditions, often encountered in aerospace applications. In order to thoroughly understand the experimental results found in the literature, it is necessary to review some important concepts related to the environmentally-assisted failure of ceramic materials.

2.4.1. Environmental Failure Mechanisms in Ceramics

When trying to understand and predict failure of brittle materials, there are some important material properties and characteristics that must be fully understood beyond the ultimate strength of the material. Brittle materials are very susceptible to catastrophic failure due to the presence of small flaws and cracks; therefore, understanding how a specific material reacts to these small imperfections and how quickly cracks can grow are very important. The field of fracture mechanics aims to determine how and why cracks propagate through a material, and must be studied to understand the failure of brittle materials.

A key material property studied in the field of fracture mechanics is the fracture toughness of a material. Fracture toughness can be defined as the ability of the material to resist fracture in the presence of cracks or voids [192]. It can also be described as the critical level of the stress intensity factor at which point a crack will become unstable and continually propagate through a material [38]. Typically, cracks will not propagate through a material causing failure until the applied stress causes the stress intensity factor to exceed the inherent fracture toughness. The

critical stress intensity factor is well understood in the field of fracture mechanics and can be defined by Equation 12 for an applied stress acting normal to the crack opening [192].

$$K_C = \sigma_{ult}\sqrt{\pi a} \quad \text{(Equ. 12)}$$

where a is the crack length and σ_{ult} is the ultimate strength of the material. This simple expression effectively describes the state of stress at the crack tip and represents the critical point at which the crack will continue to propagate through a material, generally causing catastrophic failure. The fracture toughness of brittle materials is generally much lower than that of ductile materials, which tend to inherently resist crack growth by means of various toughening mechanisms [193]. Table 9 shows some fracture toughness values for various structural materials, including several ceramic materials discussed in this study.

Table 9: Fracture Toughness values for several structural materials.

Material	Fracture Toughness (K_{1C}) $\left[MPa \cdot m^{1/2}\right]$
Aluminum	15 – 50
Steel	20 – 100
Silicon Nitride	3 – 6
Alumina	4 – 6
Silica Glass	0.7 – 0.8
Polycrystalline YAG	1.3 – 1.5
Single-Crystal YAG	2 – 8

*Fracture toughness values taken from various sources: [51], [104], [194].

There is another crack growth phenomenon, caused by a variety of factors, which allows a crack to slowly propagate through a material below the critical value defined by the stress intensity factor. This is called subcritical crack growth. Although many factors can contribute to subcritical crack growth, it is mainly the result of the applied stress combined with harmful chemical interactions between the material and the environment. When this environmental attack causes corrosion and enables crack propagation due to a reaction at the crack tip, it is known as

stress corrosion cracking, and has been observed in many of the materials described in this study [48], [130].

One of the most commonly studied chemical interactions, which enables subcritical crack growth is the reaction of a material with moisture in the environment. Simple water vapor is often enough to increase the rate of oxidation or result in the loss of volume by the formation of volatile reaction products. These processes are often enabled further by high temperatures [38]. However, stress corrosion cracking, enabling subcritical crack growth, is a highly material-specific process, and depends entirely on the chemical composition of the material and the chemical species present in the environment. Therefore, experiments are usually conducted for any material of interest while simulating the environment in which it is expected to operate. It is typically understood that ceramics are much more resistant to stress corrosion cracking than other materials, such as metals. However, there are still corrosive environments, which will cause harmful reactions in ceramics, generating subcritical crack growth.

When stress corrosion cracking occurs in ceramics, the parameter which controls the crack propagation velocity is the applied stress intensity factor. As the stress intensity factor changes based on loading or crack length, the mechanisms controlling the rate of crack propagation will also change. A plot of the logarithm of crack velocity vs. the stress intensity factor can typically be divided into three regimes, shown in Figure 18. This behavior has been noted to occur in many ceramic materials, including Silicon nitride, alumina, glasses, porcelains, and cements [38].

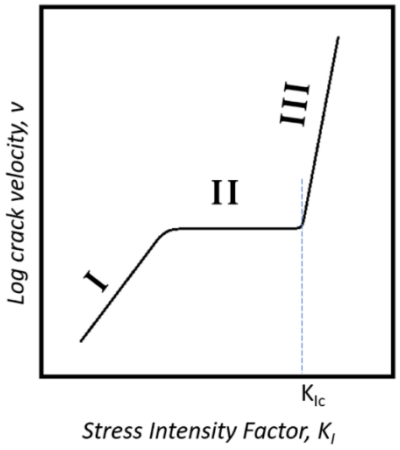

Figure 18: Three regimes found when plotting the logarithm of crack velocity vs. the stress intensity factor for several ceramic materials undergoing subcritical crack propagation.

This behavior was first observed by Wiederhorn in 1967 when studying subcritical crack growth in glass [195]. In region 1 the crack growth is typically controlled by the stress-enhanced chemical reaction between the material and the environment. This region is reaction-rate controlled, meaning the crack velocity will increase along with the concentration of the reactant. In region 2 crack propagation becomes independent of the stress intensity factor, and the crack growth is controlled by the rate of diffusion of chemicals into the crack. This region is controlled by the rate of chemical transport into the crack, rather than the reaction rate. In region 3 the stress intensity factor reaches its critical value and crack growth becomes independent of the environment. At this point the crack velocity is primarily based on temperature and material composition, and the crack will propagate rapidly to failure [38].

2.4.2. Environmental Degradation Studies of Oxide Ceramics

Investigations into the corrosion and degradation of ceramics has been ongoing since their use was adopted for engineering applications operating in extreme environments. Oxide ceramics were developed because of their inherent resistance to environmental attack, specifically

oxidation. However, these materials have still been shown to react to harsh chemical environments in several negative ways, such as microstructural changes, stress corrosion cracking, reduction in fracture toughness, the formation and evaporation of hydroxides, among others [196]–[201]. This section provides a brief overview of previous experimental studies on the degradation and corrosion of some important oxide ceramics.

Degradation of Alumina

Alumina has been a fundamental oxide ceramic material, thoroughly used across many industries because of its high-temperature stability and resistance to oxidation. However, it has been shown to be susceptible to property degradation in harsh chemical environments, and is presented here as a foundational example of oxide ceramic degradation. Blumenthal et al. in 1984 [201] and Cao in 1985 [196] observed premature cracking in polycrystalline alumina in the presence of silica at high temperatures. It was discovered that the amorphous silica particles entered the grain boundaries and enabled creep embrittlement, reducing the overall strength of the material.

Several more studies investigated the stability of alumina in the presence of water vapor. Oda et al. [197] tested polycrystalline alumina in water vapor at 300°C and a pressure of 8.6 MPa. Small amounts of impurities within the alumina enabled the dissolution of SiO_2 and Na_2O at the grain boundaries. This allowed corrosion to occur at the grain boundaries, reducing the weight, and overall strength properties of the material. Similarly Kruzic et al. [200] studied the effect of moisture on the fracture toughness of alumina at room temperature. It was determined that the intrinsic toughness at the crack tip was approximately 30% lower in the presence of moist air, likely reducing the theoretical strength of the material. It was also observed that in fatigue

experiments, crack growth rates are significantly higher and the fatigue thresholds are lower in moist air.

Tai et al. [202] observed the degradation of alumina in an argon and water vapor environment at temperatures between 1300°C and 1700°C. There was a measurable decrease in volume and flexural strength of the alumina samples after 10 hours of exposure. At the surface of the alumina specimens, substantial grain growth was observed. Additionally, grain boundary etching occurred due to the formation of volatile Al-hydroxide gasses, $Al(OH)_2$ and $Al(OH)_3$.

Kronenberg et al. [203] and Castaing et al. [204] investigated the effects of hydrogen impurities in sapphire and polycrystalline α-alumina specimens, subject to annealing in super critical water at temperatures between 850°C and 1025°C and pressures between 1500 MPa and 2000 MPa. Infrared absorption measurements were used to determine the amount of Hydrogen uptake by the specimens. Both interstitial Hydrogen impurities and OH clusters were found to rapidly diffuse into the specimens, and mainly segregate near the surfaces. It was also noted that the amount of water uptake was 100 times greater for polycrystalline alumina compared to sapphire. It was concluded that the grain boundaries become pathways for rapid transport of the Hydrogen impurities. This phenomena increased the rate of intergranular fracture, significantly reducing the strength and fracture toughness of the specimens due to grain boundary weakening [203]. Additionally, when placed under uniaxial stress, the strength of the sapphire and large-grain (30-50 μm) polycrystalline alumina was reduced by a factor of two in the presence of water. These results were attributed to the enhanced rate of dislocation mobility. However, the strength of fine-grained (3-5 μm) polycrystalline alumina was reduced by a factor of six due to the presence of water at high temperatures and pressures. This result was attributed to a change in failure mechanism from primarily dislocation glide to largely grain boundary sliding under

hydrothermal conditions [204].

Fritsch et al. [198] and Klemm et al. [199] tested alumina along with non-oxide ceramics at temperatures between 1200°C and 1500°C in a burner rig with a water vapor partial pressure of 0.24 atm for test times between 100 and 300 hours. Although the most significant degradation came in the form of active oxidation of the non-oxide ceramics, corrosion was also observed on the alumina specimens above 1300°C. Surface reaction-controlled corrosion was determined to cause weight loss in alumina due to the formation of the volatile hydroxide $Al(OH)_3$ on the surface. This would allow for significant recession on the surface of alumina over the operational life of structural components in combustion environments [198].

The effects of steam on the high temperature creep of alumina have also been thoroughly studied at the Air Force Research Laboratory. Armani et al. [29] tested the creep of polycrystalline alumina with and without silica doping, exposed to steam at 1100°C and 1300°C. Similar compressive creep tests in air were reported in the previous section on creep of ceramic oxides. The creep rates for tests conducted in air and steam are compared in Figure 19.

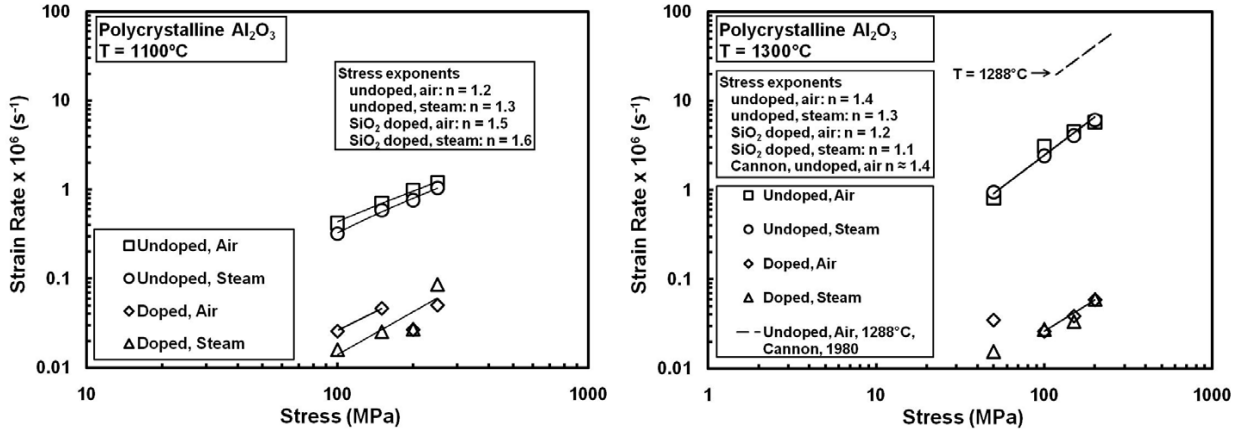

Figure 19: Steady-state creep rates vs. the applied stress for doped and undoped polycrystalline alumina at 1100°C (left) and 1300°C (right), from Armani [29] Reproduced with permission from the Air Force Institute of Technology.

At both temperatures there is very little effect of the presence of steam on the creep rate with or without silica doping. These results are compatible with the previously described study conducted by Tai et al. who showed that in the presence of water vapor, there was little effect on polycrystalline alumina prior to increasing the temperature to 1500°C [202].

Similar experiments were conducted by Fritsch et al. [198], Klemm et al. [199], and Schmucker et al. [205] on other important oxide ceramics, such as mullite. Mullite exhibited higher corrosion rates than other oxides. At temperatures above 1300°C a porous layer of alumina was formed on the surface of the mullite, due to the silica leaching out through the surface and reacting with the water vapor, causing the formation of volatile Si-hydroxides, such as $Si(OH)_4$. This is also a result of the low activation energy required for this reaction when compared to the corrosion mechanisms at work in other oxide ceramics [198], [199], [205].

Degradation of YAG

Fritsch et al. [198] and Klemm et al. [199] also observed the behavior of YAG at temperatures between 1200°C and 1500°C in a burner rig with a water vapor partial pressure of 0.24 atm. Compared with alumina and mullite, YAG exhibited a much lower rate of corrosion, which was primarily due to the formation of a small protective layer on the surface. It was suggested that a small amount of weight loss occurred due to the formation of various Al-hydroxides on the surface of the YAG specimens. However, the size of the surface layer and the overall weight loss of YAG was much less than the other oxide ceramics tested [198], [199]. The surface layer of YAG compared with that of alumina taken from the studies conducted by Fritsch et al. are shown in Figure 20.

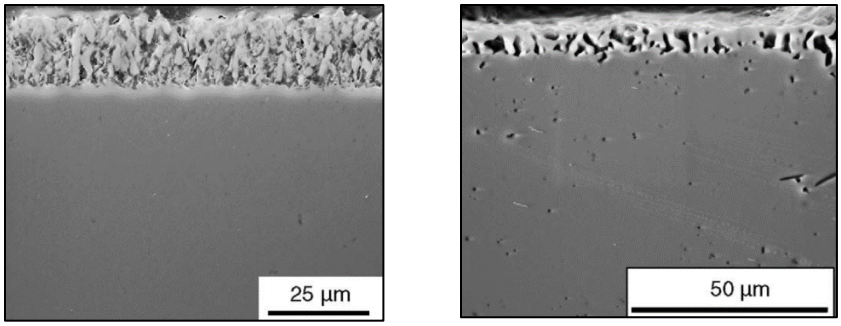

Figure 20: Surface corrosion layers observed on alumina (left) and YAG (right) from Fritsch et al. [198]. Reproduced with permission from Elsevier.

Harada et al. [206] conducted tensile creep tests on a ceramic matrix composite composed of alumina fibers embedded in a YAG matrix. The fiber volume was approximately 50%. Tests were conducted at temperatures ranging from 1773 K to 1873 K in argon, air, and water vapor with a water vapor pressure between 0.06 MPa and 0.6 MPa. At atmospheric pressure previous studies have shown that the flexural strength of such a composite composed of alumina and YAG is not affected by the presence of water vapor, indicating significant corrosion resistance of the constituent materials [207]. However, Harada et al. showed that once the water vapor pressure increased, the creep rate increased significantly. Figure 21 shows the increase in overall creep strain vs. time with the addition of water vapor under pressure [206].

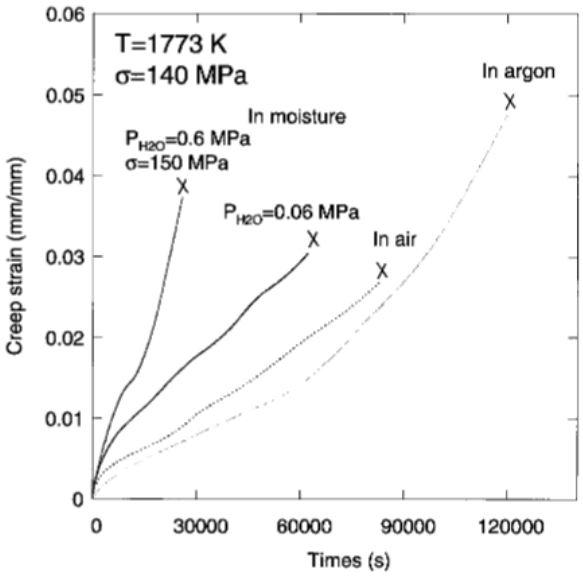

Figure 21: Creep strain of an alumina/YAG composite subject to tensile creep in argon, air, and steam from Harada et al. [206]. Reproduced with permission from John Wiley and Sons.

The increase in creep strain was attributed to a significant increase in the dislocation motion of the alumina phase. However, only a slight increase in dislocation density was observed in the YAG matrix, again, pointing to its exceptional corrosion resistance in the presence of moisture.

Armani et al. [28], [29] also demonstrated the thermal and chemical stability of single-crystal and polycrystalline YAG in creep. YAG specimens were creep tested in compression in the presence of steam at 1300°C. As was noted in the previous section, single-crystal YAG exhibited no measurable deformation under these conditions. Also, the presence of steam in this temperature range was shown to have little effect on the superior creep rate of polycrystalline YAG specimens as well, which was previously described in section 2.3.3.

2.5. Implications for Current Research

Based on this previous research and development of engineering ceramics throughout the last century, this unique class of materials has become well known and widely used in many industries due to the many known advantages and strengths. Among the most unique and important properties of engineering ceramics is their excellent resistance to high temperatures. A more recently developed group of ceramics are oxide ceramics, which are critical for applications requiring use at high temperatures in oxidizing environments. Because of their chemical composition, oxide ceramics inherently resist oxidation and provide consistent and stable properties in the most extreme environments.

The extensive development of oxide ceramics in recent years has enabled their consistent property improvement, creating solutions to many tough material challenges. Today, several oxide ceramics are widely used in many applications with tested behavior and proven properties. However, the performance of certain synthetic oxide ceramics is not entirely known, especially in extreme conditions at high temperatures. Garnet ceramics have showed the highest potential in terms of structural stability at high temperatures and chemical resistance to harsh operating environments, but previous testing has not proven their performance for all possible applications.

The creep performance of YAG has been studied by several researchers; however, its performance in air and combustion environments at the highest test temperatures is not fully known. Previous research has demonstrated its potential up to 1300°C, but has not yet proven its capabilities beyond this, which is critical before significant investment can be made in larger research efforts and in the eventual use of this costly material for critical structural applications. Additionally, the basic material properties and crystal structure of LuAG suggest that its performance may surpass all other oxide ceramics, including YAG. However, the creep

performance of LuAG at any temperature in any environment has yet to be determined.

This study will attempt to observe and analyze the creep performance of each of these high-potential, synthetic oxide ceramics. They will each be tested at high temperatures in potentially degrading environments to determine how well they can each perform under these conditions. These experiments will demonstrate the usefulness and ultimate potential of each of these materials and will inform future investment decisions concerning continued research and the eventual development of future high-performance aerospace structures.

3. Research Materials and Processing Methods

3.1. Research Materials

3.1.1. Yttrium Aluminum Garnet (YAG, $Y_3Al_5O_{12}$)

Overview

High-purity, undoped polycrystalline YAG specimens were fabricated using the state-of-the-art material processing laboratories at the Air Force Research Laboratory, Materials and Manufacturing Directorate at Wright-Patterson Air Force Base. Undoped YAG powder was processed by Nanocerox, Inc., located in Ann Arbor, MI, which specializes in the production of high-purity ceramic nanopowders. The powder was developed using flame spray pyrolysis to achieve fine nanoparticles. The YAG powder was carefully mixed into water or alcohol solution, ball-milled for 48 hours, and dried. The resultant powder was transferred from its container to a graphite die for sintering.

Spark plasma sintering (SPS) was selected as the ceramic sintering method due to its short processing time, and its effectiveness in creating near theoretical-density parts. SPS is a standard ceramic processing technique, where ceramic powder is heated below its melting point, typically under pressure, so that bonding occurs by means of atomic diffusion. This leads to the ceramic powder solidifying into a rigid structure. SPS was performed using various temperature and pressure parameters, which are discussed in more detail later in this chapter. Additionally, various heating and cooling rates were explored in order to minimize the potential cracking of the solid parts during fabrication. Following SPS, each sintered YAG puck was removed from the die and heat treated in order to remove any residual carbon contamination. Each heat treatment cycle was carried out in an alumina tube furnace at 1500°C for 10 hours in flowing O_2.

Powder Properties

According to details provided by Nanocerox, Inc., the YAG powder has an approximate particle size of 0.1 μm and a specific surface area of 20 m^2/g. An impurity analysis also revealed approximately 300 ppm impurities, mostly volatiles. Figure 22 shows SEM images of the high-purity, undoped YAG powder before any additional processing occurred. Figure 23 shows an SEM image of a solid, undoped YAG specimen following sintering, revealing an average grain size of approximately 1 μm. Both images were provided to the Air Force Institute of Technology by Nanocerox, Inc. in the YAG nanopowder data sheet [208].

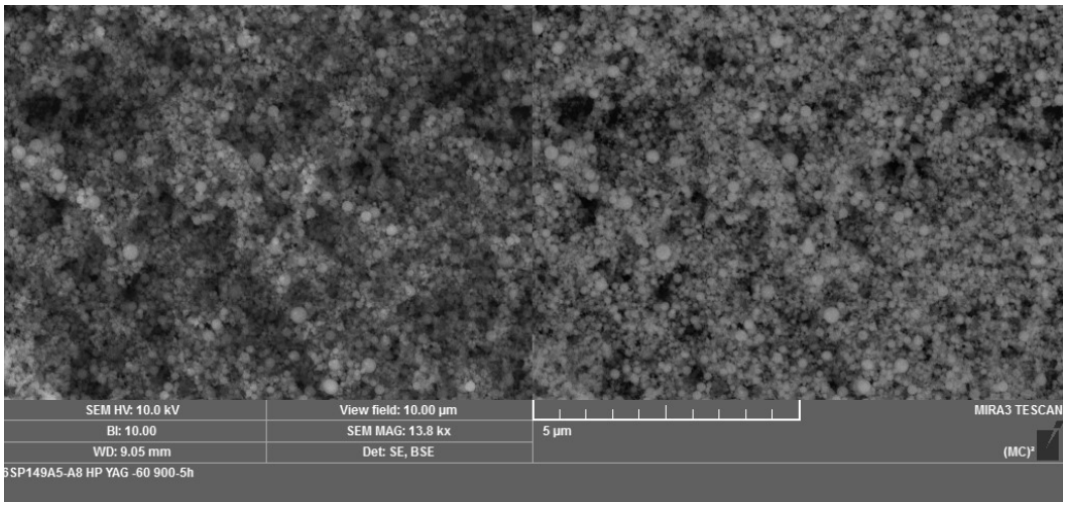

Figure 22: SEM images of high-purity, undoped YAG powder prior to processing, reproduced from the material data sheets, provided by Nanocerox, Inc. [208].

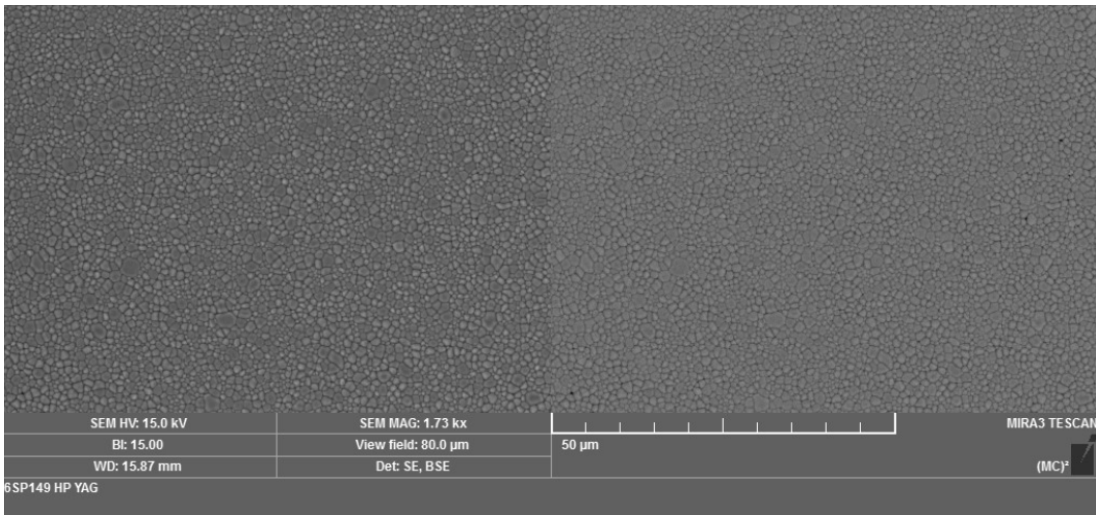

Figure 23: SEM images of a sintered high-purity, undoped YAG specimen, revealing small grains and overall phase purity, reproduced from the material data sheets, provided by Nanocerox, Inc. [208].

Yttrium Aluminum Garnet Doped Variants

In addition to undoped YAG, two doped YAG variants were also fabricated using the same methods described above. One YAG variant was doped with Ytterbium and the other was doped with Erbium. The amount of each dopant was 2 atomic percent (2at%). These elements are common dopants in many YAG solid-state laser materials due to the significant changes that they create in the overall optical properties of the host material. For example, Er:YAG lasers typically emit light with a much different wavelength of 2940 nm, which is strongly absorbed by water and other substances found in the body, allowing Er:YAG lasers to be widely used in medical procedures with less risk of human tissue damage [209]. Yb:YAG lasers emit light at 1030 nm and have a very high power output, low fractional heating, and high thermal conductivity, making Yb:YAG lasers the best medium for high-power solid state lasers [210].

Both Yb^{3+} and Er^{3+} ions possess certain properties, which make them excellent candidates for

substituting for Y^{3+} in YAG. Specifically, they possess a similar valence electron state, and have similar ionic radii (Yb_r^{3+} = 0.985 Å; Er_r^{3+}= 1.004 Å; Yb_r^{3+} = 1.019 Å) [96], [211], [212]. This allows significant doping to occur without any distortion of the crystal lattice [213]. Due to the common presence of these dopants in YAG materials used in many applications, it is desirable to understand the associated mechanical properties of each doped material variant.

Both 2at% Yb-doped YAG and 2at% Er-doped YAG were fabricated using pre-doped powder, processed by flame spray pyrolysis obtained from Nanocerox, Inc. Sintering occurred by means of SPS using the same powder preparation techniques and sintering parameters as with undoped YAG. The processing methods used to generate these materials are discussed in more detail later in this section.

3.1.2. Lutetium Aluminum Garnet (LuAG, $Lu_3Al_5O_{12}$)

Overview

High-purity, undoped polycrystalline LuAG specimens were similarly fabricated using the laboratories at the Air Force Research Laboratory, Materials and Manufacturing Directorate at Wright-Patterson Air Force Base. Undoped LuAG powder was not readily available from a commercial source, so the required LuAG powder was obtained from a stoichiometric mixture of high purity (>99.99%) alumina powder and Lutetium oxide (Lu_2O_3) powder, produced by Nanocerox, Inc. This powder was also developed using their in-house flame spray pyrolysis method to achieve fine nanoparticles. The combination of powders was mixed into a water or alcohol solution, ball-milled for 48 hours, and dried. The resultant powder was transferred from its container to a graphite die for sintering.

SPS was similarly used to processing LuAG specimens, as it was for each YAG variant as

well. SPS was performed using various temperature and pressure parameters, which are discussed in more detail later in this chapter. Additionally, various heating and cooling rates were explored in order to minimize the potential cracking of the solid parts during fabrication. Following SPS, each sintered LuAG puck was removed from the die and heat treated in order to remove any residual carbon contamination. Each heat treatment was carried out in an alumina tube furnace at 1500°C for 10 hours in flowing O_2.

Powder Properties

According to details provided by Nanocerox, Inc., the Lutetium oxide powder has an approximate particle size of 0.1 μm and a specific surface area of 22.1 m^2/g. An impurity analysis also revealed approximately 200 ppm impurities, mostly volatiles, similar to YAG. Figure 24 shows SEM images of the high-purity Lutetium oxide powder before any additional processing occurred, provided by Nanocerox, Inc. [214].

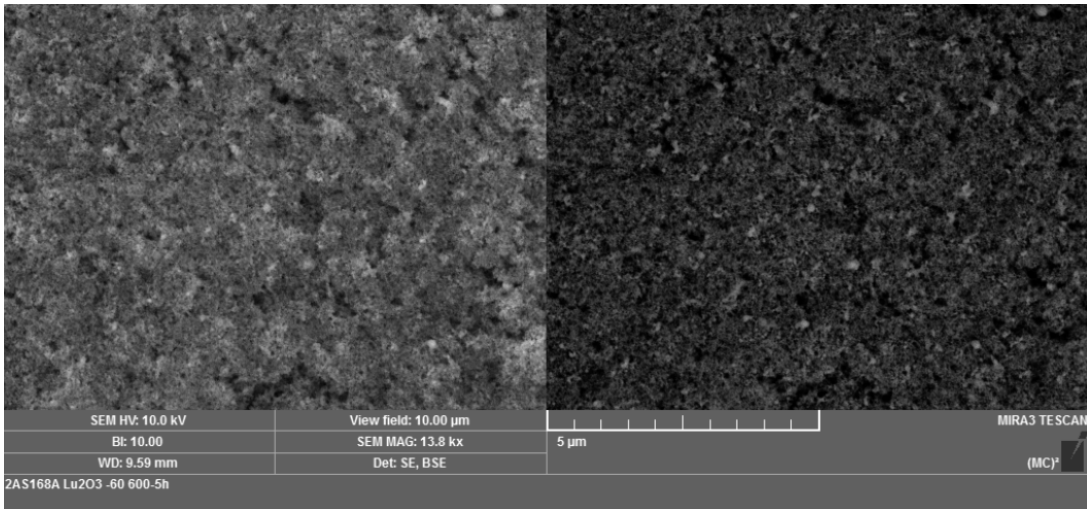

Figure 24: SEM images of high-purity Lutetium oxide powder prior to processing, reproduced from the material data sheets, provided by Nanocerox, Inc. [214].

3.2. Material Processing

3.2.1. Spark Plasma Sintering: An Introduction

The Sintering Process

The sintering process represents a basic material fabrication method where powders, particulates, or porous materials are heated to a temperature below their melting points and are converted into a dense useful solid. Sintering often occurs unassisted in nature. Examples include the slow compacting of rocks and minerals under pressure within the earth's crust, ice cubes as they heat up in a glass and join together, and individual snowflakes coming together to form a snow ball. Sintering has been adopted by material scientists as a useful way of fabricating various materials in a laboratory environment under high temperature and pressure, including metals, polymers, and ceramics. Sintering is particularly valuable in fabricating metals and ceramics with high melting points, as it can be very difficult to achieve the temperatures necessary to bind particles together in the liquid phase.

Sintering of polycrystalline ceramic powders, such as YAG and LuAG, involves forming a consolidated mass of particles in the desired final shape, and heating the mass to a temperature usually in the range of 50% to 80% of the material's melting temperature. Porosity is reduced by atomic diffusion, where atoms from neighboring particles move across boundaries, fusing the particles together. This diffusion occurs while remaining in the solid phase, and it results in a solid part with a much higher density than the un-sintered powder [215]. This sintering process, which is broken down into three stages, can be visualized by Figure 25.

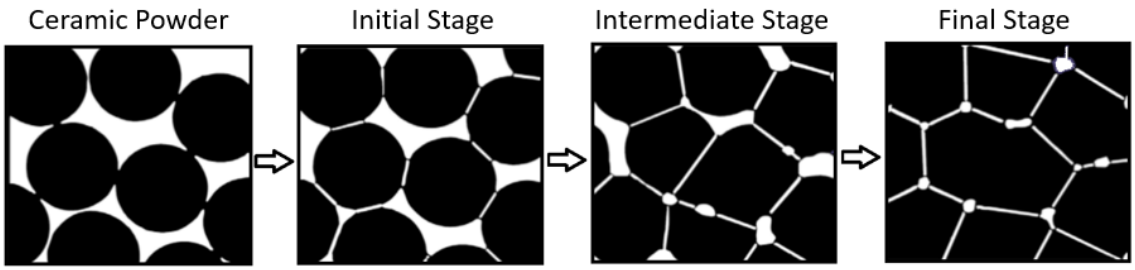

Figure 25: The three stages of sintering.

The sintering process is generally described by three stages: the initial stage, intermediate stage, and final stage. The initial stage of sintering is also known as the neck growth stage, as neighboring particles begin to form necks at the contact points. These contact points become grain boundaries through atomic diffusion. Because necking occurs at contact points, there is significant surface area loss overall; however, there is minimal densification and no shrinking of porosity in this initial sintering stage. At this stage, surface diffusion is the primary mass-transport mechanism, driven by the application of high temperature.

The second stage, or intermediate stage of sintering, is identified by the transformation of the space between particles into an inter-connected network of closed porosity [216]. These pores generally exist at the newly formed grain boundaries. In the intermediate stage, the surface energy and grain boundary energy are reduced, and shrinkage and densification begin to occur [217]. There is nearly a complete loss of open porosity, and closed pores begin to grow and elongate along with grain size.

The final stage of sintering is characterized by final densification and closure or annihilation of nearly all remaining porosity. This process is drastically aided by the application of external pressure during sintering. Most of the densification occurs during the intermediate stage, therefore, only the final and minimal increase in density occurs in the final stage. While this final stage is critical for the fabrication of fully dense parts with essentially no porosity, it is also

possible that high temperatures and extended time spent in the final stage could lead to excessive grain growth. Excessive grain growth can also lead to an increase in porosity [218]. The properties of the three stages of sintering are summarized in Table 10.

Table 10: Description of the stages of sintering [218]

Stage	**Characteristics**	**Surface area loss**	**Densification**	**Grain Growth**
Initial	Neck growth	Significant, up to 50% loss	Small at first	Minimal
Intermediate	Pore rounding and elongation	Near total loss of open porosity	Significant	Increase in grain size and pore size
Final	Pore closure, final densification	Negligible further loss	Slow and little density change	Extensive grain and pore growth

Sintering is also possible with no external pressure, which is known as pressureless sintering, and is used for the fabrication of certain metals and ceramics. However, to achieve near theoretical density of many materials, pressure must be applied to maximize displacement of the powder, and to force the material into its final desired shape and dimensions. The general type of sintering, which simultaneously applies high temperature and pressure to the powder is known as hot pressing (HP). In its simplest form, HP involves placing the powder in a die or mold, usually made of graphite or steel. The powder is pressed in the die by an upper and lower punch, which applies the desired amount of pressure, while heat is simultaneously applied to the powder by various methods. Common methods of heating during HP include indirect resistance heating, where the mold is placed inside an oven, and heating occurs by convection, inductive heating, where induction coils are wrapped around the mold creating an electromagnetic field, and heating by pulsed electric current running directly through the material, known as Spark Plasma Sintering (SPS).

Spark Plasma Sintering

Spark plasma sintering is generally used to describe a rapid sintering technique, which involves the simultaneous application of uniaxial pressure and high temperature, which is generated by high-intensity, pulsed current [219]. SPS was the processing method used for all materials in this study, so it will receive special attention in this section. The powder material is placed into a rigid mold or die, which is electrically conductive, often made of graphite, similar to other forms of hot pressing. Pressure is then applied by means of an upper and lower punch, which press on the upper and lower surfaces of the material, which is contained by the mold. The electric current passes through the punch and through the material as well if the material is conductive. This process generates precisely controlled, uniform, high temperature throughout the material.

During SPS the temperature is applied to the material in two simultaneous ways. The current passing through the graphite punch causes the punch to act as a heat source in contact with the material, and if the material is electrically conductive, it will heat internally from the pulsed current as well. This allows for rapid and uniform heating of the material during SPS [219]. A diagram of the SPS process is shown in Figure 26.

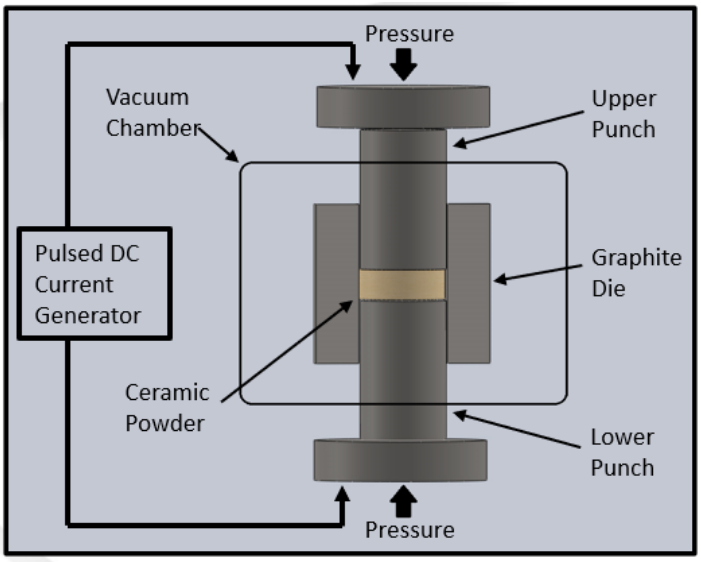

Figure 26: Diagram of SPS process.

This type of sintering, which uses pulsed direct current to generate the required temperatures, was first developed in the 1960's and published in 1966 [220]. Later, this sintering technique gained widespread popularity in Japan, where the first SPS machines for commercial use were developed, and where the term "Spark Plasma Sintering" was first established [219]. SPS has been described as a processing technique, which allows sintering at relatively low temperatures and in short periods of time compared to other techniques, by means of charging powder particles as well as the intervals between them with electrical energy. This process has also been described as effectively applying a high-temperature spark plasma generated at initial energizing, made possible by the continuous on-off DC pulsed high electric current with a low voltage [221].

The name "spark plasma sintering" and its precise definition have often been debated over the years, as it is difficult to prove the presence of plasma or electrical discharges during the process [222]–[224]. SPS has also been termed a pressure-assisted pulse energizing process or the pulsed electric current sintering (PECS) process [221]. Similar types of sintering, which have used other types of current, such as constant DC or AC, have been referred to as "Field-Assisted

Sintering" or "FAST". Therefore, this type of rapid sintering, defined by the use of electric current for heating, is sometimes known as "SPS/FAST" [219].

The appeal of SPS lies in its ability to consistently produce high-density materials in a short amount of time. It has been shown to be incredibly effective, especially when trying to fabricate parts, which are known to be "difficult to sinter", such as materials with very high melting points or materials which will typically diffuse slowly [225]. SPS is categorized as a "pressurized sintering" and "solid compaction technique". Figure 27 shows a diagram of various sintering methods, which include SPS.

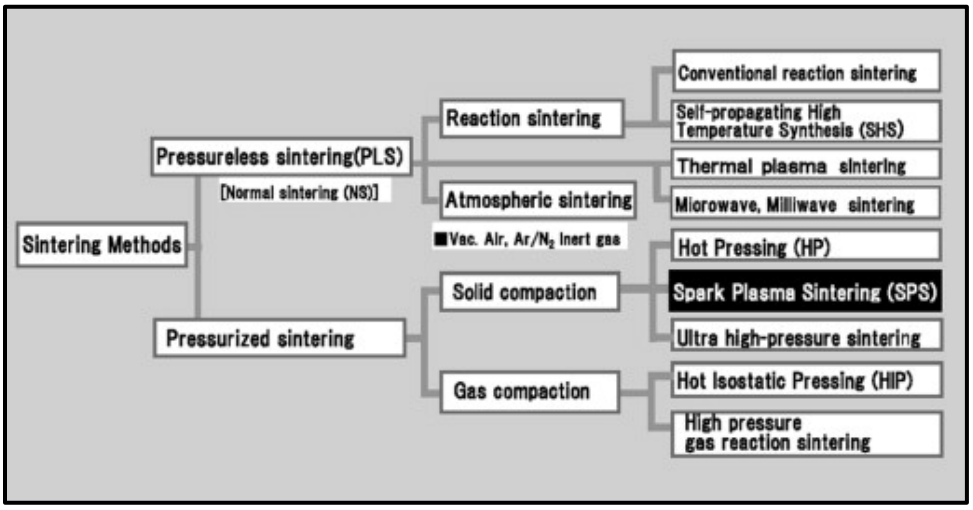

Figure 27: Various sintering techniques and how they relate to each other from the Handbook of Advanced Ceramics [226]**. Reproduced with permission from Elsevier.**

While not considered a novel technique anymore, SPS is still considered an energy saving and high-speed consolidation option over its sintering counterparts, requiring approximately 1/3 of the power required by conventional sintering [226]. Equipment used for SPS can usually generate temperatures up to 2400°C and compressive stresses up to 250 kN [227]. These capabilities of SPS lead to its ability to achieve fully dense, sintered parts in a matter of minutes, rather than several hours as is the case with traditional sintering techniques. SPS technology also

allows for very rapid heating and cooling rates, depending on the fragility of the material, and also minimal hold times at high temperature and pressure [219].

Although SPS is very similar to some other sintering techniques, such as hot pressing, it has generally resulted in more consistent, higher quality final materials. SPS has been shown to produce parts which have nearly 100% of the theoretical material density. Also, the high speeds and low temperatures required can reduce diffusion across grain boundaries, minimizing grain growth, and generating consistent, isotropic properties, causing SPS to remain one of the best ceramic processing techniques available [226], [227].

Spark Plasma Sintering of Oxide Ceramics

Oxide ceramics have been commonly sintered by SPS and reported in literature since this processing method was first adopted by the industry. The primary reasons that SPS is considered a valuable sintering method for oxides are the ability to produce consistently high-density materials in short processing times, which can help keep grain size small. Additionally, the uniform heating can be helpful in minimizing cracking of the resulting brittle ceramics.

Although SPS has been proven to be effective in fabricating oxide ceramics, it is also accompanied by unique challenges. Oxide ceramics are not electrically conductive, and therefore will not behave as other materials when subjected to the pulsed DC current within SPS. The current will typically not pass through oxides or other electrical insulating materials. Rather heating primarily occurs by contact with the upper and lower punch within the SPS mold. The electrically conductive punches are heated via electrical current, and effectively act as heating elements in a furnace. This allows SPS to maintain its effectiveness with oxide ceramics;

however, heating will potentially occur at a slower rate, and temperature gradients can develop within the material before an isothermal state is reached.

The second property of oxide ceramics, which presents a unique challenge during SPS is their extremely brittle nature. Most ceramics demonstrate brittle characteristics; however, oxide ceramics are among the most brittle and sensitive during fabrication. As a result, oxide ceramics can fracture during the SPS process unless the processing parameters are carefully optimized to allow for such delicate material. Cracking can be a result of thermal shock seen during processing, due to rapid changes in temperature. Additionally, if sintering occurs in one part of the specimen before another, internal pressure can be generated due to the continued volume change, which is more common in larger parts. Cracking can also be generated from high pressures contained in the small closed porosity that remains in the specimen after sintering. As the material sinters, and small closed pores take their final shape, the pressure within them will be equal and opposite to the pressure applied during sintering. Depending on the strength of the material, the size of the remaining pores, and the pressure parameters during the SPS process, the pressure within these pores can cause significant cracking to occur when the externally applied pressure is removed.

There have been many studies which have shown the effectiveness of SPS to process oxide ceramics, including $MgAl_2O_4$, Al_2O_3, MgO, $BaTiO_3$, and YAG [228]. Spark plasma sintered alumina has been well documented for years [229]–[231]. It has been shown that not only can SPS be used to fabricate high quality, fully dense, alumina parts, but the properties, specifically grain size and associated mechanical properties, can be easily tailored to meet the specific needs of the application. Several authors, such as Santanach et al. [232], Necina et al. [233], Vuksic et al. [234], and Pravarthana et al. [235], among others have done studies on the effects of SPS

parameters on the resulting alumina material properties, which have helped establish baselines for investigations into the SPS processing of similar oxides.

Several authors have also written about polycrystalline YAG ceramics processed by SPS. Sokol et al. demonstrates that YAG ceramics processed by SPS have excellent mechanical properties that exceed that of YAG single crystals [236]. Additionally, desirable optical properties are maintained via SPS processing as well. Wagner et al. [237], [238], Paygin et al. [239], and Chaim et al. [240]–[242], among others have shown that SPS is effective in creating transparent YAG ceramics, which are particularly useful for laser applications. Transparent ceramics require a processing method that is able to achieve near-theoretical density and remove essentially all porosity from the material. These authors have studied the effects of SPS parameters on the resultant properties of YAG ceramics, which have been useful in creating baseline recipes for the YAG materials processed in this study. These specific SPS parameters, which have been used to process dense YAG ceramics with excellent mechanical properties are reviewed in more detail in Section 3.2.3.

An et al. report the fabrication of high-quality, transparent Lu_2O_3 by means of SPS [110]. Specifically, grain size can be easily controlled by precise adjustments of the SPS parameters, which can impact density, transparency, and mechanical properties. Kumar et al. [243], Pejchal et al. [244], and Babin et al. [245] reported difficulties in processing doped and undoped LuAG transparent ceramics by means of SPS. The presence of porosity, primarily at the grain boundaries, caused the resultant materials to be opaque. Other authors, such as Cutler et al. [246] and Xu et al. [120] have had more success in processing LuAG transparent ceramics via SPS. However, even these authors report a certain amount of porosity remaining after processing. The variation in the quality of LuAG processed by SPS found in the literature suggests that LuAG

may be particularly difficult to process, especially when the need for absolute purity and density is required for transparency. However, the determination of optimal SPS parameters, which are required to achieve the highest quality materials, is still an ongoing area of study. The SPS parameters used in this study will be reported along with the associated material properties of the resultant polycrystalline LuAG ceramics.

3.2.2. Powder Preparation Procedures

Powder preparation procedures for both YAG and LuAG involve correctly portioning out the desired powder, mixing it into solution, ball-milling, drying, and straining. The final resultant powder is a soft, pure powder ready to be sintered with small particle size and minimal conglomerates. The entire process for a single material billet prepared from powder and processed into a sintered, solid material takes approximately 4-5 days. The powder preparation process described in this chapter was accomplished for all the material analyzed in this research effort, and took place in the material processing laboratories at the Air Force Research Laboratory, Materials and Manufacturing Directorate.

For all YAG variants powder preparation begins by carefully measuring out the doped or undoped YAG powder. The amount of powder that is used is based on the desired final dimensions of the sintered material. The available graphite molds for SPS were all cylindrical with inner diameters of 20 mm, 25 mm, and 40 mm. Because the final theoretical density of YAG is known, the weight of the powder can be determined. The desired volume of the resultant cylindrical material is determined by Equation 13:

$$V = t(\pi r^2) \qquad \text{(Equ. 13)}$$

where the thickness, t, was chosen to be 7 mm in order to accommodate the required thickness of the creep test specimens. Powder is measured out by weight. Therefore, in order to calculate the amount of powder needed to fabricate a specimen of known dimensions and known density, the following equation is used:

$$m = \rho v \quad \text{(Equ. 14)}$$

And substituting volume from Equation 13, the formula becomes:

$$m = \rho t(\pi r^2) \quad \text{(Equ. 15)}$$

YAG has a theoretical density of 4.56 g/cc. For a 40 mm diameter SPS mold, the equations for the necessary amount of YAG becomes:

$$m_{YAG} = \left(4.56 \frac{g}{cc}\right)(0.7\ cm)\pi(2\ cm)^2 = 40.11\ g \quad \text{(Equ. 16)}$$

Each variant of YAG was available and purchased as doped and undoped YAG powder, so it was not necessary to mix Al_2O_3 and Y_2O_3. In contrast, LuAG was fabricated by sintering a powder mixture of Lu_2O_3 and Al_2O_3. The overall weight of the LuAG powder is determined in the same fashion as with YAG, using the same sintered material dimensions and the theoretical density of LuAG, which is 6.73 g/cc. The equation used to determine the total amount of powder needed to fabricate LuAG is shown in Equation 17:

$$m_{LuAG} = \left(6.73 \frac{g}{cc}\right)(0.7\ cm)\pi(2\ cm)^2 = 59.2\ g \quad \text{(Equ. 17)}$$

Next it is necessary to determine the proportions of Lu_2O_3 and Al_2O_3 that are required to create 59.2 g of $Al_5Lu_3O_{12}$. The molar mass of Lu_2O_3 is 397.932 g/mol and Al_2O_3 is 101.96 g/mol. From the chemical formula of LuAG, the molar ratio of Lu_2O_3 to Al_2O_3 is 3:5. Therefore a ratio equation can be set up and solved for the required mass of Lu_2O_3 and Al_2O_3.

$$(3)\left(397.932 \frac{g}{mol}\right) : (5)\left(101.96 \frac{g}{mol}\right) = m_{Lu_2O_3} : m_{LuAG} - m_{Lu_2O_3} \quad \text{(Equ. 18)}$$

The powder is measured directly from the original container using a clean plastic spatula, and placed into a clean plastic container with a lid in order to be ball-milled. In addition to the powder, small alumina balls were added to the container along with approximately 200 g of either alcohol or deionized water. Different powder solutions using alcohol and water were investigated along with the associated drying methods in order to determine their effect on the resultant powder and processed material. Prior to ball milling the powder, the alumina balls were thoroughly cleaned with ethanol, put into a container, and placed on the spinner with no powder. The balls were left on the spinner for 24 hours in order to break off any small alumina shavings. Following spinning, the balls were cleaned again using ethanol. Once the powder was combined with the alumina balls and the liquid, the container was placed back on the spinner for 48 hours, shown in Figure 28. The spinner was set to a slow speed, rotating at approximately 14 rpm.

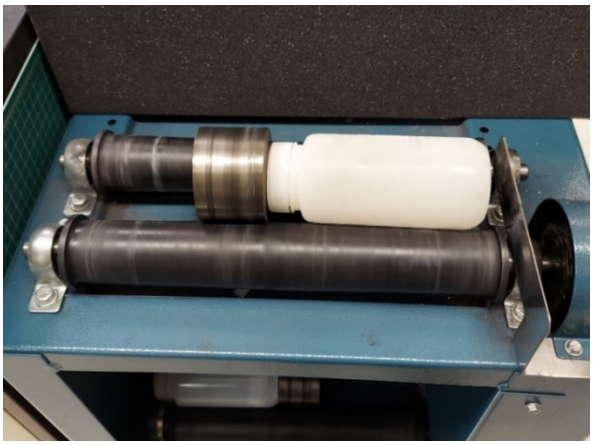

Figure 28: Ball milling powder solution on spinning rollers.

After ball milling is complete, the solution of ceramic powder in alcohol or water is carefully poured out and separated from the alumina balls. The drying method was determined based on the previous solvent chosen. Each water solution was dried by the freeze-drying method, and typically resulted in very soft, light powder, which was immediately ready for sintering. Each alcohol solution was placed in an open-air oven set to 120°C and left to dry for 24 hours. After

24 hours, the alcohol is completely evaporated, and only dry, dense powder remains. After the powder is dried in the oven, it is necessary to crush the powder into small particles using a mortar and pestle, and then pass the crushed particles through a fine-mesh sieve. For this material, a sieve with mesh number 100 and an aperture length of 150 μm was used. The result is a soft, light powder ready to be sintered.

The die and punch assembly is then constructed prior to adding any powder. The lower punch is placed into the lower opening of the graphite die, and two circular pieces of graphite foil of the same diameter as the die with a boro-nitride coating between them are placed inside the die in contact with the lower punch. Then a larger piece of graphite foil is cut and wrapped into a cylindrical shape to line the inside of the die. The powder is then carefully added inside the die, and should only be in direct contact with the graphite foil. Two more circular pieces of graphite foil with boro-nitride coating between them are placed on top of the powder, and the opening is sealed with the upper punch. The assembly laid on its side after loading the powder is shown in Figure 29.

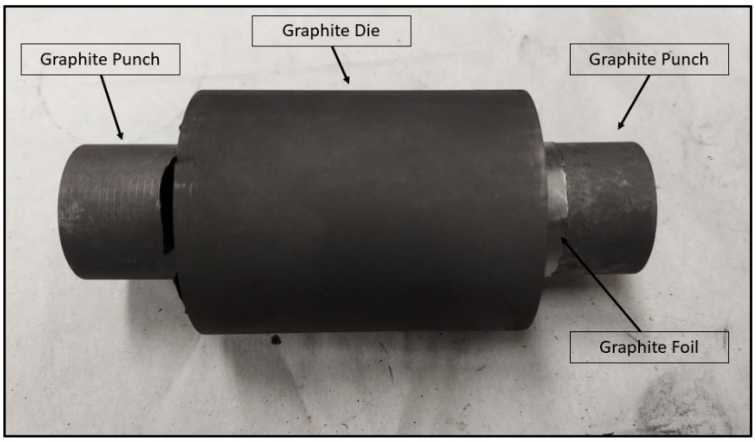

Figure 29: SPS die and punch assembly after loading the powder.

The assembly is then wrapped in a soft graphite insulation and is loaded into the SPS as is shown in Figure 30. The final step is to set the specific SPS parameters, which are discussed in the next section.

Figure 30: Loading the die and punch assembly into the enclosure for SPS.

3.2.3. Spark Plasma Sintering Parameters

There are many parameters that must be set during the SPS process. Specifically, maximum temperature, maximum pressure, hold times at the selected temperature and pressure, heating and cooling rates, and timing of pressure application and removal. For many materials, including YAG, several research studies have determined ideal ranges for the temperature and pressure that the powder should see during an SPS cycle [236], [240]–[242], [247]. These references can provide a valuable baseline; however, they may not be adequate or ideal processing parameters for all similar material types. Even when comparing different YAG materials processed by SPS, many factors, including the dopants, presence of impurities, the size of the SPS molds, and the precise care taken when loading the powder into the molds, can play a critical role in the

resulting material and its microstructure. For this reason, SPS parameters must often be investigated for a new type or quantity of material.

For this investigation into the microstructure, material properties, and mechanical behavior of YAG and LuAG, it was desired to determine ideal parameters for the SPS processing of these materials and to establish a "recipe" for their fabrication. In order to generate this recipe, SPS parameters were initially selected based on a review of published YAG and LuAG processing details. As material processing continued, and several billets were prepared for SPS, all the parameters were varied across the many SPS runs for each material. The two primary reasons for varying several SPS parameters are to determine their effects on material cracking and their effects on the resulting material grain size. These two resultant material characteristics were the most sensitive to any change in SPS parameters, and were also very significant in terms of the usability and effectiveness of the resultant material.

For each SPS run the following parameters were investigated:

- Maximum temperature
- Maximum pressure
- Hold time at maximum temperature and pressure
- Heating rate
- Cooling rate
- Addition of an isothermal hold time prior to sintering
- Removal of pressure prior to cooling

The temperature and pressure selected for SPS were carefully chosen. This selection will significantly and directly affect the final density, porosity, and grain size of the resultant ceramic material. These SPS parameters can also have a significant effect on the final material's optical

properties as well, which is valuable in laser applications. Additionally, the selected temperature and pressure will determine how much sintering time is required and will, therefore, affect the length of the SPS run time. For any material fabricated by means of SPS, there are generally a range of temperatures and pressures, which will allow sintering to successfully occur, such that a solid material will result. However, the quality may vary drastically, based on the possible effects listed above.

The specific temperatures chosen for the sintering of YAG and LuAG in this study were primarily chosen based on their effect on the resultant material's grain size. It is recognized that higher sintering temperatures lead to larger grain sizes in ceramics. This is the case with all types of ceramic sintering, including SPS. As higher sintering temperatures are chosen for SPS runs, the resultant material grain size will slowly increase until a threshold temperature is reached. At this point grain size can increase rapidly. For the purposes of obtaining an array of creep test specimens with various properties, it was desired to process ceramics with several different grain sizes. Therefore, several temperatures were selected for SPS, based on the range of acceptable temperatures from the literature and from previous in-house SPS trials. Hence different temperatures within this range were applied to the processing of both YAG and LuAG. It was determined that SPS temperatures should be set between 1300°C and 1550°C, and adjusting the temperature within this range by as little as 50°C could affect the resulting grain size [240]–[242], [247]–[250].

The pressure parameter during an SPS cycle is similarly critical in obtaining reliably consistent, high-quality materials. The amount of compressive stress applied to the powder during SPS will directly affect the amount of densification that will occur, which will determine whether or not the resultant material is fully sintered. Also, the pressure setting along with the

temperature setting will dictate for what length of time the SPS run should last. Very high pressures have been used for processing similar materials, up to 100 MPa. These high pressures are used especially for the fabrication of optically transparent ceramics, where 100% density is critical. In these cases, SPS runs only need to last a few minutes in some cases depending on the size of the part. However, the highest pressures can also cause problems during sintering, especially for large, brittle materials, which is the case for the oxide ceramics in this study.

The large diameter and thickness of the resultant materials combined with the very sensitive and fragile nature of these ceramics in the presence of any flaws, suggest that lower pressure settings for longer times could be beneficial in reducing cracking and breaking during the sintering process. Small internal porosity if not completely removed during SPS, will remain in the material after it solidifies. These small pores will maintain residual internal pressure equal to the initial external applied compressive stress. Therefore, upon pressure removal, internal voids can cause the final material to crack.

It is often necessary to obtain 100% dense materials for use in optical applications where transparency is required. The presence of voids in not fully dense ceramic materials will prevent transparency, and cause the resulting materials to be ineffective in their primary application. However, for the purposes of obtaining consistent, reliable mechanical test specimens, materials with densities of approximately 98% - 99% of the theoretical material density will exhibit near maximum mechanical performance, and very small internal porosity should not affect the overall mechanical results. Therefore, lower pressures and extended times were selected for the processing of YAG and LuAG in this study. Analysis of the results of previous oxide ceramic processing resulted in the selection of pressure settings between 20 MPa and 50 MPa as likely

parameters to produce near theoretical density parts while attempting to reduce cracking and maintain the structural integrity of the larger diameter parts.

At these temperature and pressure settings, it was determined that maximum compaction and densification will occur in less than 15 minutes. Figure 31 shows an example of an SPS cycle under the conditions mentioned above. The bulk of compaction occurs within approximately 10 minutes, while slow final densification occurs over a longer span of time during cooling. Therefore, hold times at maximum temperature and pressure were selected between 15 and 30 minutes.

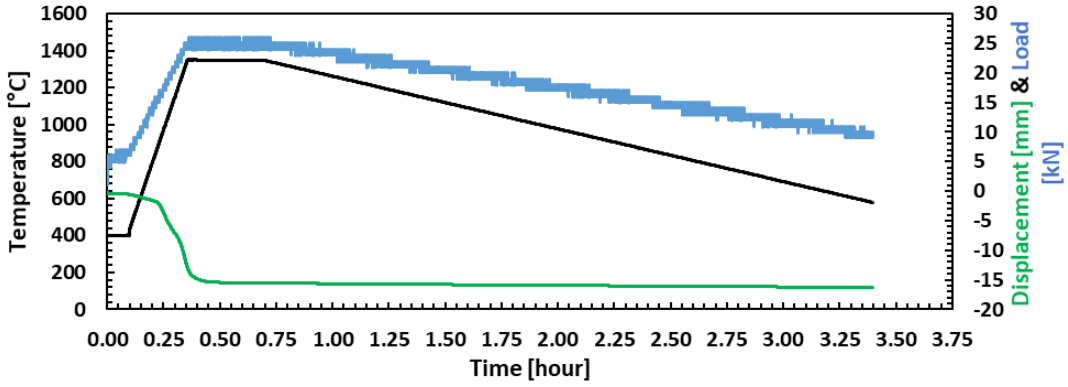

Figure 31: Typical SPS processing cycle with parameter settings of 1350°C and 20 MPa.

The hold time at maximum temperature can directly impact grain growth. The longer the material remains at maximum temperature, the more grain growth can occur. Therefore, it is not typically desired to allow SPS cycles to run excessively long, as grain growth can perpetuate and eventually the material will begin to crack and lose all strength. It was determined that by setting the SPS hold time to 15 minutes for the majority of the processing runs, grain growth remained expected and manageable, and the variation in grain size was caused primarily by the temperature setting and no by varying the hold time. Therefore, the vast majority of the SPS runs were kept to 15 minutes.

Heating and cooling rates were significant in maintaining homogeneous temperature throughout the material within the die during sintering and also minimizing the potential for cracking by reducing the possibility of thermal shock once the material was fully sintered. The materials in this study are electrical insulators, which means that heating within SPS occurs by contact with the upper and lower punch. An electric current is typically used to heat the material rapidly and evenly; however, in the case of non-electrically conductive materials, the current will not pass through the material, and heating occurs by conduction through the heated punches in contact with the powder. This also means that even heating can become a problem under such rapid sintering conditions, and temperature gradients can form causing a portion of the powder to sinter first. Specifically, as heat enters the sample powder from external contact with the heated SPS punches and die, the outside volume of powder can sinter before the center. This can constrain the inner powder during sintering and the outer solid material can crack.

As a preventative measure to ensure even heating and to minimize cracking, a typical rapid heating rate was slowed to 35°C/min and an isothermal segment was added during heating. It occurred during heat up at 1000°C just prior to sintering for 5 minutes. This allows the powder to reach a uniform temperature just prior to sintering and allow densification and sintering to occur evenly throughout the entire volume of ceramic powder [251]. Many different types of materials will be resilient and forgiving of these potential problems with cracking; however, the brittle and fragile nature of YAG and LuAG requires this type of planning and modifications to typical SPS cycles.

Similarly, the cooling rates were reduced to prevent thermal shock or rapid change in volume of the final sintered material, which could also contribute to cracking and the formation of

residual stresses within the material. Cooling rates began at 20°C/min, and were reduced to as low as 2°C/min.

All these SPS parameters were varied for different billets of each material. Parameters were adjusted in order to find the optimal settings to reduce cracking and to develop a consistent procedure for high-quality oxide ceramics processed via SPS. However, once successful billets were obtained and optimal settings and procedures were determined, the SPS parameters continued to be adjusted from run to run within the determined optimal range of settings in order to produce a wide variety of grain sizes for each material. The complete table of the SPS parameter settings that were used for each billet is shown in Appendix A. Additionally, pictures and properties of each SPS billet, along with profile graphs of each SPS cycle can be found in Appendix C.

3.2.4. Post processing and Overview of Resultant Materials

After each SPS run, the pucks were carefully removed from the mold. The appearance of both YAG and LuAG pucks is dark in color, almost black and opaque, due to the residual Carbon content absorbed during sintering. A sintered YAG puck is shown in Figure 32, prior to any heat treatment.

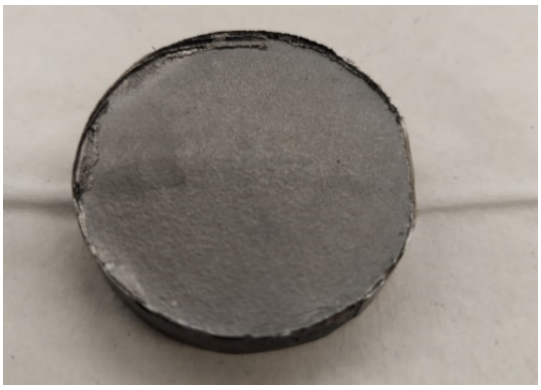

Figure 32: Example of 40-mm diameter YAG puck following SPS before heat treatment. Raised edges are due to the remaining graphite foil wrap, which is placed around the powder before sintering occurs.

Following sintering each puck is quickly sand blasted in order to remove any lose flaky material that did not fully sinter as well as the remaining graphite foil wrap, which can often stick to the sides of the puck. Next, the pucks are heat treated in order to remove the remaining Carbon content. Each puck is placed into an alumina boat and carefully placed into a tube furnace with a minimum inner diameter of 2 inches so that the 40 mm pucks can fit without contacting the sides of the tube. The steps of each heat treatment are as follows:

- Ramp from room temperature to 1500°C at 60°C/min
- Soak at 1500°C for 10 hours
- Cool slowly at 10°C/min back to room temperature

Following heat treatment, the pucks are mostly white in appearance, but vary slightly depending on the material variant and the specific physical properties of each puck. Pucks with a higher density, close to the theoretical material density, can appear partially transparent; however, the optical properties were not under investigation in this study, so SPS parameters were chosen in order to minimize transparency. Some processed materials maintained a small carbon content, and as a result, appeared slightly gray in color. Additionally, YAG pucks,

which were doped with Erbium appeared light pink in color, which was the only notable and consistent difference in appearance across each material variant. Figure 33 shows a side-by-side comparison of each YAG variant, and Figure 34 shows a similar 40 mm puck of LuAG following sintering and heat treatment.

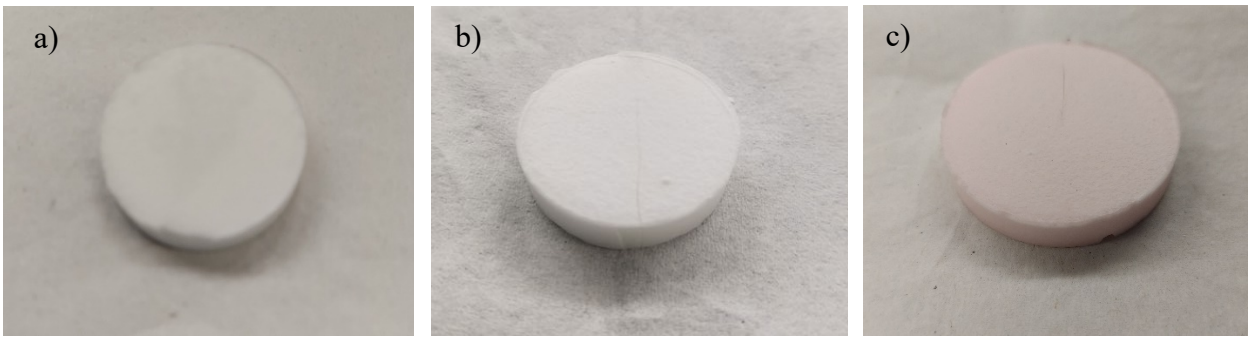

Figure 33: 40-mm diameter YAG pucks following sintering and heat treatment. Small hairline fractures are partially visible. Material variants include: a) Undoped YAG b) 2at% Yb-doped YAG c) 2at% Er-doped YAG

Figure 34: 40-mm diameter LuAG puck following sintering and heat treatment.

Each processed material was approximately 7 mm thick following SPS, but varied slightly based on the final amount of densification that occurred during processing. Additionally, throughout this entire SPS study, pucks were processed using SPS molds of three different diameters: 20 mm, 25 mm, and 40 mm. Larger puck sizes are ideal for obtaining mechanical test specimens, as more specimens can be produced for microstructural analysis and mechanical

testing from a single processing run. This also ensures more continuity of properties across more specimens, which come from one processed puck. However, significant cracking was observed in several of the larger pucks, while the smaller pucks were typically undamaged. As a result, several SPS runs were conducted with smaller mold sizes.

SPS parameters were tailored slightly, in order to determine their effects on the structural integrity of the resultant material, and to ultimately minimize cracking in the 40 mm diameter pucks. The varying SPS parameters certainly had significant effects on the material microstructure and the associated material properties, as is shown in the later chapter focusing on the material microstructure; however, adjusting specific SPS parameters proved to be less effective at minimizing the inevitable cracking that often occurred within the 40 mm diameter pucks. Figure 35 shows a damaged 40 mm diameter puck following processing.

Figure 35: A damaged 40-mm diameter LuAG puck following processing with several distinct cracks through the thickness.

After conducting a thorough investigation into the possible causes of cracking during SPS processing, it was concluded that varying the SPS parameters within reasonable limits does not have a significant and consistent effect on the final cracking of the material. Rather, the most effective way to minimize cracking was to ensure that uniform heating occurs across the cross section of the material by careful and delicate handling of the powder and die preparation prior to

sintering. In order to minimize temperature gradients within the specimen during heating, excessive care must be taken while loading the powder, ensuring that the graphite foil wrap and upper and lower covers are perfectly cut to the inner dimensions of the mold, leaving no uncovered powder and no overlapping of graphite. The addition of a boro-nitride coating onto the upper and lower punches during SPS was also added in order to reduce cracking by minimizing excessive heating along the puck edges by means of electric current.

Each specimen was given an alphanumeric designation in order to keep track of processing parameters and material properties. The format of each designation is as follows:

Material Abbreviation – Dopant Abbreviation – Overall Billet # – Puck Diameter

The first character identifying the material is the first letter of the material (either L or Y for LuAG or YAG, respectively). Additionally, if no dopant was present then the second field is removed. For example, the second YAG billet, which had a 40 mm diameter, would be written as follows: *Y-2-40*. The first LuAG billet, which had a 20 mm diameter, would be written as follows: *L-1-20*. Finally, the third 2at% Yb-doped YAG billet, which had a 40 mm diameter, would be written as follows: Y-Yb-3-40.

In total 20 LuAG pucks were processed via SPS. Initially a single 20-mm LuAG puck was processed to prove the processing method and results. Seven more 25-mm LuAG pucks were processed, and 12 more 40-mm LuAG pucks were processed. These quantities are tabulated in Table 11. 14 undoped YAG billets were processed, three of which were 25 mm in diameter and the remaining were all 40 mm. Undoped YAG names and sizes are tabulated in Table 12. 10 billets were processed for 2at% Er-doped YAG, four of which were 25 mm in diameter and the remaining were all 40 mm. Er-doped YAG names and sizes are tabulated in Table 13. Finally, 10 billets were processed for 2at% Yb-doped YAG, one of which was 20 mm in diameter, three

were 25 mm in diameter, and the remaining were all 40 mm. Yb-doped YAG names and sizes are tabulated in Table 14.

Table 11: LuAG Sample Data

Processed LuAG Pucks								
Billet Number	Billet Name	Diameter [mm]	Billet Number	Billet Name	Diameter [mm]	Billet Number	Billet Name	Diameter [mm]
1	L-1-20	20	8	L-8-25	25	15	L-15-25	25
2	L-2-25	25	9	L-9-25	25	16	L-16-25	25
3	L-3-40	40	10	L-10-40	40	17	L-17-40	40
4	L-4-40	40	11	L-11-40	40	18	L-18-40	40
5	L-5-40	40	12	L-12-40	40	19	L-19-40	40
6	L-6-40	40	13	L-13-40	40	20	L-20-25	25
7	L-7-40	40	14	L-14-25	25			

Table 12: Undoped YAG Sample Data

Processed YAG Pucks								
Billet Number	Billet Name	Diameter [mm]	Billet Number	Billet Name	Diameter [mm]	Billet Number	Billet Name	Diameter [mm]
1	Y-1-25	25	6	Y-6-25	25	11	Y-11-40	40
2	Y-2-40	40	7	Y-7-40	40	12	Y-12-40	40
3	Y-3-40	40	8	Y-8-40	40	13	Y-13-40	40
4	Y-4-40	40	9	Y-9-40	40	14	Y-14-40	40
5	Y-5-25	25	10	Y-10-40	40			

Table 13: 2at% Er-Doped YAG Sample Data

Processed 2at% Er-Doped YAG Pucks								
Billet Number	Billet Name	Diameter [mm]	Billet Number	Billet Name	Diameter [mm]	Billet Number	Billet Name	Diameter [mm]
1	Y-Er-1-40	40	5	Y-Er-5-25	25	9	Y-Er-9-40	40
2	Y-Er-2-40	40	6	Y-Er-6-25	25	10	Y-Er-10-40	40
3	Y-Er-3-25	25	7	Y-Er-7-40	40			
4	Y-Er-4-25	25	8	Y-Er-8-40	40			

Table 14: 2at% Yb-Doped YAG Sample Data

Processed 2at% Yb-Doped YAG Pucks								
Billet Number	Billet Name	Diameter [mm]	Billet Number	Billet Name	Diameter [mm]	Billet Number	Billet Name	Diameter [mm]
1	Y-Yb-1-20	20	5	Y-Yb-5-25	25	9	Y-Yb-9-40	40
2	Y-Yb-2-25	25	6	Y-Yb-6-40	40	10	Y-Yb-10-40	40
3	Y-Yb-3-40	40	7	Y-Yb-7-40	40			
4	Y-Yb-4-25	25	8	Y-Yb-8-40	40			

Each puck was cut into several specimens following processing. Small pieces of essentially any shape, which were too small to be used for any mechanical test, were cut from each puck in order to conduct a thorough microstructural investigation, primarily by means of scanning electron microscopy. Remaining small pieces with unspecified dimensions were used to determine the material density, the possible presence of impurities, and to analyze the material composition. A detailed description of specimens used for microstructural evaluation is included in Section 4.1. Larger specimens of specific dimensions and geometry were also cut from each puck and used for creep testing. A 40-mm diameter puck with no cracks could theoretically be used to fabricate up to six creep test specimens. However, it was more common to only produce between two and four creep test specimens due to cracking and chipping during processing and specimen fabrication. A detailed description of creep test specimen design and fabrication is included in Section 5.1.

4. Characterization and Microstructural Analysis

4.1. Scanning Electron Microscope Specimen Preparation

Once processing via SPS was complete, and each puck was heat treated to remove any remaining Carbon content, each puck was cut into small specimens for microstructural analysis. At least 3 small pieces were removed from each puck in order to take density measurements, undergo impurity analysis, and to be analyzed in the scanning electron microscope (SEM). The specific size and shape of these specimens was not critically important. However, specimens prepared for the SEM were typically cut from each puck with one flat surface at least 10 mm in length.

In order to obtain clear images of each specimen in the SEM, they were each mounted in epoxy and polished so that small details and features would be visible on the surface and would not be obstructed by imperfections in a rough, scratched finish. For a clear view of the surface porosity and the grain structure within the SEM, a detailed sample preparation procedure was developed and applied to each specimen prior to viewing. For standard microstructural evaluation in the SEM, each specimen was mounted in an epoxy puck in order to easily handle the specimen during polishing. Two examples are shown in Figure 36.

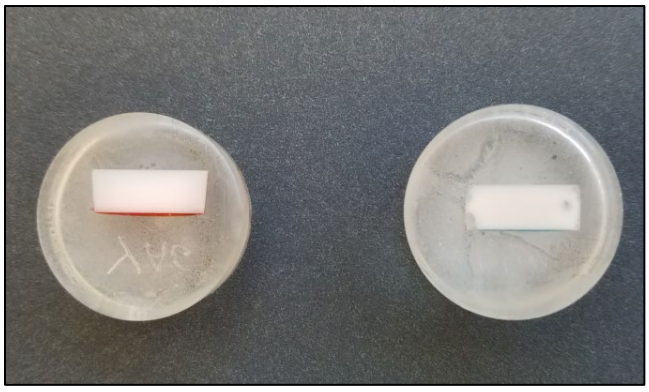

Figure 36: YAG and LuAG specimens mounted in epoxy pucks for microscopic evaluation.

Once the specimens were mounted in epoxy, the surfaces could be thoroughly polished. All pucks were leveled, ground, and polished using a Buehler Polimet I manual polishing wheel, shown in Figure 37.

Figure 37: Buehler Polimet I manual polishing wheel.

Each sample must be polished using a sequential order of polishing pads, beginning with a relatively rough low-grit abrasive pad to remove the outer layer of epoxy and level the surface of the specimen. Then various polishing pads were used with sequentially finer diamond particle, water-based suspensions. For YAG and LuAG specimens, each polishing step lasts for approximately 5-10 minutes and requires a moderate amount of pressure placed evenly on the backside of the puck while held on the polishing wheel. Several iterations of sample polishing were required in order to develop a specific procedure, which successfully removed enough imperfections and scratches from the sample surface, producing a mirror-like finish. Several dissertations and published papers were reviewed in order to determine the general procedures for polishing hard ceramic specimens [30], [31], [252], [253]; however, specific procedures with adequate details for these materials were not found in the literature. Ultimately, the most effective method for producing successful polishing procedures came from trial and error based

loosely on procedures established previously for similar materials. A detailed procedure for sample preparation, to include mounting in epoxy as well as the order and type of polishing pads used to prepare the surface of each specimen for the SEM, can be found in Appendix D.

4.2. Density Measurements

The density of each specimen was measured prior to any creep testing or further material characterization. Density is a critical material property when determining the porosity present in the material and is important when comparing creep rates to similar materials. It also helps determine the success of SPS as a processing method, as it is typically chosen because of its ability to create near theoretical density ceramics. The measured density can then be compared to the theoretical density of each material to determine the overall quality of the processed ceramic and to determine expectations of mechanical performance.

Density was determined for each specimen by two methods: the Archimedes density measurement method and by Helium pycnometry. Results were averaged together to obtain the most accurate approximation of the true bulk density of each specimen.

Density Measurements by the Archimedes Method

To obtain the bulk density of a material one must simply divide the total mass by the volume of the material. This becomes more difficult when the material has an irregular shape or small imperfections, making the precise volume difficult to determine. In order to determine the accurate volume of each specimen, the Archimedes principle is used. The Archimedes principle states that “a body immersed in fluid is buoyed up by a force equal to the weight of the fluid

displaced" [254]. Therefore, the buoyancy force acting on the object is equal to the volume of the object multiplied by the density of the fluid and the force of gravity, represented by Equation 19.

$$F_b = (\rho_f V)g \quad \text{(Equ. 19)}$$

Because the density of a common fluid, such as water, ρ_f, is well known along with the force due to gravity, g, the volume, V, can be found by determining the buoyancy force, F_b. The buoyancy force can be determined by simply subtracting the weight of the material in water from the weight of the material in air. Therefore, the precise volume of the material specimen can be determined by combining these two ideas into the following equation:

$$V = \frac{W_{air} - W_{water}}{g\rho_f} \quad \text{(Equ. 20)}$$

The final density of the material is then calculated using Equation 21 [254]:

$$\rho = \frac{m}{V} = \frac{W_{air}\rho_f}{W_{air} - W_{water}} \quad \text{(Equ. 21)}$$

The Archimedes density measurement was accomplished by using a laboratory balance and an apparatus that allows the material to be immersed in water and the corresponding mass to be measured, which includes the opposite buoyancy force. Three mass measurements are taken during the Archimedes density measurement procedure: the dry mass of the material, the mass of the material while fully immersed in water, and the "wet" mass of the material, which is measured in air with all open porosity fully saturated with water. The procedures for the Archimedes density measurements are visualized in the following Figures. Figure 38 shows the dry sample weighed in a standard sample tray. Figure 39 shows the wire basket held above the scale with no water. Figure 40 shows the sample held in the wire basket immersed in water.

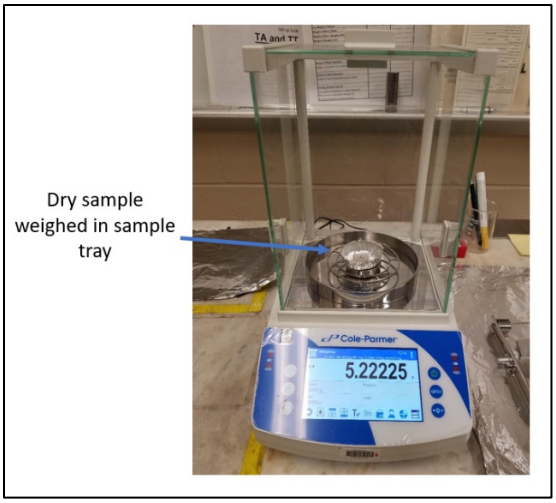

Figure 38: Dry sample weighed on a laboratory balance.

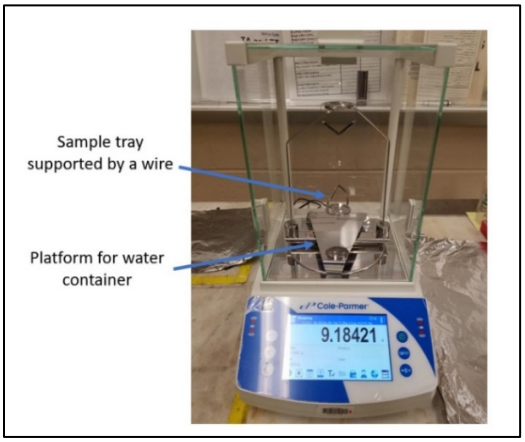

Figure 39: Archimedes wire basket hanging above scale with no water.

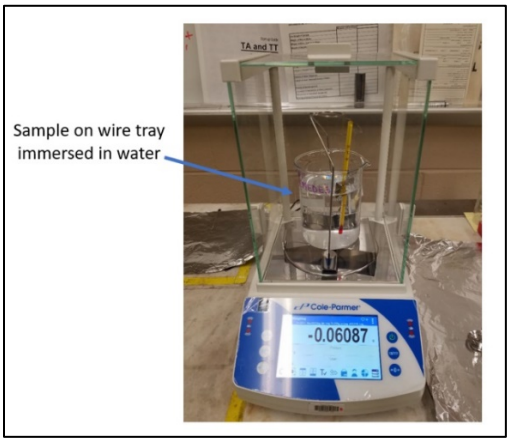

Figure 40: Sample immersed in water and held in wire basket.

The Archimedes density measurement procedures were accomplished three separate times over three different days for each specimen. The water temperature was measured during each procedure in order to ensure the density of the distilled water was accurate. Once the dry mass, the mass of the sample immersed in water, and the mass of the wet sample in air were recorded, the density was calculated using Equation 21 described above.

Density Measurements by a Helium Pycnometer

In order to obtain the most accurate density measurements for each specimen and to verify density measurements found by means of the Archimedes method, the densities of each specimen was measured by means of a Helium pycnometer. A pycnometer measures the volume of a small material specimen by injecting a gas, such as Helium, into a chamber of known volume, containing the specimen. The resulting equilibrium pressure change is measured and compared with the corresponding pressure obtained from the empty chamber with calibrated volume [255]. If the mass of the specimen is known, the apparent density of the material can be determined. Helium pycnometry is considered an accurate method of determining specimen density for small samples of unknown or irregular volumes [255]. Figure 41 shows a diagram of the Micromeritics AccuPyc 1330 Helium pycnometer, which was used to measure the density of each specimen. Figure 42 shows a schematic of the internal layout of the pipes and chambers within the pycnometer system, presented in the AccuPyc 1330 operator's manual [256].

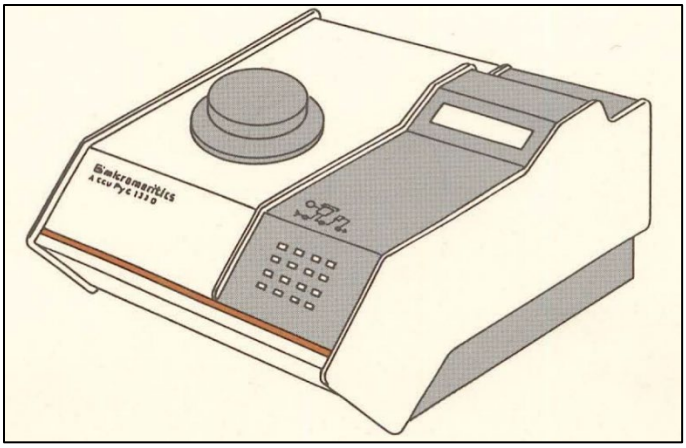

Figure 41: AccuPyc 1330 Helium Pycnometer used for density measurements. Reproduced with permission from the Micromeritics Instrument Corporation [256]**.**

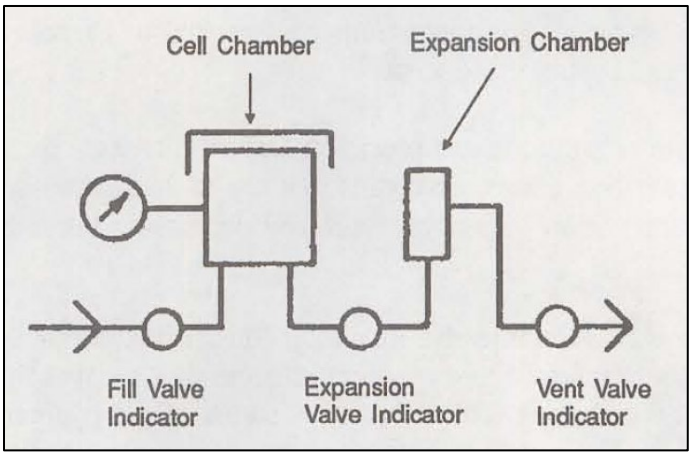

Figure 42: Schematic of the internal layout of the AccuPyc 1330 Helium Pycnometer. Reproduced with permission from the Micromeritics Instrument Corporation [256]**.**

Summary of Density Results

For each specimen multiple density measurements were averaged and then compared to the theoretical density of each material found in the literature. The density measurements can be found in the tables in Appendix B, which lists all the creep specimen dimensions, mass, and density. Appendix B also shows the densities of each creep specimen from the same SPS billet

averaged together, which are then shown as a percentage of the theoretical density of each material.

The theoretical density of YAG as reported in the literature is 4.6 g/cc. It should be noted that the published theoretical density of YAG has varied between sources [27], [257], [258]. The higher published density of 4.6 g/cc was chosen for use here to provide a conservative comparison [257]. However, some sources report theoretical densities from 4.53 to 4.56 g/cc for YAG [27], [258]. Similarly the higher published theoretical density of LuAG is 6.71 g/cc as found in literature [109].

Generally, the densities of the YAG and LuAG specimens were found to be very near theoretical density, indicating the high quality of the processing method. For YAG specimens, doped and undoped, the measured densities were found to be between 97% and 100% of the theoretical density, with the majority of specimens falling between 98% and 99.5%. The densities of the LuAG specimens were found to be slightly lower on average, with a range between 96% to 100% of the theoretical density.

4.3. Grain Size Analysis

4.3.1. Overview of Grain Size Analysis in the SEM

Grains in a crystalline material refer to individual crystals with long range atomic order and consistent orientation [259]. Each grain contains a consistent pattern of atoms. Polycrystalline materials possess many crystal grains in many orientations. The size of each grain may be small (< 1 μm), but they can contain thousands or millions of atoms. The regions between each grain are called grain boundaries, which are regions of short-range disorder and inconsistent atomic

arrangements [259]. Atoms along a grain boundary may not align with any of the adjacent grains, and are not as densely packed. These atoms are not ordered like the adjacent crystal structures, and typically possess a higher internal energy. A diagram of the atomic arrangement and orientation within crystal grains is shown in Figure 43.

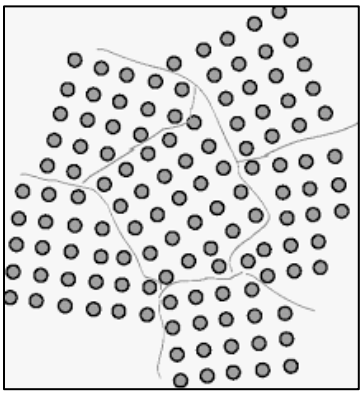

Figure 43: Diagram of crystal orientations within ceramic grains.

These characteristics of grains in a polycrystalline ceramic material significantly impact the mechanical properties. Additionally, the size and shape of grains and grain boundaries impact diffusion in a material, which greatly affects deformation at high temperatures. Since grain boundaries are regions of less densely-packed, disordered atoms, the rate of diffusion can be increased at the grain boundaries, as there are generally more vacancies than are found in the crystal lattice within a grain. Therefore, the characteristics of grains, specifically their size, are critical when studying the creep behavior of ceramics, especially when creep primarily occurs by atomic diffusion.

For this reason, grain size and structure are typically analyzed in order to understand the high-temperature behavior of polycrystalline, ceramic materials. Ceramic grains are not perfect spheres, but rather are irregular polyhedrons, and are generally closely packed together, encompassing the entire material microstructure. Quantifying the size of the grains within a polycrystalline ceramic can be an efficient way to understand and predict the material behavior,

and compare performance with similar materials. Fine-grained materials are generally denser with less porosity, and are stronger at room temperature than materials with larger grains. However, larger grains contribute to increased creep resistance at elevated temperature. A material with larger grains will have fewer grain boundaries, and therefore, will see less grain boundary sliding during deformation.

The microstructural characteristics of each SPS billet was determined by analysis in a TESCAN MIRA 3 scanning electron microscope (SEM), shown in Figure 44.

Figure 44: The Tescan Mira 3 Scanning electron microscope, used for all microstructural analysis and grain size measurements.

The various SEM settings were carefully scrutinized in order to determine the parameters that resulted in the best images of the ceramic grains. This issue is complicated further due to the fact that these oxide ceramics are nonconductive, which means they must be carefully prepared and coated with a conductive material, in order to obtain clear images in the SEM. In this case, it was necessary to coat each polished SEM sample with approximately 10 nm of Carbon.

The grains of YAG and LuAG became the most visible in the SEM when receiving a signal from the detection of backscattered electrons. The two primary types of electrons detected in an SEM are secondary electrons (SEs) and backscattered electrons (BSEs), which both result from a targeted beam of primary electrons coming in contact with the surface of a sample. SEs originate from the specimen itself. They are low-energy electrons that have been excited and ejected from their positions within the target atoms by contact with the primary electron beam. SEs are a result of inelastic interactions between the beam and the specimen. Because SEs are low energy electrons, they typically originate from only a few nanometers below the sample surface. This SEM mode is typically used for imaging very precise and detailed surface topography of a specimen.

BSEs are electrons that originated from the primary electron beam and have been reflected back after elastic interactions with the specimen. They typically can reach deeper below the surface of the specimen, so features just below the surface can be observed, such as sub-surface porosity. BSEs are highly sensitive to the specific attributes of the atoms with which they interact, so they typically reveal significant contrast between different elements. This can be useful for identifying various elemental phases within a specimen. BSEs can also provide similar contrast due to interactions with different crystal orientations, and, therefore, can detect grains and grain boundaries present at the sample surface.

Grain sizes for each billet of YAG and LuAG were widely varied due to the different SPS parameter settings used during processing. The smallest grain sizes in fine-grained materials were determined to be approximately 0.3 μm. The largest grain sizes were determined to be greater than 10 μm. These grain sizes, as well as several other grain sizes within this range, were similarly found for billets of each material variant in this study, including doped YAG.

Examples of SEM micrographs obtained from fine-grained billets of each material variant used in this study are shown in Figure 45.

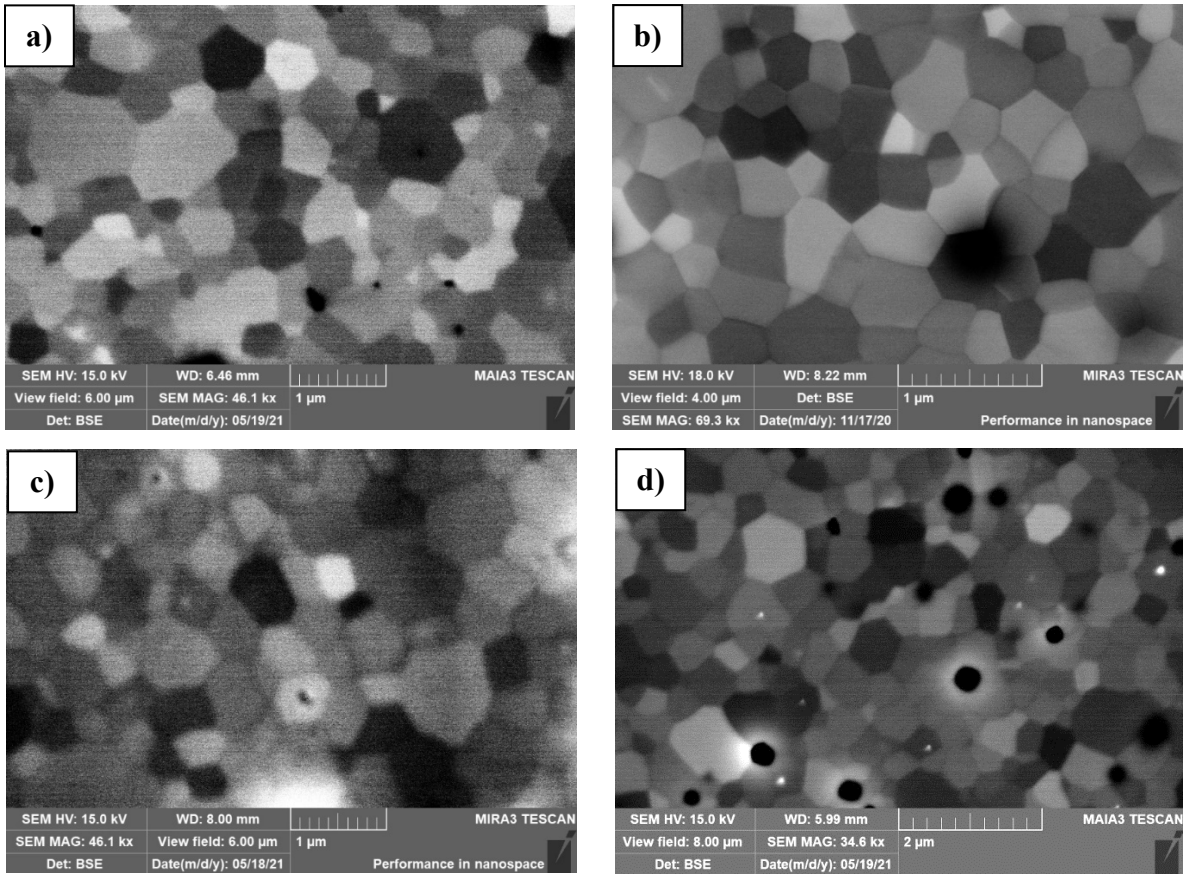

Figure 45: SEM micrographs of fine-grained billets of YAG and LuAG: a) Undoped YAG from billet Y-6-40; b) Yb-doped YAG from billet Y-Yb-1-20; c) Er-doped YAG from billet Y-Er-8-40, d) Undoped LuAG from billet L-7-40.

A primary observation from Figure 45 is that the microstructures of each material variant are nearly identical. They each possess close-packed, polyhedron grains, and also reveal minimal porosity. These characteristics suggest that each material would perform similarly in creep under the same conditions. Two more examples of SEM micrographs obtained from large-grained billets of YAG and LuAG are shown in Figure 46.

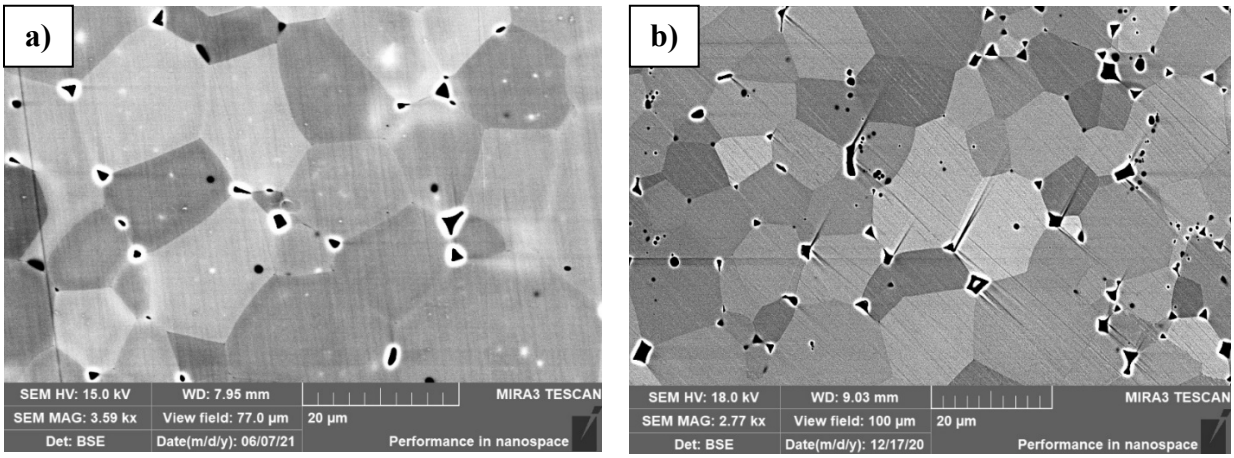

Figure 46: SEM micrographs of large-grained billets of YAG and LuAG: a) Undoped YAG from billet Y-13-40; b) Undoped LuAG from billet L-1-40.

The grains observed in Figure 46 are significantly larger than the grains observed in Figure 45. There is also additional porosity observed in the larger-grained specimens. The vast majority of the pores appear along the grin boundaries, which are formed during sintering. Generally, large-grained ceramics tend to be more porous, which also contributes to their reduced strength compared to fine-grained ceramics. However, large grains can be very advantageous in creep, which will be investigated in later sections.

4.3.2. Grain Size Measurement Techniques

These SEM micrographs were also used to quantify the average grain size of each material billet. Ceramic grains can be measured in a variety of ways. One such way is by determining the grain size number, described by ASTM E112-13 [260]. This ASTM standard describes two primary methods: the *planimetric method* and the *intercept method*. The planimetric method involves counting the number of grains within a known area. A commonly used version of this method typically utilizes Equation 22, where n is the number of grains per square inch, and G is the ASTM grain size number.

$$n = 2^{G-1} \quad \text{(Equ. 22)}$$

The grain size number is inversely proportional to the actual size of the grains. In other words, for smaller grains, the grain size number is larger. The second method for determining the grain size number is the intercept method. This involves drawing a line over an image of the surface of the material containing grains. Then the number of intersected grains or grain boundaries are counted to reveal the number of grains per line of known length. From this measurement, the grain size number can be determined.

Besides the ASTM grain size number, the most common way to quantify the average size of grains is by determining the average grain diameter. Since grains are not circular, the average grain diameter is actually the diameter of a circle of equivalent area. This equivalent diameter of grains is typically referred to as the average grain size. The intercept method is commonly used to determine the average grain size as well. As was described above, a line, or several lines are drawn over a clear surface image of a material containing visible grains. The length of the line is divided by the number of intersected grains to reveal the average grain size. The greater the length of the lines and the more grains intersected, the more accurate this method will be.

In recent years, the most accurate method considered by many for determining grain size is the use of image analysis software. If there is significant visual contrast between neighboring grains, then the details each grain can be quantified including its diameter, area, aspect ratio, length of grain boundaries, among others. Because this method can be automated, it can be performed over thousands of grains, creating much more statistically significant results.
In order to analyze the grains and quantify the average grain size in polycrystalline YAG and LuAG in this study, the average grain diameter was determined by the manual intercept method, and also by digital image analysis of grains after thresholding. These two methods gave very

consistent results, and eventually became equally valuable and interchangeable when analyzing grain size.

When determining grain size by means of the intercept method, at least five lines were manually drawn over an SEM image with clearly visible grains using Adobe Photoshop. The five lines were spread out over the entire image, and were drawn such that they overlapped as many grains as possible. Figure 47 shows micrographs of two different YAG specimens and Figure 48 shows micrographs of two different LuAG specimens, whose grain sizes were quantified by the use of the intercept method. The five lines are visible in each micrograph.

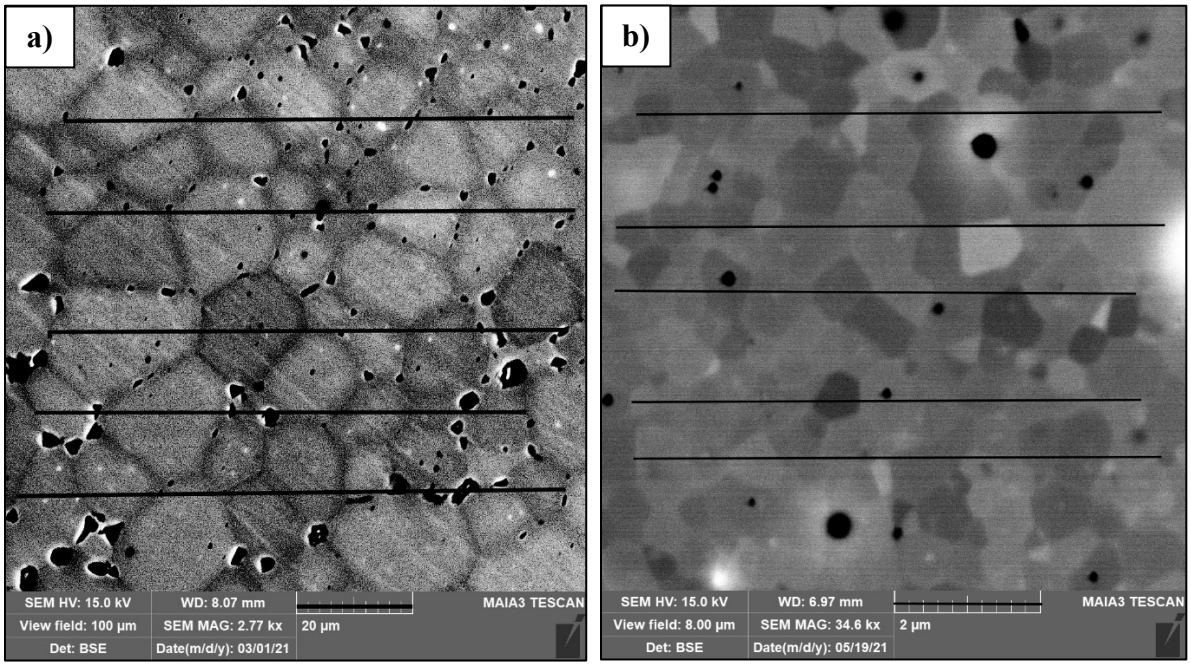

Figure 47: Micrographs of two different YAG specimens with lines used to determine the average grain size by means of the intercept method: a) Image from billet Y-2-40 and b) Image from billet Y-4-40.

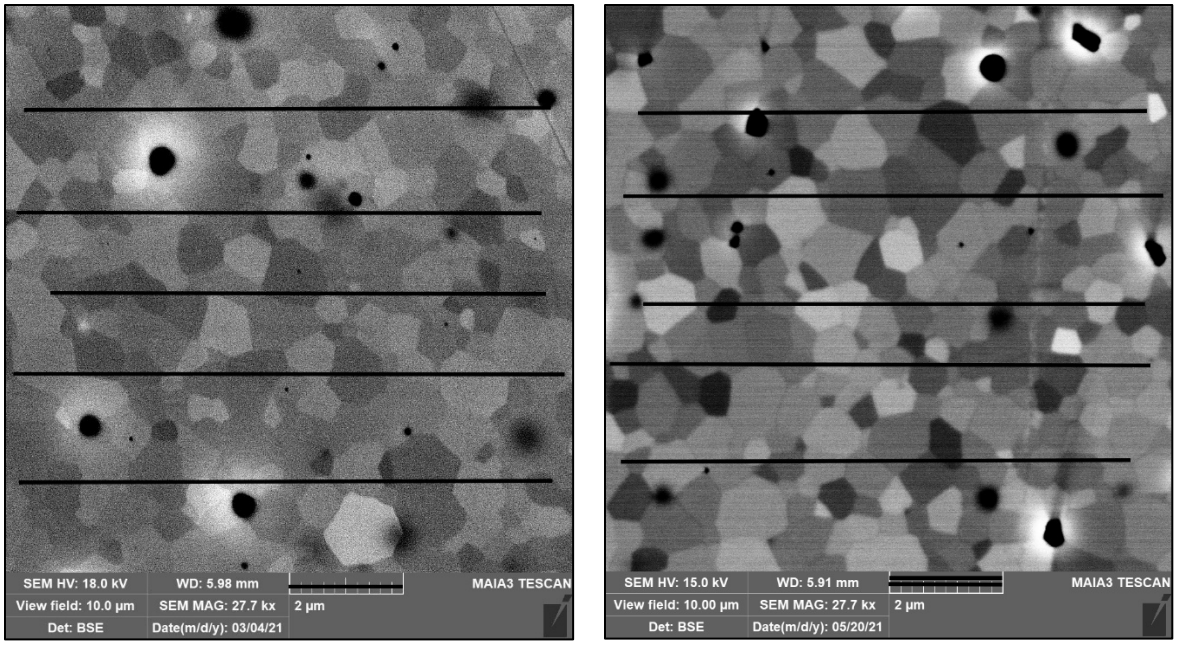

Figure 48: Micrographs of two different LuAG specimens with lines used to determine the average grain size by means of the intercept method: a) Image from billet L-6-40 and b) Image from billet L-8-40.

The second method used to quantify the average grain size of each billet in this study was the measuring the area of each grain from an SEM micrograph by the use of digital image analysis software. In order for each grain to be visually identified and separated from the adjacent grains, the color contrast from each SEM image first had to be exaggerated, creating a more significant threshold between each grain and the surrounding background. In order to accomplish this, Adobe Photoshop was used to capture each grain and copy the identical shape in black onto a white background. An example of this procedure, which was accomplished for LuAG billet L-1-20, is shown in Figure 49. In this case 275 grains were copied from one SEM image. The scale bar was also copied and is visible in Figure 49 in order to maintain an accurate reference to determine the grain size.

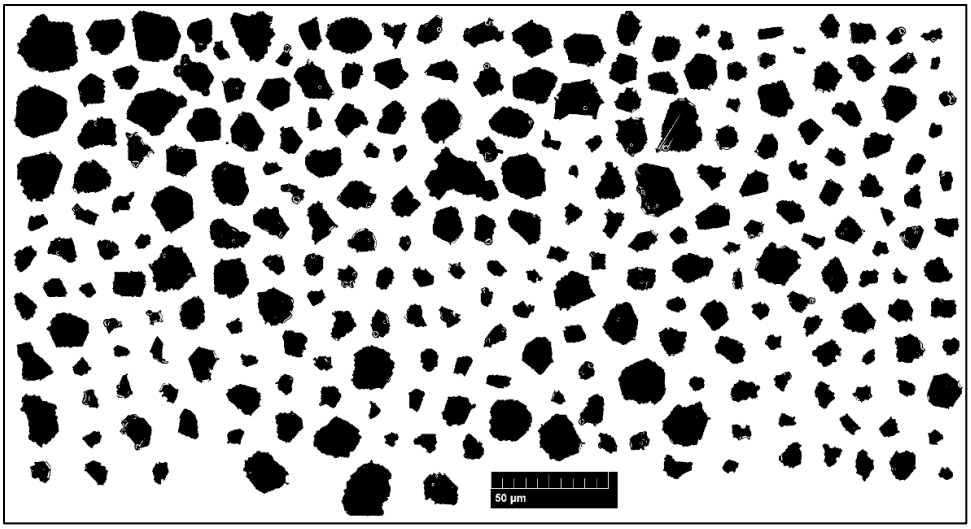

Figure 49: Grain thresholding procedure for digital image analysis of LuAG billet L-1-20.

The standard image analysis add-on in Adobe Photoshop is adequate for capturing the size and shape of grains. Using the threshold image, shown in Figure 49, each grain is analyzed using number of pixels, which can be translated into meaningful units, such as micrometers, in Photoshop. The software outputs the area, perimeter/circumference, the height, and the width of each grain. Using the area obtained for each grain, the diameter of an equivalent circle can be determined. These diameters are then averaged for each grain from the original SEM image, resulting in the average grain size for that billet.

These two measurement techniques consistently resulted in grain size agreement within 5%. Therefore, the grain size measurement process was eventually reduced to solely using the intercept method. The measured grain size for each billet, as well as the accompanying SEM images, can be seen in Appendix C.

4.3.3. Effects of SPS Processing Parameters on Grain Size

The grain size of each billet of YAG and LuAG was determined and correlated with the individual processing parameters used during SPS. The primary parameters that consistently

varied between different billets were the SPS temperature and pressure. As was discussed in Section 3.2.3, a range of temperature and pressure parameter settings were used in order to determine their effects on the microstructure and the overall quality and consistency of each processed billet. These two parameters were identified for each billet and their individual effects on the resultant grain size of each material was determined. Graphs of SPS temperature vs. grain size for YAG billets are shown in Figure 50. Each graph demonstrates the grin size dependence on SPS temperature for a given pressure. Each of the billets included in an individual graph were processed at the same identified pressure and a consistent hold time of 15 minutes. Not all SPS billets are included in these figures, as some of them were processed using inconsistent settings, such as extended hold times, and cannot be directly compared.

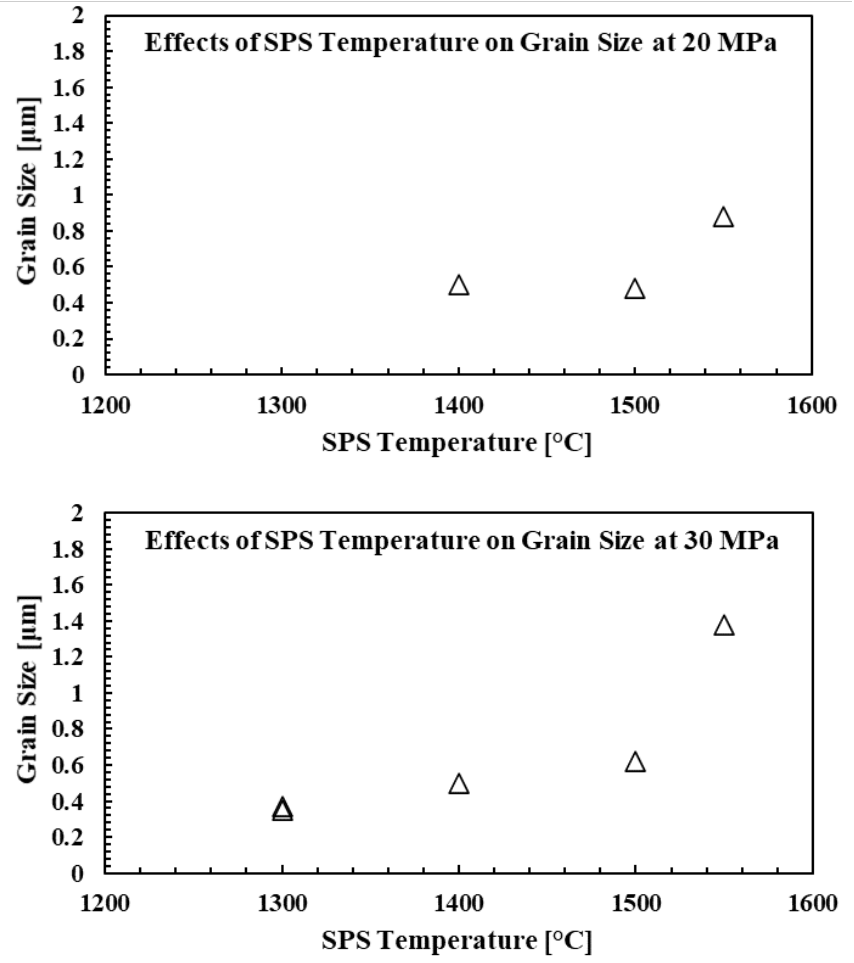

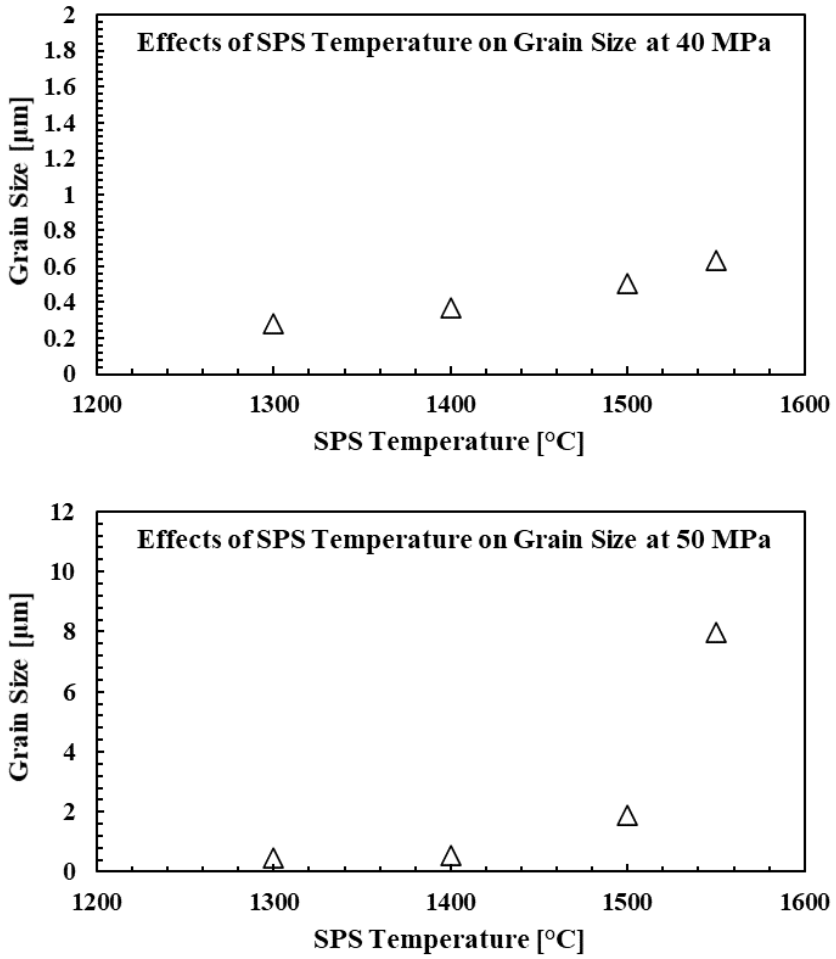

Figure 50: The effects of the SPS temperature setting combined with various pressure settings during sintering on the resulting grain size of YAG.

These four graphs are overlaid in Figure 51 in order to more easily observe the overall effects of temperature for each individual pressure setting.

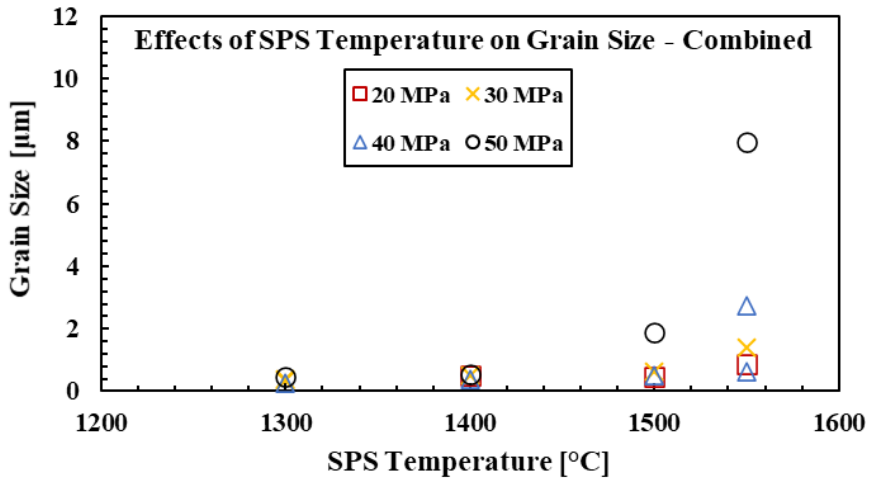

Figure 51: Summary graph of the effects of temperature on the resultant grain size of YAG.

Figure 50 and Figure 51 reveal an increasing trend in grain size based on increasing SPS temperature. There is very little grain size variation between 1300°C and 1400°C sintering temperatures; however, at 1500°C and 1550°C the average grain size of the YAG billets tends to be larger with more variation between SPS runs. Due to the limited number of specimens processed at each temperature and pressure setting, these results only provide a potential correlation between temperature and grain size, and more SPS runs are necessary to produce more statistically significant results. However, the consistency of the temperature effects at each pressure setting suggests that at 1550°C, significantly more grain growth occurs in a short amount of time.

This is consistent with what has been determined in other investigations of grain growth in YAG during sintering. In each case grain size slightly increases with increasing sintering temperature until a threshold temperature is reached, after which grain growth increases rapidly. Kochwattana et al. [261] identified this phenomenon occurring at 1700°C when sintering YAG by means of cold isostatic pressing, then heating in a vacuum. Jia et al. [262], [263] also

observed this occurring in YAG above 1500°C with the same sintering method. Chaim et al. [242] observed rapid grain growth in YAG occurring at 1450°C during SPS. Similarly, Perez et al. [228] identified only minimal grain growth due to SPS sintering temperature up to 1500°C, but did not perform sintering runs at higher temperatures.

Any potential effects of SPS pressure on the resultant grain size in YAG were similarly characterized. Graphs of SPS pressure vs. grain size for YAG billets are shown in Figure 52. Each graph demonstrates the grain size dependence on SPS pressure for a given temperature setting. Each of the billets included in an individual graph were processed at the same identified temperature and a consistent hold time of 15 minutes.

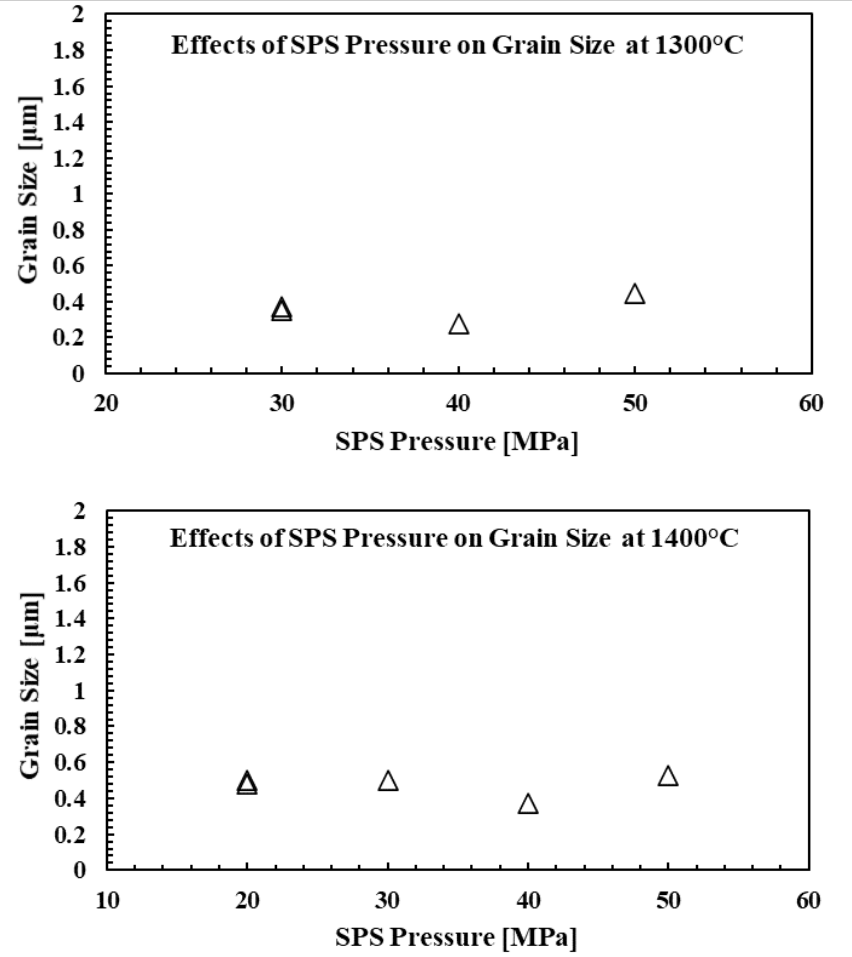

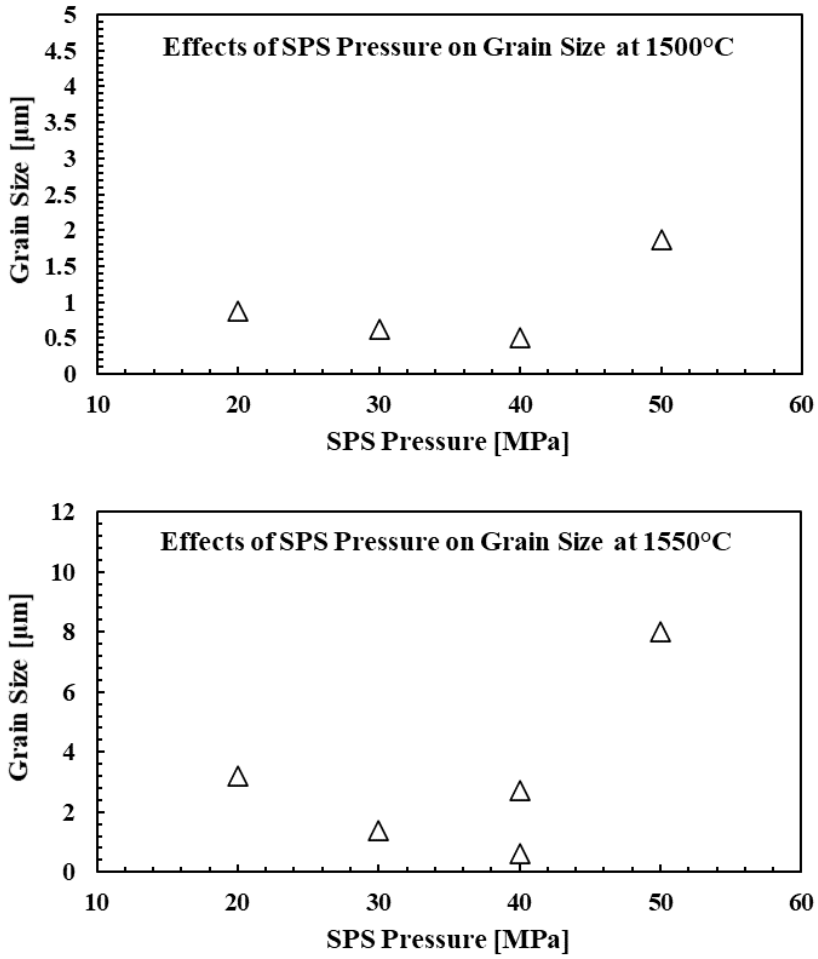

Figure 52: The effects of the SPS pressure setting combined with various temperature settings during sintering on the resulting grain size of YAG.

Once again, these four graphs are overlaid in Figure 53 in order to more easily observe the overall effects of pressure for each individual temperature setting during the processing of YAG.

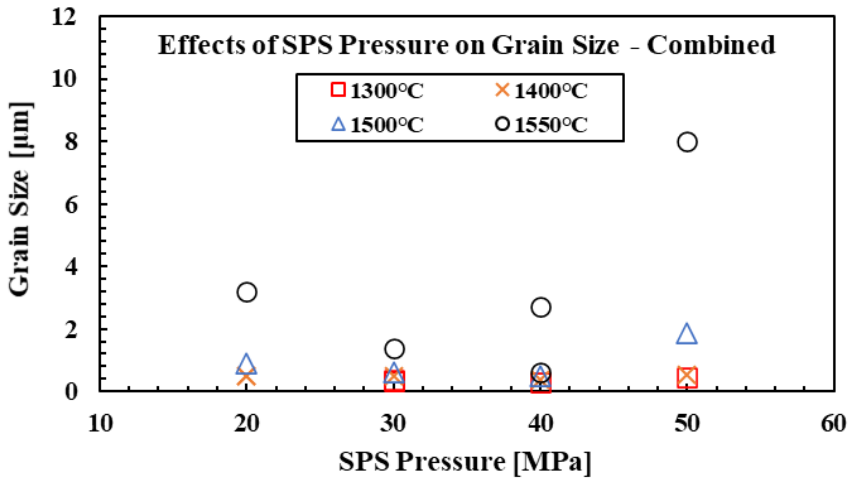

Figure 53: Summary graph of the effects of pressure on the resultant grain size of YAG.

The effects of SPS pressure on the resultant grain size are less clear and robust than the correlation with temperature; however, two consistent trends emerged. First, at each temperature, grain size tends to be smallest at 40 MPa. Again, more SPS runs are necessary to obtain more conclusive results, but this was the consistent observation for the SPS runs conducted in this study. Secondly, grain size appears to be more varied and less consistent at 20 MPa and 50 MPa. This may have been expected at 20 MPa, as this pressure is rarely cited in the literature as a typical SPS setting, due to the fact that with such a low pressure, densification may not fully occur. However, 50 MPa is a common SPS pressure setting for YAG and similar ceramics. The variation in grin size, resulting from this pressure setting is surprising, and additional SPS runs followed by microstructural analysis may help to explain this phenomenon.

Graphs of SPS temperature vs. grain size for LuAG billets are shown in Figure 54. Each graph demonstrates the grain size dependence on SPS temperature for a given pressure. Each of the billets included in an individual graph were processed at the same identified pressure and a consistent hold time of 15 minutes. Once again, not all SPS billets of LuAG are included in these

figures, as some of them were processed using inconsistent settings, such as extended hold times, and cannot be directly compared.

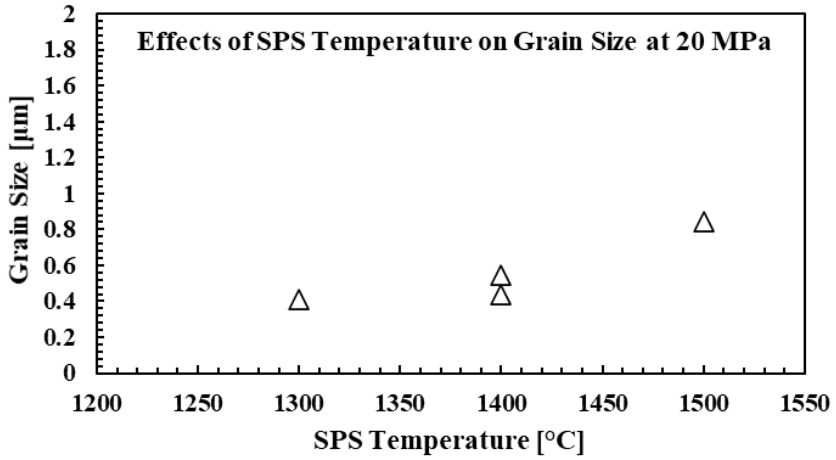

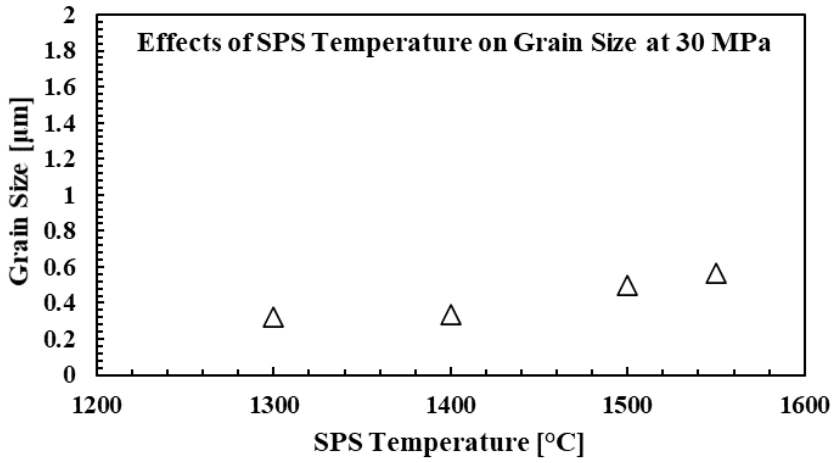

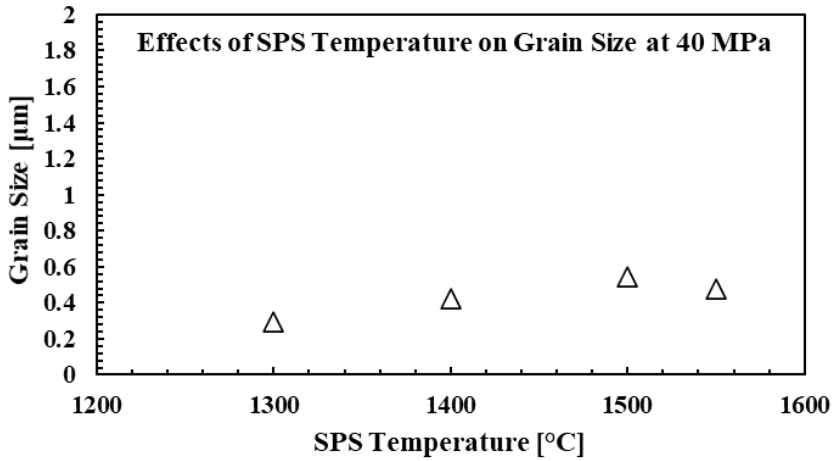

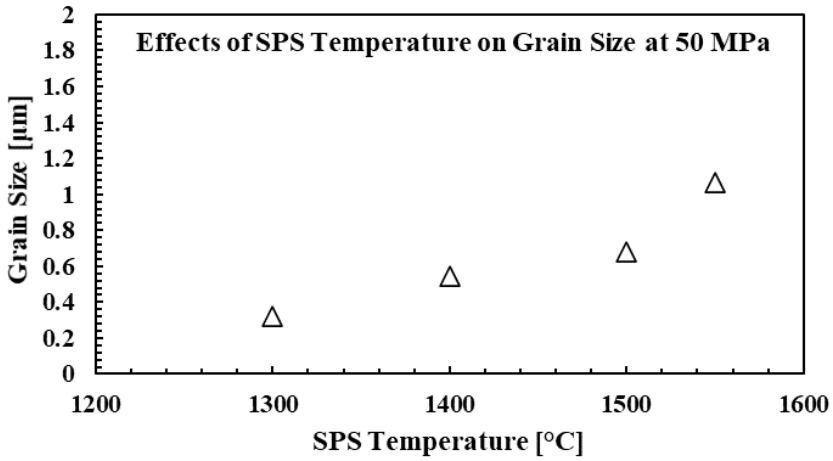

Figure 54: The effects of the SPS temperature setting combined with various pressure settings during sintering on the resulting grain size of LuAG.

The overall trend in grain size of LuAG billets based on the SPS temperature setting is more easily visualized in Figure 55, where the results of grain size vs. temperature at each corresponding pressure setting have been overlaid.

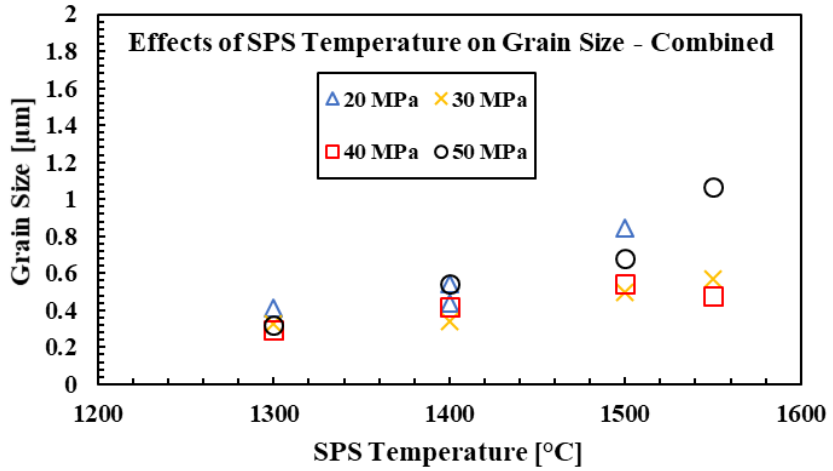

Figure 55: Summary graph of the effects of temperature on the resultant grain size of LuAG.

Very similar results were obtained by analyzing the grain sizes of LuAG billets and correlating them with SPS temperature. In general, there is a slight increasing trend in grain size as the SPS temperature setting is increased from 1300°C to 1400°C. At 1500°C and 1550°C the

upward trend in grain size appears to grow significantly. Similar to YAG, these temperatures may represent a sintering temperature threshold, above which the grain size of LuAG will increase significantly in a short amount of time.

Trofimov et al. conducted a study of the effects of sintering temperature on the resultant grain size of LuAG [264]. It was concluded that LuAG grain size increases as the sintering temperature is increased. Furthermore, they observed that the rate of grain growth increases as well from 1400°C to 1700°C, with a significant jump above 1600°C. A very similar result as obtained by Marchewka [265]. He determined that LuAG grain sizes and grain growth rates will increase based on sintering temperatures from 1400°C to 1700°C. LuAG materials in these investigations were not sintered by SPS, as it is an uncommon sintering method for LuAG. However, the relationship between grain size and sintering temperature is very similar to what was obtained in this study.

The effects of SPS pressure on the resultant grain size in LuAG were similarly characterized as they were for YAG previously. Graphs of SPS pressure vs. grain size for LuAG billets are shown in Figure 56. Each graph demonstrates the grain size dependence on SPS pressure for a given temperature setting. Each of the billets included in an individual graph were processed at the same identified temperature with a consistent hold time of 15 minutes.

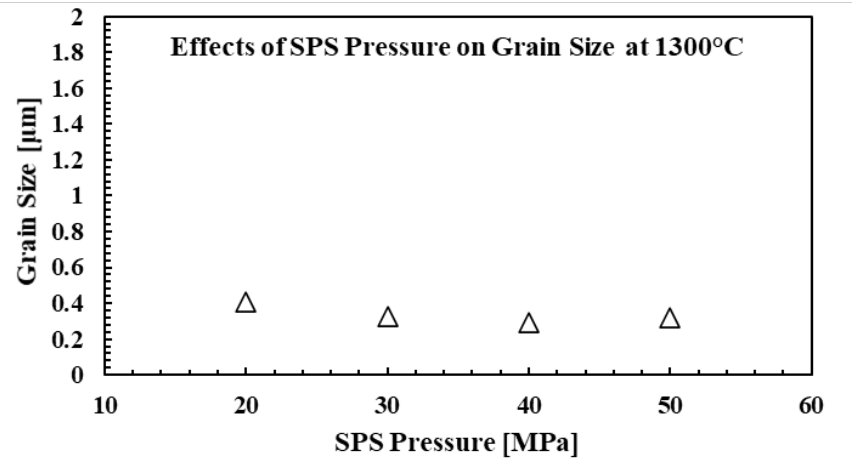

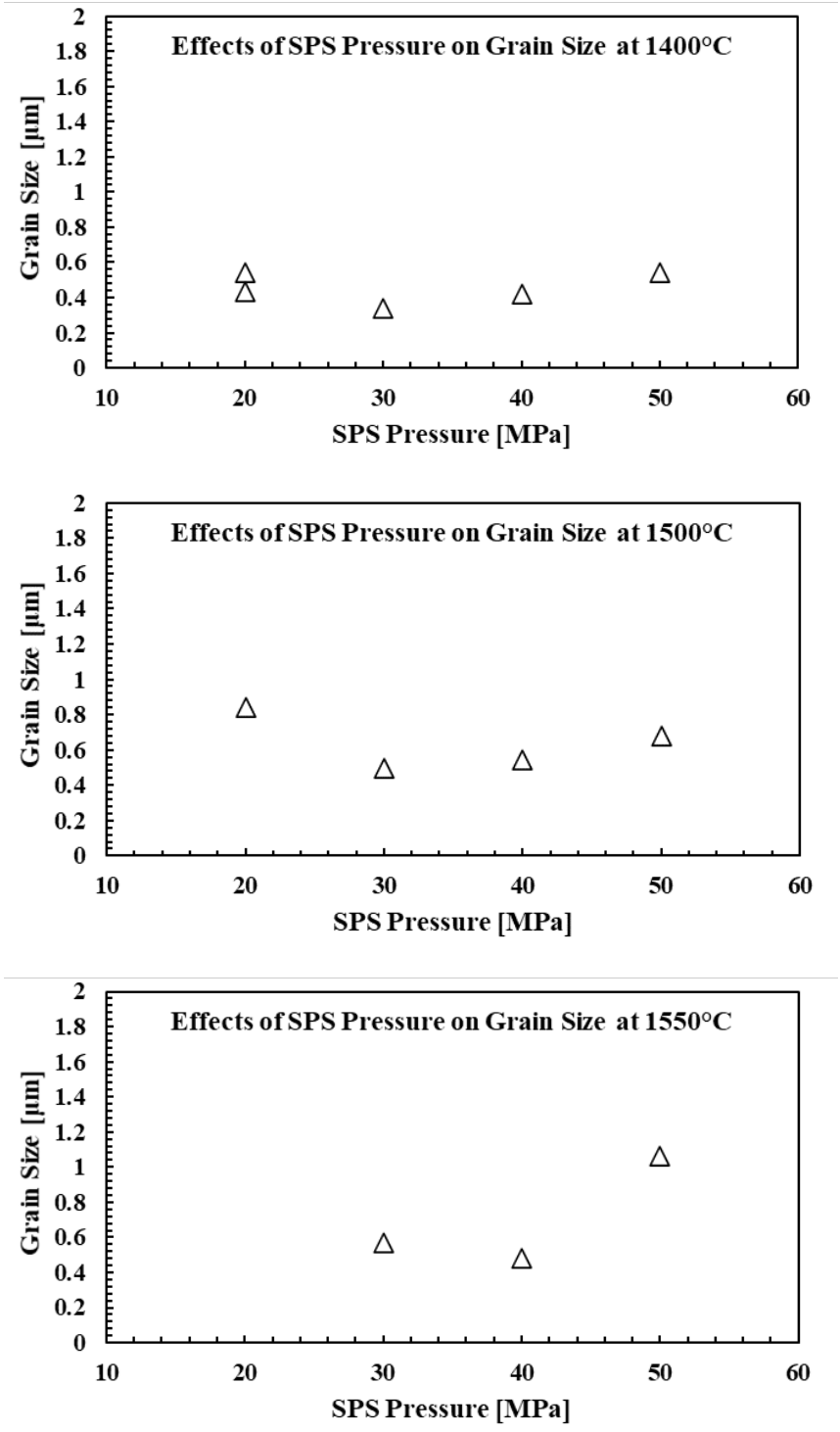

Figure 56: The effects of the SPS pressure setting combined with various temperature settings during sintering on the resulting grain size of LuAG.

These four graphs are overlaid in Figure 57 in order to more easily observe the overall effects of pressure for each individual temperature setting during the processing of LuAG.

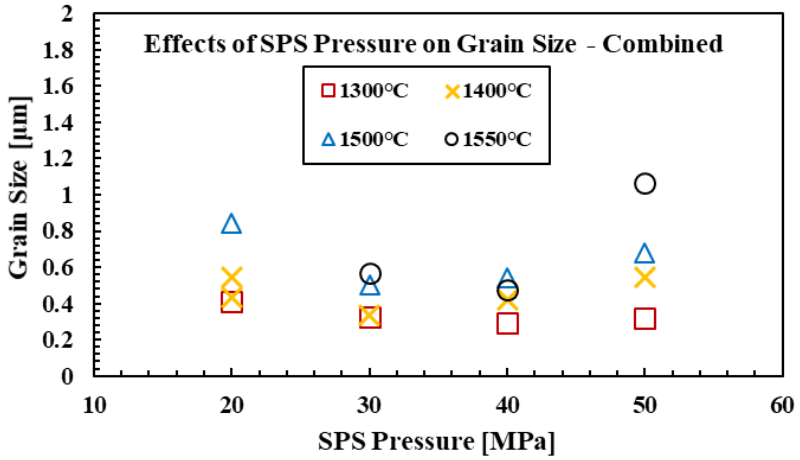

Figure 57: Summary graph of the effects of pressure on the resultant grain size of LuAG.

Similar observations can be made regarding grain size of LuAG as for YAG, based on the pressure settings during SPS. The grain size does not fluctuate significantly with pressure settings between 20 MPa and 50 MPa. However, consistently smaller grains are observed for SPS runs at 30 MPa and 40 MPa. Again, many more SPS runs under these same conditions are necessary in order to obtain more conclusive results; however, this result is consistent across all the SPS runs conducted on LuAG billet in this study.

Additionally, there is once again more grain size variation at pressures of 20 MPa and 50 MPa. It is likely that this phenomenon is due to both the densification, and also the heat transfer rates during SPS, which can both influence the resultant grain size and are both related to the applied pressure.

4.4. Porosity Analysis

Specimens from each puck were analyzed in the SEM in order to understand the general pore size and distribution for each SPS billet. The density of each material was already determined, which gives insight into the associated porosity; however, porosity was still examined in order to ensure that there were no extremely large pores or internal cracks that could lead to premature failure during creep.

Due to the various SPS parameters selected during processing, each resulting material billet had a unique microstructure with various properties, including the size, shape, and location of pores. The majority of the different billets of each material variant possessed small pores, which were easily visible in the SEM. Typical pore size was less than 1 μm in length, and were polyhedrons in shape, similar to grains with sharp edges, which indicates that the pores were often formed by material breaking and chipping at the grain boundaries. Figure 58 shows two SEM micrographs of typical sample surfaces with visible pores. The SEM micrograph on the left is from the undoped YAG billet Y-3-40, and the micrograph on the right is from the 2at% Yb-doped YAG billet Y-Yb-3-40.

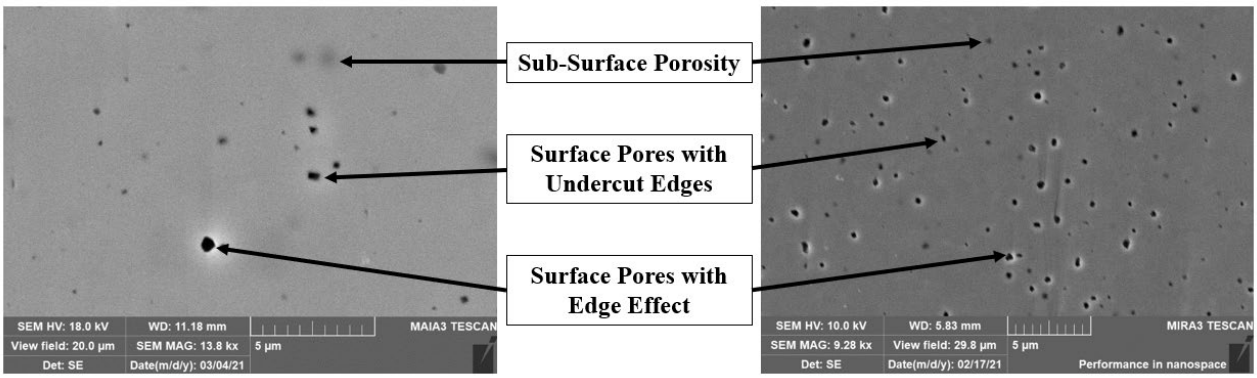

Figure 58: SEM micrographs showing typical porosity in YAG specimens. Left: Billet Y-3-40 with 98.9% theoretical density. Right: Billet Y-Yb-3-40 with 99.5% theoretical density.

When viewing porosity using the backscattered electron detector in the SEM, three variations of pores can be observed and identified. BSEs make this possible as the shape and location of the pores affect the resulting image characteristics. As was described in Section 4.3.1, BSEs can originate from deeper regions of the sample below the surface. As a result, porosity below the surface can be identified. However, due to their depth below the surface, they can appear blurry and out of focus. Examples for sub-surface porosity are also identified in Figure 58. Surface porosity is generally characterized by clear, dark regions, with sharp edges, often along grain boundaries. Some surface pores simply appear as dark regions, while others appear dark with a bright ring around the edges. This is known as the "edge effect" in SEM imaging. The edge effect occurs when the primary electron beam hits the edges of pores, which results in significantly more backscattered electrons being detected than a flat surface. This results in excessive charging around the edges of the pore. If a surface pore has no edge effect, then it could be that the pore edges are undercut and are not visible at all. In this case the majority of the pore volume is beneath the surface. A diagram of the edge effect is shown in Figure 59.

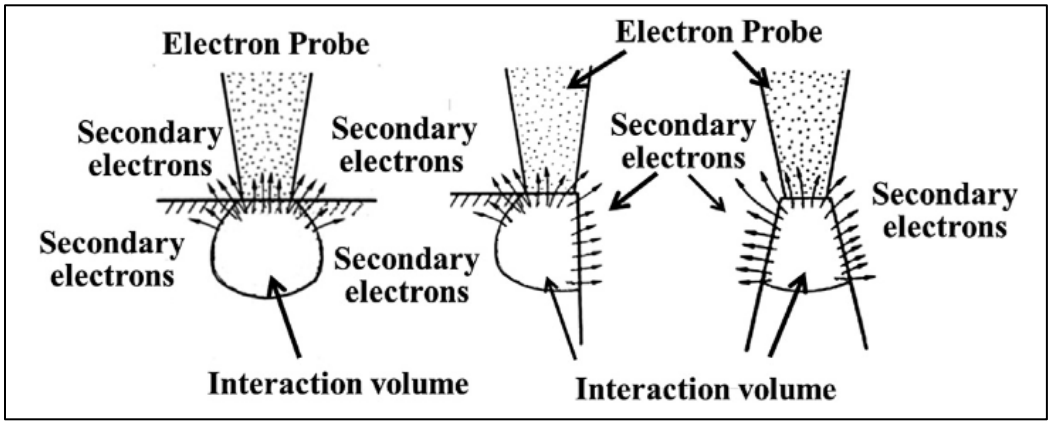

Figure 59: Diagram of the edge effect when imaging a sample surface in the SEM from Yoshida et al. [266]**. Reproduced with permission from Elsevier.**

Significantly more porosity was observed in certain material billets, especially those with larger grain sizes. Higher quantities and larger sizes of surface porosity was easily visible in some SEM images; however, it was not always clear from density measurements. All SPS billets in this study had a measured density between 96% and 100% of the theoretical density of the material. Additionally, this small difference in specimen density did not always correlate to grain size or differences in visible porosity. This could be due to variations in grain size and porosity throughout a material billet. A specimen prepared for SEM imaging was much smaller than the entire surface of an SPS billet, and an individual SEM image only captures a few micrometers of distance on the specimen surface. Therefore, the overall porosity, density, and grain size were difficult to correlate.

Several SEM micrographs of billets with much larger visible pores were obtained for some billets. Figure 60 shows an SEM micrograph of the surface of the undoped YAG billet Y-2-40. Several large surface pores with a bright edge effect are visible. The average measured density of all specimens from Y-2-40 was 97.5% of the theoretical density of YAG.

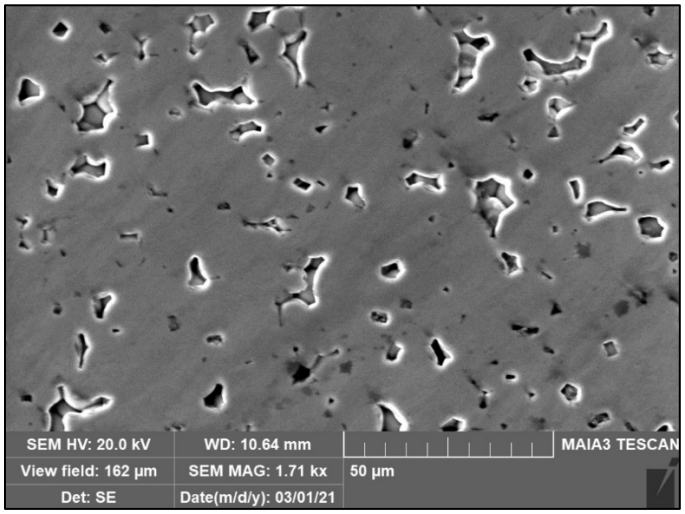

Figure 60: SEM micrograph of billet Y-2-40, showing surface porosity.

Significantly larger surface pores with lengths of approximately 5-10 μm are clearly visible. Furthermore, sintering may have only been partially completed during the processing of this billet, as individual particles are visible within the larger pores. This specimen was analyzed further in the SEM, and the location of these pores relative to the grain boundaries can be viewed in Figure 61.

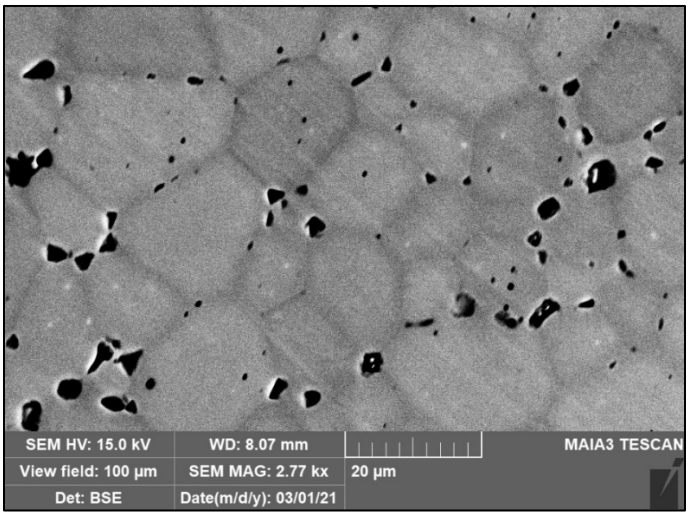

Figure 61: SEM micrograph of billet Y-2-40 with visible grain boundaries.

The majority of the pores seen in Figure appear along the grain boundaries. Perhaps sintering and densification was not fully completed, as these pores along the grain boundaries should have been removed during the final stage of sintering. This is likely the case based on the SPS parameters selected for processing this billet. High temperature (1500°C) and low pressure (20 MPa) was chosen in combination with a longer hold time (20 minutes), which can enable further grain growth. This combination of increased grain growth with minimal SPS pressure, which decreases overall densification, can lead to increased porosity or cavity formation along the grain boundaries. A clear example of this is seen in a separate SEM micrograph shown in Figure 62.

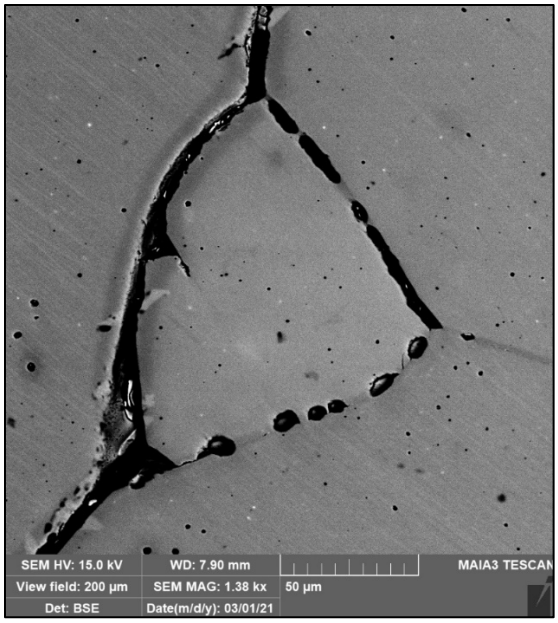

Figure 62: SEM micrograph of undoped YAG billet Y-2-40, showing porosity joining together along a grain boundary.

Despite the variation in porosity that was identified during microstructural examination of all the different billets and all the material variants in this study, the measured densities did not significantly vary. Furthermore, no consistent correlation could be made between specimen density, pore size from individual SEM images, and the mechanical properties investigated later in this study. Grain size and not porosity ultimately had the greatest impact on creep resistance. In fact, larger grains, often associated with greater porosity, exhibited the highest creep resistance for each material variant, which is discussed in Sections 6 and 7.

4.5. Microhardness Evaluation

Generally speaking, hardness is a material characteristic that identifies the material's resistance to indentation. Using a known force, a small indenter is pressed into the flat surface of the material, and the characteristics of the permanent indent, such as area or depth, reveal the hardness of the material [267]. Although there are many different specific types of hardness tests, the Vickers hardness test, also known as the microhardness test, was the most appropriate for these materials. It is typically used for small, thin specimens, and it is also helpful in determining the hardness of very brittle materials, which have the tendency to crack under a very small load.

The Vickers hardness test uses a very small, pyramid shape, diamond indenter, and uses very light loads to try to create a permanent indentation on the material surface. Because the loads are so light and the indentations are so small, the Vickers hardness test requires that the specimens be polished prior to testing, so that the indentations can be clearly seen and measured. Therefore, the same polishing procedures as was used for SEM specimens, which were described in Section 4.1, were also used to prepare specimens for hardness testing. The final depth of the indentation was measured using an optical microscope.

Each hardness value presented for an individual specimen is the average of five individual tests across the surface of each polished specimen. Hardness tests were not determined for all specimens; however, several specimens were selected from each material variant that was investigated in each study. Furthermore, several hardness tests were unsuccessful as the material cracked during application of the load. Even as the load was lessened to the minimum amount, certain samples still cracked at the point where the indenter came into contact with the surface of the specimen. This is due to the extremely brittle nature of these oxide ceramics.

Due to the tendency of the materials to crack during hardness testing, the load used to create an indentation on the surface was lowered when necessary, in order to minimize cracking. Generally, it is desired to use a larger load so that the visible indentation is larger. The larger the indentation, the more reliable the resulting hardness value will be. The smaller the indentation, the less reliable the hardness value will be due to the possibility of measurement error. Therefore, each specimen was first tested using a larger applied load, typically between 100 g and 500 g. If the specimen cracked immediately, then the load was lowered for the next test on the same sample surface. This continued until the load reached 25 g, and in some extreme cases, even 10 g. This is the lowest load value that could still produce a visible indentation.

Because several different loads were used to create the indentations on different specimens, it was necessary to determine if the amount of load had an inconsistent effect on the final hardness measurement. In other words, it must be determined if this particular material responds differently under smaller vs. larger loads. It is already expected that the load directly impacts the potential size of the indentation based on the following relationship:

$$H_V = 1854.4\left(\frac{P}{d^2}\right) \quad \text{(Equ. 23)}$$

where H_V is the Vickers hardness number, P is the load in kg, and d is the indentation diagonal dimension in mm. However, some materials have been shown to deviate from this relationship for particularly small or large loads. To determine if this is the case, the Meyer equation must be considered as follows:

$$P = kd^n \quad \text{(Equ. 24)}$$

Once again, P is the test load, d is the diagonal length of the indentation, and k is a constant. The exponent, n, represents the degree in which the material is affected by the test load. These two equations can be combined, which results in the equation below:

$$H_V = Cd^{n-2} \quad \text{(Equ. 25)}$$

In order to determine the effects of test load on hardness, the indentation size vs. test load is plotted on a log-log-scale. By applying a best fit line to the data, the exponent, n, can be determined. Then by plotting hardness vs. indentation size on the same log-log scale, the effect of test load can be visualized. A best fit line is similarly plotted over this data, and its slope represents the degree to which the test load affects the resulting hardness. If *n* is found to be equal to 2, then based on Equation 25, the slope of second line would be 0. These plots are shown in Figure 63 and Figure 64 for the hardness of YAG and LuAG.

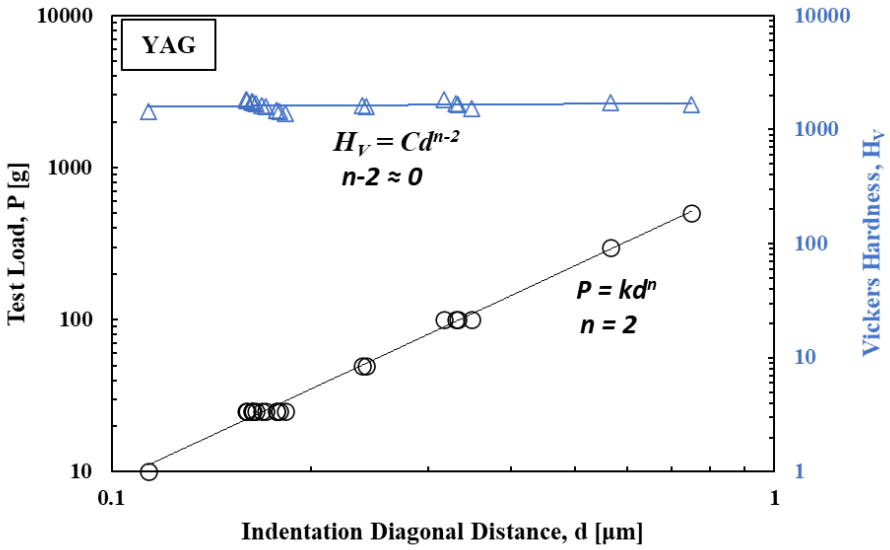

Figure 63: Determination of the impact of test load on Vickers hardness results for YAG.

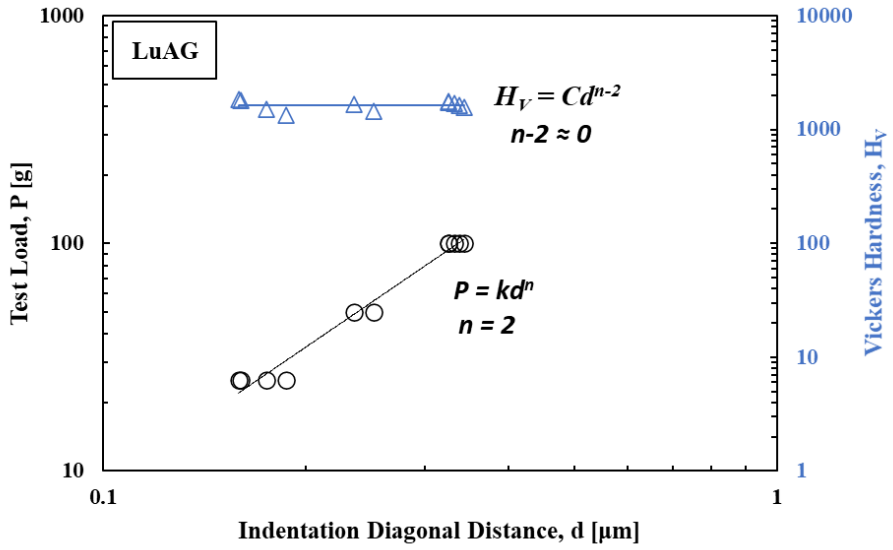

Figure 64: Determination of the impact of test load on Vickers hardness results for YAG.

As Figure 63 and Figure 64 indicate, the exponent, n, was found to be 2 in both cases, and the slope of the Meyer hardness line (shown in blue), is nearly zero. Therefore, the test load has been adequately taken into account by using the original equation for Vickers hardness, shown in Equation 23.

The individual results of hardness tests for each specimen are included in the tables in Appendix A. Additionally, the results of the hardness tests for each material variant are summarized in Table 15, which lists the number of specimens tested for each material, the average hardness value, the range of grain sizes tested, and the maximum and minimum hardness values determined for each material.

Table 15: Summary of hardness results for each material.

Material	Number of Samples tested	Average Hardness [H_V]	Range of Grain Size [µm]	Minimum Hardness [H_V]	Maximum Hardness [H_V]
LuAG	10	1625	0.32 – 10.78	1328	1839
Undoped YAG	8	1668	0.35 – 7.99	1390	1848
2at% Yb-Doped YAG	8	1651	0.37 – 4.83	1442	1747
2at% Er-Doped YAG	4	1591	0.45 – 2.82	1436	1742

The hardness for each material is very high, well beyond that of most metals, and alongside other similar ceramics, such as alumina. Table 15 indicates that there is a wide range of hardness values obtained for the different specimen, even for the same material types. This is due to the variation in grain size across specimens of each material. Hardness is usually correlated directly with other material properties such as tensile strength. Increased grain size, although advantageous for creep resistance, is typically detrimental to material strength. Therefore, it is expected that the hardness would decrease with increasing grain size. This relationship was originally discovered by Hall and Petch, and termed the Hall-Petch relationship [268]–[271]. It is now defined as follows:

$$\sigma_y = \sigma_0 \left(\frac{k}{\sqrt{d}}\right) \quad \text{(Equ. 26)}$$

where σ_y is the yield stress of the material, σ_0 is a material property related to the stress required to initiate dislocation motion, d is the grain size, and k is a strengthening coefficient, which is unique to individual materials. Although most often applied to metals, the Hall-Petch relationship has been shown to hold true for polycrystalline ceramics as well. The hardness values determined for YAG and LuAG were plotted vs. grain size in Figure 65 and Figure 66, respectively.

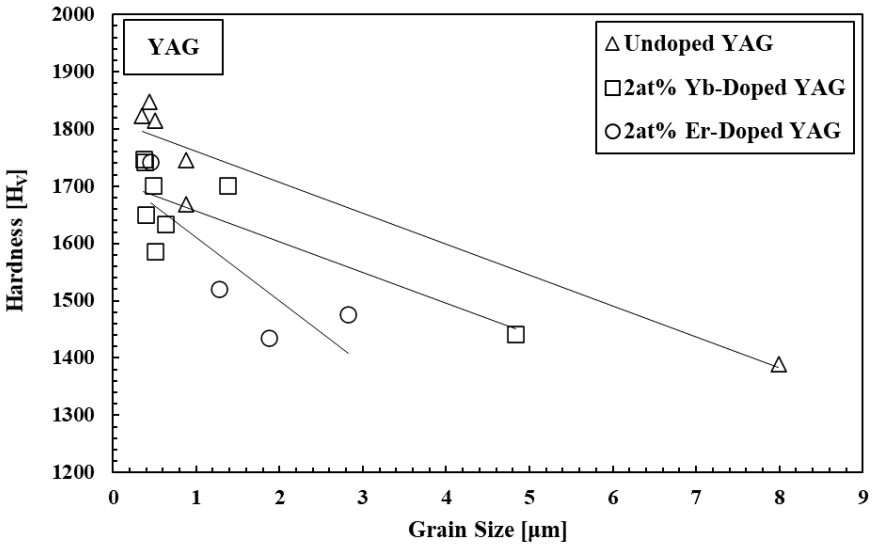

Figure 65: Hardness vs. grain size for three variants of YAG.

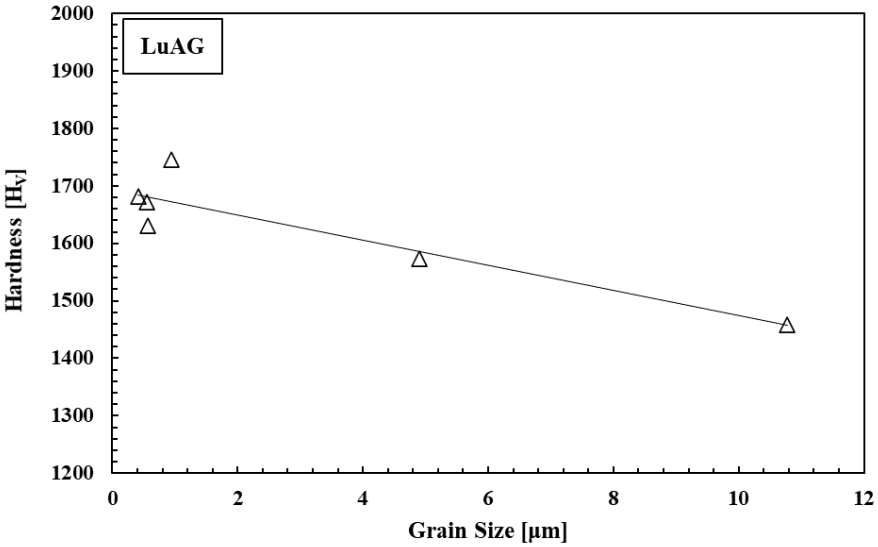

Figure 66: Hardness vs. grain size for various LuAG specimens.

The Hall-Petch relationship appears to hold true for the hardness of YAG and LuAG, similar to other materials. There is significant scatter in the hardness results, especially for specimens with smaller grain size. This could be due to a variety of reasons, but most likely due to error associated with grain size measurements and indentation size measurements during hardness testing. In order to arrive at more concrete conclusions about the specific relationship between

hardness and grain size for garnet ceramics, several more specimens would have to be tested at each grain size.

Once additional specimens of each material variant are tested, then the potential difference in hardness associated with the dopants in YAG could be determined more conclusively. Figure 65 shows three different groups of hardness results associated with undoped YAG, Yb-doped YAG, and Er-doped YAG. The lines are nearly parallel, but stacked up, and not overlapping. This suggests that the presence of dopants may negatively impact the hardness of YAG. However, this is inconclusive, as the lines are not perfectly parallel, and the data appears scattered, especially at lower grain sizes. Many more hardness tests are required in order to obtain more confident conclusions about hardness and the presence of dopants.

5. Creep Experimental Arrangements

5.1. Creep Specimen Design

Specimen Geometry and Dimensions

Following sintering and heat treatment, each puck was sectioned into small rectangular creep test specimens. The initial geometry and dimensions for small compressive creep test specimens were developed, tested, and validated by several previous students at AFIT, and this proven specimen design was only minimally altered for this investigation. All specimen fabrication was accomplished by the machinists at the AFIT Model Shop, and is described in detail in the following paragraphs. Each specimen was cut according to the specifications shown in the sample diagram in Figure 67. A more detailed fabrication drawing, which shows all the creep specimen dimensions, including the size of the small grooves for extensometer mounting, is shown in Appendix G.

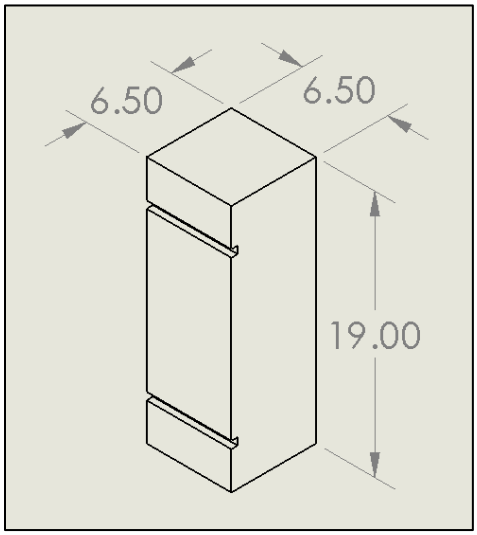

Figure 67: Creep test specimen design with dimensions shown in millimeters.

Current processing limitations, excessive material costs, and the small size of the furnace cavity, all require the use of small test specimens. Specifically, their thickness was limited by the thickness of the SPS billets. Although thicker SPS billets can be fabricated, it was determined

that it would be more cost effective to continue with small specimen dimensions. The creep specimens must also fit inside a small furnace cavity. This cavity is small so that it can effectively be heated and maintained at the desired temperature up to 1400°C. Additionally, the small cross-sectional area of each specimen was also a result of the small surface area of the compression push rods, which are part of the load train and are discussed in more detail later in this section. These different factors all require that the small sides of the creep test specimens be approximately 6.5 mm in length.

The height of each creep test specimen was determined primarily based on the extensometer gauge length used in creep testing, which is 12.7 mm (0.5 in). Small grooves must be carefully machined into one side of each specimen in order for the extensometer rods to remain in position and not move or slide on the sample surface during testing. Therefore, the specimen height must be greater than the extensometer gauge length, and the grooves must be far enough from the upper and lower ends of each sample to ensure they do not affect the mechanical behavior of the material and the associated test results. Additionally, the creep specimens cannot be excessively long, as this will increase the potential for introducing bending effects during compression.

Previous creep studies at AFIT have established a baseline for the required height of each creep specimen, based on these requirements, which was determined to be approximately 19 mm (0.748 in). This allows for the center of each groove to be exactly 12.7 mm (0.5 in) apart, with approximately 2.5 mm (0.098 in) in length above and below the upper and lower grooves, respectively. This height also allows for the specimen to easily fit inside the furnace cavity [29], [30]. The cross-section dimensions were chosen to provide each specimen with the required stability while not laterally supported during each test. Additionally, the cross-sectional area is not so large that the specimen could not be placed on and centered between the small

compression push rods.

The extensometer groove shape and dimensions were determined based on the angle of the extensometer rod tips and the desired contact points. Multiple groove shapes and associated dimensions were attempted during this investigation. The initial grooves were rectangular and were designed so that the chisel-shaped ends or cone-shaped ends of the extensometer rods will contact the outer edges of the grooves and remain in place even during specimen deformation. The groove depth was determined to ensure the extensometer rod tip would not contact the back surface of the groove, where sliding can occur. This will ensure more consistent contact between the specimen and extensometer, which will minimize any slipping during testing. A diagram of the extensometer rod tip in contact with a specimen with rectangular grooves is shown in Figure 68.

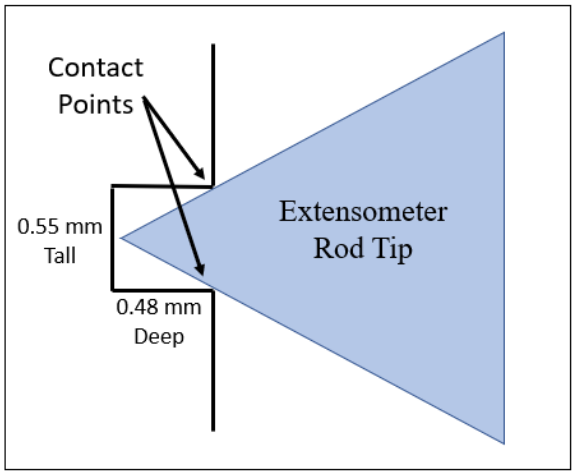

Figure 68: Diagram of extensometer rod tip and rectangular groove contact points.

During this investigation of creep behavior, it was determined that the presence of large rectangular grooves could negatively impact the creep results. Therefore, a second extensometer groove geometry was proposed and machined into several creep test specimens. This second groove shape was designed to minimize the impact on the cross-sectional area. The shape was

changed from a rectangle to a triangular groove, and the depth was determined based on the minimum required depth to effectively catch the tip of the extensometer and restrain movement. Each triangular groove was approximately 0.25 mm (0.0098 in) deep and 0.25 mm (0.0098 in) wide at the opening. A diagram of the extensometer rod tip in contact with a specimen with triangular grooves is shown in Figure 69.

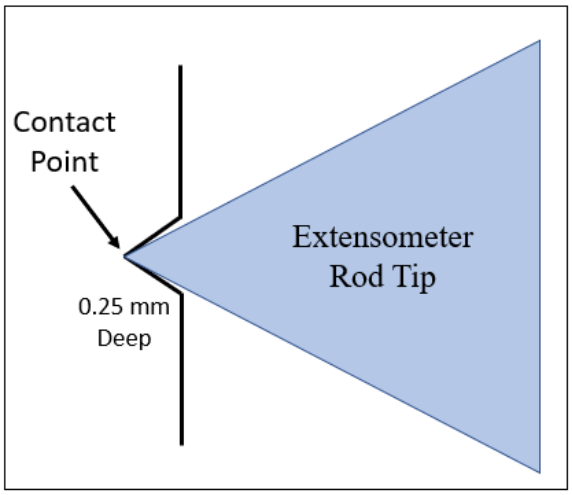

Figure 69: Diagram of extensometer rod and triangular groove contact point.

After a preliminary and thorough investigation into the effects of these two extensometer notch sizes, which were machined into several creep test specimens, it was determined that the larger, yet more stable and secure, rectangular notches have too great of an impact on the resulting mechanical tests. The rectangular notches are simply too large, and they created a complex state of stress that resulted in inconsistent and, in some cases, unusually high creep strain rates, which were observed during preliminary creep tests. It was determined that the small triangular notches have a minimal impact on the mechanical behavior of each specimen, and that this specimen design will likely produce the most consistent and reliable results. The details of this preliminary investigation into the effectiveness of each notch size, and a comparison of the associated creep results for specimens with both notch designs is shown in Appendix F.

Creep Specimen Fabrication

Each creep test specimen was cut directly from the large circular pucks following SPS, previously discussed in Section 3.2.4. In order to section each puck into creep specimens, the following procedures were utilized. Each puck or cracked section of a puck was fixed onto a custom mounting fixture by using a UV-curable adhesive. Specimens were rough-cut from each puck with measurements slightly larger than the desired specimen dimensions using a diamond slitting wheel on a surface grinder. A diamond grinding wheel was then used to slowly cut away excess material to the exact desired dimensions. The extensometer grooves were also cut using the same diamond slitting wheel. The rectangular grooves were cut using standard perpendicular alignment of the wheel, and the triangular grooves were cut using the wheel positioned at a 45° angle.

Occasionally the brittle specimens would chip or crack during fabrication, which could result in the creep test specimen being unusable. However, creep test specimens were salvaged whenever possible by reducing the final dimensions as necessary until a lower dimensional limit was reached. This created the need for establishing minimum specimen dimensions and maximum chip/flaw depth allowances. The primary requirements for cutting each specimen to the desired dimensions and creating specific tolerances were as follows:

1. Extensometer mounting notches need to be approximately 12.7 mm (0.5 in) apart.
2. Opposite sides must be parallel
3. Adjacent sides must be perpendicular in order to maintain balance and alignment during creep tests.

Tolerances were established that were acceptable for precision tests yet were also repeatable with the machining equipment available. All tolerances are shown in inches, as is standard for

the AFIT Model Shop. The long sides of the specimens were required to be cut parallel or perpendicular to each other within +/- 0.0002 in. The top and bottom ends were also cut parallel to each other within 0.0002 in. The grooves were cut 0.25 in from the specimen centerline within +/- 0.0002 in. Additionally, the rectangular grooves were all cut 0.038 in tall and 0.035 in deep within +/- 0.002 in. The triangular grooves were all cut 0.0095 in within +/- 0.002 in. Finally, dimensions could be ground further down in order to smooth out any chips that would break off during cutting and grinding until any visible chip was less than 0.02 in deep. Specimens could be used until dimensions were reduced to less than 6 mm (0.24 in) in width or depth and 16 mm (0.63 in) in height. Two views of a typical creep test specimen are shown in Figure 70.

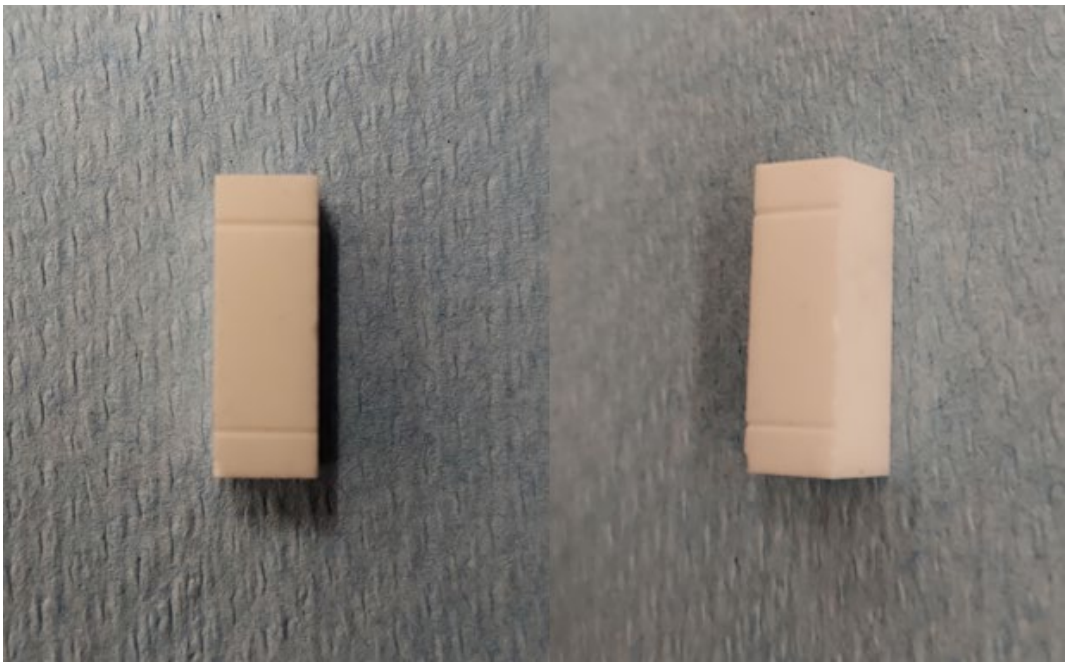

Figure 70: Front view and side view of a typical LuAG creep test specimen. Small chips from the fabrication process are visible along the edges of the specimen.

Creep Specimen Quantity and Dimensions

As many creep specimens as possible were cut from each puck following SPS processing. If no flaws or cracks were present from processing, a 20 mm diameter puck could theoretically yield just one creep test specimen, a 25 mm diameter puck could yield 2 creep test specimens, and a 40 mm diameter puck could yield up to 6 creep test specimens. However, the cracking that was present in many of the 40 mm diameter sintered pucks, as well as small defects, which would lead to chipping during specimen fabrication, often limited the number of specimens that could be fabricated. The overall quantity of creep test specimens that were fabricated from all billets processed via SPS is shown in Table 16. Detailed tables of creep specimen properties, including dimensions, mass, and density for all material variants are shown in Appendix B.

Table 16: Quantity of cylindrical SPS billets and fabricated Creep Test Specimens

Material	Total # of SPS Billets	# of 20 mm Billets	# of 25 mm Billets	# of 40 mm Billets	Total # of Creep Specimens
Undoped LuAG	20	1	7	12	42
Undoped YAG	14	0	3	12	37
2at% Er:YAG	10	0	4	6	20
2at% Yb:YAG	10	1	3	6	24

5.2. Creep Test Facility

5.2.1 Test Equipment

The experimental facility for compression creep testing of small ceramic samples at high temperature in air and in steam consisted of a universal material testing machine coupled with a compact box furnace surrounding a specimen carefully mounted on extension rods. All creep testing was done in compression due to the small specimen size, which made it difficult to grip the material in tension. Additionally, the small size of the specimens required that the entire specimen, not just a center gauge section, be placed entirely within the furnace. Therefore, in

order for creep tests to be conducted in tension, theoretical tensile grips would have to withstand the high temperatures within the furnace surrounding the specimen up to 1430°C. For these reasons, all creep tests in this study were accomplished in compression.

The experimental setup utilized a servo-hydraulic MTS 810 mechanical testing machine equipped with an MTS 609 alignment fixture, an MTS 5.5 kip load cell, and water-cooled MTS 647.02B hydraulic wedge grips, shown in Figure 71. This testing system has a load capacity up to 5,500 lbs (25 kN). An MTS FlexTest 40 digital controller was used for all input signal generation and data acquisition.

Figure 71: MTS 810 Mechanical Testing Machine.

An AMTECO Hot Rail compact two-zone resistance-heated furnace (Model #: HRFS-400-2700-2Z) and MTS 409.83 temperature controllers were used in conjunction with the MTS material testing machine for elevated temperature testing. The furnace is shown in

Figure **72**. This furnace is split into two sides, which slide along a rail in the back and open in the middle. The maximum operating temperature, according to the specifications, is 1500°C with the ability to ramp up to temperature at 100°C/min. Furnace specifications are shown below in Table 17.

Figure 72: AMTECO Hot Rail compact two-zone resistance-heated furnace.

Table 17: AMTECO HRFS-400-2700-2Z Furnace Specifications [272].

Max/Min Temperature (°C)	Control Point Stability (°C)	Hot Zone Height (mm)	Hot Zone Depth (mm)	Hot Zone Width (mm)	Overall Height (mm)
1500/100	±1	56	41	70	93

In order for the specimen and steam enclosure (susceptor) to fit inside the furnace without contacting the heating elements and thermocouples, which are already built into the sides of the furnace, a special furnace insert was designed and fabricated to expand the overall furnace cavity width. The furnace insert was also split into two pieces, which each attached to the middle sections of each side of the original furnace. The two parts of the furnace insert were mirror images of each other, each composed of M310 alumina insulation surrounded by a two-piece steel frame, which screwed directly into the existing furnace. The furnace along with the custom inserts, fully integrated into the material testing machine and load train, is shown in Figure 73. All critical elements of the creep test facility and load train, which are visible in Figure 73, are discussed in more detail later in this section.

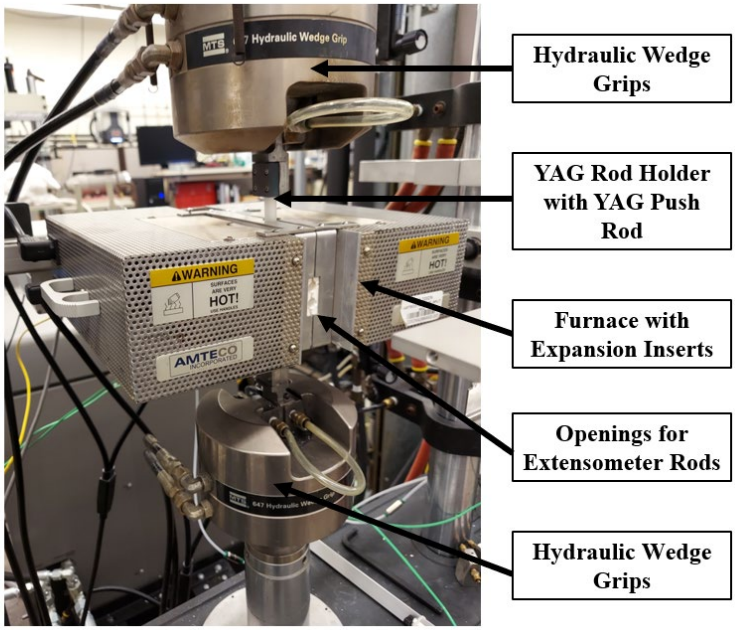

Figure 73: Overview of creep test facility.

An alumina susceptor (a ceramic tube with endcaps) was placed within the furnace surrounding the specimen. The primary purpose of the susceptor is to contain the steam and protect the furnace heating elements during steam environment creep tests. The susceptor is a custom enclosure, designed at AFIT, and fabricated out of alumina by Machined Ceramics, Inc, located in Bowling Green, KY. Figure 74 shows the parts of the susceptor laid out, and Figure 75 shows the fully assembled susceptor.

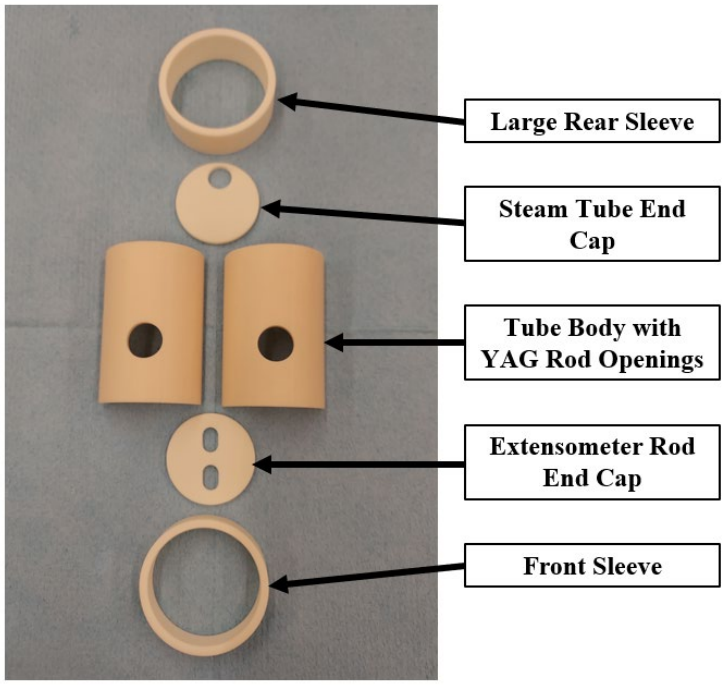

Figure 74: Alumina susceptor parts laid out.

Figure 75: Fully assembled alumina susceptor.

The cylindrical alumina susceptor consists of two separate semi-cylindrical halves, two ceramic hoops used to secure the assembly during testing, and two circular endplates, one with holes for the extensometer rods and the other with a hole for the steam feeding tube. The susceptor was specifically designed to accommodate the desired specimen size and to fit snugly

inside the furnace. The susceptor allows heat transfer from the heating elements to the specimen, while protecting the interior of the furnace, the heating elements, and the thermocouples from the degrading effects of steam environment. In addition to providing a contained steam environment, the use of the susceptor should result in a more stable and repeatable temperature profile for the specimen, as has been observed in previous experiments [29]. Therefore, the susceptor will be used in all tests. The steam will enter the susceptor through a feeding tube inserted into the back endcap of the susceptor. The extensometer rods will be inserted into the susceptor through the small openings in the front endcap. The open furnace with a specimen mounted onto the single-crystal YAG push rods surrounded by the susceptor is shown in Figure 76.

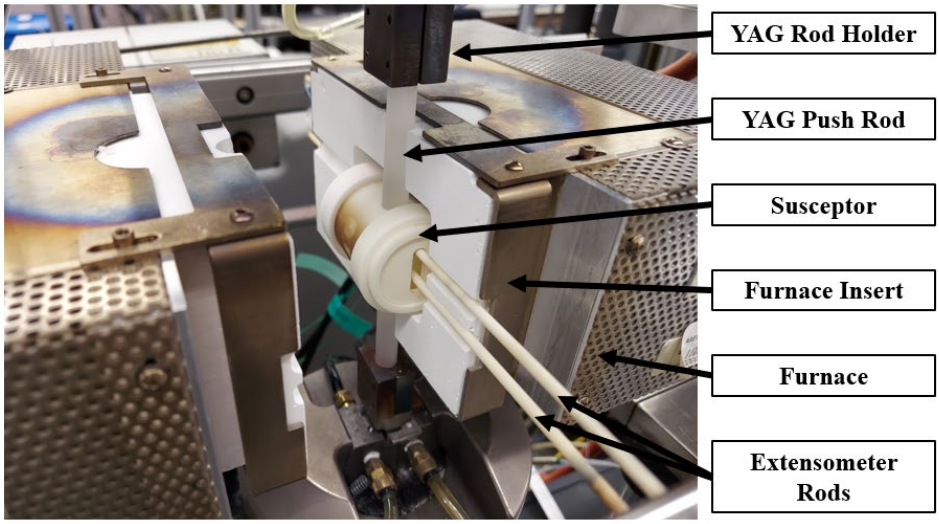

Figure 76: Creep test facility with the furnace opened prior to testing.

Strain measurements were accomplished with an MTS 632.53E-14 high temperature, low contact force extensometer with a 12.7 mm (0.5 in) gauge length and a range of +20% to -10% (maximum nonlinearity of 0.15%). The extensometer was equipped with two 152.4 mm (6 in) sapphire rods in order to reach the specimen within the furnace, which were able to withstand the

temperature and maintain rigidity. The extensometer and attached sapphire rods are shown in Figure 77.

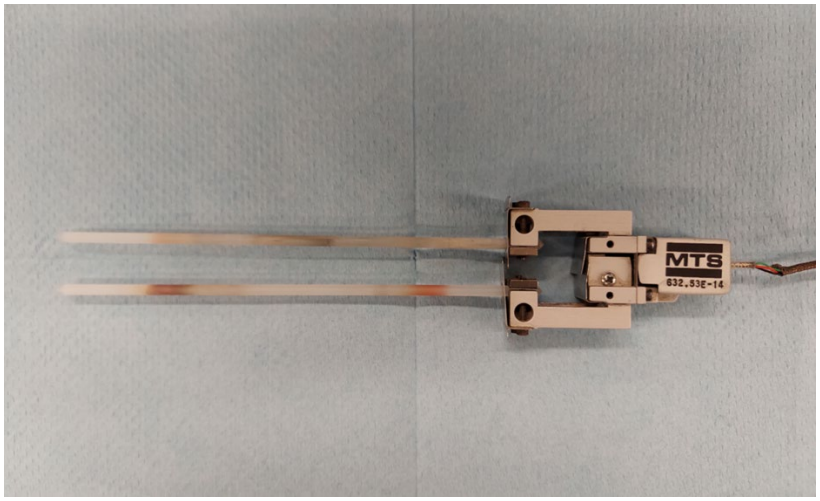

Figure 77: MTS 632.53E-14 high temperature, low contact force extensometer with 6 in high-temperature resistant sapphire rods.

To ensure that the extensometer did not slip during a test, the ends of the extensometer rods were carefully machined into chiseled ends or pointed ends. The extensometer rods tips would rest in the two horizontal grooves, which were machined into one side of all specimens, as was described previously. The extensometer was held by a fixture that was attached to the front of the testing facility. A spring-loaded mounting system was used to suspend the extensometer in the air, creating minimal contact with anything but the sample itself within the furnace. The spring-loaded mounting system generated a compressive force from the extensometer rods onto the sample surface. This enabled the extensometer rod tips to remain in place on the specimen without slipping. Finally, a custom cooling system was attached to the end of the extensometer mounting fixture in order to cool the extensometer during testing. This mounting system is shown in Figure 78.

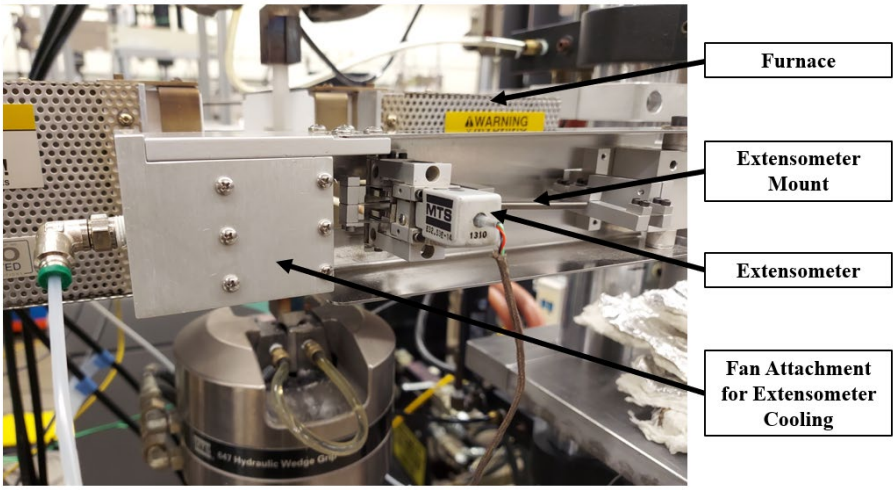

Figure 78: Extensometer mounting system.

An AMTECO HRFS-STMGEN steam generator using de-ionized water was used to generate the steam at a rate of 35 mL/hr. Steam was supplied into the susceptor through a ceramic feeding tube in a continuous flow with a slightly positive pressure, expelling the dry air and creating a very high partial pressure of water inside the susceptor. The presence of steam inside the susceptor was easily verified visually by observing condensation on various components above the susceptor prior to and during each test.

5.2.2 Load Train and Test Setup

The test method developed for testing polycrystalline YAG and LuAG specimens in compression employs a load train with several components, which are used to hold the specimen in place and to transfer the compressive force from the upper and lower hydraulic wedge grips to the specimen within the furnace. The critical elements of the load train that extended from the grips into the furnace and contacted the specimen were single-crystal YAG push rods of 10.16 mm (0.4 in) diameter. Push rods that could withstand high temperatures were necessary to extend the load train from the hydraulic wedge grips into the hot zone of the furnace, where the

specimen was placed. Single-crystal YAG was chosen as an appropriate material for compression extension rods because of their excellent deformation resistance at high temperature. Previous tests have been conducted, which demonstrated the exceptional creep resistance of single-crystal YAG at 1300°C in air and in steam. It was determined that at these test conditions, there was essentially no measurable deformation. This quality of single-crystal YAG has made it a very effective material for transferring the compressive load to the specimen without excessive deformation and without sustaining significant damage during each test.

The push rods were mounted on two custom-built stainless-steel fixtures, which were gripped by the water-cooled hydraulic wedge grips. These YAG rod holders were fabricated by the AFIT Model Shop, and were designed such that one end was machined flat in order to be gripped by the flat wedge grips attached to the material testing machine. The hydraulic wedge grips provided enough lateral pressure that the YAG rod holders would not slip in compression. At the other end of the YAG rod holder was a cylindrical opening, approximately 1” in length, which held the YAG rod. This portion of the YAG rod holder was split into two halves and held together by four screws. The YAG rod holder could be opened at any time in order to remove a YAG rod and clean out any debris from the opening. A small slot was machined into each YAG rod holder just below the cylindrical opening in order to hold a small piece of thin copper foil (0.0004” thick). Copper foil was used to cushion the ends of the YAG rods. Additionally, strips of copper foil were wrapped around the lower portion of the YAG rods where they contact the YAG rod holders in order to soften the contact points between the YAG rods and holders and to also assist in the removal of the YAG rods after high temperature exposure. The custom YAG rod holders are shown in Figure 79. The YAG rods and the custom YAG rod holders are also visible in use in Figure 76.

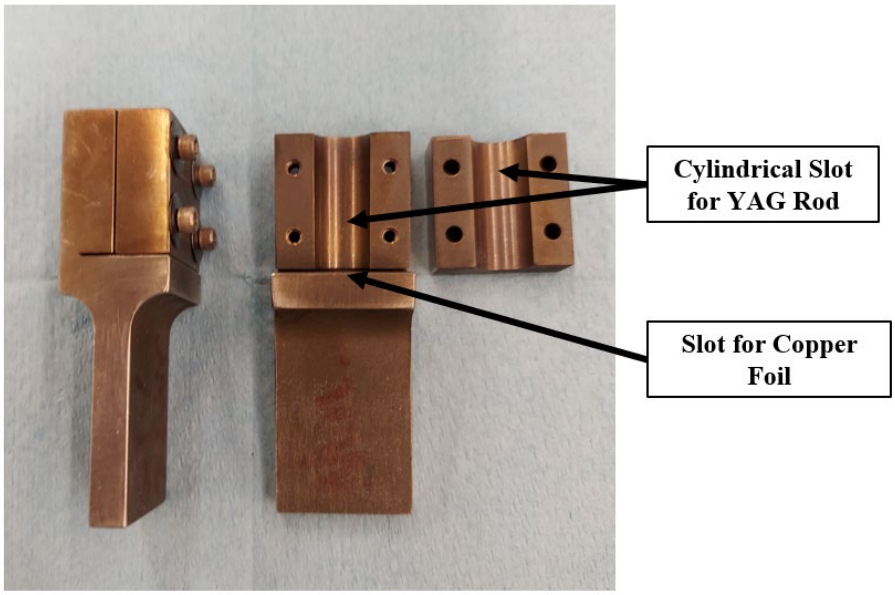

Figure 79: Custom stainless-steel YAG rod holders, developed for compressive creep tests at AFIT.

The test specimens were compressed between the push rods. Compressive loading is transferred through the ends of the single-crystal YAG push rods to the compression specimens. The close fit of the circumference of the push rods and the cylindrical openings of the YAG rod holders is designed to ensure proper alignment, and it was designed not to transfer the desired compressive load through lateral force. The loads induced on the circumference of the push rod due to any small misalignment would be relieved by loosening the set screws on the YAG rod holders after the load train had been assembled, immediately prior to conducting each test. For elevated temperature testing the furnace was positioned such that the test specimen was centered in the hot section. A portion of the top and bottom push rods were also located inside the hot section of the furnace in contact with the specimen. A diagram of this creep test setup and load train is shown in Figure 80.

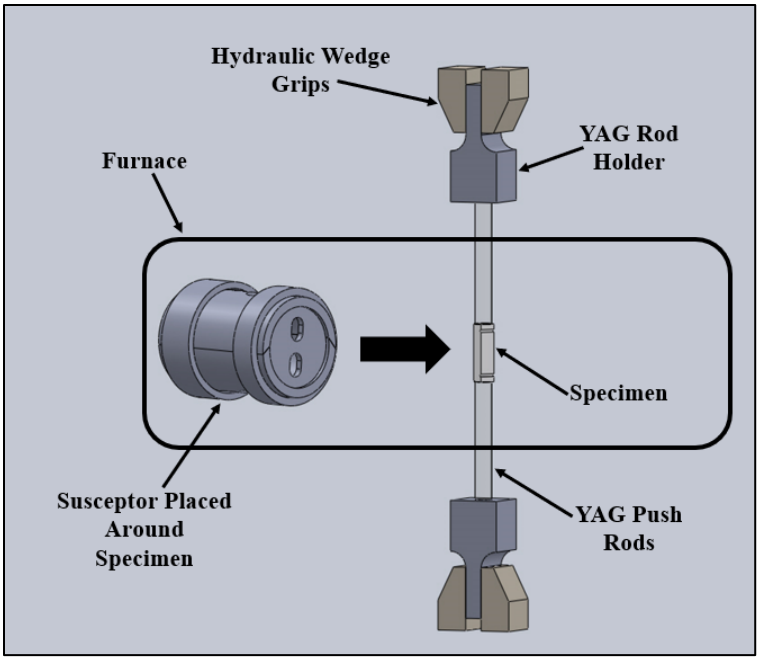

Figure 80: Diagram of the compression creep test setup.

5.3. Creep Test Preparation and Procedures

The following paragraphs describe the activities that were accomplished prior to, during, and after each creep test. Prior to executing the creep test procedures, equipment calibration was required to ensure the resulting data was accurate. It was necessary to calibrate the furnace temperature in order to determine the appropriate temperature controller set points, which would result in the desired specimen temperature. Additionally, it was necessary to calibrate the extensometer to ensure that the strain values, which were output by the testing software, were accurate. Following equipment calibration, the creep test procedures could be followed. These procedures are summarized in this section, and are also listed in much more detail in Appendix E. The equipment calibration, creep test procedures, and data acquisition processes, which are discussed in this section, were utilized for all creep tests in this study for all materials.

5.3.1. Temperature Calibration and Determination of Thermal Strain

The temperature within the furnace is controlled by two upper and two lower Molybdenum Disilicide ($MoSi_2$) heating elements. These elements are controlled by a temperature controller, which receives feedback from two thermocouples placed inside the furnace, measuring the ambient temperature of the hot zone of the furnace. This system is able to control and maintain a very stable and consistent temperature based on the internal temperature measurements. However, the thermocouples, which take the internal temperature reading and influence the temperature controller command signal are not in contact with the specimen. Because there is constant heat loss from small gaps in the furnace insulation as well as from conduction through the YAG rods and load train, there can be significant internal temperature gradients between different parts of the furnace cavity and within the specimen itself. The actual temperature of the specimen inside the hot section of the furnace during creep testing can differ substantially from the temperature controller set points. Therefore, prior to creep testing, the required temperature set points for the temperature controller, which would result in a precise specimen temperature, must be determined.

This temperature calibration was accomplished by bringing the furnace up to a desired temperature and simultaneously measuring the sample surface temperature, revealing any disparity between the temperature controller settings and the sample temperature. This enabled the temperature set points on the temperature controller, which produced the desired specimen temperature, to be determined. In order to accomplish this calibration, all the equipment was first set up as for a standard creep test. An actual specimen was placed between two single-crystal YAG push rods, and surrounded by the susceptor and furnace. A small load was applied to the specimen to maintain contact between the specimen and YAG rods in order to simulate the exact

conditions during creep testing. As the temperature was ramping up, a high-temperature Type S thermocouple protected by a rigid alumina sheath was inserted through the front opening of the susceptor and furnace, which was designed for the extensometer rods, and the thermocouple was placed in contact with the front surface of the specimen. It was assumed that due to the small size of the specimen, measuring the front surface was adequate in determining the homogeneous temperature throughout the specimen. In actuality, there was likely a small temperature difference from the front to the back of the specimen; however, this potential difference was assumed to be negligible.

Initial temperature calibrations were conducted for each material and for each target creep test temperature in air and in steam environments. With one contacting thermocouple held onto the surface of the specimen and two non-contacting thermocouples measuring the ambient within the furnace, the temperature was slowly increased and the offsets required to reconcile the controller set points and the specimen temperature were noted. The temperature was increased at a rate of 30°C/min up to the target temperature (either 1300°C or 1400°C). Once the desired controller temperature was reached, the temperature set point was held in place. The initial specimen temperature was noted as well as the length of time required for specimen temperature fluctuations to stop, which took approximately 15 minutes, and typically resulted in approximately a 25°C difference between the controller set point and the specimen surface temperature. The controller set point was then increased again slowly in small increments of a few degrees in order to slowly track the specimen temperature increase. Once the specimen reached the desired temperature, the temperature increase was stopped, and the temperatures of both the ambient and the specimen were observed for 30 minutes. If the specimen surface reading remained at the desired temperature for 30 minutes without fluctuation, then the

controller set point was noted, and the calibration was finished.

There was no difference in temperature calibration results for both YAG and LuAG specimens, indicating that they have similar thermal properties. For the specimen surface to reach 1300°C in air, the temperature controller set point must be 1328°C. For the specimen surface to reach 1300°C in steam, the temperature controller set point must be 1351°C. Similarly, for the specimen surface to reach 1400°C in air, the temperature controller set point must be 1435°C. Calibrations were not performed at 1400°C in steam as no creep tests were performed under these conditions. Each calibration was assumed to be valid for creep tests indefinitely until a furnace heating element failed. Once any heating element was replaced with a new one, temperature calibrations were conducted again to determine if any change in the power output of the elements had occurred. Typically, there was minimal difference, but the temperature offsets listed above were adjusted slightly whenever necessary.

During each creep test, the strain during heat up and soak was recorded. This was useful for several reasons. It allowed the thermal strain of the material to be quantified, it helped visualize the temperature offset between the furnace temperature reading and the sample surface temperature during heat up, and it allowed the thermal properties of the materials to be quantified. Measuring the thermal strain of the material was useful in validating the similarity and quality of each specimen used for creep testing. Every specimen tested behaved very similarly during heat up with almost identical thermal strain, ensuring that no individual specimen had significant defects or impurities.

Figure 81 and Figure 82 show the thermal strain measurements for three YAG and LuAG specimens, respectively, obtained during heat up prior to creep testing. A variety of specimens were chosen with different grain sizes. Each graph shows the accumulated thermal strain and the

furnace set temperature vs. time during heat up.

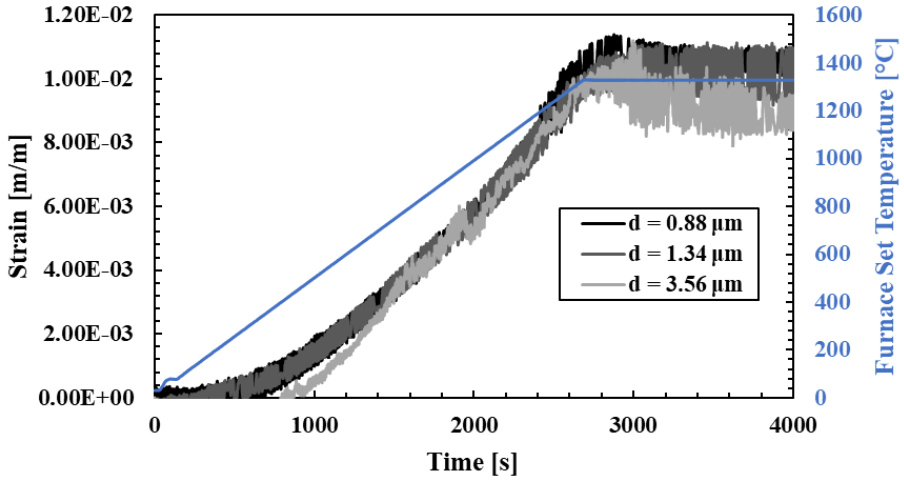

Figure 81: Thermal strain and furnace set temperature vs. time for three undoped YAG specimens during heat up to 1300°C prior to creep testing.

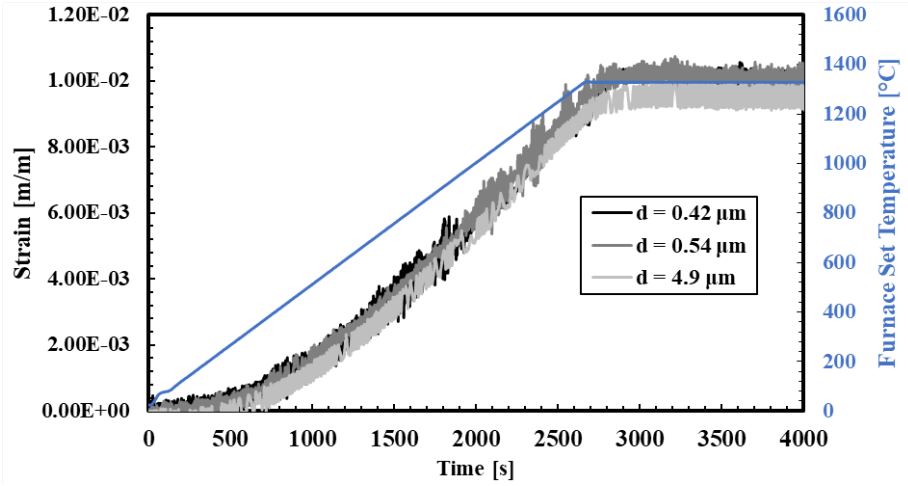

Figure 82: Thermal strain and furnace set temperature vs. time for three undoped LuAG specimens during heat up to 1300°C prior to creep testing.

The thermal strain measured for each specimen is very consistent for each material. Only minor variations are observed for specimens with different grain sizes. For both YAG and LuAG it appears that thermal strains are lower for specimens with larger grains. This is consistent with previous reports that certain materials have reduced coefficients of thermal expansion with

increased grain size [273]–[276]. However, this affect seems to be very small, almost negligible, for YAG and LuAG, at least for the grain sizes shown here. In each case the specimens accumulate approximately 1% strain during heat up to 1300°C. There also appears to be a significant discrepancy in the rate of strain accumulation vs. temperature. However, this could also be related to the discrepancy between the furnace temperature and the sample surface temperature.

The specimen surface temperature was measured during heat up for both YAG and LuAG. In order to accomplish this, the specimens were instrumented with the extensometer rods contacting the front surface, while a type-S thermocouple with an alumina sheath was placed in contact with the back surface of the specimen. Figure 83 and Figure 84 show the thermal strain vs. time as well as the furnace set temperature and the sample surface temperature rise during heat up.

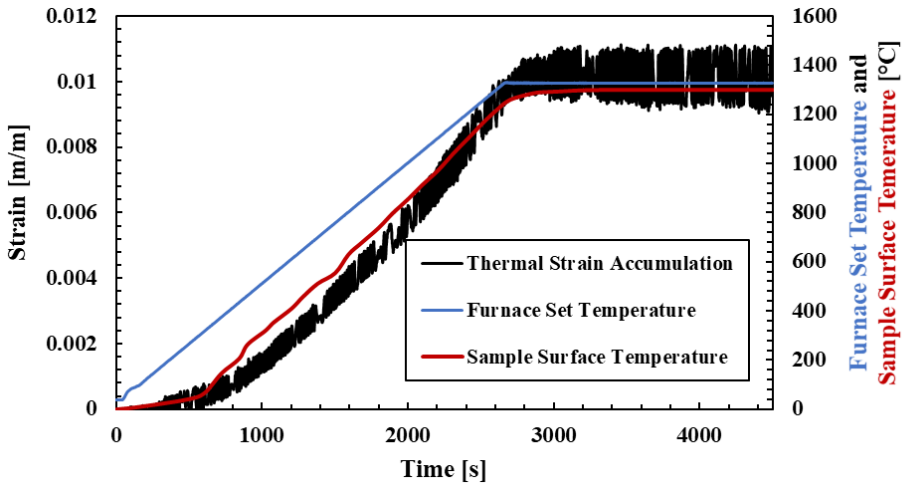

Figure 83: Thermal strain, furnace set temperature, and sample surface temperature vs. time for one undoped YAG specimen during heat up to 1300°C prior to creep testing.

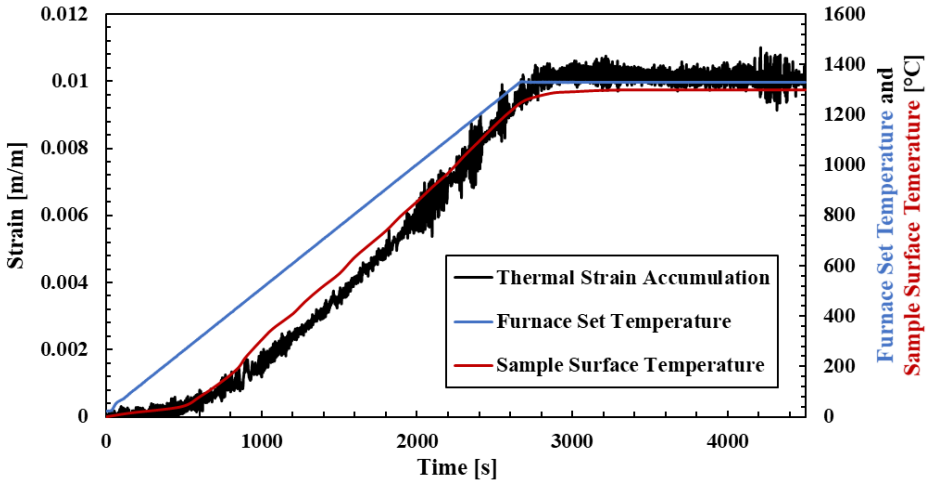

Figure 84: Thermal strain, furnace set temperature, and sample surface temperature vs. time for one undoped LuAG specimen during heat up to 1300°C prior to creep testing.

After observing the temperature discrepancy between the furnace temperature and the sample surface temperature, seen in Figure 83 and Figure 84 for YAG and LuAG, respectively, the slow rise in thermal strain at low temperature is understood. As the furnace temperature increases, there is a significant delay in the rise of the sample surface temperature. As is expected, there is a close correlation between the heating rate of the sample and the thermal strain.

In order to more closely compare the thermal strain observed in YAG and LuAG, the measured strain was plotted vs. the sample surface temperature for both materials, shown in Figure 85. Plotting strain vs. sample surface temperature enables the rate of heating to be removed, and to isolate the thermal expansion properties of both materials. Figure 85 shows that there is a small difference in the thermal strains measured for each material. Once the sample surface temperature increases beyond 500°C, YAG begins to achieve higher more thermal strain than LuAG, and this trend continues for the duration of heat up. Recall that LuAG has a higher melting temperature than YAG, which could lead to LuAG being more thermally stable and more resistant to thermal strain than YAG.

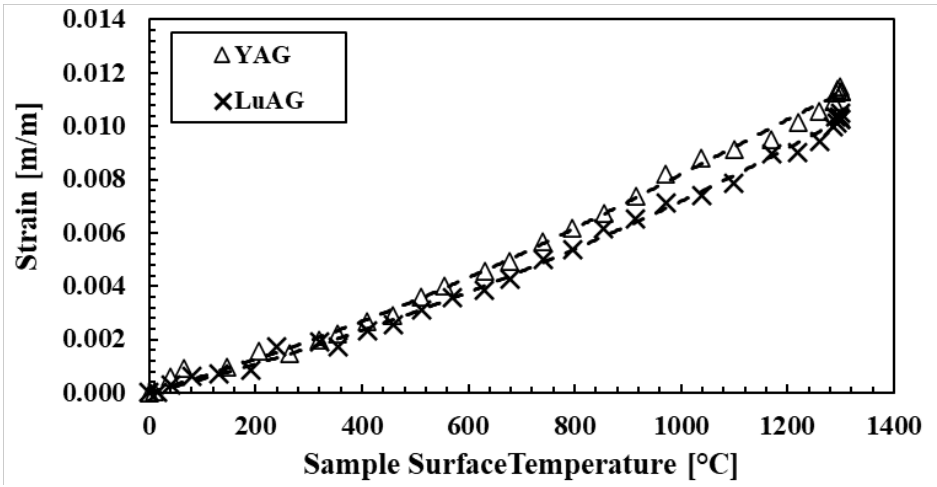

Figure 85: Thermal strain accumulation vs. sample surface temperature for YAG and LuAG.

From these thermal strain measurements, rough approximations of the coefficients of thermal expansion for both YAG and LuAG at temperatures ranging from room temperature to 1300°C was determined. The general equation for the coefficient of thermal expansion is as follows:

$$\alpha = \frac{1}{L}\frac{dL}{dT} \qquad \text{(Equ. 27)}$$

Using this equation, the approximate coefficients of thermal expansion can be determined for YAG and LuAG from the relationship between strain and sample surface temperature observed in Figure 83 and Figure 84. Individual coefficients were calculated for the strain measurements, which were associated with approximately every 100°C increase in sample surface temperature. The results for YAG are shown in Figure 86 along with some previously published values [277], [278]. Results for LuAG are shown in Figure 87.

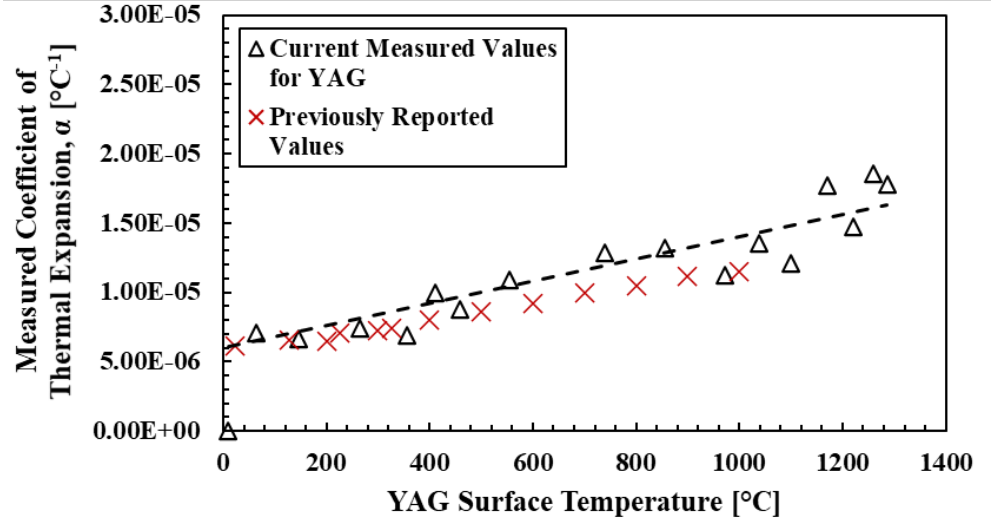

Figure 86: Approximate values of the coefficient of thermal expansion of YAG vs. temperature. Previously published values, shown in red, were determined by Furuse et al. and Sokol et al. [277], [278].

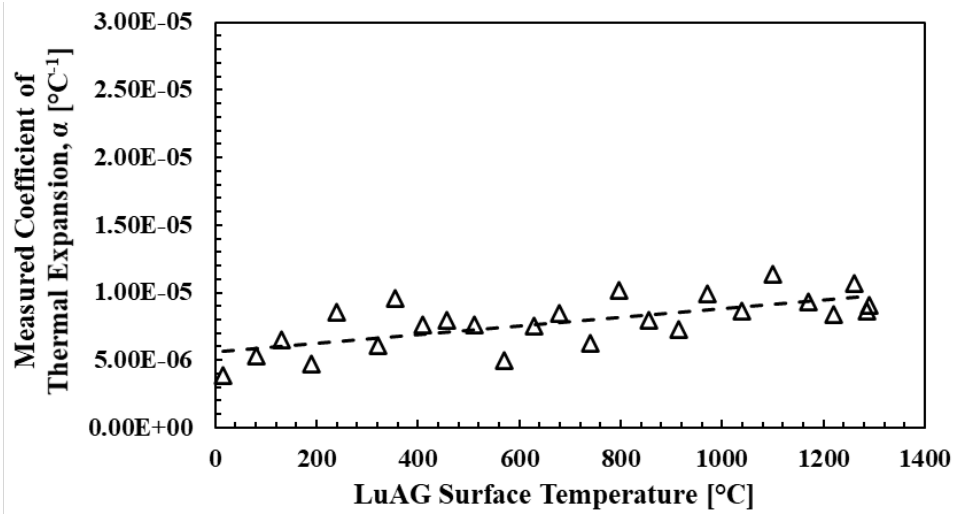

Figure 87: Approximate values of the coefficient of thermal expansion of LuAG vs. temperature.

There is a small but notable difference in the coefficients determined for YAG and LuAG. As was seen in Figure 85, LuAG has a greater resistance to thermal strain accumulation at a given temperature, compared to YAG. This difference is amplified as the sample surface temperature

increases. This comparison between the coefficients of thermal expansion of YAG and LuAG vs. temperature is shown in Figure 88.

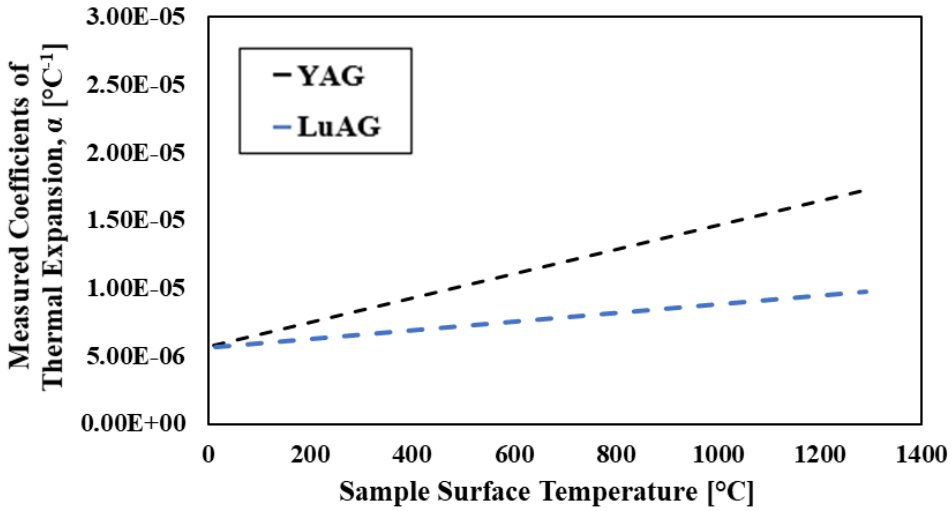

Figure 88: Comparison of the approximate coefficients of thermal expansion for YAG and LuAG vs. sample surface temperature.

Results in Figure 88 represent approximate values of the coefficients of thermal expansion for YAG and LuAG, as this is not a standard measurement method used in the analysis of thermal properties for these materials. There is significant noise in the thermal strain measurements due to the limitations in the precision of the extensometer. Therefore, the potential error associated with the noise in strain measurements not only affects the determination of total accumulated strain, but also the strain vs. sample temperature, shown in Figure 85. In order to plot the strain vs. sample temperature, individual strain values were taken from Figure 83 and Figure 84. Therefore, the resultant data can be significantly affected by the noise in the raw strain data. This source of potential error carries over into the determination of the coefficients of thermal expansion. Therefore, these measurements are should simply be used as a check into the quality of the processed material, and also to determine the relative thermal expansion properties of YAG vs. LuAG.

5.3.2. Extensometer Calibration and Measurement Limitations

Extensometers are tools used to measure the deformation of a material under stress during any kind of mechanical test. In the case of creep tests in this study, an extensometer, shown in Figure 77, was used to measure the total axial strain over time under a compressive stress. The strain measurement must be used to determine the total strain accumulated during creep, and also to determine the steady-state creep rate of each material. Extensometers typically need to be calibrated to ensure that the voltage output from the extensometer to the testing software equates to the correct amount of strain. The calibration also takes into account the length of the extension rods that are used to connect the extensometer to the specimen. For all the tests in this study, the extensometer rods were 6 inches long. The maximum voltage signal from the extensometer must equate to the maximum positive movement of the tips of the extension rods. Similarly, the minimum voltage signal from the extensometer must equate to the maximum negative movement of the tips of the extension rods. Rods of different lengths will require a new calibration to account for the associated change in the range of movement of the rod tips.

The gauge length of the extensometer is the space between the extension rod tips when the device is set to its center location, or more specifically, it is the axial length measurement that equates to zero strain. In this case, the gauge length of the extensometer used in these creep tests was 0.5 in. The extensometer calibration took place by mounting the extensometer onto a precision micrometer, which measured the distance between the tips of the extensometer rods. By using the extensometer zero bar, provided by MTS, the precise gauge length could be established, and the voltage output was set to zero. A detailed calibration procedure was followed, which involved moving the extensometer rods to different distances, and adjusting the output voltage to correspond to the correct strain. A calibration window was used within the

MTS software, which enabled the adjustment of the strain output based on the extensometer voltage and the micrometer reading.

The use of this specific extensometer and associated data acquisition software resulted in strain measurement limitations. As is the case with any distance measurement device, there are set maximum and minimum values, as well as precision limits. The maximum strain that could be measured by this extensometer was approximately 15% strain. This value was affected each time the rods were mounted on a specimen and the strain reading was zeroed out. If the extensometer was in a positive strain position, then the maximum strain value would increase beyond 15%. The minimum strain capability of this extensometer was dependent on the sensitivity and precision of the measurements. This particular extensometer is capable of measuring very small strains associated with strain rates of approximately 10^{-10} s^{-1}. This precision makes it an effective instrumentation device for creep testing. However, even after a precise calibration of the extensometer, there was typically a fluctuation of approximately ±100 mV, which equates to 0.2% strain. Therefore, when measuring the strain of the most creep resistant specimens in this study, there could be significant noise observed in the data, and this must be acknowledged as a potential source of error.

5.3.3. Creep Test Procedures

Compressive creep tests were performed on polycrystalline YAG and LuAG specimens at 1300°C and 1400°C in air and in steam. Creep stress levels during all creep tests ranged from 50 MPa to 200 MPa. Typically, specimens from the same sample set or different sample sets with similar microstructure and grain size were tested at various stress levels under the same

temperature and environmental conditions. In these cases, stress levels were adjusted from 50 MPa to 200 MPa in 50 MPa increments for each specimen.

Specimens were loaded into the furnace and placed between the YAG push rods, as was described previously in this section. A force of 100 lbf was applied to the specimen to ensure it stayed in place during heat up. The susceptor was enclosed around the specimen, and the extensometer was placed onto the mounting fixture, with rods extending through the opening in the susceptor, with the rod tips placed in the horizontal grooves on the specimen. If the specific test required the addition of steam, then the steam delivery tube was connected to the steam generator and the back opening of the susceptor. The furnace was then closed around the specimen and susceptor. Additional soft insulation pieces were placed on the top of the furnace to help protect the upper grips, and the extensometer cooling fan was attached to the mounting fixture and turned on.

Each creep test procedure consisted of three segments: heat up, creep, and cool down. During heat up, the temperature within the furnace was ramped up to the desired temperature at a rate of 0.5°C/s, and the temperature was maintained for 30 minutes in order to achieve thermal equilibrium within the specimen.

After the specimen soaked at the desired temperature for 30 minutes, the creep stress was applied at a rate of approximately 15 MPa/min. Each specimen remained under load at the desired temperature for 5 hours or until specimen failure occurred. In most cases, the specimen did not fail within the 5-hour test time. After 5 hours, the load was removed and the temperature was lowered back to room temperature. The internal furnace cavity and specimen were left to cool unassisted, which took approximately 90 minutes.

Creep test parameters, including temperature, stress level, and environment were adjusted sequentially between tests in order to isolate the effects of each setting individually. Additionally, the same test conditions were often repeated for specimens of various properties and microstructures in order to determine their potential effects on the resulting creep behavior. In most cases only one specimen with a given microstructure and grain size was tested under specific conditions due to the limited number of available specimens.

Throughout all three segments of each test, stress-strain data was collected as well as the associated furnace temperature setting. The data recorded during the heat up portion of the test enabled observations of thermal strain and determination of certain thermal properties of each material. Data recorded during the creep portion of each test enabled the observation and analysis of creep strain over time. These results contributed to the determination of the steady-state creep strain rates for each material under each test condition.

Detailed creep test procedures, which include the test setup process and the execution of a creep test, are included in Appendix E. The specific desired goals/outcomes of creep testing can be summarized as follows:

1. Conduct creep tests on each material variant at 1300°C in air and in steam at 50, 100, 150, and 200 MPa
2. Conduct creep tests on undoped YAG and LuAG at 1400°C in air at 50, 100, 150, and 200 MPa
3. Repeat similar test conditions for specimens of different grain sizes for each material variant
4. Determine creep strain as a function of time for each specimen after each creep test

5. Determine the maximum accumulated strain and the steady-state creep strain rate for each specimen after each creep test
6. Determine the creep stress exponent at each temperature for each material variant
7. Determine the grain size exponent at each temperature for each material variant
8. Determine the activation energy for undoped YAG and LuAG
9. Determine active mechanisms controlling the creep of all material variants

6. Creep Behavior of Undoped and Doped Yttrium Aluminum Garnet ($Y_3Al_5O_{12}$) at Elevated Temperature

This chapter describes the compressive creep behavior of polycrystalline Yttrium Aluminum Garnet ($Y_3Al_5O_{12}$, YAG). Creep specimens, which are described in detail in Section 5.1, were tested in compression at 1300°C and 1400°C at various stress levels, between 50 MPa and 200 MPa. Each creep test consisted of the following parts:

1. Heat furnace up to the desired temperature (45 mins)
2. Hold to allow the specimen to reach uniform temperature (30 mins)
3. Apply compressive creep stress and hold stress constant (5 hrs)
4. Simultaneously reduce temperature and remove compressive stress (5 mins)
5. Allow specimen to cool to room temperature (90 mins)

This investigation of the compressive creep behavior of polycrystalline YAG builds on the work of Armani et al. [28], [29], where undoped and silica-doped, polycrystalline YAG specimens were similarly tested in air and in steam at 1300°C. During this previous work, due to the material limitations as well as the time and equipment required for each test, only a limited number of creep tests were accomplished, which included testing specimens with only one grain size for each type of material. The work of Armani et al. was very valuable to the material science community, as it demonstrated the impressive creep performance of YAG compared to other oxide ceramics [28], [29]. Therefore, the test results presented in this chapter will validate as well as build on the work of Armani et al. by testing the same material in similar environments, and will then expand on the previous work by testing several more undoped, polycrystalline YAG specimens with several different grain sizes in air and in steam, at 1300°C and 1400°C. Two additional doped YAG variants will be tested as well: 2at% Yb-doped YAG

and 2at% Er-doped YAG, both of which are common, doped YAG variants, typically used in optical material applications.

The results from each creep test consisted of the measured creep strain over time. From these strain vs. time curves, the steady-state creep strain rates were determined and analyzed. This minimum creep strain rate, described by Equation 4, is the primary focus of this investigation. This chapter will demonstrate the effects of temperature, applied creep stress, grain size, environment, and material dopant on the total accumulated strain during creep and the resultant steady-state creep strain rate. In order to determine these effects on strain rate, a test plan was developed where each of these variables were isolated and adjusted, while all others remained constant, in order to understand the effects of each individually. Finally, the stress exponents and grain size exponents, used in Equation 4, were determined from the results of these creep tests by analyzing the steady-state creep strain rates at various stress levels and various grain sizes. These exponents, which were determined experimentally for each sample set, can be averaged together to obtain an approximation of the true exponents, which represent inherent material properties of YAG, and can be used in Equation 4 to predict the steady-state creep strain rates of YAG, including material variants and environmental conditions that were not tested in this study.

6.1. Creep of Undoped, Polycrystalline Yttrium Aluminum Garnet at 1300°C in Air

6.1.1. Validation of Creep Test Method Based on Published Results

The original creep strain vs. time curves, obtained by Armani et al. for undoped, polycrystalline YAG specimens at 1300°C in air with a grain size of 0.92 μm, are displayed in

Figure 89 [28], [29]. These original results were obtained with permission from the authors and are displayed here in a format, which is consistent with the rest of the results in this chapter. Figure 89 shows the resulting creep strain for four different compression creep tests, conducted at 50, 100, 150, and 200 MPa, originally presented by Armani et al [28], [29]. All the creep tests in this study have been conducted within this same compressive stress range in order to achieve consistency with the previous results.

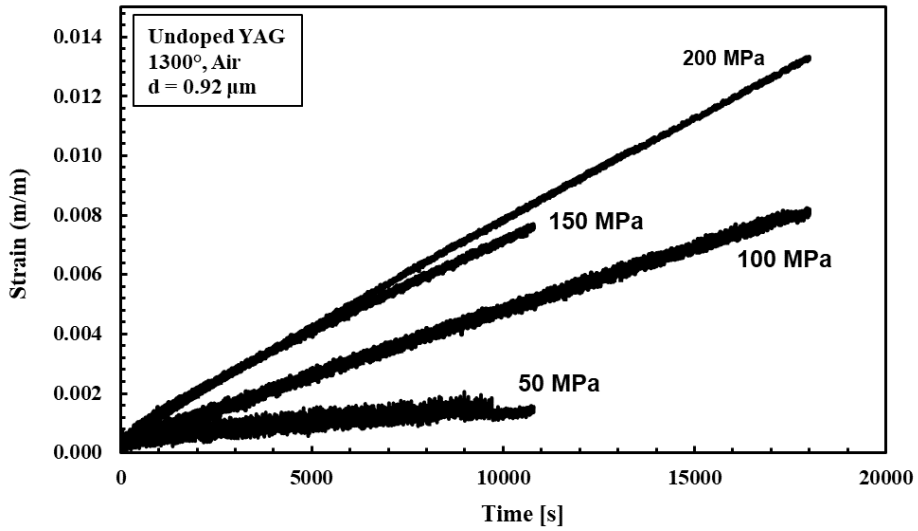

Figure 89: Creep strain vs. time curves obtained by Armani et al. for undoped, polycrystalline YAG specimens with grain size of 0.92 µm at 1300°C in air [28], [29].

For this material at these test conditions (stress, temperature, environment, test length), the results are nearly linear. There is minimal primary creep and no apparent tertiary creep reached in the allotted five-hour test time. Two of the four specimens were tested for 5 hours, while the other two were removed from testing earlier. In order to validate the consistency and quality of the materials and test methods used in this study, it was necessary to first achieve results consistent with these previous creep results found for undoped, polycrystalline YAG. It is necessary to mention that the two test methods are similar, but slightly different. The previous

creep tests by Armani et al. utilized shorter creep specimens (10 mm height), without any notches machined into the side of the specimens for extensometer mounting. Instead, similar notches were machined into the sides of the single-crystal YAG push rods, and the extensometer rods were mounted in these grooves, having no direct contact with the specimens. Within the test conditions selected by Armani et al, it was determined that the single-crystal YAG push rods do not exhibit any measurable strain; therefore, it was deemed acceptable to mount the extensometer rods on the push rods instead of directly on the short samples, which were too small for the available extensometer, which had a gauge length of 0.5 inches (12.7 mm). The resultant creep strain readings were numerically adjusted in order to compensate for the fact that the gauge length was longer than the actual material being tested.

The new specimens used in this investigation were fabricated with greater height (h = approximately 19 mm, as was described in Section 5.1), which means that the notches for mounting the extensometer rods could be machined directly into the side the specimen. In order to validate this new test method for testing polycrystalline YAG specimens in creep, identical test conditions were used, to include the same material and a similar grain size. Even when attempting to recreate identical test conditions as was previously used by Armani et al, some variation was unavoidable. Although both materials are undoped, polycrystalline YAG specimens, processed from 99.999% pure YAG powder, the processing methods were different, as this work is focusing on the effects of spark plasma sintering. Additionally, if each specimen was processed at different times and came from different billets, then the grain size and densities will never be identical. Therefore, there exists some inherent error when comparing the creep results. However, these small sources of potential error proved to be insignificant after all other test conditions were held constant.

The specimens chosen to compare directly to the creep results obtained by Armani et al. were from the SPS billet Y-7-40, and were determined to have an average grain size of 1.17 μm. This billet was selected due to the number of available creep test specimens and because the grain size is very close to the value determined for specimens tested by Armani, which was 0.92 μm. Figure 90 shows an SEM image of the microstructure and grains of a specimen from Y-7-40. The grain size was measured by multiple methods as was described in Section 4.3.2. Some porosity was observed, but the density measurements for specimens from Y-7-40 were determined to be within the acceptable range for creep testing.

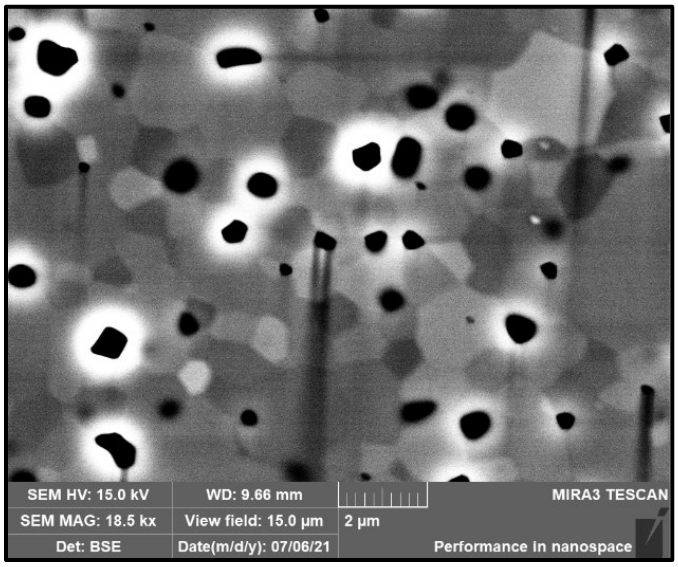

Figure 90: SEM image depicting the microstructure and grain size of a specimen from SPS billet Y-7-40.

The creep strain vs. time curves of undoped, polycrystalline YAG specimens at 1300°C in air with a grain size of 1.17 μm, are displayed in Figure 91. Three tests were conducted in order to compare these results with the previous work of Armani et al. The three tests were run at stress levels of 50, 100, and 150 MPa.

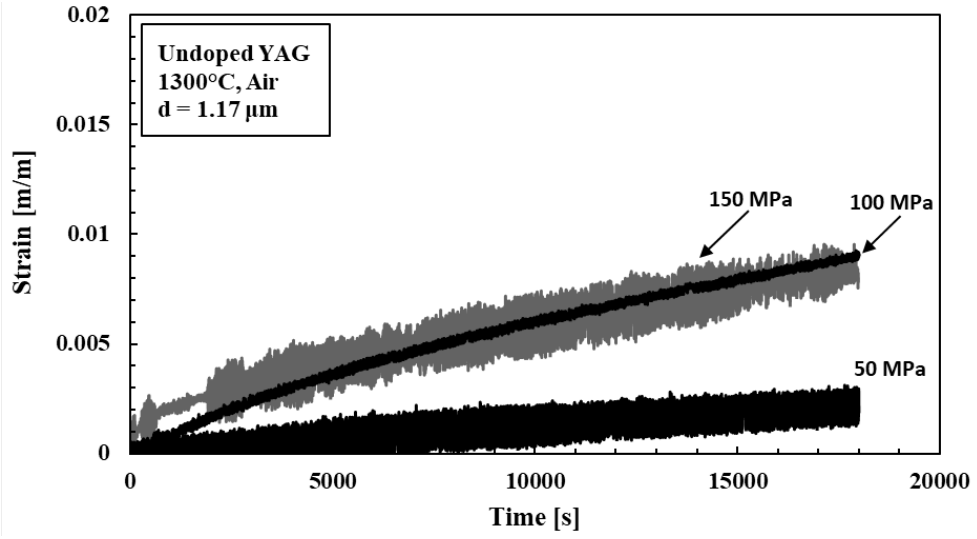

Figure 91: Creep strain vs. time curves obtained for undoped, polycrystalline YAG specimens with grain size of 1.17 µm at 1300°C in air.

From each strain vs. time curve, the total accumulated strain was determined as well as the minimum, steady-state creep strain rates. The strain rates were determined by measuring the slope of the flattest portion of the curve, which was typically at the end of each strain vs. time curve. This method has been used previously to determine the best approximation of the steady-state creep strain rate [28], [29]. A summary of these initial results, including the creep strain accumulated after 5 hours and the measured steady-state creep strain rate, for undoped, polycrystalline YAG specimens at 1300°C in air with grain sizes of 0.92 µm and 1.17 µm, is displayed in Table 18.

Table 18: Summary of creep results for undoped, polycrystalline YAG with comparable grain sizes at 1300°C in air. Results for specimens with grain size of 0.92 μm from Armani et al. (2011) are included for comparison [28], [29].

Specimen Name	Grain Size [μm]	Creep Stress [MPa]	Total Accumulated Strain after 5 hrs [%]	Steady-State Creep Rate [s^{-1}]
Armani-1*	0.92	50	Not Available**	1.09×10^{-7}
Armani-2*	0.92	100	0.81	3.94×10^{-7}
Armani-3*	0.92	150	Not Available**	5.69×10^{-7}
Armani-4*	0.92	200	1.33	6.91×10^{-7}
Y-7-40-1	1.17	50	0.30	9.49×10^{-8}
Y-7-40-2	1.17	100	0.92	3.21×10^{-7}
Y-7-40-3	1.17	150	0.95	3.42×10^{-7}

*Results obtained by Armani et al. and referenced in this work for comparison [28], [29].
**Creep tests ended early, and total strain accumulation after 5 hrs is unknown.

The steady state creep rates were then plotted versus the amount of compressive stress applied during each test in order to determine how the change in creep stress affects the steady-state creep strain rate. The exact force applied during each test varied based on the specific cross-sectional area of each specimen. This plot is shown in Figure 92 for the Y-7-40 sample set at 1300°C in air with a grain size of 1.17 μm along with the previous results from Armani et al. which were included for comparison [28], [29].

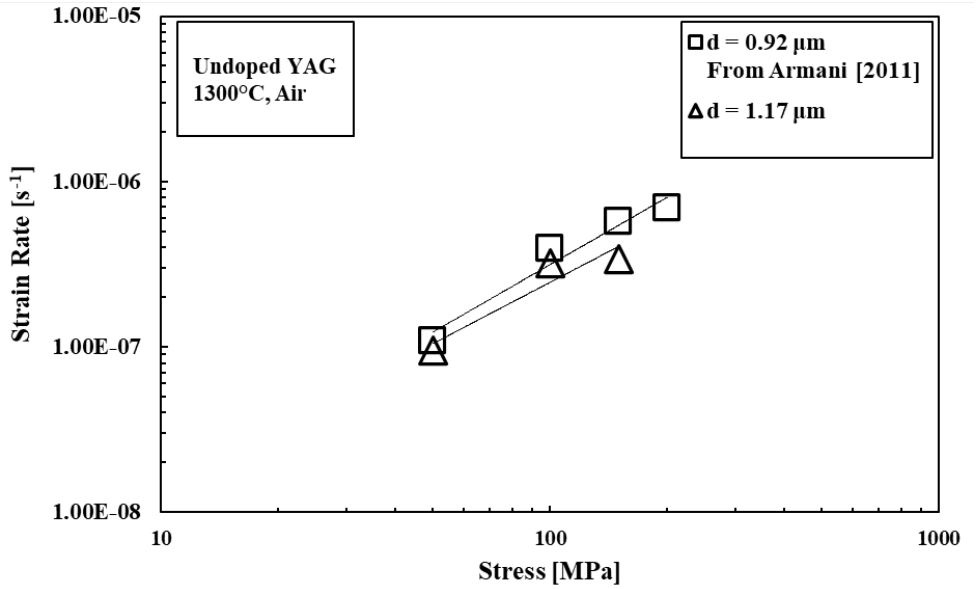

Figure 92: The steady-state creep strain rate vs. applied stress of undoped, polycrystalline YAG specimens with grain sizes of 0.92 µm and 1.17 µm at 1300°C in air. Results for specimens with grain size of 0.92 µm from Armani et al. (2011) are included for comparison [28], [29].

The strain rate vs. stress curves were plotted using a log-log scale in Figure 92, resulting in an apparently linear relationship as is typically found in the steady-state creep rates observed for similar materials. The relationship observed between the strain rates and the applied stress in Figure 92 follows a power law, which is based on a form of the Arrhenius strain rate equation, described by Equation 4 in Section 2.3.1. In this case all equation parameters are constant across each test except for the independent variable, which is the applied stress. This exponential relationship, which appears linear on the graph with a log-log scale, is validated with these initial tests using specimens from the Y-7-40 sample set for undoped, polycrystalline YAG at 1300°C in air. Also, from Figure 92, it is observed that the previous creep results from Armani et al. are very close, and nearly overlapping, which was expected for samples of such similar grain sizes.

Based on these nearly identical creep results for similar specimens of very similar grain sizes, it was concluded that both of these test methods, which utilize different specimen geometry, are effective in determining accurate creep strain rates of this material. The measured strain rates determined for specimens from the Y-7-40 sample set appear to be slightly lower than the that from the previously published results from Armani et al [28], [29]. Although this difference is very small and could easily be assumed to be within the noise from the strain measurements during each creep test, the difference could also be attributed to the small difference in material grain size (0.92 μm and 1.17 μm). As is observed in the next section, the material grain size is a critical material property, which greatly affects the overall creep behavior of YAG.

6.1.2. The Effects of Grain Size on the Creep Behavior of Yttrium Aluminum Garnet at 1300°C in Air

Additional undoped YAG specimens were tested in a similar manner in order to determine the effect of grain size on the overall creep behavior. The creep test results were compared for specimens from sample sets: Y-7-40, Y-14-40, and Y-13-40. Details of these billets, including the SPS processing parameters, test specimen dimensions, density, hardness, and grain size, can be found in Appendix A and B. They were primarily selected because of the variation in their grain sizes, which were measured to be 1.17 μm, 3.19 μm, and 7.99 μm. An SEM image from Y-7-40 is shown in Figure 90. SEM images taken from sample sets Y-14-40 and Y-13-40 are shown in Figure 93 and Figure 94, respectively.

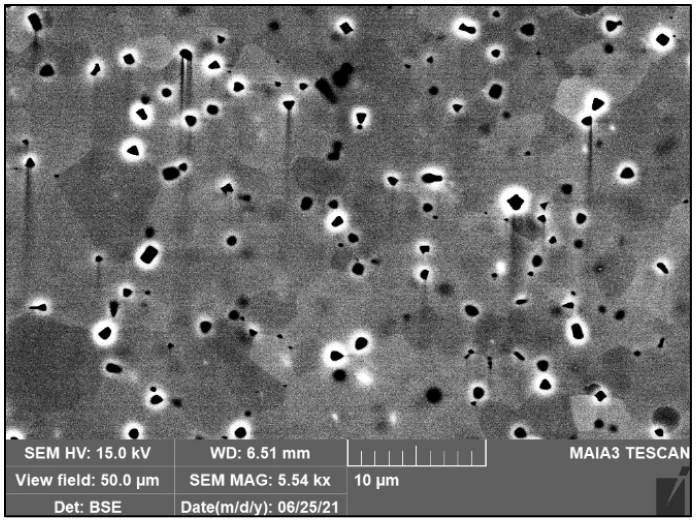

Figure 93: SEM image of a specimen cut from the SPS billet Y-14-40, with a measured average grain size of 3.19 µm.

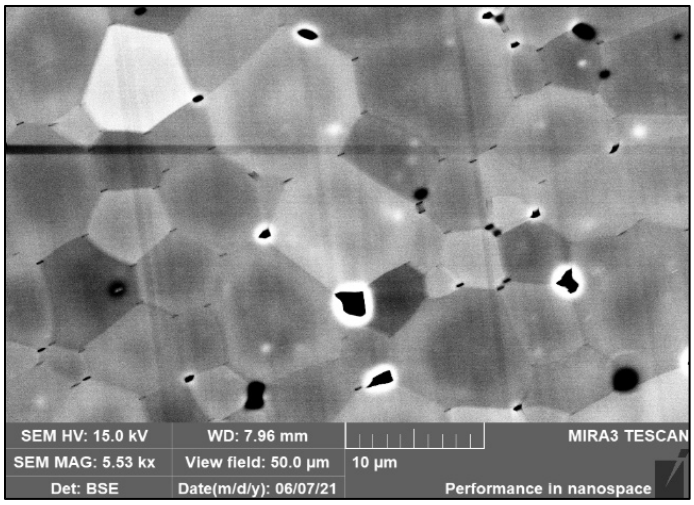

Figure 94: SEM image of a specimen cut from the SPS billet Y-13-40, with a measured average grain size of 7.99 µm.

Despite the different appearances of the SEM images, which are due to the inconsistent and sensitive nature of observing grains within these types of non-conductive oxide ceramics in an SEM, it is still apparent that the grain structure is generally consistent for each material. All grains have a sharp geometric shape, and do not possess smooth, curving edges. Each material possesses a considerable number of larger and smaller grains, which are apparent even within

such small view fields. This is due to the potentially large variation in size of neighboring grains, and also due to the use of a 2-dimensional view of the surface of a 3-dimensional material. Each grain is a 3-dimensional object, which has depth that cannot be seen by the SEM. Therefore, it is possible that small grains could actually be the visible tips of large grains, similar to an iceberg in the ocean. For these reasons, many grains must be averaged to determine a good approximation of the overall grain size for comparison between materials. Refer to Section 4.3.2 for a more detailed description of the grain size measurement methods used in this study.

In order to determine the effects of grain size, all other material properties and all test conditions were kept constant including the material type, processing method, test temperature, stress range, and environment. The creep strain vs. time curves for specimens with a grain size of 3.19 μm and 7.99 μm are shown in Figure 95 and Figure 96, respectively. Both sets of specimens were tested at 50, 100, 150, and 200 MPa.

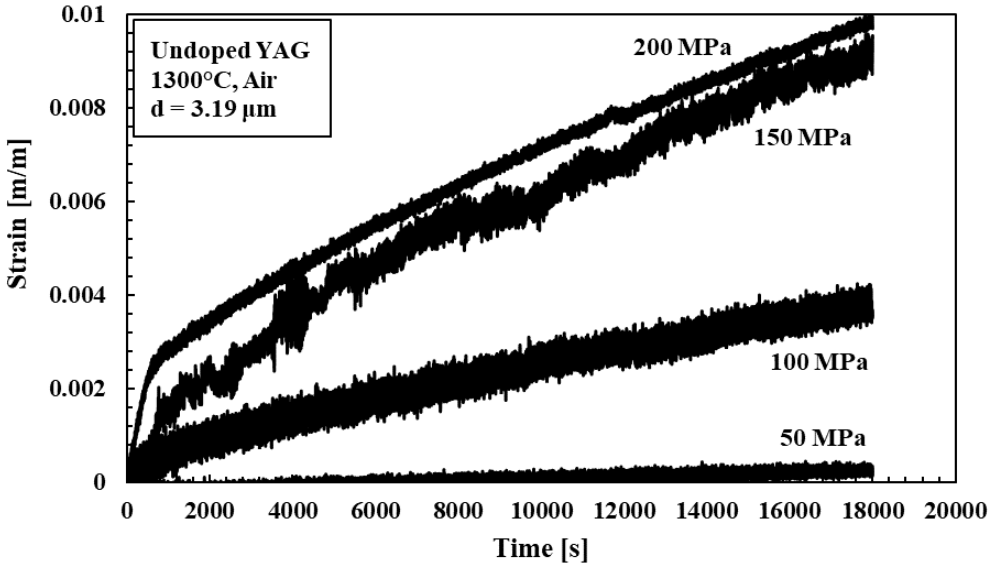

Figure 95: Creep strain vs. time curves obtained for undoped, polycrystalline YAG specimens with grain size of 3.19 μm at 1300°C in air.

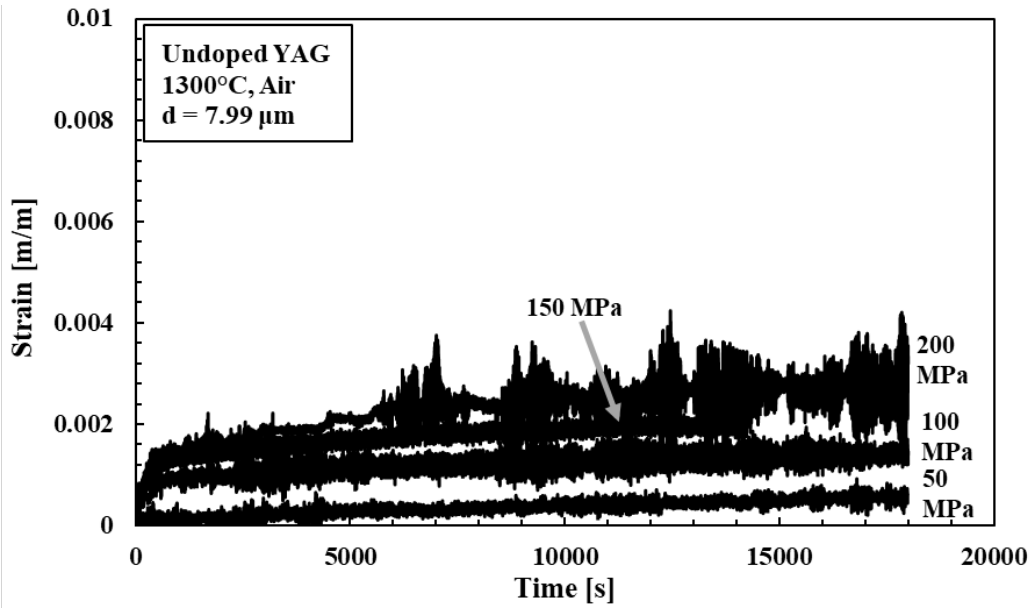

Figure 96: Creep strain vs. time curves obtained for undoped, polycrystalline YAG specimens with grain size of 7.99 µm at 1300°C in air.

Specimens with larger grain sizes exhibit significantly less creep strain under the same test conditions. As is seen in Figure 96, the total accumulated creep strain for specimens with a grain size of 7.99 µm only reaches 0.3%, even with 200 MPa applied during the test. This is close to the maximum sensitivity of the extensometer used in this study, and as a result, the strain vs. time curves exhibit significant noise during the creep tests. However, a clear trend is observed, and can still be used to determine the steady-state creep rates. These results as well as the steady-state creep rates and total accumulated strains for all the undoped YAG specimens tested at 1300°C in air are summarized in Table 19.

Table 19: Summary of creep results for undoped, polycrystalline YAG specimens with different grain sizes at 1300°C in air. Results for specimens with grain size of 0.92 μm from Armani et al. (2011) are included for comparison [28], [29].

Specimen Name	Grain Size [μm]	Creep Stress [MPa]	Total Accumulated Strain after 5 hrs [%]	Steady-State Creep Rate [s^{-1}]
Armani-1*	0.92	50	Not Available**	1.09×10^{-7}
Armani-2*	0.92	100	0.81	3.94×10^{-7}
Armani-3*	0.92	150	Not Available**	5.69×10^{-7}
Armani-4*	0.92	200	1.33	6.91×10^{-7}
Y-7-40-1	1.17	50	0.30	9.49×10^{-8}
Y-7-40-2	1.17	100	0.92	3.21×10^{-7}
Y-7-40-3	1.17	150	0.95	3.42×10^{-7}
Y-14-40-1	3.19	50	0.363	3.17×10^{-8}
Y-14-40-2	3.19	100	0.423	1.21×10^{-7}
Y-14-40-3	3.19	150	0.940	2.01×10^{-7}
Y-14-40-4	3.19	200	0.480	1.40×10^{-7}
Y-13-40-1	7.99	50	0.0648	1.34×10^{-9}
Y-13-40-2	7.99	100	0.152	4.16×10^{-9}
Y-13-40-3	7.99	150	0.23**	6.53×10^{-9}
Y-13-40-4	7.99	200	0.318	9.13×10^{-9}

*Results obtained by Armani et al. and referenced in this work for comparison [28], [29].
**Creep tests ended early, and strain accumulation after 5 hrs is approximated or unknown.

The results in Table 19 clearly illustrate the significant effect of grain size on the creep strain accumulated after five hours and on the overall steady-state creep strain rates of undoped, polycrystalline YAG. As grain size increases, the steady-state creep strain rates of YAG decrease drastically. Specimens with grain size of 7.99 μm reached minimum strain rates between 1.34×10^{-9} s^{-1} and 9.13×10^{-9} s^{-1} depending on the applied stress level. These results represent the lowest strain rates reported for polycrystalline YAG at 1300°C. At this grain size, these specimens achieved steady-state creep strain rates that are two orders of magnitude lower than the previously tested YAG material with grain size of 0.92 μm.

Additional plots are shown below, which illustrate the significant effects of grain size on the creep behavior of undoped, polycrystalline YAG at 1300°C in air. Figure 97 shows the strain vs. time curves for two sample sets with grain sizes of 1.17 μm and 3.19 μm. All strains shown in Figure 97 are very small; however, a significant difference is still observed. The 50 MPa curve for the smaller grain size is close to the 100 MPa curve for the larger grain size. Similarly, the 100 MPa curve for the smaller grain size nearly overlaps the 150 MPa curve for the larger grain size.

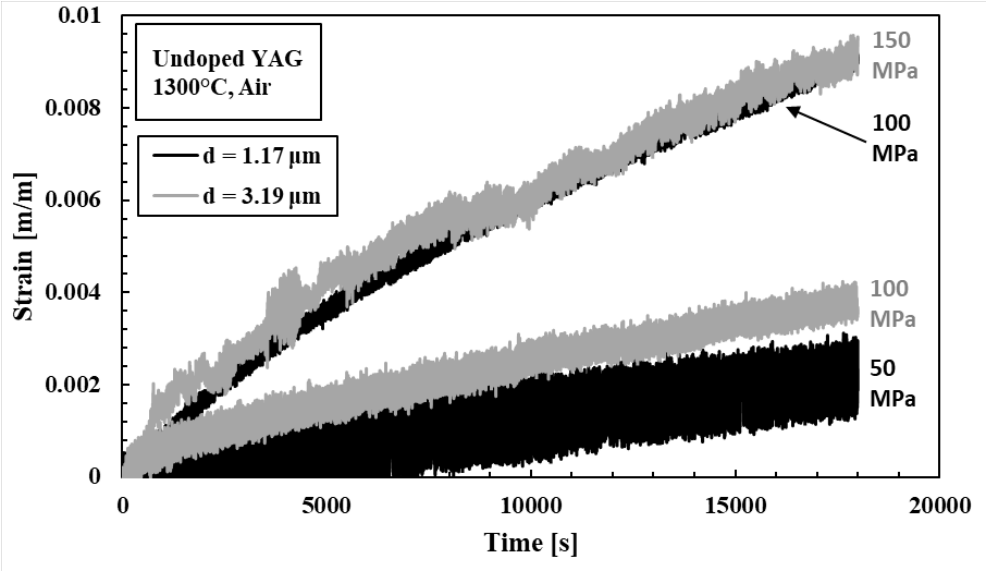

Figure 97: Comparison of the creep strain vs. time curves obtained for undoped, polycrystalline YAG specimens with grain sizes of 1.17 μm and 3.19 μm at 1300°C in air.

Similarly in Figure 98 the significant effects of grain size are illustrated by the strain vs. time curves for the three sample sets with grain sizes of 1.17 μm, 3.19 μm, and 7.99 μm. The same trend is observed, where the smaller grain sizes correspond to the highest accumulated creep strains. The one exception is creep results obtained at the lowest stress level. With an applied stress of 50 MPa, some tests showed that the effects of grain size were less pronounced. In this case the significant effect of grain size can be minimized by such a low applied stress. It appears

that for creep stresses of 50 MPa or lower, specimens will exhibit very low strain regardless of grain size.

In Figure 98 the strain accumulated by a specimen with a grain size of 3.19 was lower than the strain accumulated by a specimen with a grain size of 7.99. This is attributed to the diminished effects of grain size at 50 MPa. In other sections of this study a similar phenomenon was observed.

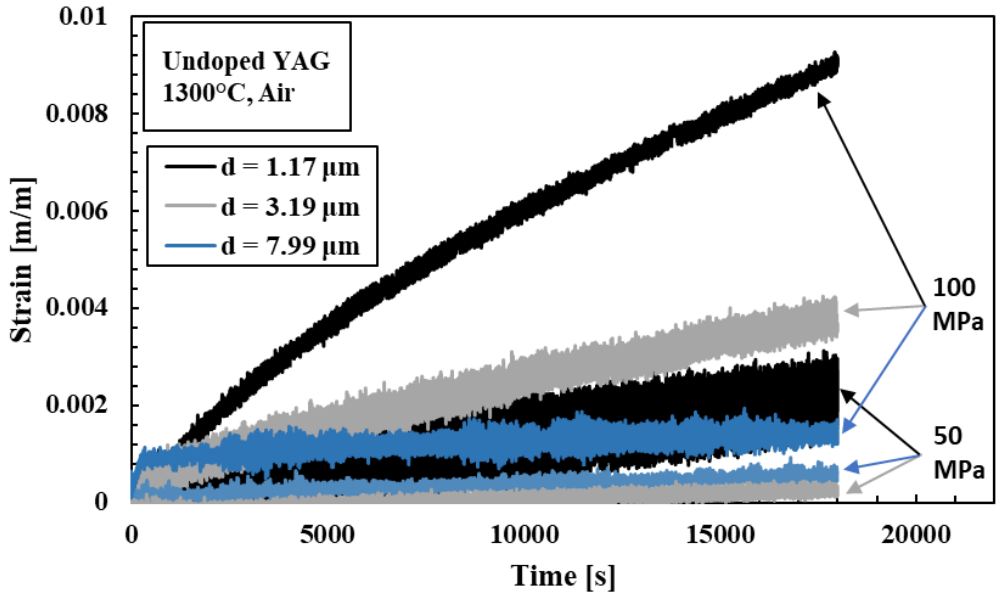

Figure 98: Comparison of creep strain vs. time curves obtained for undoped, polycrystalline YAG specimens with different grain sizes at 50 MPa and 100 MPa at 1300°C in air.

6.1.3. Determination of the Stress Exponent and Grain Size Exponent from the Steady-State Creep Results of Yttrium Aluminum Garnet at 1300°C in air

The creep results from each sample set described above were plotted on a log-log plot of strain rate vs. stress, shown in Figure 99. This graph illustrates the significant difference in steady-state

creep strain rates due to the difference in material grain size. Four different sample sets are shown in Figure 99 with grain sizes between 0.92 μm and 7.99 μm.

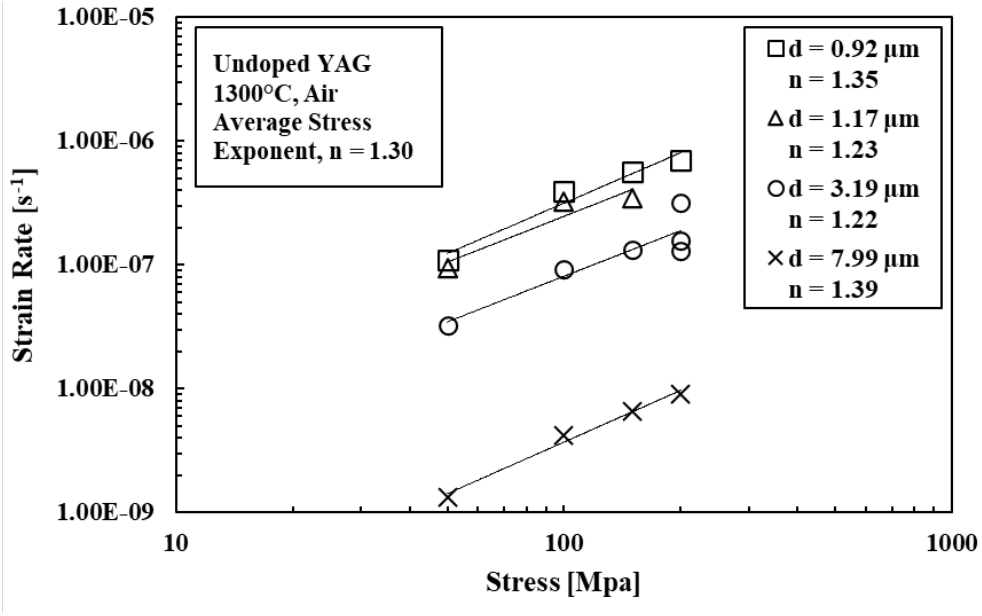

Figure 99: The steady-state creep strain rate vs. applied stress and the stress exponents, *n*, of undoped, polycrystalline YAG specimens with different grain sizes at 1300°C in air. Results for specimens with grain size of 0.92 μm from Armani et al. (2011) are included for comparison [28], [29].

It is also seen from Figure 99 that although grain size significantly affects the magnitude of the creep strain rates of YAG, it does not significantly alter the effect of stress on the resulting strain rate. The relationship between the applied creep stress and the resulting creep strain rate can be determined by plotting strain rate vs. stress on a log-log scale, as is shown in Figure 99. This plot allows the effects of stress to be isolated and measured by using linear regression to find a best-fit line associated with each set of date. Because the data is plotted on a log-log scale, each line corresponds to an exponential equation of the form:

$$\dot{\varepsilon} = A\sigma^n \qquad \text{(Equ. 28)}$$

Where σ is the applied stress during creep, n is the stress exponent, and A incorporates all other parts of the steady-state creep equation from Equation 4. From these Equations, the stress exponent can be determined. As is shown in the legend of Figure 99, and also in Table 20 below, the stress exponents for each set of samples with similar grain sizes are almost identical, and average to $n = 1.30$. This value of n is very close to that previously determined by Parthasarathy et al. and Armani et al. in their work on the creep of YAG [27]–[29]. Therefore, it was concluded that the grain size of undoped, polycrystalline YAG has a significant effect on the steady-state creep strain rates, but not on the stress exponent, for the range of grain sizes studied here (0.92 μm – 7.99 μm).

Table 20: The stress exponent, n, for undoped, polycrystalline YAG specimens with different grain sizes at 1300°C in air. Results for specimens with grain size of 0.92 μm from Armani et al. (2011) are included for comparison [28], [29].

Sample Set	**Grain Size [μm]**	**Stress Range [MPa]**	**Stress Exponent, *n***	**Average Stress Exponent, *n***
Armani 1 - 4*	0.92	50 - 200	1.35	**1.30**
Y-7-40	1.17	50 - 150	1.23	
Y-14-40	3.19	50 - 200	1.22	
Y-13-40	7.99	50 - 200	1.39	

*Results obtained by Armani et al. and referenced in this work for comparison [28], [29].

The grain size exponent, m, from Equation 4 was also determined in a similar manner to the stress exponent, n. The effect of grain size was isolated by grouping test results together based on the applied stress. Steady-state creep rates were plotted versus grain size on a log-log scale in Figure 100. Each specimen that was tested at a particular stress level was grouped with the others at that same stress level, and they were plotted as a series on the graph.

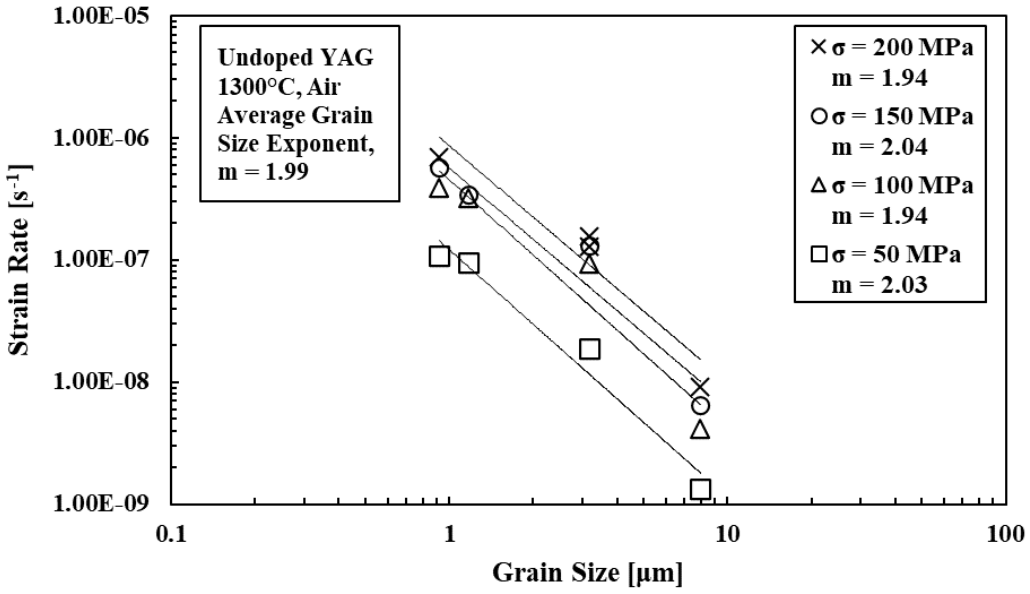

Figure 100: The steady-state creep strain rate vs. grain size and the grain size exponents, *m*, of undoped, polycrystalline YAG specimens at different creep stress levels at 1300°C in air. Results for specimens with grain size of 0.92 µm from Armani et al. (2011) are included for comparison [28], [29].

For each data series plotted in Figure 100, the stress, temperature, and environment were held constant, and the effects of grain size were isolated. To quantify this effect, a best-fit line was determined by linear regression for each group of results. The corresponding equation for each best-fit line on the log-log scale contains an exponent, similar to the analysis of the stress exponent above. In this case the exponent is a negative number, which corresponds to the inverse relationship between grain size and steady-state creep rate. This negative exponent represents the experimentally determined value of the grain size exponent, *m*. As is shown in the legend of Figure 100, and also in Table 21 below, the grain size exponents for each set of samples and applied stress values are almost identical, and average to $m = 1.99$.

Table 21: Grain size exponent, m, for undoped, polycrystalline YAG specimens at different creep stress levels at 1300°C in air. Results for specimens with grain size of 0.92 μm from Armani et al. (2011) are included for comparison [28], [29].

Creep Stress [MPa]	Grain Sizes [μm]	Grain Size Exponent, *n*	Average Grain Size Exponent, *n*
50	0.92*, 1.17, 3.19, 7.99	2.03	**1.99**
100	0.92*, 1.17, 3.19, 7.99	1.94	
150	0.92*, 1.17, 3.19, 7.99	2.04	
200	0.92*, 3.19, 7.99	1.94	

*Results obtained by Armani et al. (2011) and referenced in this work for comparison [28], [29].

6.2. Creep of Undoped, Polycrystalline Yttrium Aluminum Garnet at 1300°C in Steam

Undoped, polycrystalline YAG specimens were tested under similar creep conditions in steam in order to assess the effects of the environment on the overall creep behavior. Armani et al. previously tested undoped, polycrystalline YAG specimens with a grain size of 0.92 μm at 1300°C in steam and determined that the presence of steam had no significant effect on the creep behavior for that material at this temperature. The small differences between the current creep test method and previous work were already discussed and found to have no significant effects on the creep results. Therefore, results of this work can be directly compared to results obtained previously by Armani et al. For this reason, creep experiments on similar grain-sized YAG specimens were not repeated in steam. Rather specimens with a larger grain size of 7.99 μm (from the same sample set as was previously tested in air) were tested in steam in order to determine the effects of grain size in steam, and to determine any potential effects of environment on specimens with two different grain sizes.

6.2.1. The Effects of Grain Size on the Creep Behavior of Undoped Yttrium Aluminum Garnet at 1300°C in Steam

The first published results of the creep of undoped, polycrystalline YAG at 1300°C in steam were obtained by Armani et al [28], [29]. The creep strain vs. time curves from this earlier research are shown in Figure 101. These results were obtained with permission from the authors and are displayed here in a format, which is consistent with the rest of the results in this chapter. These first specimens tested in steam had a grain size of 0.92 μm, and came from the same sample set as the undoped YAG specimens tested in air by Armani et al.

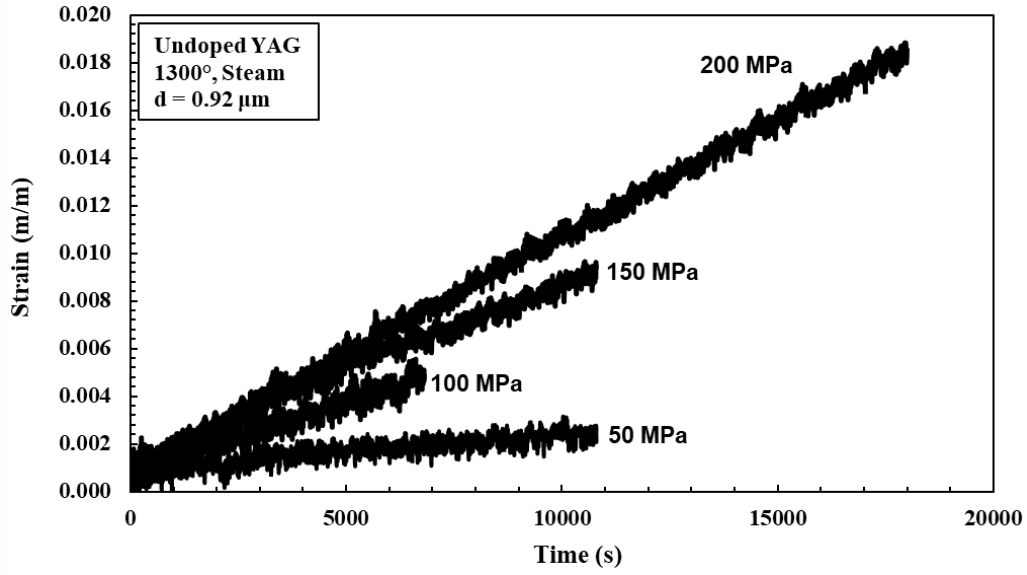

Figure 101: Creep strain vs. time curves obtained by Armani et al. for undoped, polycrystalline YAG specimens with grain size of 0.92 μm at 1300°C in steam [28], [29].

Specimens with a grain size of 7.99 μm, obtained from the same sample set as was tested in air, were also tested in steam. The resulting creep strain vs. time curves are shown in Figure 102. Due to the limited number of specimens, only three tests were performed, with creep stress levels of 50, 100, and 200 MPa.

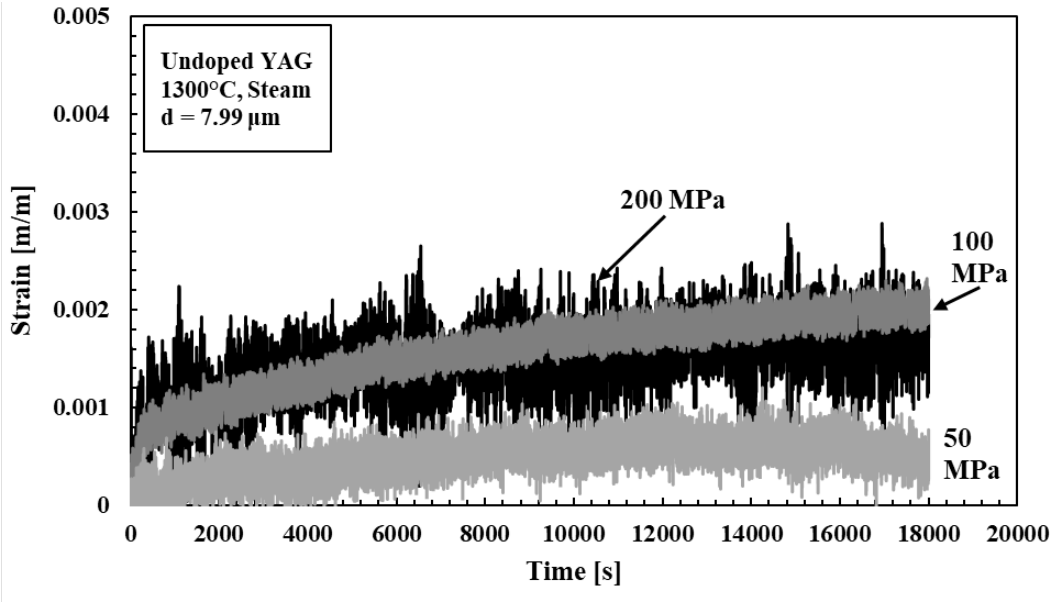

Figure 102: Creep strain vs. time curves obtained for undoped, polycrystalline YAG specimens with grain size of 7.99 µm at 1300°C in steam.

As was observed from the results of YAG specimens with grain size of 7.99 µm tested in air, creep strains are very low at all creep stress levels. The largest creep strain of 0.23% was accumulated at 200 MPa. The creep strains observed for specimens with larger grains are significantly less than those for specimens with smaller grains, as evidenced with results in Figure 101 and Figure 102. Table 22 below shows the accumulated strain as well as the steady-state creep rates for specimens with larger grains and for specimens tested previously by Armani et al. with grain size of 0.92 µm.

The steady state creep rates of undoped, polycrystalline YAG with a grain size of 7.99 at 1300°C in steam were determined to be between 1.66×10^{-9} and 1.21×10^{-8} s^{-1}. These creep rates are very similar to those found for specimens from the same sample set, which were tested in air. The steady-state creep rates were measured after careful examination of the creep strain vs. time curves in Figure 102. Part of the curves level out and are completely horizontal, and small portions of the curves actually possess a negative slope. These characteristics of the strain vs.

time curves can make it difficult to identify the steady-state portion for analysis. However, after careful examination, portions of the curves that most likely represent the steady-state creep regimes were isolated, and the steady-state creep strain rates were determined.

Table 22: Summary of creep results for undoped, polycrystalline YAG with grain sizes of 0.92 μm and 7.99 μm at 1300°C in steam. Results for specimens with grain size of 0.92 μm from Armani et al. (2011) are included for comparison [28], [29].

Specimen Name	**Grain Size [μm]**	**Creep Stress [MPa]**	**Total Accumulated Strain after 5 hrs [%]**	**Steady-State Creep Rate [s^{-1}]**
Armani-5*	0.92	50	0.32**	1.29×10^{-7}
Armani-6*	0.92	100	Not Available**	5.29×10^{-7}
Armani-7*	0.92	150	1.24**	7.31×10^{-7}
Armani-8*	0.92	200	1.83	9.46×10^{-7}
Y-13-40-1	7.99	50	0.097	1.66×10^{-9}
Y-13-40-2	7.99	100	0.22	5.26×10^{-9}
Y-13-40-5	7.99	200	0.23	1.21×10^{-8}

*Results obtained by Armani et al. and referenced in this work for comparison [28], [29].
**Creep tests ended early, and total strain accumulation after 5 hrs is approximated or unknown.

In order to compare the results obtained for specimens with the same grain size tested in air and in steam, the steady-state creep strain rates for all specimens with grain size of 7.99 μm were plotted on the same graph in Figure 103. There is little difference in the creep strain rates for specimens tested in air and in steam, and any small visual difference seen in Figure 103 is well within the potential error that could be present in these tests.

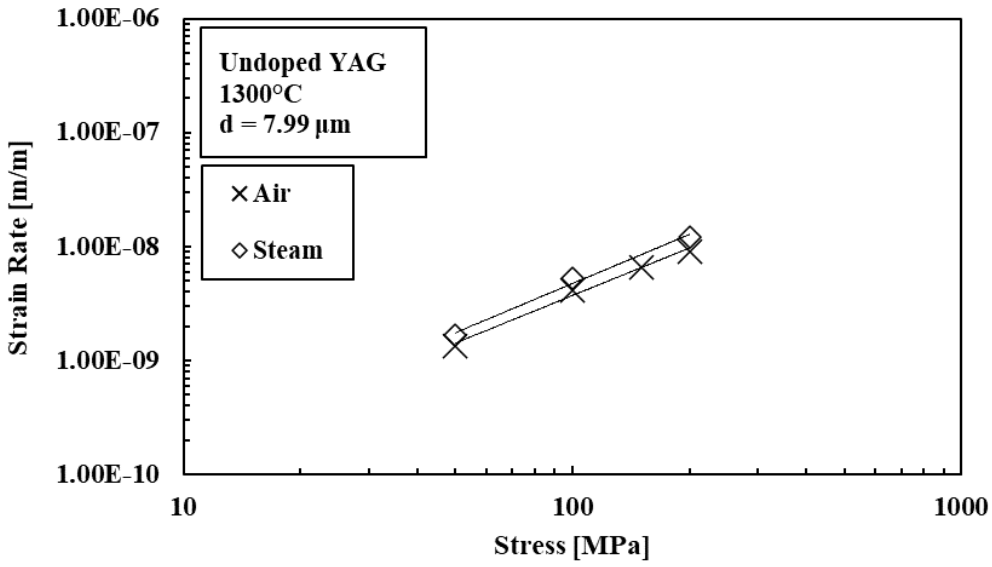

Figure 103: The steady-state creep strain rate vs. applied stress of undoped YAG specimens with grain size of 7.99 µm at 1300°C in air and in steam.

Therefore, the effect of steam on the creep rates of YAG at 1300°C for specimens with grain size of 7.99 µm appears to be negligible. This observation supports the same conclusion developed by Armani et al. who found that the presence of steam has no significant effect on the creep strain rates of undoped, polycrystalline YAG at 1300°C with grain size of 0.92 µm [28], [29]. Now that the same conclusion has been reached for a second and much larger grain size, it is apparent that the presence of steam has no significant effect on the creep rates of YAG, and also the effect of grain size, which was observed in air, holds true in steam as well.

6.2.2. Determination of the Stress Exponent and Grain Size Exponent for the Steady-State Creep Behavior of Yttrium Aluminum Garnet at 1300°C in steam

In order to determine the stress exponent for undoped YAG at 1300°C in steam, the creep results from each sample set described above were plotted on a log-log plot of strain rate vs. stress, shown in Figure 104. One sample set with grain size of 0.92 µm was obtained from the results presented by Armani et al. [28], [29]. The second sample set came from SPS billet Y-13-

40 with a grain size of 7.99 µm. Figure 104 illustrates the significant difference in steady-state creep strain rates between the sample sets due to the difference in material grain size.

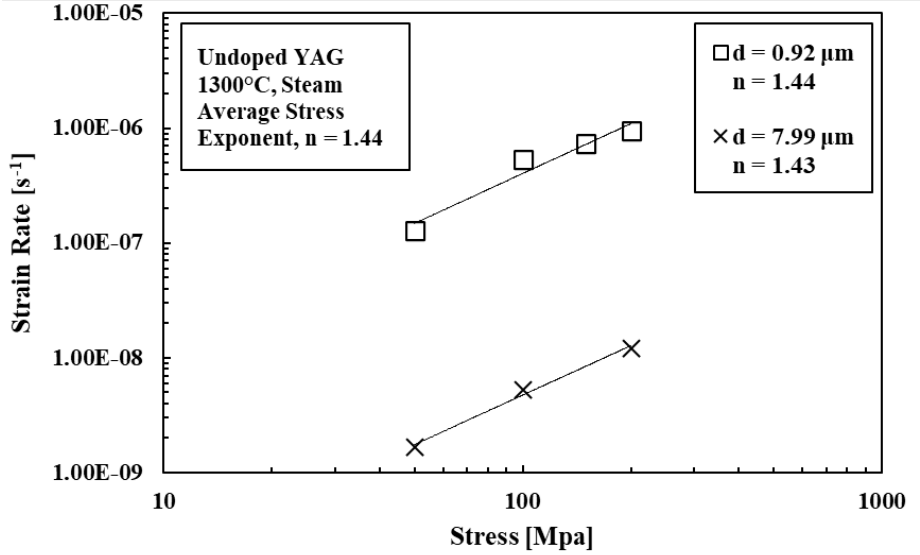

Figure 104: The steady-state creep strain rate vs. applied stress and the stress exponents of undoped, polycrystalline YAG specimens with different grain sizes at 1300°C in steam. Results for specimens with grain size of 0.92 µm from Armani et al. (2011) are included for comparison [28], [29].

Figure 104 reveals additional information about the creep of YAG in steam. First it successfully demonstrates the significant effect of grain size on the steady state creep rates for all stress levels. As in air, the difference in the steady-state creep rates is approximately 2 orders of magnitude for specimens with these specific grain sizes. The stress exponents were determined by finding the exponent associated with the best-fit line on a log-log scale for the data points of each sample set of a particular grain size. The stress exponent for the specimens tested by Armani et al. in steam with a grain size of 0.92 µm was 1.43. This stress exponent was validated by testing specimens with the larger grain size of 7.99 µm. The stress exponent for specimens from Y-13-40 was determined to be approximately 1.44, as is shown in Figure 104 and Table 23

below. When comparing these stress exponents to those determined for undoped, polycrystalline YAG at 1300°C in air, it is observed that the stress exponents are very close, 1.30 in air and 1.44 in steam.

Table 23: The stress exponent, n, for undoped, polycrystalline YAG specimens with different grain sizes at 1300°C in steam. Results for specimens with grain size of 0.92 µm from Armani et al. (2011) are included for comparison [28], [29].

Sample Set	**Grain Size [µm]**	**Stress Range [MPa]**	**Stress Exponent, *n***	**Average Stress Exponent, *n***
Armani 5 - 8*	0.92	50 - 200	1.43	**1.44**
Y-13-40	7.99	50 - 200	1.44	

*Results obtained by Armani et al. and referenced in this work for comparison [28], [29].

The grain size exponent, *m*, was also determined for creep of undoped, polycrystalline YAG at 1300°C in steam. The effect of grain size was isolated by plotting test results together as log(strain rate) vs. log(grain size), shown in Figure 105. Each set of specimens that was tested at a particular stress level, which is composed of specimens from each sample set and associated grain size, was grouped as a series on the graph and a best-fit line was applied to each set of results. The corresponding equation for each best-fit line contains an exponent, similar to the analysis of the stress exponent above. In this case the exponent is a negative number, which corresponds to the inverse relationship between grain size and creep rate in Equation 4.

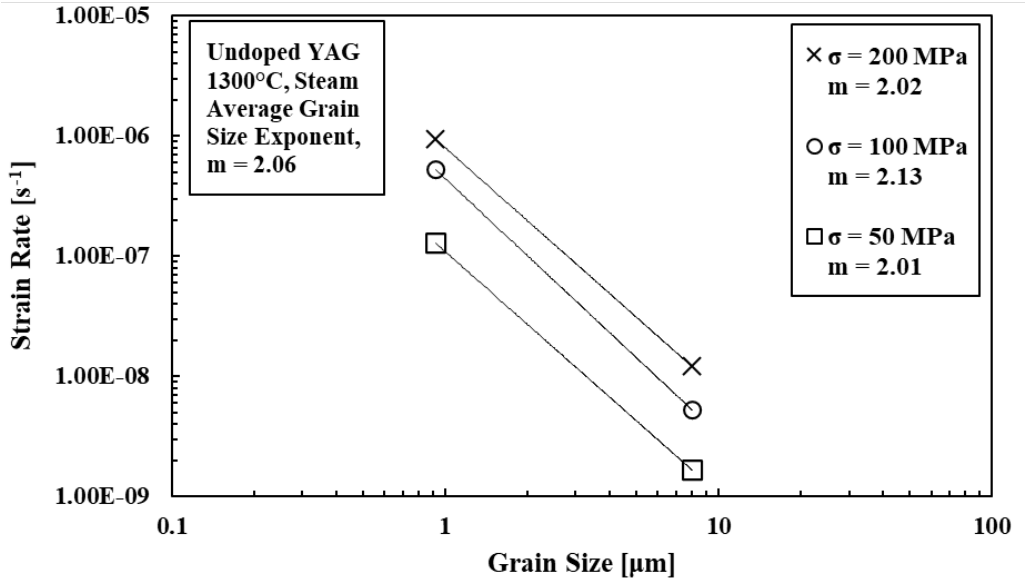

Figure 105: The steady-state creep strain rate vs. grain size and the grain size exponents, *m*, of undoped, polycrystalline YAG specimens with different grain sizes at 1300°C in steam. Results for specimens with grain size of 0.92 µm from Armani et al. (2011) are included for comparison [28], [29].

As is shown in the legend of Figure 105, and also in Table 24 below, the grain size exponents for each set of samples are very close to each other, and average to $m = 2.06$. When comparing this grain size obtained in steam to that obtained in air ($m_{air} = 1.99$), it is concluded that the effect of grain size on the steady-state creep behavior of undoped, polycrystalline YAG at 1300°C in steam is the same as in air. Once again, the presence of steam has little influence on creep behavior of YAG at 1300°C.

Table 24: The grain size exponent, m, for undoped, polycrystalline YAG specimens at different creep stress levels at 1300°C in steam. Results for specimens with grain size of 0.92 µm from Armani et al. (2011) are included for comparison [28], [29].

Creep Stress [MPa]	Grain Sizes [µm]	Grain Size Exponent, *n*	Average Grain Size Exponent, *n*
50	0.92*, 7.99	2.01	**2.06**
100	0.92*, 7.99	2.13	
200	0.92*, 7.99	2.02	

*Results obtained by Armani et al. and referenced in this work for comparison [28], [29].

6.3. Creep of Undoped Yttrium Aluminum Garnet at 1400°C in Air

6.3.1. Determination of the Stress Exponent for Undoped Yttrium Aluminum Garnet at 1400°C in Air

Creep tests were performed on three specimens from the SPS billet Y-7-40 at 1400°C in air in the same manner as 1300°C. The specimens were tested at compressive stress levels of 50 MPa, 100 MPa, and 150 MPa in order to be able to directly compare the results of specimens from the same billet tested at 1300°C. All specimens from Y-7-40 have an average grain size of 1.17 μm. The resulting creep strain vs. time curves are shown in Figure 106.

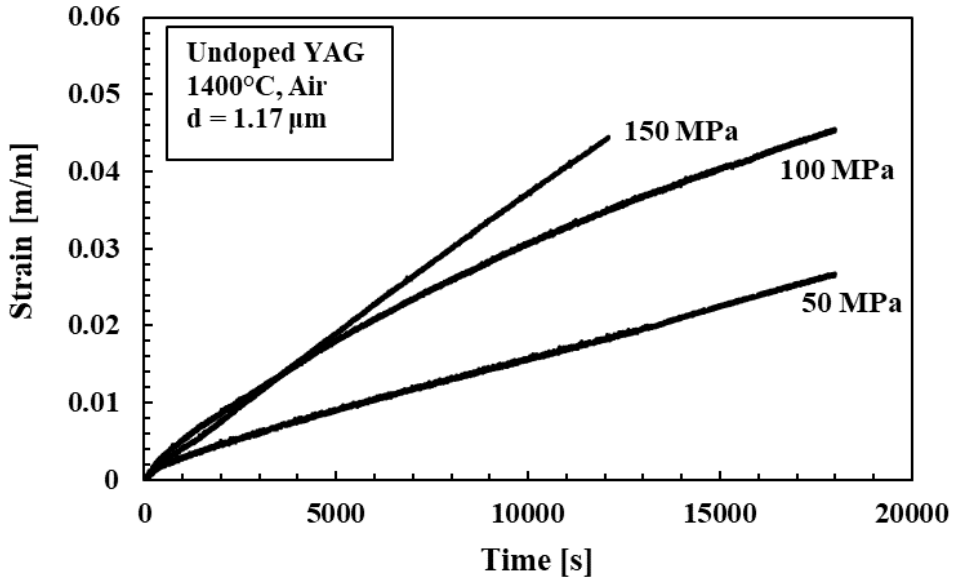

Figure 106: Creep strain vs. time curves obtained for undoped, polycrystalline YAG specimens with grain size of 1.17 μm at 1400°C in air.

Table 25 summarizes results for creep tests conducted at 1400°C, including the creep strain accumulated after 5 hours and the steady-state creep strain rates. The accumulated strain was between 2.64% at 50 MPa and approximately 6% at 150 MPa. Steady-state creep strain rates were determined to be between 1.28 x 10^{-6} s^{-1} for 50 MPa and 3.50 x 10^{-6} s^{-1} for 150 MPa. Both the accumulated strain and the steady-state strain rates are significantly higher at 1400°C than at

1300°C. The accumulated strains are approximately 7-8 times greater at 1400°C than at 1300°C. The creep rates at 1400°C are about one order of magnitude higher than those at 1300°C.

Table 25: Summary of creep results for undoped, polycrystalline YAG with grain size of 1.17 µm at 1400°C in air.

Specimen Name	Grain Size [µm]	Creep Stress [MPa]	Total Accumulated Strain after 5 hrs [%]	Steady-State Creep Rate [s^{-1}]
Y-7-40-4	1.17	50	2.64	1.28×10^{-6}
Y-7-40-5	1.17	100	4.54	1.80×10^{-6}
Y-7-40-6	1.17	150	6.00*	3.50×10^{-6}

*Creep test ended early, and total strain accumulation after 5 hrs is approximated.

The steady-state creep rates obtained at 1300°C and 1400°C in air were plotted on a log-log plot in Figure 107. This graph illustrates the significant difference in steady-state creep strain rates due to the difference in temperature. All other parameters, which could affect the creep rates, were held constant between the two sample sets, including material type, grain size, applied stress, and testing environment.

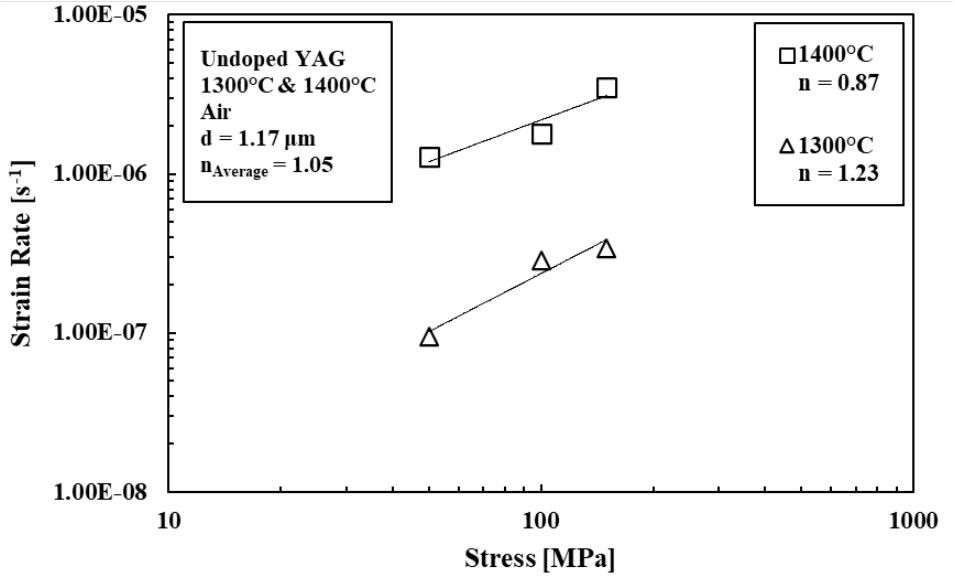

Figure 107: The steady-state creep strain rate vs. applied stress and the stress exponents of undoped, polycrystalline YAG specimens with grain size of 1.17 µm at 1300°C and 1400°C.

The significant effect of temperature on the steady-state creep strain rates of undoped YAG is apparent in Figure 107. The stress exponent for the creep of undoped YAG at 1400°C in air was also determined from the strain rate vs. stress plot in the same way as it was determined previously for specimens tested at 1300°C. The stress exponent at 1400°C was determined to be 0.87. This value is lower than the other stress exponents determined so far for undoped, polycrystalline YAG at 1300°C, which was 1.23. It is possible that the effect of varying the applied stress during creep tests is less significant at 1400°C than at 1300°C. However, several more creep tests using specimens from different sample sets are necessary to determine if this is a consistent trend for all undoped YAG specimens at 1400°C or if this stress exponent is unique to specimens from Y-7-40.

6.3.2. Determination of the Creep Activation Energy for Undoped Yttrium Aluminum Garnet in Air

The apparent activation energy with respect to plastic deformation is a material characteristic that describes the temperature dependence of the steady-state creep rate. It is represented by Q in Equation 5, which describes the diffusivity of a material, which is also critical to the steady-state creep rate, described by Equation 4. The diffusivity of a material is important because diffusion has been recognized as a primary mechanism that can enable creep in YAG. In order for an atom to move to a new location during diffusion, it must reach a certain energy level, known as the activation energy [279].

Once the steady-state creep rates have been determined for a material at different temperatures under the same stress, the activation energy can be determined. In order to accomplish this task, creep tests at different temperatures must be performed using specimens of similar grain size and subject to the same stress level and environment. To meet these

requirements, specimens from the same SPS billet (Y-7-40) with a grain size of 1.17 μm, were tested at the same stress level at 1300°C in air and at 1400°C in air. The activation energy was determined by plotting the results as the natural logarithm of strain rate [$\ln(\dot{\varepsilon})$] vs. the reciprocal of temperature [1/T]. Recall that the steady-state creep rate can be expressed as follows:

$$\dot{\varepsilon} = \frac{AD\mu b}{kT}\left(\frac{b}{d}\right)^m \left(\frac{\sigma}{\mu}\right)^n \quad \text{(Equ. 29)}$$

where D is the diffusion coefficient given by:

$$D = D_0 e^{-\frac{Q}{RT}} \quad \text{(Equ. 30)}$$

By rearranging and combining these equations, and removing any variation due to stress or grain size, Equation 29 becomes:

$$\dot{\varepsilon} = X\left(\frac{1}{T}\right) e^{-\frac{Q}{RT}} \quad \text{(Equ. 31)}$$

where *X* incorporates the portion of Equation 29 that can be held constant. By plotting the natural logarithm of strain rate vs. the reciprocal of temperature, and using linear regression to obtain a best fit line for each set of data, the equation for each line becomes:

$$\ln(\dot{\varepsilon}) = -\frac{Q}{R}\left(\frac{1}{T}\right) + X \quad \text{(Equ. 32)}$$

Using linear regression and Equation 32, the expression (-Q/R) can be determined by finding the slope of each line. These data for specimens from SPS billet Y-7-40 was plotted in Figure 108 along with the best-fit lines for each set of specimens tested under similar conditions but different temperatures.

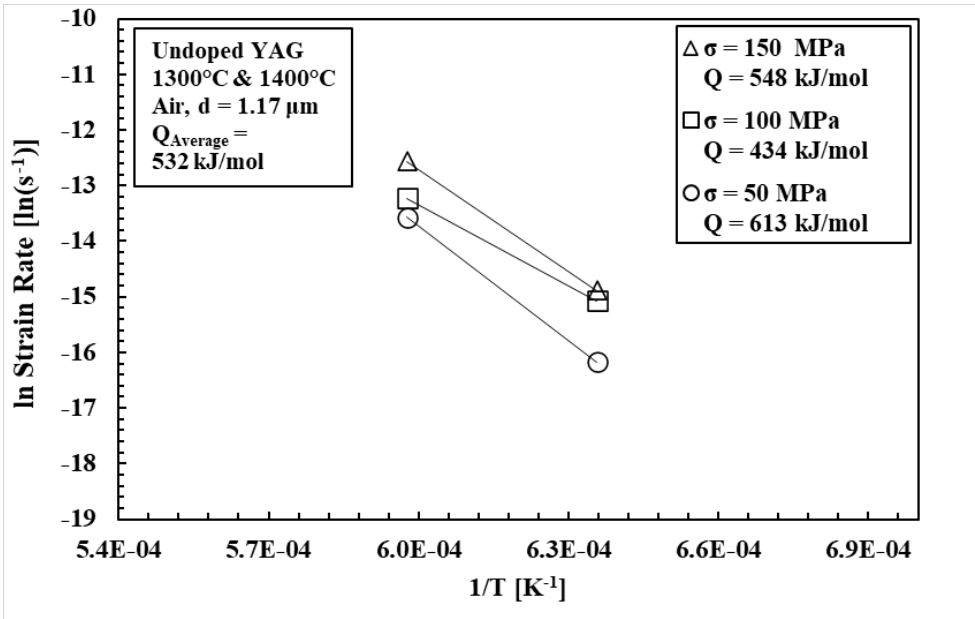

Figure 108: The natural log of steady-state creep strain rate vs. inverse temperature for undoped, polycrystalline YAG at 1300°C and 1400°C in air.

The activation energy was determined for each set of strain rate results associated with a specific stress level. The activation energies for undoped, polycrystalline YAG were determined to be 613 kJ/mol, 434 kJ/mol, and 548 kJ/mol for creep stresses of 50, 100, and 150 MPa, respectively. These three activation energies were averaged together to get a better approximation of the true activation energy for the creep of YAG, which was found to be 532 kJ/mol.

The creep activation energy of YAG has been previously reported by Parthasarathy et al. to be 584 kJ/mol [190]. They determined that activation energy was associated with Nabarro-Herring diffusional creep, where diffusion of the Yttrium cation (Y^{3+}) was the rate limiting factor. Similarly, additional authors have cited the activation energy associated with Y^{3+} cation in YAG to be between 500 and 565 kJ/mol [280], [281]. This high activation energy in YAG above 500 kJ/mol indicates that the Y^{3+} cation must be the rate limiting diffusional species, as the activation energy associated with the diffusion of Oxygen has been found to be much lower,

approximately 300 – 350 kJ/mol [96]. Similarly, a lower activation energy would be associated with the diffusion of Aluminum, approximately 440 kJ/mol [282]. An additional discussion of the creep activation energy and its implications for the most likely creep mechanisms at work in YAG can be found in Section 6.5.

6.4. Creep of Yb- and Er-doped Yttrium Aluminum Garnet at 1300°C in Air

This chapter presents the creep results obtained for 2at% Yb-doped YAG and 2at% Er-doped YAG specimens, which were fabricated by means of SPS. Details of the doped YAG materials are discussed in Section 3.1.1 and the characteristics of each SPS billet are tabulated in Appendix A. Due to the limited number of creep test specimens that were fabricated from the doped-YAG billets, only two sets of creep specimens were tested for each material variant. This chapter is organized into two parts: first, the results obtained for 2at% Yb-doped YAG are presented, and then the results obtained for 2at% Er-doped YAG. In each of these sections, the creep results are summarized and compared to the results from corresponding tests for undoped YAG, presented in the previous section.

In order to determine the effects of dopants on the creep behavior of polycrystalline YAG, each test was conducted in the same manner as those for undoped YAG. Each creep test was performed at 1300°C in air, with stress levels between 50 MPa and 200 MPa, so that direct comparisons could be made, and the effects of dopants could be isolated. Specimens from each billet had different grain size, which enabled the effect of grain size to be determined for doped, polycrystalline YAG. For each material variant, the stress exponent and grain size exponent were determined and compared to that of undoped YAG.

This analysis of the effects of dopants on the creep behavior of polycrystalline YAG is designed to build on the previous work of Armani et al. [28], [29], who conducted creep tests on 0.15wt% SiO_2-doped YAG specimens at 1300°C in air and in steam. Armani et al. concluded that for materials with identical grain size under similar test conditions, the presence of the silica dopant may have a small increasing effect on the diffusion rates in YAG and, therefore, on the creep rates as well [28], [29]. Assuming that the creep of polycrystalline YAG of this grain size is dominated by lattice diffusion, based on the Nabarro-Herring creep mechanism, then the rate-limiting species in the lattice of YAG is the Yttrium cation (Y^{3+}). It has been shown that the presence of silica doping in YAG can results in Si^{4+} cation being in solution with YAG at these temperatures. This can lead to increased densification and grain growth, and can also contribute to an increased rate of diffusion, due to possible increased mass transport effects from the silica dopant [261].

However, perhaps due to the small amount of the silica dopant, this potential increase in creep rate, was observed to be very small, almost negligible, in the work of Armani et al [28], [29]. YAG was processed in this previous work with a silica dopant as a sintering aid. YAG is also commonly processed with other various dopants, such as Yb and Er, primarily due to their effects on the optical properties of doped YAG, when used as a laser material. However, very little work has been done to determine the potential effects of these dopants on the mechanical properties of YAG. Therefore, the effects of these dopants on the mechanical behavior of YAG is still a topic of interest.

6.4.1. Creep Results of 2at% Yb-Doped Yttrium Aluminum Garnet at 1300°C in Air

Two sample sets from two different SPS billets were creep tested at 1300°C in air. These billets were Y-Yb-7-40 and Y-Yb-5-40 with grain sizes of 0.37 μm and 1.38 μm, respectively. The microstructure of each billet was analyzed in the SEM, in order to determine grain size, as well as to quantify the presence of porosity and any cracking. SEM images are shown for specimens from Y-Yb-7-40 and Y-Yb-5-40 in Figure 109 and Figure 110, respectively.

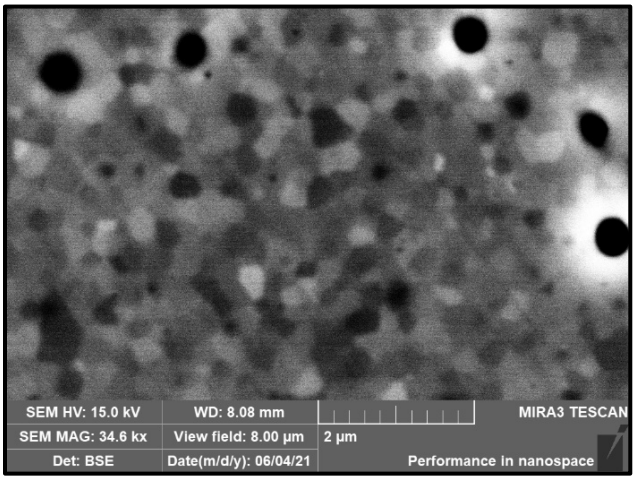

Figure 109: SEM image of a specimen cut from the SPS billet Y-Yb-7-40, with a measured average grain size of 0.37 μm.

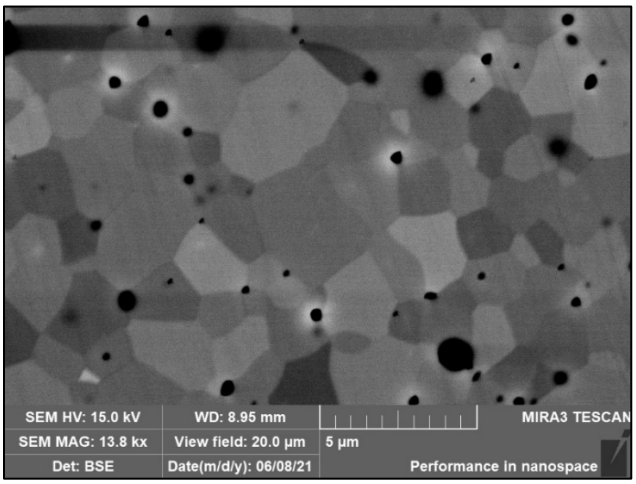

Figure 110: SEM image of a specimen cut from the SPS billet Y-Yb-5-40, with a measured average grain size of 1.38 μm.

Each SEM image shows a similar grain structure as was seen before with other specimens. There is significant variation in grain size within the view field, and grains tend to have sharp geometric shapes with no round edges. Figure 111 shows the creep strain vs. time curves for three samples from the Y-Yb-7-40 sample set. They were tested at 50 MPa, 100 MPa, and 200 MPa.

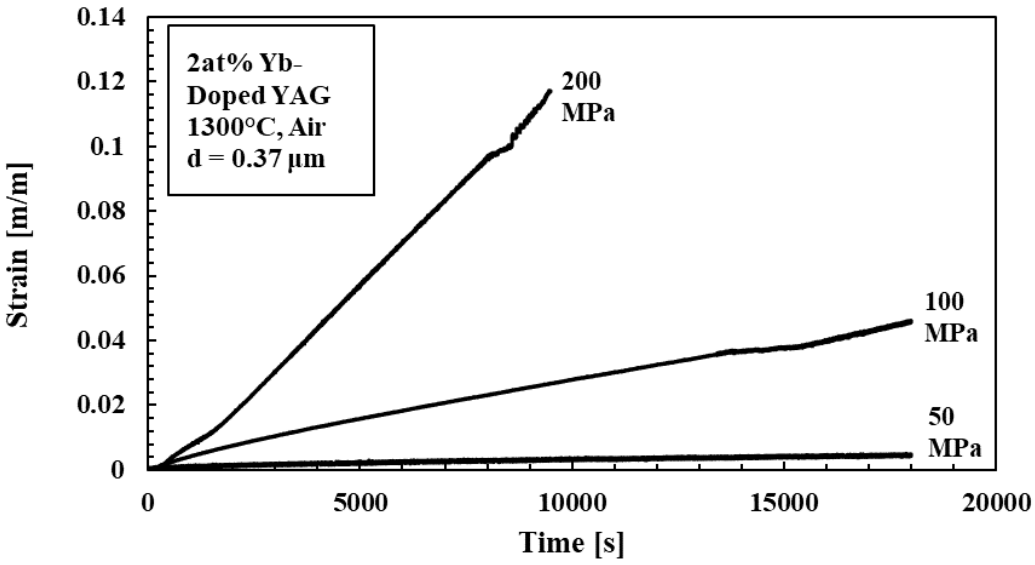

Figure 111: Creep strain vs. time curves obtained for 2at% Yb-doped, polycrystalline YAG specimens with grain size of 0.37 µm at 1300°C in air.

It is apparent from **Figure 111** that the accumulated creep strains are significantly higher than what was previously observed for undoped YAG. Creep strain for the specimen subjected to 200 MPa at 1300°C in air reached over 12% strain in approximately 3 hrs. However, the grain size for the Y-Yb-7-40 billet is very small (0.37 µm), which likely has a significant impact on the creep rates, and is analyzed later in this section.

Specimens from the second 2at% Yb-doped YAG billet, Y-Yb-5-40, have a grain size of 1.38 µm. The creep strain vs. time curves for these specimens are shown in Figure 112. Three specimens were tested at 50 MPa, 100 MPa, and 200 MPa.

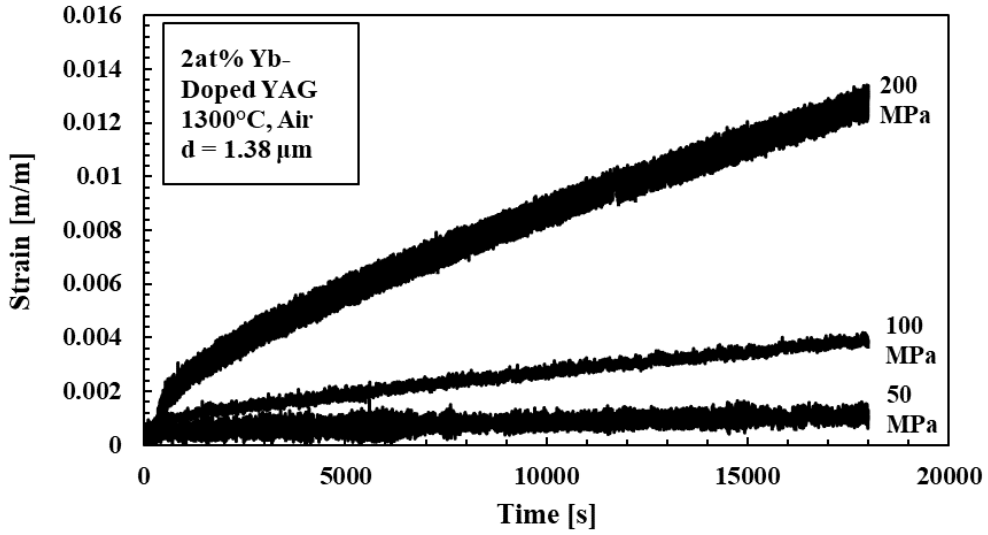

Figure 112: Creep strain vs. time curves obtained for 2at% Yb-doped, polycrystalline YAG specimens with grain size of 1.38 µm at 1300°C in air.

Specimens from this billet with larger grain size accumulated significantly less creep strain than observed for the previous billet. The specimen subjected to 200 MPa reached approximately 1.3% strain after 5 hrs. The creep strain vs. time curves obtained for both Yb-doped YAG billets, are mostly smooth and linear. They exhibit minimal primary creep, and most of the five-hour long creep test was dominated by secondary creep. These results are summarized in Table 26.

Table 26: Summary of creep results for 2at% Yb-doped, polycrystalline YAG with grain sizes of 0.37 µm and 1.38 µm at 1300°C in air.

Specimen Name	Grain Size [µm]	Creep Stress [MPa]	Total Accumulated Strain after 5 hrs [%]	Steady-State Creep Rate [s^{-1}]
Y-Yb-7-40-1	0.37	50	0.49	2.18×10^{-7}
Y-Yb-7-40-2	0.37	100	4.57	2.21×10^{-6}
Y-Yb-7-40-3	0.37	200	Not Available*	5.88×10^{-6}
Y-Yb-5-40-1	1.38	50	0.15	7.37×10^{-8}
Y-Yb-5-40-2	1.38	100	0.41	1.21×10^{-7}
Y-Yb-5-40-3	1.38	100	0.42	1.59×10^{-7}
Y-Yb-5-40-4	1.38	200	1.34	4.73×10^{-7}

*Creep tests ended early, and total strain accumulation after 5 hrs is unknown.

The steady-state creep strain rates were determined by measuring the slope of the flattest portion of each strain vs. time curve. The strain rates for each Yb-doped YAG specimen from each SPS billet were plotted vs. stress and are shown in Figure 113.

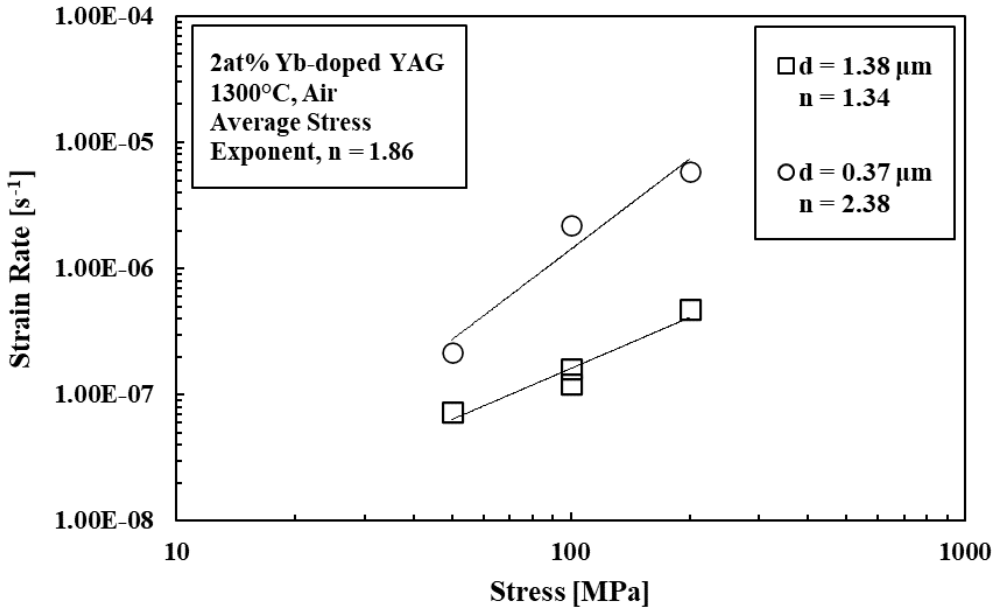

Figure 113: The steady-state creep strain rate vs. applied stress and the stress exponents, *n*, of 2at% Yb-doped, polycrystalline YAG specimens with different grain sizes at 1300°C in air.

The stress exponents were obtained from the strain rate vs. stress curves as they were previously for undoped YAG specimens. The stress exponent for Yb-doped YAG specimens from billet Y-Yb-5-40 with a grain size of 1.38 µm was found to be 1.34. This is right in line with stress exponents obtained for undoped YAG, which was approximately 1.30. However, the stress exponent for billet Y-Yb-7-40 with grain size of 0.37 was found to be much larger, with a value of 2.38. This stress exponent is consistent with the apparent steep trend seen in Figure 113 for the three specimens with smaller grain size. The two stress exponents determined for Yb-doped YAG specimens are summarized and averaged in Table 27.

Table 27: The stress exponent, n, for 2at% Yb-doped, polycrystalline YAG specimens with different grain sizes at 1300°C in air.

Sample Set	Grain Size [μm]	Stress Range [MPa]	Stress Exponent, *n*	Average Stress Exponent, *n*
Y-Yb-7-40	0.37	50 - 200	2.38	**1.86**
Y-Yb-5-25	1.38	50 - 200	1.34	

As is shown in Table 27, the two stress exponents can be averaged together, which results in an average stress exponent of 1.86 for Yb-doped YAG at 1300°C in air. However, it is likely that this large discrepancy in the two stress exponents is due to a change in creep mechanism for materials with small grains. It has been shown that the creep of large grained (d > 1 μm) ceramic materials, including alumina, and likely YAG, is typically dominated by the Nabarro-Herring diffusional creep mechanism. However, the creep mechanism for similar materials with smaller grains can change to become interface-reaction controlled, a mechanism associated with a higher stress exponent, as seen here.

For diffusional creep mechanisms, such as Nabarro-Herring and Coble creep, the grain boundaries are assumed to act as perfect sources and sinks for vacancies, enabling diffusion that controls the creep rates. However, the small grain size and the increased amount of grain boundaries in fine-grained materials can lead to reactions at the interface. In these cases, the typical lattice or grain boundary diffusion becomes so rapid, that creation and removal of vacancies and defects at the grain boundaries can become the rate-controlling mechanism of diffusion [147], [283]–[285]. This is discussed further in Section 6.5, summarizing the creep mechanisms observed in doped and undoped YAG.

In order to determine a grain size exponent for Yb-doped YAG, the steady-state creep strain rates of all Yb-doped YAG specimens were grouped according to the creep stress value, and plotted vs. grain size on a log-log scale in Figure 114.

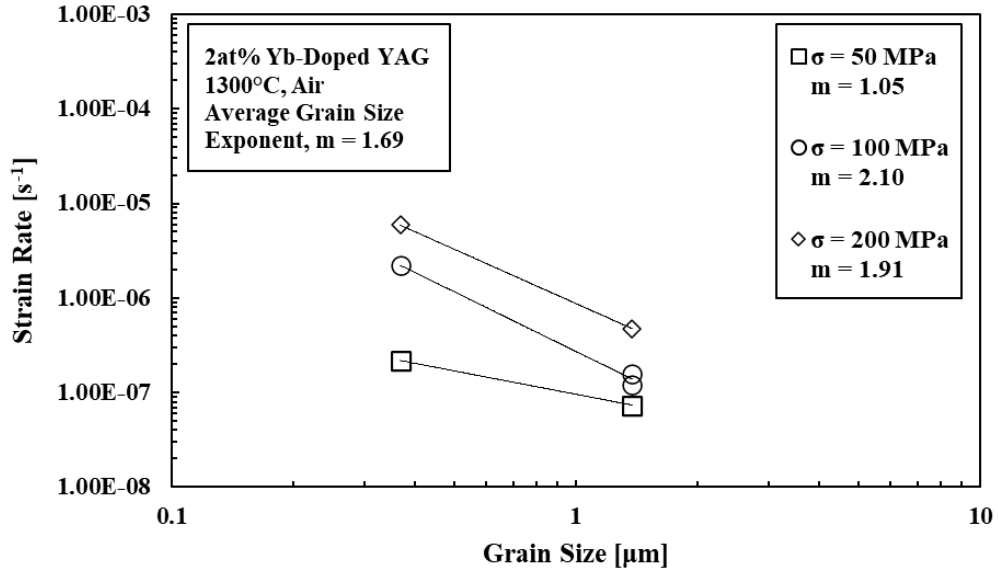

Figure 114: The steady-state creep strain rate vs. grain size and the grain size exponents, *m*, of 2at% Yb-doped, polycrystalline YAG specimens at different creep stress levels at 1300°C in air.

Creep tests were performed at three different stress values: 50 MPa, 100 MPa, and 200 MPa, so three grain size exponents were determined for Yb-doped YAG at 1300°C in air. These three grain size exponents were averaged together to obtain a better approximation of the grain size exponent associated with the creep of this material, which was 1.69. These exponents are shown in Figure 114 and Table 28.

There was a larger discrepancy between the three grain size exponents, than was seen for undoped YAG. At 50 MPa the grain size exponent was determined to be 1.05, and at 100 MPa the grain size exponent was determined to be 2.10. This variation in grain size exponent may be due to a change in creep mechanisms associated with different grain sizes, which was discussed earlier in this section. It is possible that the two creep mechanisms are associated with two different strain regimes. Nabarro-Herring diffusional creep will typically result in a grain size exponent of 2, while interface reaction-controlled creep will typically see a grain size exponent

of 1. This could explain the range of grain size exponents that were obtained in this case using these two sets of specimens.

Table 28: The grain size exponent, m, for 2at% Yb-doped, polycrystalline YAG specimens at different creep stress levels at 1300°C in air.

Creep Stress [MPa]	Grain Sizes [µm]	Grain Size Exponent, *n*	Average Grain Size Exponent, *n*
50	0.37, 1.38	1.05	**1.69**
100	0.37, 1.38	2.10	
200	0.37, 1.38	1.91	

The steady-state creep strain rates obtained for 2at% Yb-doped YAG specimens were compared to those obtained for undoped YAG in Figure 115. Both the doped and undoped specimens were tested at 1300°C in air in order to remove other sources of variation and to determine the effects of the dopant. However, the grain sizes of each SPS billet are different, for both the doped and undoped billets. Each grain size is shown in Figure 115 along with the steady-state creep strain rates.

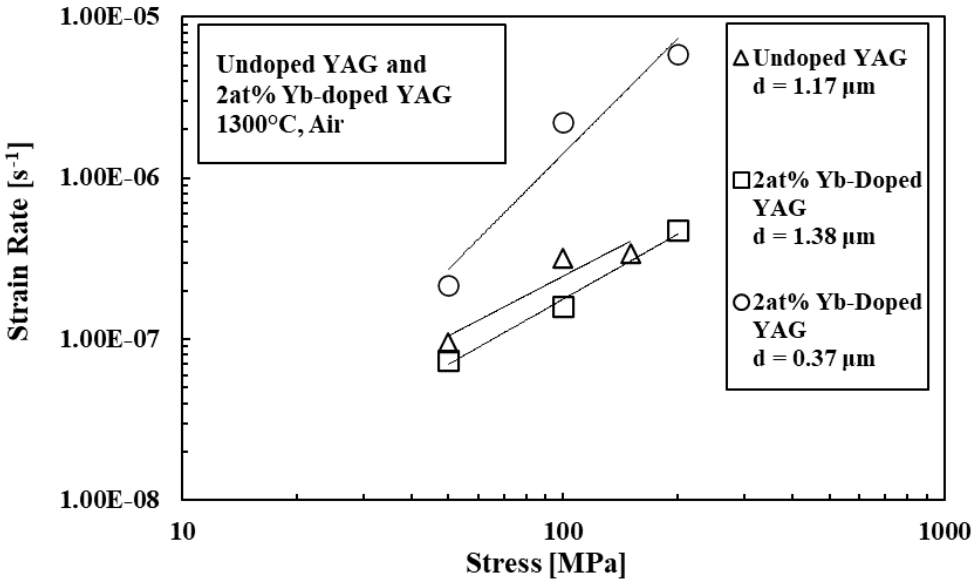

Figure 115: The steady-state creep strain rate vs. applied stress of 2at% Yb-doped and undoped, polycrystalline YAG specimens with different grain sizes at 1300°C in air.

In order to fully assess the effects of the dopant on the creep behavior of YAG at 1300°C in air, it was necessary to remove any possible effect of grain size. Therefore, the steady-state creep strain rates were normalized for a grain size equal to d = 1 μm. The creep rates were normalized by using the average measured grain size exponent determined for undoped YAG, shown in Table 21, and the following equation:

$$\dot{\varepsilon}_{Norm} = \dot{\varepsilon}_{Actual}\left(\frac{d_{Actual}}{1\ \mu m}\right)^{m} \qquad \text{(Equ. 33)}$$

Figure 116 shows the steady-state creep strain rates for Yb-doped and undoped YAG specimens at 1300°C in air; however, in this case, the creep rates have all been normalized to a common grain size of d = 1 μm. The original grain size of each group of specimens is also shown in Figure 116.

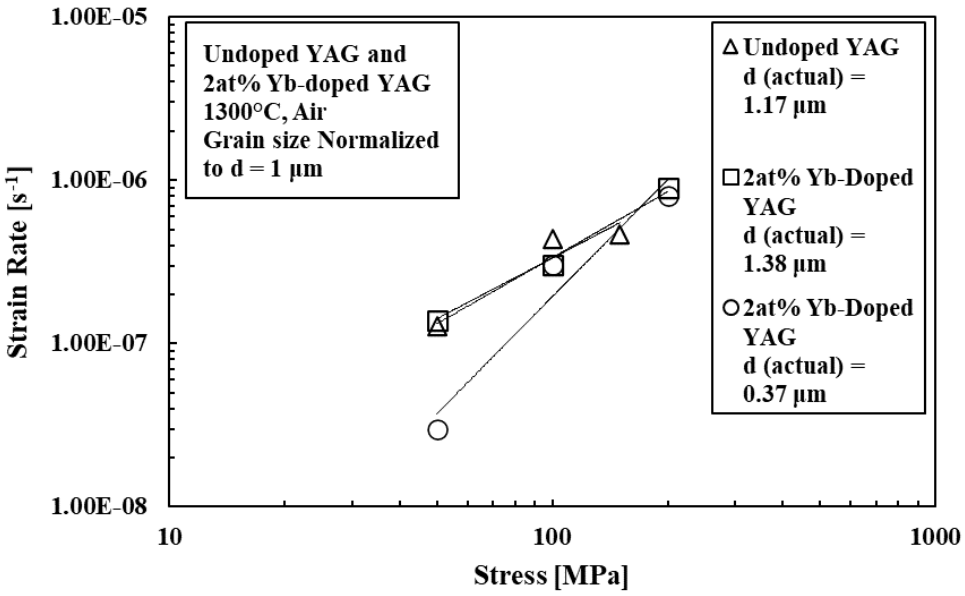

Figure 116: The normalized steady-state creep strain rate vs. applied stress of 2at% Yb-doped and undoped, polycrystalline YAG specimens for grain sizes of d = 1 μm at 1300°C in air.

Once the creep rates were normalized to a common grain size, the results in Figure 116 were analyzed to identify any possible effects of the dopant on the creep behavior of YAG. The steady-state strain rates for undoped YAG with grain size of 1.17 μm and the Yb-doped YAG with grain size of 1.38 μm are directly on top of each other, indicating that once grain size effect was accounted for, there was essentially no significant difference between the creep behavior, and that an effect of dopant was negligible.

Previous research has suggested that for undoped YAG with grain sizes of $d > 1$ μm, the dominant creep mechanism is Nabarro-Herring diffusional creep, and that the rate-limiting species in the lattice of YAG is the Yttrium cation (Y^{3+}) [190]. When these materials are doped with another element, the rate-limiting species during diffusion can change, thus affecting the creep rates. However, because the creep rates of 2at% Yb-doped YAG and undoped YAG with similar grain sizes are overlapping with no apparent difference, this indicates that the presence of the dopant is not significantly affecting the rate of diffusion during creep.

This conclusion is consistent with several observations regarding the similarities of the rare-earth elements, Yb and Y. Although the atomic mass of Y is 88.9 amu and the atomic mass of Yb is 173.04 amu, it has been determined that the diffusivity of each species is minimally affected by the atomic mass, when compared to other considerations. The diffusivity of each element is approximately equivalent to the square root of the reciprocal of the atomic mass. Therefore, the difference would only be approximately a factor of two, due only to the mass effect [96]. However, the more significant attributes affecting the diffusivity of elements are the valence state and the ionic radii of each species. The large trivalent Yttrium ions occupy dodecahedral sites with ionic radii of 0.102 nm. Similarly, the Ytterbium ions have the same valence as the Yttrium with ionic radii of 0.099 nm. These attributes are nearly identical.

Therefore, the diffusivity of Yb^{3+} is assumed to closely correspond to the diffusivity of Y^{3+} self-diffusion in YAG, and the elements can almost fully replace one-another [96]. When considering this phenomenon, recall that the activation energy associated with the diffusional creep for undoped YAG was determined to be approximately 532 kJ/mol. It has also been shown that when Yb is added to a solution with YAG, the activation energy associated with diffusion was found to be approximately 550 kJ/mol. These activation energies are nearly identical. It is likely that the Yb atoms replace a certain amount of Y atoms, but this exchange has no effect on the rates of diffusion.

However, there is a significant difference in creep strain rates of Yb-doped YAG and undoped YAG when considering the SPS billet with grain size of 0.37 μm. Even though the strain rates have been normalized to a common grain size, this normalization process assumes identical creep mechanisms and overall similar creep behavior. Recall that the small grain size of this doped YAG billet contributed to different stress and grain size exponents than what was expected for YAG, based on the earlier results presented in this chapter. Therefore, the normalization process did not fully remove the variation in the creep behavior between these specimens. The steeper slope, which is observed for specimens from billet Y-Yb-7-40 was expected, and was also seen in Figure 113 and Figure 115. This higher stress exponent was attributed to the interface reaction-controlled creep mechanism. It has also been shown that for small grain sizes and low stress values, that interface reaction-controlled creep can contribute to surprisingly low steady-state creep rates [286], [287]. This is apparent in this case of 50 MPa in Figure 116. This stress level can also represent an amount of stress that is below some threshold value where very little creep will occur. This trend has also been seen in the creep of similar materials [288], [289].

6.4.2. Creep of 2at% Er-Doped Yttrium Aluminum Garnet at 1300°C in Air

Two sample sets from two 2at% Er-doped YAG SPS billets were creep tested at 1300°C in air. These billets were Y-Er-9-40 and Y-Er-7-40 with grain sizes of 0.45 μm and 1.87 μm, respectively. The microstructure of each billet was analyzed in the SEM, in order to determine grain size, and to quantify the presence of porosity and any cracking. SEM images are shown for specimens from Y-Er-9-40 and Y-Er-7-40 in Figure 117 and Figure 118, respectively.

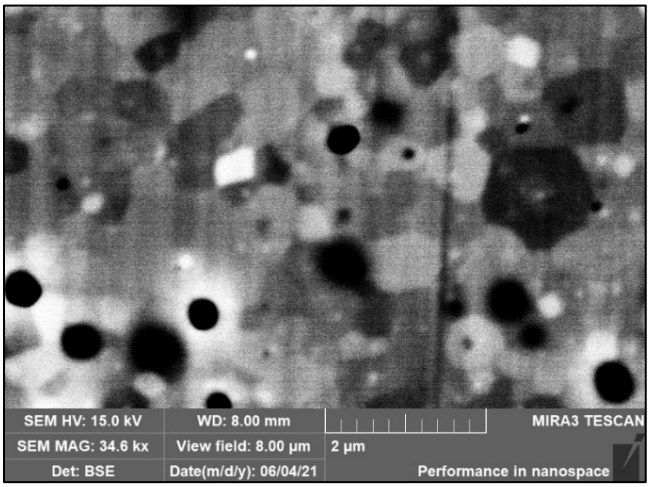

Figure 117: SEM image of a specimen cut from the SPS billet Y-Er-9-40, with a measured average grain size of 0.45 μm.

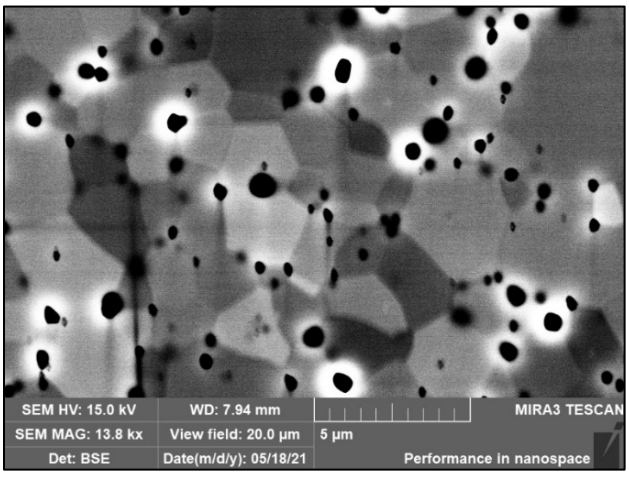

Figure 118: SEM image of a specimen cut from the SPS billet Y-Er-7-40, with a measured average grain size of 1.87 μm.

The grains visible in Figure 117 and Figure 118 are similar in shape as was seen before with other specimens. There is some variation in grain size within the view field, and grains tend to have sharp geometric shapes with no round edges. Figure 119 shows the creep strain vs. time curves for three samples from the Y-Er-9-40 sample set. They were tested at 50 MPa, 100 MPa, and 150 MPa.

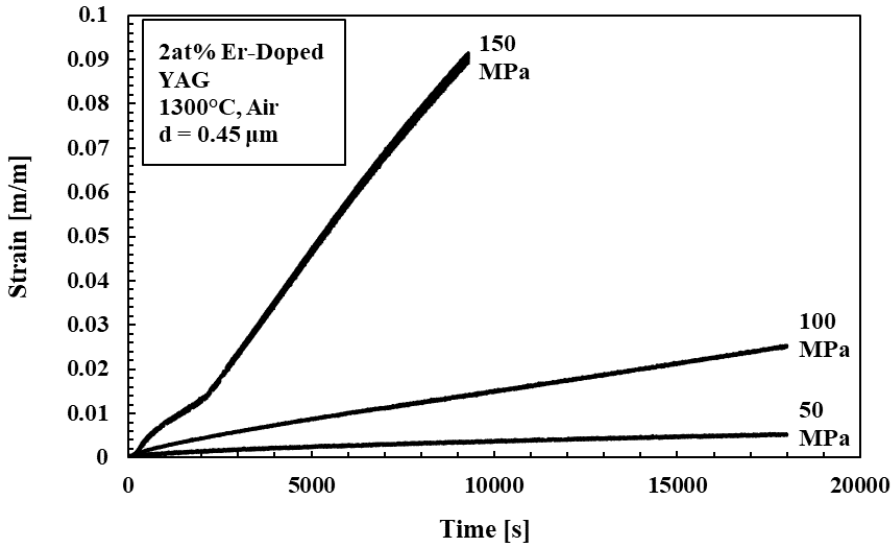

Figure 119: Creep strain vs. time curves obtained for 2at% Er-doped, polycrystalline YAG specimens with grain size of 0.45 µm at 1300°C in air.

Once again, the accumulated creep strains are significantly larger than those observed for undoped YAG specimens with larger grain sizes. These three specimens have a grain size of 0.45 µm, so larger accumulated strains are expected due to the smaller grain size. The accumulated creep strain for the specimen subjected to 150 MPa at 1300°C in air reached over 9% strain in approximately 2.5 hrs. A test was attempted with an applied stress of 200 MPa; however, the specimen failed early, and the results could not be used. At 150 MPa, the shape of the strain vs. time curve is not consistent and smooth, but rather a significant slope change is apparent during the test. This could indicate a transition from secondary to tertiary creep, but it also could

indicate shearing within the specimen or some other phenomenon, which could impact the strain response in creep.

Specimens from the second 2at% Er-doped YAG billet, Y-Er-7-40, have a grain size of 1.87 μm. The creep strain vs. time curves for these specimens are shown in Figure 120. Three specimens were tested at 50 MPa, 100 MPa, and 200 MPa.

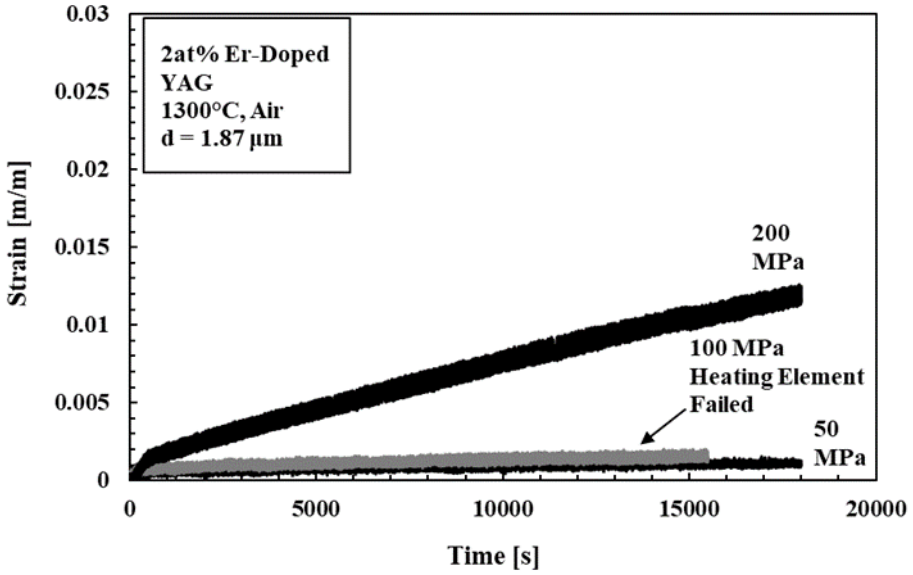

Figure 120: Creep strain vs. time curves obtained for 2at% Er-doped, polycrystalline YAG specimens with grain size of 1.87 μm at 1300°C in air.

Specimens from this billet with larger grain size revealed significantly less accumulated creep strain than those from the previous billet. The specimen subjected to 200 MPa only reached approximately 1.2% strain after 5 hrs. The specimen subjected to 100 MPa only reached approximately 0.16% strain after 4 hrs, which barely surpasses the creep strain produced at 50 MPa. However, this small amount of strain is due to a furnace malfunction. A heating element failed at the beginning of the test resulting in a low temperature setting (approximately 75°C below the set point). It is expected that this temperature deviation did cause the observed strain to be lower than expected. However, the temperature deviation of 75°C is small, and the

difference in creep strain is likely small as well. Therefore, the resultant creep strain data is still presented here for comparison.

Each strain vs. time curve in Figure 120 is smooth and nearly linear. This indicates that there is minimal primary creep, and most of the five-hour long creep tests were dominated by secondary creep. The creep results for Er-doped YAG specimens are summarized in Table 29.

Table 29: Summary of creep results for 2at% Er-doped, polycrystalline YAG with grain sizes of 0.45 μm and 1.87 μm at 1300°C in air.

Specimen Name	**Grain Size [μm]**	**Creep Stress [MPa]**	**Total Accumulated Strain after 5 hrs [%]**	**Steady-State Creep Rate [s^{-1}]**
Y-Er-9-40-1	0.45	50	0.52	1.80×10^{-7}
Y-Er-9-40-2	0.45	100	2.49	1.29×10^{-6}
Y-Er-9-40-3	0.45	200	Not Available*	5.13×10^{-6}
Y-Er-7-40-1	1.87	50	0.10	2.52×10^{-8}
Y-Er-7-40-2	1.87	100	Not Available*	4.89×10^{-8}
Y-Er-7-40-3	1.87	200	1.21	2.87×10^{-7}

*Creep tests ended early, and total strain accumulation after 5 hrs is estimated or unknown.

A significant difference in accumulated strain and steady-state creep rate is observed for these two sample sets; which was expected due to the significantly different grain sizes. The two sets of creep strain vs. time curves were plotted on the same graph in Figure 121 in order to demonstrate the significant difference in strain accumulation due to grain size. A strain vs. time for a specimen with grain size of 1.87 μm at 200 MPa is nearly identical to the strain vs. time for a specimen with grain size of 0.45 μm at 100 MPa.

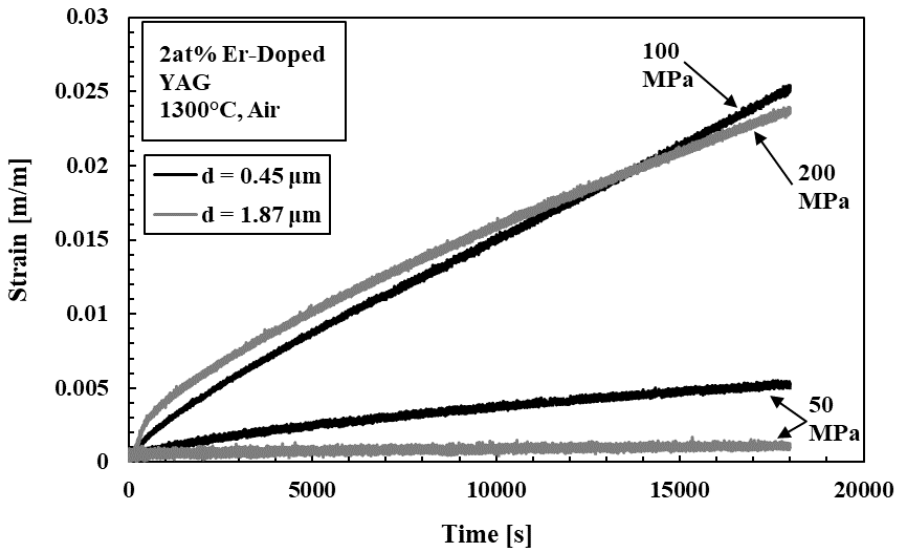

Figure 121: Creep strain vs. time curves for specimens from billet Y-Er-9-40 and Y-Er-7-40 with grain sizes of 0.45 µm and 1.87 µm, respectively.

The steady-state creep strain rates were determined by measuring the slope of the flattest portion of each strain vs. time curve. The strain rates for each Er-doped YAG specimen from each SPS billet were plotted vs. stress and are shown in Figure 122.

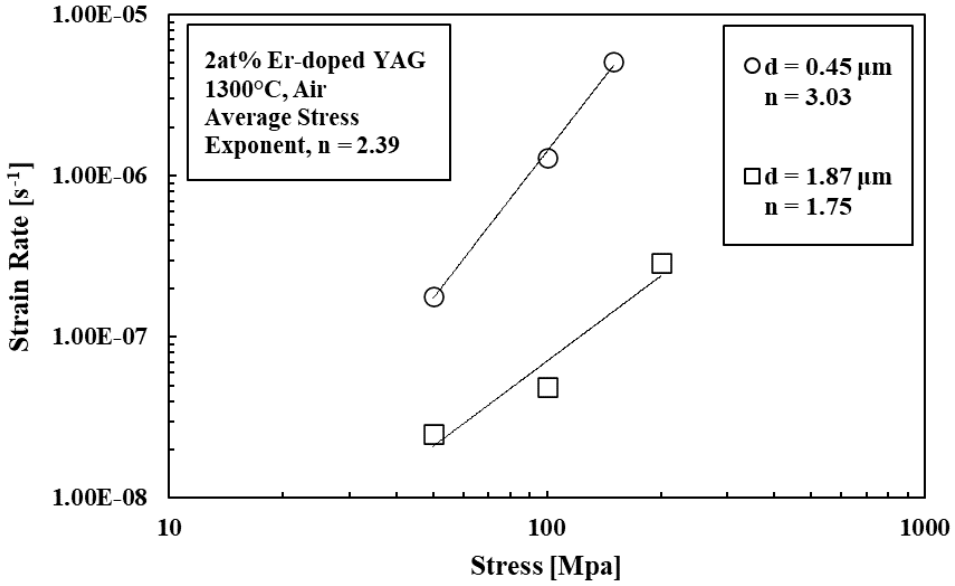

Figure 122: The steady-state creep strain rate vs. applied stress and stress exponents, *n*, of 2at% Er-doped, polycrystalline YAG specimens with different grain sizes at 1300°C in air.

The stress exponents were obtained from the strain rate vs. stress curves as they were previously for undoped YAG specimens. The stress exponent for Er-doped YAG specimens from billet Y-Er-7-40 with a grain size of 1.87 μm was found to be 1.75. This stress exponent is higher than those determined for undoped YAG, which were approximately 1.30. One possible cause of this unusually high exponent is the heater failure, which occurred during the 100 MPa test. As was described earlier, the temperature output of the furnace was approximately 75°C below the set point, which resulted in a low apparent creep strain rate. Due to specimen limitations the test could not be repeated using a specimen from the same billet. Without this equipment malfunction, the stress exponent obtained from the higher stress tests would have likely been lower and within the range of those determined for undoped YAG.

The stress exponent for billet Y-Er-9-40 with grain size of 0.45 was found to be much larger, with a value of 3.03. This stress exponent is consistent with the apparent steep trend seen in Figure 122 for the three specimens with smaller grain size. This result is also consistent with the unusually high stress exponent found for specimens with small grain size of Yb-doped YAG. The two stress exponents determined for Er-doped YAG specimens are summarized and averaged in Table 30.

Table 30: The stress exponent, n, for 2at% Er-doped, polycrystalline YAG specimens with different grain sizes at 1300°C in air.

Sample Set	**Grain Size [μm]**	**Stress Range [MPa]**	**Stress Exponent, *n***	**Average Stress Exponent, *n***
Y-Er-9-40	0.45	50 - 150	3.03	**2.39**
Y-Er-7-40	1.87	50 - 200	1.75	

As is shown in Table 30, the two stress exponents can be averaged together, which results in an average stress exponent of 2.39 for Er-doped YAG at 1300°C in air. As was seen with Yb-doped YAG, it is likely that the high stress exponent for Y-Er-9-40 is due to the change in creep

mechanism for certain materials with small grains. As was discussed in the previous section, it is possible that the creep mechanism for specimens with very small grains changes from Nabarro-Herring diffusional creep to interface reaction-controlled creep. This can be indicated by a higher stress exponent, as seen here.

In order to determine the grain size exponent for Er-doped YAG, the same steady-state creep strain rates of all Yb-doped YAG specimens were grouped according to the creep stress value, and plotted vs. grain size on a log-log scale in Figure 123.

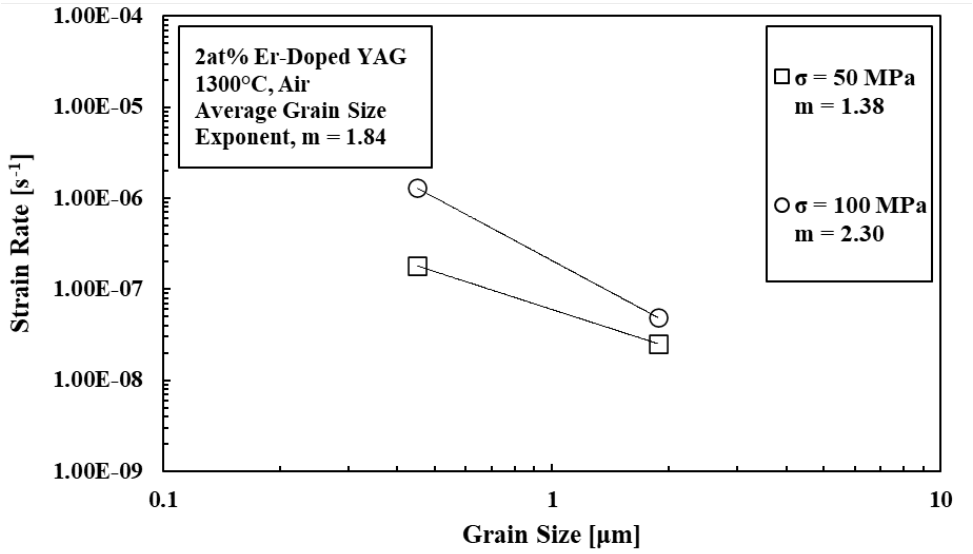

Figure 123: The steady-state creep strain rate vs. grain size and the grain size exponents, *m*, of 2at% Er-doped, polycrystalline YAG specimens at different creep stress levels at 1300°C in air.

Creep tests included only two different stress values: 50 MPa and 100 MPa. Although three stress levels were used to test specimens from each sample set, the third stress level did not match (150 MPa and 200 MPa for the two billets). So only two grain size exponents were determined for Er-doped YAG at 1300°C in air. These two grain size exponents were averaged together to obtain a best approximation of the grain size exponent describing the creep of this material, which was 1.84. These exponents are shown in Figure 123 and Table 31.

As was observed for Yb-doped YAG, there is a large discrepancy between the two grain size exponents, which correspond to 50 MPa and 100 MPa. This variation in grain size is likely due to the two different creep mechanisms that may be occurring during creep of these two sets of samples with two very different grain sizes, which was discussed earlier in this section. Nabarro-Herring diffusional creep will typically result in a grain size exponent of approximately 2, while interface reaction-controlled creep will typically see a grain size exponent of approximately 1. This could explain the range of grain size exponents that were obtained in this case using these two sets of specimens. The grain size exponents are presented again in Table 31.

Table 31: The grain size exponent, m, for 2at% Er-doped, polycrystalline YAG specimens at different creep stress levels at 1300°C in air.

Creep Stress [MPa]	**Grain Sizes [µm]**	**Grain Size Exponent, *n***	**Average Grain Size Exponent, *n***
50	0.45, 1.87	1.38	**1.84**
100	0.45, 1.87	2.30	

The steady-state creep strain rates obtained for 2at% Er-doped YAG specimens were compared to those obtained for undoped YAG, shown in Figure 124. Both the doped and undoped specimens were tested at 1300°C in air in order to remove other sources of variation and to isolate the effects of the dopant. However, the grain sizes of each SPS billet are different for both the doped and undoped billets. Each grain size is shown in Figure 124 along with the steady-state creep strain rates.

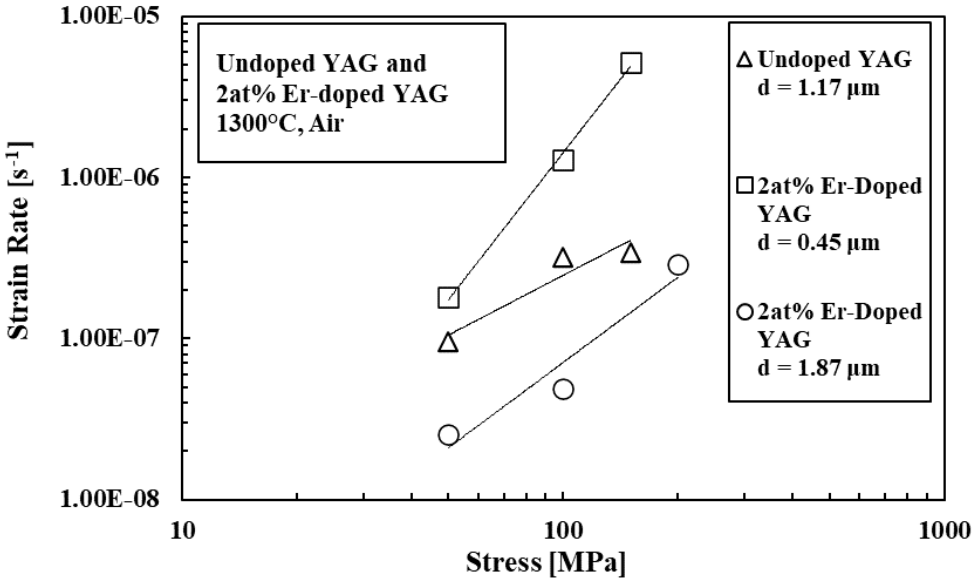

Figure 124: The steady-state creep strain rate vs. applied stress of 2at% Er-doped and undoped, polycrystalline YAG specimens with different grain sizes at 1300°C in air.

In order to fully assess the effects of the dopant on the creep behavior of YAG at 1300°C in air, it was necessary to remove any possible effect of grain size. Therefore, the steady-state creep strain rates were normalized for a grain size equal to d = 1 µm. As with Yb-doped YAG specimens, the creep rates were normalized by using the average measured grain size exponent determined for undoped YAG, shown in Table 21 and Equation 33. The resulting, normalized steady-state creep strain rates are shown in Figure 125.

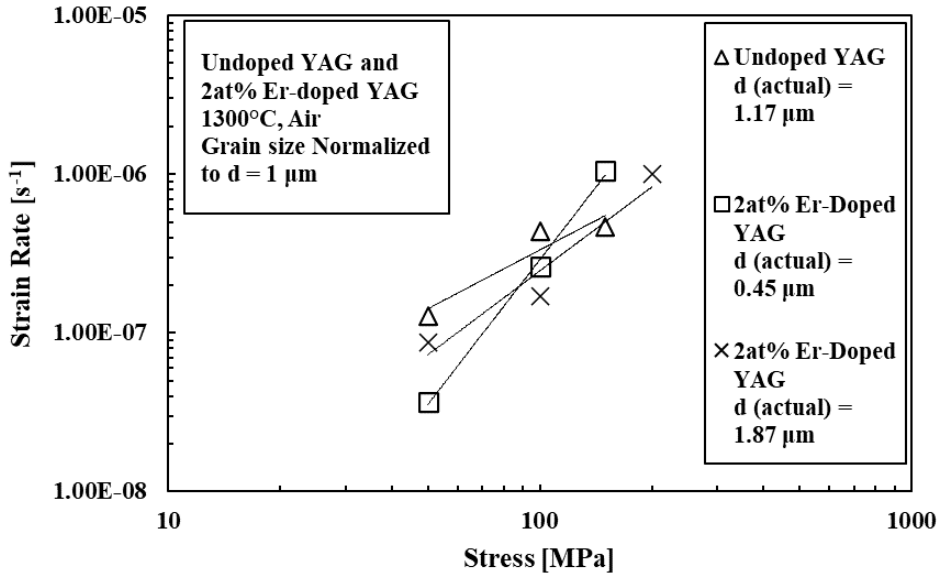

Figure 125: The normalized steady-state creep strain rate vs. applied stress of 2at% Yb-doped and undoped, polycrystalline YAG specimens for grain sizes of d = 1 µm at 1300°C in air.

Once the creep rates were normalized for grain size, the results in Figure 125 were analyzed to determine any possible effects of the dopant on the creep behavior of YAG. The steady-state strain rates for undoped YAG with original grain size of 1.17 µm and the Er-doped YAG with grain size of 1.87 µm are very close to each other. Recall that the 100 MPa test for Er-doped YAG with grain size of 1.87 µm was performed at a lower temperature, and would likely have resulted in a higher strain rate with no furnace malfunction. Based on these results for specimens with larger grain size, there is minimal difference observed in Figure 125, which may indicate that there is no significant effect of the dopant on the steady-state creep behavior of YAG.

This same observation was made for Yb-doped YAG in the previous section, and was attributed to the similarities of the rare-earth ions, Y^{3+} and Yb^{3+}. Therefore, these ion substitutions have minimal effects on the rates of diffusion during creep. These similarities extend to the Er^{3+} ion as well, which has an ionic radius of 0.100 nm, which falls between Y^{3+}

and Yb^{3+}. Therefore, the diffusivity of Er^{3+} is expected to closely correspond to the diffusivity of Y^{3+} self-diffusion in YAG, and these elements can almost fully replace one-another [96], [290], [291].

However, there is a significant difference in creep strain rates of Er-doped YAG and undoped YAG when considering the SPS billet with grain size of 0.45 μm. Even though the strain rates have been normalized for grain size, this normalization process assumes identical creep mechanisms and overall similar creep behavior. Recall that the small grain size of this doped YAG billet contributed to a different stress and grain size exponent than what was expected for YAG, based on the earlier results presented in this chapter. Therefore, the normalization process described for Figure 125 did not fully remove the variation in the creep behavior between these specimens. Just as with Yb-doped YAG, this higher stress exponent was attributed to the interface reaction-controlled creep mechanism, which could be present in YAG materials with smaller grain size. Also recall that interface reaction-controlled creep can contribute to surprisingly low steady-state creep rates [29], as was observed at 50 MPa in the current work.

A comparison of the steady-state creep strain rates of Yb- and Er-doped YAG is presented in Figure 126 and Figure 127. Figure 126 shows the results for doped YAG specimens with smaller grain sizes compared to undoped YAG with a grain size of 1.17 μm. Results are presented for actual grain sizes in Figure 126(a) and normalized to d = 1 μm in Figure 126(b). Figure 127 shows the results for doped YAG specimens with larger grain sizes compared to undoped YAG with a grain size of 1.17 μm. Results are presented for actual grain sizes in Figure 127(a) and normalized to d = 1 μm in Figure 127(b).

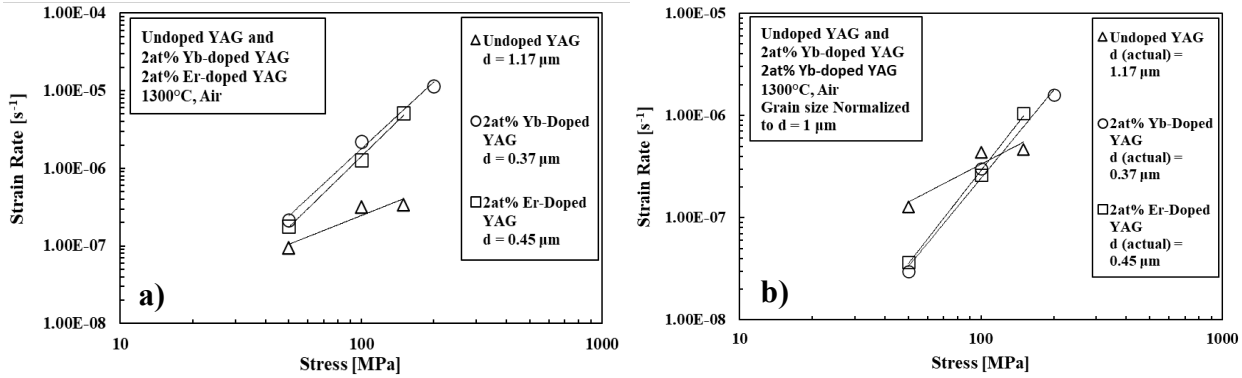

Figure 126: Comparison of Yb- and Er-doped YAG specimens with grain sizes of 0.37 µm and 0.45 µm, respectively and undoped YAG with grain size of 1.17 µm. Steady-state creep strain rates vs. applied stress are presented for original grain size (a) and normalized to d = 1 µm (b).

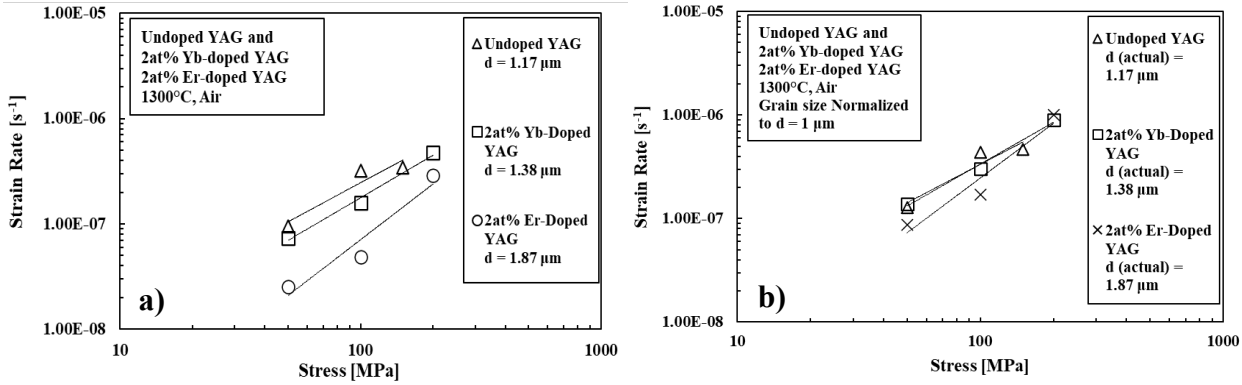

Figure 127: Comparison of Yb- and Er-doped YAG specimens with grain sizes of 1.38 µm and 1.87 µm, respectively and undoped YAG with grain size of 1.17 µm. Steady-state creep strain rates vs. applied stress are presented for original grain size (a) and normalized to d = 1 µm (b).

These results demonstrate the similarity of the creep behavior of 2at% Yb-doped YAG and 2at% Er-doped YAG. Multiple conclusions can be drawn from Figure 126 and Figure 127. First, it appears that grain size is the most significant factor that influences the steady-state creep rates of each material variant, including undoped YAG. Once creep rates have been normalized to one

common grain size, Figure 127 reveals that there is essentially no effect of each dopant for grain sizes above 1 μm.

Figure 126 reveals a different phenomenon altogether. There is a significant difference in the effects of creep stress on the resultant creep strain rates for each doped YAG material variant with smaller grain sizes ($d < 0.5$ μm). This was previously manifested by the higher stress exponents obtained for specimens with smaller grain sizes. This result indicates that there may be a different creep mechanism controlling the creep rates of YAG with very small grain sizes. Previous research has suggested that ceramic material specimens with smaller grain sizes tested at low creep stress levels may see a shift from Nabarro-Herring diffusional creep to interface reaction-controlled diffusional creep as the dominant creep mechanism. Furthermore, interface reaction-controlled creep has been associated with higher stress exponents, as was discussed previously in Section 2.3.2. This conclusion would explain the results obtained for YAG specimens of particularly small grain size.

6.5. Determination of the Dominant Creep Mechanisms for Yttrium Aluminum Garnet at 1300°C and 1400°C in Air and in Steam

Undoped, Polycrystalline YAG at 1300°

Recall from Section 2.3.2 that there are several different possible creep mechanisms in ceramic materials that lead to different behavior. Identifying these creep mechanisms can lead to a better understanding of how a material will perform in creep and will enable performance predictions and material design for structural applications. Previous research has established the behavioral trends associated with different mechanisms, so they can be determined by analyzing

the steady-state creep rates, which are described by Equation 4. Typically, by determining the stress exponent, *n*, and the grain size exponent, *m*, along with some other observations, the dominant creep mechanisms can be determined. Parthasarathy et al. [26] and Armani et al. [28], [29] found that the creep of YAG was primarily caused by grain boundary sliding accommodated by diffusion, according to the Nabarro-Herring creep model. This creep mechanism is typically identified by a stress exponent of 1 and a grain size exponent of 2. The average stress exponent for all the undoped, polycrystalline YAG specimens tested in this study was 1.33 in air and 1.44 in steam. The average grain size exponent for all the undoped, polycrystalline YAG specimens tested in this study was 1.99 in air and 2.06 in steam. Therefore, this research supports the previous conclusion that Nabarro-Herring diffusional creep is likely the dominant creep mechanism controlling the strain rates of undoped, polycrystalline YAG at 1300°C in air and in steam.

Undoped, polycrystalline YAG at 1400°C

Similarly for creep of undoped, polycrystalline YAG at 1400°C, the stress exponent was determined to be 0.87, based on the results of three specimens tested from one sample set. Although this stress exponent is lower than what was determined at 1300°C, it still supports the conclusion that Nabarro-Herring diffusional creep with an approximate stress exponent of 1 is likely the dominant creep mechanism at 1400°C. Additional experimentation at 1400°C with more specimens would be necessary to determine with certainty if the stress exponent is consistently lower than that at 1300°C.

The investigation into the activation energy of undoped YAG at 1300°C and 1400°C suggests Nabarro-Herring diffusional creep with diffusion of the Y^{3+} cation as the rate limiting

species. The activation energy for the creep of undoped, polycrystalline YAG in this study was found to be approximately 534 kJ/mol. This is very close to 584 kJ/mol, which was the activation energy associated with of the Y^{3+} cation in YAG, reported by Parthasarathy et al. who came to the same conclusion about creep mechanisms in YAG, when conducting creep experiments in a vacuum.

2at% Yb-Doped YAG at 1300°C

The investigation into the creep behavior of 2at% Yb-doped YAG not only revealed effects of the dopant, but also provided additional information about the overall creep of YAG with small grains. First, creep tests conducted with 2at% Yb-doped YAG specimens with a grain size of 1.38 μm, revealed that the presence of Yb had no apparent effect on the creep of YAG. Once the steady-state creep rates were normalized to a common grain size, the resulting strain rates for doped and undoped YAG were nearly identical. Also, the stress exponent for 2at% Yb-doped YAG specimens with a grain size of 1.38 μm was determined to be 1.34, which is nearly identical to that found for undoped YAG for all grain sizes tested, between 0.92 μm (from the work of Armani et al. [28], [29]) and 7.99 μm. This identical behavior of Yb-doped YAG and undoped YAG is supported by the previous conclusions about the similarities of Yb and Y. When considering rare-earth dopants, suitable for YAG, Yb is widely considered the most equivalent element, that can be substituted for Y with minimal effect [96].

Secondly, the creep behavior of 2at% Yb-doped YAG specimens with grain size of 0.37 μm was different than that of all the previously tested YAG specimens. The creep rates were much higher than those obtained for YAG with larger grains, as was expected, due to the inverse relationship between the grain size and steady-state creep rates. However, the creep rates showed

a stronger sensitivity to the applied stress as evidenced by a higher stress exponent of 2.38. Additionally, the grain size exponent associated with Yb-doped YAG was found to be 1.69, slightly lower than that found for undoped YAG. These variations in the stress exponent and the grain size exponent suggest that the creep mechanism is different for YAG with the much smaller grain size, and that it is the grain size and not the presence of a dopant that causes the change in creep mechanism.

The higher stress exponent and lower grain size exponent indicate that for small grain sizes, significantly less than 1 μm, the dominant creep mechanism changes from Nabarro-Herring diffusional creep to interface reaction-controlled diffusional creep. This type of diffusional creep no longer assumes perfect sources and sinks at the grain boundaries, but assumes that the rate of bulk diffusion increases, and the creation and annihilations of vacancies at the grain boundaries can become the rate-controlling mechanism of diffusion.

Reaction controlled diffusional creep typically has a stress exponent of 2 and a grain size exponent of 1, and has been considered the dominant creep mechanism for fine-grained alumina and alumina fibers [29], [292], [293]. Additionally, some research suggests that in fine-grained ceramics, a larger stress exponent could be related to the presence of basal slip dislocation motion, or the simultaneous occurrence of dislocation motion, grain boundary sliding, and cavity formation [29], [147], [283]–[285], [287]. Only one set of YAG specimens with grain size of less than 0.5 μm was tested in this study. Additional tests of YAG specimens with similar grain size might give more insight into the potential shift in creep mechanism.

2at% Er-Doped YAG at 1300°C

The results obtained for 2at% Er-doped YAG specimens support those previously obtained for Yb-doped YAG specimens. For specimens with large grain sizes ($d > 1$ μm), there is no significant difference in the steady-state creep strain rates for doped or undoped YAG. The small differences observed may be within the noise associated with each test and measurement method, and are likely negligible. Graphs were created to demonstrate the similar creep behavior of doped and undoped YAG (see Figure 127), including one with creep rates normalized to a common grain size ($d_{norm} = 1$ μm).

A significant difference in creep behavior was noted for both Er- and Yb-doped YAG specimens with smaller grains sizes ($d < 0.5$ μm). The greater dependence on creep stress was identified based on the stress exponents obtained for billets Y-Yb-7-40 and Y-Er-9-40. Based on these results along with the other results for doped and undoped YAG specimens, and considering the grain sizes of all the specimens that were tested, it is likely that this different behavior is not due to the presence of a dopant, but rather due to a change in creep mechanism for YAG specimens with smaller grain sizes. Based on the stress exponents obtained for these two different doped YAG billets (n = approximately 2 and 3), the creep mechanism is likely grain boundary sliding accommodated by interface reaction-controlled diffusion.

Interface Reaction-Controlled Diffusional Creep

The creep behavior of YAG that was presented in this section has resulted in several observations about creep mechanisms. The results indicate that the steady-state creep strain rates for the majority of specimens tested are controlled by grain boundary sliding, accommodated by Nabarro-Herring diffusional creep. This was indicated by the stress exponent (n = 1.30) and

grain size exponent (m = 2.01), shown in Figure 99 and Figure 100. This is in close agreement with previous studies, which also suggest Nabarro-Herring diffusional creep as the dominant creep mechanism for YAG under these test conditions.

However, there are two possible exceptions to this conclusion that have been identified in this section. First, it has been observed that the creep of YAG with small grain sizes (d < 0.5 μm) may be interface reaction-controlled, which was indicated by higher stress exponents and lower grain size exponents obtained for YAG billets Y-Yb-7-40 and Y-Er-9-40, as summarized in Sections 6.4.1 and 6.4.2. These two billets were doped with Yb and Er; however, these were also the only YAG billets with such small grain sizes. It was concluded that it is the grain size and the associated creep mechanism that directly contributed to the creep behavior, and likely not the presence of either dopant. However, further study of the creep behavior of undoped YAG with small grain sizes is required in order to validate this conclusion.

The second exception to Nabarro-Herring creep as the dominant mechanism for the creep of YAG was identified by the non-linear trends observed in Figure 99 and Figure 100. These plots show the steady state creep rate results of undoped, polycrystalline YAG at 1300°C. A more detailed analysis of these plots indicates that the interface reaction-controlled creep mechanism may be present for YAG specimens with low applied creep stress.

The curves used to generate the stress exponents and grain size exponents plotted as log(strain rate) vs. log(stress) and log(strain rate) vs. log(grain size), respectively, are not perfectly linear. Using linear regression on a log-log scale, a good linear approximation of the trends can be obtained and exponents can be approximately determined for the entire range of stresses. However, as is shown in Figure 128 and Figure 129, if the creep rate vs. stress curves are separated into lower and higher stress regimes, and similarly, if the creep rate vs. grain size

curves are separated into lower and higher grain sizes, the slopes of the curves associated with each separate regime change drastically.

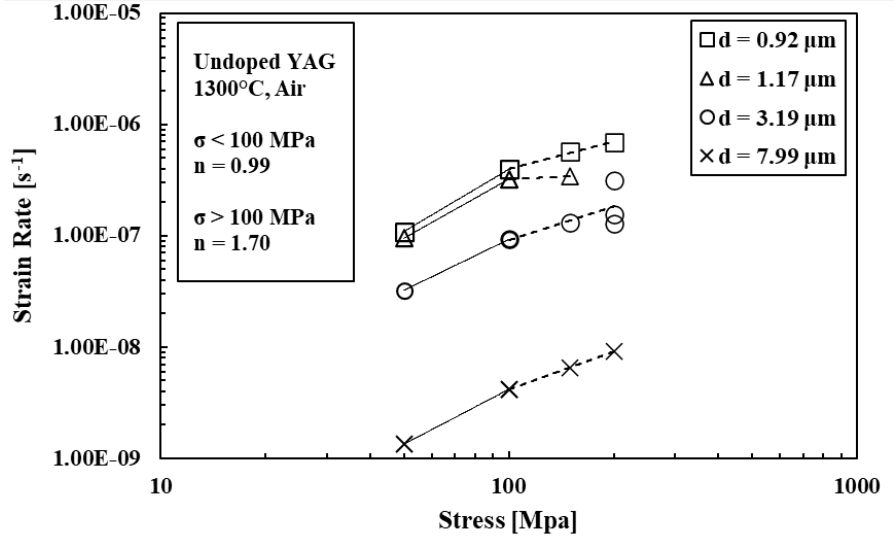

Figure 128: Determination of the stress exponents of undoped YAG at 1300°C in air. Each set of specimens of a particular grain size has been divided into low stress and high stress regimes, demonstrating the consistent change in slope of each line.

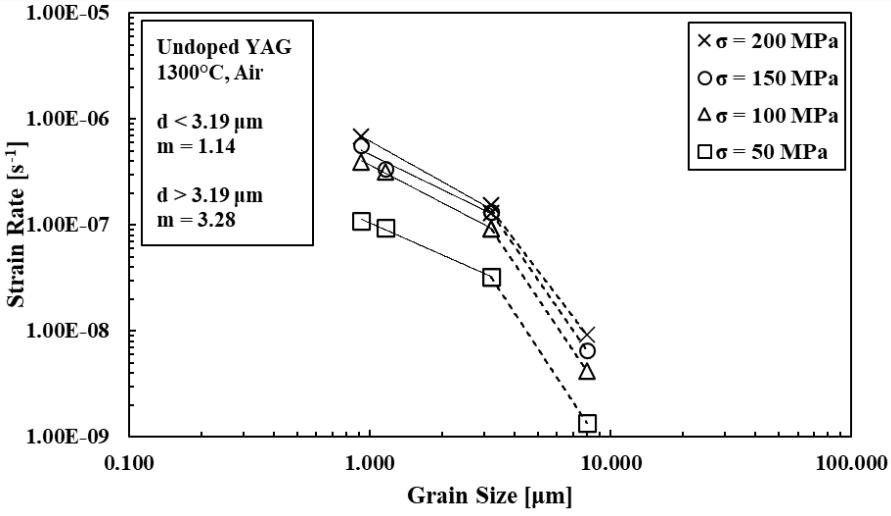

Figure 129: Determination of the grain size exponents of undoped YAG at 1300°C in air. Each set of specimens at a particular stress level has been divided into smaller grains and larger grains, demonstrating the consistent change in slope of each line.

For higher stress, the stress exponent of approximately 1 is as expected for Nabarro-Herring creep. For lower stress, the associated creep rates are lower than expected, causing the measured stress exponent to be approximately 1.7. This same phenomenon was observed in the steady-state creep rates of 2at% Yb-doped YAG, and was even more pronounced for specimens with smaller grain size. This suggests that creep of YAG at 50 MPa may transition from Nabarro-Herring diffusion creep to interface-reaction controlled creep. Previous research has suggested that this is more likely at low stresses, and that in these cases, the resultant creep rates could be lower than expected [147], [284], [285]. It is also possible that 50 MPa may be below some stress threshold, where very little creep occurs at these test conditions [288], [289].

A similar effect is observed when determining grain size exponents in Figure 129. When larger grain sizes are isolated, the grain size exponent is observed to be approximately 3.28. And when the smaller grain sizes are isolated, the grain size exponent is observed to be approximately 1.14. This also suggests that lower grains increase the occurrence of interface reaction-controlled creep as an active mechanism in YAG. Similar to what was discovered for 2at% Yb-doped YAG, specimens with smaller grains are less sensitive to grain size and have a smaller grain size exponent, as is the case with interface reaction-controlled creep. Again, this has been observed in materials with smaller grains as the increased amount of grain boundaries in fine-grained materials can lead to reactions at the interface. In these cases, the rate of bulk diffusion increases such that the creation and annihilation of vacancies and defects at the grain boundaries can become the rate-controlling mechanism of diffusion. This has also been observed in materials subject to creep at lower stress values, and has contributed to surprisingly low creep rates, as is seen at low stresses and for smaller grain sizes in YAG.

7. Creep Behavior of Undoped Lutetium Aluminum Garnet ($Lu_3Al_5O_{12}$) at Elevated Temperature

This chapter presents the experimental results of creep tests performed on undoped, polycrystalline Lutetium Aluminum Garnet (LuAG). Creep tests were performed in the same manner as with YAG, using the same experimental facility, identical specimen design, and the same experimental procedures, which are written out in detail in Appendix E. Compressive creep experiments were performed at 1300°C and 1400°C with creep stresses between 50 MPa and 200 MPa in air and in steam environments. Specimens from several different sample sets were selected for creep tests based on specimen quantity and grain size. All specimens were processed via SPS, which was discussed in more detail in Section 3.2.1.

This chapter first presents the creep results obtained at 1300°C in air for LuAG specimens with various grain sizes. Specimens from six different SPS billets were selected for creep testing at 1300°C in air, and these specimens were grouped into four different sample sets based on average grain size. The analysis of these four sample sets will demonstrate the effect of grain size on the creep behavior of LuAG at 1300°C in air.

Creep tests were also conducted in steam in order to demonstrate the effects of steam environment on the creep behavior of LuAG. Specimens from three different SPS billets were grouped into two different sample sets based on grain size. This approach enabled the determination of the effect of grain size on the creep behavior of LuAG at 1300°C in steam.

Finally, the creep behavior of LuAG at 1400°C in air is also presented in order to assess the effects of temperature on the overall creep behavior of LuAG and to determine the creep activation energy.

For each temperature and environment, the creep behavior is investigated by obtaining the creep strain vs. time curves associated with each test, as well as by determining the steady-state creep strain rates. From these results, the stress exponent, grain size exponent, and the activation energy were obtained. This information was then used to determine the most likely creep mechanisms responsible for the creep behavior of LuAG. The creep behavior of LuAG is presented and compared to the creep behavior of YAG under similar test conditions in order to understand similarities between materials in the garnet family and to assess the feasibility of LuAG as a structural material.

7.1. Creep of Undoped, Polycrystalline Lutetium Aluminum Garnet at 1300°C in air

7.1.1. The Effects of Grain Size on the Creep Behavior of Lutetium Aluminum Garnet at 1300°C in Air

LuAG specimens from six different SPS billets were selected for creep testing at 1300°C in air, and these specimens were grouped into four different sample sets based on average grain size. Certain SPS billets possessed very similar grain sizes, and in these cases, specimens from these billets were grouped together in order to test more specimens with one approximate grain size. This approach enabled the effects of the applied stress to be isolated, and a better approximation of the stress exponent could be determined. The analysis of these four sample sets, comprised of specimens from six SPS billets, will demonstrate the effect of grain size on the creep behavior of LuAG at 1300°C in air.

LuAG specimens were tested at stress levels between 50 MPa and 200 MPa in the same manner as with YAG. Specimens available for testing had a variety of grain sizes between 0.32 μm and 4.90 μm. Figure 130 shows an SEM image of the polished surface of a specimen from SPS billet L-12-40, which has the smallest grain size of 0.32 μm.

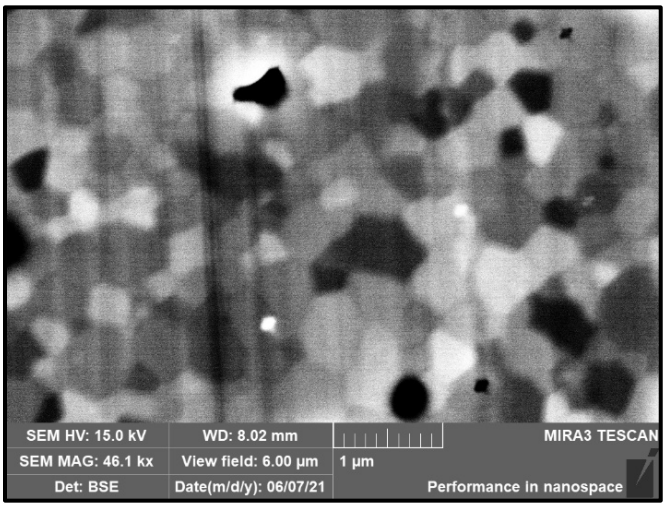

Figure 130: SEM image of a specimen cut from the SPS billet L-12-40, with a measured average grain size of 0.32 μm.

This SEM image demonstrates that the microstructure of LuAG is similar to that of the YAG specimens discussed in the previous chapter. The visible grains possess a sharp geometric shape with no smooth, round edges. There is also significant variation in the apparent grain size within the small field of view of the image in Figure 130. Some small open porosity is also observed, and is identified by the darkest shapes surrounded by a light ring, indicating charging in the SEM. Three specimens from billet L-12-40 were creep tested at 1300°C in air under compressive stresses of 50 MPa, 100 MPa, and 200 MPa. Figure 131 shows the creep strain vs. time curves obtained for LuAG specimens from billet L-12-40 with a grain size of 0.32 μm.

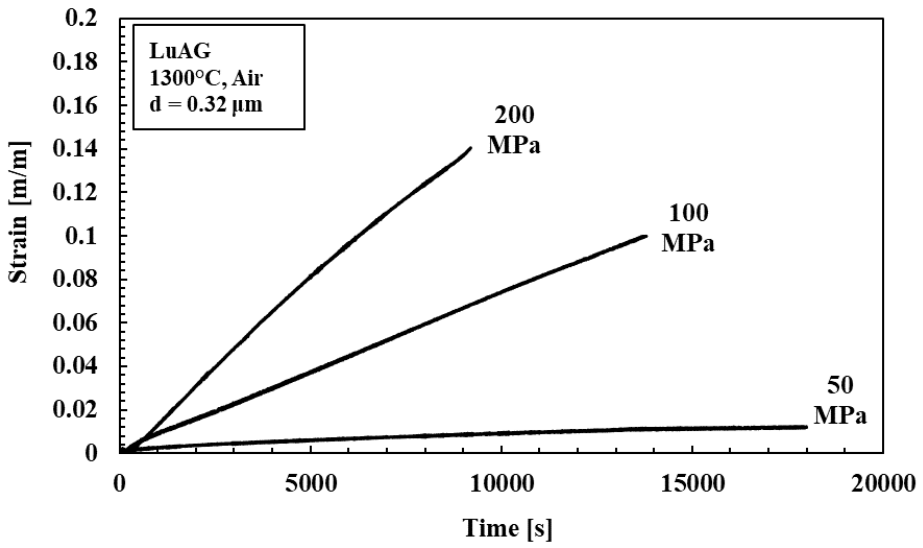

Figure 131: Creep strain vs. time curves obtained for polycrystalline LuAG specimens with grain size of 0.32 µm at 1300°C in air.

As is common with each ceramic material tested in this study, there is little primary creep and no apparent tertiary creep seen in Figure 131. The majority of the five-hour creep test is dominated by nearly linear secondary creep. It is also apparent from the creep strain vs. time curves that there is significant strain accumulation for the higher stress tests. The specimen tested with 200 MPa applied stress reached nearly 15% strain in 2.5 hours. The specimen tested with 100 MPa applied stress reached 10% strain in four hours. Even at 50 MPa applied stress, the strain reached 1.2% after five hours.

To determine if grain size was the primary cause of these high accumulated strains, specimens from several other SPS billets with several different grain sizes were tested under similar conditions. SEM micrographs of specimens from billets L-10-40 and L-18-40 are shown in Figure 132 and Figure 133, respectively.

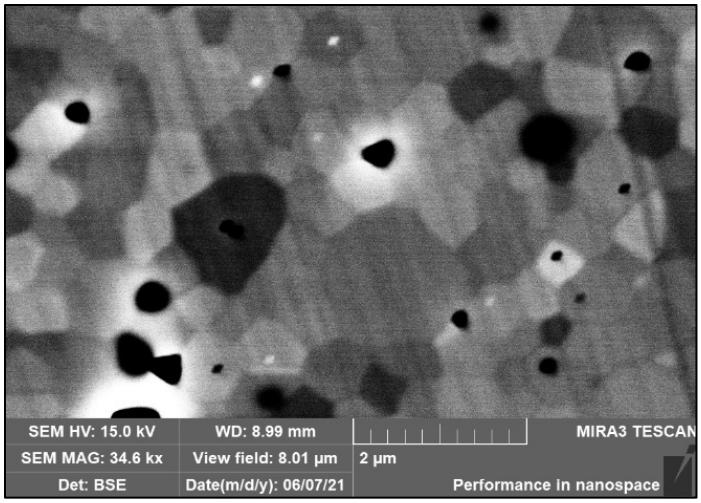

Figure 132: SEM image of a specimen cut from the SPS billet L-10-40, with a measured average grain size of 0.54 µm.

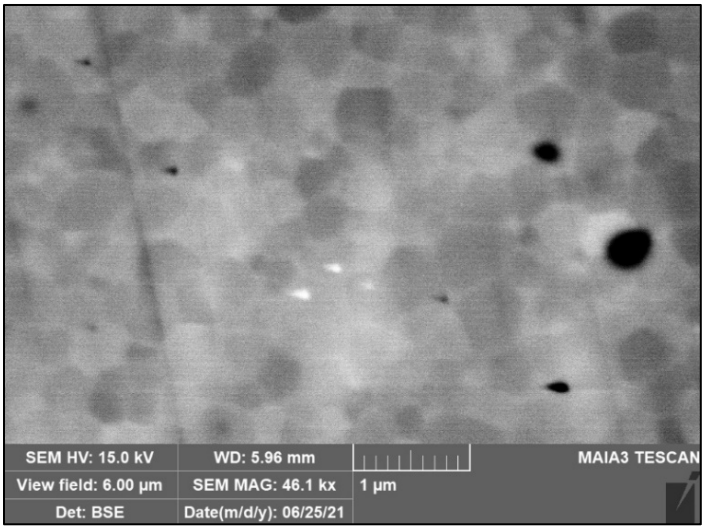

Figure 133: SEM image of a specimen cut from the SPS billet L-18-40, with a measured average grain size of 0.42 µm.

Figure 134 shows the creep strain vs. time curves for LuAG specimens from SPS billets L-10-40 and L-18-40 with an average grain size of 0.48 µm. In this case not all of the specimens were from the same billet, so their grain sizes were not all identical; however, they were chosen and grouped together due to the very close similarity in grain size. Three of the specimens presented in Figure 134 were from L-10-40 with a measured grain size of 0.54 µm. A fourth

specimen from L-18-40 with a very similar grain size of 0.42 μm was also tested in order to determine the strain at a fourth stress level. It was assumed that this small difference in grain size will not cause any major effect on the creep strain beyond the noise associated with this type of test. Therefore, Figure 134 shows results obtained for all four specimens grouped together in order to compare the effects of applied stress on creep. The sample set in Figure 134 is identified by the average of the two grain sizes, which is 0.48 μm.

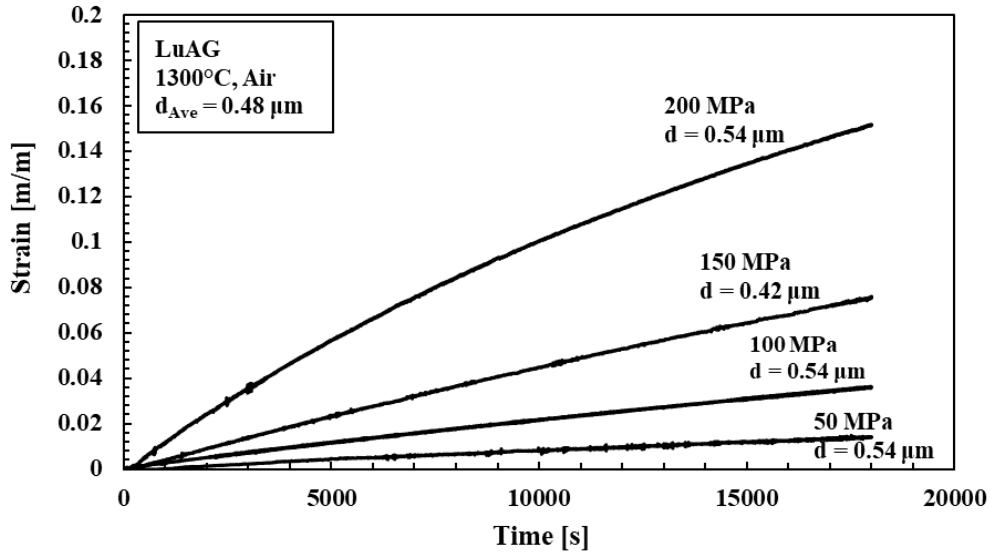

Figure 134: Creep strain vs. time curves obtained for polycrystalline LuAG specimens with an average grain size of 0.48 μm at 1300°C in air. Specimens with grain size of 0.54 μm were tested at 50, 100, and 200 MPa, and a specimen with grain size of 0.42 μm was tested at 150 MPa.

The total accumulated strain for specimens with an average grains size of 0.48 μm was between 1.5% and 15% strain, which is similar to the results for LuAG specimens with grain size of 0.32 μm. This result is expected due to the similarity in grain size between specimens presented in Figure 132 and Figure 133. Two more sample sets were tested at 1300°C in air, each having larger grains, in order to quantify the effect of grain size on the creep behavior of LuAG.

SEM micrographs from billets L-4-40 and L-19-40 are shown in Figure 135 and Figure 136, respectively.

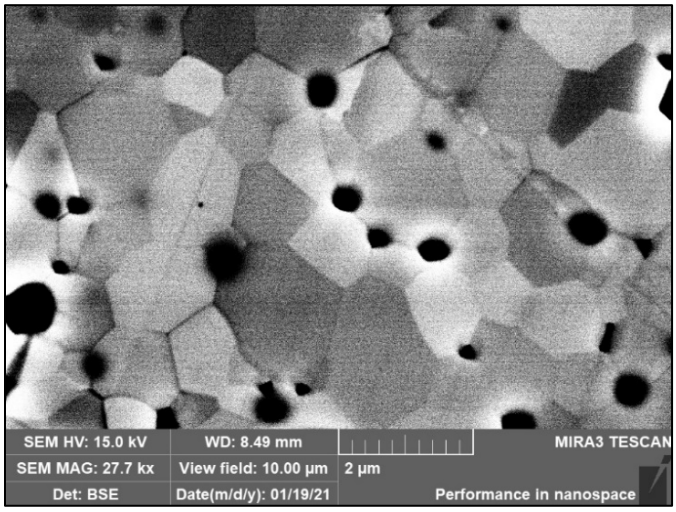

Figure 135: SEM image of a specimen cut from the SPS billet L-4-40, with a measured average grain size of 0.95 µm.

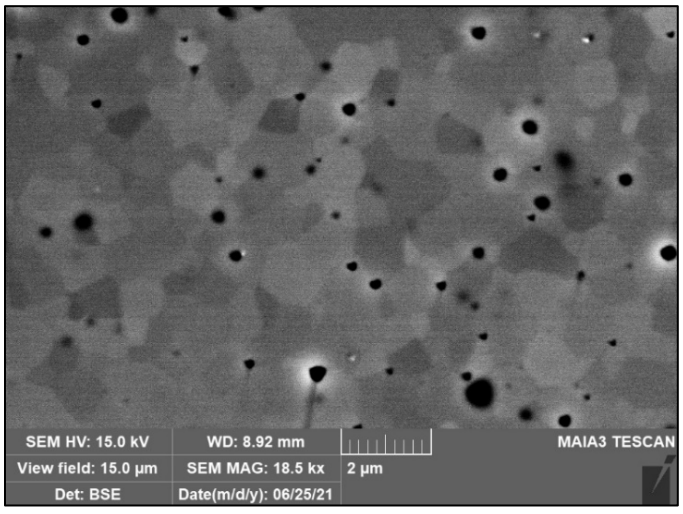

Figure 136: SEM image of a specimen cut from the SPS billet L-19-40, with a measured average grain size of 0.84 µm.

Figure 137 shows the creep strain vs. time curves for specimens with an average grain size of 0.90 µm. In this case, as with Figure 134 above, not all of the specimens were from the same sample set, so their grain sizes are not all identical. However, they were chosen due to the very

close similarity in grain size. Two of the specimens presented in Figure 137 were from one sample set with a measured grain size of 0.95 μm. A third specimen with a very similar grain size of 0.84 μm was also tested in order to determine the strain at a third stress level. Figure 137 shows all three specimens grouped together. The sample set is identified by the average of the two grain sizes, which is 0.90 μm.

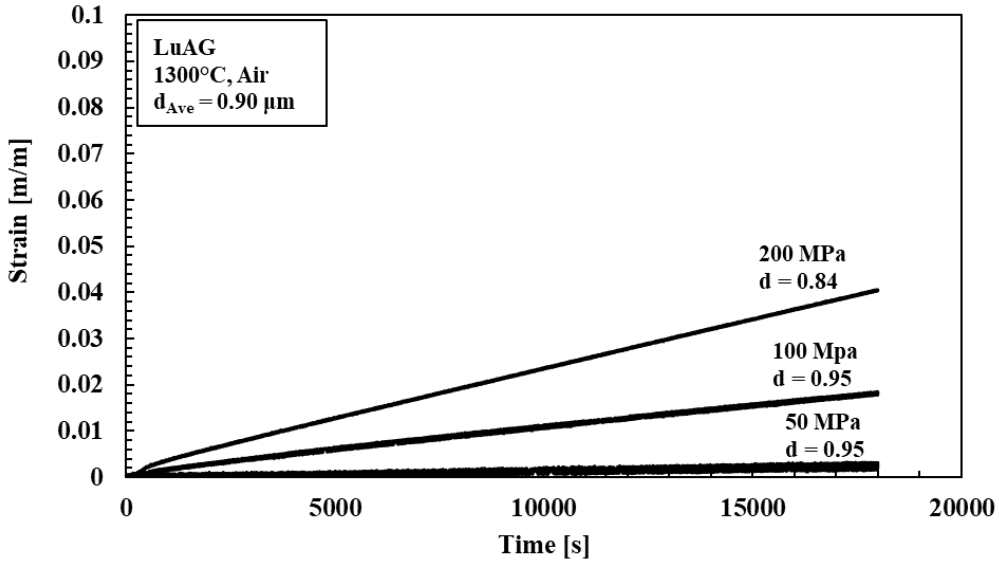

Figure 137: Creep strain vs. time curves obtained for polycrystalline LuAG specimens with an average grain size of 0.90 μm at 1300°C in air. Specimens with grain sizes of 0.95 μm were tested at 50 MPa and 100 MPa, and a specimen with grain size of 0.84 μm was tested at 200 MPa.

The total accumulated strain for specimens with an average grains size of 0.90 μm was between 0.25% and 4% strain. One more sample set with a larger grain size was tested for comparison. An SEM micrograph from billet L-3-40 is shown in Figure 138.

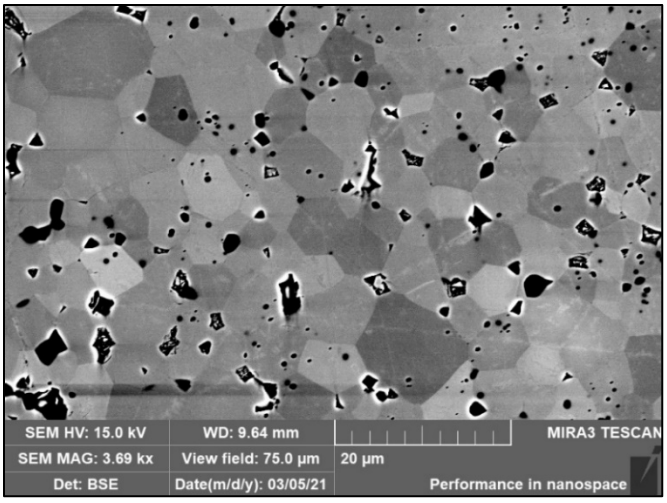

Figure 138: SEM image of a specimen cut from the SPS billet L-3-40, with a measured average grain size of 4.90 µm.

Figure 139 shows the creep behavior of specimens with a grain size of 4.90 µm. For specimens with this larger grain size, the total accumulated strain is much lower, reaching less than 1% strain at all stress levels. Table 32 lists all the LuAG specimens tested at 1300°C in air and summarizes the associated creep results including the total accumulated strain after five hours and the steady-state creep strain rates for each specimen at each grain size.

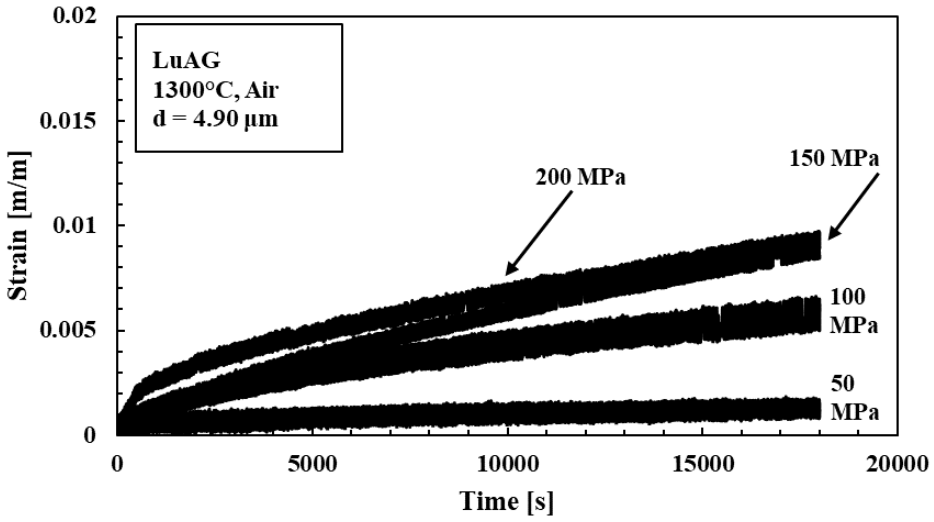

Figure 139: Creep strain vs. time curves obtained for polycrystalline LuAG specimens with grain size of 4.90 µm at 1300°C in air.

Table 32: Summary of creep results for polycrystalline LuAG with different grain sizes at 1300°C in air.

Specimen Name	Grain Size [μm]	Creep Stress [MPa]	Total Accumulated Strain after 5 hrs [%]	Steady-State Creep Rate [s^{-1}]
L-12-40-1	0.32	50	1.20	6.27×10^{-7}
L-12-40-2	0.32	100	Not Available*	6.77×10^{-6}
L-12-40-3	0.32	200	Not Available*	1.28×10^{-5}
L-10-40-1	0.54	50	1.48	5.87×10^{-7}
L-10-40-2	0.54	100	3.58	1.70×10^{-6}
L-18-40-1	0.42	150	7.53	3.59×10^{-6}
L-10-40-3	0.54	200	15.16	5.36×10^{-6}
L-4-40-1	0.95	50	0.26	1.17×10^{-7}
L-4-40-2	0.95	100	1.78	8.67×10^{-7}
L-19-40-1	0.84	200	4.06	2.09×10^{-6}
L-3-40-1	4.90	50	0.17	2.65×10^{-8}
L-3-40-2	4.90	100	0.65	1.45×10^{-7}
L-3-40-3	4.90	150	0.93	2.55×10^{-7}
L-3-40-4	4.90	200	0.97	2.83×10^{-7}

*Creep tests ended early, and strain accumulation after 5 hrs is unknown.

As with YAG specimens discussed in Section 6, the steady state creep strain rates shown in Table 32 represent the minimum creep strain rates obtained during each five-hour long creep test. The strain rates are determined by finding the slope of the shallowest portion of each strain vs. time curve. From Table 32, there is a significant difference in the steady-state creep strain rates for specimens with different grain sizes. The lowest steady-state creep strain rate for a LuAG specimen with a grain size of 4.90 μm was found to be 2.65×10^{-8} s^{-1}, while similar test conditions resulted in a steady-state creep strain rate of 6.27×10^{-7} s^{-1} for a specimen with a grain size of 0.32 μm. There is also significant variation in the steady-state creep rates within the individual sample sets, due only to the difference in applied stress. In most cases there is a single order of magnitude difference between the steady-state creep rates at 50 MPa and 200 MPa. For

specimens with the smallest grain size there is nearly a two orders of magnitude difference between the steady-state creep rates at 50 MPa and 200 MPa.

7.1.2. Determination of the Stress Exponent and the Grain Size Exponent for the Steady-State Creep Behavior of Lutetium Aluminum Garnet at 1300°C in Air

Once the steady-state creep strain rates are obtained from the strain vs. time curves, then the stress exponent can be determined. Recall that the stress exponent, *n*, is a critical element in the steady state creep rate equation (Equation 4), described in Section 2.3.1. The stress exponent describes to what degree the applied creep stress effects the final steady-state creep rate. It can be determined by plotting strain rate vs. stress on a log-log scale. Linear regression is used to determine the best-fit line for each set of data, and the associated exponent represents the stress exponent for a particular grain size. The steady-state creep strain rates for LuAG specimens with four different average grain sizes and the associated stress exponents are shown in Figure 140.

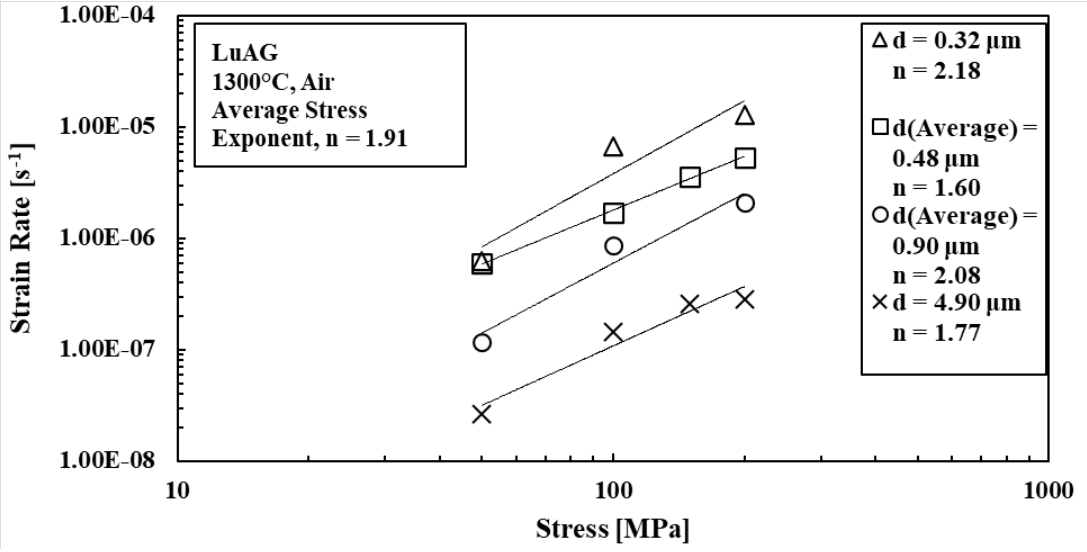

Figure 140: The steady-state creep strain rate vs. applied stress and stress exponents, *n*, determined for polycrystalline LuAG specimens with different grain sizes at 1300°C in air.

A different stress exponent was calculated for each sample set associated with each grain size. The stress exponents were then averaged together to determine one approximate stress exponent, which best describes the effects of stress on the steady-state creep rates of LuAG at 1300°C in air. Table 33 shows the stress exponents determined for each sample set associated with a different grain size, as well as the final averaged stress exponent.

Table 33: The stress exponent, n, for polycrystalline LuAG specimens with different grain sizes at 1300°C in air.

Sample Set	**Average Grain Size [µm]**	**Stress Range [MPa]**	**Stress Exponent, *n***	**Average Stress Exponent, *n***
L-12-40	0.32	50 - 200	2.18	**1.91**
L-10-40 L-18-40	0.48	50 - 200	1.60	
L-4-40 L-19-40	0.90	50 - 200	2.08	
L-3-40	4.90	50 - 200	1.77	

The stress exponent for LuAG at 1300°C in air was determined to be 1.91. This is a higher stress exponent than that found for YAG under the same conditions, which indicates that the applied stress has a greater effect on the steady-state creep rate of LuAG during creep. Recall from Section 2.3.2 that there have been several different stress exponents observed in ceramic materials, which correspond to different creep mechanisms. While it is expected that the creep mechanisms are similar for YAG and LuAG, this higher stress exponent suggests something different is occurring. In this case, a stress exponent of 2 may indicate that interface reaction-controlled diffusional creep could be the rate-controlling creep mechanism. This was observed in YAG specimens with smaller grains, which was described in the previous chapter; however, this creep mechanism is evident in the behavior of LuAG with a much larger range of grain sizes, given the consistently higher stress exponents, determined from Figure 140.

Using the same process, the grain size exponent was determined for LuAG at 1300°C in air by plotting strain rate vs. grain size on a log-log scale, shown in Figure 141. A different grain size exponent was calculated for each group of creep tests associated with each compressive stress value. The grain size exponents were then averaged together to determine one approximate grain size exponent for the steady-state creep of LuAG at 1300°C in air. *Table 34* shows the grain size exponents determined for each sample set associated with a different compressive stress value, as well as the final averaged grain size exponent.

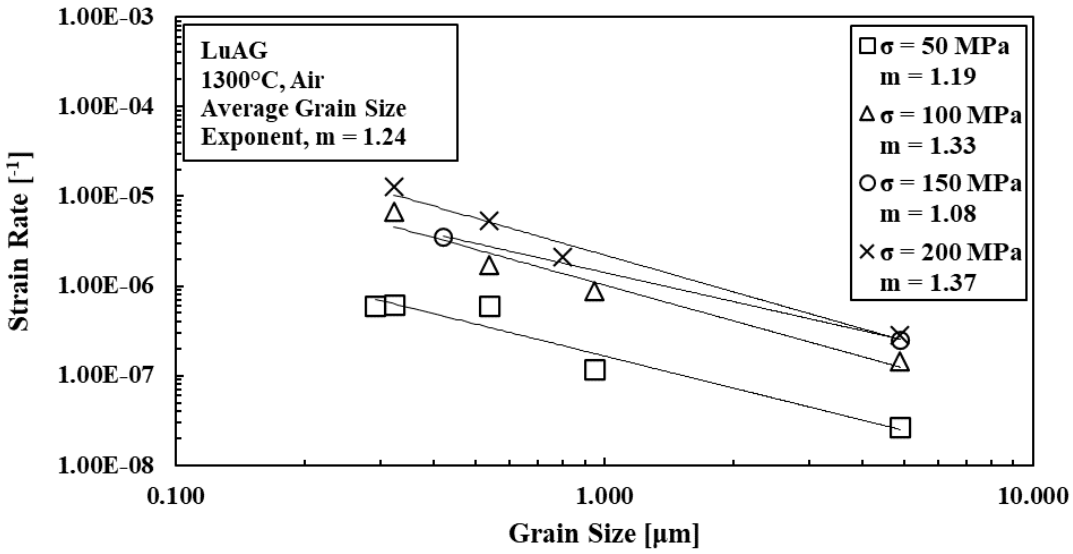

Figure 141: The steady-state creep strain rate vs. grain size and grain size exponents, *m*, of polycrystalline LuAG specimens at different creep stress levels at 1300°C in air.

Table 34: The grain size exponent, m, for polycrystalline LuAG specimens at different creep stress levels at 1300°C in air.

Creep Stress [MPa]	Grain Sizes [µm]	Grain Size Exponent, *n*	Average Grain Size Exponent, *n*
50	0.32, 0.54, 0.95, 4.90	1.19	**1.24**
100	0.32, 0.54, 0.95, 4.90	1.33	
150	0.42, 4.90	1.08	
200	0.32, 0.54, 0.84, 4.90	1.37	

The grain size exponents determined by analyzing the creep behavior of LuAG with grain sizes between 0.32 μm and 4.90 μm, was found to be 1.24. This value is the average of four different grain size exponents, which correspond to the four different creep stress values used in the tests described in this chapter. The four grain size exponents were found to be between 1.08 and 1.37. Recall from Section 2.3.2 that a grain size exponent of 1 indicates that interface reaction-controlled diffusional creep may be the rate-controlling creep mechanism, which is consistent with the stress exponent of 2, as was determined in Figure 140.

7.2. Creep of Undoped, Polycrystalline Lutetium Aluminum Garnet at 1300°C in Steam

7.2.1. The Effects of Grain Size on the Creep Behavior of Lutetium Aluminum Garnet at 1300°C in Steam

Two sample sets with different grain sizes were tested at 1300°C in steam to determine the effects of steam environment on the creep behavior of undoped, polycrystalline LuAG. Testing specimens with different grain sizes will allow the effects of grain size in steam to be determined and compared to the effects of grain size in air. The first sample set included specimens from billet L-13-40 and L-18-40 and had an average grain size of 0.44 μm. Figure 142 shows an SEM micrograph from billet L-13-40. A micrograph from L-18-40 was shown previously in Figure 133.

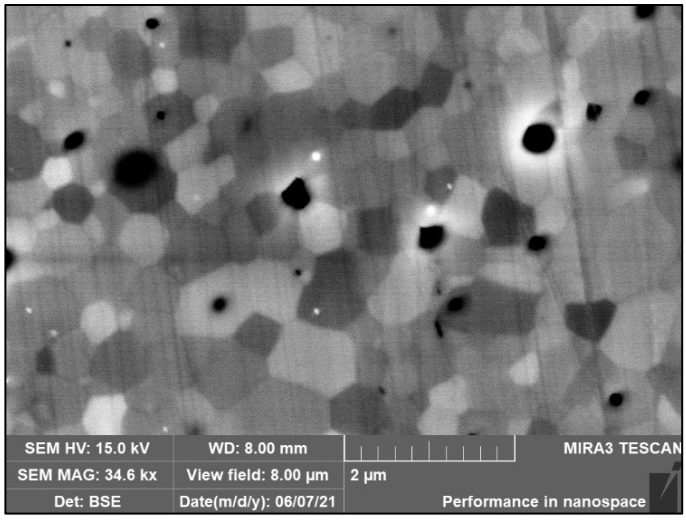

Figure 142: SEM image of a specimen cut from the SPS billet L-13-40, with a measured average grain size of 0.45 µm.

This set of specimens, tested at 50 MPa, 100 MPa, and 200 MPa, consisted of one specimen from the SPS billet L-13-40 with a measured grain size of 0.45 µm. This specimen was tested at 50 MPa. The other two specimens were taken from the SPS billet L-18-40 with a measured grain size of 0.42 µm. These two specimens were tested at 100 MPa and 200 MPa. These three specimens were grouped together on the same graph due to the very close similarity in grain size, and were identified by the average grain size of 0.44 µm. The strain vs. time curves for these three specimens tested in steam are shown in Figure 143.

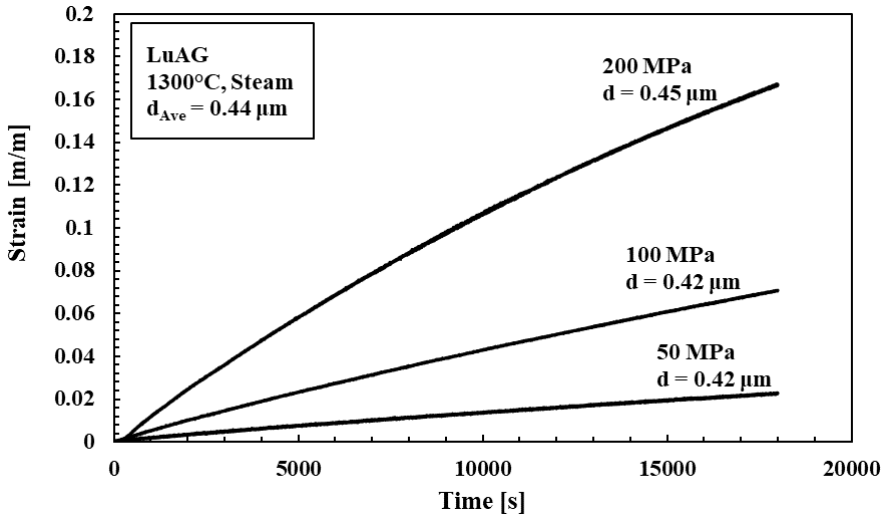

Figure 143: Creep strain vs. time curves obtained for polycrystalline LuAG specimens with an average grain size of 0.44 µm at 1300°C in steam. Specimens with grain sizes of 0.42 µm were tested at 50 MPa and 100 MPa, and a specimen with grain size of 0.45 µm was tested at 200 MPa.

Each specimen survived the entire five-hour long test without reaching failure. Each strain vs. time curve includes a slightly steeper section at the beginning of the test and then continues to level out toward the end. The steady-state creep rates were obtained by measuring the slopes of the final linear sections of the strain vs. time curves. The total accumulated strains for these specimens with an average grain size of 0.44 µm were between 2.26% at 50 MPa applied stress and 16.66% at 200 MPa applied stress. A second group of LuAG specimens was also tested in steam in order to determine the effect of grain size. The specimens within the second sample set were taken from the SPS billet L-3-40, and had a measured grain size of 4.90 µm. Due to the larger grain size, it was expected that these specimens would have a much higher resistance to creep under the same test conditions. The creep strain vs. time curves for these specimens are shown in Figure 144. The total accumulated strains for these specimens with an average grain size of 4.90 µm were between 0.35% at 50 MPa applied stress and approximately 1% at 200 MPa

applied stress, although this test did not last the entire 5 hours due to complications with the extensometer.

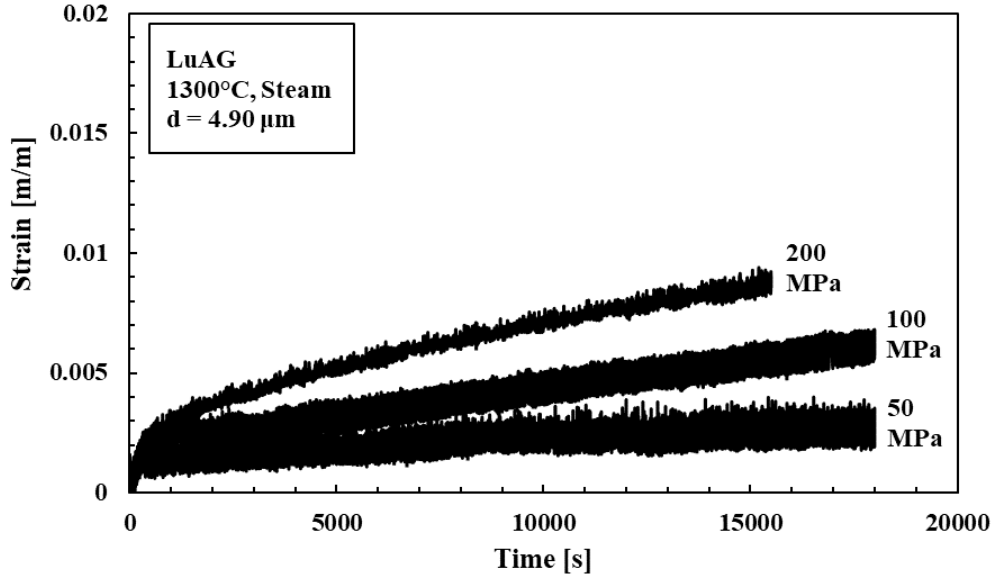

Figure 144: Creep strain vs. time curves obtained for polycrystalline LuAG specimens with grain size of 4.90 µm at 1300°C in steam.

The creep results for the two LuAG sample sets tested at 1300°C in steam are shown in Table 35. The table includes the specimen grain sizes, the total strains accumulated after five hours, and the steady-state creep strain rates.

Table 35: Summary of creep results for polycrystalline LuAG with different grain sizes at 1300°C in steam.

Specimen Name	Grain Size [µm]	Creep Stress [MPa]	Total Accumulated Strain after 5 hrs [%]	Steady-State Creep Rate [s^{-1}]
L-13-40-1	0.45	50	2.26	1.07×10^{-6}
L-18-40-2	0.42	100	7.06	3.25×10^{-6}
L-18-40-3	0.42	200	16.66	6.72×10^{-5}
L-3-40-1	4.90	50	0.35	3.34×10^{-8}
L-3-40-2	4.90	100	0.66	1.94×10^{-7}
L-3-40-5	4.90	150	Not Available*	3.50×10^{-7}

*Creep tests ended early, and strain accumulation after 5 hrs is unknown.

7.2.2. Determination of the Stress Exponent and the Grain Size Exponent for the Steady-State Creep Behavior of Lutetium Aluminum Garnet at 1300°C in steam

The stress exponent and grain size exponent, describing the steady-state creep behavior of LuAG at 1300°C in steam were determined in the same manner as they were for creep in air. As in Section 7.1.2, the stress exponent was determined from the strain rate vs. stress curves. Linear regression was used to determine the best-fit line for each set of data on a log-log scale; the associated exponent represents the stress exponent for a particular grain size. The steady-state creep strain rates for LuAG specimens with two different average grain sizes tested in steam are shown in Figure 145.

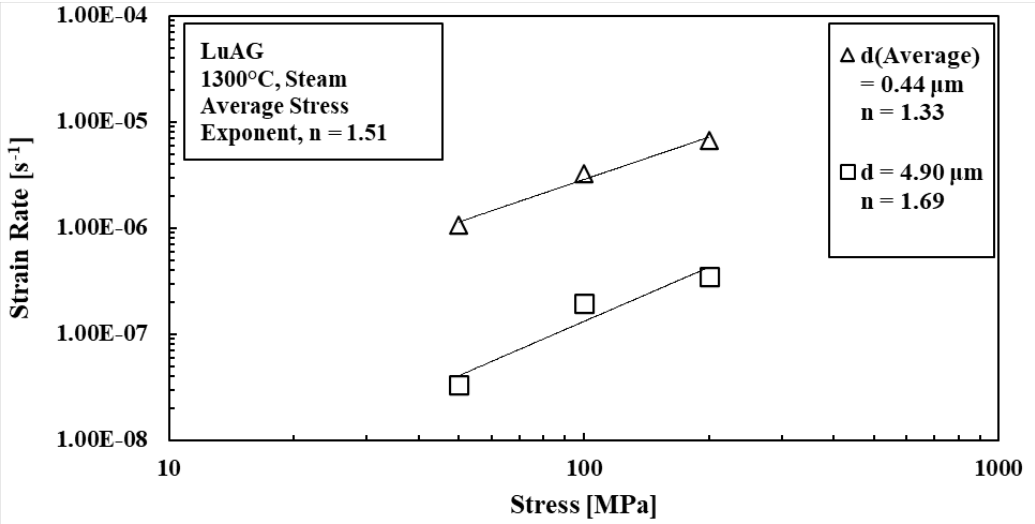

Figure 145: The steady-state creep strain rate vs. applied stress and stress exponents, *n*, of polycrystalline LuAG specimens with different grain sizes at 1300°C in steam.

A different stress exponent was calculated for each sample set with a different grain size. The stress exponents were then averaged together to determine an approximate stress exponent for the steady-state creep of LuAG at 1300°C in steam. Table 36 shows the stress exponents determined for each sample set associated with a different grain size, as well as the final averaged stress exponent.

Table 36: The stress exponent, n, for polycrystalline LuAG specimens with different grain sizes at 1300°C in steam.

Sample Set	Average Grain Size [µm]	Stress Range [MPa]	Stress Exponent, *n*	Average Stress Exponent, *n*
L-13-40 L-18-40	0.44	50 - 200	1.33	**1.51**
L-3-40	4.90	50 - 200	1.69	

The stress exponent for the steady-state creep of LuAG at 1300 in steam was determined to be 1.51. This value of *n* falls in the middle of the two stress exponents associated with the diffusional creep mechanisms discussed in this chapter: Nabarro-Herring creep with a stress exponent of 1 and interface reaction-controlled creep with a stress exponent of 2. Creep in ceramics has often been attributed to multiple mechanisms occurring simultaneously, which could account for the value of the stress exponent of 1.51.

The same process was used to determine the grain size exponent. By plotting log(strain rate) vs. log(grain size), the effect of grain size at each stress level could be determined for creep in steam. This plot is shown in Figure 146. By finding a best fit line for each set of data associated with an individual creep stress value, the grain size exponent was determined.

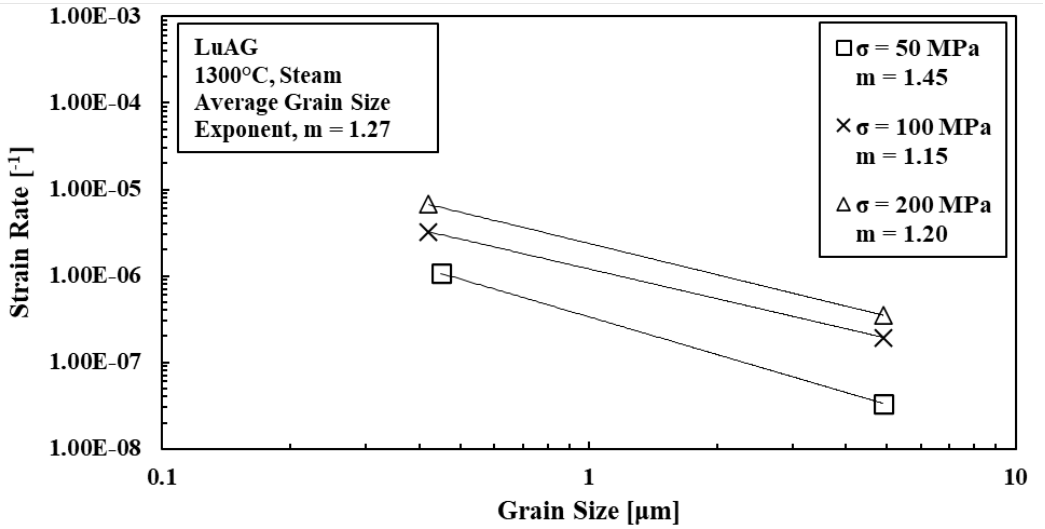

Figure 146: The steady-state creep strain rate vs. grain size and grain size exponents, *m*, of polycrystalline LuAG specimens at different creep stress levels at 1300°C in steam.

A different grain size exponent was calculated for each group of creep tests associated with each compressive stress value. The grain size exponents were then averaged together to determine the approximate grain size exponent for the steady-state creep of LuAG at 1300°C in steam. Table 37 shows the grain size exponents determined for each sample set associated with a different compressive stress value, as well as the final averaged grain size exponent.

Table 37: The grain size exponent, m, for polycrystalline LuAG specimens at different creep stress levels at 1300°C in steam.

Creep Stress [MPa]	**Grain Sizes [µm]**	**Grain Size Exponent, *n***	**Average Grain Size Exponent, *n***
50	0.45, 4.90	1.45	**1.27**
100	0.42, 4.90	1.15	
200	0.42, 4.90	1.20	

The grain size exponent for the steady-state creep of LuAG at 1300°C in steam was determined to be 1.27. Again, this indicates that interface reaction-controlled diffusional creep is likely the dominant creep mechanism for LuAG. Recall from Section 2.3.2, that this creep mechanism, which is also described earlier in this chapter, is typically identified by a grain size exponent of 1. A small difference was observed in the exponents determined for different creep stress values, which were between 1.15 and 1.45, as shown in Table 37. This indicates that the effect of grain size may be slightly greater at the lowest creep stress value of 50 MPa. However, this small difference observed in the grain size exponents may also be due to various sources of error associated with experimental results.

7.2.3. A Comparison of the Creep Behavior of LuAG at 1300°C in air and in steam

A comparison of the creep behavior of LuAG at 1300°C in air and in steam reveals very minimal, perhaps negligible, effects of steam. Figure 147 shows the creep vs. time curves of specimens with small, similar grain sizes tested in air and steam. It is apparent that there is a

consistent difference in the results in air vs. steam. In each case the specimens tested in steam creep a little more than the specimens tested in air. However, the grain sizes of specimens tested in air and those tested in steam are not identical. Each of the three specimens tested in air had a grain size of 0.54 μm, while the specimens tested in steam had grain sizes of 0.42 μm and 0.45 μm. It is possible that the small and consistent difference in total accumulated creep strain is due to the steam environment. One could conclude that the presence of steam at 1300°C causes LuAG to creep more when subjected to a compressive stress between 50 MPa and 200 MPa. However, grain size has already been shown to have a significant effect on the accumulated creep strain and the associated steady-state creep rate in LuAG in both air and steam. Therefore, it is likely that the differences observed in Figure 147 may be due to the difference in grain size of the two sample sets.

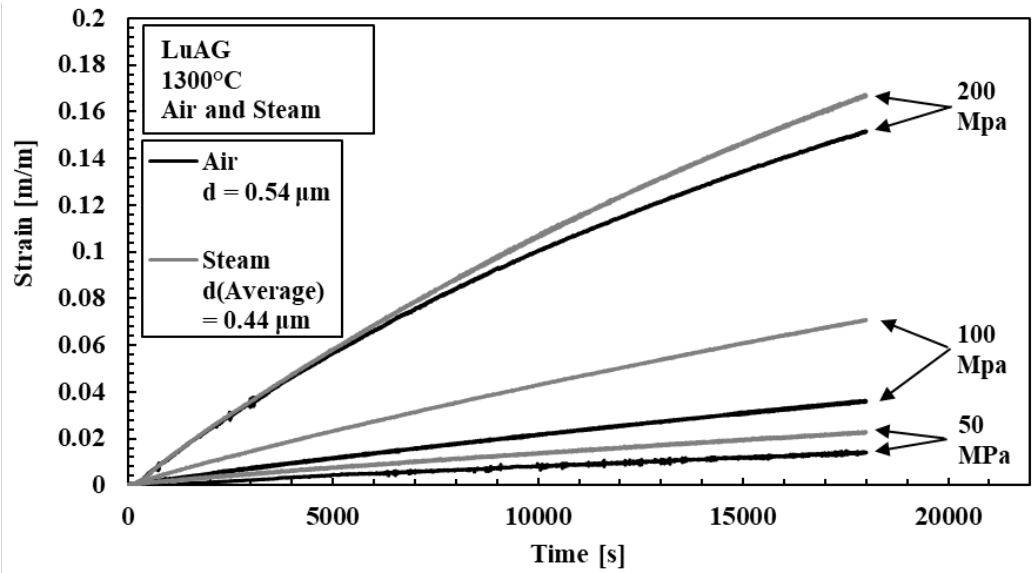

Figure 147: Creep strain vs. time curves for LuAG specimens at 1300°C in air and steam. Specimens in air have an average grain size of 0.48 μm and specimens in steam have an average grain size 0f 0.44 μm.

In order to shed more light on the true cause of the difference in accumulated strain, observed in Figure 147, a similar comparison was made between results obtained for specimens of larger grain size tested in air and steam. In this case all specimens came from the same SPS billet and should have a more consistent grain size. Figure 148 shows the creep strain vs. time curves for specimens with a grain size of 4.90 μm tested in air and in steam. This comparison reveals a much more negligible difference in the creep strain due to steam. Specimens subjected to 100 MPa and 200 MPa show essentially no difference in creep strain due to the environment, while specimens tested at 50 MPa show a very small difference. Figure 148 indicates that creep response of specimens with identical grain size is not significantly affected by the presence of steam, creep behaviors in both environments are nearly identical.

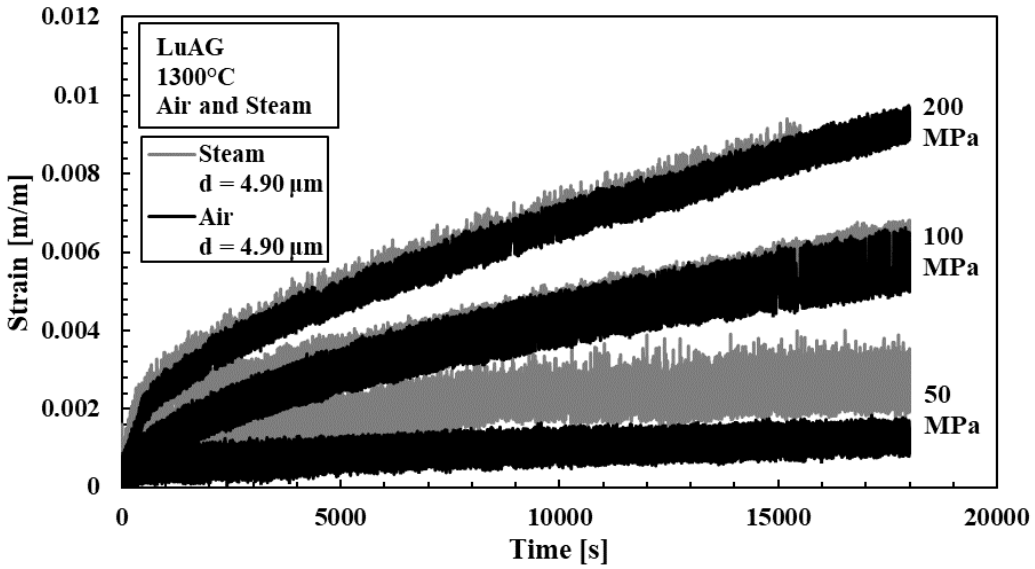

Figure 148: Creep strain vs. time curves for LuAG specimens at 1300°C in air and steam. Specimens in air and in steam have a grain size of 4.90 μm from the same sample set.

In order to further assess any potential effects of steam on the creep behavior of LuAG, and to determine if steam has a different effect on specimens with small grain size vs. large grain size, the steady-state creep rates were compared. The creep rates associated with each sample set,

tested in air and in steam with comparable grain sizes, are shown in Figure 149. Just as the creep strain vs. time graph above from Figure 147 suggests, there is a small apparent difference in the steady-state creep strain rates for smaller-grained sample sets. However, for specimens with larger grain sizes, the steady-state creep strain rates obtained in air and in steam fall directly on top of one another with no apparent difference.

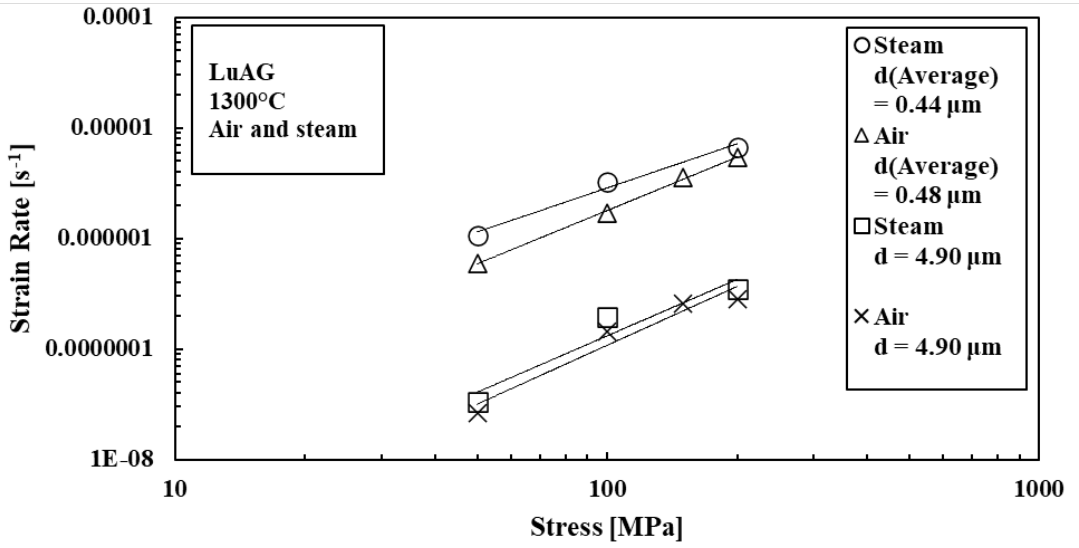

Figure 149: A comparison of the steady-state creep strain rates of LuAG specimens at 1300°C in air and in steam. Specimens are compared at two different grain sizes. Small average grain sizes of 0.48 µm and 0.44 µm are compared in air and steam, respectively. Large grain sizes of 4.90 µm are compared in air and in steam.

Recall that the smaller-grained specimens, compared in Figure 147, came from multiple sample sets with similar, but not identical grain sizes, and it has been shown that grain size has a significant effect on creep rate. Therefore, in order to fully assess the effect of environment, any potential effect of grain size must be removed from this comparison. As was described earlier in this section, small-grained specimens, tested in air were found to have grain sizes of 0.42 µm and 0.54 µm, and small-grained specimens, tested in steam were found to have grain sizes of 0.42 µm and 0.54 µm. In order to remove any potential effect of grain size on the resulting creep rates

observed in Figure 149, the steady-state creep strain rates were all normalized to a grain size of d = 1 μm. The strain rate normalization process described in the previous chapter was used in this case as well.

The strain rates were normalized by using the average measured grain size exponent determined for LuAG, which was m = 1.25. This grain size exponent was input into Equation 33, described in the previous section. Figure 150 shows the steady-state creep strain rates for specimens tested in air and steam; however, in this case, results for specimens with smaller grains have been normalized to d = 1 μm. Results for specimens with larger grain sizes were not normalized because all specimens tested in air and in steam were taken from the same SPS billet and had the same grain size of 4.90 μm.

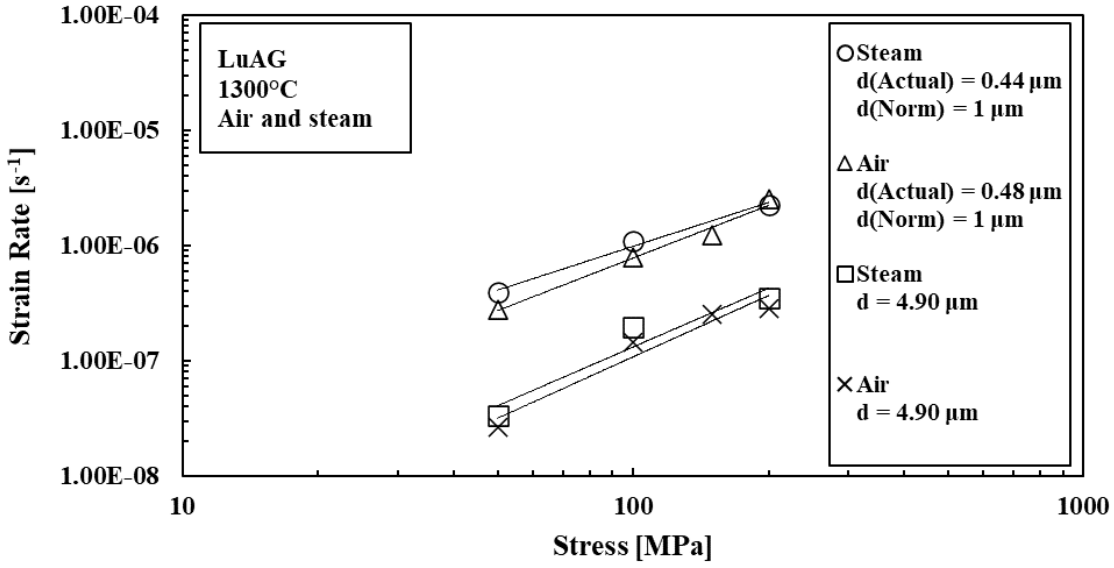

Figure 150: A comparison of the steady-state creep strain rates of LuAG specimens at 1300°C in air and in steam. Specimens are compared at two different grain sizes. Strain rates of small-grained specimens have been normalized to d = 1 μm. Specimens with large grain sizes are from the same sample set and the results were not normalized.

There are two observed differences between Figure 149 and Figure 150 due to the normalization process. First, the difference in strain rates associated with the sample sets with smaller grain sizes and the sample sets with larger grain sizes is much smaller. Due to normalizing the strain rates, the apparent difference in grain size between sample sets is smaller. This is expected, as it has been clearly demonstrated that specimens with larger grain sizes creep less under the same test conditions. Therefore, after normalizing strain rates from grain sizes of 0.44 μm and 0.48 μm to d = 1 μm, the associated strain rates will be lowered significantly after applying Equation 33.

The second difference seen in Figure 150 after removing the effect of grain size is the small difference in strain rate between the small-grained sample set tested in air and the small-grained sample set tested in steam had been reduced. It appears that any potential effect of steam on the strain rates of LuAG at 1300°C for any grain size may be negligible. It is likely that the previously observed differences in Figure 149 between the creep of LuAG specimens tested in air and those tested in steam, incorporated grain size effects as well as effect of environment. These results indicate that LuAG is just as resilient as YAG against any possible environmental degradation due to the presence of steam during creep at 1300°C.

7.3. Comparison of the Creep Behavior of Undoped YAG and LuAG at 1300°C in air

Now that the creep behaviors of YAG and LuAG have been observed and analyzed, they can now be directly compared. The following figures demonstrate the differences in the creep behavior of YAG and LuAG at 1300°C in air. Since the effects of steam were observed to be

negligible on the creep behavior of both YAG and LuAG, this section focuses on YAG and LuAG in air, and a comparison of creep in steam is not discussed.

In order to effectively compare the creep behavior of YAG and LuAG, all other possible factors that could influence the material performance must be held constant for the two different materials. Therefore, all test conditions are identical for all specimens selected for comparison. Additionally, the steady-state creep rates have all been normalized to a common grain size of d = 1 µm, using the grain size exponents obtained in the previous sections. Figure 151 shows the steady-state creep strain rates of YAG and LuAG specimens, normalized to a common grain size. The specimens selected for comparison in Figure 151 include smaller-grained sample sets for both YAG and LuAG.

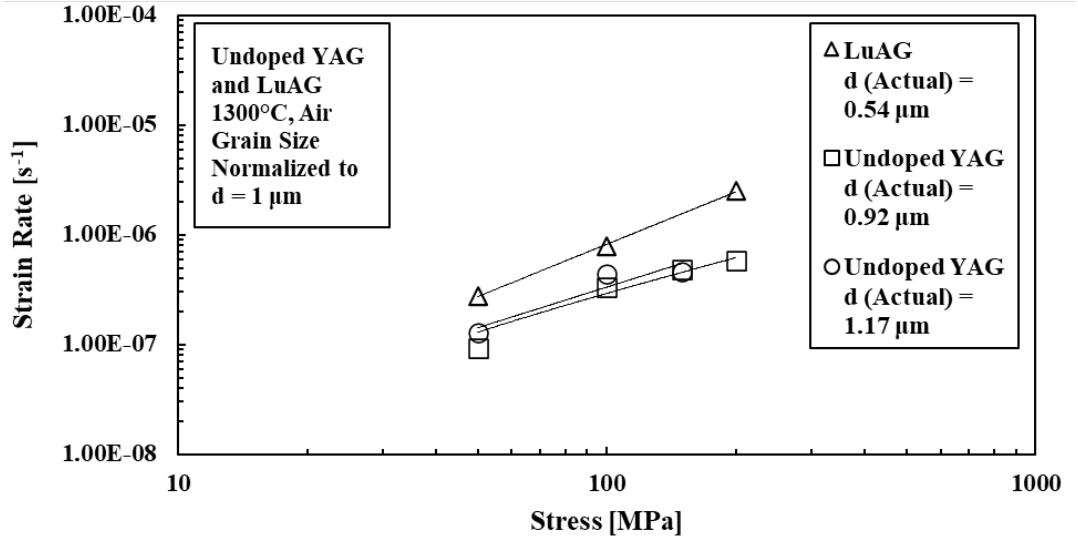

Figure 151: A comparison of the steady-state creep strain rates of YAG and LuAG specimens at 1300°C in air. All strain rates have been normalized to a common grain size of d = 1 µm. Results for YAG specimens with grain size of 0.92 µm from Armani et al. (2011) are included for comparison [28], [29].

Even after accounting for grain size, a significant difference in the steady-state creep rates is observed. At each stress level LuAG specimens creep significantly more. At low stress of 50

MPa, a difference of approximately half an order of magnitude is observed, and at high stress of 200 MPa, a difference of almost one order of magnitude is observed. In addition to the difference in creep rate, there is also a difference in the creep rate vs. stress trends of YAG and LuAG. The LuAG specimens appear to be more sensitive to the compressive applied stress as evidenced by the steeper trend associated with LuAG specimens. Recall that the average stress exponent for LuAG at 1300°C in air was found to be 1.91 for LuAG, which is much larger than the corresponding stress exponent of 1.30 determined for YAG.

A similar comparison between YAG and LuAG is shown in Figure 152 for specimens with larger grain size. It is beneficial to know if the relative behavior of YAG and LuAG depends on the grain size of each material. Figure 152 shows the steady-state creep strain rates for YAG and LuAG at 1300°C, all normalized to a common grain size. These sample sets include YAG specimens with an original measured grain size of 7.99 μm and LuAG specimens with an original measured grain size of 4.90 μm. These are the largest grain sizes of undoped YAG and LuAG in this study.

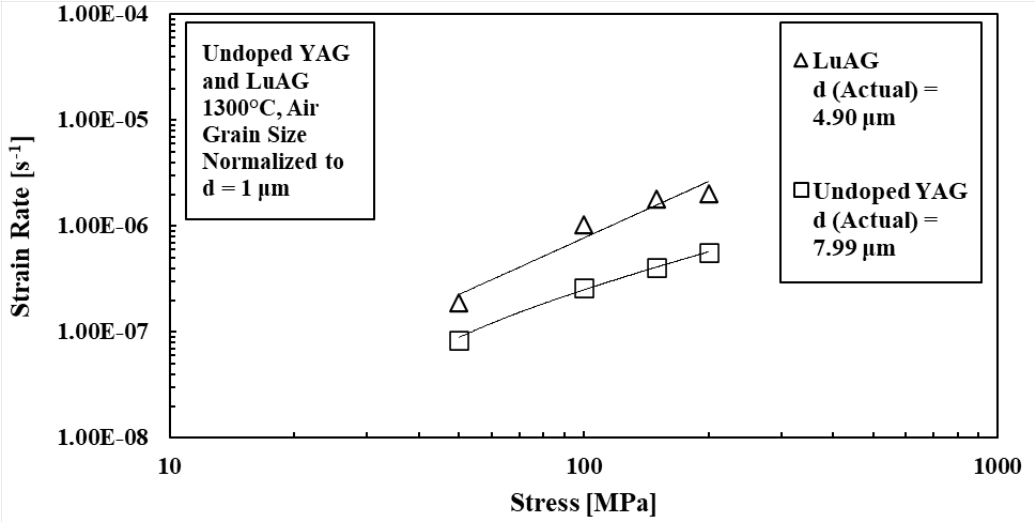

Figure 152: A comparison of the steady-state creep strain rates of YAG and LuAG specimens at 1300°C in air, normalized to a grain size of d = 1 μm.

It appears that grain size does not significantly affect the difference in creep behavior between undoped YAG and LuAG, as the observed differences in the steady-state creep rates in Figure 152 are nearly identical to those seen in Figure 151 for smaller-grained specimens. Once again there is a significant difference in creep rates for YAG and LuAG specimens tested under the same conditions; LuAG creeps significantly more than YAG. Also, as with smaller-grained specimens, the creep of LuAG is more affected by the applied creep stress. This is once again evidenced by the steeper trend associated with the LuAG specimens.

Simply comparing the steady-state creep rates is not enough to understand the difference in creep behaviors of YAG and LuAG. The total accumulated strains obtained for specimens with similar grain size are critical when comparing the two materials and understanding the performance associated with each. Therefore, Figure 153 was created to demonstrate the difference in accumulated creep strain after five hours of compressive creep for YAG and LuAG. Specimens with similar grain size were selected to isolate the impact of material only.

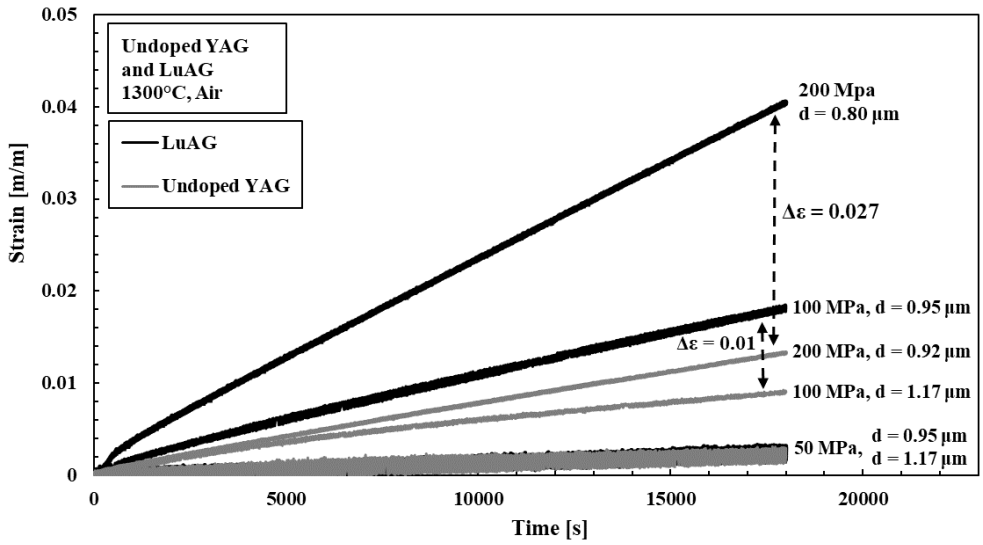

Figure 153: Comparison of the strain vs. time curves for YAG and LuAG specimens with comparable grain sizes at 1300°C in air. Results for YAG specimens with grain size of 0.92 µm from Armani et al. (2011) are included for comparison [28], [29].

In Figure 153 YAG specimens have grain sizes of 0.92 μm and 1.17 μm, and LuAG specimens have a grain size of 0.80 μm and 0.95 μm. These are not identical grain sizes; however, they are close enough to illustrate the difference in accumulated strains for each material during similar creep tests while minimizing any effect of grain size. Specimens tested with a small applied creep stress of 50 MPa do not show any difference in accumulated strain. However, at 100 MPa a 1% difference in creep strain is observed, and then at 200 MPa a 2.7% difference in accumulated creep strain is observed.

Based on the results displayed in Figure 151-Figure 153, it is clear that there is a significant difference in the creep behavior of undoped YAG and LuAG. YAG appears to be much more creep resistant for all grain sizes than LuAG. Additionally, the effects of applied stress and grain size appear to be different for the two materials as well. This phenomenon and the associated conclusions about creep mechanisms is discussed further and in more detail in the following section concerning the creep mechanisms for LuAG.

7.4. Determination of the Dominant Creep Mechanisms for Lutetium Aluminum Garnet at 1300°C in Air and in Steam

Undoped, Polycrystalline LuAG at 1300°

Similar to the discussion in Section 2.3.2 concerning the creep mechanisms of YAG, the determination of the dominant creep mechanisms in LuAG begins by reviewing the stress exponents and grain size exponents that were obtained from the creep results in this chapter. These exponents are critical inputs to Equation 4, describing the steady-state creep strain rate of ceramics. The average stress exponent for LuAG at 1300°C in air was determined to be 1.91, and

the average stress exponent for LuAG at 1300°C in steam was determined to be 1.51. The average grain size exponent for LuAG at 1300°C in air was determined to be 1.24 and the average grain size exponent for LuAG at 1300°C in steam was determined to be 1.27. Based on these exponents, the most likely creep mechanisms controlling the steady-state creep of LuAG are grain boundary sliding, accommodated by diffusion, similar to YAG. However, the differences in both the stress exponent and the grain size exponent indicate that grain boundary sliding controlling the creep of LuAG is partially or entirely accommodated by interface reaction-controlled diffusion. Recall from Section 2.3.2 that this type of diffusion can be identified by a stress exponent of 2 and a grain size exponent of 1. This result is in contrast to what was observed for YAG, which indicated that diffusion occurred according to the Nabarro-Herring creep mechanism, based on observing a stress exponent close to 1 and a grain size exponent close to 2.

Interface reaction-controlled creep was observed only in YAG specimens with the smallest grain size. It was suggested that this mechanism may also occur at the lowest creep stress in YAG. Interface reaction-controlled creep has also been observed in bulk alumina and alumina fiber materials, typically with very fine grain sizes [29]. These similar trends have been observed in essentially all the creep behavior of LuAG for all grain sizes, indicating that grain boundary sliding, accommodated by interface reaction-controlled diffusion. Typically, in ceramics, bulk diffusion occurs much slower than diffusion at the grain boundaries. It has been reported that the bulk diffusion coefficients can be as much as five orders of magnitude lower than the diffusion coefficients at the grain boundaries [294]–[296]. During interface reaction-controlled creep, the rate of bulk diffusion increases, which causes the creation and annihilation of vacancies and defects at the grain boundaries to become the rate-controlling mechanism of diffusion.

Creep Rates of LuAG vs. YAG

In addition to the different effects of stress and grain size on the steady-state creep rates observed in YAG and LuAG, which were identified by the stress exponents and grain size exponents, the overall creep strains in LuAG were much higher than in YAG. In other words, YAG appears to be more creep resistant than LuAG. This could be due to various phenomena. First, the occurrence of interface reaction-controlled creep, indicates that the rate of bulk diffusion has increased and the rate of diffusion along the grain boundaries has decreased. During interface reaction-controlled creep, the grain boundaries are no longer considered perfect sources and sinks for vacancies during diffusion. This process could lead to the overall increase in steady-state creep rate, and this conclusion supports the difference in stress exponent and grain size exponent obtained for LuAG.

The increased creep rates observed in LuAG could also be attributed to various other phenomena. Multiple creep mechanisms could be occurring simultaneously, which could have an additive effect on the overall creep rate. The simultaneous occurrence of basal slip, dislocation motion, grain boundary sliding, and cavity formation, specifically for fine-grained ceramics has been observed. However, this is only speculation at this point, and further research is required to validate this potential cause of increased strain rates. An additional possible cause of apparent increased strain rates in LuAG when compared to YAG is a difference in material quality and purity.

The analysis of each material in this study, specifically the determination of grain size and density, as well as porosity observations, did not indicate any significant difference in the microstructures of YAG and LuAG specimens. However, a determination of any potential impurities by chemical analysis would be beneficial in the comparison of the two materials.

Furthermore, analysis of each material using a transmission electron microscope (TEM), would be able to identify any potential impurities that may be segregating to the grain boundaries, impacting diffusion.

Creep Mechanisms at Low Creep Stress

The strain rate vs. stress curves for LuAG at 1300°C in air, which were plotted in Figure 140, were separated into the lower and higher stress regimes. Figure 154 shows the strain rate data for LuAG specimens, where the trends are analyzed separately for creep stresses below and above 100 MPa.

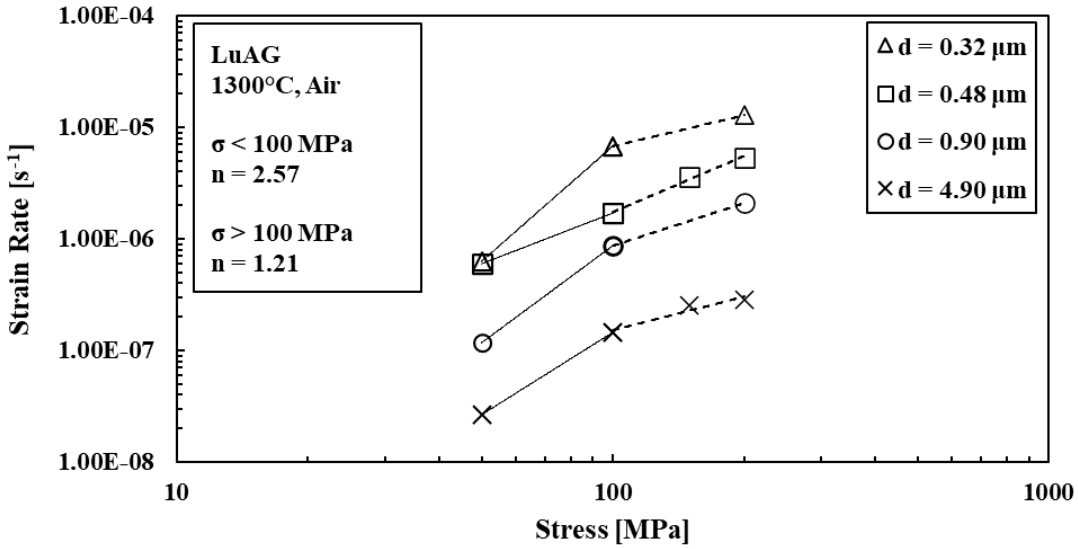

Figure 154: The stress exponents of undoped YAG at 1300°C in air. Each set of strain rates obtained for specimens of a particular grain size has been divided into low stress and high stress regions, demonstrating the consistent change in slope of each line.

Once the stress exponents from the lower stress regime (below 100 MPa) were averaged together, the approximate stress exponent was determined to be 2.57. Similarly, once the stress exponents from the higher stress regime were averaged together, the approximate stress exponent was determined to be 1.21. This observation is similar to what was determined for YAG in the

previous chapter, and it calls into question the likely creep mechanisms occurring during creep of LuAG. It is possible that interface reaction-controlled creep, which is assumed to be the rate-controlling mechanism of the creep in LuAG, is only occurring at low stresses. As is seen in Figure 154, the stress exponent for creep of LuAG in the low stress regime (below 100 MPa) was determined to be 2.57, which is consistent with interface reaction-controlled creep. If two different creep mechanisms were controlling the creep rates of LuAG in different stress regimes, then this would indicate that Nabarro-Herring creep may be the dominant creep mechanism at higher stresses. This same observation was made for Nextel 720 fibers by Armani et al. [23]. It was concluded that a significantly different stress exponent was observed at lower stresses, and, therefore, interface reaction-controlled creep must be rate-limiting.

Recall that a similar observation was made regarding the grain size exponent in undoped YAG, described in Section 6.5. The creep rate vs grain size plot, which was used to obtain the grain size exponent was separated into lower and higher grain size regimes. A similar conclusion was made that creep of YAG specimens with lower grain sizes may be partially interface reaction-controlled, and creep of YAG specimens with larger grain sizes is likely still controlled by Nabarro-Herring diffusion. However, it was determined that a similar conclusion could not be made for the creep of LuAG. The effects of grain size on the strain rates of LuAG are much more consistent than they were with YAG, and a different creep mechanism was not observed for LuAG specimens with smaller grains.

8. Post-Creep Microstructural Analysis

8.1. Motivation and Analysis Methods

The purpose of this chapter is to determine and report any potential changes in the microstructural characteristics of YAG and LuAG brought on by creep experiments at 1300°C and 1400°C. The primary method of characterizing any variations to the microstructure of each material was investigation in the SEM with emphasis on grain size and shape. It is well known that exposure to high temperatures above a certain threshold can lead to grain growth. This phenomenon has been observed through the effects of sintering parameters, which were documented in this study as well as others [240], [242], [261], [262]. This phenomenon has also been reported in the context of heat treatment after sintering for the specific purpose of grain growth [297]–[299]. For high density, oxide ceramics, heat treatments for the purposes of grain growth are typically performed at temperatures above the sintering temperature. As is seen during the processing of YAG and LuAG, heat treatment at 1500°C does not significantly increase grain size. This is evidenced by the many material billets with submicron grain size following heat treatment in air at 1500°C for 10 hours.

Effects of high temperature on the microstructure of ceramics, specifically the grain structure, also include grain boundary migration brought on by diffusion [300], and by mass redistribution and possible phase evaporation at the grain boundaries, as seen in thermal etching [250]. Typically, thermal etching involves exposure to temperatures that are 100°C – 200°C below the sintering temperature for short durations (approximately 15 min) in order to prevent unwanted grain growth. Because grain growth is known to occur at high temperatures, it is necessary to assess the grain growth during high-temperature creep. Based on temperature alone, prolonged exposure at 1300°C would not be expected to influence grain size. However, the

application of compressive stress and forced atomic diffusion curing creep may create an environment which accommodates grain growth.

Furthermore, the resulting shape of the grains in each material following creep is an important attribute of each material, as it contributes to evidence of various creep mechanisms at work. Grain boundary sliding, is a large part of the established creep mechanisms for YAG and LuAG, as discussed in Sections 6 and 7. Significant discussion surrounded the type and location of atomic diffusion as well as the associated rates, but this phenomenon does not occur alone, and is not solely responsible for creep deformation. Recall that diffusion is simply the accommodating mechanism for grain boundary sliding, where grains shift and move past one-another due to the combination of temperature and pressure during creep. In Nabarro-Herring diffusion creep, grain boundary sliding contributes to at least 50%-60% of deformation and is the primary cause of material failure. In the case of compression creep, grains will begin to compress due to the applied stress, and as grain shape is altered, cavities can form along the moving grain boundaries. However, some materials resist cavity formation by movement of the grains, which can slide around each other, largely maintaining their shape, and filling the voids formed at the grain boundaries.

Recall from Section 2, the two primary methods of grain boundary sliding: Rachinger sliding and Lifshitz sliding. In Rachinger sliding the grains retain most of their original shape, and the internal stress is balanced out by grain movement. Lifshitz sliding, which occurs during Nabarro-Herring and Coble creep, involves the diffusion of vacancies brought on by the applied stress, and leads to changes in grain shape during grain boundary sliding. Diffusion within the crystal lattice of the grains allows for grain elongation in the direction of the applied stress [301].

Therefore, the average grain shape before and after creep is analyzed for both YAG and LuAG in this chapter. The average grain shape is determined by digital image analysis of the grains visible in SEM micrographs of the surfaces of various specimens. The overall grain shape is quantified by determining the average aspect ratio, and this attribute as well as the average grain size are compared for pre-test and post-test micrographs of specimens from the same billets.

Multiple specimens from individual billets were chosen for analysis in the SEM in order to compare the microstructures of similar specimens of undoped YAG and LuAG before and after creep experiments at 1300°C and 1400°C in air. The original microstructural analysis specimens, which were cut from each billet, but were not part of the fabricated creep test specimens, were used in this section in order to determine the baseline characteristics of each billet prior to creep testing. Although there is likely some amount of variation in grain size and structure throughout a 40 mm diameter billet processed via SPS, the assumption was made at various times throughout this study that the grain characteristics across each billet are similar, and different specimens from the same billet can be used for comparison.

The first specimen used to elucidate the effects of creep on microstructure represented the baseline properties of that billet and was not subject to creep testing. The surface analyzed in the SEM was the rectangular surface adjacent to one of the creep test specimens. This selection was necessary so that the orientation of each SEM image was identical and the average grain shape could be directly compared for pre- and post-creep specimens. A diagram of the location of the polished surface of each specimen, which was not subject to creep testing, is shown in Figure 155.

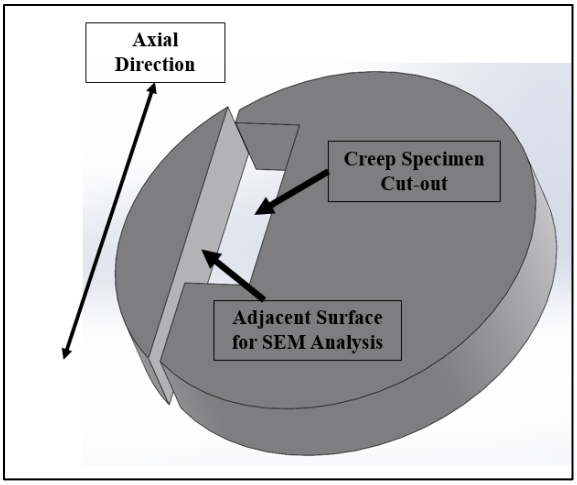

Figure 155: Diagram of a location of a pre-test microstructural analysis specimen, cut adjacent to a creep specimen.

During SEM imaging, the surface was always oriented in axial direction prior to capturing images. This was the case for all SEM analysis on this study. Therefore, the average aspect ratio of the grains, which are determined from various SEM images are consistent. The grain aspect ratio discussed in this section is defined as follows:

$$AR_{Grain} = w/h \qquad \text{(Equ. 34)}$$

where w is the width of the grain, and h is the height of the grain. In each case the measured height is the length of the grain in the axial direction, or the direction of the applied load during creep. The width of each grain is the perpendicular length on the 2-dimensional surface.

Each micrograph was analyzed using the digital image analysis software within Adobe Photoshop, as described in Section 4.3.2. This software is capable of determining the average grain size. Additionally, this software displays the precise height and width of each grain that is selected to be analyzed. Therefore, the aspect ratio of each grain can be determined. Once hundreds of grain aspect ratios are determined from analysis of the SEM micrographs, they are averaged together, revealing one average grain aspect ratio for the specimen. In most cases

between 100 and 200 grains were analyzed for each specimen in this section. In addition to the baseline microstructure obtained from specimens that were not subject to creep testing, the average aspect ratio and average grain size were also determined for several specimens following creep testing in order to observe any potential changes.

In order to determine the characteristics of the post-creep microstructure, the internal surface of each specimen with the same axial orientation must be selected for analysis in the SEM. Once a specimen was selected for post-creep microstructural analysis, it was cut in half in the axial direction by means of water-cooled, diamond blade, wheel saw. A diagram of the cutting plane and exposed surface is shown in Figure 156.

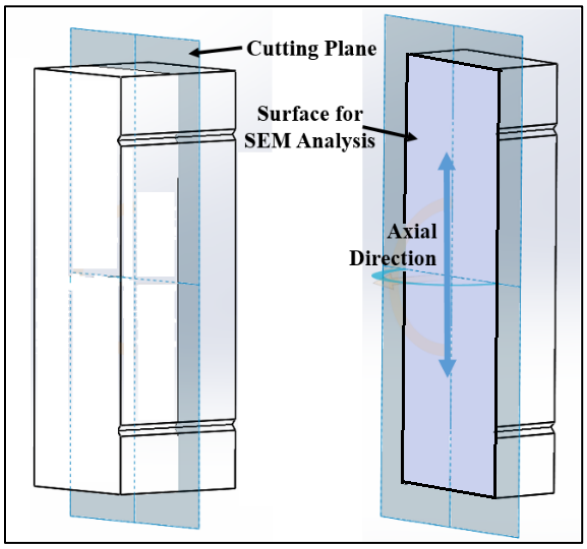

Figure 156: The cutting plane and internal surface used for SEM analysis in the axial direction for each creep test specimen.

The cut surface was perpendicular to the specimen cross-section. Each half of the specimens were oriented parallel with the cut surfaces facing out. They were then mounted in epoxy and polished for analysis in the SEM. In each case the specimens selected for post-creep microstructural analysis were those with the highest observed creep strains, which means they were the specimens that saw 200 MPa compressive creep stress. Changes in the microstructure,

specifically grain size and shape, can only be determined if the creep strains are high enough to allow detection by analysis of a limited number of grains. Creep strains of less than approximately 10% may not be detectable by this type of measurement method. And, if very small changes in grain size or aspect ratio are observed, they may not be considered conclusive due to the potential error associated with these measurement techniques.

8.2. Analysis of Yttrium Aluminum Garnet

Two creep specimens from billet Y-7-40 were selected for SEM analysis. Specimen Y-7-40-5 was tested at 1400°C and 100 MPa and saw the highest strain of 4.54%. Therefore, any microstructural effects of creep will be most apparent in this specimen. Specimen Y-7-40-3, tested at 1300°C and 200 MPa, saw only 1% strain, but analysis of this specimen will still enable a comparison of microstructural changes due to creep at both temperatures. Prior to analyzing these post-creep specimens, a baseline untested microstructure was established. The SEM micrographs of a specimen from billet Y-7-40, which was not subject to creep testing, are shown in Figure 157.

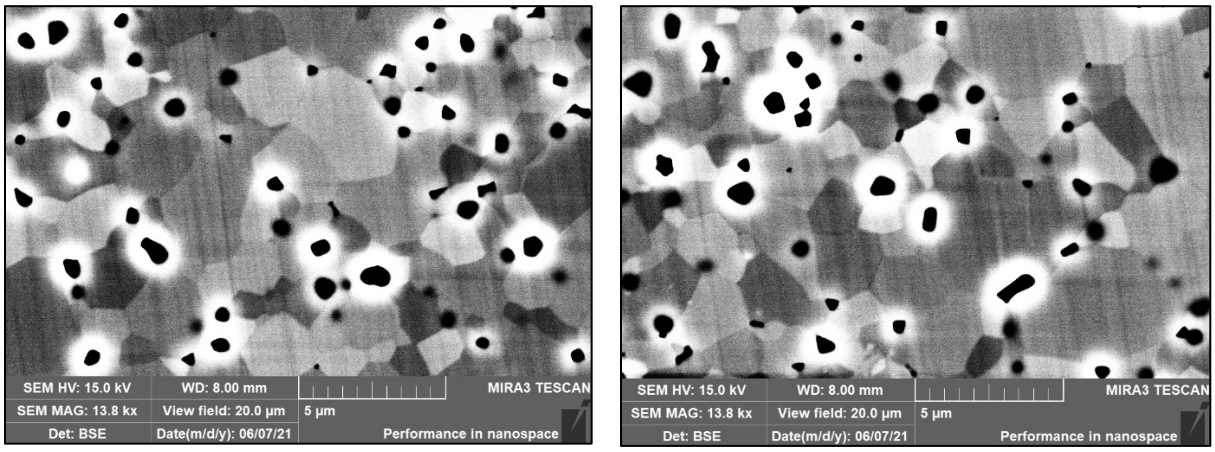

Figure 157: SEM micrographs of specimen from billet Y-7-40 prior to creep testing with an average grain size of 1.17 µm.

The microstructural characteristics of a specimen from billet Y-7-40 were briefly discussed in Section 6.1. The SEM images reveal attributes similar to those seen in other YAG specimens presented in this study, including grain size and shape, and presence of porosity. The grain size for this billet immediately after processing was determined to be 1.17 μm. Two SEM micrographs of specimen Y-7-40-3 following creep testing at 1300°C are shown in Figure 158. These images came from the internal surface after sectioning the specimen, as described in Figure 156, and are oriented in the axial direction.

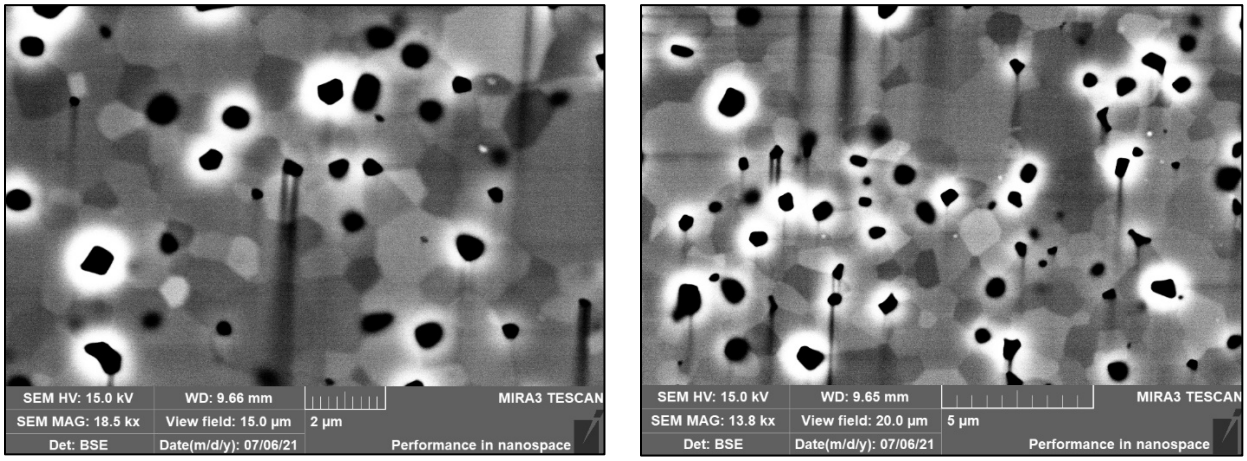

Figure 158: SEM micrographs of specimen Y-7-40-3 after creep at 1300°C in air. Average measured grain size is 1.21 μm.

The average grain size of specimen Y-7-40-3 following creep at 1300°C was determined to be 1.21 μm. Armani et al. had previously reported that similar creep testing at 1300°C did not lead to any apparent grain growth in YAG [29]. This conclusion is also validated here as the grain sizes of specimens from billet Y-7-40 prior to creep and after creep at 1300°C are essentially identical. The average grain aspect ratio determined for specimen Y-7-40-3 was 1.04. This is identical to the measured aspect ratio for the specimen, which was not subject to creep. This observation suggests that the small amount of accumulated creep strain of approximately 1% at 1300°C in air with an applied compressive stress of 200 MPa does not significantly alter

the shape of the grains. Furthermore, if changes in grain shape are occurring during creep of YAG at 1300°C, it is likely that these changes would not be detectable due to the small amount of strain.

Two SEM micrographs of specimen Y-7-40-5 following creep testing at 1400°C are shown in Figure 159.

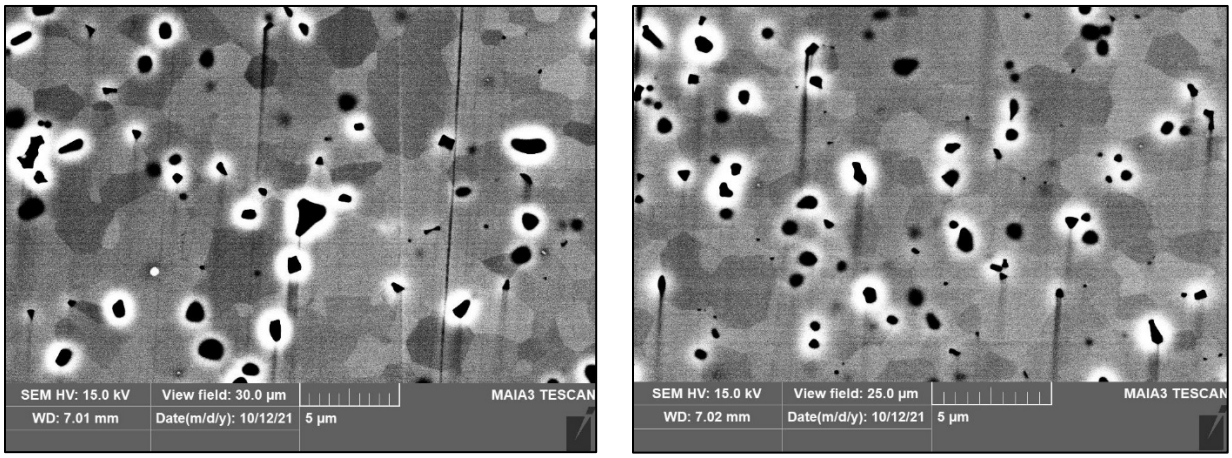

Figure 159: SEM micrographs of specimen Y-7-40-5 after creep at 1400°C in air. Average measured grain size is 2.16 µm.

The measured average grain size for Y-7-40-5 after creep at 1400°C was determined to be 2.16 µm. This is significantly larger than the grain size measured after creep at 1300°C. While a certain amount of grain size fluctuation is expected throughout a 40 mm diameter SPS billet, the SEM images appear consistent. Hence it is likely that creep at 1400°C in air may have induced grain growth in this YAG specimen.

The average grain aspect ratio was determined to be 1.14, which is approximately 10% greater than that determined for the specimen not subjected to creep. This result may indicate that there was a small increase in the relative width of the grains during creep, which is consistent with compression. Additionally, this small increase in aspect ratio is also consistent with the total amount of accumulated creep strain, which was approximately 4.5%. This result

indicates that the shape of the grain may be affected by compression during creep, which is consistent with Lifshitz grain boundary sliding, and Nabarro-Herring creep. However, this small change in aspect ratio also falls within the possible amount of error associated with these measurement techniques and is not fully conclusive. Significantly higher strains were observed in LuAG specimens; therefore, the same analysis is conducted for LuAG in the following section in order to determine if similar observations can be made.

The average grain size and average grain aspect ratio for all specimens from billet Y-7-40, which were analyzed in the SEM are summarized in Table 38.

Table 38: Summary of grain size and aspect ratio for specimens from billet Y-7-40.

Specimen	Creep Temperature [°C]	Average Grain Size [µm]	Average Grain Aspect Ratio	Accumulated Creep Strain [%]	Amount of Grain Growth [%]	Amount of Grain Elongation [%]
Post-SPS Y-7-40	N/A	1.17	1.04	N/A	N/A	N/A
Post-Creep Y-7-40-3	1300	1.21	1.04	0.95	3.42	0
Post-Creep Y-7-40-5	1400	2.16	1.14	4.54	84.62	9.62

8.3. Analysis of Lutetium Aluminum Garnet

The same process and analysis methods were used to determine the effects of creep on the microstructure of LuAG specimens. However, LuAG specimens were only tested in creep at 1300°C; therefore, any effects of exposure to 1400°C during creep are not presented in this study. Recall that significantly more creep strain was observed in LuAG specimens, specifically the smaller-grained specimens. Larger accumulated strains are advantageous when comparing the average shape of grains before and after creep, because the greater the observed difference in aspect ratio, the more likely that difference is due to the effects of creep and not due to small measurement errors. Three different LuAG billets were examined prior to creep and after creep

at 1300°C in air. Each billet has a different original grain size; therefore, any potential effects of grain size on grain growth and change in grain shape can be observed.

The three LuAG billets, which were analyzed in the SEM were L-12-40 with an average grain size of 0.32 μm, L-10-40 with an average grain size of 0.54 μm, and L-19-40 with an average grain size of 0.84 μm. Again, a baseline untested microstructure was established by first analyzing untested specimens. Two SEM micrographs taken from a specimen from billet L-12-40, which was not subject to creep testing, are shown in Figure 160.

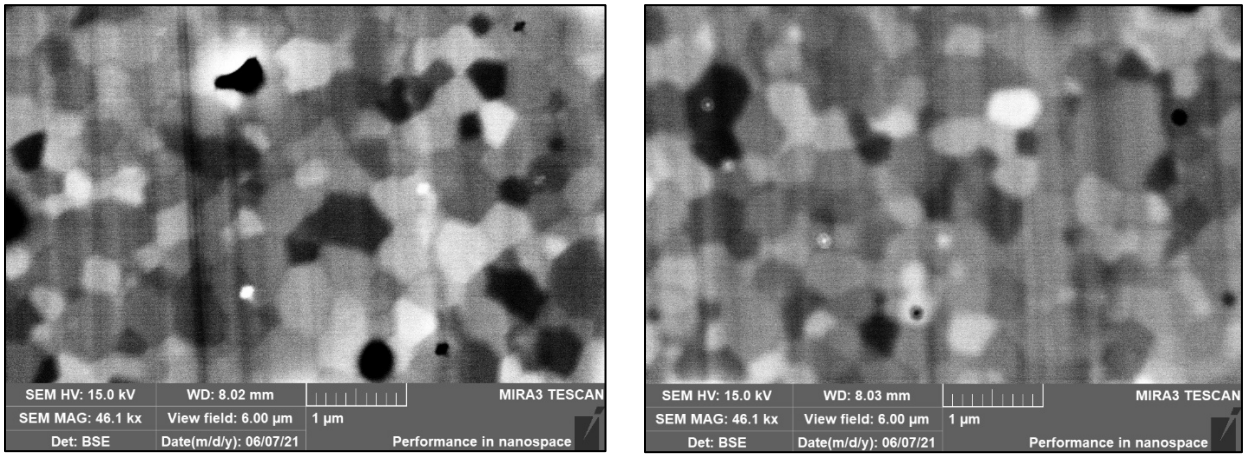

Figure 160: SEM micrographs of billet L-12-40 prior to creep testing with an average grain size of 0.32 μm.

From analysis of these micrographs, the average grain size was determined to be 0.32 μm and the average grain aspect ratio was determined to be 0.96. This aspect ratio of approximately 1 is very similar to that determined for YAG. This result is also consistent with the visual appearance of the nearly-circular grains observed in Figure 160. These micrographs were compared to micrographs of specimen L-12-40-5 following creep at 1300°C in air, which are shown in Figure 161. Just as with the post-creep YAG specimens, these micrographs were taken from the internal specimen surface after sectioning, with the axial direction oriented vertically.

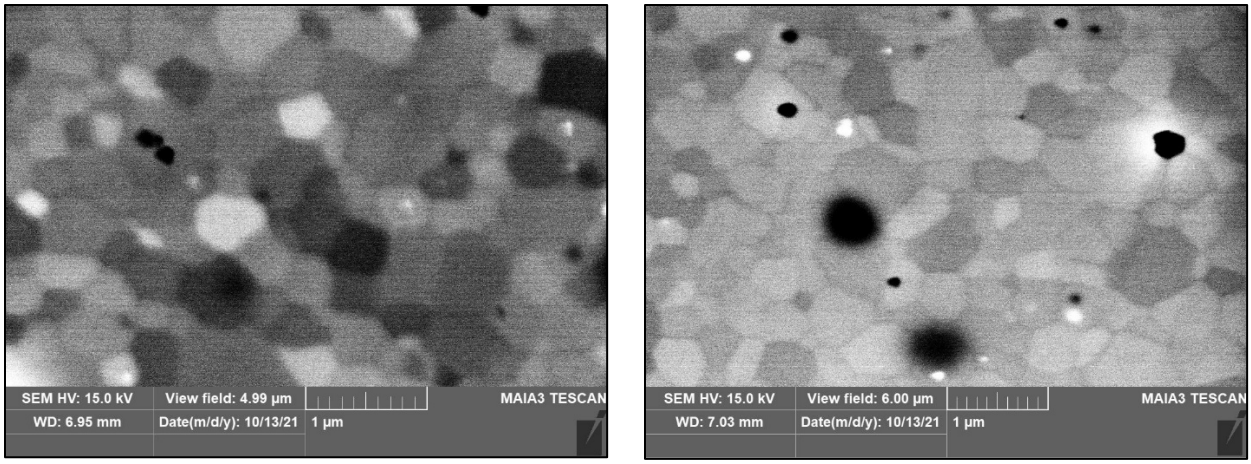

Figure 161: SEM micrographs from specimen L-12-40-5 after creep at 1300°C in air. Average measured grain size is 0.37 µm.

The average grain size for specimen L-12-40-5 following creep at 1300°C was determined to be 0.37 µm, indicating that there was essentially no grain growth during creep at 1300°C. This observation is consistent with what was observed for YAG. Specimen L-12-40-5, which was subject to a compressive creep stress of 200 MPa, saw a total accumulated creep strain of 14%, as noted in Section 7.1.1. The average grain aspect ratio for this specimen following creep was determined to be 1.12. Again, an increase in aspect ratio indicates a relative increase in width and a decrease in height of the grains, which is consistent with compression. This difference in aspect ratio represents an increase of almost 17%, which is consistent with the amount of creep strain observed. These results, as well as the results from analysis of the other LuAG billets in this section are presented in Table 39.

SEM micrographs were also analyzed before and after creep at 1300°C in air for specimens from billet L-10-40, with an average pre-test grain size of 0.54 µm. Micrographs of specimens, which were not subject to creep, are shown in Figure 162.

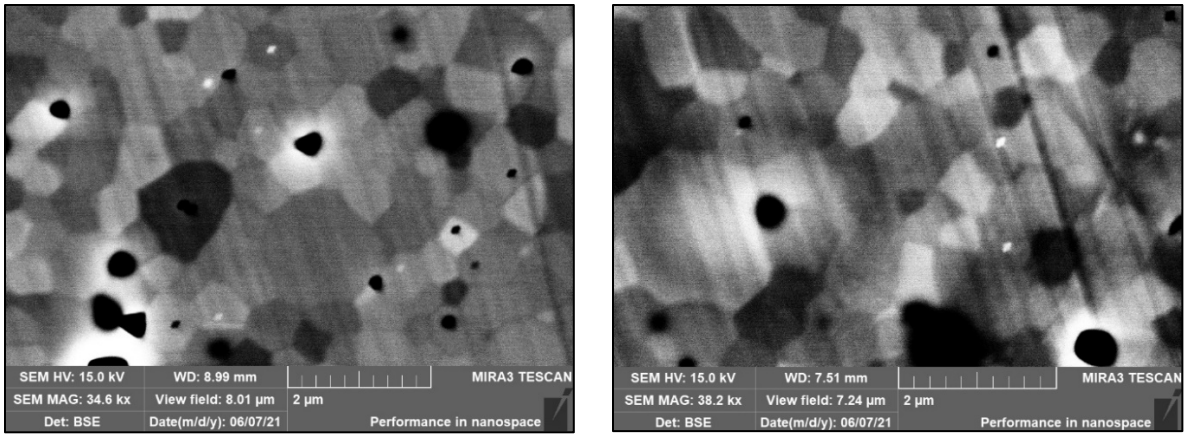

Figure 162: SEM micrographs of billet L-10-40 prior to creep testing with an average grain size of 0.54 µm.

After analysis of these micrographs, the average grain size was determined to be 0.54 µm and the average grain aspect ratio was determined to be 1.01. Once again, this aspect ratio of approximately 1 is very close to that determined for YAG and to that of the previously discussed LuAG billet. These micrographs established the baseline microstructure for L-10-40 and were compared to similar micrographs of specimen L-10-40-3 following creep at 1300°C in air, which are shown in Figure 163.

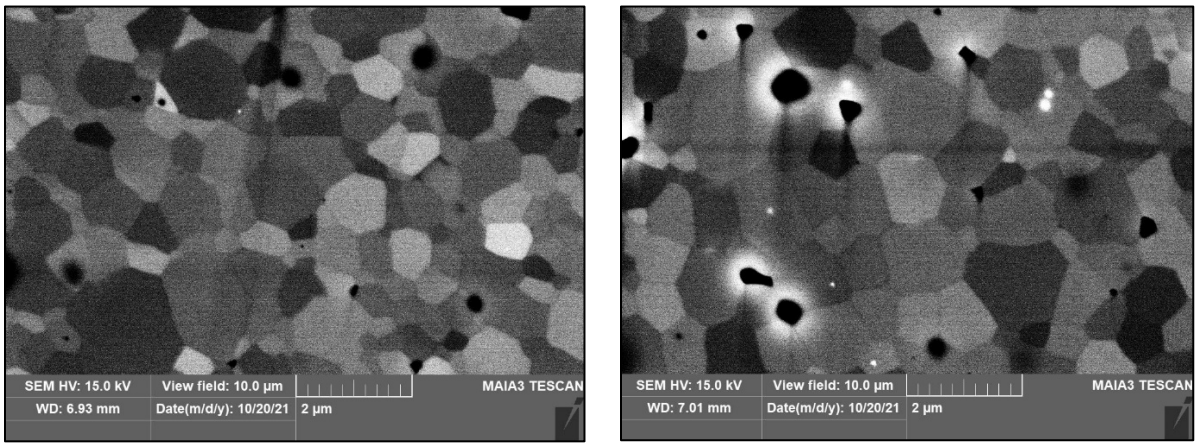

Figure 163: SEM micrographs of Specimen L-10-40-3 after creep at 1300°C in air. Average measured grain size is 0.57 µm.

The average grain size for specimen L-10-40-3 following creep at 1300°C was determined to be 0.57 μm, which represents a small increase in grain size of approximately 5%. However, this small difference in grain size is well-within the potential error of the grain size measurement methods. These numbers indicate that there was likely no significant grain growth during creep at 1300°C. Specimen L-10-40-3, which was subject to a compressive creep stress of 200 MPa, saw a total accumulated creep strain of 15%, as was presented in Section 7.1.1. The average grain aspect ratio for this specimen following creep was determined to be 1.16. This difference in aspect ratio represents an increase of almost 16%, which is very consistent with the amount of creep strain observed. These results are also summarized in Table 39.

Similar SEM micrographs were also analyzed before and after creep at 1300°C in air for specimens from billet L-19-40, with an average grain size of 0.84 μm. Specimens not subject to creep are shown in Figure 164.

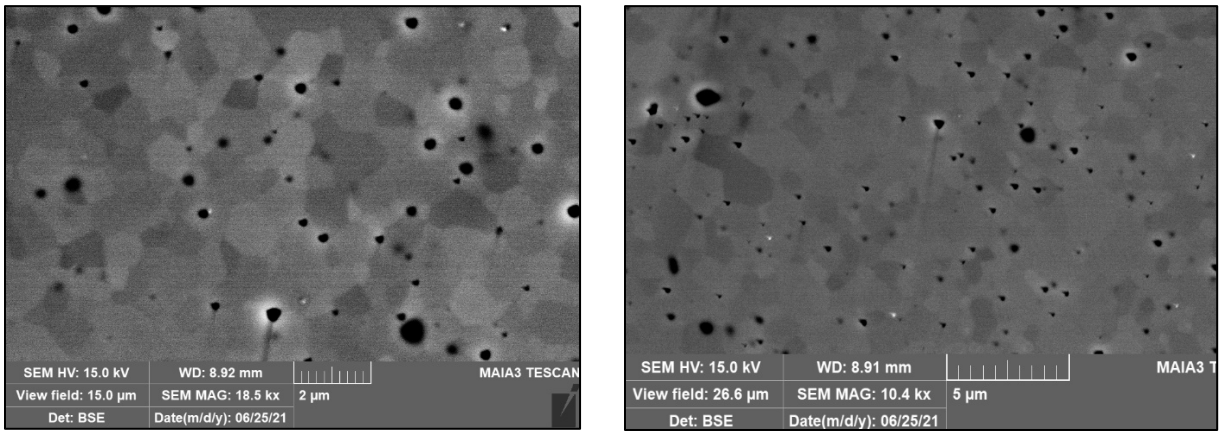

Figure 164: SEM micrographs of billet L-19-40 prior to creep testing with an average grain size of 0.84 μm.

After analysis of these micrographs, the average grain size was determined to be 0.84 μm and the average grain aspect ratio was determined to be 1.04. Again, this aspect ratio of approximately 1 is very similar to that previously determined for YAG and LuAG specimens.

This aspect ratio is also consistent with the visual appearance of the nearly-circular grains in Figure 164. These micrographs were compared to similar micrographs of specimen L-19-40-1 following creep at 1300°C in air, which are shown in Figure 165.

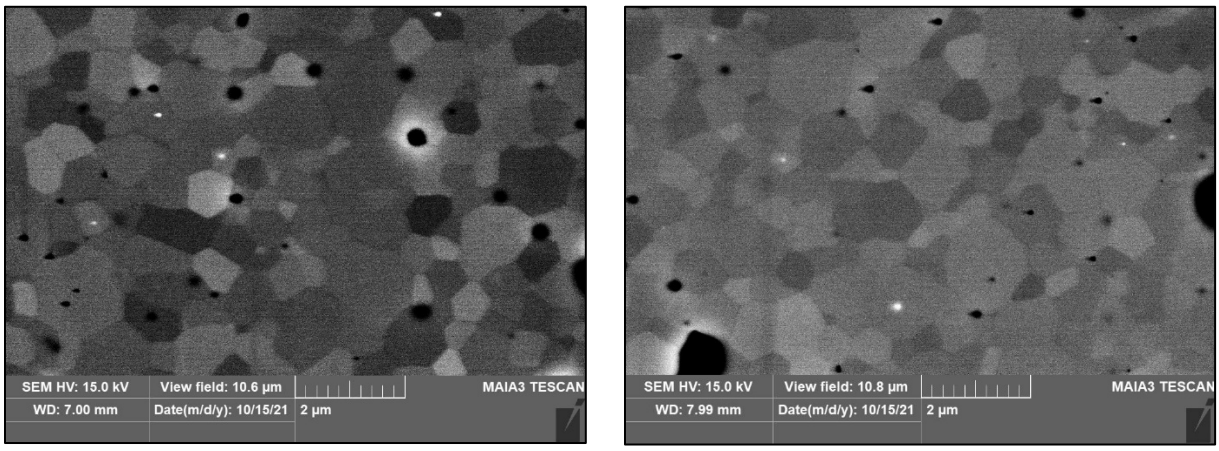

Figure 165: SEM micrographs of Specimen L-19-40-1 after creep at 1300°C in air. Average measured grain size is 0.84 µm.

Analysis of the micrographs of the post-creep specimen L-19-40-1 revealed the average grain size to be 0.82 µm and the average grain aspect ratio to be 1.10. This measured grain size is technically smaller than that measured for a specimen not subject to creep. However, this small difference is well within the possible amount of error associated with grain size measurements. Hence, we conclude that there was no apparent grain growth during creep at 1300°C.

Specimen L-19-40-1, which was subject to a compressive creep stress of 200 MPa, saw a total accumulated creep strain of 4%, as was presented in Section 7.1.1. The average grain aspect ratio for this specimen following creep was determined to be 1.10, which represents an increase of almost 6%. As was observed for the previously analyzed YAG and LuAG specimens, this increase in aspect ratio is consistent with compression and is also consistent with the amount of creep strain observed. The effects of creep on the average grain size and the average grain aspect ratio for all three LuAG billets are summarized in Table 39.

Table 39: Summary of the creep effects at 1300°C in air on the grain size and shape of various LuAG specimens.

Specimen	Creep Temperature [°C]	Average Grain Size [µm]	Average Grain Aspect Ratio	Accumulated Creep Strain [%]	Amount of Grain Growth [%]	Amount of Grain Elongation [%]
Post-SPS L-12-40	N/A	0.32	0.96	N/A	N/A	N/A
Post-Creep L-12-40-3	1300	0.37	1.12	14.00	15.63	16.67
Post-SPS L-10-40	N/A	0.54	1.01	N/A	N/A	N/A
Post-Creep L-10-40-3	1300	0.57	1.16	15.16	5.56	14.85
Post-SPS L-19-40	N/A	0.84	1.04	N/A	N/A	N/A
Post-Creep L-19-40-1	1300	0.82	1.1	4.06	0.00	5.77

Each LuAG billet, which was analyzed before and after creep at 1300°C, exhibited similar grain deformation consistent with the amount of creep strain observed. This indicates that creep of LuAG under these conditions is controlled by Lifshitz grain boundary sliding, which is accommodated by vacancy diffusion within grains, which further results in grain shape change due to the applied stress. This type of grain boundary sliding is associated primarily with Nabarro-Herring creep.

9. Conclusions and Recommendations

9.1. Spark Plasma Sintering of Oxide Ceramics

Several different oxide ceramic billets were prepared and processed via SPS. Processed materials included undoped, polycrystalline YAG, 2at% Yb-doped YAG, 2at% Er-doped YAG, and undoped, polycrystalline LuAG. SPS parameters were changed for the processing of different billets of each material variant in order to assess the effects of SPS parameters on overall material quality and grain size, and to determine the most effective combination of processing parameters for synthesizing creep resistant oxide ceramics.

SPS has been shown to be an effective processing method for YAG in many published material studies, which gave a baseline for the target SPS parameters that were likely to be effective in making fully dense, fine-grained ceramics. SPS has been used to fabricate LuAG specimens, primarily for optical applications, but consistent SPS settings, which are capable of producing high quality LuAG specimens, have not been established. Therefore, the assumption was made that LuAG would respond similarly to YAG during processing, and the parameters were kept consistent between each material.

Many SPS parameters were varied in order to identify their effects on the resulting material. These parameters include pressure, temperature, hold time, heating rate, cooling rate, powder packing methods, powder drying methods, and the timing associated with releasing pressure and temperature. Many of these parameters and procedural alterations did not have a significant influence on the resulting material. However, the temperature and pressure used during SPS had a significant effect on the resulting material grain size, which also has a significant impact on strength and creep resistance. In general, the grain size of the material appears to increase as the SPS temperature is increased. However, this increase in grain size is very minimal below a

certain temperature threshold. This threshold was identified to be approximately 1500° - 1550°C for YAG, and perhaps slightly higher, >1550°C for LuAG. The effect of pressure on the resultant grain size were more difficult to analyze. The plots of grain size vs. pressure produce nearly flat curves for both materials; however, 40 MPa seems to represent a point of slightly reduced grain growth, while the results are much less consistent at 20 MPa and 50 MPa.

The majority of the materials processed via SPS were high-quality materials suitable for mechanical testing. Most of the YAG billets had a measured density between 97% and 100% of the published theoretical density of YAG, while most of the LuAG billets had a measured density between 96% and 99% of the theoretical density of LuAG. The reasons for these slightly lower densities observed for LuAG specimens are unknown. A wide range of apparent porosity was observed within SEM micrographs during microstructural analysis. While some YAG and LuAG billets possessed large pores on the order of 10 μm in length, the majority of billets only had small pores less than 1 μm in length.

The grain size was determined for each SPS billet following processing in the SEM. The majority of billets possessed grains sizes between 0.3 μm and 5 μm. However, some very large grains, greater than 10 μm, were observed in some materials, possibly due to abnormal grain growth, which has been known to occur during processing of these ceramics.

In conclusion, SPS is an effective processing method for both YAG and LuAG. The parameters can be adjusted in order to tailor the resulting material properties to the intended material use or application. SPS consistently produced near-theoretical density oxide ceramics, with mostly consistent grain sizes for similar parameter settings. The presence of significant, but small, porosity did not allow for transparent materials. However, it is expected that adjusting parameters as necessary, and specifically increasing the applied pressure during SPS, may result

in fully transparent billets, which was not necessary for this study to assess the creep behavior of YAG and LuAG.

The primary goal of this work was to determine the creep behavior of these materials under various conditions. Therefore, the fabrication of additional materials did not continue once mechanical testing began. In order to produce a more thorough and conclusive study of the effects of SPS parameters on the resulting material characteristics of oxide ceramics, many more SPS runs must be accomplished. By carefully adjusting each SPS parameter setting for a large group of materials, the specific capabilities of SPS could be conclusively identified. Specific processing recipes could be determined for specific resulting densities and grain sizes. This represents a very valuable area of future work for the material science community.

9.2. Creep Behavior of Yttrium Aluminum Garnet

Undoped and doped, polycrystalline YAG specimens with several different grain sizes were tested in compressive creep in air and in steam at 1300°C and 1400°C. The two doped variants of YAG were 2at% Yb-doped YAG and 2at% Er-doped YAG, both of which are common, doped YAG materials, typically used in optical material applications. By individually varying and isolating the parameters in this creep study, the impacts of temperature, compressive stress, and steam environment, as well as the significant impact of grain size were determined for each material variant.

The results from each creep test consisted of the measured creep strain over time. From the strain vs. time curves, the steady-state creep strain rates were determined and analyzed. This creep strain rate, described by the standard steady-state creep rate equation, was the primary

focus of this investigation. By determining the effects of temperature, stress, and grain size on the steady-state creep strain rates of each material, the stress exponents, grain size exponents, and creep activation energy were identified.

Determination of these creep performance characteristics was accompanied by a thorough investigation into the post-creep microstructure of each material, including changes to the average grain size and grain aspect ratio following creep. This analysis of the post creep microstructure coupled with the creep results obtained for each material contributed to the determination of the creep mechanisms responsible for the deformation observed at high temperature.

YAG demonstrated the highest creep resistance of any oxide ceramic previously investigated, displaying steady-state creep rates on the order of 10^{-9} s^{-1} at 1300°C for large grain sizes. The impact of grain size on the steady-state creep rates of YAG was significant. Grain sizes of undoped YAG between approximately 1 μm and 8 μm caused a difference in the creep rates of approximately 2 orders of magnitude. Increasing the temperature from 1300°C to 1400°C caused an increase in the steady state creep rate by approximately one order of magnitude.

The average stress exponent, *n*, for YAG was determined to be 1.30 and the average grain size exponent, *m*, for YAG was determined to be 1.99. The activation energy associated with diffusion during creep of undoped YAG was determined to be 532 kJ/mol, which is consistent with the known in activation energy associated with the Y^{3+} cation during self-diffusion. These values are consistent with the creep mechanism identified as grain boundary sliding accommodated by Nabarro-Herring diffusional creep, which suggests a stress exponent of 1 and a grain size exponent of 2. Furthermore, the rate limiting species during diffusion is the large Y^{3+} cation, identified by the observed activation energy. Small grain shape changes were identified

by comparing the pre- and post-creep grain aspect ratios. These shape changes are caused by diffusion occurring through the grains during grain boundary sliding, which is also consistent with Nabarro-Herring diffusional creep

The presence of steam appears to have no significant impact on the creep behavior of YAG at 1300°C; however, YAG specimens were not tested in steam at 1400°C, so the effects of steam at higher temperatures remain unknown. The presence of the two dopants appears to have no significant impact on the creep behavior of YAG. Very fine-grained doped YAG specimens were tested, and they demonstrated higher stress exponents and lower grains size exponents than the larger-grained specimens, doped or undoped. However, these effects are assumed to be primarily due to the grain size and not the presence of dopants. These changes in the determined exponents suggest that the mechanism associated with the creep of YAG with very small grains, < 0.5 μm, changes or partially changes to interface reaction-controlled creep, similar to what was observed in previously tested alumina. This would indicate that the grain boundaries can no longer be assumed to be the location of perfect sources and sinks for vacancy diffusion, but rather the diffusion of species during creep pile up at the grain boundaries and the resulting reactions are rate-limiting.

Recommendations for future work in the area of creep of YAG primarily include testing more specimens under the same conditions. This would allow for more statistically relevant data and more conclusive results. Additionally, more creep experiments at 1400°C should take place in air and in steam. The effects of grain size should be determined at 1400°C and compared to those at lower temperatures. Due to the observed grain size increase during creep of YAG at 1400°C, it is likely that this temperature represents a significant turning point in the abilities of this material to continue to perform for long durations.

Future work on the creep of YAG should also target fine-grained materials, specifically those with grain sizes below 0.5 μm. The limited amount of these tests in this study suggests that the creep mechanisms may change for such fine-grained YAG materials. However, only fine-grained doped YAG specimens were tested in creep. Therefore, more testing needs to accomplished on undoped YAG specimens in order to verify these results, and determine more conclusively if the creep mechanism changes based on grain size.

9.3. Creep Behavior of Lutetium Aluminum Garnet

The creep behavior of undoped LuAG was compared to that of YAG under the same test conditions and similar material characteristics. Compressive creep tests took place at 1300°C in air and in steam for a range of stress values between 50 and 200 MPa. Specimens from several billets were tested in order to assess the effects of grain size on the resultant creep performance of LuAG. Due to material quantity limitations, LuAG was not tested at 1400°C. This represented the first creep study of LuAG specimens, and the first investigation into the potential use of LuAG as an aerospace structural material.

LuAG surprisingly demonstrated strain rates between one and two orders of magnitude greater than those of YAG for similar grain sizes, despite the higher density and melting temperature of LuAG. The most creep resistant LuAG specimen was tested at 1300°C in air, had a grain size of approximately 5 μm, and produced a steady-state strain rate on the order of 10^{-8} s^{-1} at 50 MPa. While still an impressive creep rate result, this creep rate represents significantly less creep resistance than that seen in similar YAG specimens under similar conditions. Material grain size had a significant effect on the creep behavior of LuAG. Grain sizes in this study were

between 0.32 μm and 4.90 μm. This variation in grain size caused a difference of approximately two orders of magnitude in the creep rates of LuAG. Very large creep strains were also observed during creep of LuAG. Accumulated strains above 15% were observed for fine-grained LuAG specimens. Even specimens with grain size close to 1 μm reached strains of 4%, which is much higher than that observed for YAG. The presence of steam appears to have no significant impact on the creep behavior of LuAG at 1300°C, as was the case for YAG. Two sets of LuAG specimens with two different gran sizes were tested in steam. In each case the resulting creep behavior was nearly identical to the creep behavior in air for specimens with similar grain sizes.

The average stress exponent, *n*, for LuAG was determined to be 1.91 and the average grain size exponent, *m*, for LuAG was determined to be 1.24. This stress exponent is higher, and the grain size exponent is lower than those observed for YAG. This difference appears to be significant enough to suggest that the creep mechanisms operating in LuAG may be different from those operating in YAG, despite the material similarities. A stress exponent close to 2 and a grain size exponent close to 1 would suggest that the creep is occurring by grain boundary sliding accommodated by interface reaction-controlled diffusional creep, similar to that observed for very fine-grained YAG. However, these trends were observed for LuAG across all grain sizes.

Significant grain shape changes were identified by comparing the pre- and post-creep grain aspect ratios. Even more identifiable in LuAG specimens with significant accumulated creep strains, these shape changes are likely caused by diffusion occurring through the grains during grain boundary sliding, which is also consistent with Nabarro-Herring diffusional creep. It is likely that multiple diffusion mechanisms are occurring in LuAG during creep, which would account for all these observations.

Future research into the creep behavior of LuAG should also involve large quantities of materials in order to create statistically relevant and conclusive results. Specifically, more creep experiments should focus on the creep of LuAG at 1400°C, as no tests were conducted at that temperature during this study. It would be beneficial to test LuAG specimens with larger grains to see if any LuAG specimen could produce the same impressive creep resistance as YAG. The discrepancies between the creep behavior of YAG and LuAG should be investigated further. It is possible that LuAG is inherently less creep resistant than YAG, as the results of this study suggest.

However, it is also possible that the lower creep resistance of LuAG is due to specific material defects, rather than intrinsic material properties. In order to reach this conclusion for LuAG, the specimens, which were used throughout this study, must be examined further. The potential presence of impurities must be determined by chemical analysis. Impurities and their potential segregation at the grain boundaries must be analyzed in thin specimens by observations in the TEM. These potential defects in LuAG specimens could account for the increased creep strains and creep rates observed throughout this study, and should be investigated in future work.

Appendix A: Tables of Spark Plasma Sintering Parameters and Resultant Material Properties

Table A-1: Undoped YAG Spark Plasma Sintering Parameters and Resultant Material Properties.

Identification		SPS Parameter Settings					Material Results				
Billet Name	Billet Diameter [mm]	SPS Temperature [°C]	SPS Pressure [MPa]	Heating Ramp Rate [°C/min]	Hold Time [min]	Cooling Rate [°C/min]	# of Resultant Creep Specimens	Grain Size [µm]	Density [g/cc]	Density [%]	Material Hardness [Vickers]
Y-1-25	25	1500	30	70	20	20	2	0.43	4.52	99.13	1848
Y-2-40	40	1500	20	70	20	5	2	11.65	4.44	97.48	1585
Y-3-40	40	1500	20	70	15	5	4	0.88	4.51	98.90	1669
Y-4-40	40	1400	20	70	30	5	2	0.50	4.42	96.84	1814
Y-5-25	25	1500	30	35	15	2	1	0.81	4.53	99.44	
Y-6-25	25	1500	30	35	15	2	2	0.34	4.56	100.00	
Y-7-40	40	1500	30	35	15	2	6	1.17	4.53	99.24	1470
Y-8-40	40	1400	40	35	15	5	1	0.88	4.45	97.55	1746
Y-9-40	40	1300	30	35	15	5	0	0.35	4.56	99.94	1823
Y-10-40	40	1300	40	35	15	5	3	0.28	4.56	100.00	
Y-12-40	40	1300	20	35	15	5	0	3.07	4.51	98.95	
Y-13-40	40	1550	50	35	15	5	5	7.99	4.46	97.85	1390
Y-14-40	40	1550	20	35	15	5	4	3.19	4.54	99.62	

Table A-2: 2at% Yb-Doped YAG Spark Plasma Sintering Parameters and Resultant Material Properties.

Identification		SPS Parameter Settings					Material Results				
Billet Name	Billet Diameter [mm]	SPS Temperature [°C]	SPS Pressure [MPa]	Heating Ramp Rate [°C/min]	Hold Time [min]	Cooling Rate [°C/min]	# of Resultant Creep Specimens	Grain Size [µm]	Density [g/cc]	Density [%]	Material Hardness [Vickers]
Y-Yb-1-20	20	1500	30	70	20	20	1	0.39	4.56	99.96	1651
Y-Yb-2-25	25	1500	30	70	20	20	2	0.38	4.59	100.00	1743
Y-Yb-3-40	40	1400	20	70	20	5	4	0.48	4.54	99.48	1701
Y-Yb-4-25	25	1500	30	35	15	2	2	4.83	4.57	100.00	1442
Y-Yb-5-40	25	1550	30	35	15	5	4	1.38	4.50	98.76	1701
Y-Yb-6-40	40	1500	40	35	15	2	3	0.51	4.52	99.21	1587
Y-Yb-7-40	40	1300	30	35	15	2	3	0.37	4.47	97.97	1747
Y-Yb-8-40	40	1400	50	35	15	2	1	0.53	4.56	100.00	
Y-Yb-9-40	40	1550	40	35	15	2	3	0.63	4.53	99.45	1634
Y-Yb-10-40	40	1550	30	35	20	2	3	15.02	4.54	99.52	

Table A-3: 2at% Er-Doped YAG Spark Plasma Sintering Parameters and Resultant Material Properties.

Identification		SPS Parameter Settings					Material Results				
Billet Name	Billet Diameter [mm]	SPS Temperature [°C]	SPS Pressure [MPa]	Heating Ramp Rate [°C/min]	Hold Time [min]	Cooling Rate [°C/min]	# of Resultant Creep Specimens	Grain Size [µm]	Density [g/cc]	Density [%]	Material Hardness [Vickers]
Y-Er-1-40	40	1400	10	70	20	5	2	24.30	4.47	97.93	1627
Y-Er-2-40	40	1400	30	70	20	2	2	0.50	4.55	99.72	
Y-Er-3-25	25	1500	30	35	20	2	2	1.28	4.80	100.00	1520
Y-Er-4-25	25	1500	30	35	20	2	2	2.83	4.61	100.00	1476
Y-Er-5-25	25	1500	30	20	20	2	0	0.33	N/A	N/A	
Y-Er-6-25	25	1500	30	35	20	2	1	0.47	4.58	100.00	
Y-Er-7-40	40	1500	50	35	15	2	3	1.87	4.53	99.34	1436
Y-Er-8-40	40	1400	40	35	15	2	4	0.37	4.55	99.84	
Y-Er-9-40	40	1300	50	35	15	2	3	0.45	4.51	98.94	1742
Y-Er-10-40	40	1550	40	35	15	2	1	2.72	4.52	99.21	

Table A-4: LuAG Spark Plasma Sintering Parameters and Resultant Material Properties.

Identification		SPS Parameter Settings					Material Results				
Billet Name	Billet Diameter [mm]	SPS Temperature [°C]	SPS Pressure [MPa]	Heating Ramp Rate [°C/min]	Hold Time [min]	Cooling Rate [°C/min]	# of Resultant Creep Specimens	Grain Size [µm]	Density [g/cc]	Density [%]	Material Hardness [Vickers]
L-1-20	20	1550	30	70	25	20	1	10.78	6.57	97.67	1459
L-2-25	25	1550	30	70	20	20	1	0.57	6.55	97.40	1630
L-3-40	40	1550	30	70	20	20	5	4.90	6.47	96.20	1574
L-4-40	40	1450	20	70	20	5	3	0.95	6.54	97.23	1745
L-5-40	40	1350	20	70	20	5	1	0.41	6.57	97.66	1681
L-6-40	40	1450	20	70	40	5	3	0.55	6.60	98.11	1672
L-7-40	40	1450	20	70	40	2	2	0.44	6.65	98.86	1328
L-8-25	25	1500	30	35	15	2	1	0.50	6.57	97.64	
L-9-25	25	1300	30	35	15	2	0	0.32	6.49	96.48	1811
L-10-40	40	1500	40	35	15	2	3	0.54	6.65	98.84	
L-11-40	40	1300	40	35	15	2	4	0.55	6.57	97.62	
L-12-40	40	1300	50	35	15	5	3	0.32	6.50	96.55	1515
L-13-40	40	1400	50	35	15	5	2	0.45	6.58	97.78	1839
L-14-25	25	1400	30	35	20	2	0	0.34	6.66	98.99	
L-15-25	25	1400	40	35	15	2	0	N/A	N/A	N/A	
L-16-25	25	1550	40	35	15	2	1	0.48	6.57	97.64	
L-17-40	40	1500	50	35	15	2	3	0.68	6.58	97.77	
L-18-40	40	1400	40	35	15	2	3	0.42	6.49	96.43	
L-19-40	40	1500	20	35	15	2	1	0.84	6.68	99.23	
L-20-25	25	1550	50	35	15	2	1	1.06	6.66	98.99	

Appendix B: Tables of Creep Specimen Dimensions

Table B-1: Undoped YAG Creep Specimen Dimensions.

Material Type	Specimen Name	Height (mm)	Width (mm)	Depth (mm)	X1 (mm)	X2 (mm)	X3 (mm)	Mass (g)
YAG - Undoped	Y-1-25-1	19.54	6.50	6.50	3.11	12.00	3.11	3.710
YAG - Undoped	Y-1-25-2	18.82	6.46	6.45	2.76	12.10	2.71	3.470
YAG - Undoped	Y-2-40-1	19.87	6.39	6.43	3.12	11.72	3.13	3.575
YAG - Undoped	Y-2-40-2	19.35	6.43	6.42	3.02	11.95	2.86	3.499
YAG - Undoped	Y-3-40-1	18.59	6.25	6.25	2.59	11.79	2.61	3.220
YAG - Undoped	Y-3-40-2	19.73	6.24	6.24	3.00	11.75	3.09	3.400
YAG - Undoped	Y-3-40-3	17.48	5.60	5.60	1.91	11.73	1.95	3.020
YAG - Undoped	Y-3-40-4	18.75	6.25	6.24	2.64	11.77	2.53	3.28
YAG - Undoped	Y-4-40-1	19.12	6.04	6.04	2.77	11.80	2.76	3.118
YAG - Undoped	Y-4-40-2	19.69	6.02	6.02	3.09	11.76	3.03	3.157
YAG - Undoped	Y-5-25-1	20.25	7.26	7.26	3.10	11.78	3.62	4.761
YAG - Undoped	Y-6-25-1	19.34	6.85	6.89	2.89	11.78	2.85	4.025
YAG - Undoped	Y-6-25-2	17.95	6.65	6.65	2.55	11.06	2.51	3.517
YAG - Undoped	Y-7-40-1	19.03	6.74	6.74	3.05	11.98	3.44	3.800
YAG - Undoped	Y-7-40-2	20.62	6.11	6.11	3.16	11.92	3.65	4.010
YAG - Undoped	Y-7-40-3	18.99	6.73	6.73	3.52	11.87	2.98	3.770
YAG - Undoped	Y-7-40-4	18.46	6.54	6.54	2.75	11.76	3.33	3.340
YAG - Undoped	Y-7-40-5	19.22	6.02	6.02	3.12	11.92	3.54	3.640
YAG - Undoped	Y-7-40-6	17.65	5.88	5.88	2.45	11.76	2.78	3.210
YAG - Undoped	Y-8-40-1	18.99	6.51	6.51	2.85	12.27	3.20	3.620
YAG - Undoped	Y-9-40-1	No Creep Specimens						
YAG - Undoped	Y-10-40-1	19.49	6.00	6.00	2.69	11.79	3.31	3.030
YAG - Undoped	Y-10-40-2	19.64	6.25	6.25	3.42	11.72	2.78	3.360
YAG - Undoped	Y-10-40-3	20.03	6.50	6.50	3.57	11.82	3.11	3.710
YAG - Undoped	Y-12-40-1	No Creep Specimens						
YAG - Undoped	Y-13-40-1	19.06	6.61	6.61	2.82	12.34	3.12	3.730
YAG - Undoped	Y-13-40-2	18.97	6.61	6.61	3.26	12.40	2.78	3.700
YAG - Undoped	Y-13-40-3	19.09	6.62	6.62	3.56	12.30	2.40	3.740
YAG - Undoped	Y-13-40-4	19.00	6.63	6.63	3.12	12.25	2.65	3.720
YAG - Undoped	Y-13-40-5	18.95	6.62	6.62	3.12	12.48	2.76	3.680
YAG - Undoped	Y-14-40-1	18.98	5.54	5.55	3.14	12.34	2.77	2.600
YAG - Undoped	Y-14-40-2	17.97	6.40	6.40	2.85	12.42	2.23	3.300
YAG - Undoped	Y-14-40-3	18.97	6.26	6.26	2.39	12.42	3.61	3.300
YAG - Undoped	Y-14-40-4	17.87	6.41	6.41	2.14	12.30	2.82	3.240

Table B-2: 2at% Yb-Doped YAG Creep Specimen Dimensions.

Material	Specimen Name	Height (mm)	Width (mm)	Depth (mm)	X1 (mm)	X2 (mm)	X3 (mm)	Mass (g)
YAG - Yb Doped	Y-Yb-1-20-1	18.96	6.49	6.56	2.69	12.08	2.91	3.610
YAG - Yb Doped	Y-Yb-2-25-1	18.98	6.47	6.56	2.71	12.11	2.98	3.630
YAG - Yb Doped	Y-Yb-2-25-2	19.06	6.49	6.49	2.92	12.10	2.74	3.540
YAG - Yb Doped	Y-Yb-3-40-1	16.84	6.21	6.22	1.67	11.71	1.60	2.903
YAG - Yb Doped	Y-Yb-3-40-2	19.63	6.38	6.37	3.02	11.73	2.94	3.573
YAG - Yb Doped	Y-Yb-3-40-3	18.71	6.50	6.52	2.60	11.74	2.53	3.535
YAG - Yb Doped	Y-Yb-3-40-4	18.15	6.48	6.49	2.30	11.73	2.31	3.412
YAG - Yb Doped	Y-Yb-4-25-1	20.51	6.83	6.83	3.41	11.76	3.53	4.315
YAG - Yb Doped	Y-Yb-4-25-2	21.41	6.87	6.87	3.99	11.80	3.91	4.540
YAG - Yb Doped	Y-Yb-5-25-1	18.99	6.49	6.45	3.10	12.40	2.71	3.630
YAG - Yb Doped	Y-Yb-5-25-2	18.97	6.49	6.49	3.05	12.45	2.75	3.600
YAG - Yb Doped	Y-Yb-5-25-3	18.87	6.48	6.48	2.81	12.46	3.15	3.550
YAG - Yb Doped	Y-Yb-5-25-4	18.97	6.44	6.44	2.91	12.44	3.10	3.590
YAG - Yb Doped	Y-Yb-6-40-1	20.04	6.14	6.14	3.27	11.74	3.29	3.372
YAG - Yb Doped	Y-Yb-6-40-2	19.59	6.14	6.16	2.95	11.75	3.01	3.318
YAG - Yb Doped	Y-Yb-6-40-3	18.94	6.15	6.15	2.68	11.75	2.71	3.203
YAG - Yb Doped	Y-Yb-7-40-1	18.94	6.47	6.47	3.08	12.33	2.89	3.510
YAG - Yb Doped	Y-Yb-7-40-2	19.01	6.50	6.50	3.01	12.23	2.99	3.590
YAG - Yb Doped	Y-Yb-7-40-3	18.64	6.34	6.34	2.65	11.89	3.34	3.220
YAG - Yb Doped	Y-Yb-8-40-1	19.20	6.00	6.01	2.54	11.81	3.10	3.096
YAG - Yb Doped	Y-Yb-9-40-1	18.78	5.45	5.45	2.59	12.59	3.10	2.530
YAG - Yb Doped	Y-Yb-9-40-2	18.57	5.47	5.47	2.43	12.32	2.91	2.510
YAG - Yb Doped	Y-Yb-9-40-3	18.87	5.47	5.47	2.75	12.40	3.00	2.540
YAG - Yb Doped	Y-Yb-10-40-1	19.19	6.48	6.48	3.03	12.55	3.20	3.680
YAG - Yb Doped	Y-Yb-10-40-2	18.94	6.54	6.54	2.72	12.56	3.20	3.620
YAG - Yb Doped	Y-Yb-10-40-3	19.05	6.48	6.48	2.96	3.05	12.44	3.650

Table B-3: 2at% Er-Doped YAG Creep Specimen Dimensions.

Material Type	Specimen Name	Height (mm)	Width (mm)	Depth (mm)	X1 (mm)	X2 (mm)	X3 (mm)	Mass (g)
YAG - Er Doped	Y-Er-1-40-1	18.05	6.38	6.39	2.36	11.82	2.16	3.232
YAG - Er Doped	Y-Er-1-40-2	16.92	6.74	6.76	2.01	10.76	2.38	3.383
YAG - Er Doped	Y-Er-2-40-1	19.20	6.56	6.55	2.76	11.75	2.84	3.675
YAG - Er Doped	Y-Er-2-40-2	18.95	6.54	6.54	2.69	11.76	2.69	3.599
YAG - Er Doped	Y-Er-3-25-1	18.65	6.47	6.45	2.48	11.75	2.44	3.460
YAG - Er Doped	Y-Er-3-25-2	21.83	6.49	6.49	4.14	11.74	4.14	4.109
YAG - Er Doped	Y-Er-4-25-1	18.03	6.79	6.79	2.64	11.17	2.61	3.728
YAG - Er Doped	Y-Er-4-25-2	20.44	6.99	6.99	3.52	11.76	3.43	4.478
YAG - Er Doped	Y-Er-5-25	No Creep Specimens						
YAG - Er Doped	Y-Er-6-25-1	18.07	6.89	6.87	2.53	11.06	2.60	3.840
YAG - Er Doped	Y-Er-7-40-1	19.12	5.98	5.98	2.78	11.74	2.76	3.035
YAG - Er Doped	Y-Er-7-40-2	19.33	5.99	5.99	2.88	11.86	2.90	3.060
YAG - Er Doped	Y-Er-7-40-3	18.69	6.14	6.14	2.72	11.58	2.73	3.030
YAG - Er Doped	Y-Er-8-40-1	18.87	6.06	6.06	2.67	11.75	2.67	3.087
YAG - Er Doped	Y-Er-8-40-2	19.21	6.03	6.04	2.81	11.75	2.76	3.119
YAG - Er Doped	Y-Er-8-40-3	18.29	6.04	6.04	2.36	11.77	2.31	2.965
YAG - Er Doped	Y-Er-8-40-4	18.20	6.00	6.06	2.34	11.80	2.39	2.938
YAG - Er Doped	Y-Er-9-40-1	18.07	6.89	6.87	2.53	11.06	2.60	3.840
YAG - Er Doped	Y-Er-9-40-2	18.57	6.54	6.54	2.78	11.32	2.65	3.640
YAG - Er Doped	Y-Er-9-40-3	19.02	6.41	6.41	2.75	12.11	3.10	3.510
YAG - Er Doped	Y-Er-10-40-1	19.14	6.33	6.33	2.79	12.31	3.12	3.460

Table B-4: LuAG Creep Specimen Dimensions.

Material	Specimen Name	Height (mm)	Width (mm)	Depth (mm)	X1 (mm)	X2 (mm)	X3 (mm)	Mass (g)
LuAG	L-1-20-1	18.82	6.56	6.53	2.58	12.13	2.88	5.200
LuAG	L-2-25-1	18.93	5.62	5.62	2.78	11.92	2.67	3.870
LuAG	L-3-40-1	19.69	6.39	6.39	3.10	11.73	3.15	5.109
LuAG	L-3-40-2	19.89	6.33	6.34	3.21	11.71	3.09	5.081
LuAG	L-3-40-3	19.77	6.51	6.52	3.01	11.75	3.12	5.360
LuAG	L-3-40-4	19.71	6.40	6.40	3.10	11.75	3.01	5.140
LuAG	L-3-40-5	19.66	6.43	6.43	3.13	11.87	2.02	5.050
LuAG	L-4-40-1	19.13	6.25	6.24	2.89	11.93	2.82	4.830
LuAG	L-4-40-2	19.79	6.24	6.25	3.19	11.97	3.25	4.990
LuAG	L-4-40-3	17.50	6.37	6.37	2.81	10.45	2.81	4.610
LuAG	L-5-40-1	19.05	6.49	6.48	2.78	11.75	2.78	5.201
LuAG	L-6-40-2	20.02	6.24	6.24	3.26	11.73	3.24	5.080
LuAG	L-6-40-3	16.96	6.09	6.09	2.11	10.74	2.25	4.087
LuAG	L-6-40-4	16.75	6.24	6.24	2.26	10.83	2.18	4.242
LuAG	L-7-40-1	18.59	6.30	6.23	2.53	11.85	2.44	4.709
LuAG	L-7-40-2	19.95	6.31	6.31	3.21	11.75	3.25	5.173
LuAG	L-8-25	19.40	6.87	6.85	2.92	11.76	2.94	5.970
LuAG	L-9-40-1	No Creep Specimens						
LuAG	L-10-40-1	19.13	5.98	5.98	2.50	12.38	3.50	4.460
LuAG	L-10-40-2	18.28	6.38	6.38	2.50	12.50	2.60	4.890
LuAG	L-10-40-3	18.98	6.37	6.37	2.81	12.34	3.20	5.010
LuAG	L-11-40-1	18.73	6.64	6.64	2.77	12.43	2.98	5.380
LuAG	L-11-40-2	19.00	6.56	6.56	3.04	12.39	2.86	5.350
LuAG	L-11-40-3	19.02	6.66	6.67	3.15	12.35	2.79	5.540
LuAG	L-11-40-4	18.64	6.38	6.38	2.57	12.24	2.81	4.990
LuAG	L-12-40-2	18.91	6.47	6.47	3.06	12.11	2.75	5.050
LuAG	L-12-40-3	19.10	6.47	6.47	3.14	12.61	2.84	5.320
LuAG	L-12-40-5	19.01	6.41	6.47	2.77	12.54	3.04	5.220
LuAG	L-13-40-1	17.69	6.13	6.13	2.55	12.42	2.15	4.590
LuAG	L-13-40-2	17.67	6.13	6.13	2.52	12.40	2.22	4.480
LuAG	L-14-40-1	No Creep Specimens						
LuAG	L-15-40-1	No Creep Specimens						
LuAG	L-16-25-1	18.66	6.46	6.47	2.52	12.23	3.04	5.190
LuAG	L-17-40-1	20.28	6.24	6.24	3.47	11.99	3.36	5.220
LuAG	L-17-40-2	20.16	6.25	6.25	3.50	12.21	3.23	5.150
LuAG	L-17-40-3	18.47	6.13	6.13	2.49	12.00	2.61	4.530
LuAG	L-18-40-1	19.45	6.47	6.47	3.29	12.38	3.08	5.360
LuAG	L-18-40-2	19.41	6.48	6.48	3.40	12.36	2.96	5.390
LuAG	L-18-40-3	19.35	6.48	6.48	3.22	12.15	2.75	5.030
LuAG	L-19-40-1	18.90	6.46	6.46	3.32	12.41	2.94	4.760
LuAG	L-20-25-1	17.78	5.84	5.84	2.21	12.35	2.49	4.020

Appendix C: Summary of Materials

- **Billet Pictures**
- **Creep Test Specimen Dimensions**
- **SEM Micrographs**
- **Material Properties (Density, Grain Size, Hardness)**
- **Spark Plasma Sintering Profiles**

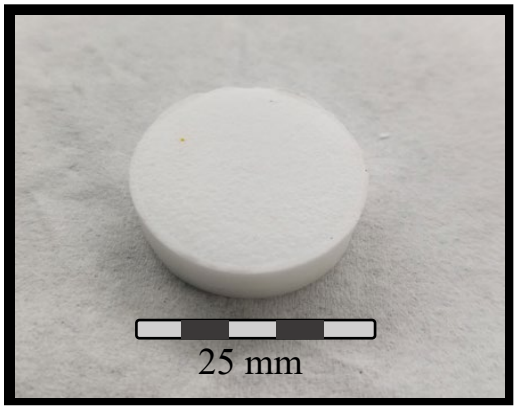

Specimen Name	Specimen Dimensions [mm]						Mass [g]
	Height	Width	Depth	X_1	X_2	X_3	
Y-1-25-1	19.54	6.50	6.50	3.11	12.00	3.11	3.710
Y-1-25-2	18.82	6.46	6.45	2.76	12.10	2.71	3.470

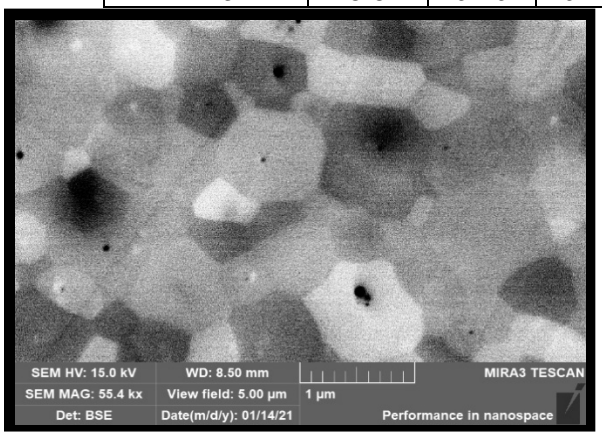

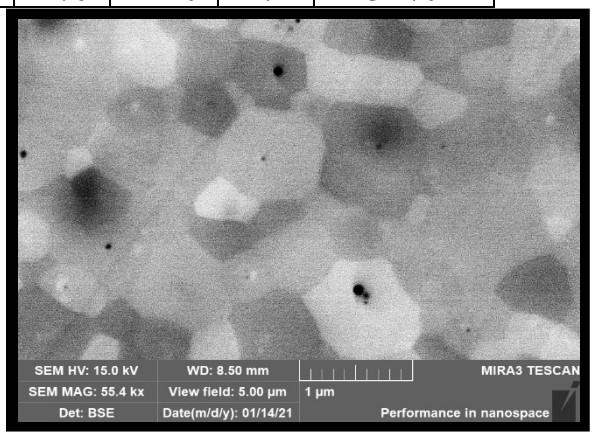

Material Properties			
Density [g/cc]	Density [%]	Grain Size [µm]	Hardness
4.52	99.13	0.43	1848

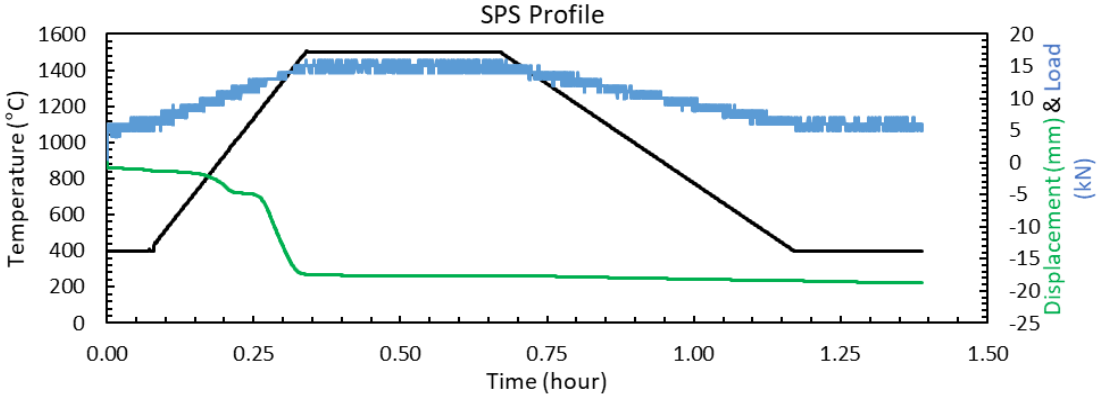

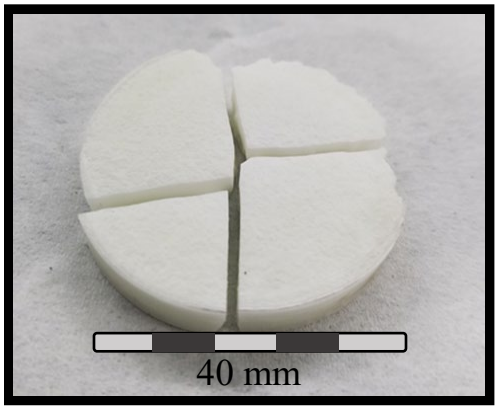

Specimen Name	Specimen Dimensions [mm]						Mass [g]
	Height	Width	Depth	X_1	X_2	X_3	
Y-2-40-1	19.87	6.39	6.43	3.12	11.72	3.13	3.575
Y-2-40-2	19.35	6.43	6.42	3.02	11.95	2.86	3.499

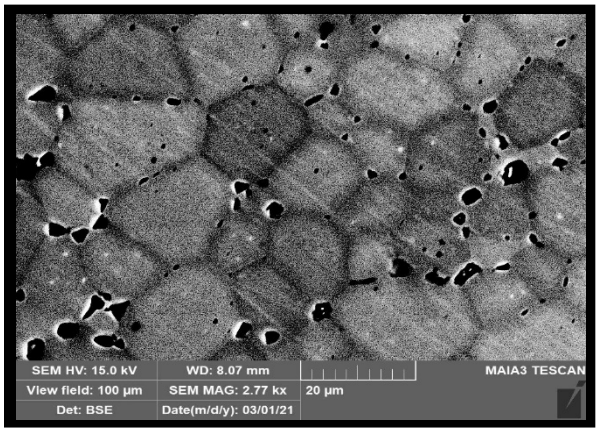

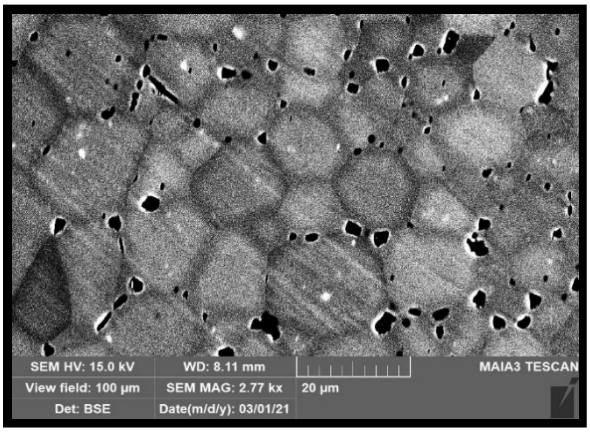

Material Properties			
Density [g/cc]	Density [%]	Grain Size [µm]	Hardness
4.44	97.48	11.65	1585

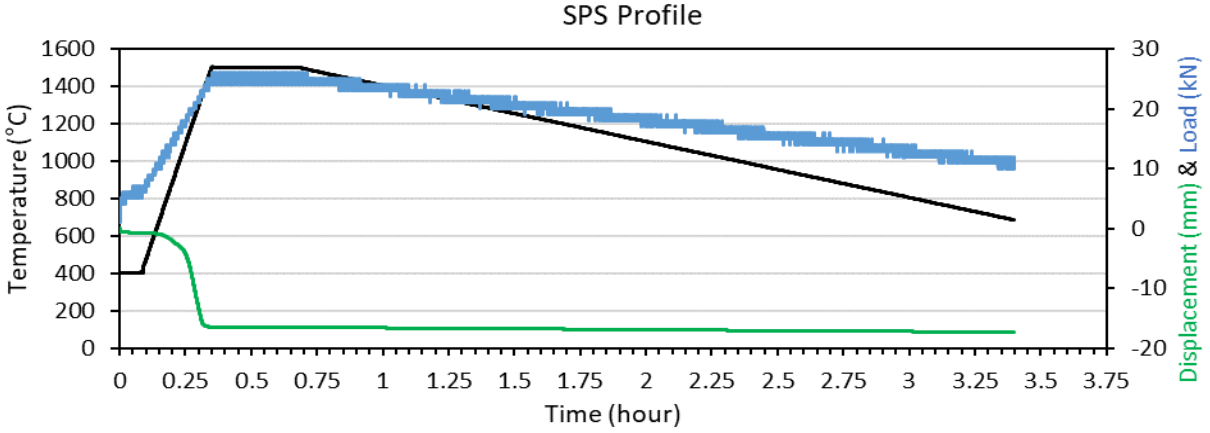

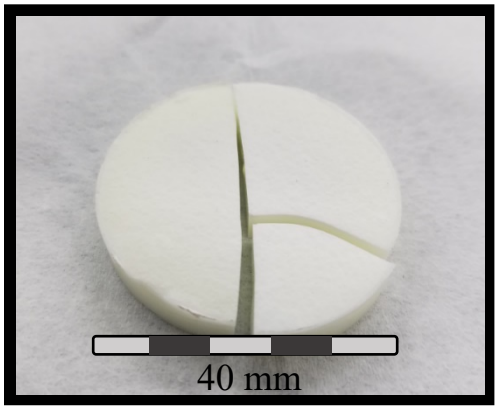

Specimen Name	Specimen Dimensions [mm]						Mass [g]
	Height	Width	Depth	X_1	X_2	X_3	
Y-3-40-1	18.59	6.25	6.25	2.59	11.79	2.61	3.220
Y-3-40-2	19.73	6.24	6.24	3.00	11.75	3.09	3.400
Y-3-40-3	17.48	5.60	5.60	1.91	11.73	1.95	3.020
Y-3-40-4	18.75	6.25	6.24	2.64	11.77	2.53	3.28

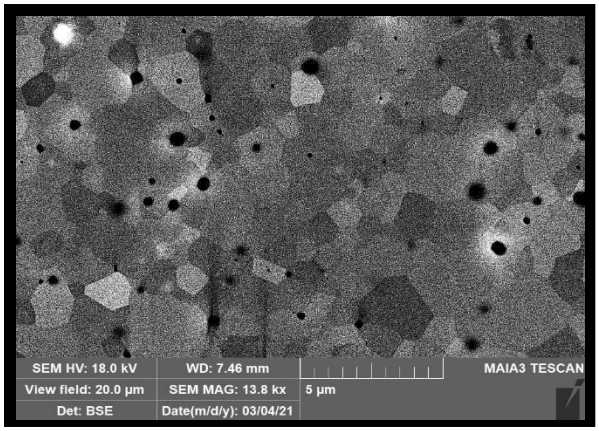

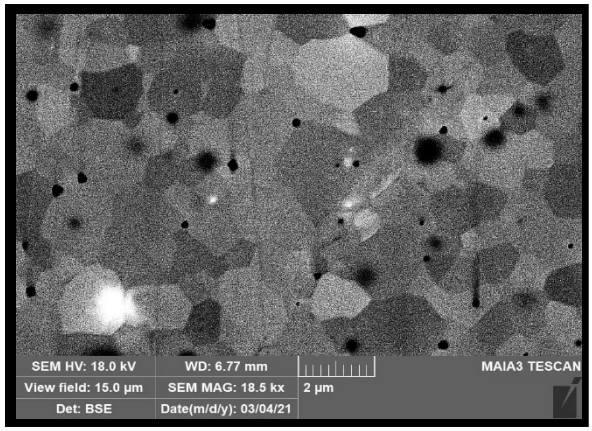

Material Properties			
Density [g/cc]	Density [%]	Grain Size [µm]	Hardness
4.51	98.90	0.88	1669

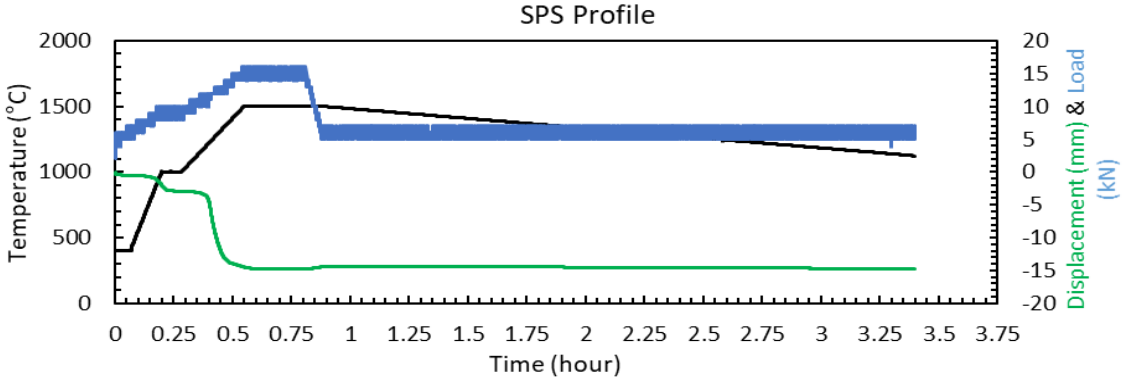

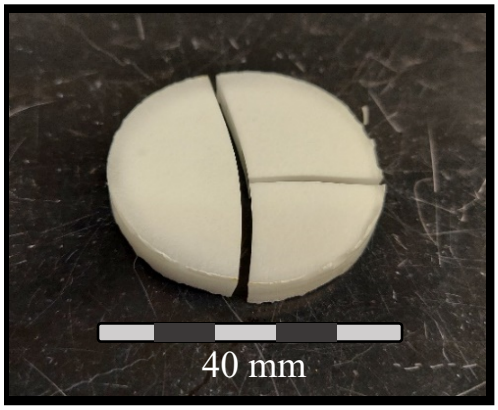

Specimen Name	Specimen Dimensions [mm]						Mass [g]
	Height	Width	Depth	X_1	X_2	X_3	
Y-4-40-1	19.12	6.04	6.04	2.77	11.80	2.76	3.118
Y-4-40-2	19.69	6.02	6.02	3.09	11.76	3.03	3.157

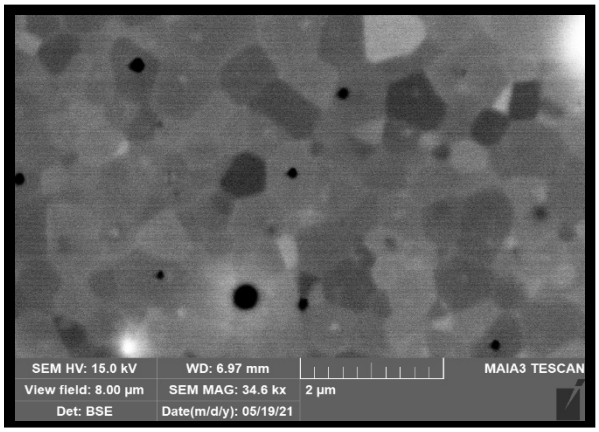

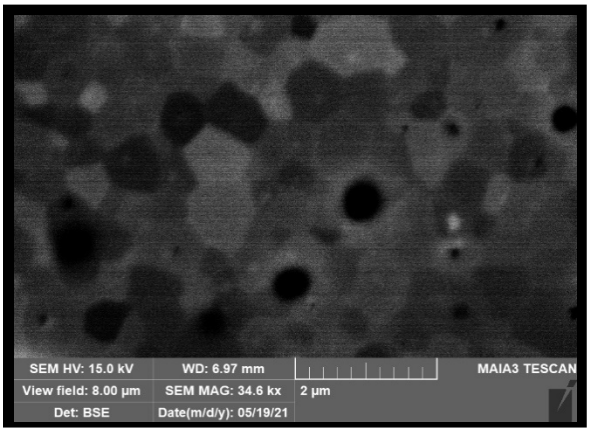

Material Properties			
Density [g/cc]	Density [%]	Grain Size [µm]	Hardness
4.42	96.84	0.50	1814

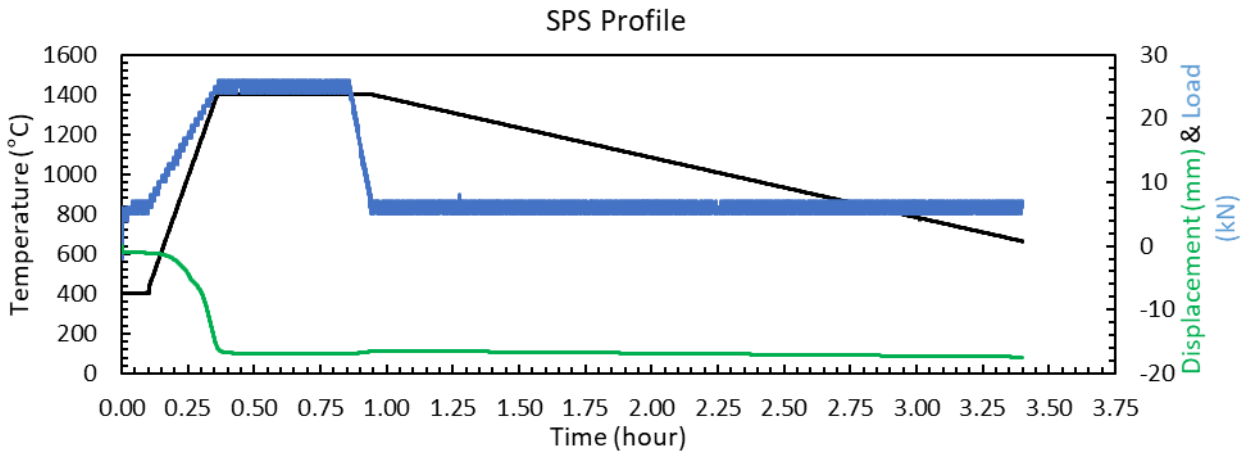

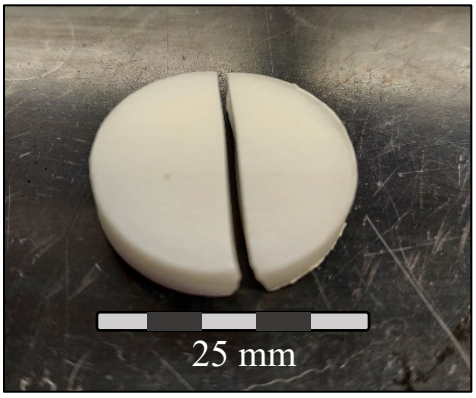

Specimen Name	Specimen Dimensions [mm]						Mass [g]
	Height	Width	Depth	X_1	X_2	X_3	
Y-5-25-1	20.25	7.26	7.26	3.10	11.78	3.62	4.761

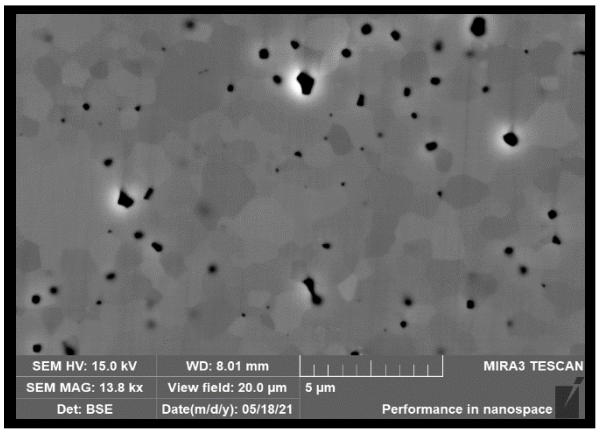

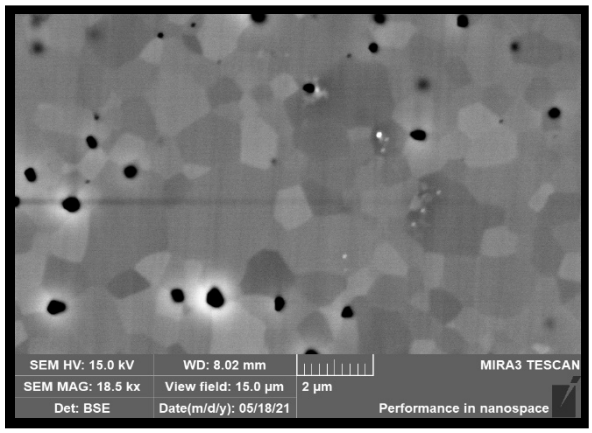

Material Properties			
Density [g/cc]	Density [%]	Grain Size [µm]	Hardness
4.53	99.44	0.81	N/A

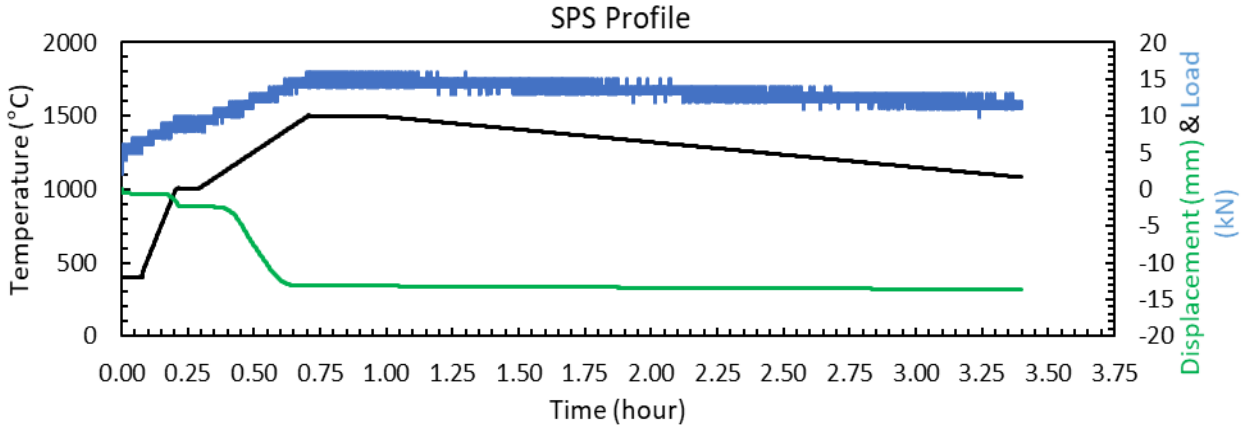

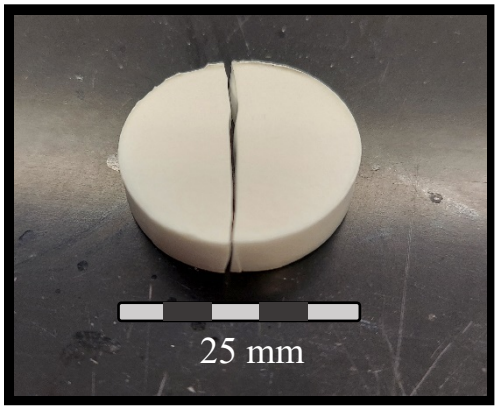

Specimen Name	Specimen Dimensions [mm]						Mass [g]
	Height	Width	Depth	X_1	X_2	X_3	
Y-6-25-1	19.34	6.85	6.89	2.89	11.78	2.85	4.025
Y-6-25-2	17.95	6.65	6.65	2.55	11.06	2.51	3.517

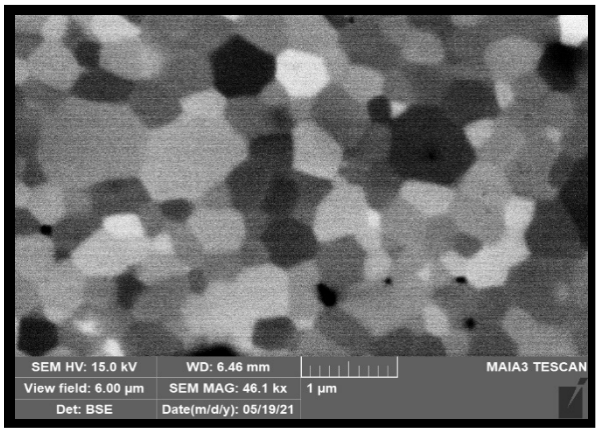

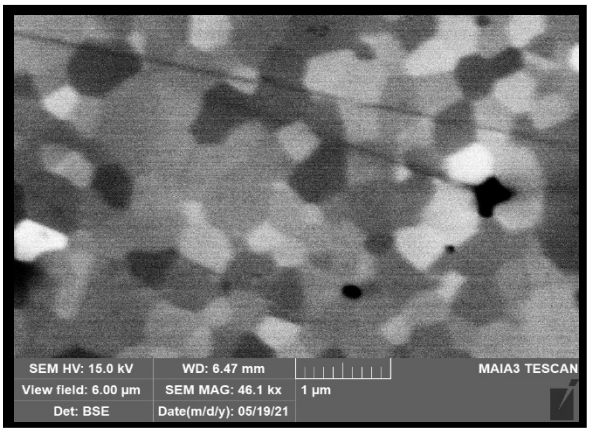

Material Properties			
Density [g/cc]	Density [%]	Grain Size [µm]	Hardness
4.79	100.00	0.34	N/A

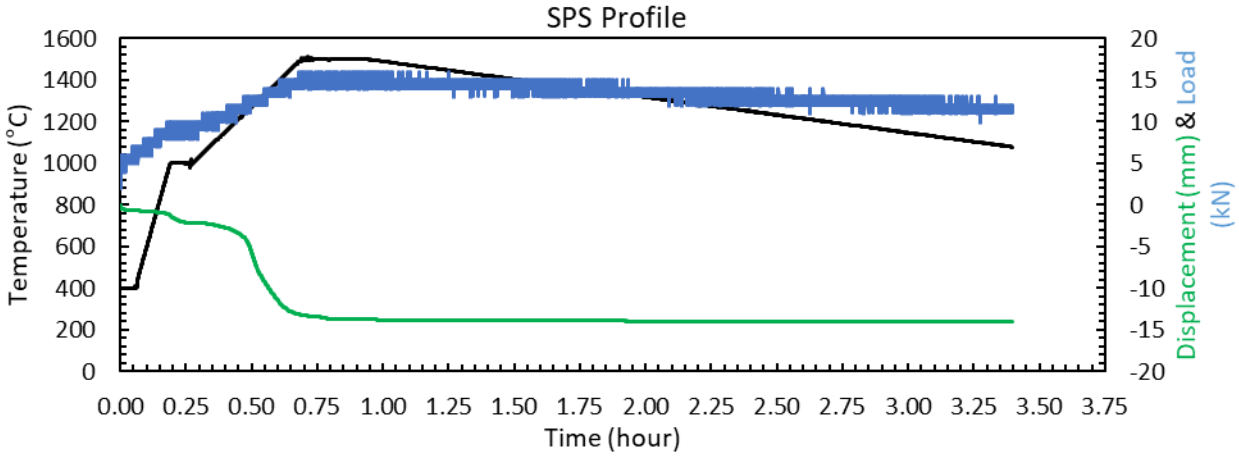

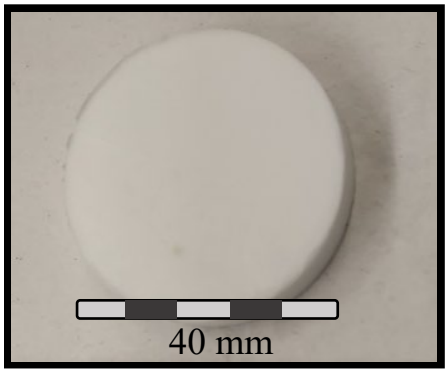

Specimen Name	Specimen Dimensions [mm]						Specimen Mass [g]
	Height	Width	Depth	X_1	X_2	X_3	
Y-7-40-1	19.03	6.74	6.74	3.05	11.98	3.44	3.800
Y-7-40-2	20.62	6.11	6.11	3.16	11.92	3.65	4.010
Y-7-40-3	18.99	6.73	6.73	3.52	11.87	2.98	3.770
Y-7-40-4	18.46	6.54	6.54	2.75	11.76	3.33	3.340
Y-7-40-5	19.22	6.02	6.02	3.12	11.92	3.54	3.640
Y-7-40-6	17.65	5.88	5.88	2.45	11.76	2.78	3.210

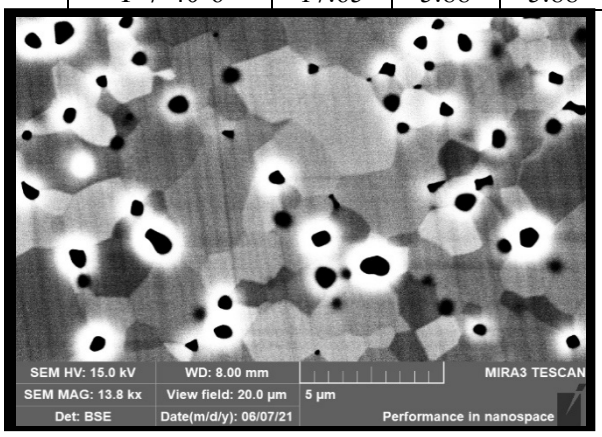

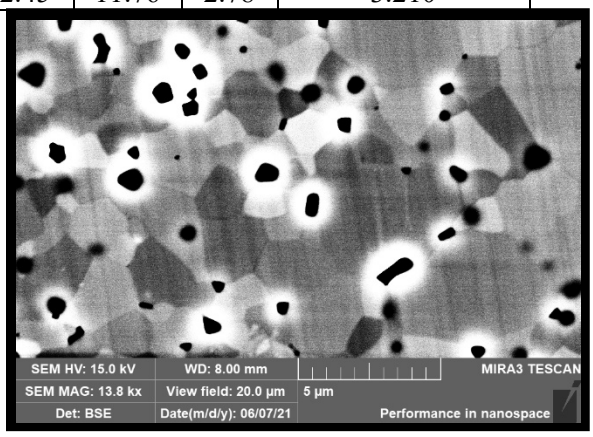

Material Properties			
Density [g/cc]	Density [%]	Grain Size [µm]	Hardness
4.53	99.24	1.17	1470

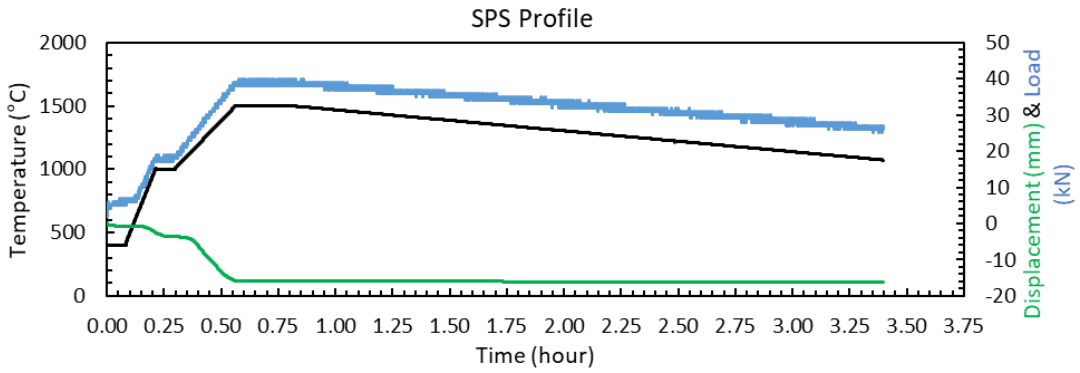

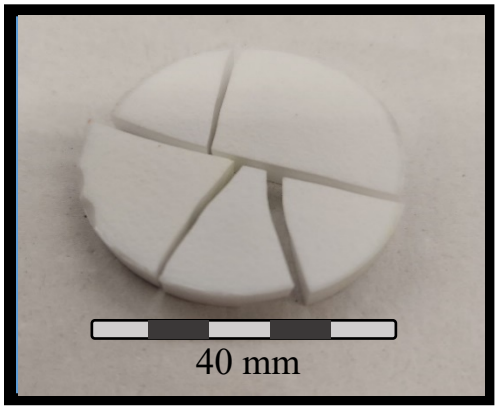

Specimen Name	Specimen Dimensions [mm]						Specimen Mass [g]
	Height	Width	Depth	X_1	X_2	X_3	
Y-8-40-1	18.99	6.51	6.51	2.85	12.27	3.20	3.620

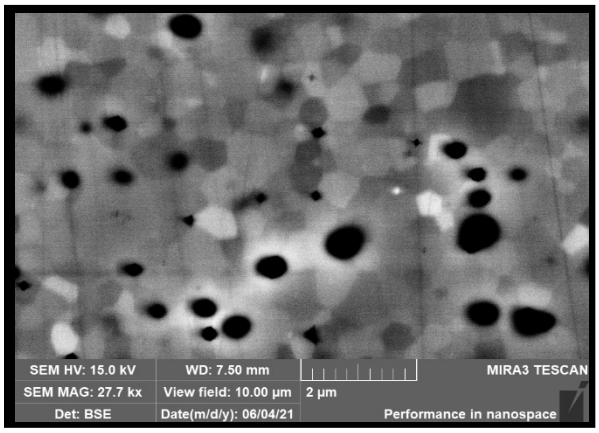

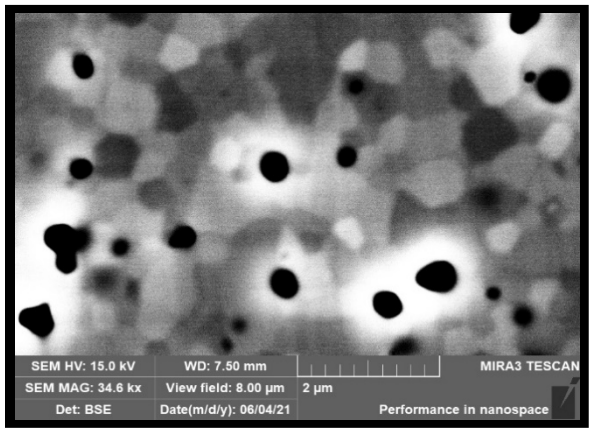

Material Properties			
Density [g/cc]	Density [%]	Grain Size [µm]	Hardness
4.45	97.55	0.88	1746

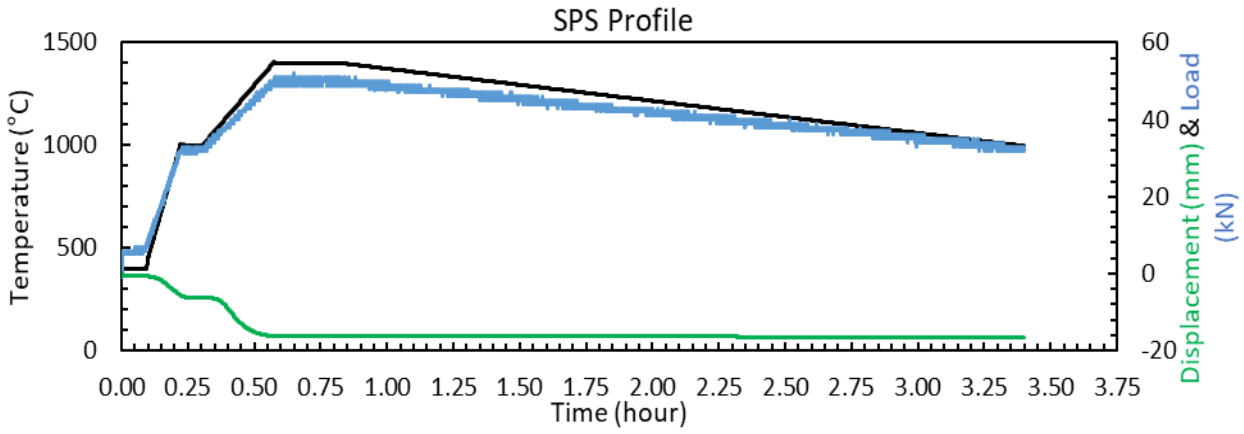

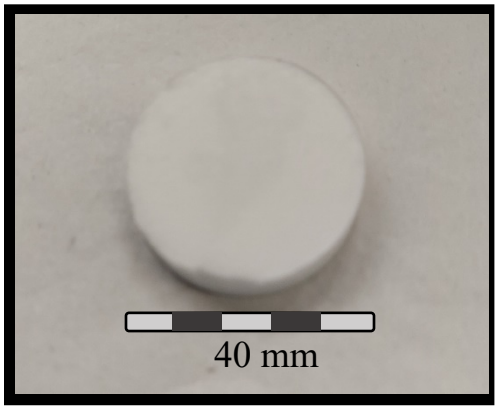

Specimen Name	Specimen Dimensions [mm]						Specimen Mass [g]
	Height	Width	Depth	X_1	X_2	X_3	
No Creep Specimens							

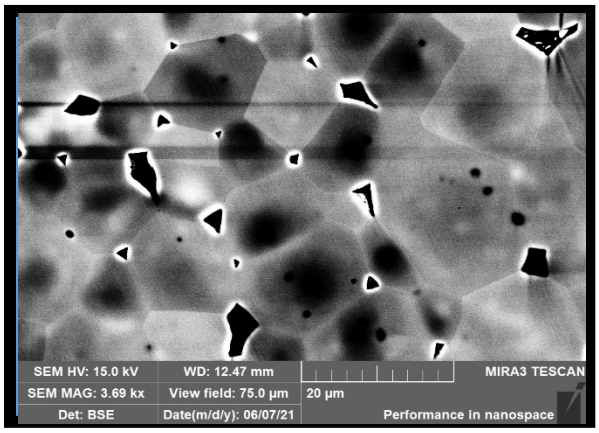

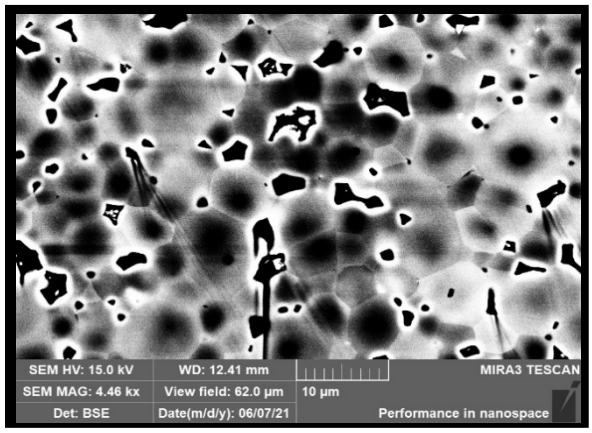

Material Properties			
Density [g/cc]	Density [%]	Grain Size [µm]	Hardness
4.56	99.94	6.12	1823

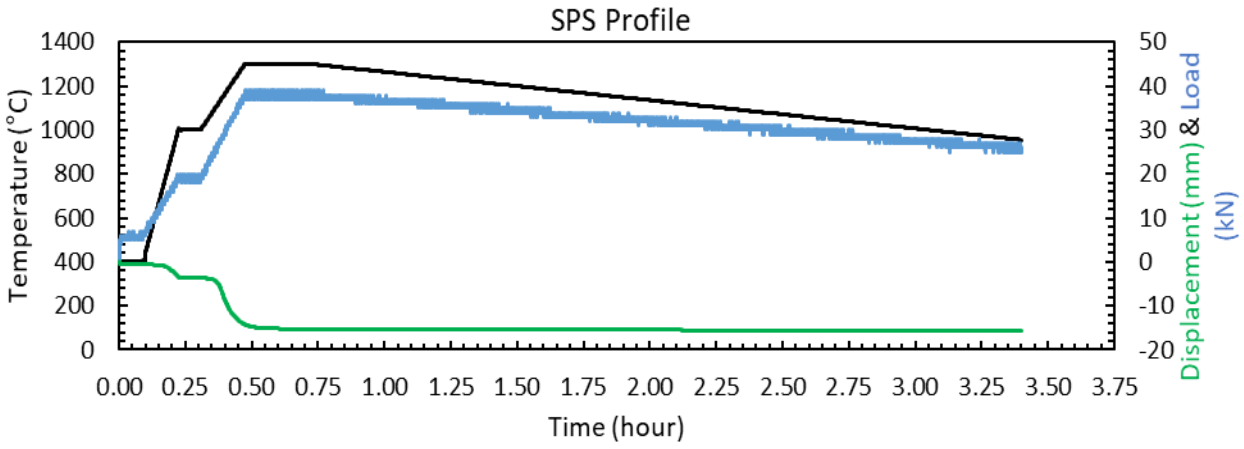

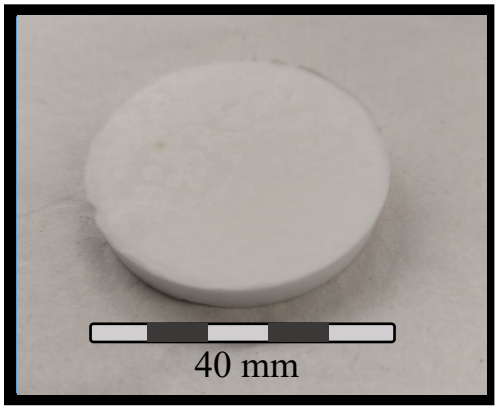

Specimen Name	Specimen Dimensions [mm]						Specimen Mass [g]
	Height	Width	Depth	X_1	X_2	X_3	
Y-10-40-1	19.49	6.00	6.00	2.69	11.79	3.31	3.030
Y-10-40-2	19.64	6.25	6.25	3.42	11.72	2.78	3.360
Y-10-40-3	20.03	6.50	6.50	3.57	11.82	3.11	3.710

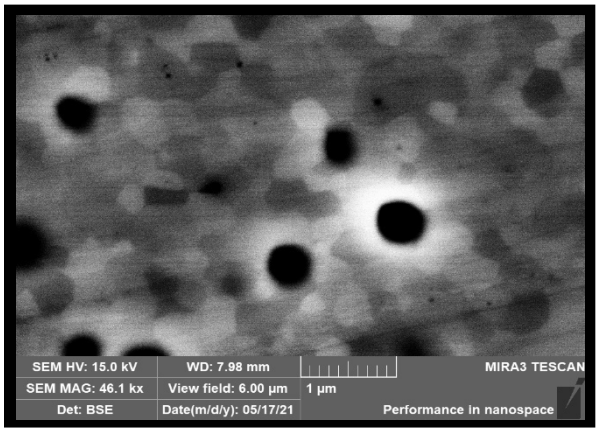

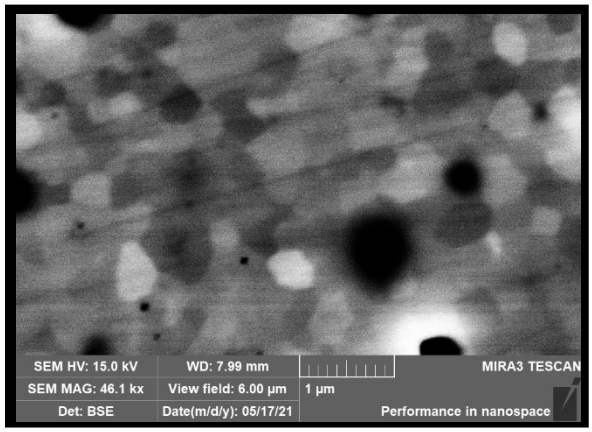

Material Properties			
Density [g/cc]	Density [%]	Grain Size [µm]	Hardness
4.56	100.00	0.28	N/A

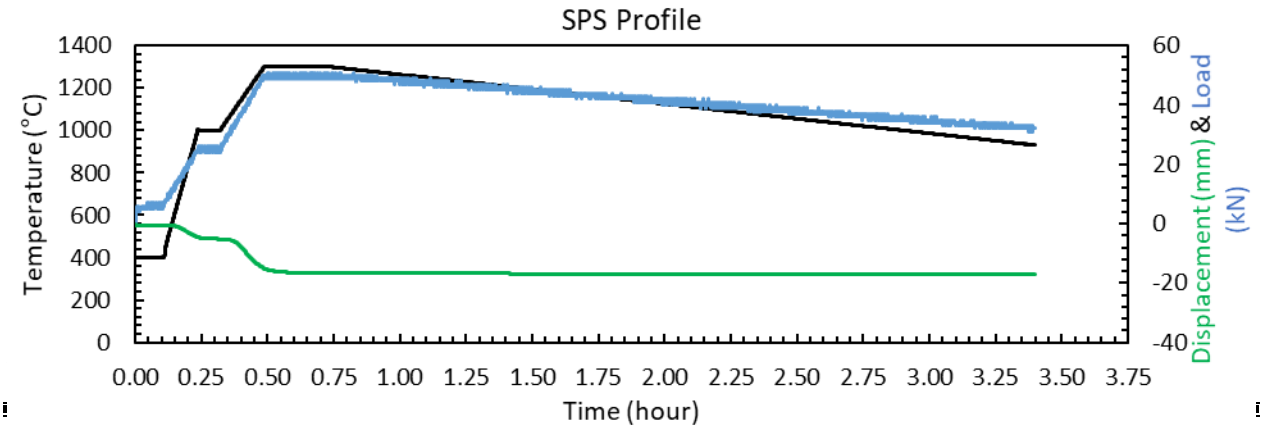

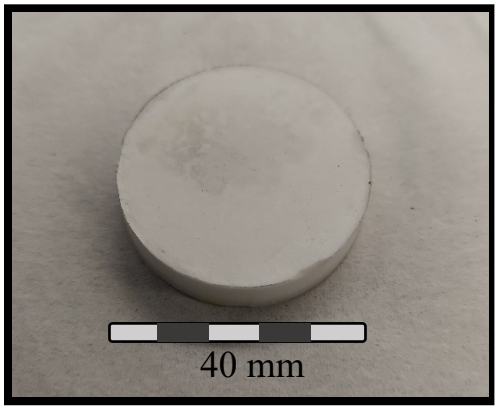

Specimen Name	Specimen Dimensions [mm]						Specimen Mass [g]
	Height	Width	Depth	X_1	X_2	X_3	
No Creep Specimens							

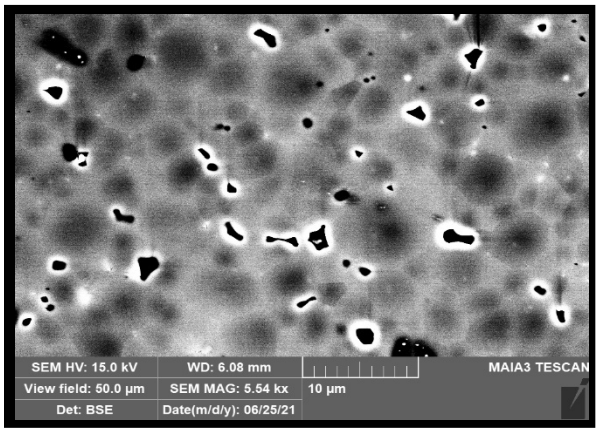

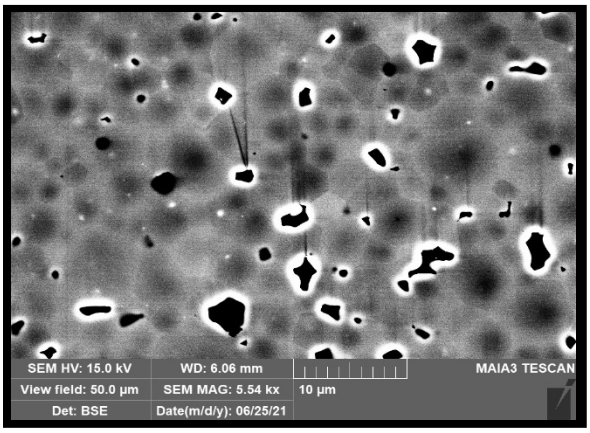

Material Properties			
Density [g/cc]	Density [%]	Grain Size [µm]	Hardness
4.51	98.95	3.07	N/A

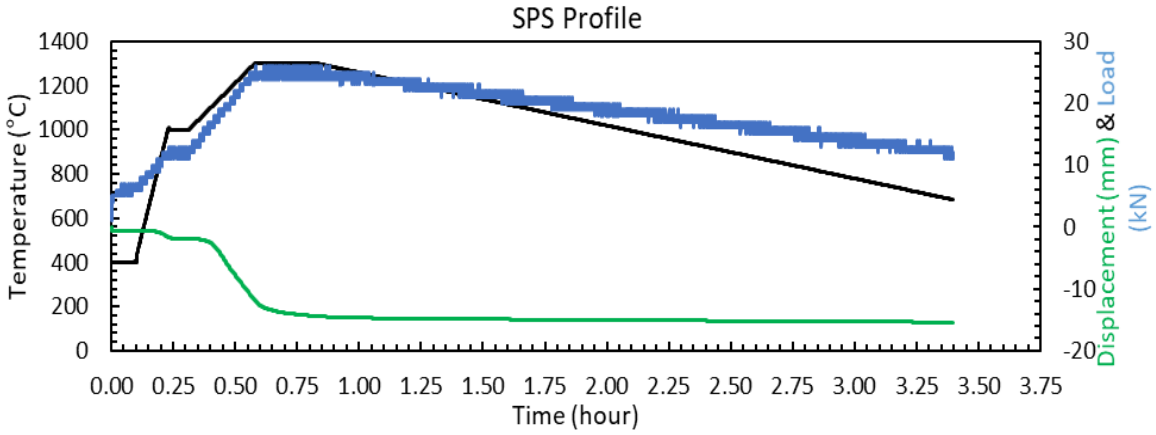

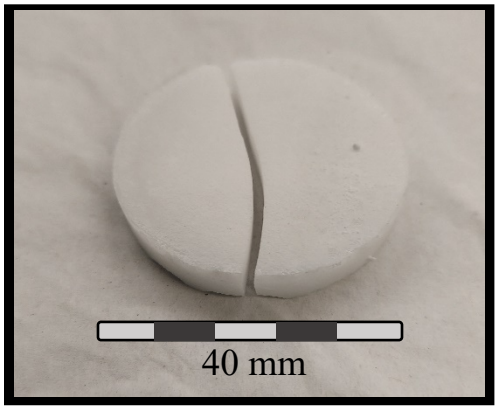

Specimen Name	Specimen Dimensions [mm]						Specimen Mass [g]
	Height	Width	Depth	X_1	X_2	X_3	
Y-13-40-1	19.06	6.61	6.61	2.82	12.34	3.12	3.730
Y-13-40-2	18.97	6.61	6.61	3.26	12.40	2.78	3.700
Y-13-40-3	19.09	6.62	6.62	3.56	12.30	2.40	3.740
Y-13-40-4	19.00	6.63	6.63	3.12	12.25	2.65	3.720
Y-13-40-5	18.95	6.62	6.62	3.12	12.48	2.76	3.680

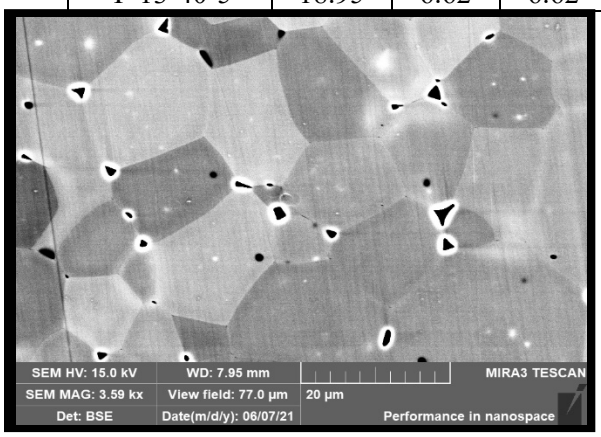

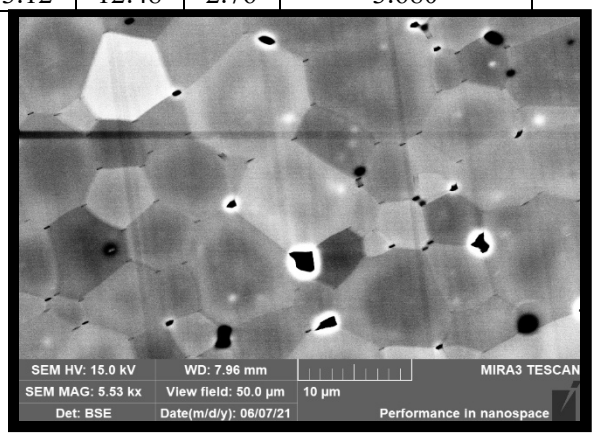

Material Properties			
Density [g/cc]	Density [%]	Grain Size [µm]	Hardness
4.46	97.85	7.99	1390

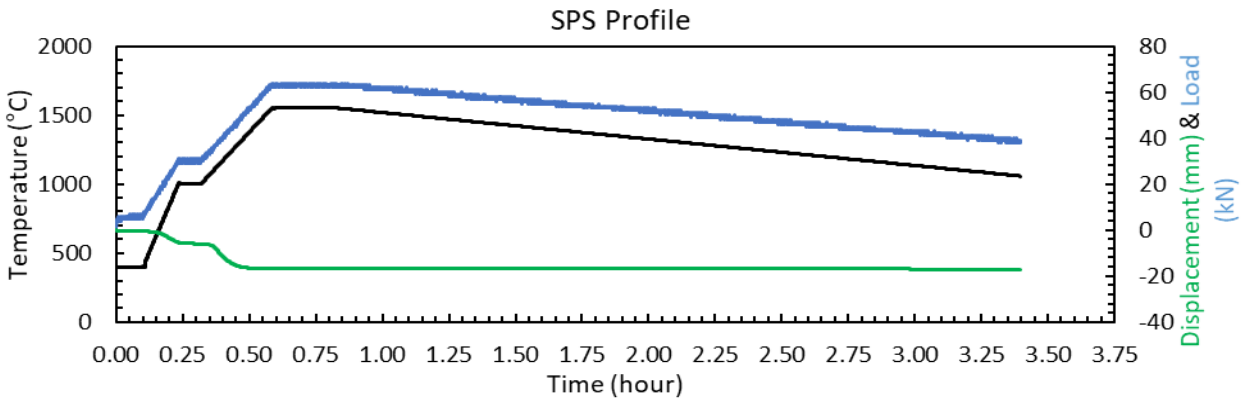

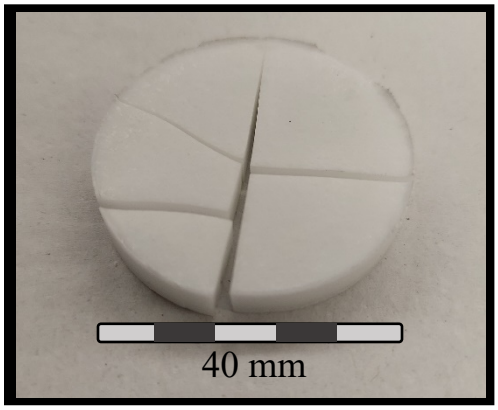

Specimen Name	Specimen Dimensions [mm]						Specimen Mass [g]
	Height	Width	Depth	X_1	X_2	X_3	
Y-14-40-1	18.98	5.54	5.55	3.14	12.34	2.77	2.600
Y-14-40-2	17.97	6.40	6.40	2.85	12.42	2.23	3.300
Y-14-40-3	18.97	6.26	6.26	2.39	12.42	3.61	3.300
Y-14-40-4	17.87	6.41	6.41	2.14	12.30	2.82	3.240

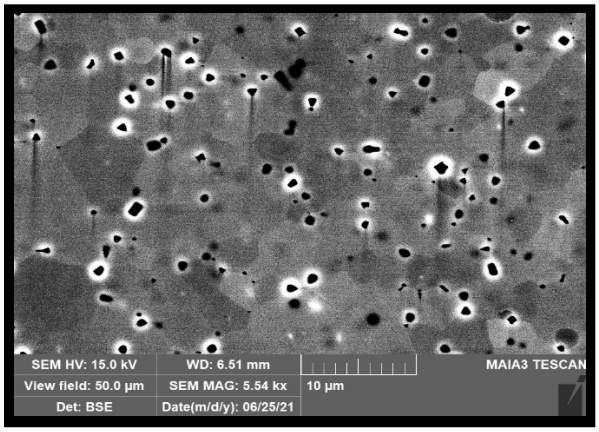

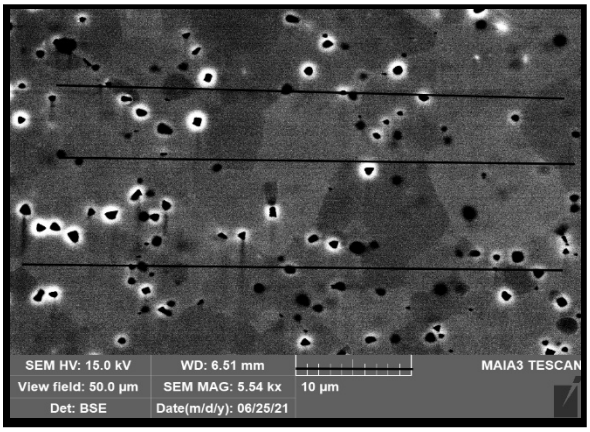

Material Properties			
Density [g/cc]	Density [%]	Grain Size [µm]	Hardness
4.54	99.62	3.19	N/A

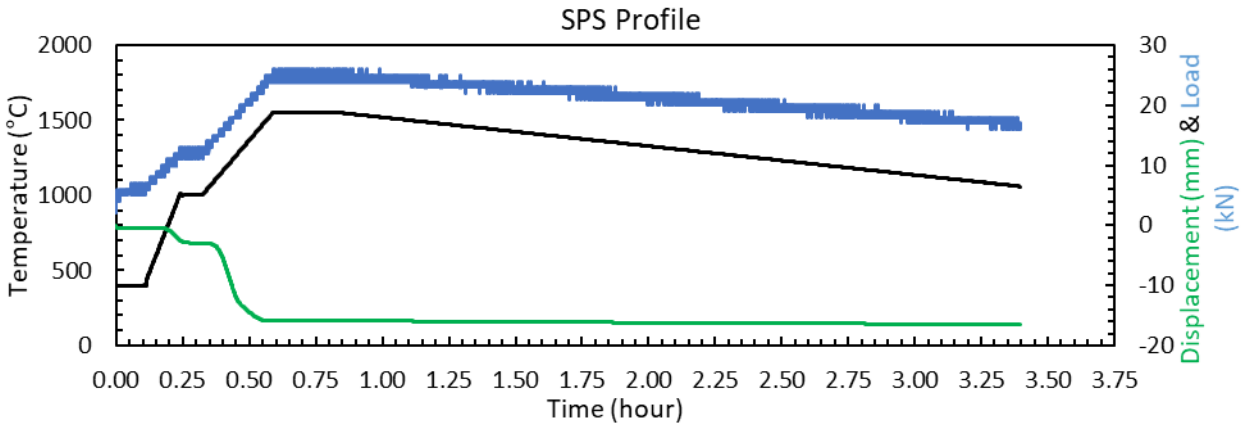

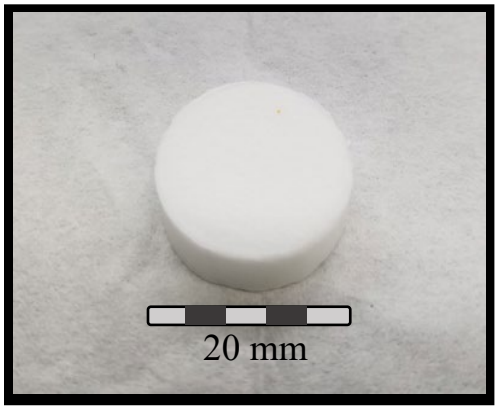

Specimen Name	Specimen Dimensions [mm]						Mass [g]
	Height	Width	Depth	X_1	X_2	X_3	
Y-Yb-1-20-1	18.96	6.49	6.56	2.69	12.08	2.91	3.610

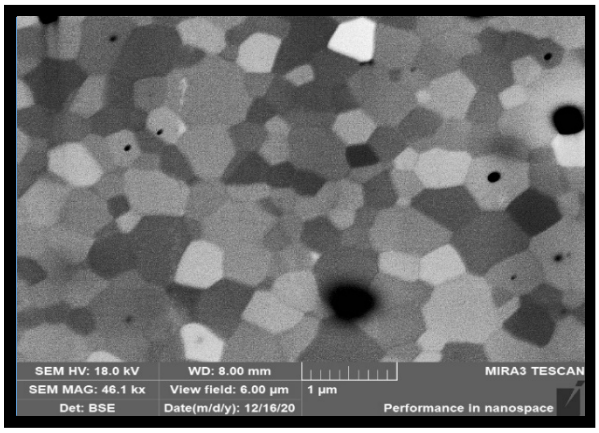

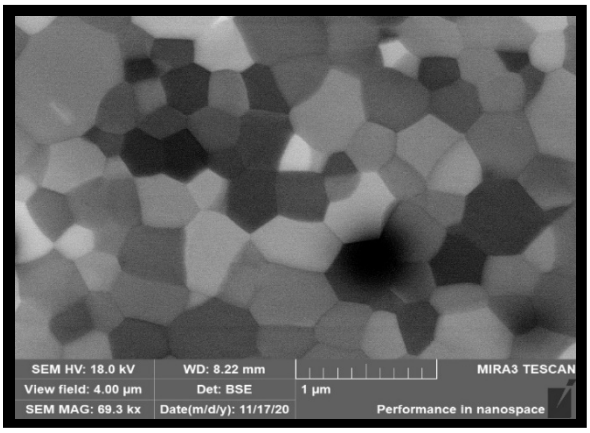

Material Properties			
Density [g/cc]	Density [%]	Grain Size [µm]	Hardness
4.56	99.96	0.39	1651

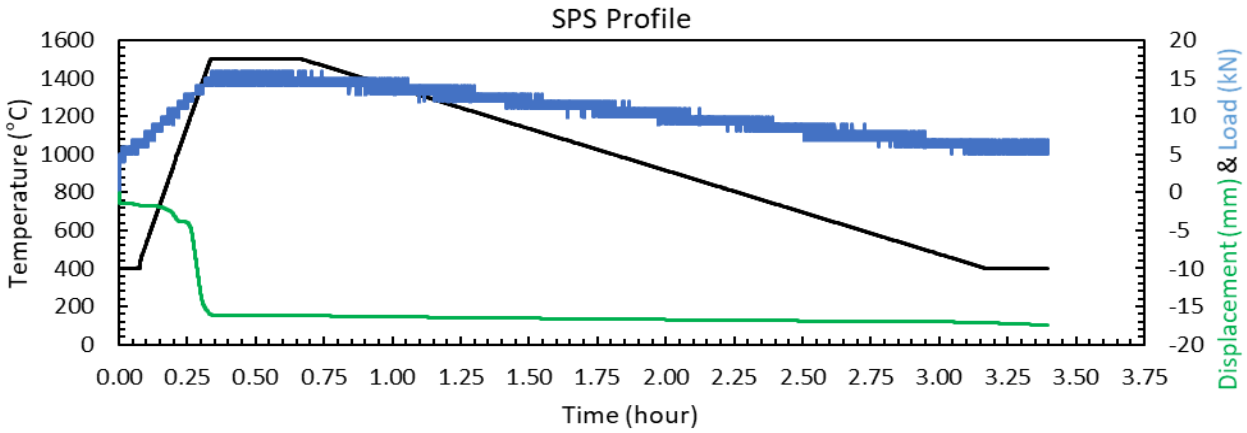

Specimen Name	Specimen Dimensions [mm]						Mass [g]
	Height	Width	Depth	X_1	X_2	X_3	
Y-Yb-2-25-1	18.98	6.47	6.56	2.71	12.11	2.98	3.630
Y-Yb-2-25-2	19.06	6.49	6.49	2.92	12.10	2.74	3.540

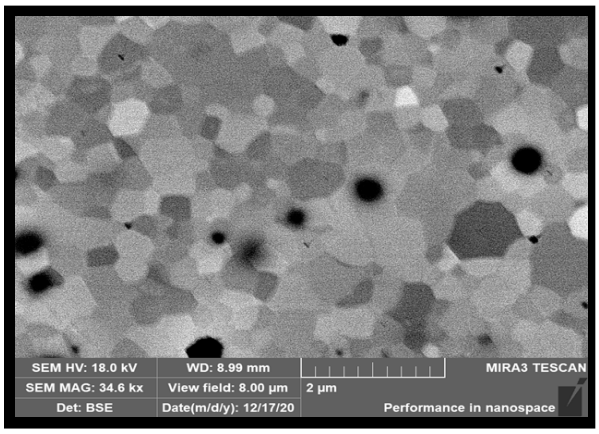

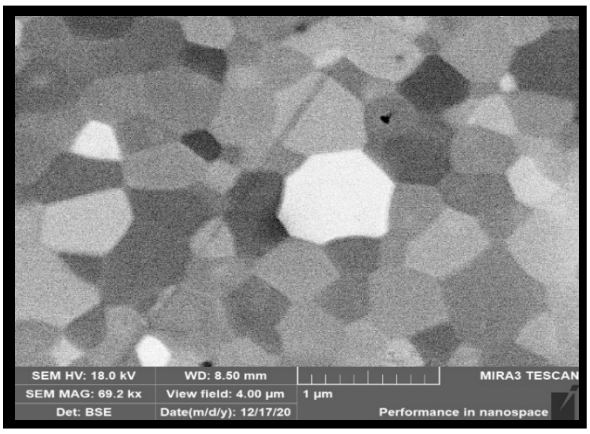

Material Properties			
Density [g/cc]	Density [%]	Grain Size [µm]	Hardness
4.59	100.00	0.38	1743

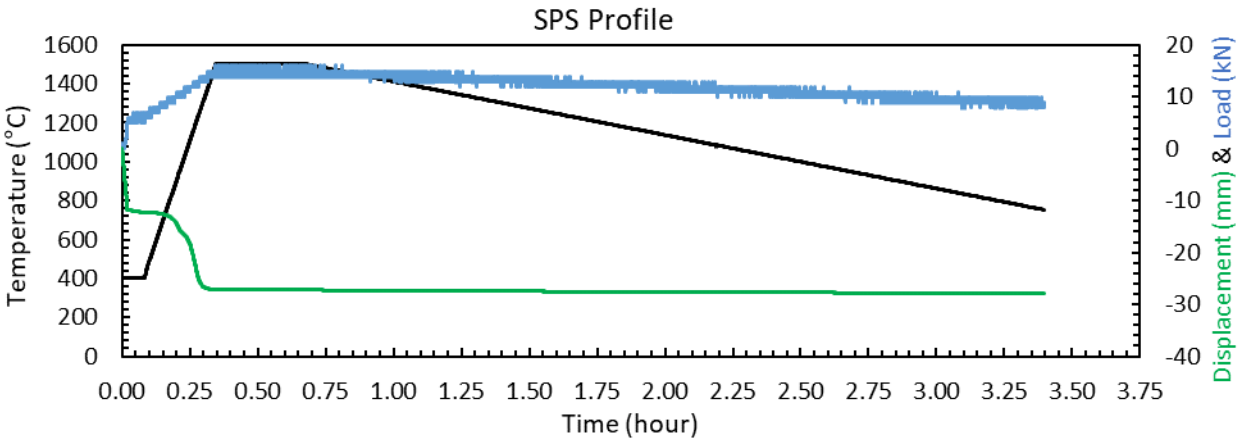

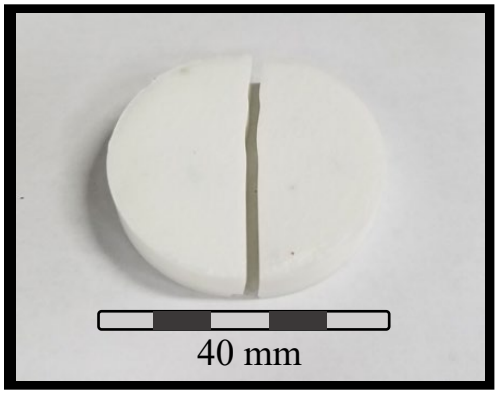

Specimen Name	Specimen Dimensions [mm]						Mass [g]
	Height	Width	Depth	X_1	X_2	X_3	
Y-Yb-3-40-1	16.84	6.21	6.22	1.67	11.71	1.60	2.903
Y-Yb-3-40-2	19.63	6.38	6.37	3.02	11.73	2.94	3.573
Y-Yb-3-40-3	18.71	6.50	6.52	2.60	11.74	2.53	3.535
Y-Yb-3-40-4	18.15	6.48	6.49	2.30	11.73	2.31	3.412

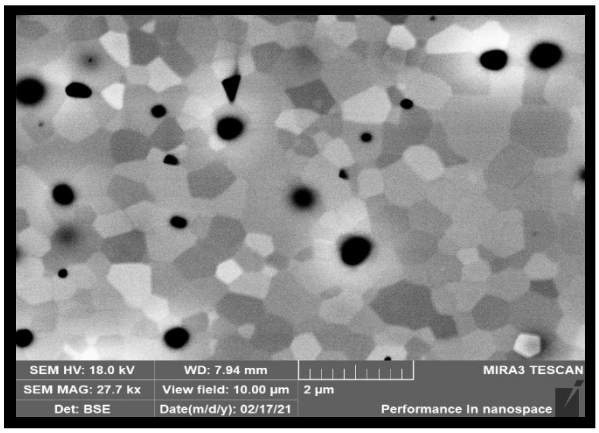

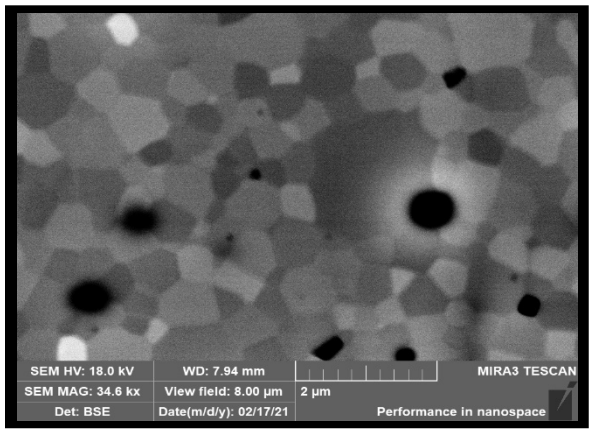

Material Properties			
Density [g/cc]	Density [%]	Grain Size [µm]	Hardness
4.54	99.48	0.48	1701

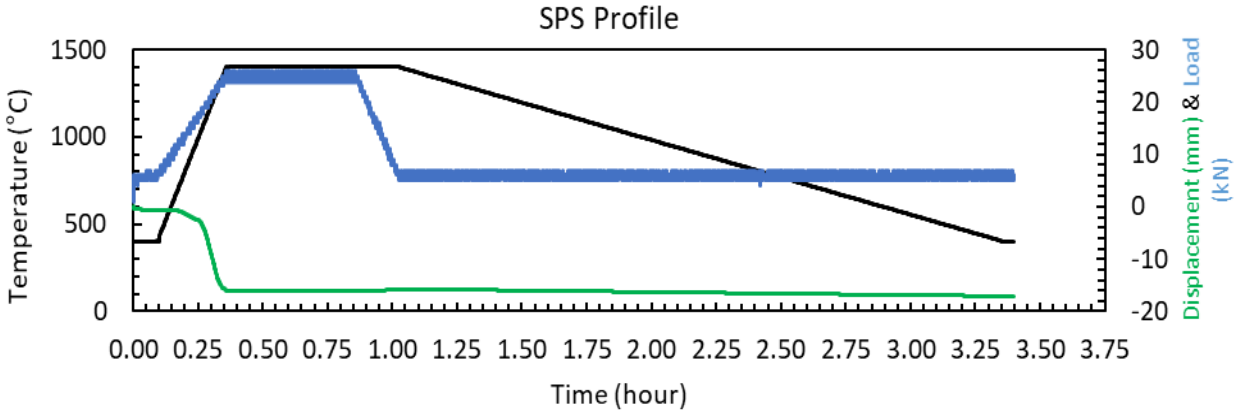

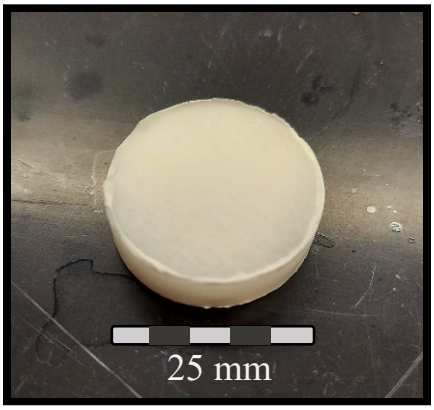

Specimen Name	Specimen Dimensions [mm]						Mass [g]
	Height	Width	Depth	X_1	X_2	X_3	
Y-Yb-4-25-1	20.51	6.83	6.83	3.41	11.76	3.53	4.315
Y-Yb-4-25-2	21.41	6.87	6.87	3.99	11.80	3.91	4.540

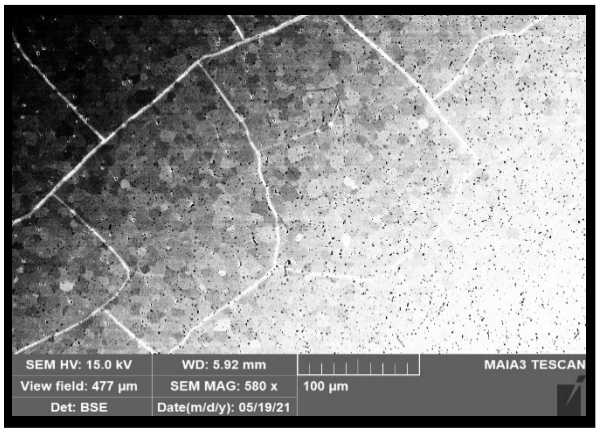

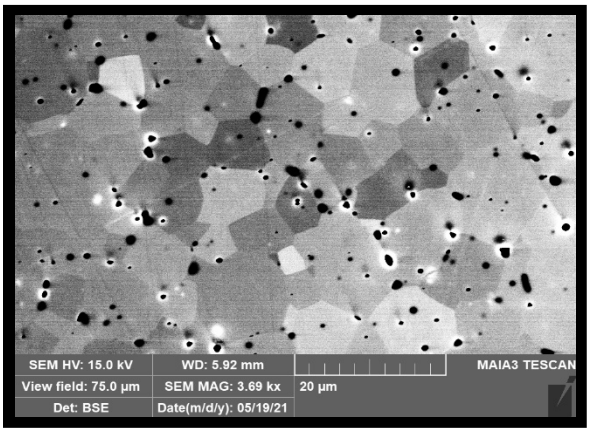

Material Properties			
Density [g/cc]	Density [%]	Grain Size [µm]	Hardness
4.57	100.00	4.83	1442

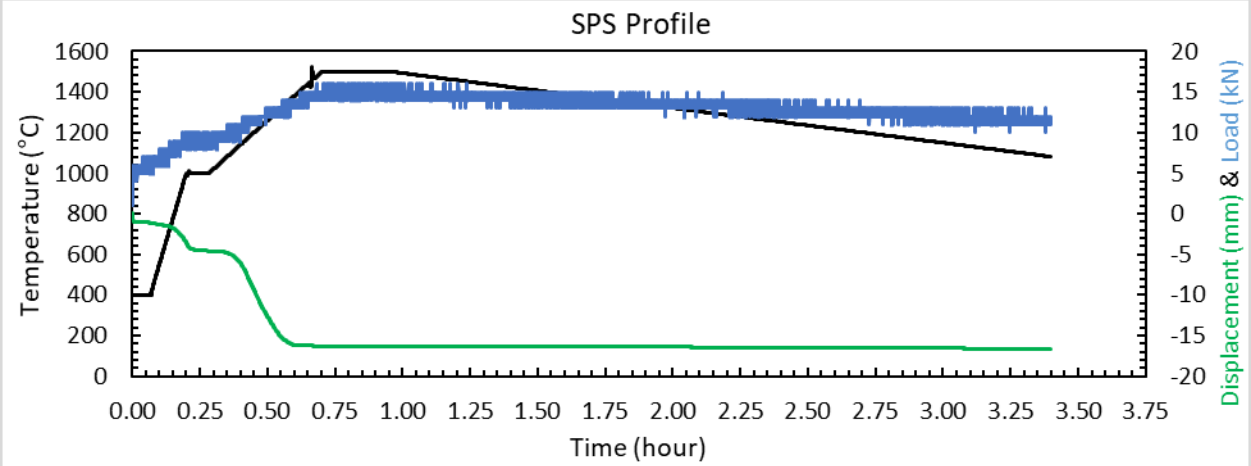

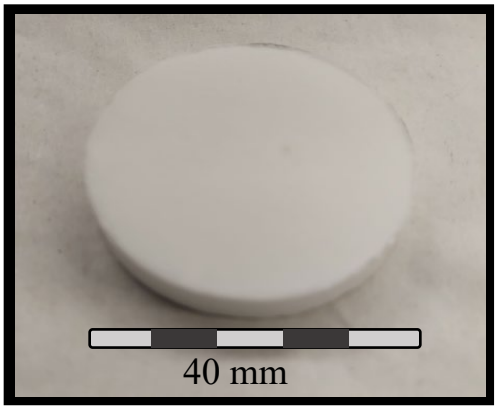

Specimen Name	Specimen Dimensions [mm]						Mass [g]
	Height	Width	Depth	X_1	X_2	X_3	
Y-Yb-5-25-1	18.99	6.49	6.45	3.10	12.40	2.71	3.630
Y-Yb-5-25-2	18.97	6.49	6.49	3.05	12.45	2.75	3.600
Y-Yb-5-25-3	18.87	6.48	6.48	2.81	12.46	3.15	3.550
Y-Yb-5-25-4	18.97	6.44	6.44	2.91	12.44	3.10	3.590

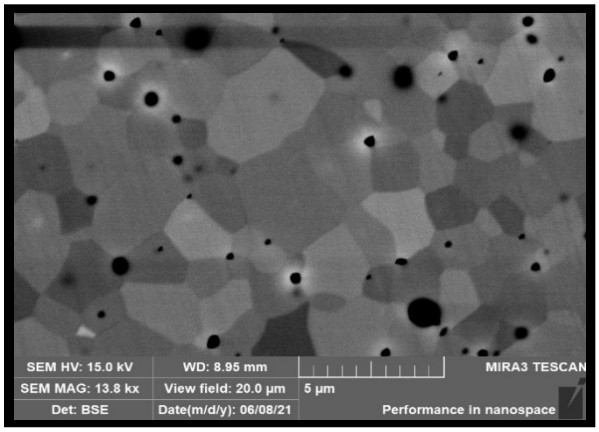

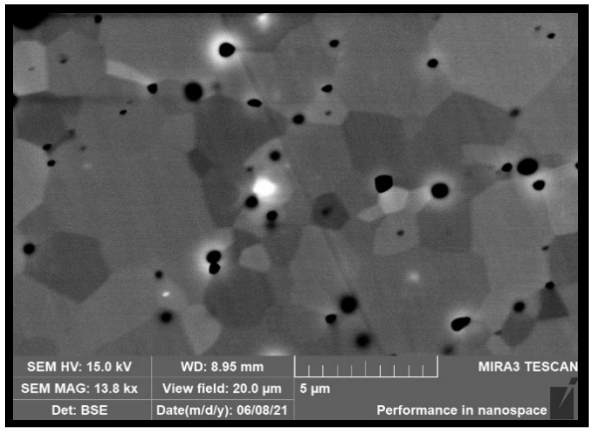

Material Properties			
Density [g/cc]	Density [%]	Grain Size [µm]	Hardness
4.50	98.76	1.38	1701

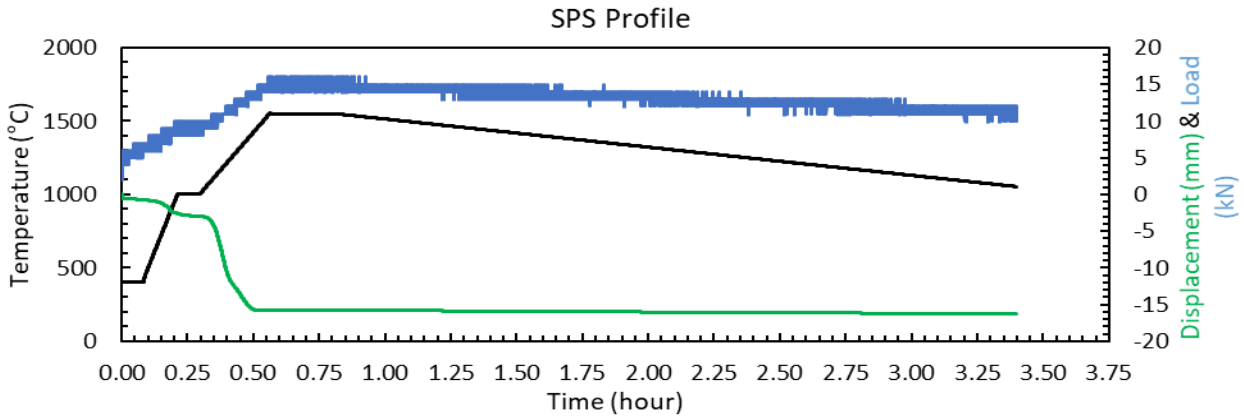

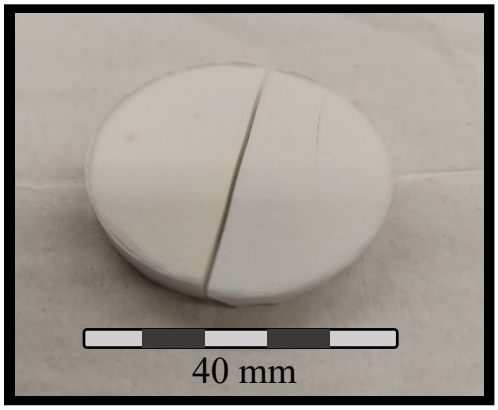

Specimen Name	Specimen Dimensions [mm]						Mass [g]
	Height	Width	Depth	X_1	X_2	X_3	
Y-Yb-6-40-1	20.04	6.14	6.14	3.27	11.74	3.29	3.372
Y-Yb-6-40-2	19.59	6.14	6.16	2.95	11.75	3.01	3.318
Y-Yb-6-40-3	18.94	6.15	6.15	2.68	11.75	2.71	3.203

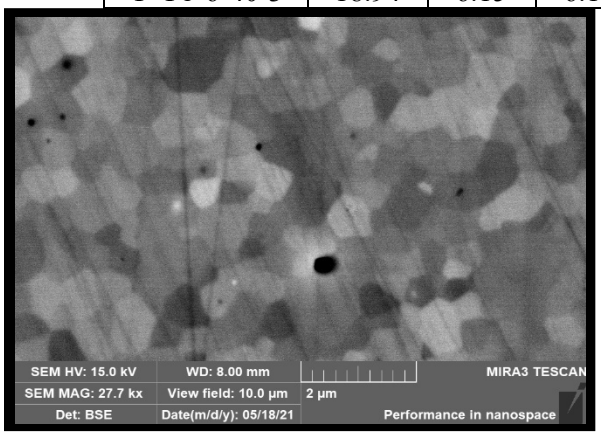

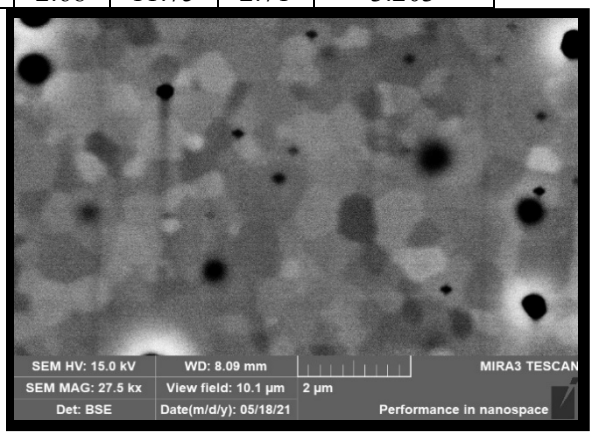

Material Properties			
Density [g/cc]	Density [%]	Grain Size [µm]	Hardness
4.52	99.21	0.51	1587

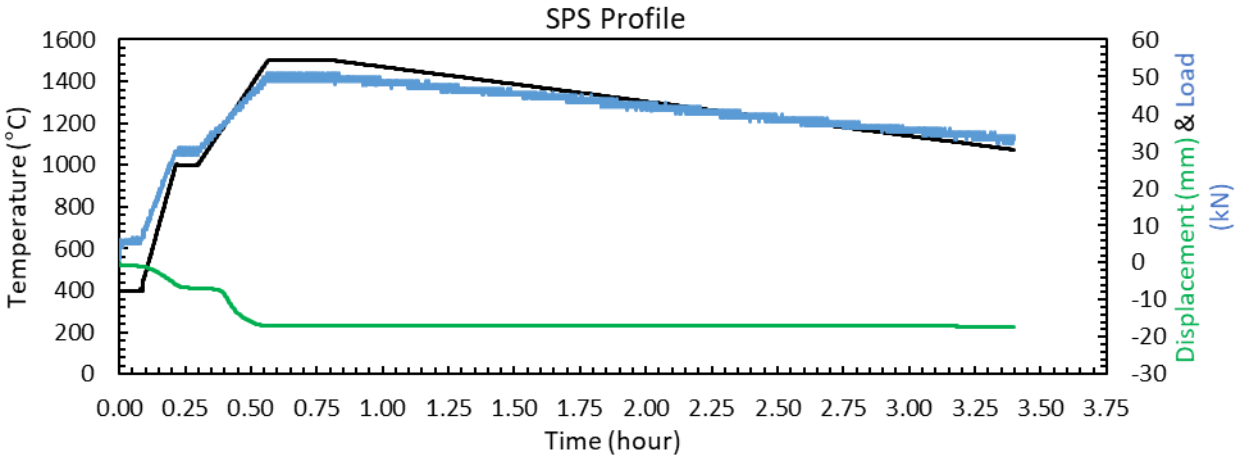

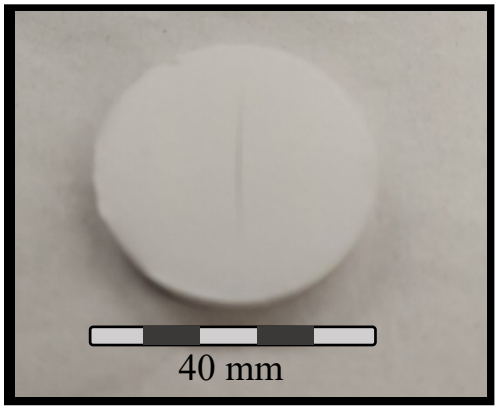

Specimen Name	Specimen Dimensions [mm]						Mass [g]
	Height	Width	Depth	X_1	X_2	X_3	
Y-Yb-7-40-1	18.94	6.47	6.47	3.08	12.33	2.89	3.510
Y-Yb-7-40-2	19.01	6.50	6.50	3.01	12.23	2.99	3.590
Y-Yb-7-40-3	18.64	6.34	6.34	2.65	11.89	3.34	3.220

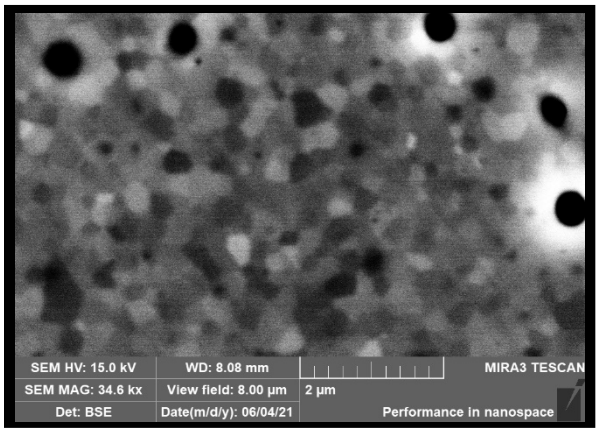

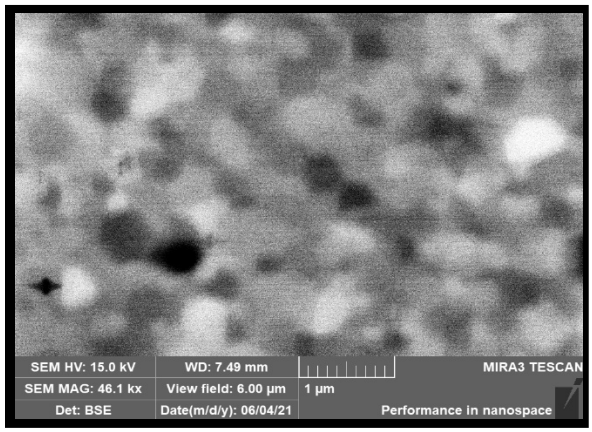

Material Properties			
Density [g/cc]	Density [%]	Grain Size [µm]	Hardness
4.47	97.97	0.37	1747

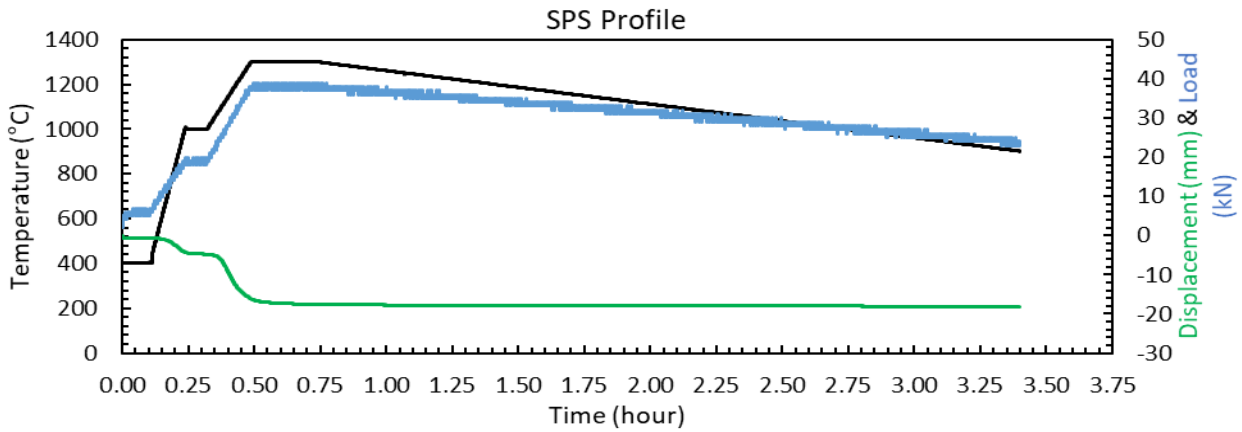

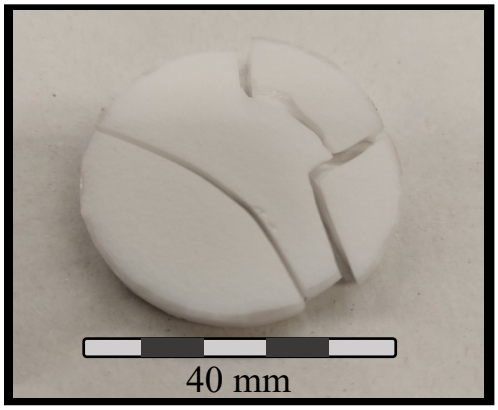

Specimen Name	Specimen Dimensions [mm]						Mass [g]
	Height	Width	Depth	X_1	X_2	X_3	
Y-Yb-8-40-1	19.20	6.00	6.01	2.54	11.81	3.10	3.096

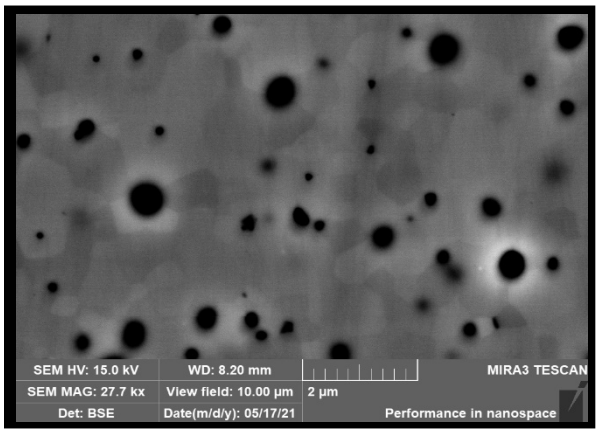

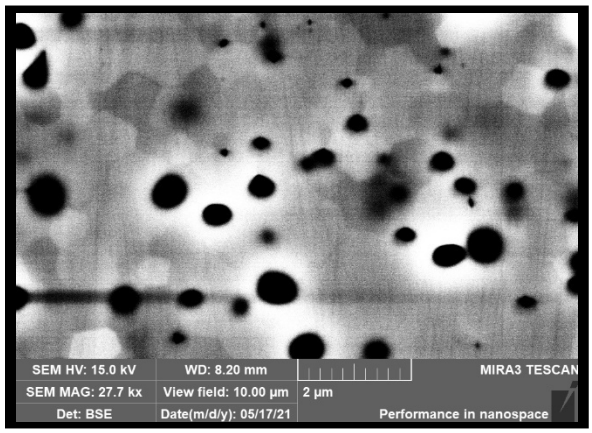

Material Properties			
Density [g/cc]	Density [%]	Grain Size [µm]	Hardness
4.56	100.00	0.53	N/A

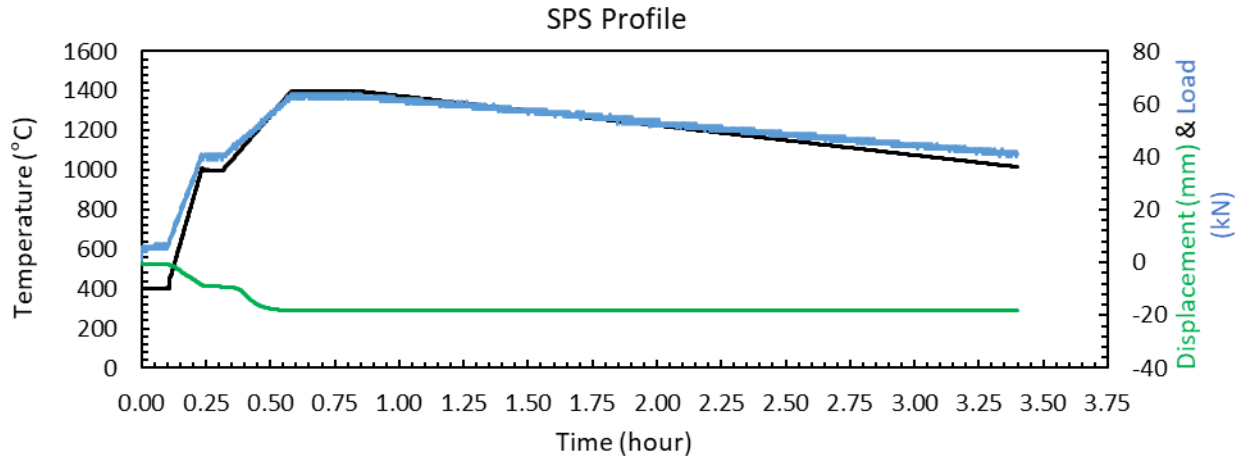

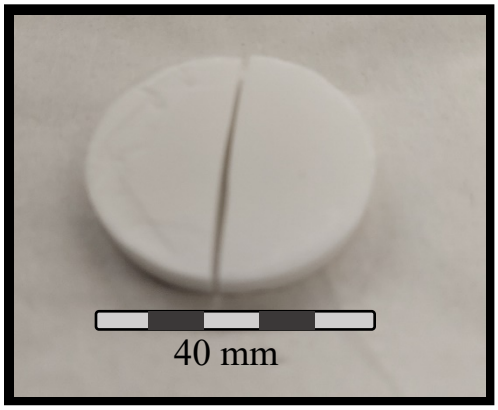

Specimen Name	Specimen Dimensions [mm]						Mass [g]
	Height	Width	Depth	X_1	X_2	X_3	
Y-Yb-9-40-1	18.78	5.45	5.45	2.59	12.59	3.10	2.530
Y-Yb-9-40-2	18.57	5.47	5.47	2.43	12.32	2.91	2.510
Y-Yb-9-40-3	18.87	5.47	5.47	2.75	12.40	3.00	2.540

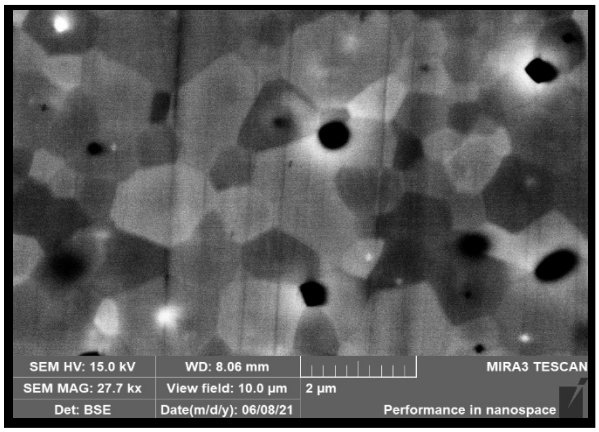

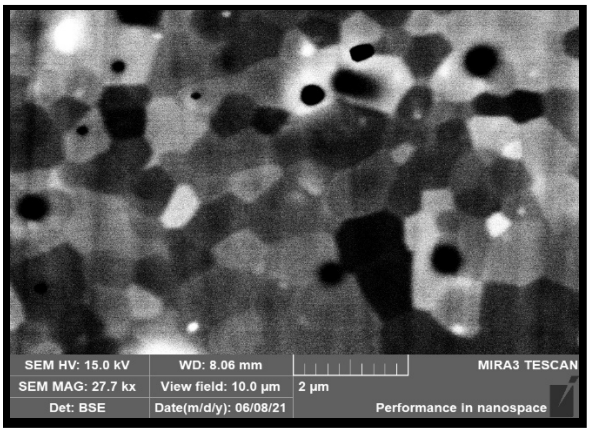

Material Properties			
Density [g/cc]	Density [%]	Grain Size [µm]	Hardness
4.53	99.45	0.63	1634

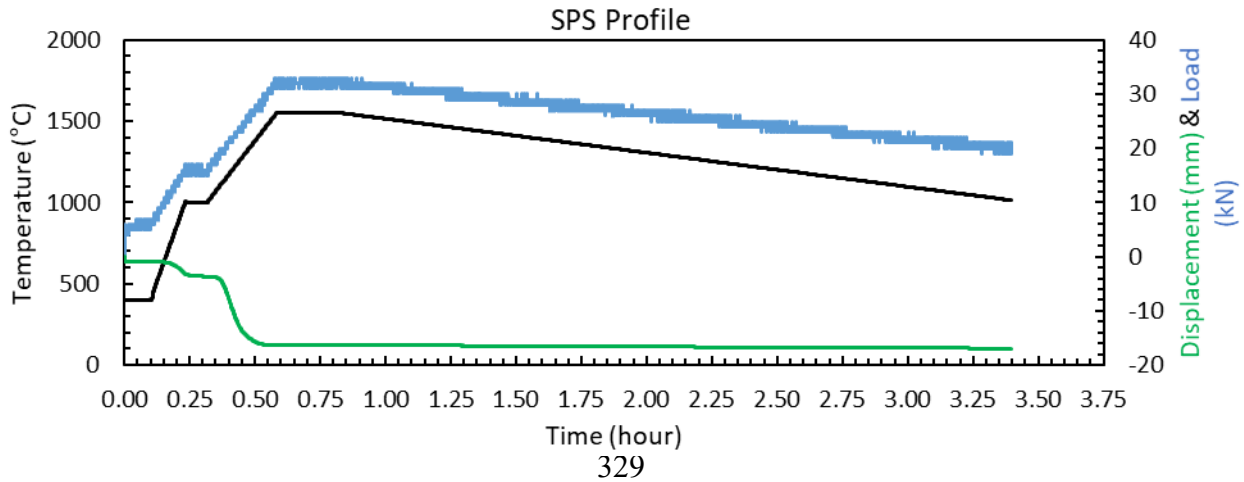

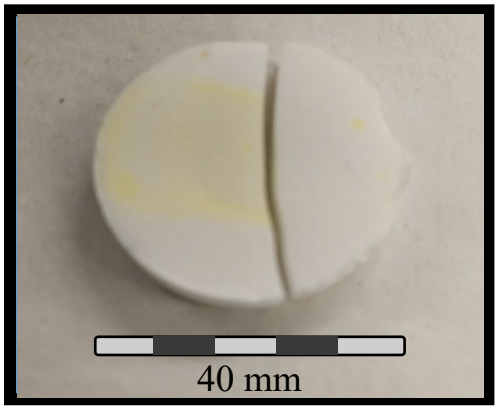

Specimen Name	Specimen Dimensions [mm]						Mass [g]
	Height	Width	Depth	X_1	X_2	X_3	
Y-Yb-10-40-1	19.19	6.48	6.48	3.03	12.55	3.20	3.680
Y-Yb-10-40-2	18.94	6.54	6.54	2.72	12.56	3.20	3.620
Y-Yb-10-40-3	19.05	6.48	6.48	2.96	3.05	12.44	3.650

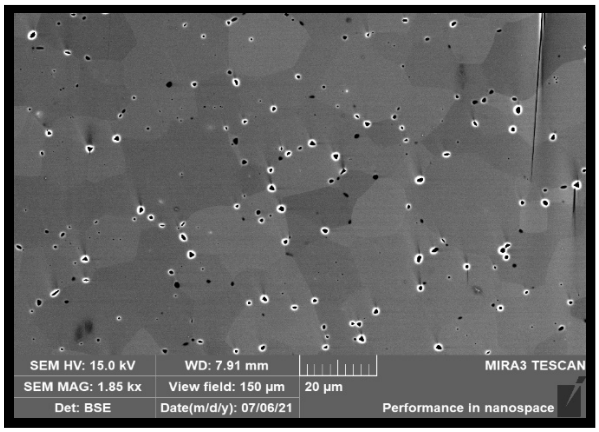

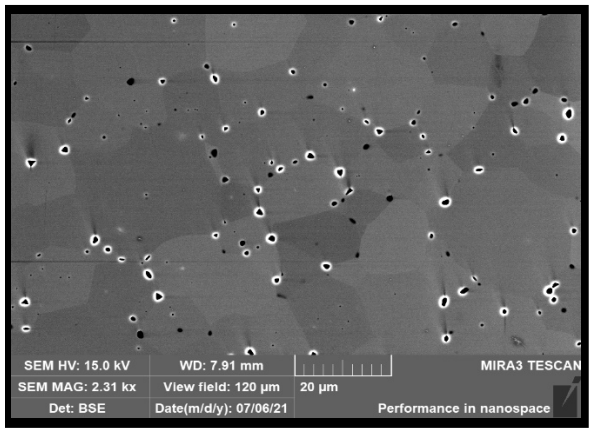

Material Properties			
Density [g/cc]	Density [%]	Grain Size [µm]	Hardness
4.54	99.52	15.02	N/A

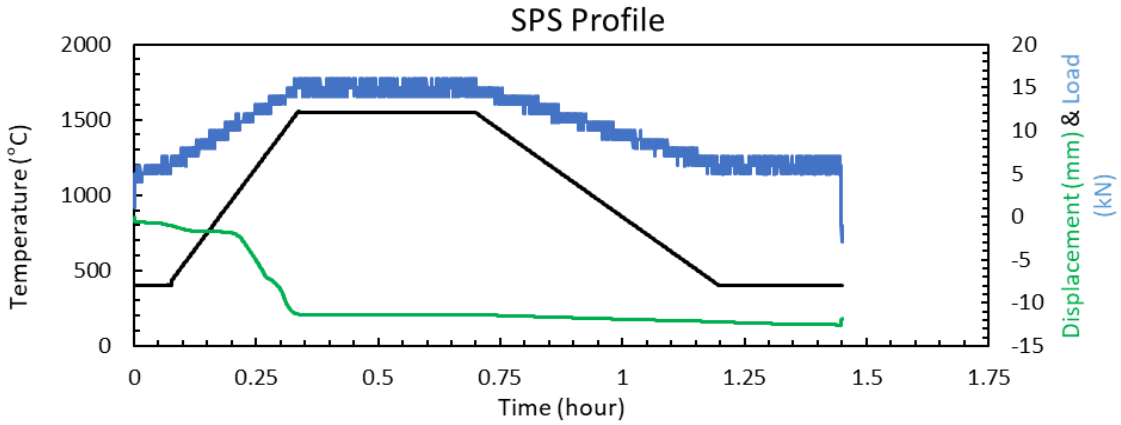

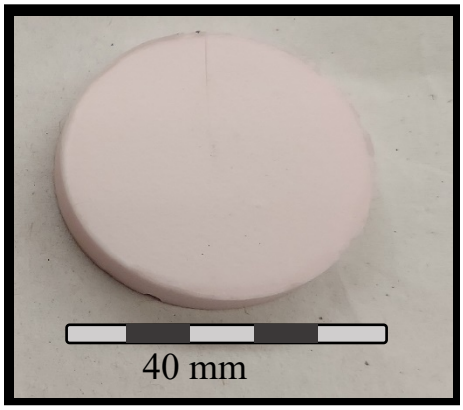

Specimen Name	Specimen Dimensions [mm]						Mass [g]
	Height	Width	Depth	X_1	X_2	X_3	
Y-Er-1-40-1	18.05	6.38	6.39	2.36	11.82	2.16	3.232
Y-Er-1-40-2	16.92	6.74	6.76	2.01	10.76	2.38	3.383

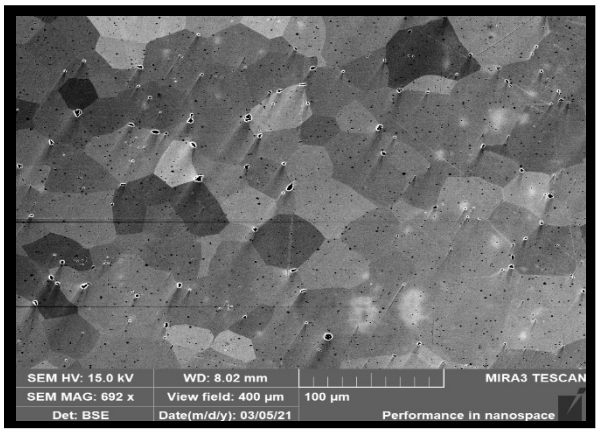

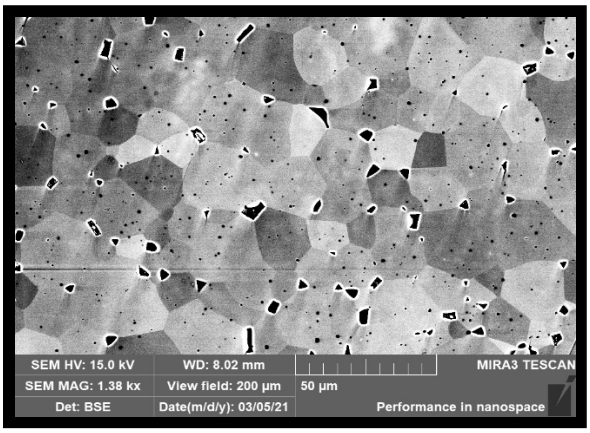

Material Properties			
Density [g/cc]	Density [%]	Grain Size [µm]	Hardness
4.47	97.93	24.30	1627

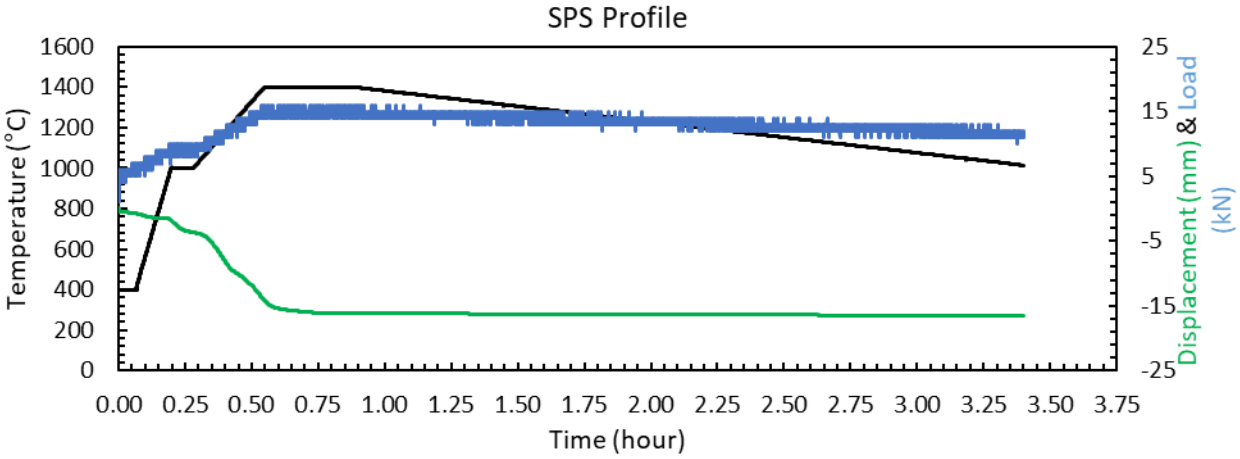

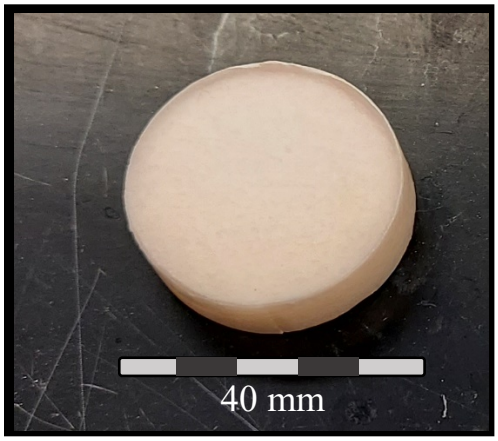

Specimen Name	Specimen Dimensions [mm]						Mass [g]
	Height	Width	Depth	X_1	X_2	X_3	
Y-Er-2-40-1	19.20	6.56	6.55	2.76	11.75	2.84	3.675
Y-Er-2-40-2	18.95	6.54	6.54	2.69	11.76	2.69	3.599

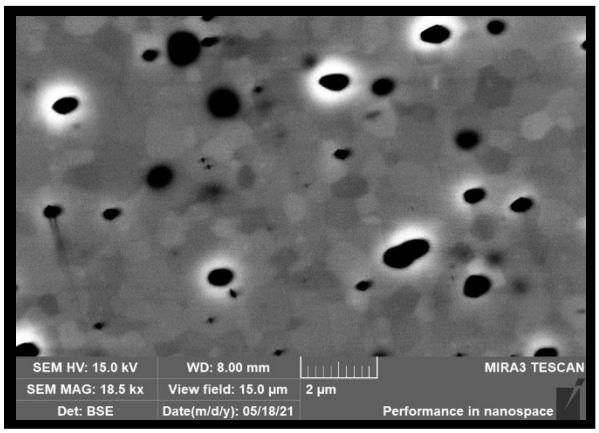

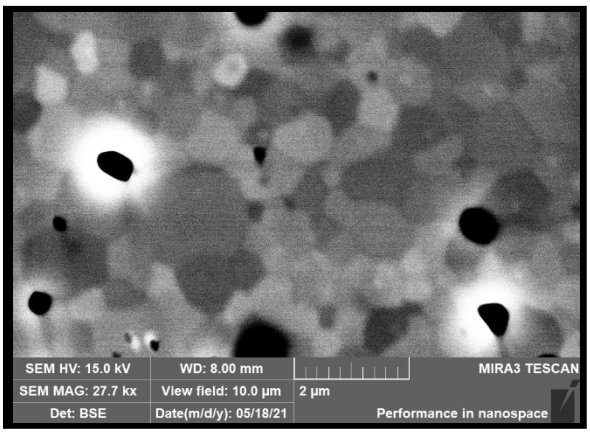

Material Properties			
Density [g/cc]	Density [%]	Grain Size [µm]	Hardness
4.55	99.72	0.50	N/A

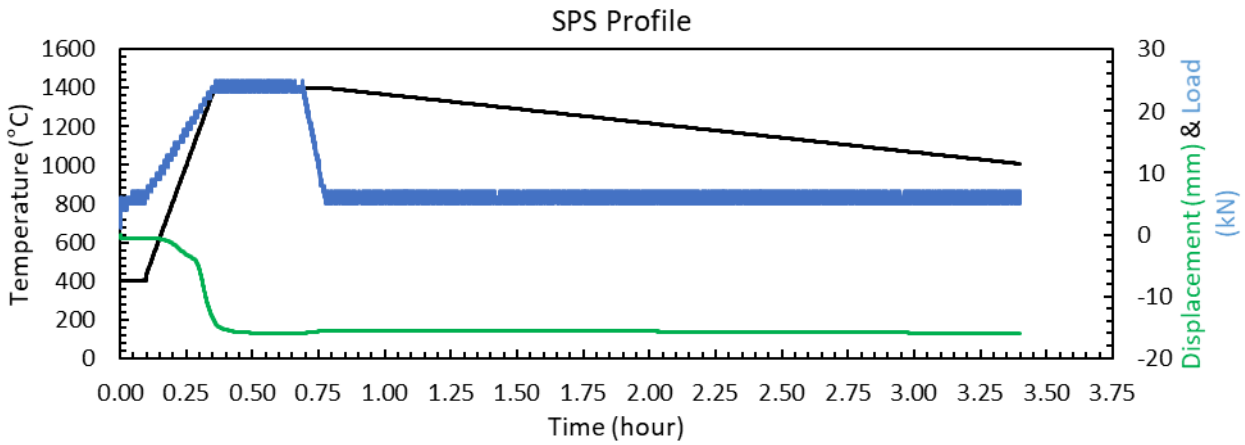

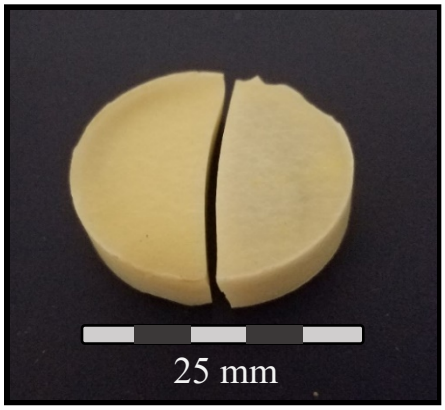

Specimen Name	Specimen Dimensions [mm]						Mass [g]
	Height	Width	Depth	X_1	X_2	X_3	
Y-Er-3-25-1	18.65	6.47	6.45	2.48	11.75	2.44	3.460
Y-Er-3-25-2	21.83	6.49	6.49	4.14	11.74	4.14	4.109

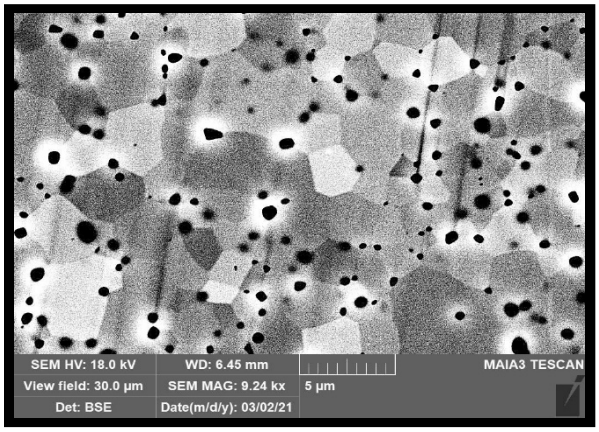

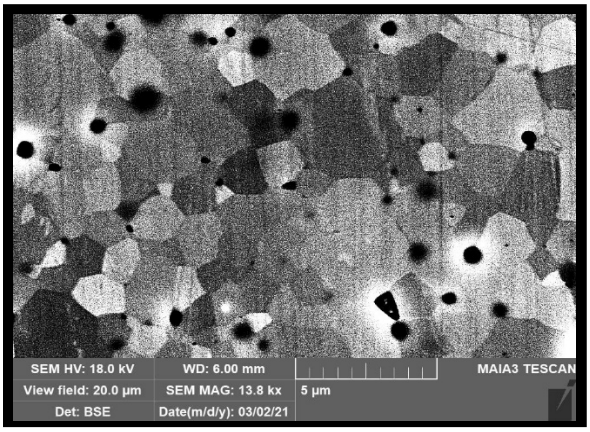

Material Properties			
Density [g/cc]	Density [%]	Grain Size [µm]	Hardness
4.80	100.00	1.28	1520

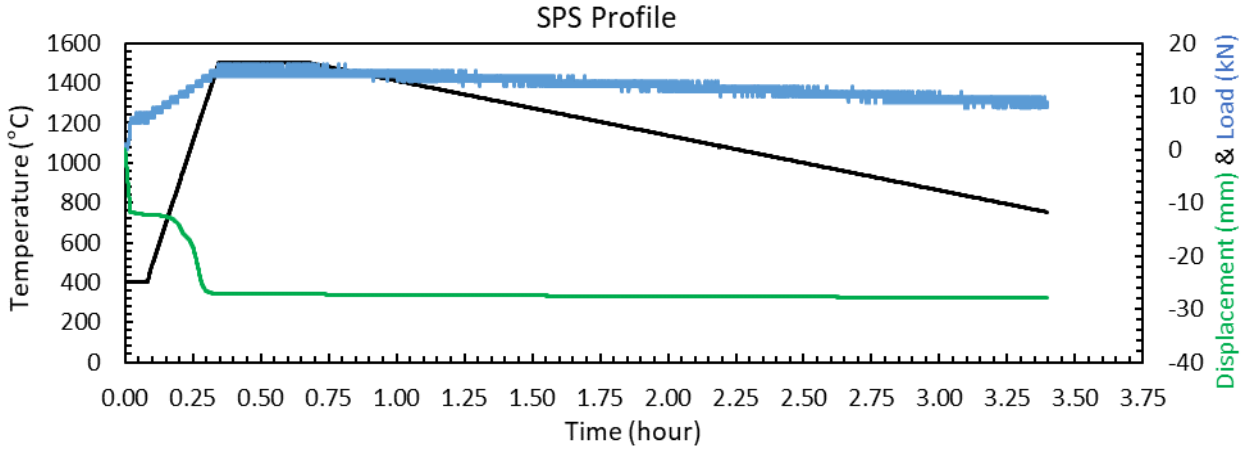

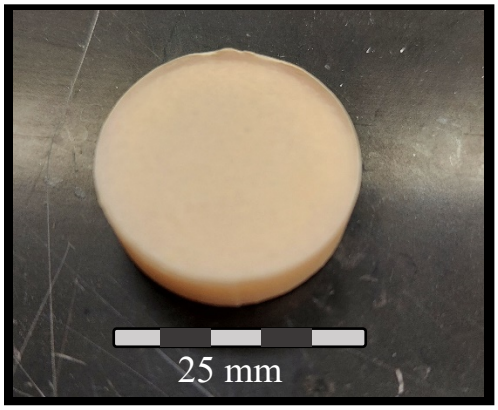

Specimen Name	Specimen Dimensions [mm]						Mass [g]
	Height	Width	Depth	X_1	X_2	X_3	
Y-Er-4-25-1	18.03	6.79	6.79	2.64	11.17	2.61	3.728
Y-Er-4-25-2	20.44	6.99	6.99	3.52	11.76	3.43	4.478

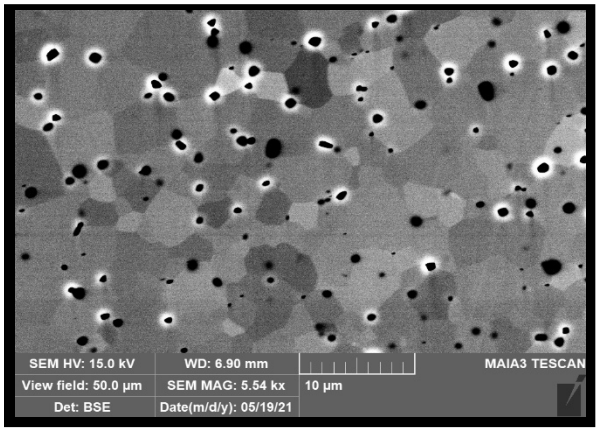

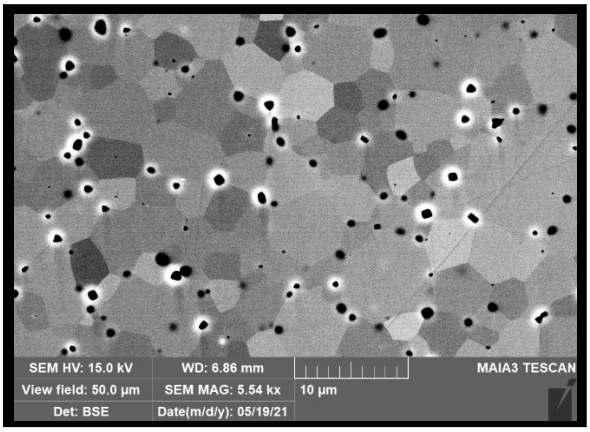

Material Properties			
Density [g/cc]	Density [%]	Grain Size [µm]	Hardness
4.61	100.00	2.83	1476

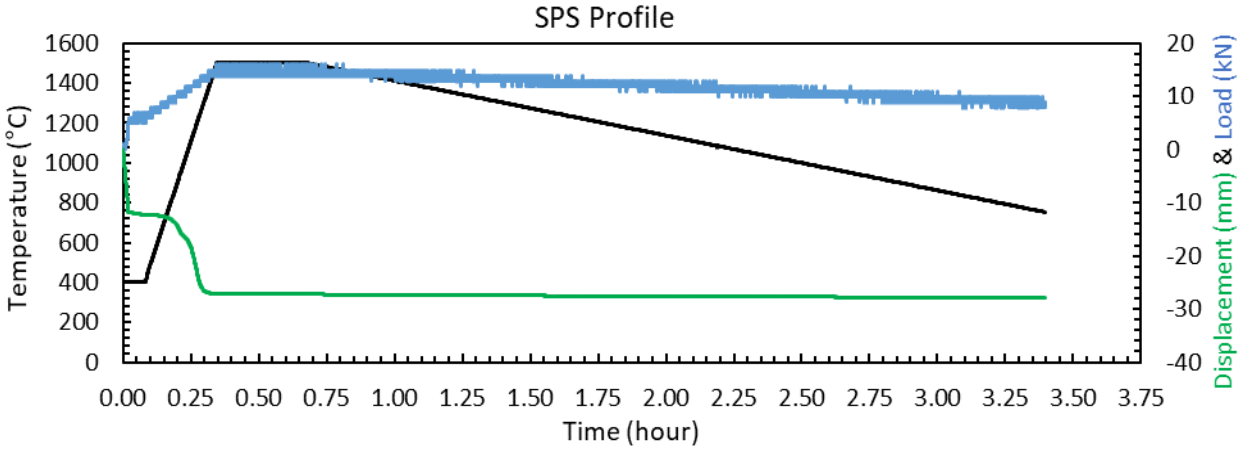

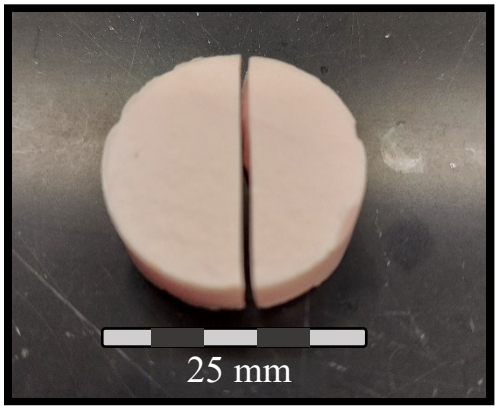

Specimen Name	Specimen Dimensions [mm]						Mass [g]
	Height	Width	Depth	X_1	X_2	X_3	
No Creep Specimens							

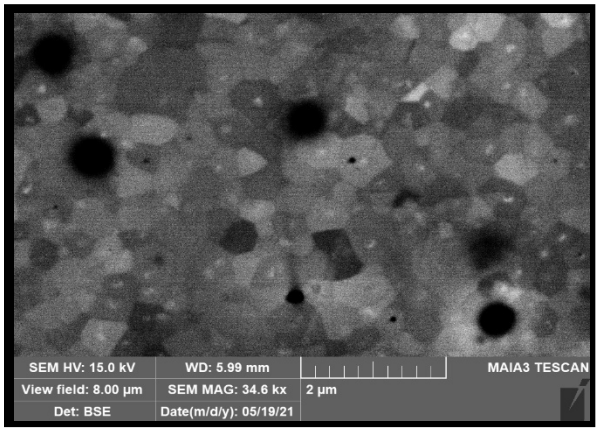

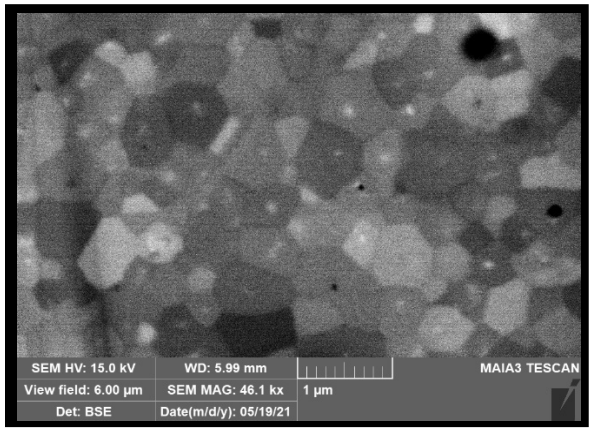

Material Properties			
Density [g/cc]	Density [%]	Grain Size [µm]	Hardness
N/A	N/A	0.33	N/A

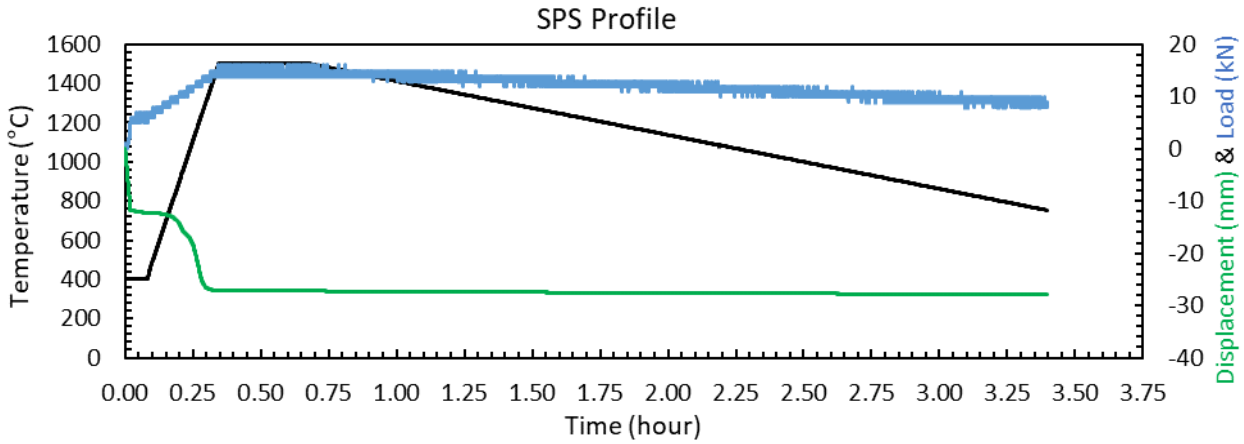

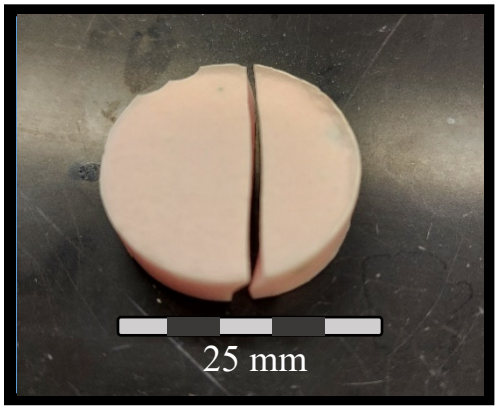

Specimen Name	Specimen Dimensions [mm]						Mass [g]
	Height	Width	Depth	X_1	X_2	X_3	
Y-Er-6-25-1	18.07	6.89	6.87	2.53	11.06	2.60	3.840

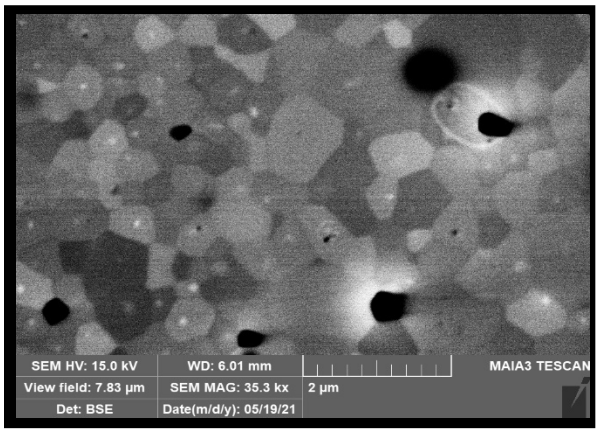

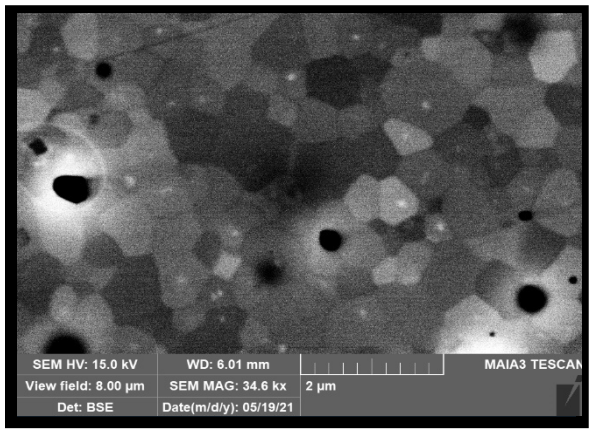

Material Properties			
Density [g/cc]	Density [%]	Grain Size [µm]	Hardness
4.58	100.00	0.47	N/A

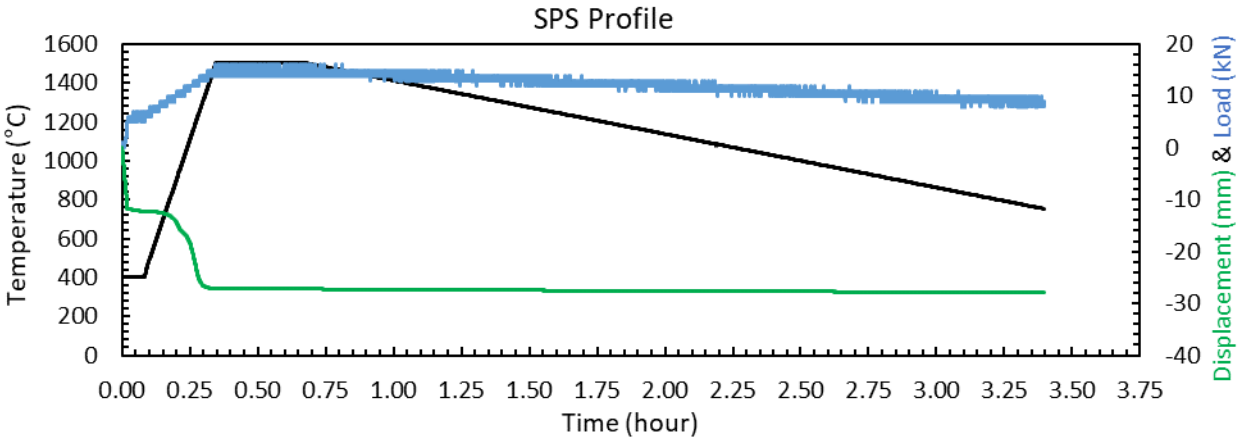

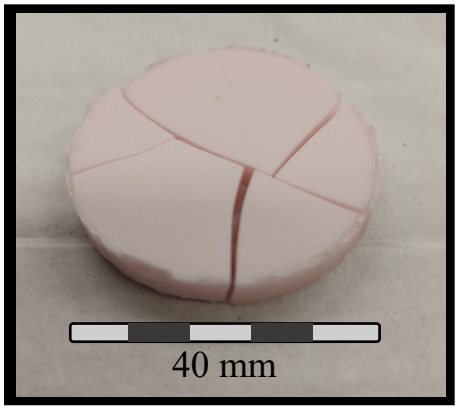

Specimen Name	Specimen Dimensions [mm]						Mass [g]
	Height	Width	Depth	X_1	X_2	X_3	
Y-Er-7-40-1	19.12	5.98	5.98	2.78	11.74	2.76	3.035
Y-Er-7-40-2	19.33	5.99	5.99	2.88	11.86	2.90	3.060
Y-Er-7-40-3	18.69	6.14	6.14	2.72	11.58	2.73	3.030

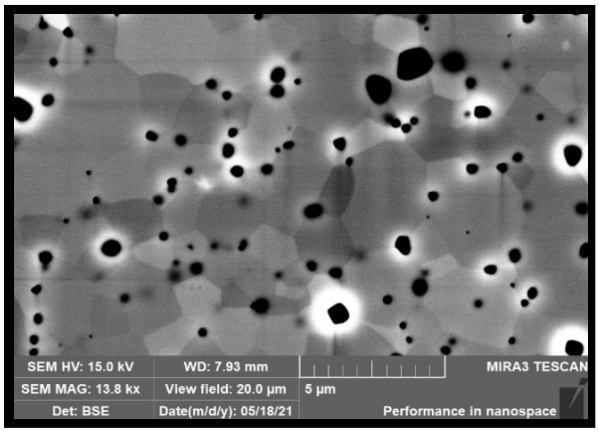

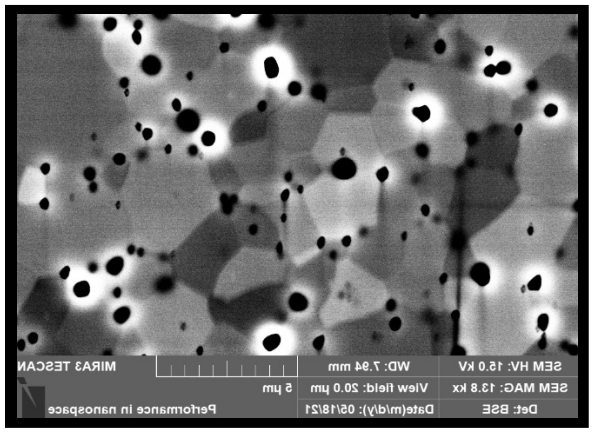

Material Properties			
Density [g/cc]	Density [%]	Grain Size [µm]	Hardness
4.53	99.34	1.87	1436

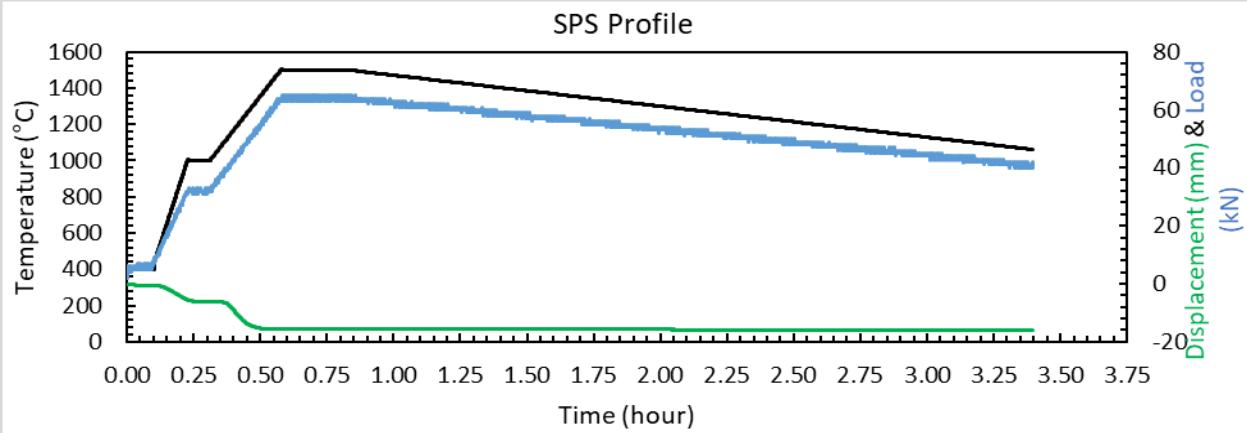

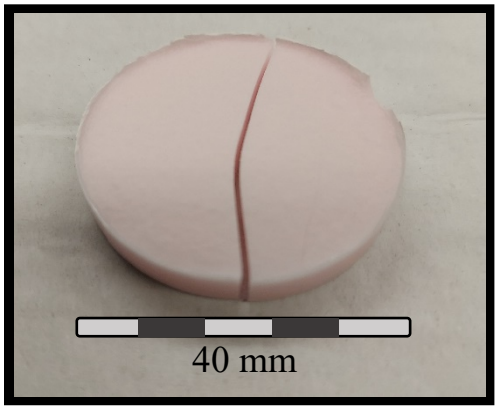

Specimen Name	Specimen Dimensions [mm]						Mass [g]
	Height	Width	Depth	X_1	X_2	X_3	
Y-Er-8-40-1	18.87	6.06	6.06	2.67	11.75	2.67	3.087
Y-Er-8-40-2	19.21	6.03	6.04	2.81	11.75	2.76	3.119
Y-Er-8-40-3	18.29	6.04	6.04	2.36	11.77	2.31	2.965
Y-Er-8-40-4	18.20	6.00	6.06	2.34	11.80	2.39	2.938

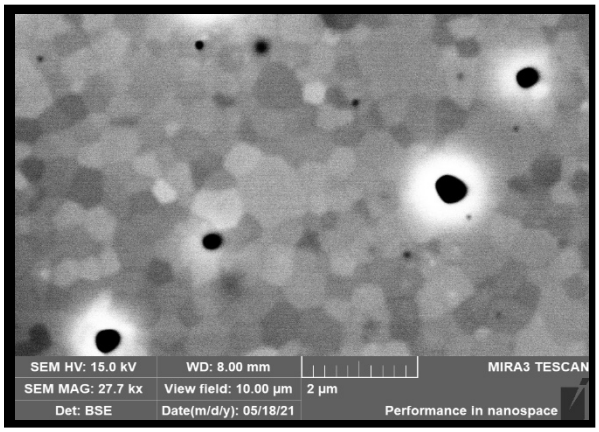

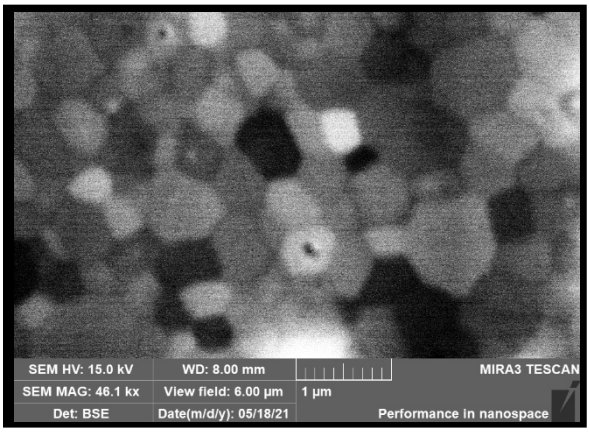

Material Properties			
Density [g/cc]	Density [%]	Grain Size [µm]	Hardness
4.55	99.84	0.37	N/A

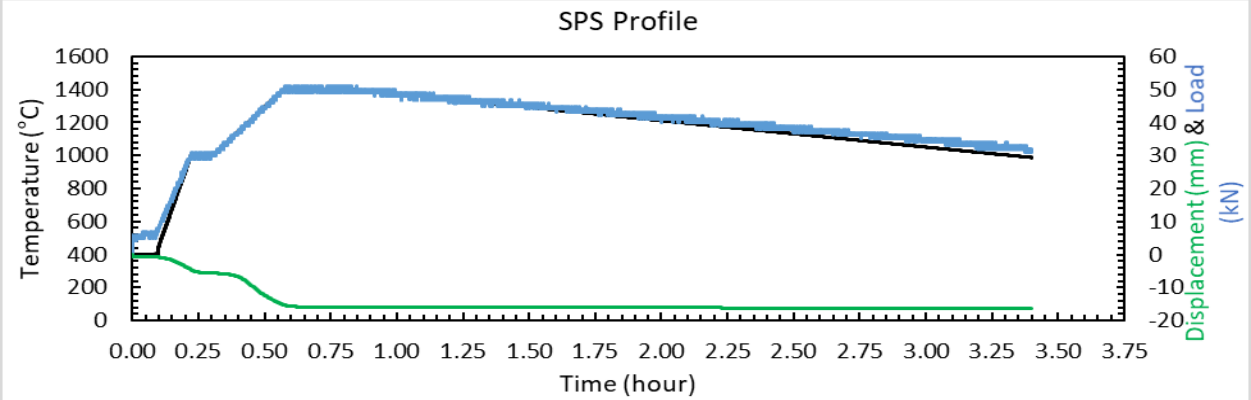

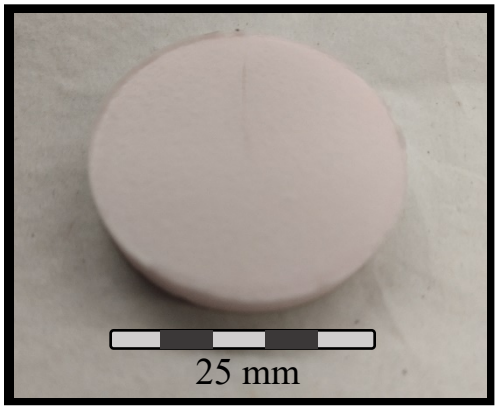

Specimen Name	Specimen Dimensions [mm]						Mass [g]
	Height	Width	Depth	X_1	X_2	X_3	
Y-Er-9-40-1	18.07	6.89	6.87	2.53	11.06	2.60	3.840
Y-Er-9-40-2	18.57	6.54	6.54	2.78	11.32	2.65	3.640
Y-Er-9-40-3	19.02	6.41	6.41	2.75	12.11	3.10	3.510

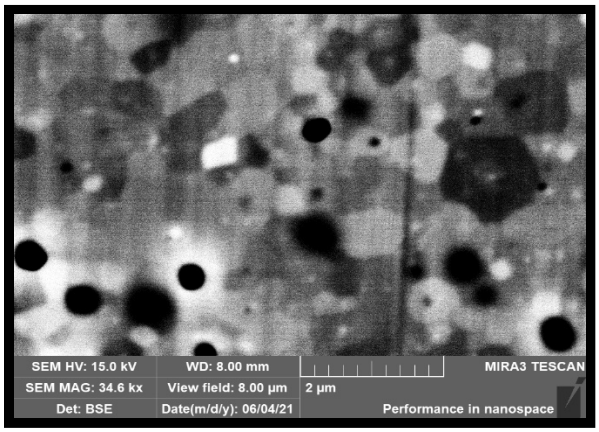

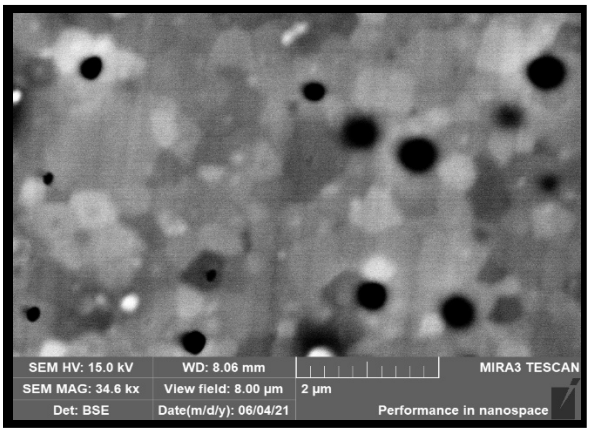

Material Properties			
Density [g/cc]	Density [%]	Grain Size [µm]	Hardness
4.51	98.94	0.45	1742

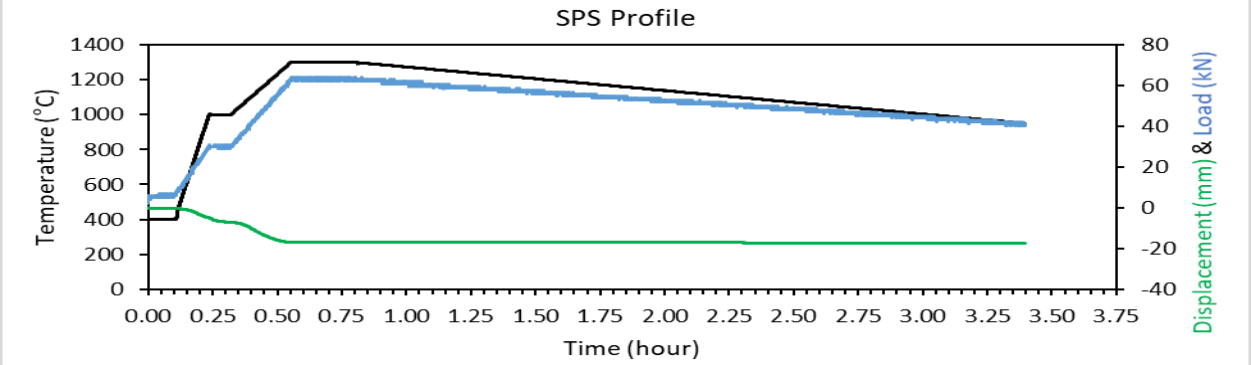

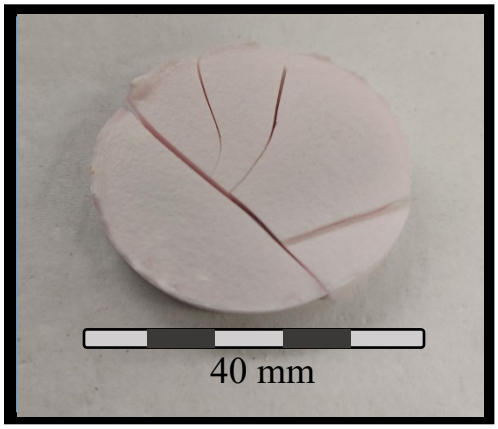

Specimen Name	Specimen Dimensions [mm]						Mass [g]
	Height	Width	Depth	X_1	X_2	X_3	
Y-Er-10-40-1	19.14	6.33	6.33	2.79	12.31	3.12	3.460

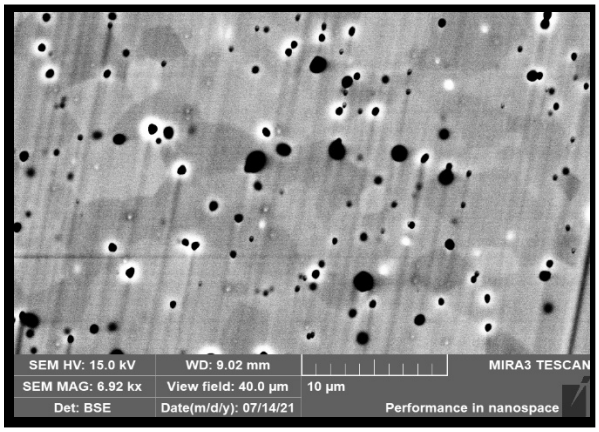

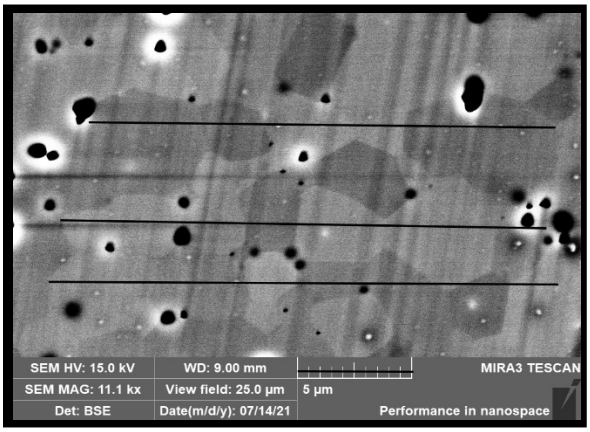

Material Properties			
Density [g/cc]	Density [%]	Grain Size [µm]	Hardness
4.52	99.21	2.72	N/A

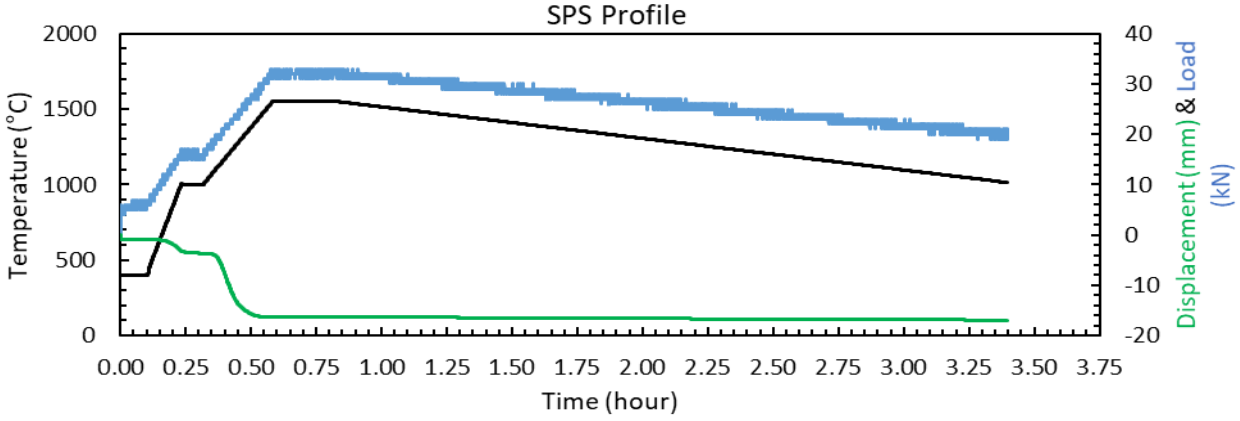

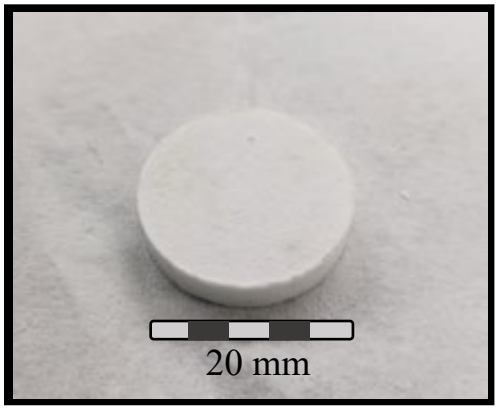

Specimen Name	Specimen Dimensions [mm]					
	Height	Width	Depth	X_1	X_2	X_3
L-1-20-1	18.82	6.56	6.53	2.58	12.13	2.88

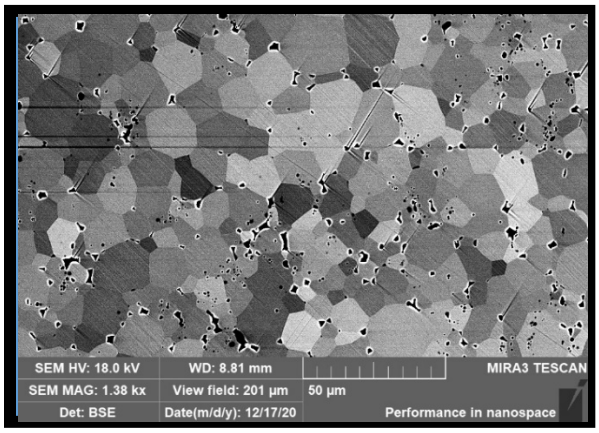

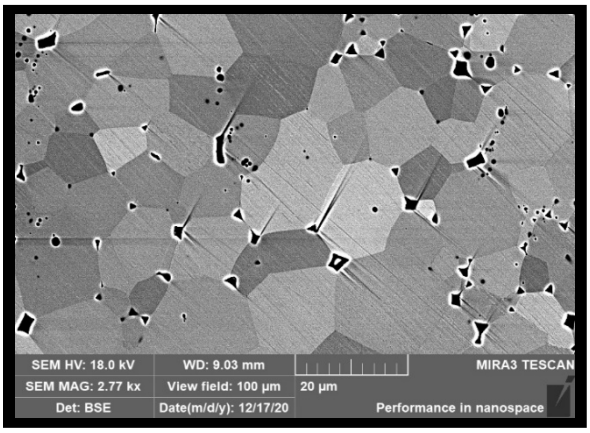

Material Properties			
Density [g/cc]	Density [%]	Grain Size [µm]	Hardness
6.57	97.70	10.78	1459

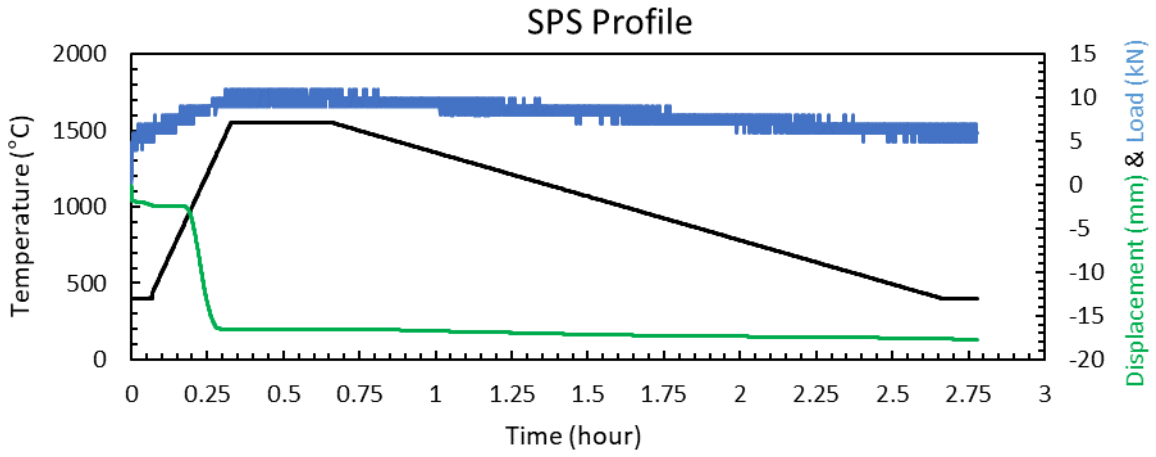

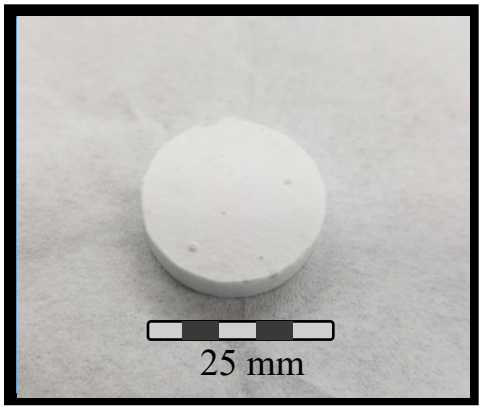

Specimen Name	Specimen Dimensions [mm]						Mass [g]
	Height	Width	Depth	X_1	X_2	X_3	
L-2-25-1	18.93	5.62	5.62	2.78	11.92	2.67	3.87

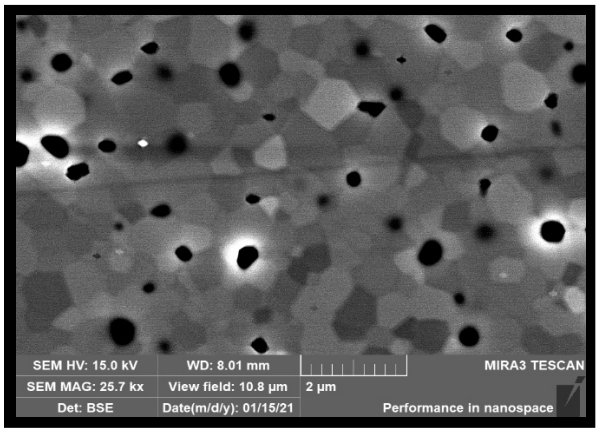

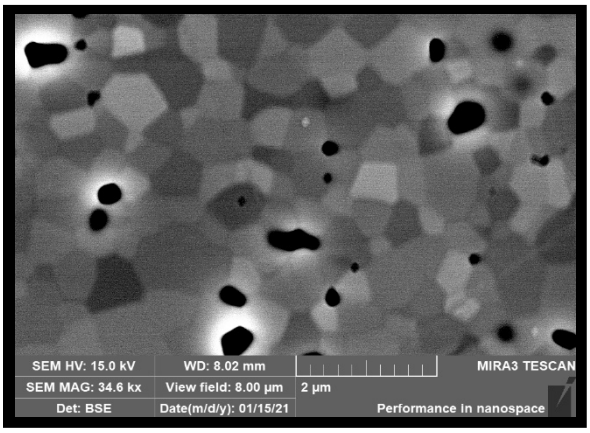

Material Properties			
Density [g/cc]	Density [%]	Grain Size [µm]	Hardness
6.56	97.40	0.57	1630

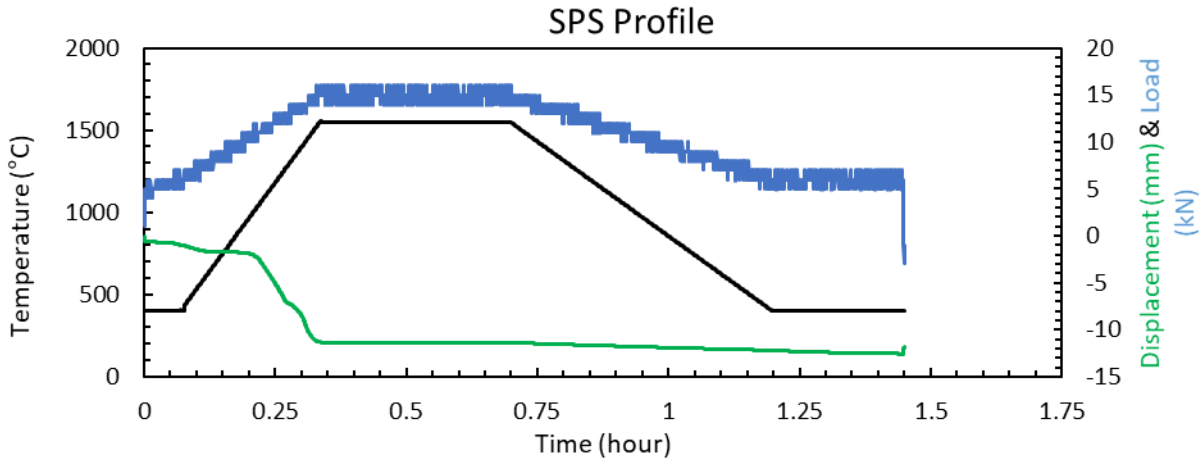

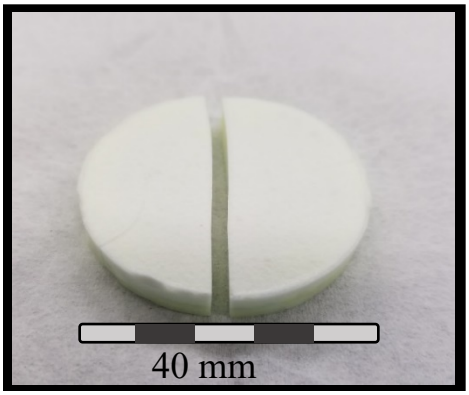

Specimen Name	Specimen Dimensions [mm]						Mass [g]
	Height	Width	Depth	X_1	X_2	X_3	
L-3-40-1	19.69	6.39	6.39	3.10	11.73	3.15	5.109
L-3-40-2	19.89	6.33	6.34	3.21	11.71	3.09	5.081
L-3-40-3	19.77	6.51	6.52	3.01	11.75	3.12	5.360
L-3-40-4	19.71	6.40	6.40	3.10	11.75	3.01	5.140
L-3-40-5	19.66	6.43	6.43	3.13	11.87	2.02	5.050

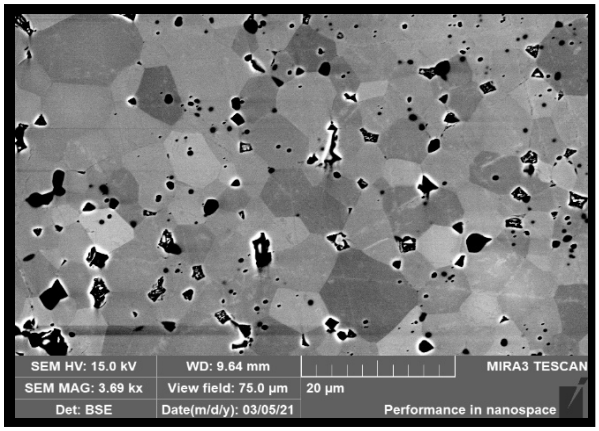

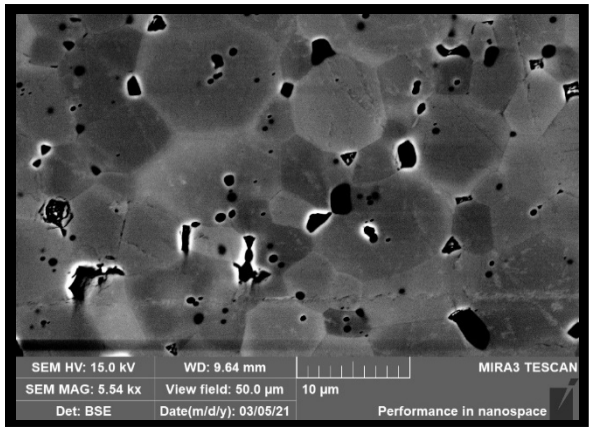

Material Properties			
Density [g/cc]	Density [%]	Grain Size [µm]	Hardness
6.47	96.20	4.90	1574

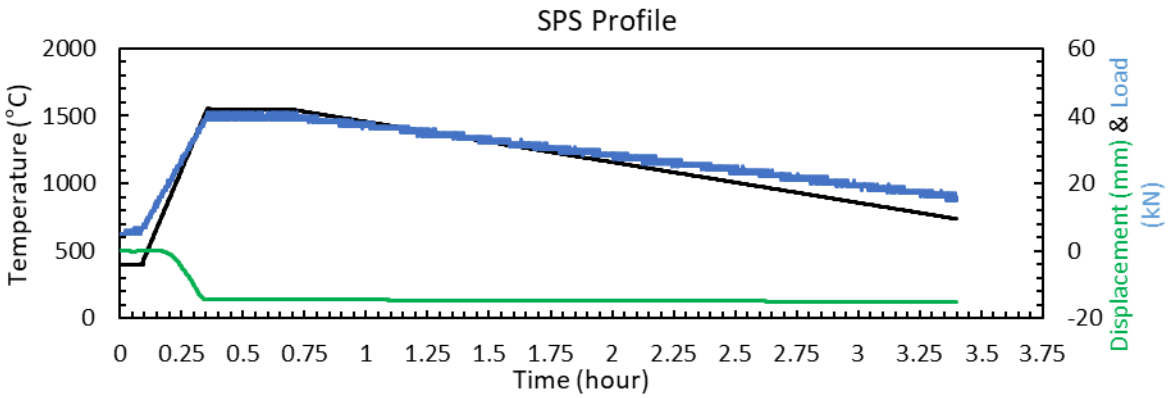

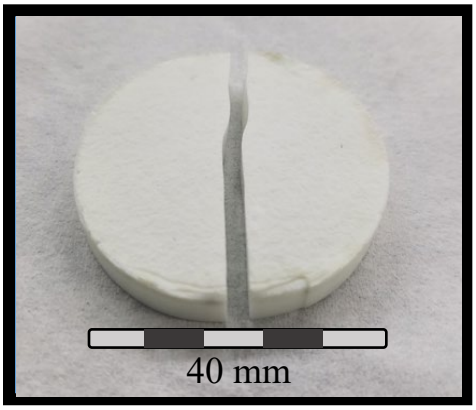

Specimen Name	Specimen Dimensions [mm]						Mass [g]
	Height	Width	Depth	X_1	X_2	X_3	
L-4-40-1	19.13	6.25	6.24	2.89	11.93	2.82	4.83
L-4-40-2	19.79	6.24	6.25	3.19	11.97	3.25	4.99
L-4-40-3	17.5	6.37	6.37	2.81	10.45	2.81	4.61

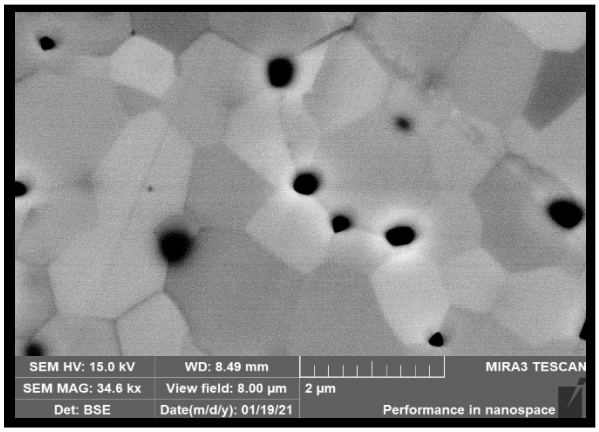

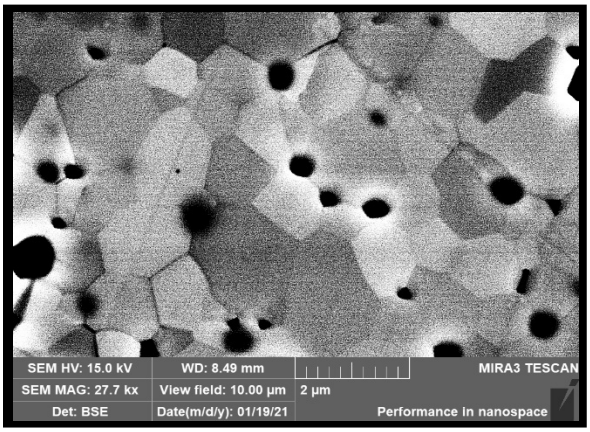

Material Properties			
Density [g/cc]	Density [%]	Grain Size [µm]	Hardness
6.54	97.23	0.95	1745

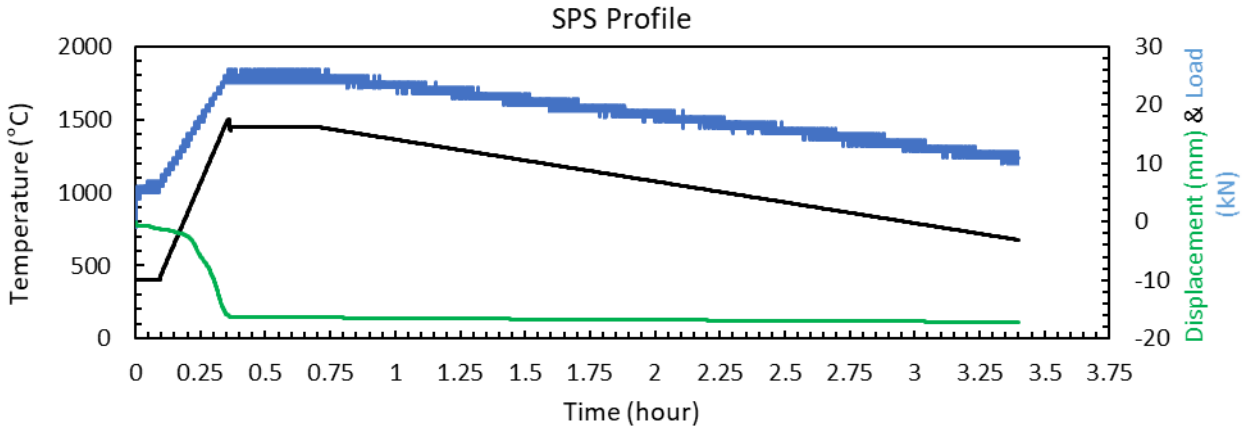

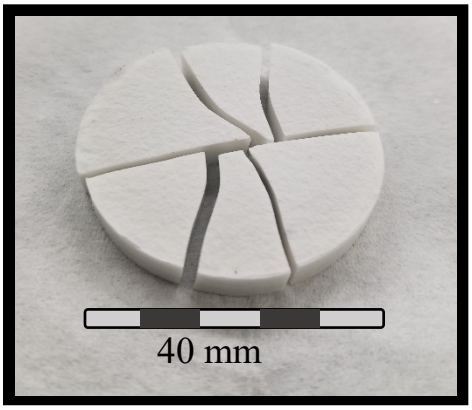

Specimen Name	Specimen Dimensions [mm]						Mass [g]
	Height	Width	Depth	X_1	X_2	X_3	
L-5-40-1	19.05	6.49	6.48	2.78	11.75	2.78	5.20

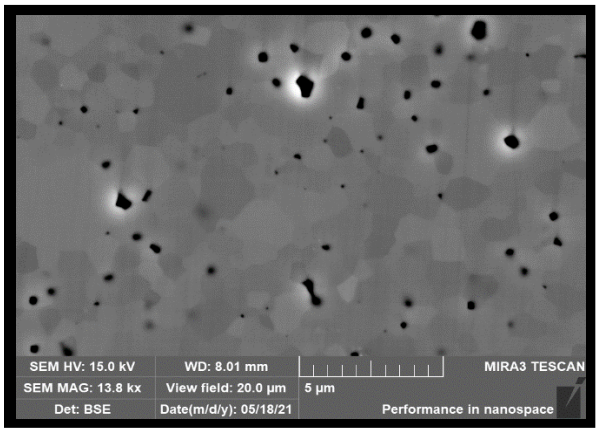

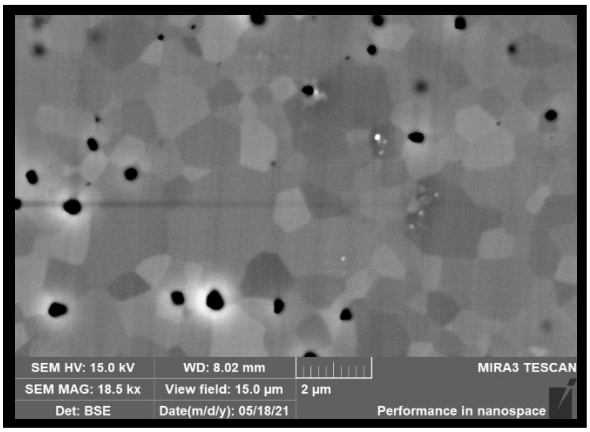

Material Properties			
Density [g/cc]	Density [%]	Grain Size [µm]	Hardness
6.57	97.66	0.41	1681

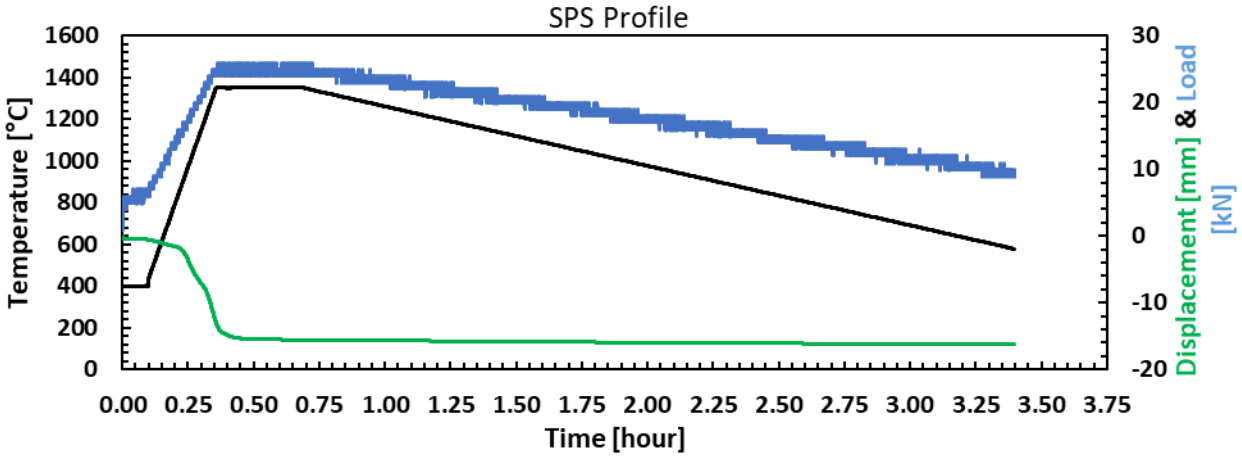

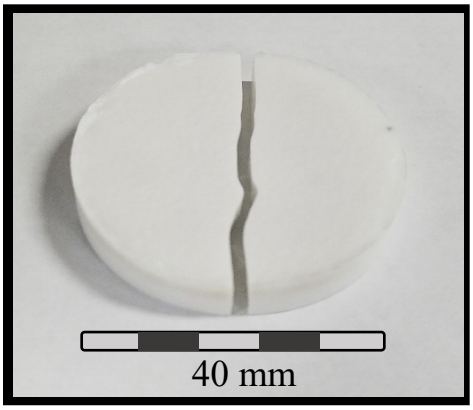

Specimen Name	Specimen Dimensions [mm]						Mass [g]
	Height	Width	Depth	X_1	X_2	X_3	
L-6-40-1	20.02	6.24	6.24	3.26	11.73	3.24	5.08
L-6-40-2	16.96	6.09	6.09	2.11	10.74	2.25	4.09
L-6-40-3	16.75	6.24	6.24	2.26	10.83	2.18	4.24

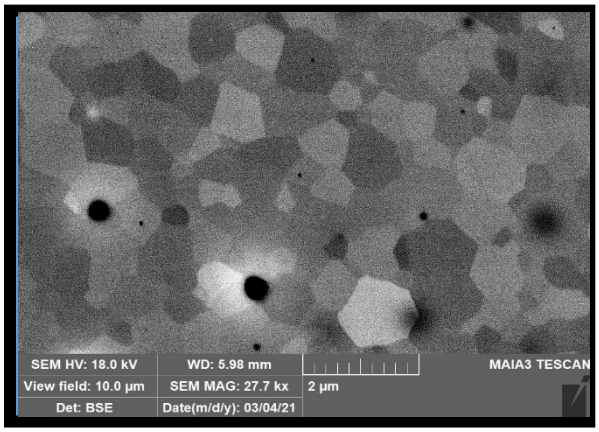

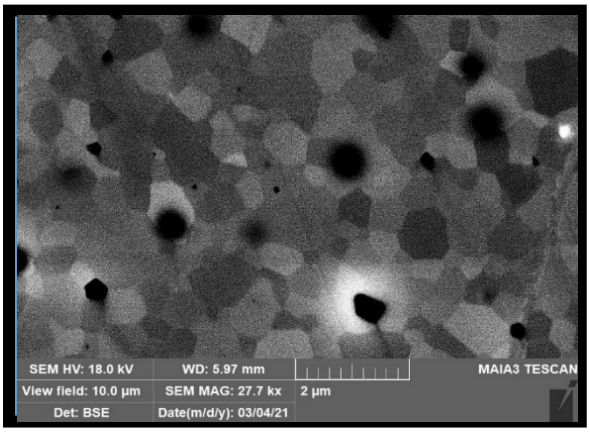

Material Properties			
Density [g/cc]	Density [%]	Grain Size [µm]	Hardness
6.60	98.11	0.55	1672

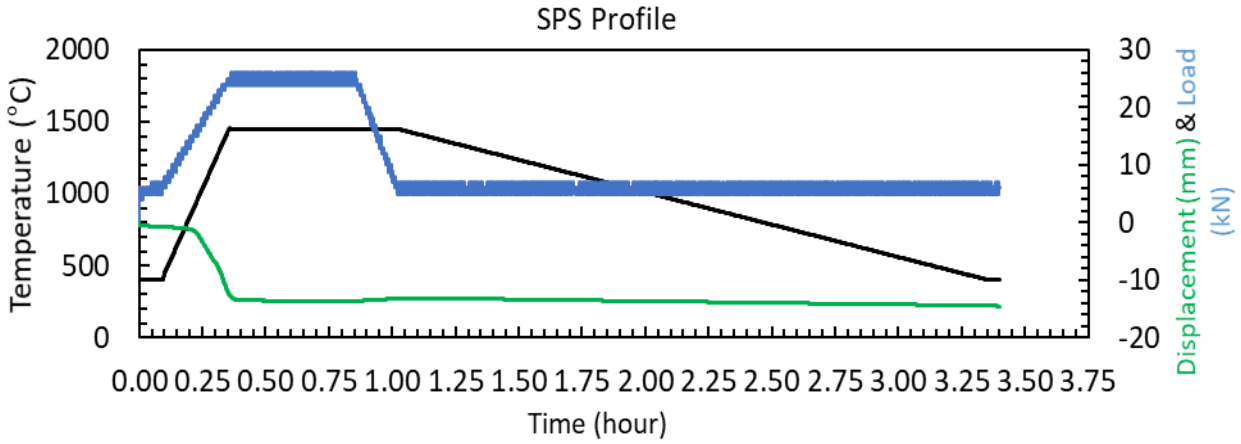

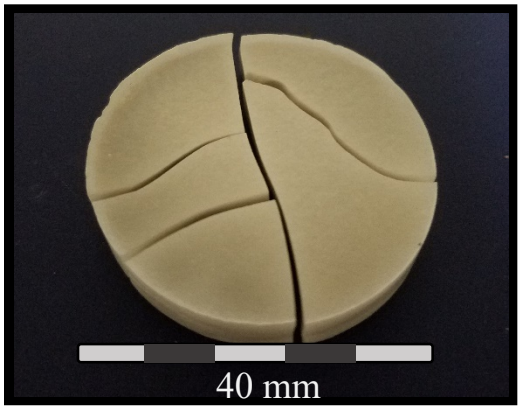

Specimen Name	Specimen Dimensions [mm]						Mass [g]
	Height	Width	Depth	X_1	X_2	X_3	
L-7-40-1	18.59	6.3	6.23	2.53	11.85	2.44	4.71
L-7-40-2	19.95	6.31	6.31	3.21	11.75	3.25	5.17

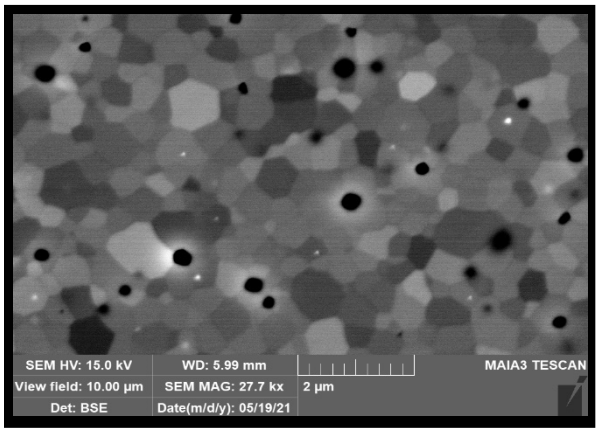

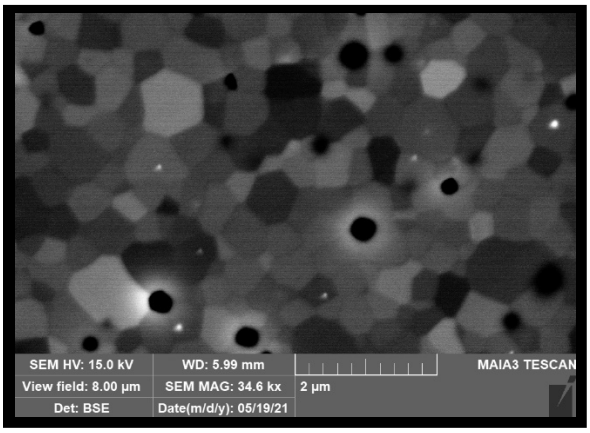

Material Properties			
Density [g/cc]	Density [%]	Grain Size [µm]	Hardness
6.65	98.86	0.44	1328

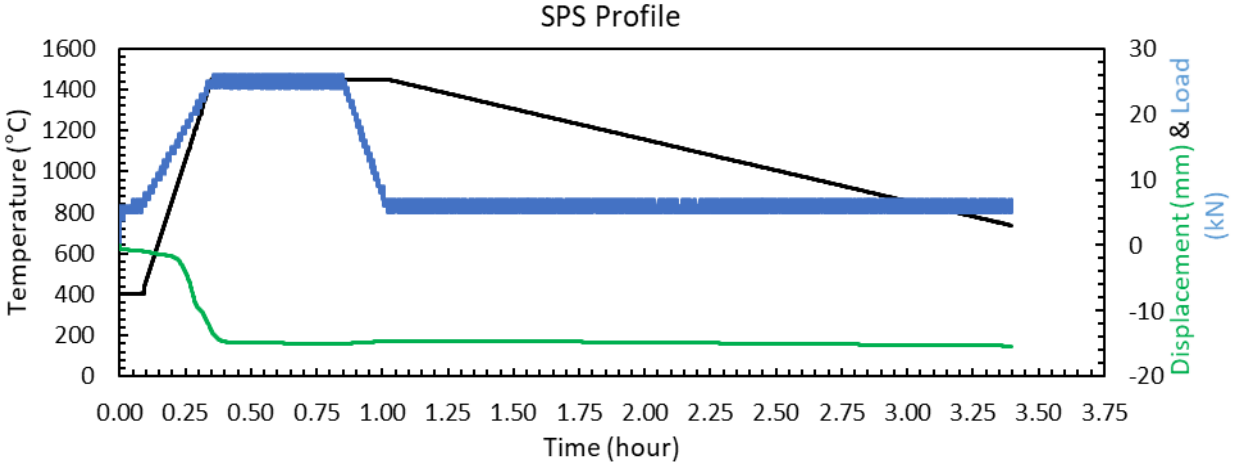

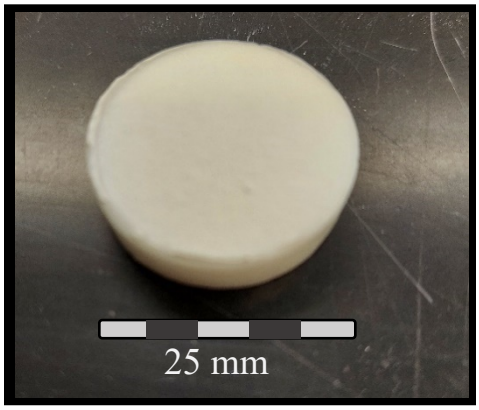

Specimen Name	Specimen Dimensions [mm]						Mass [g]
	Height	Width	Depth	X_1	X_2	X_3	
L-8-25-1	19.40	6.87	6.85	2.92	11.76	2.94	5.97

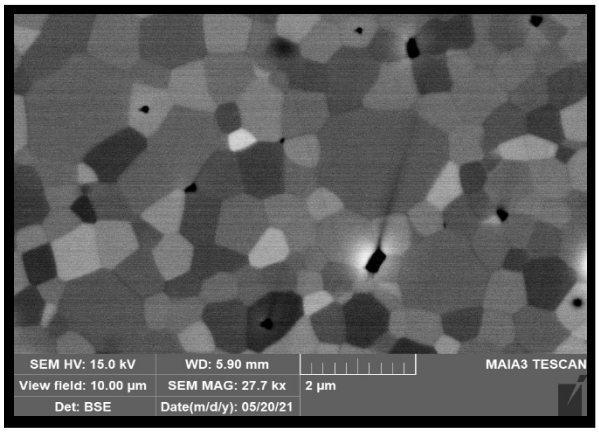

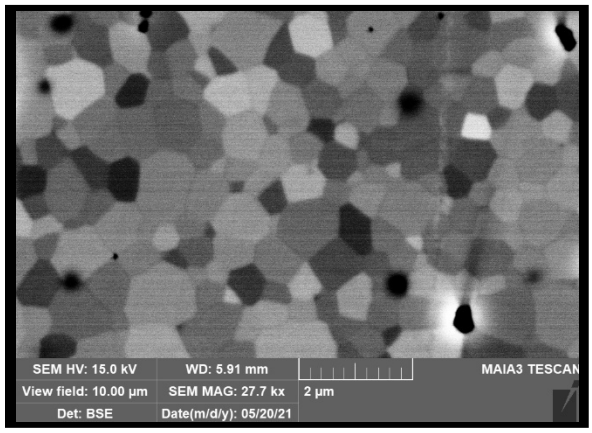

Material Properties			
Density [g/cc]	Density [%]	Grain Size [µm]	Hardness
6.57	97.64	0.50	N/A

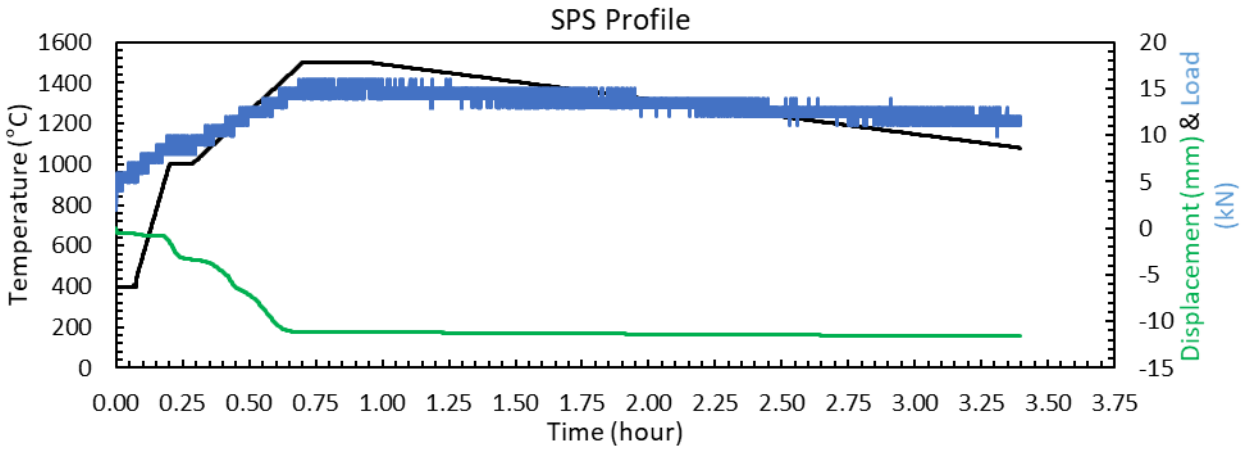

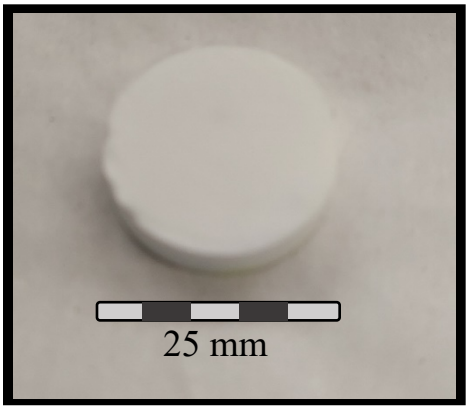

Specimen Name	Specimen Dimensions [mm]						Mass [g]
	Height	Width	Depth	X_1	X_2	X_3	
No Creep Specimens							

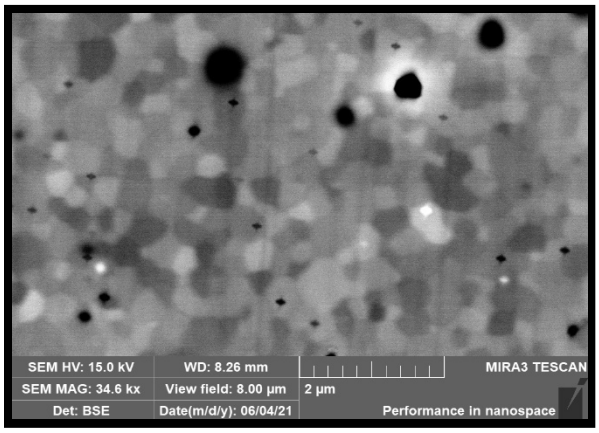

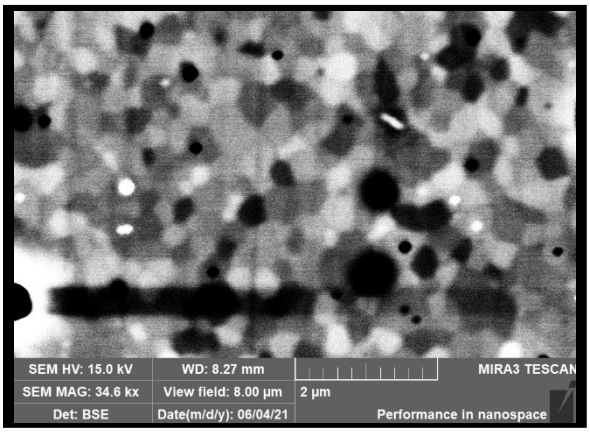

Material Properties			
Density [g/cc]	Density [%]	Grain Size [µm]	Hardness
6.49	96.48	0.32	1811

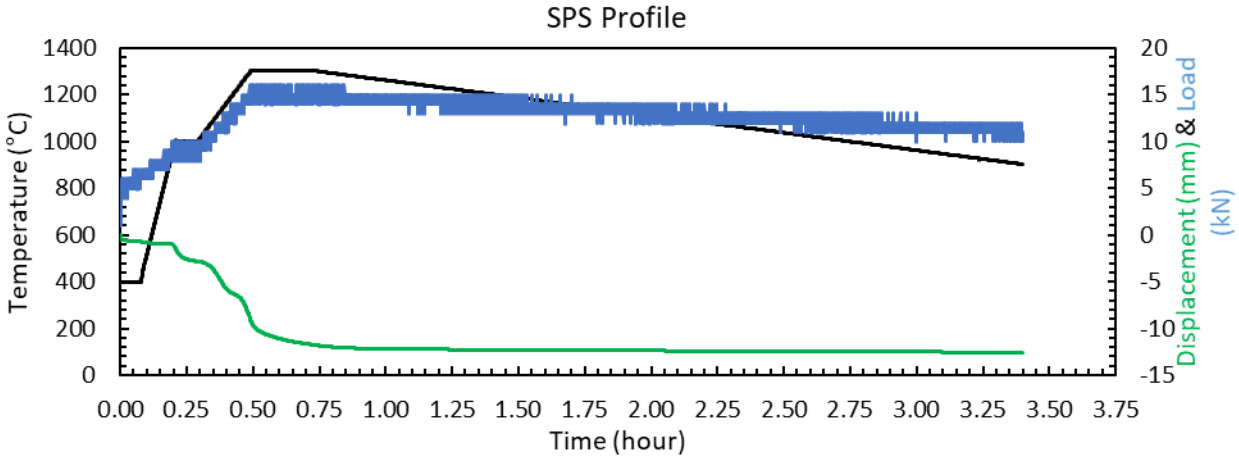

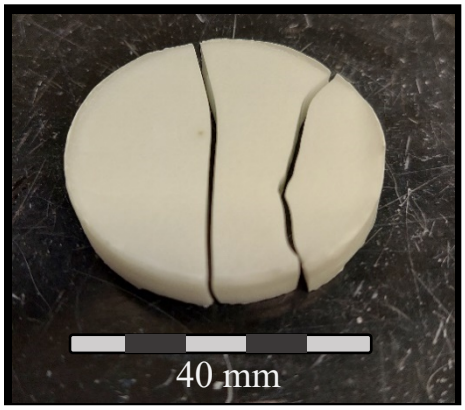

Specimen Name	Specimen Dimensions [mm]						Mass [g]
	Height	Width	Depth	X_1	X_2	X_3	
L-10-40-1	19.13	5.98	5.98	2.50	12.38	3.50	4.460
L-10-40-2	18.28	6.38	6.38	2.50	12.50	2.60	4.890
L-10-40-3	18.98	6.37	6.37	2.81	12.34	3.20	5.010

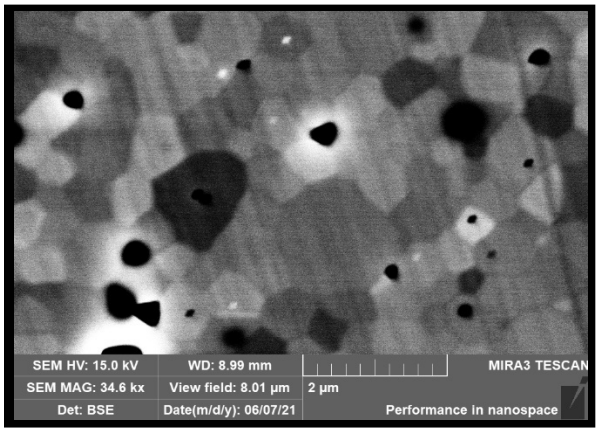

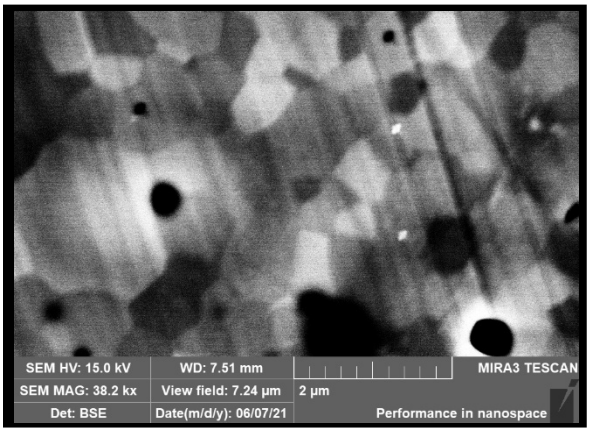

Material Properties			
Density [g/cc]	Density [%]	Grain Size [µm]	Hardness
6.65	98.84	0.54	N/A

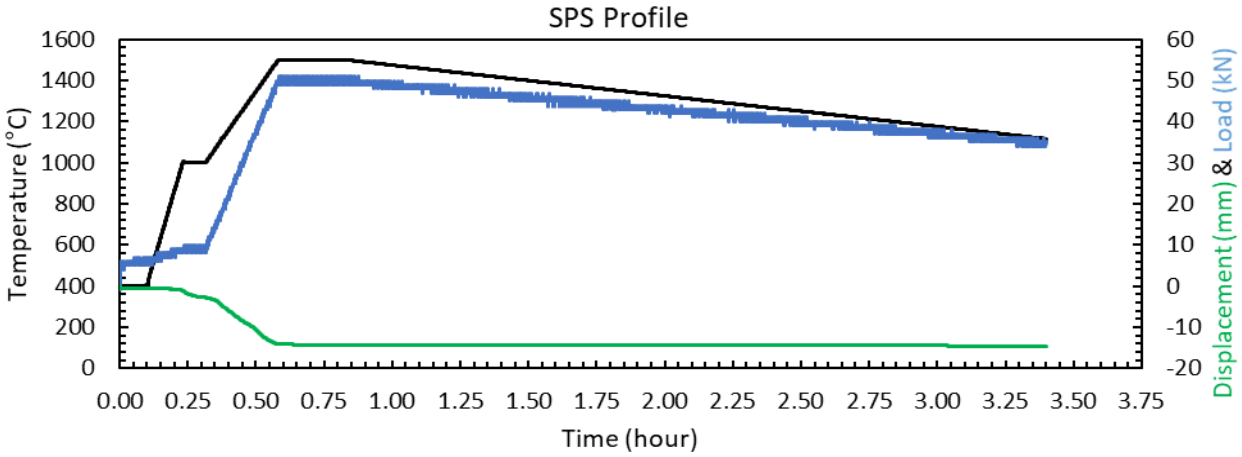

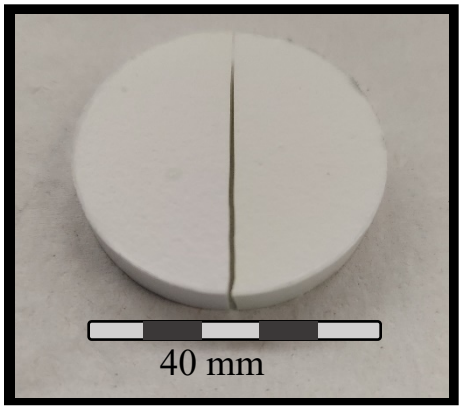

Specimen Name	Specimen Dimensions [mm]						Mass [g]
	Height	Width	Depth	X_1	X_2	X_3	
L-11-40-1	18.73	6.64	6.64	2.77	12.43	2.98	5.380
L-11-40-2	19.00	6.56	6.56	3.04	12.39	2.86	5.350
L-11-40-3	19.02	6.66	6.67	3.15	12.35	2.79	5.540
L-11-40-4	18.64	6.38	6.38	2.57	12.24	2.81	4.990

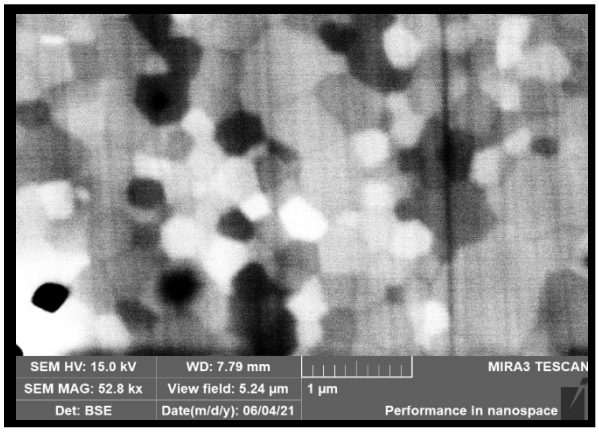

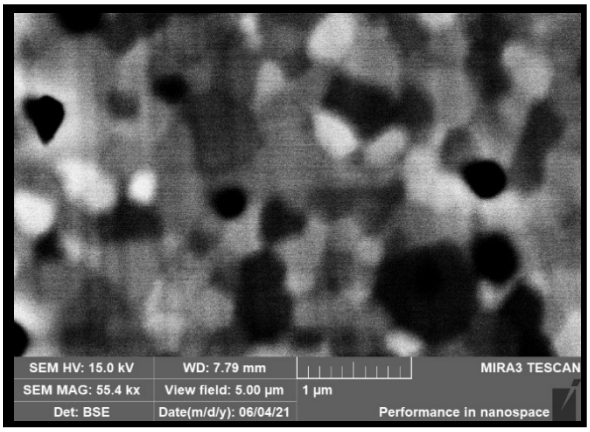

Material Properties			
Density [g/cc]	Density [%]	Grain Size [µm]	Hardness
6.57	97.62	0.55	N/A

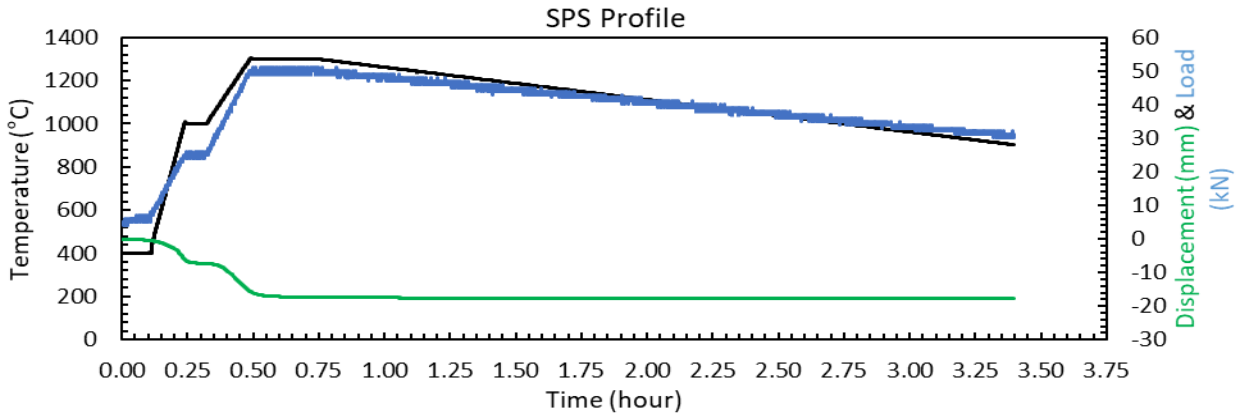

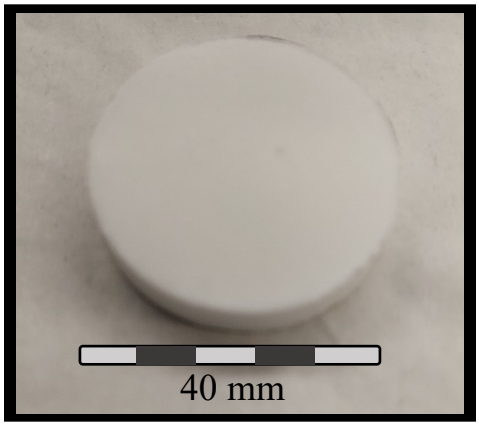

Specimen Name	Specimen Dimensions [mm]						Mass [g]
	Height	Width	Depth	X_1	X_2	X_3	
L-12-40-1	18.91	6.47	6.47	3.06	12.11	2.75	5.050
L-12-40-2	19.10	6.47	6.47	3.14	12.61	2.84	5.320
L-12-40-3	19.01	6.41	6.47	2.77	12.54	3.04	5.220

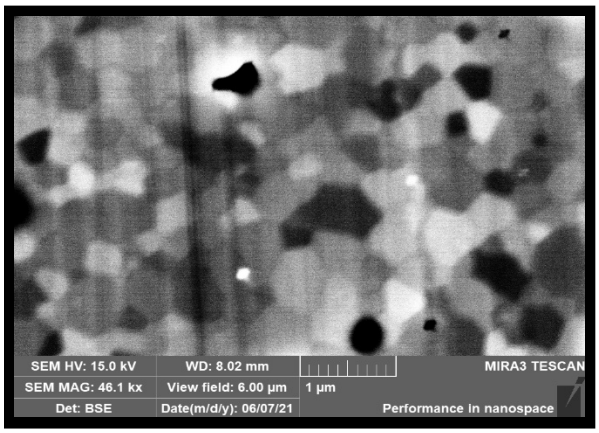

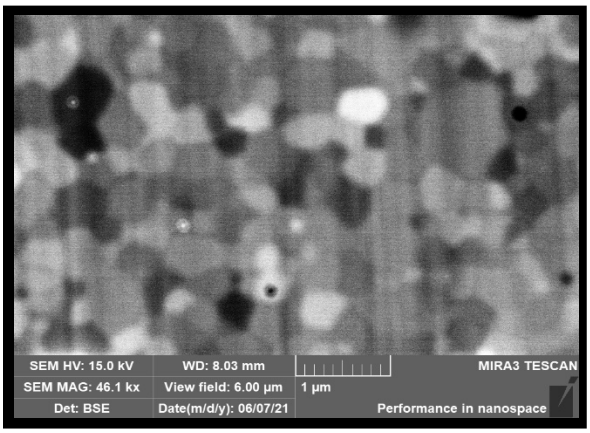

Material Properties			
Density [g/cc]	Density [%]	Grain Size [µm]	Hardness
6.50	96.55	0.32	1515

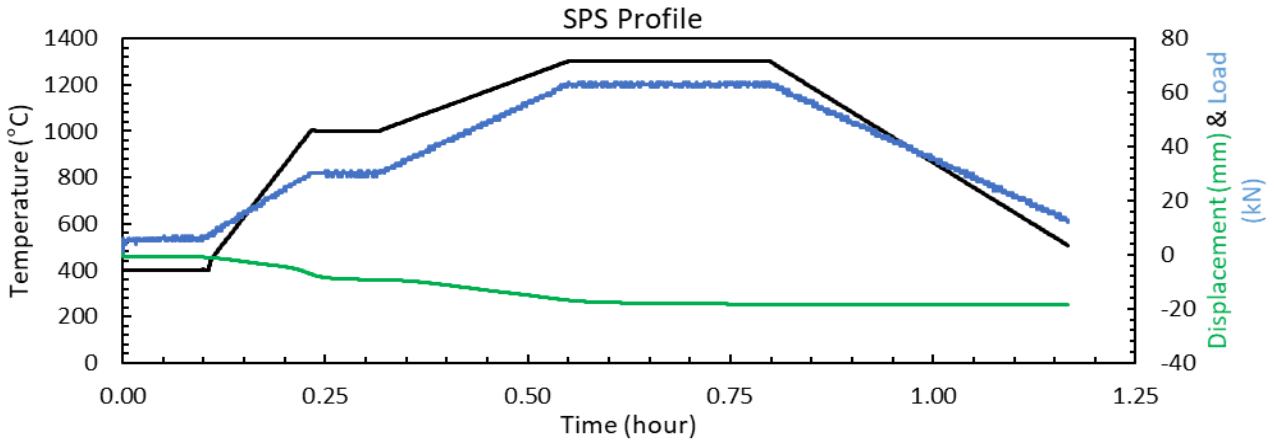

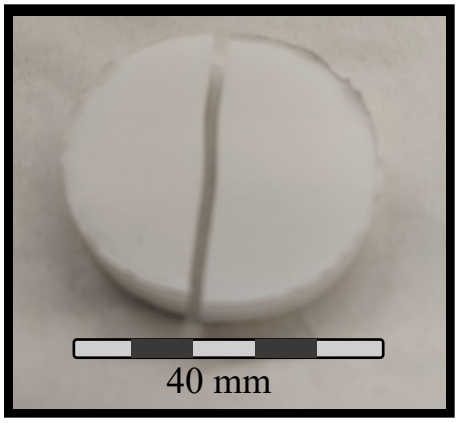

Specimen Name	Specimen Dimensions [mm]						Mass [g]
	Height	Width	Depth	X_1	X_2	X_3	
L-13-40-1	17.69	6.13	6.13	2.55	12.42	2.15	4.590
L-13-40-2	17.67	6.13	6.13	2.52	12.40	2.22	4.480

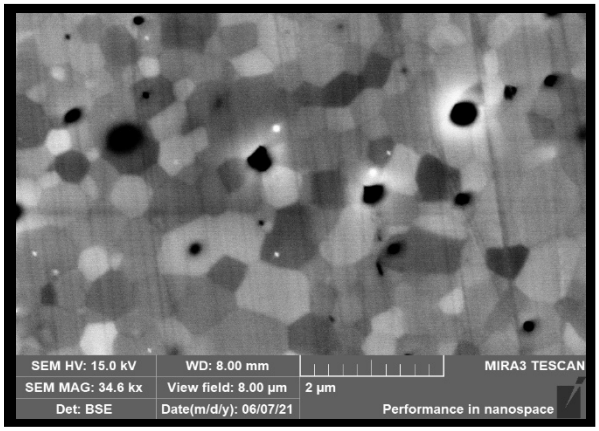

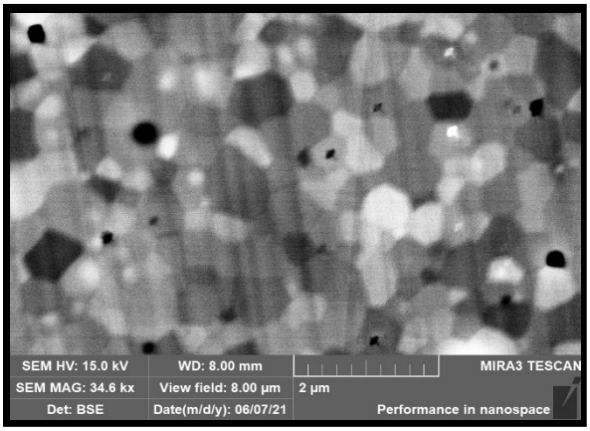

Material Properties			
Density [g/cc]	Density [%]	Grain Size [µm]	Hardness
6.58	97.78	0.45	1839

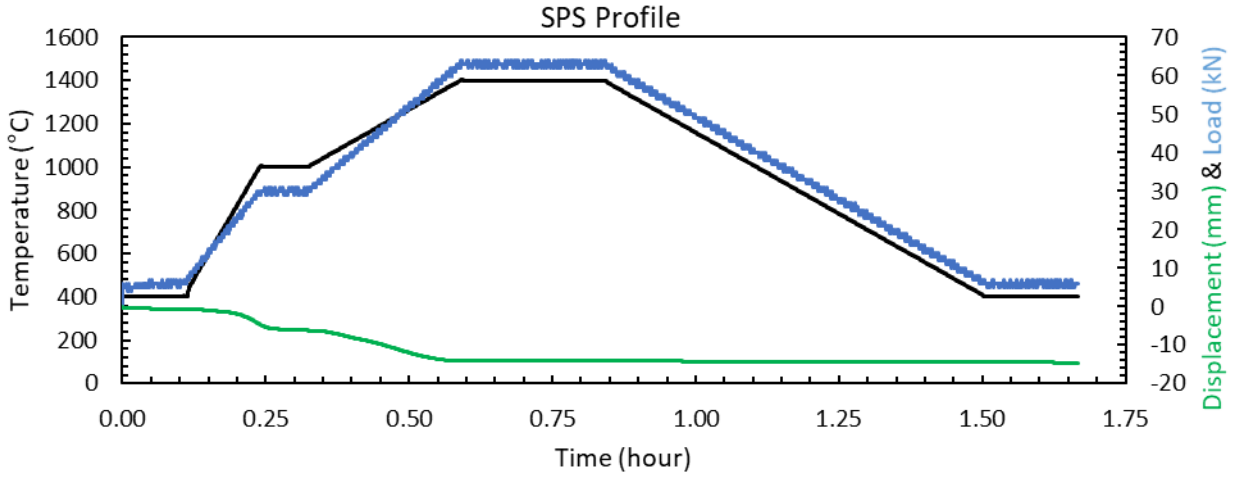

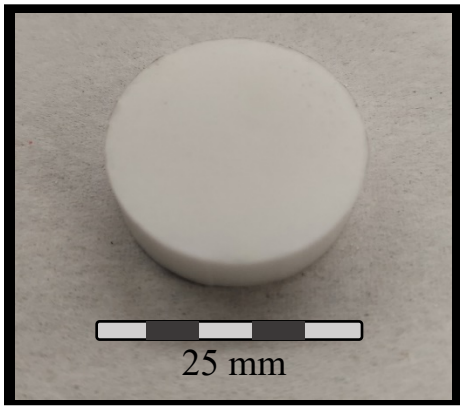

Specimen Name	Specimen Dimensions [mm]						Mass [g]
	Height	Width	Depth	X_1	X_2	X_3	
No Creep Specimens							

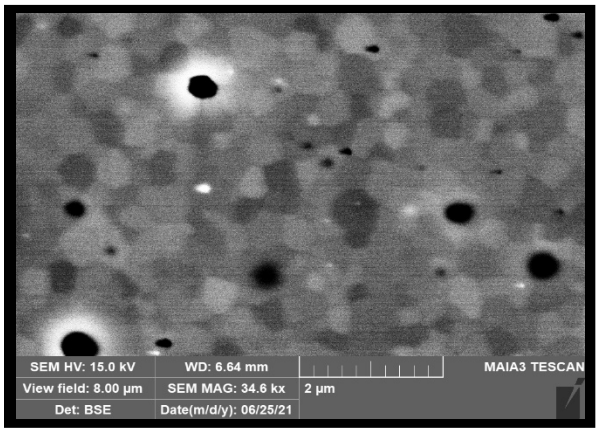

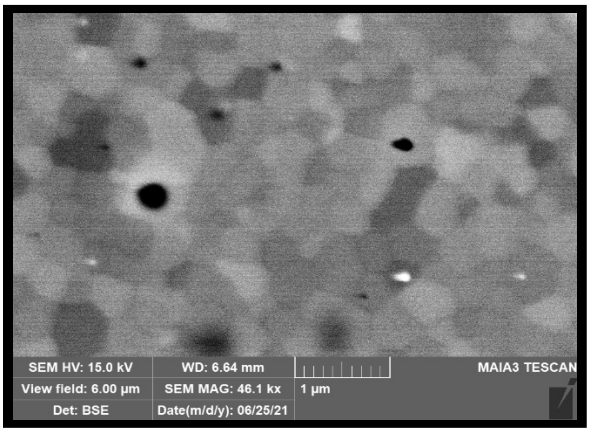

Material Properties			
Density [g/cc]	Density [%]	Grain Size [µm]	Hardness
6.66	98.99	0.34	N/A

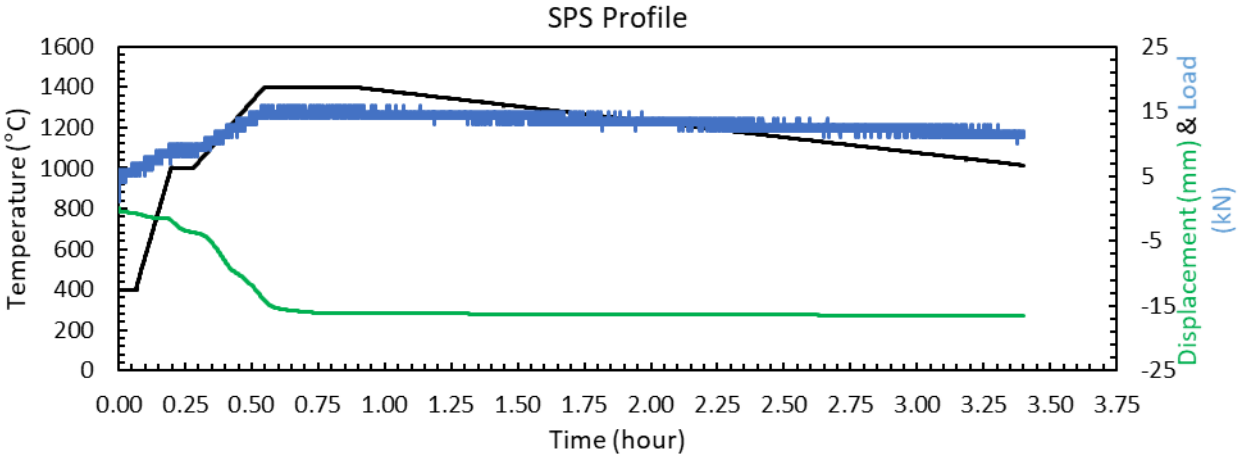

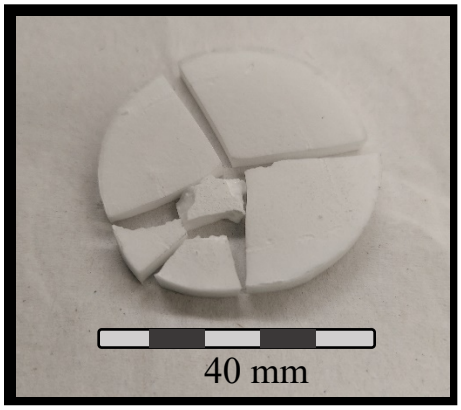

Specimen Name	Specimen Dimensions [mm]						Mass [g]
	Height	Width	Depth	X_1	X_2	X_3	
No Creep Specimens							

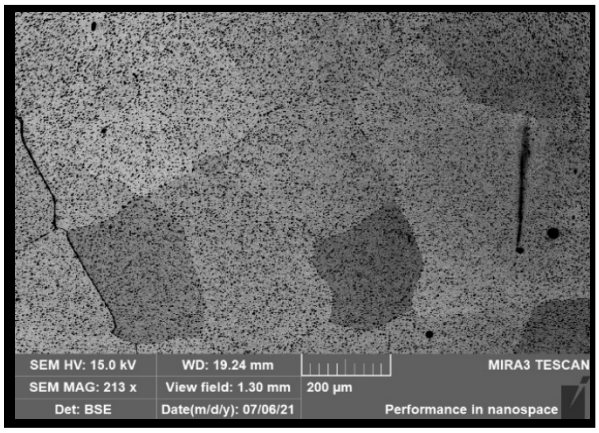

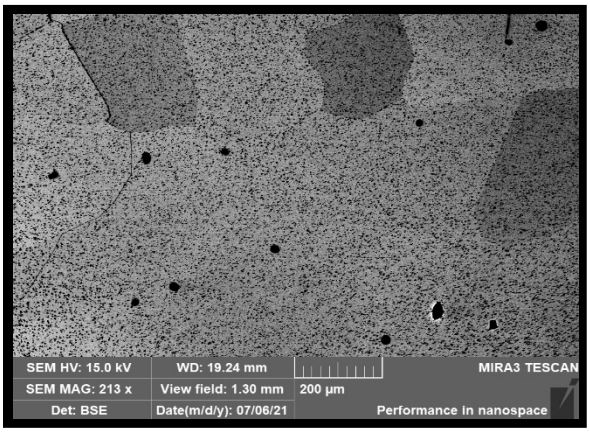

Material Properties			
Density [g/cc]	Density [%]	Grain Size [µm]	Hardness
N/A	N/A	N/A	N/A

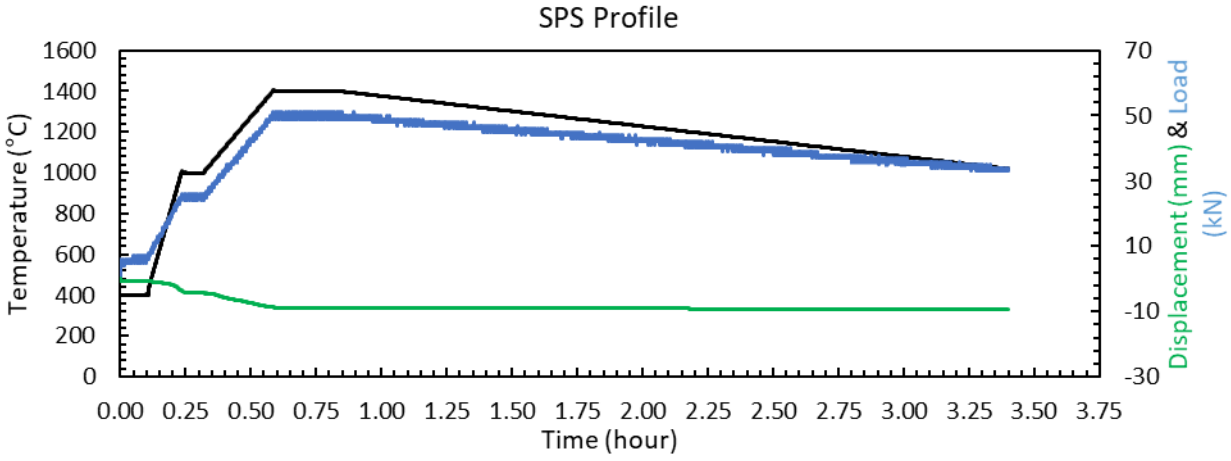

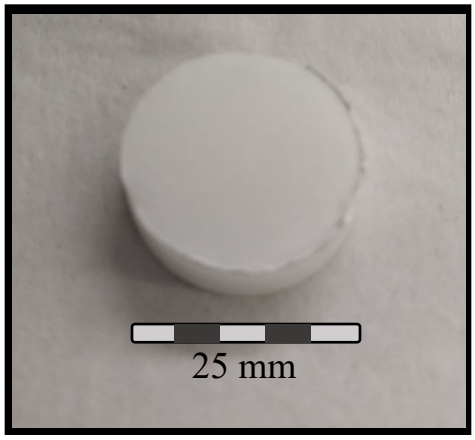

Specimen Name	Specimen Dimensions [mm]						Mass [g]
	Height	Width	Depth	X_1	X_2	X_3	
L-16-25-1	18.66	6.46	6.47	2.52	12.23	3.04	5.190

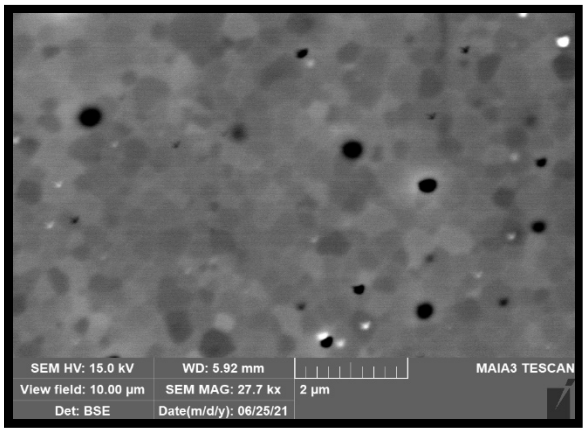

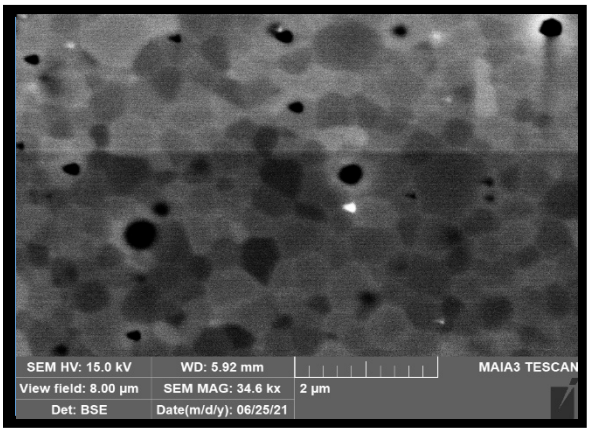

Material Properties			
Density [g/cc]	Density [%]	Grain Size [µm]	Hardness
6.57	97.64	0.48	N/A

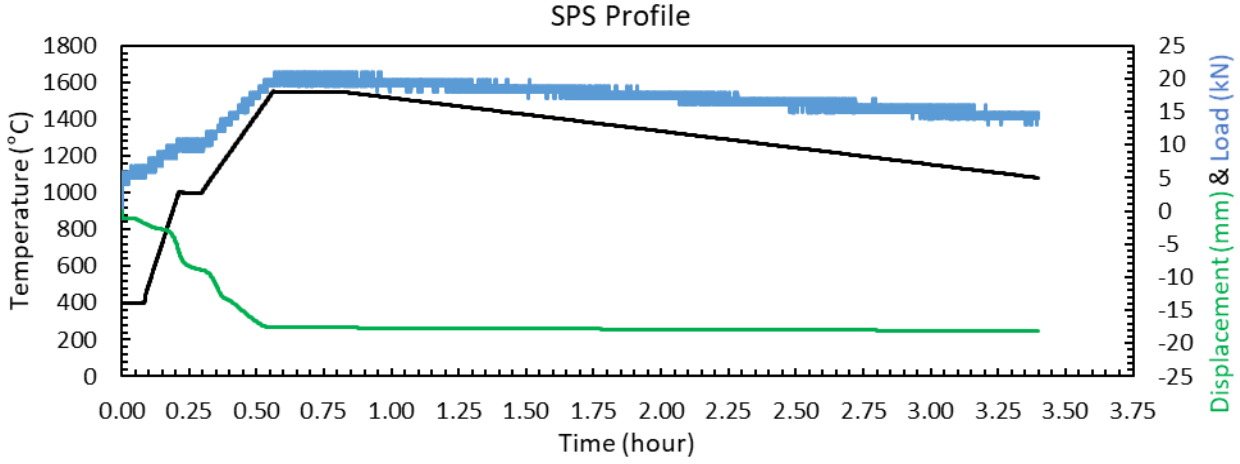

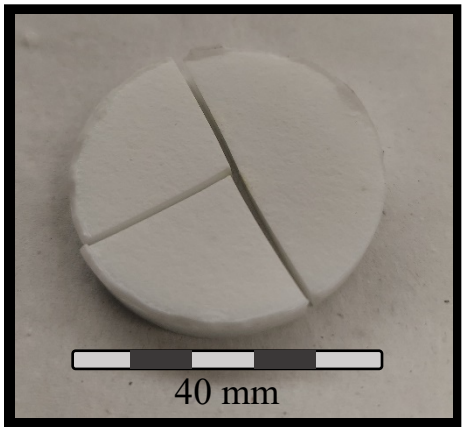

Specimen Name	Specimen Dimensions [mm]						Mass [g]
	Height	Width	Depth	X_1	X_2	X_3	
L-17-40-1	20.28	6.24	6.24	3.47	11.99	3.36	5.220
L-17-40-2	20.16	6.25	6.25	3.50	12.21	3.23	5.150
L-17-40-3	18.47	6.13	6.13	2.49	12.00	2.61	4.530

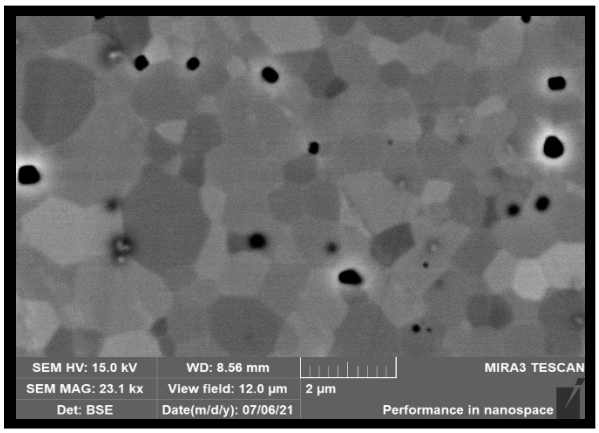

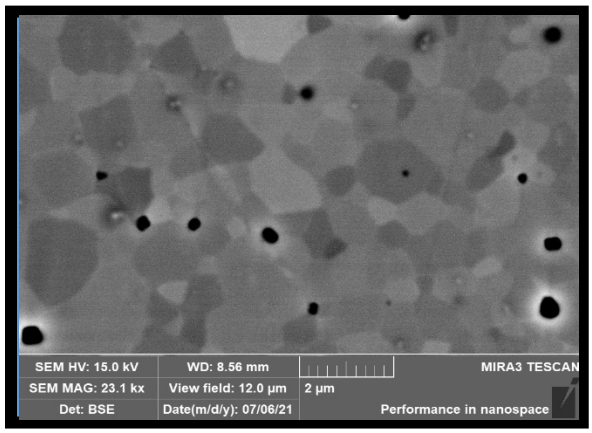

Material Properties			
Density [g/cc]	Density [%]	Grain Size [µm]	Hardness
6.58	97.77	0.68	N/A

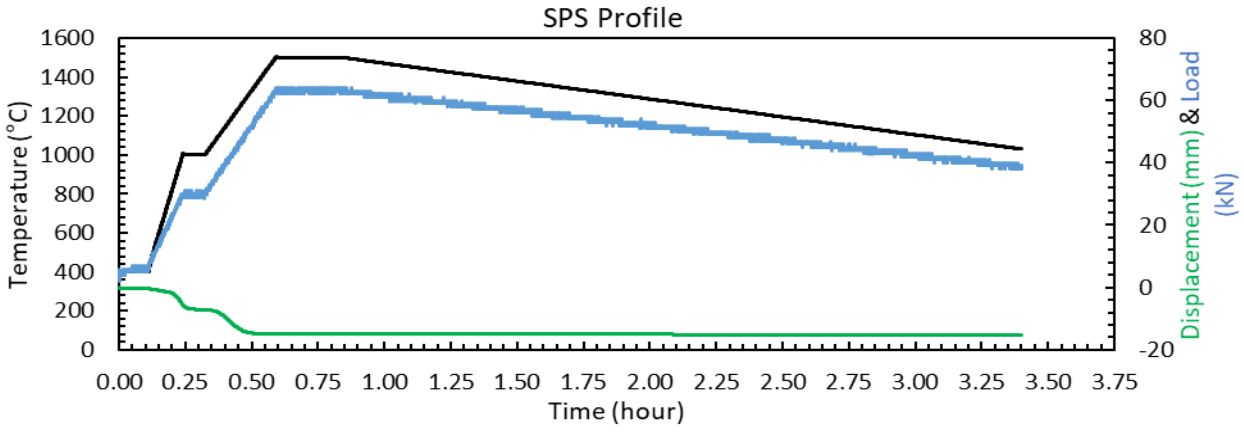

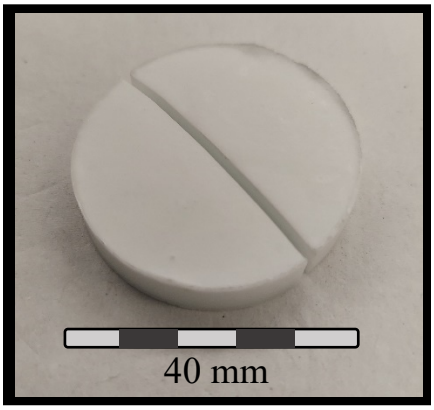

Specimen Name	Specimen Dimensions [mm]						Mass [g]
	Height	Width	Depth	X_1	X_2	X_3	
L-18-40-1	19.45	6.47	6.47	3.29	12.38	3.08	5.360
L-18-40-2	19.41	6.48	6.48	3.40	12.36	2.96	5.390
L-18-40-3	19.35	6.48	6.48	3.22	12.15	2.75	5.030

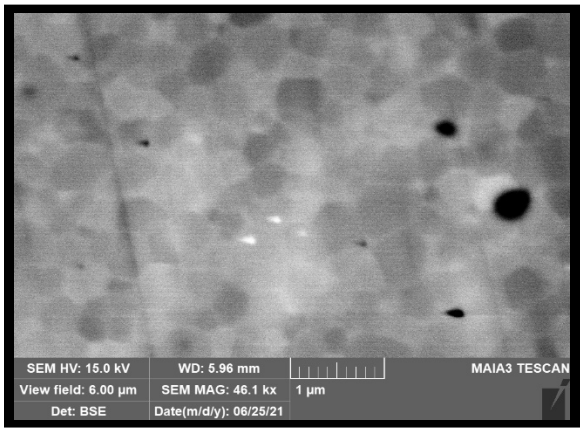

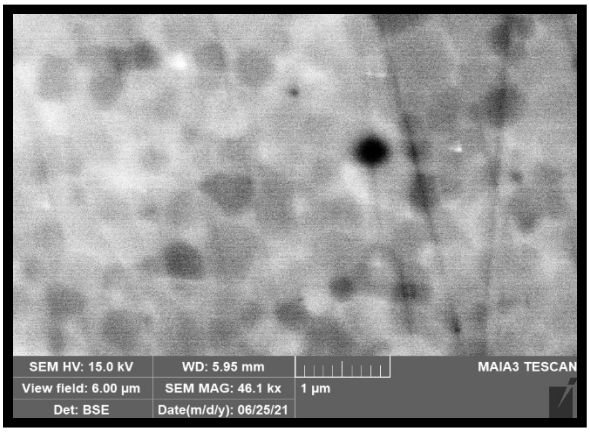

Material Properties			
Density [g/cc]	Density [%]	Grain Size [µm]	Hardness
6.49	96.43	0.42	N/A

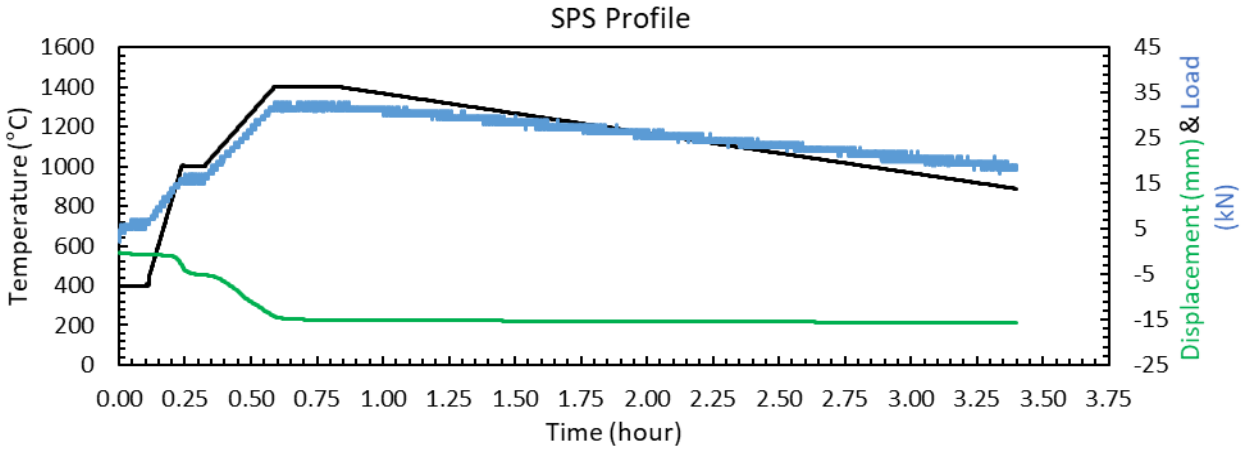

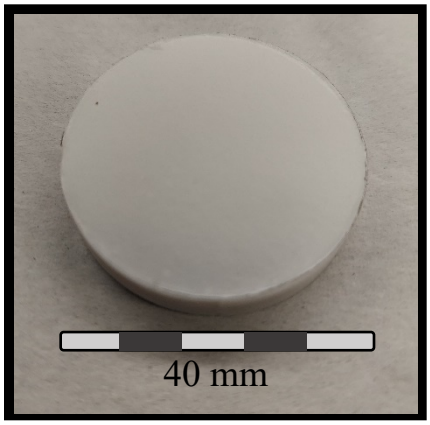

Specimen Name	Specimen Dimensions [mm]						Mass [g]
	Height	Width	Depth	X_1	X_2	X_3	
L-19-40-1	18.90	6.46	6.46	3.32	12.41	2.94	4.760

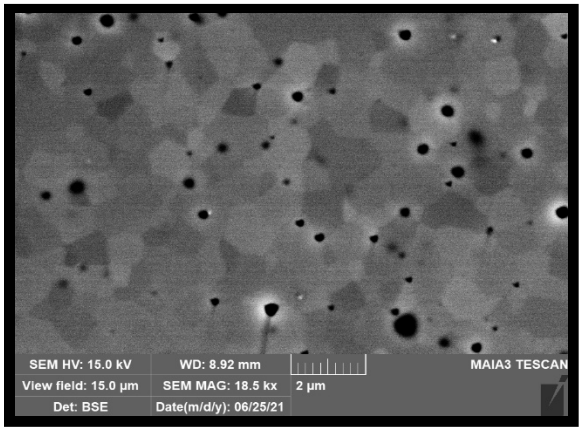

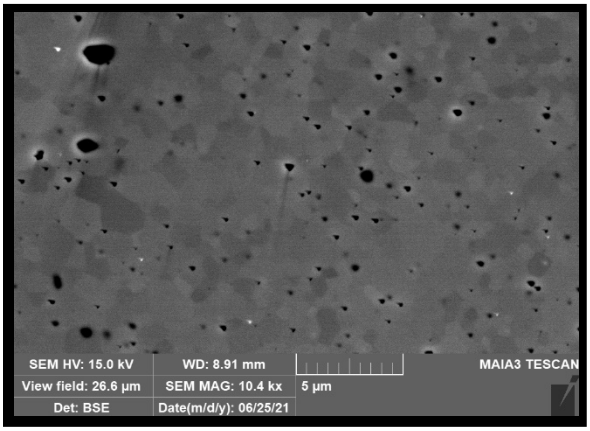

Material Properties			
Density [g/cc]	Density [%]	Grain Size [µm]	Hardness
6.68	99.23	0.84	N/A

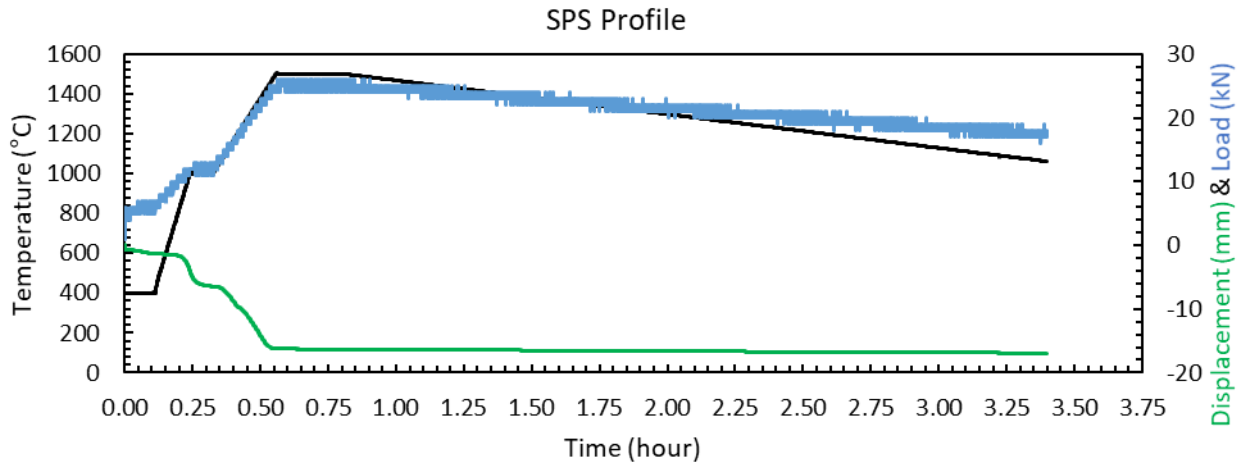

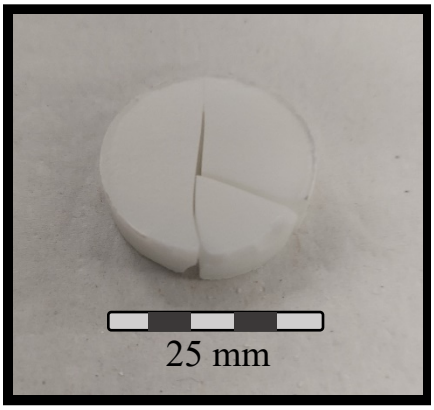

Specimen Name	Specimen Dimensions [mm]						Mass [g]
	Height	Width	Depth	X_1	X_2	X_3	
L-20-25-1	17.78	5.84	5.84	2.21	12.35	2.49	4.020

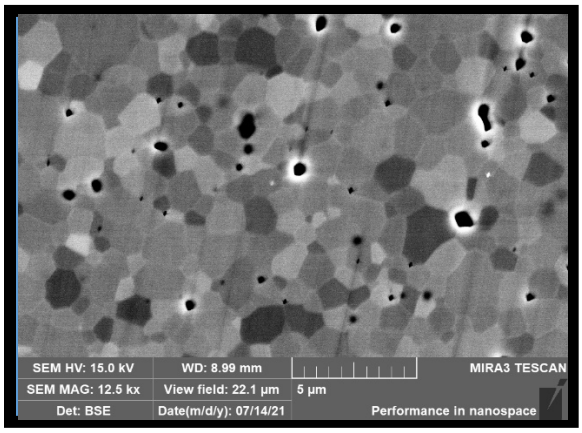

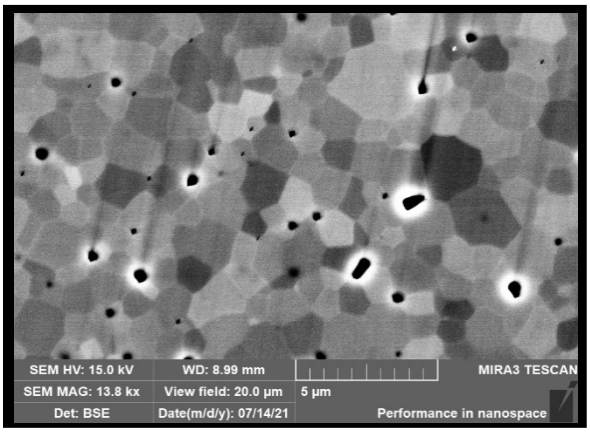

Material Properties			
Density [g/cc]	Density [%]	Grain Size [µm]	Hardness
6.66	98.99	1.06	N/A

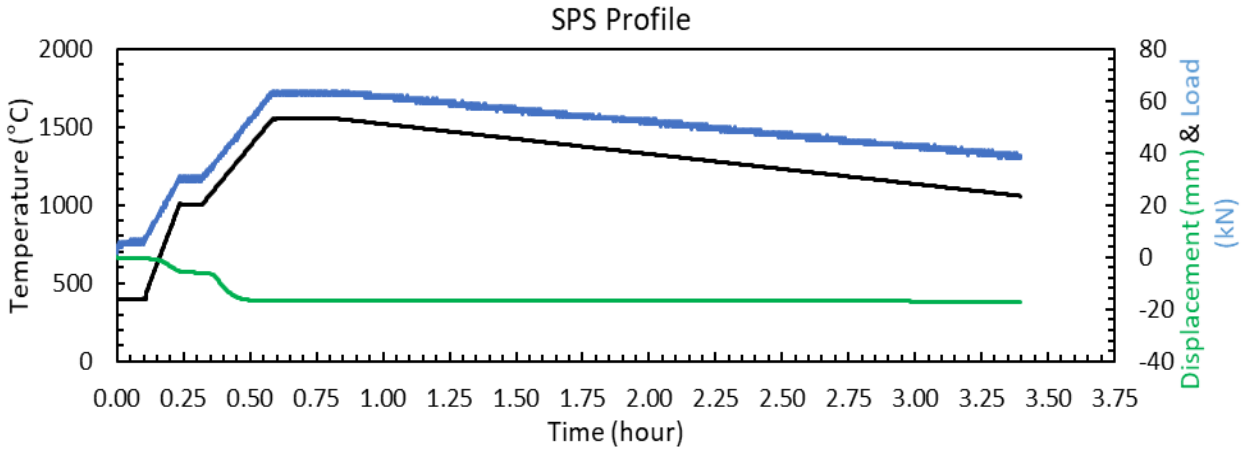

Appendix D: Specimen Preparation Procedures for Microscopy

The procedures described herein are required to prepare a material specimen for microscopic examination. These procedures describe mounting and polishing steps, which could affect the material dimensions and associated properties, and may not be appropriate for specimens prior to creep testing. However, pre-creep test examination can often be accomplished using excess material cut away from the creep test samples, such as the rounded edges of a puck following initial fabrication. These procedures may need to be adjusted accordingly if they are applied to test specimens prior to creep testing.

Specimen Mounting Procedures

- Obtain an appropriately sized sample mounting mold and apply a quick-release coating to the inner surface to allow the epoxy puck to be removed without sticking. Liquid Teflon Mold Release from Allied High Tech Products was used.
- Place the specimen in the center of the mold.
- Prepare the epoxy mixture by mixing the appropriate ratio of epoxy and hardener in a separate container. A standard laboratory scale was used to determine the appropriate amounts based on the instructed ratio by weight. Buehler EpoThin 2 Epoxy Resin and Buehler EpoThin 2 Epoxy Hardener were used with a 2:1 ratio by weight.
- Both substances are thoroughly mixed by hand and are poured into the mold containing the sample.
- The mold containing the sample and resin mixture is placed in a Struers CitoVac vacuum chamber, set at 10 psi for 10 minutes in order to remove any air bubbles from the epoxy.
- The mold is left to cure in air overnight.

Figure D-1: Struers CitoVac vacuum chamber.

Specimen Polishing Procedures

The final epoxy mounts containing the samples are removed from the molds, and polished based on the following procedures. All abrasive and fine polishing pads as well as all diamond particle water-based suspensions were obtained from Allied High-Tech Products. Polishing steps were tailored differently for each specimen depending on the depth of scratches. Typical polishing steps are listed in Table D-1. After each step, the mounted specimen was rinsed thoroughly with water, dried with pressurized nitrogen gas, and was examined under an optical microscope to ensure scratches were become smaller and smaller. The final polished specimen was also placed in an ultrasonic bath of isopropanol for 30 s to remove any remaining debris, and was dried again with nitrogen gas.

Table D-1: Typical polishing steps

Step	Abrasive/ Polishing Pad	Particle Size (µm)	Time (min)	Spin Speed (RPM)	Pressure (lbs)
1	SiC Abrasive	-	20	300	10
2	Orange Label	45	5	250	10
3	Orange Label	15	5	200	8
4	Orange Label	9	5	200	8
5	White Label	3	5	200	8
6	White Label	1	5	200	8
7	Red Final C	0.25	3-5	150	6
8	Red Final C	0.05	3-5	150	6

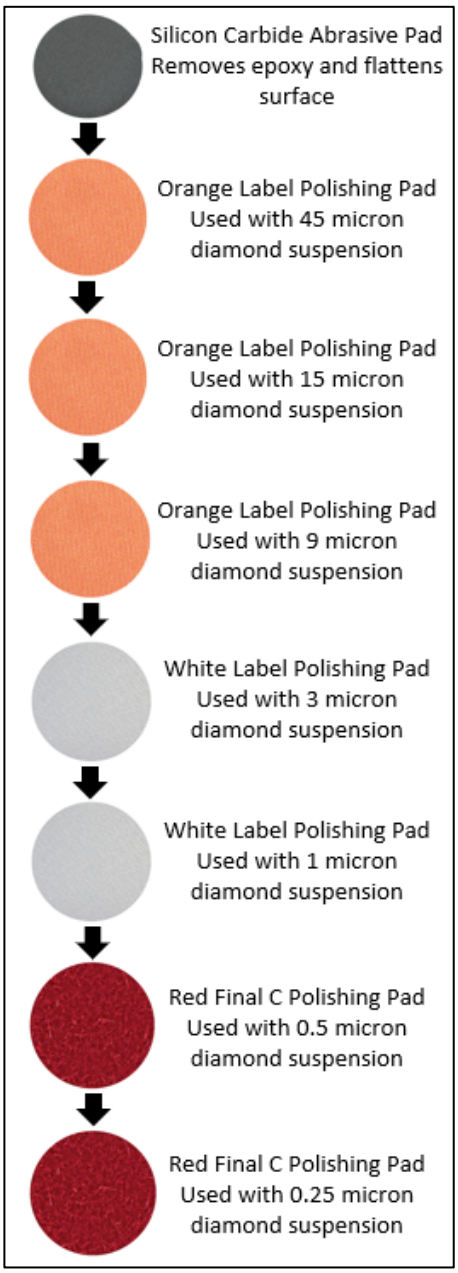

Figure D-2: Various polishing pads used for polishing samples for microscopy.

The polishing pads are visualized along with a brief description in Figure D-2. The Allied Silicon Carbide abrasive discs are designed for metallographic applications to coarse and fine grind a wide variety of materials. They feature superior mineral grading, a unique resin top coat, and a latex additive in the paper. The Orange Label polishing pads are dense, uniquely woven nylon pads and are extremely durable for use with diamond lubricants (15-3 micron). They produce excellent flatness and provides a very high material removal rate on a wide variety of materials. They are designed for intermediate polishing of refractory metals, glass, ceramics, coatings, and composites. White Label polishing pads are very dense, woven, low-nap silk for use with diamond lubricants (6-0.25 micron). They provide excellent flatness and edge retention prior to final polishing on a wide variety of materials. Finally, the Red Final C polishing pads are dense, medium-nap synthetic silk flock for use with diamond lubricants (3-0.25 micron) to provide an excellent final

polish on a wide variety of materials.

After all polishing was completed, the sample was sputter coated with a Carbon coating to approximately 10 nm thickness using an EMS150T ES sputter coater, model #Q150T (Quorum Technologies Ltd.), to prevent surface charging during SEM and EBSD analysis. Prior to analysis in the SEM, Carbon tape is placed in contact with one edge of the specimen and wrapped around the epoxy puck to reduce charging effects further during analysis.

Appendix E: Creep Test Procedures

1) *Load Test Specimen into Universal Material Testing Machine*

   a) Ensure Furnace is aligned correctly in all directions and appears level

   b) Ensure Furnace inserts are connected to furnace to allow room for susceptor to fit

   c) Separately on a flat horizontal surface attach YAG rod holders to steel alignment rod

   d) Tighten YAG rod holder screws

   e) Load YAG rod holders attached to alignment rod into hydraulic wedge grips

   f) Ensure alignment rod is vertical using a level

   g) Adjust lower grip height, ensuring that both YAG rod holders are 1 inch into each grip

   h) Close upper grip

   i) Switch manual control mode to “Force Control” and set force to “0”

   j) Close lower grip

   k) Switch manual control mode to “Displacement Control”

   l) Loosen YAG rod holder screws on both the upper and lower holders

   m) Manually lower the actuator and remove the alignment rod, leaving the YAG rod holders in the grips

   n) Insert YAG rods into YAG rod holders, ensuring copper foil is placed beneath each YAG rod and surrounding the lower portion of each YAG rod

   o) Gently tighten the YAG rod holder screws to grip the YAG rods (only finger tight)

   p) Manually lower or raise the upper crosshead to the desired position (this will always change based on the specimen height and the upper YAG rod length).

      i) The upper crosshead should be high enough, along with the furnace, so that the lower YAG rod holder can never contact the furnace. In order to ensure this setup, with the

crosshead in a high position, raise the lower grip with the YAG rod holder and YAG rod inserted to its highest position. Position the furnace so that it sits just above the YAG rod holder by several millimeters. Then lower the upper crosshead to the desired position above the furnace based on the length of the YAG rod and specimen.

q) Manually lower the lower grip actuator to allow approximately 1 inch gap between the ends of each YAG rod

r) Loosely close furnace around YAG rods and ensure that the YAG rods are centered inside the circular YAG rod openings in the insulation. If not centered, then the furnace location must be adjusted

s) Insert specimen onto the lower YAG rod. There should only be a couple millimeters between the top of the specimen and the upper YAG rod.

t) Using the specimen alignment tool, center the specimen on the lower YAG rod with extensometer grooves facing forward

u) Zero out the force by pressing the auto offset button in the Station Signals window

v) While the alignment tool is closed around the specimen and YAG rods, switch to force control in the manual command window, and apply "-40 lbf" to the specimen. This will ensure that the specimen is held tightly between each YAG rod

w) Remove the alignment fixture and ensure specimen appears fully straight and aligned

x) Loosen YAG rod holder screws so that the YAG rods are no longer clamped

y) Check extensometer alignment:

    i) Load extensometer into the extensometer holder

    ii) Place extensometer rod ends into specimen grooves

    iii) Ensure Extensometer is not touching any part of the holder edges

iv) Loosely close one side of the furnace ensuring the extensometer rods are inside the small openings in the front furnace insulation. If not the specimen must be raised or lowered accordingly, and test setup must be restarted.

v) Remove extensometer from holder and set aside

z) Construct the alumina susceptor around the specimen, ensuring that the specimen and YAG rods are not bumped out of place

aa) Place extensometer back into the holder and ensure the rod tips are in contact with the specimen grooves

bb) Check that the strain reading is somewhat close to zero, ensuring that rods are in contact with the specimen grooves

cc) Screw on the extensometer cooling attachment

dd) With the susceptor held up by the right side furnace insulation, close the left side of the furnace, and lock the furnace halves with the cross bar in the back

ee) Ensure that YAG rods are not touching the furnace insulation and that the extensometer rods are also not touching the furnace insulation or the forward metal portion of the extensometer mount

ff) Place additional soft insulation over the upper part of the furnace

gg) Turn on the air flowing to both furnace sides and to the extensometer cooling attachment

hh) Turn on the chiller and ensure that cold water is flowing to the grips

2) *Initiate Creep Test Procedure*

a) Switch manual control to “Force Control”, and adjust force to “-100 lbf”

b) Leave manual command in “Force Control”

c) Zero out the strain measurement

d) Open appropriate procedure

e) Click “New Specimen” and type the specimen name

f) Lock procedure

g) Ensure that limits are set for upper and lower displacement values. These should be approximately 10 mm above and below the current displacement value. Set these limits as program stop interlocks in the “Detectors” window.

h) Click “Run Test”

3) <u>Creep Test Procedure</u>

a) Force is maintained at -100 lbf

b) Right and left temperature settings are increased to the desired temperature set point at 30°C/min

c) Once the desired furnace temperature settings are achieved, the specimen is held at that temperature for 30 minutes to ensure that the specimen reaches uniform temperature

d) After temperature soak for 30 minutes, the desired creep load is applied at 10 kN/min

e) The specimen will remain under the desired creep load for 5 hours

f) After 5 hours the load is removed back down to -100 lbf, and the temperature is reset to room temperature allowing the furnace and specimen to cool slowly

Appendix F: Effects of Notch Size on the Creep Behavior of YAG and LuAG

Creep specimens were designed with two parallel, horizontal notches machined into one side in order to allow the tips of the extensometer rods to maintain contact with the specimen during creep without slipping on the smooth surface. Initially, large rectangular notches were machined into creep specimens in order to create the most reliable and consistent connection between the extensometer rods and the specimen. However, it was hypothesized that the presence of these large, rectangular notches may affect the state of stress within the specimens to such a degree that the creep behavior could change.

In order to test this hypothesis, a second notch style was designed and implemented on the remaining creep specimens. This iteration of the extensometer rod contact joint was smaller and triangular in shape, and represented the smallest indentation within the specimen, which still allowed for consistent contact between the specimen and the extensometer rods. Diagrams and dimensions of both notches are included in Section 5.1. Preliminary creep tests were performed at 1300°C in air using specimens with each notch design in order to determine the potential effects on the creep behavior. Creep tests were accomplished using both YAG and LuAG specimens. Creep results are displayed here in the same format as they were in Sections 6 and 7. Figure F-1 shows a comparison of the creep strain vs. time curves for undoped, polycrystalline YAG specimens with small and large notches.

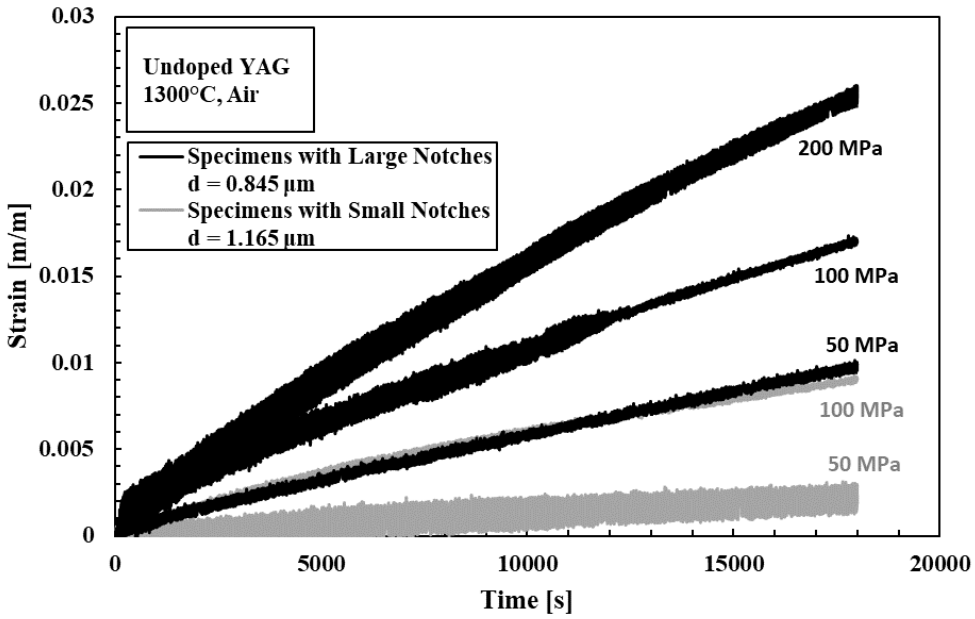

Figure F-1: The creep strain vs. time curves for undoped, polycrystalline YAG specimens with two different notch sizes at 1300°C in air.

There is a significant difference in the strain vs. time curves for YAG specimens with small and large notches. Although the grain sizes of each sample set are not identical, they are close enough to suggest that the difference in notch design is impacting these strain results. The steady-state creep strain rates were determined from the strain vs. time curves, and are summarized in *Table F-1* for YAG specimens with large notches, small notches, and no notches. The specimens with no notches were previously tested by Armani et al. and included here for comparison.

Table F-1: Summary of creep results for undoped, polycrystalline YAG with comparable grain sizes and different notch sizes at 1300°C in air. Results for specimens with grain size of 0.92 µm from Armani et al. (2011) have no notches and are included for comparison [28], [29].

Specimen Name	Grain Size [µm]	Notch Size	Creep Stress [MPa]	Total Accumulated Strain after 5 hrs [%]	Steady-State Creep Strain Rate [s^{-1}]
Y-3-40-1	0.881	Large	50	1.01	4.51×10^{-7}
Y-3-40-2	0.881	Large	100	1.73	7.14×10^{-7}
Y-5-40-1	0.809	Large	150	2.60	1.08×10^{-6}
Y-7-40-1	1.165	Small	50	0.31	9.19×10^{-8}
Y-7-40-2	1.165	Small	100	0.92	3.32×10^{-7}
Y-7-40-3	1.165	Small	150	0.95	3.42×10^{-7}
Armani-1*	0.92	None	50	Not Available**	1.09×10^{-7}
Armani-2*	0.92	None	100	0.81	3.94×10^{-7}
Armani-3*	0.92	None	150	Not Available**	5.69×10^{-7}
Armani-4*	0.92	None	200	1.33	6.91×10^{-7}

*Results obtained by Armani et al. and referenced in this work for comparison [28], [29].
**Creep tests ended early, and strain accumulation after 5 hrs is unknown.

Figure F-2 shows the three sets of steady-state creep strain rates plotted vs. stress on a log-log scale. While specimens with small notches behave very similarly to specimens with no notches, the specimens with large notches show higher strain rates and a flatter slope, revealing a different sensitivity to the applied stress during creep.

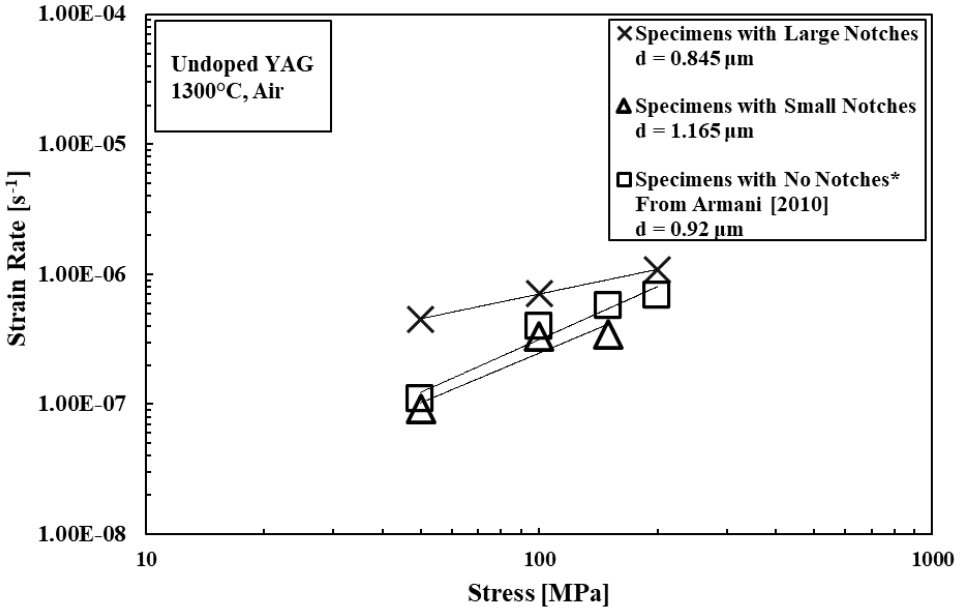

Figure F-2: The steady-state creep strain rates of YAG specimens with comparable grain sizes and different notch sizes at 1300°C in air. Results for specimens with grain size of 0.92 µm from Armani et al. (2010) have no notches and are included for comparison [28], [29].

This analysis was accomplished for LuAG specimens with two different notch sizes as well. Specimens with large notches came from two SPS billets with similar grain sizes. Two specimens were tested from billet L-6-40 with an average grain size of 0.55 µm, and two specimens were tested from billet L-7-40 with an average grain size of 0.44 µm. Specimens with small notches were from billet L-10-40 with an average grain size of 0.54 µm. The creep strain vs. time curves for all these specimens are shown in Figure F-3.

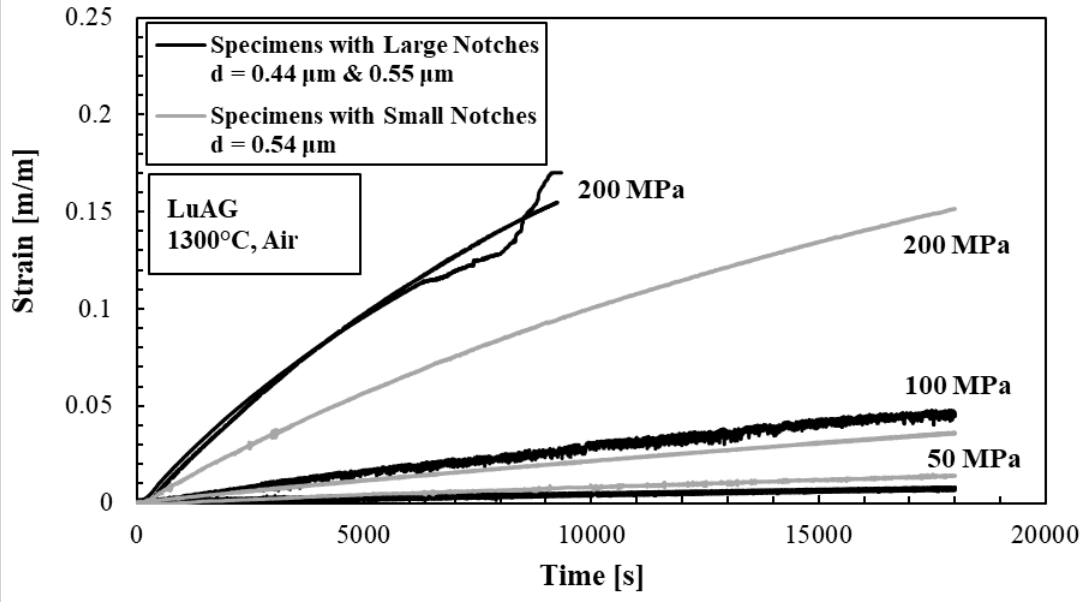

Figure F-3: The creep strain vs. time curves for undoped, polycrystalline LuAG specimens with two different notch sizes at 1300°C in air.

The observed difference in the creep strain results for LuAG specimens with large and small notches is not as consistent as it was for YAG. However, there is still some notable variation. While at 50 MPa the difference appears to be negligible, the difference at 200 MPa is very significant. The steady-state creep strain rates were determined from the strain vs. time curves, and are summarized in *Table F-2* for LuAG specimens with small and large notches.

Table F-2: Summary of creep results for undoped polycrystalline LuAG with comparable grain sizes at 1300°C in air with two different extensometer notch sizes.

Specimen Name	Grain Size [µm]	Notch Size	Creep Stress [MPa]	Total Accumulated Strain after 5 hrs [%]	Steady-State Creep Strain Rate [s^{-1}]
L-6-40-1	0.55	Large	50	0.66	1.80×10^{-7}
L-6-40-2	0.55	Large	100	4.47	1.60×10^{-6}
L-7-40-1	0.44	Large	200	15.35	9.47×10^{-6}
L-7-40-2	0.44	Large	200	17.01	1.11×10^{-5}
L-10-40-1	0.54	Small	50	1.48	7.09×10^{-7}
L-10-40-2	0.54	Small	100	3.58	1.70×10^{-6}
L-10-40-3	0.54	Small	200	15.16	5.36×10^{-6}

Figure F-4 shows two sets of steady-state creep strain rates plotted vs. stress on a log-log scale. Specimens with large notches have higher strain rates at 200 MPa than specimens with small notches. Additionally, a much steeper trend in creep rate vs. stress is apparent for large notches. It is unclear as to why the specimen with large notches at 50 MPa has the lowest creep strain rate; however, it is apparent that the presence of the large notches is introducing a new variable into the potential material properties and test conditions that influence creep behavior.

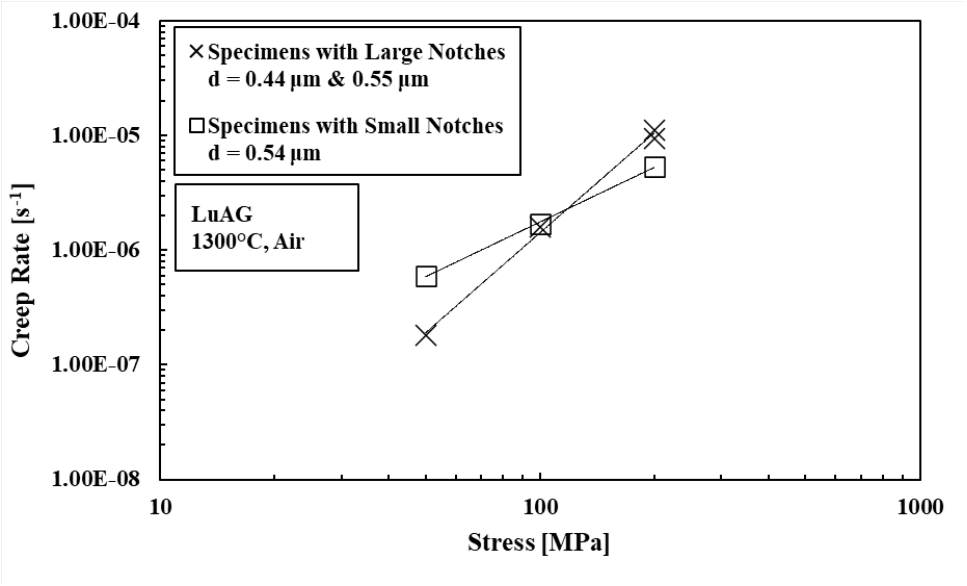

Figure F-4: The steady-state creep rates of LuAG specimens with two different extensometer notch sizes with average grain sizes of 0.49 µm and 0.54 µm for large and small notch sizes, respectively, tested at 1300°C in air.

Appendix G: Fabrication Drawings

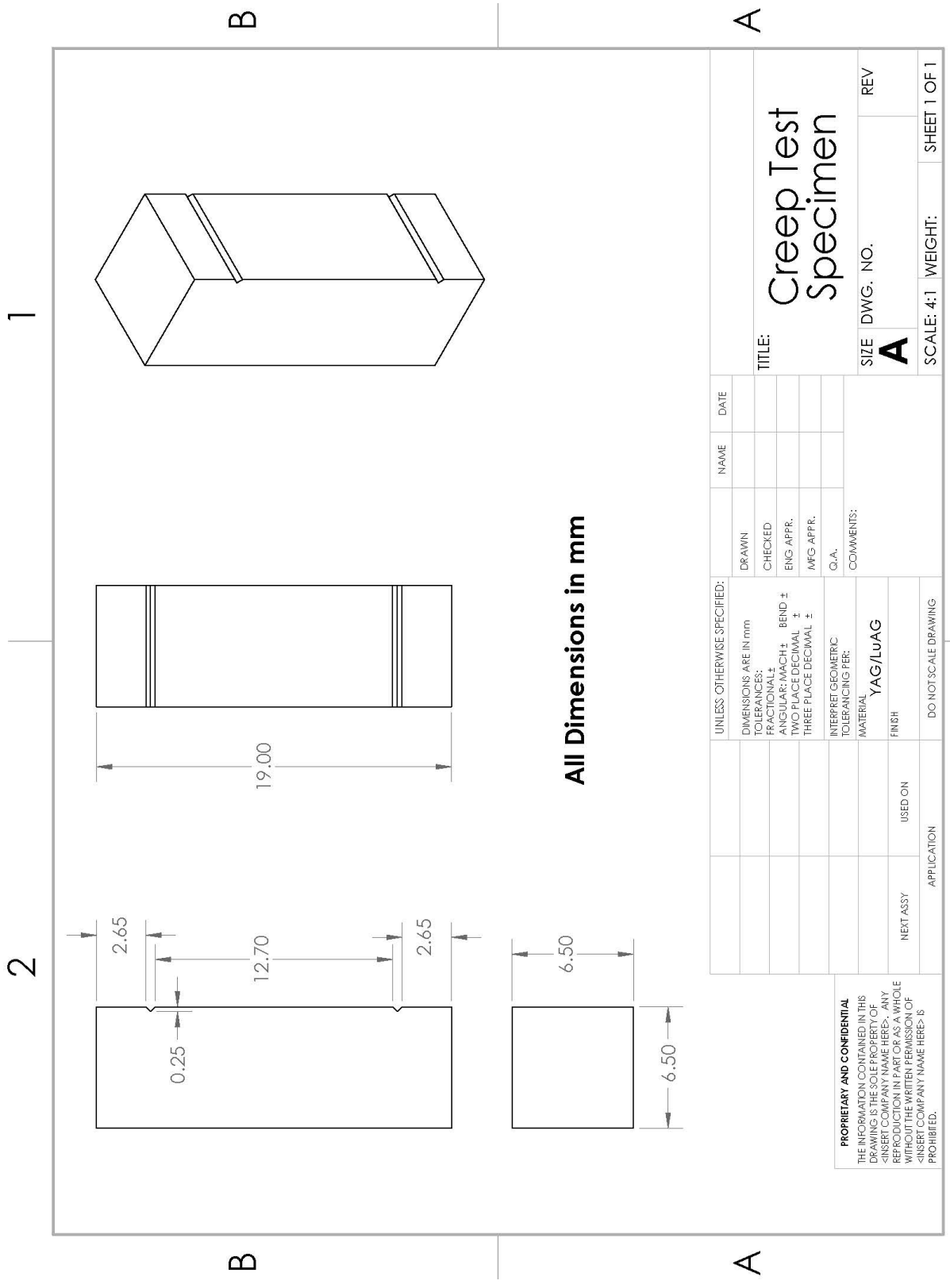

Figure G-1: Creep Specimen Drawing

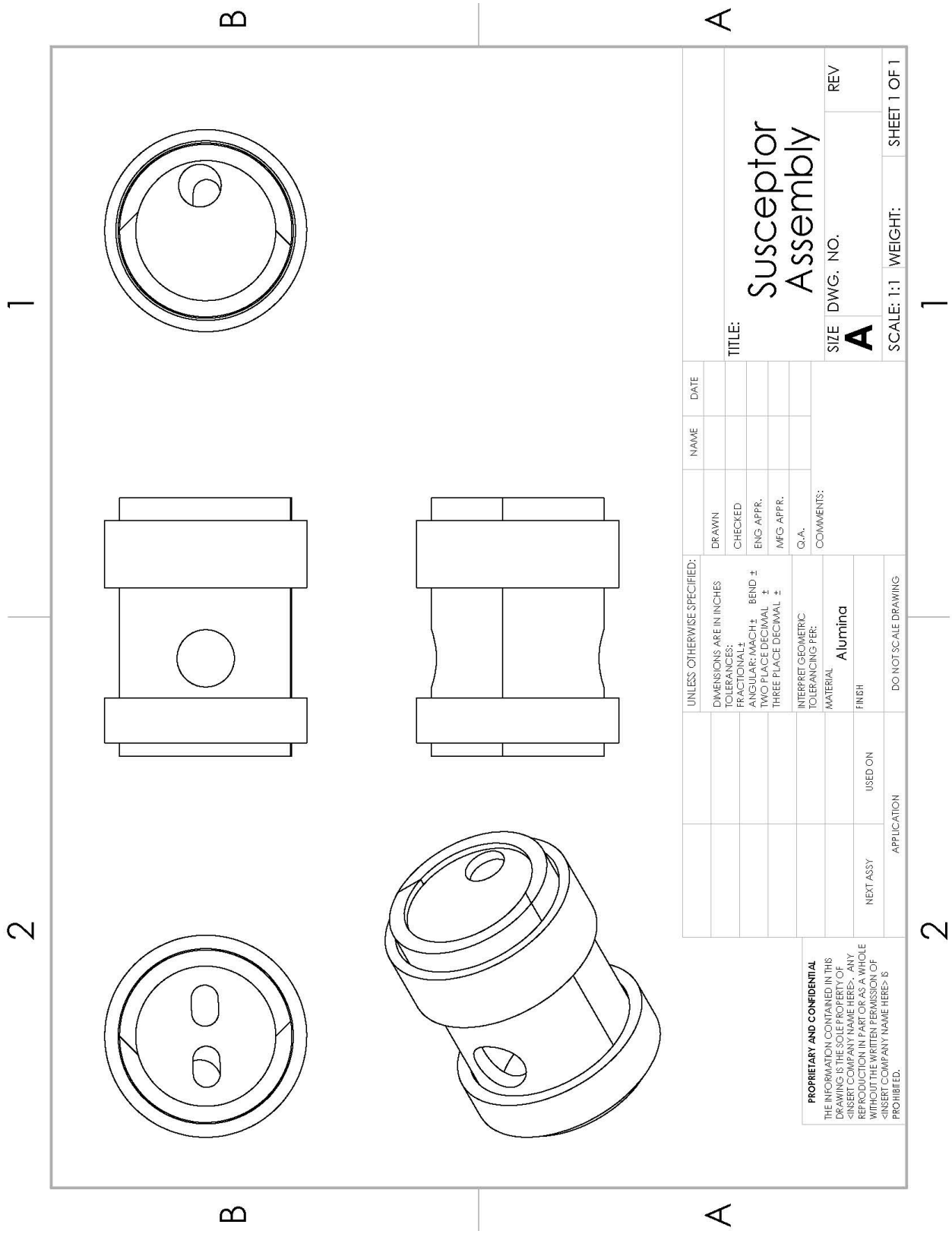

Figure G-2: Susceptor Assembly Drawing

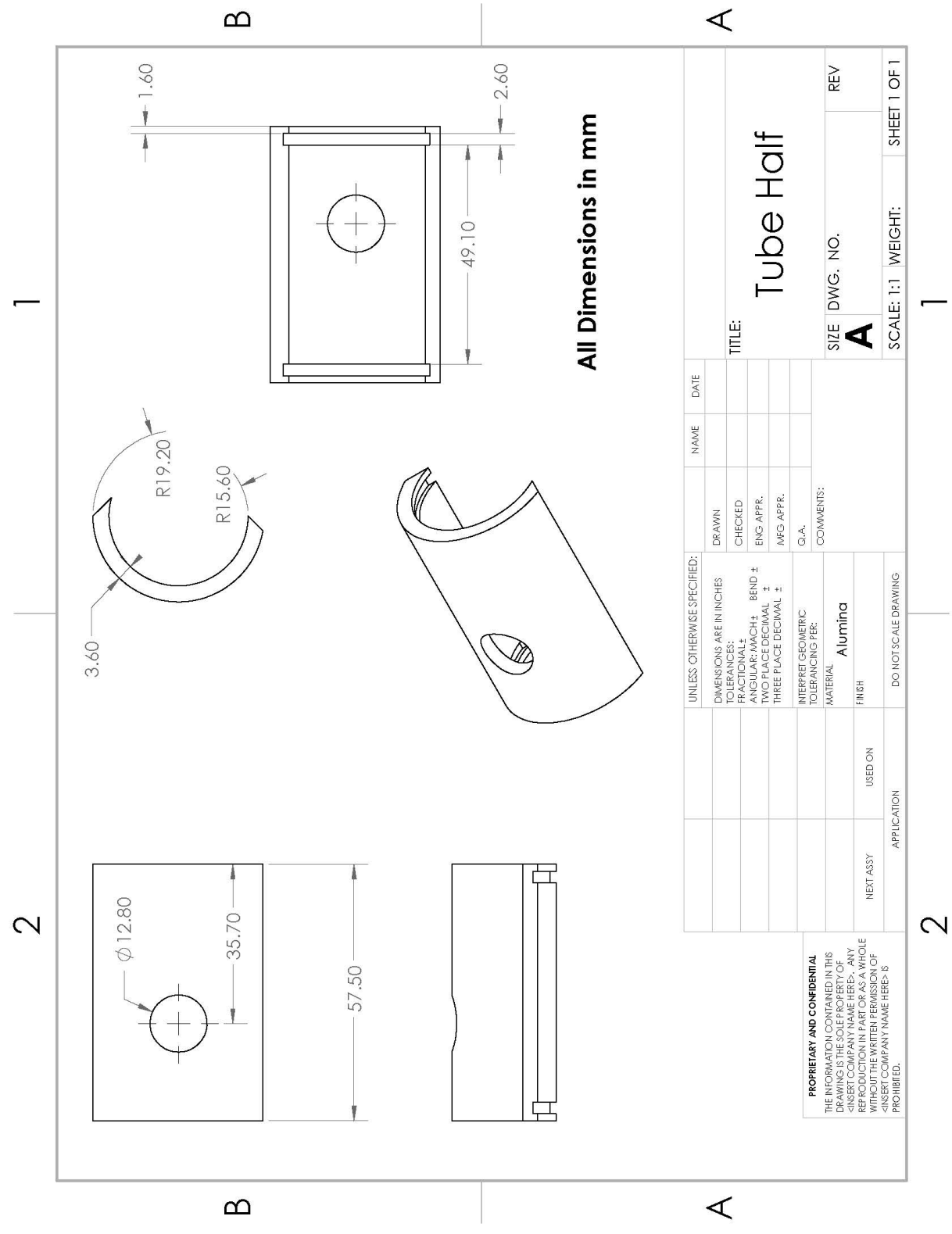

Figure G-3: Susceptor - Tube Half Drawing

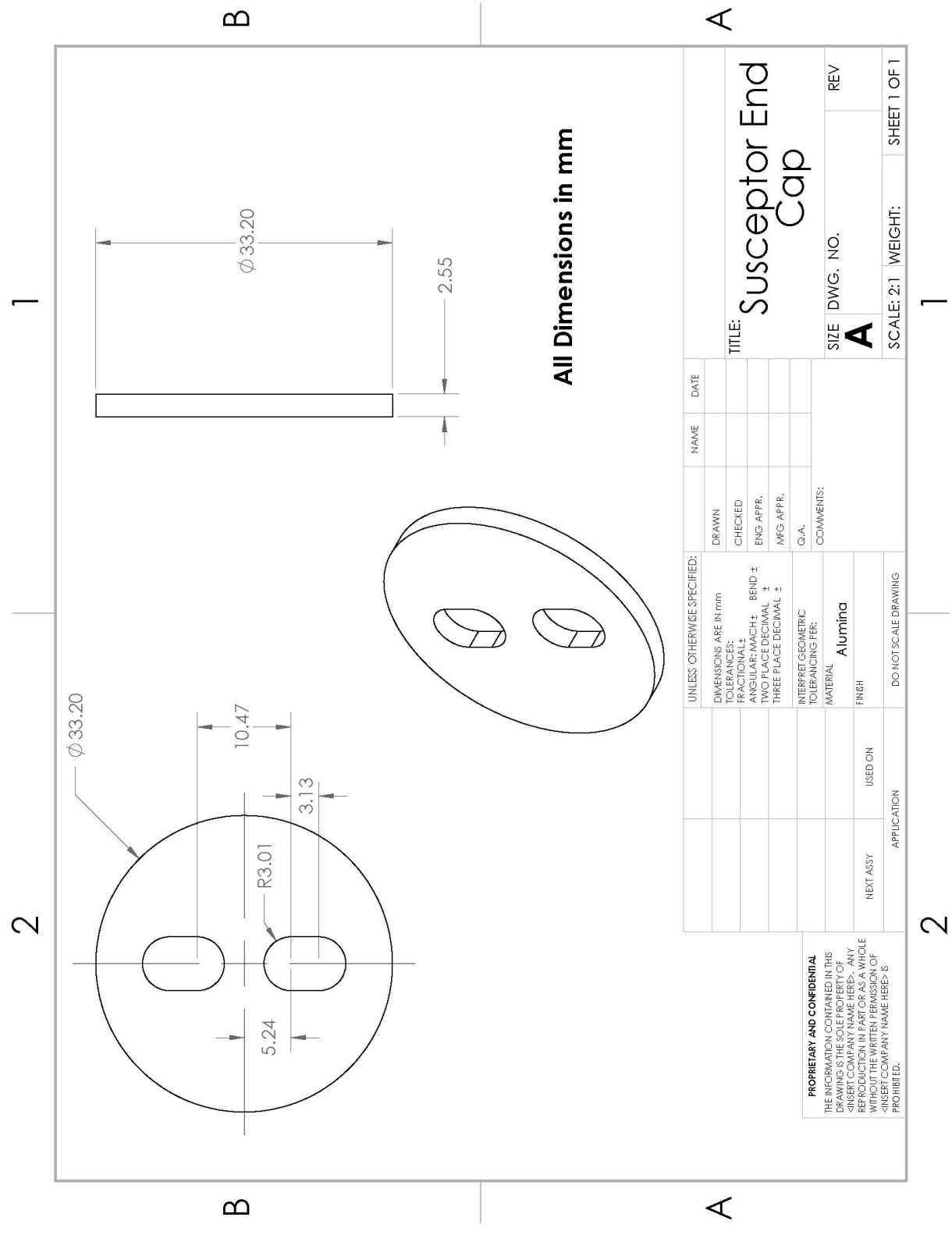

Figure G-4: Susceptor – Extensometer End Cap Drawing

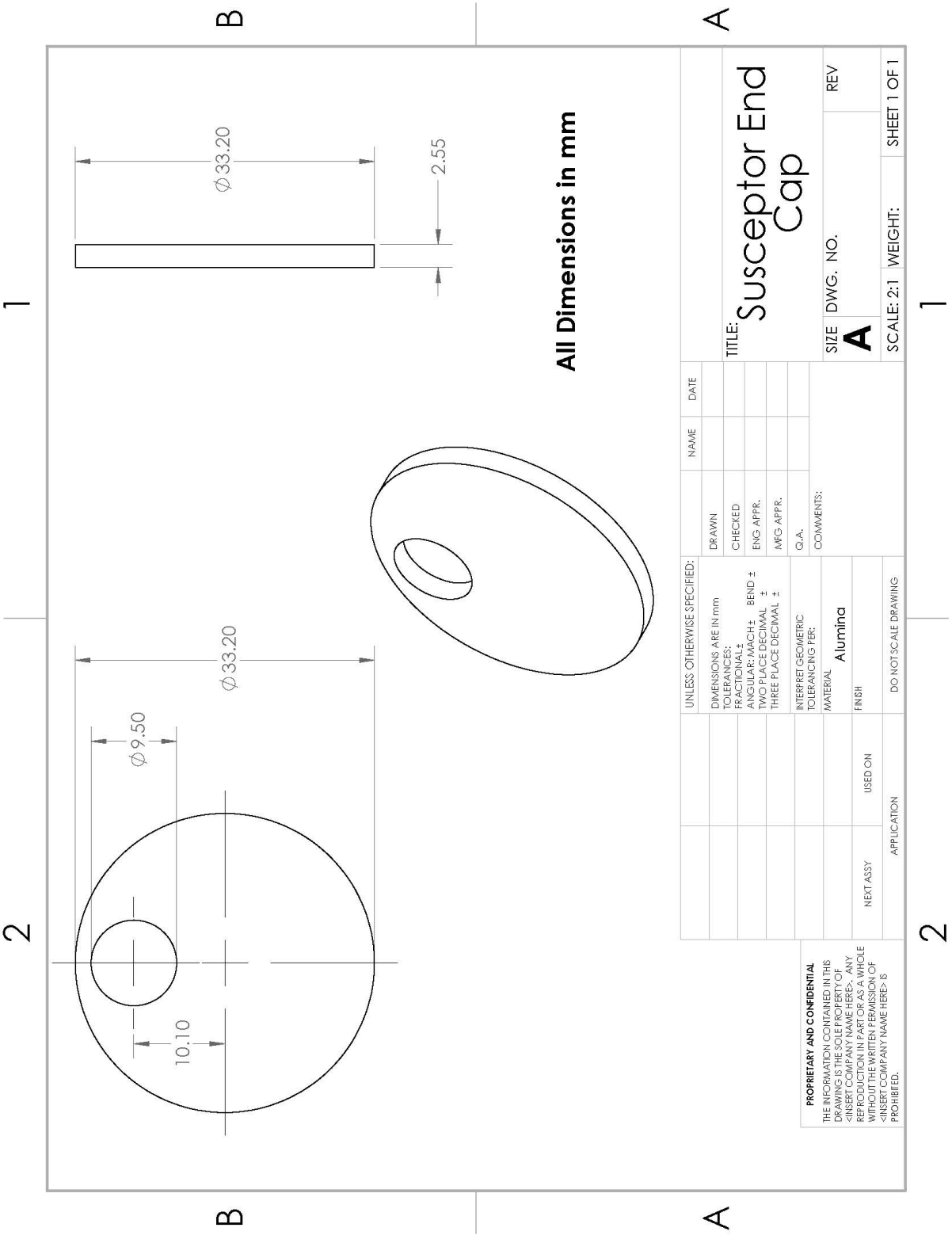

Figure G-5: Susceptor – Steam Tube End Cap Drawing

Figure G-6: Susceptor – Sleeve Drawing

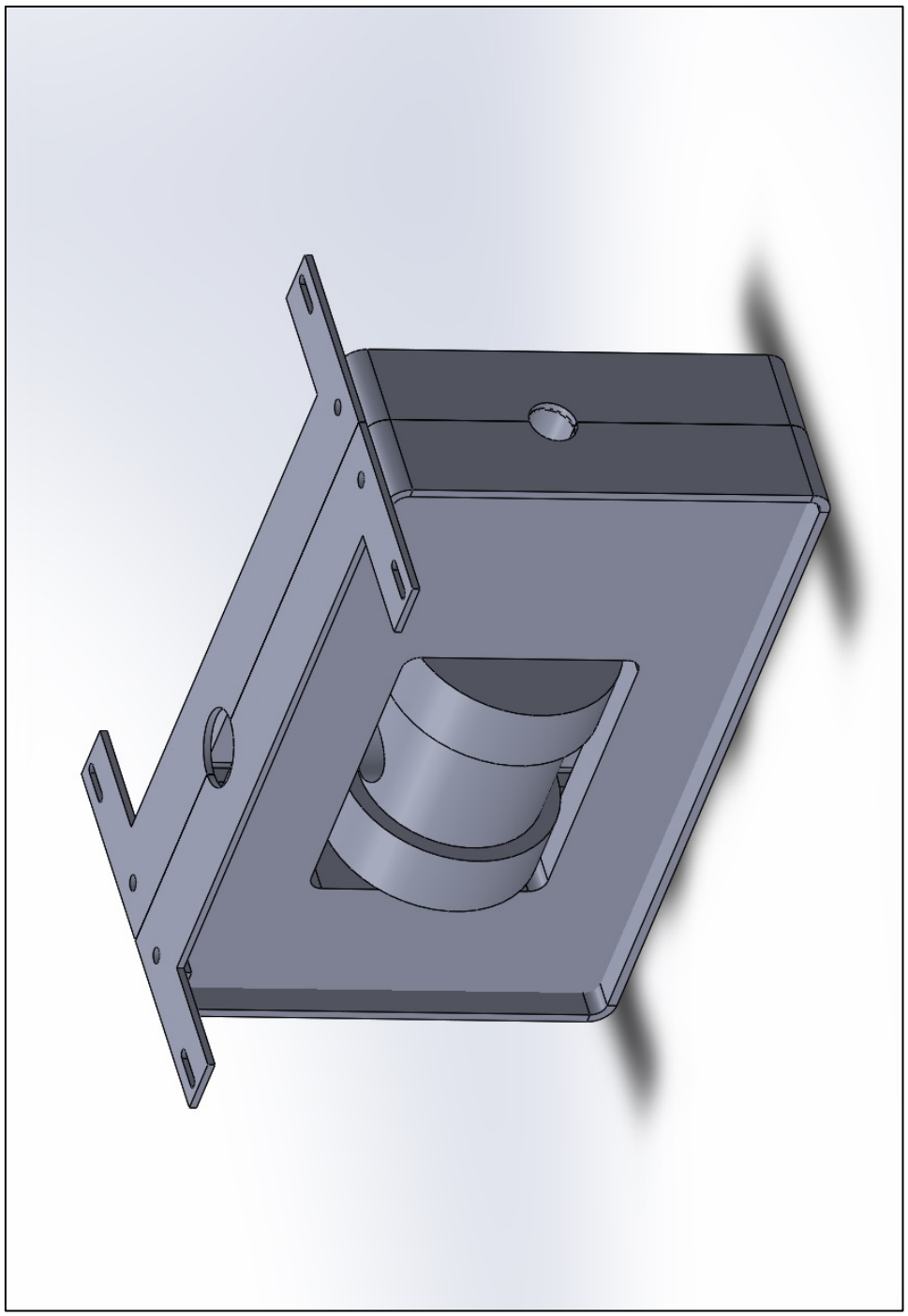

Figure G-7: Furnace Insert with Susceptor

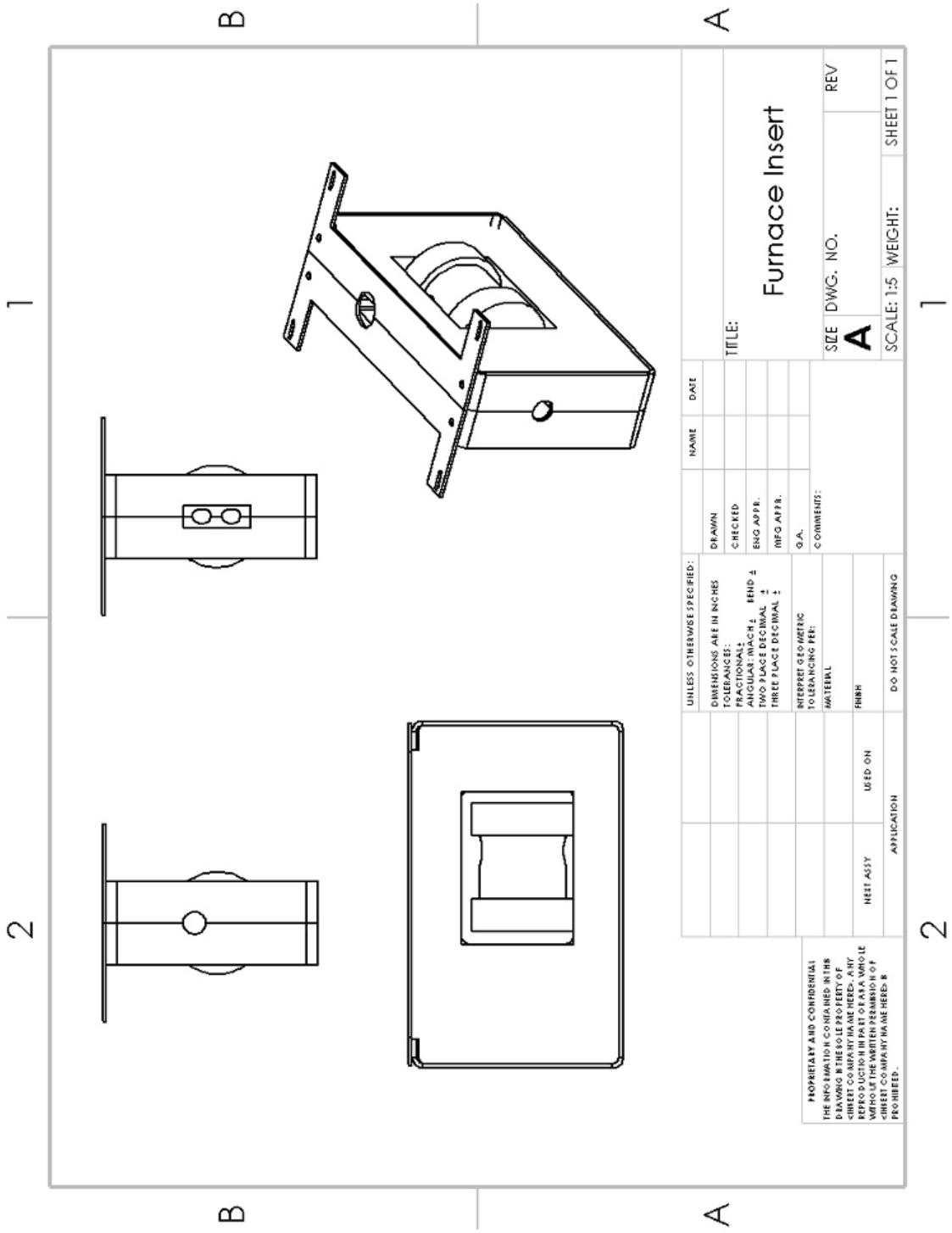

Figure G-8: Furnace Insert Drawing

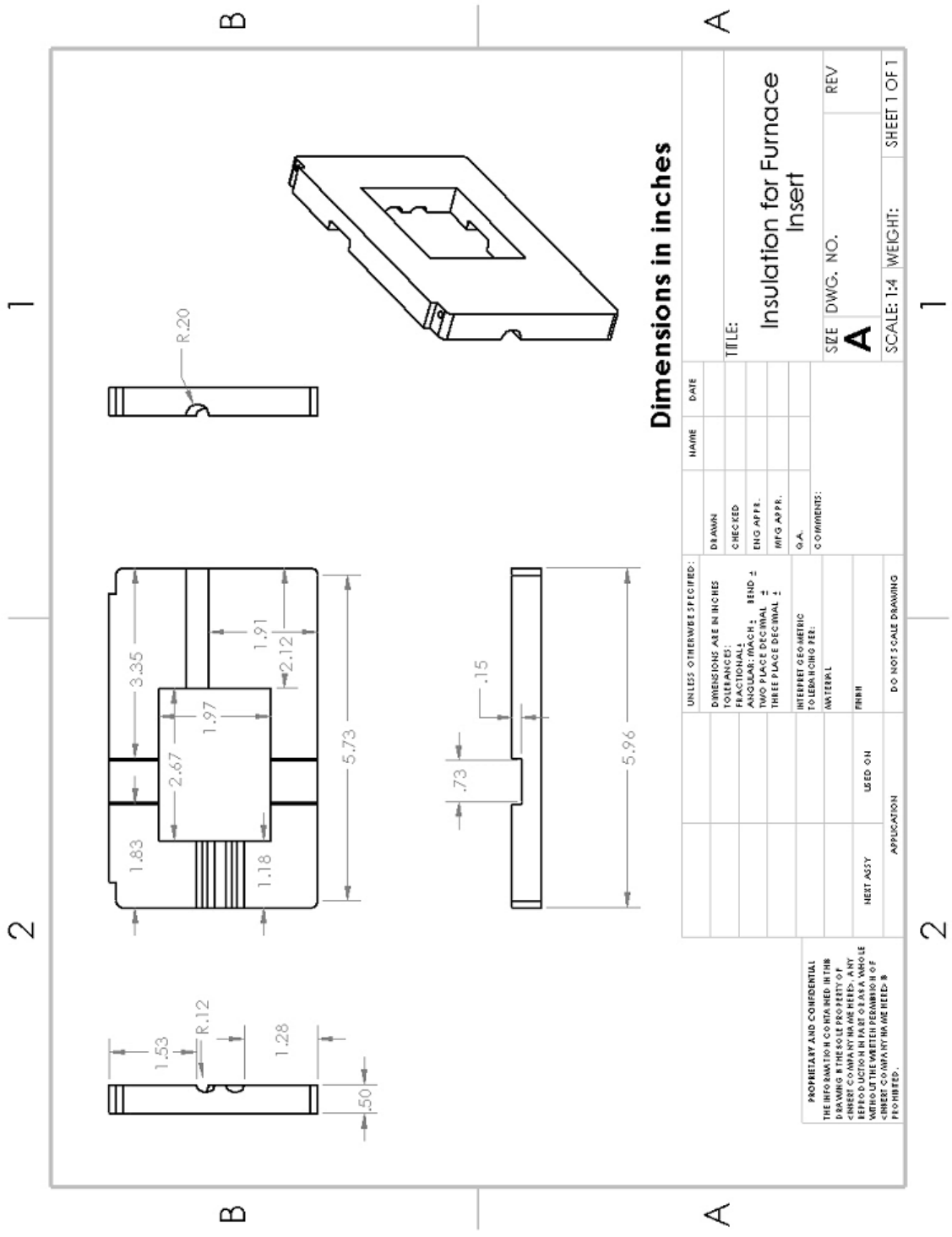

Figure G-9: Furnace Insert - Insulation Drawing

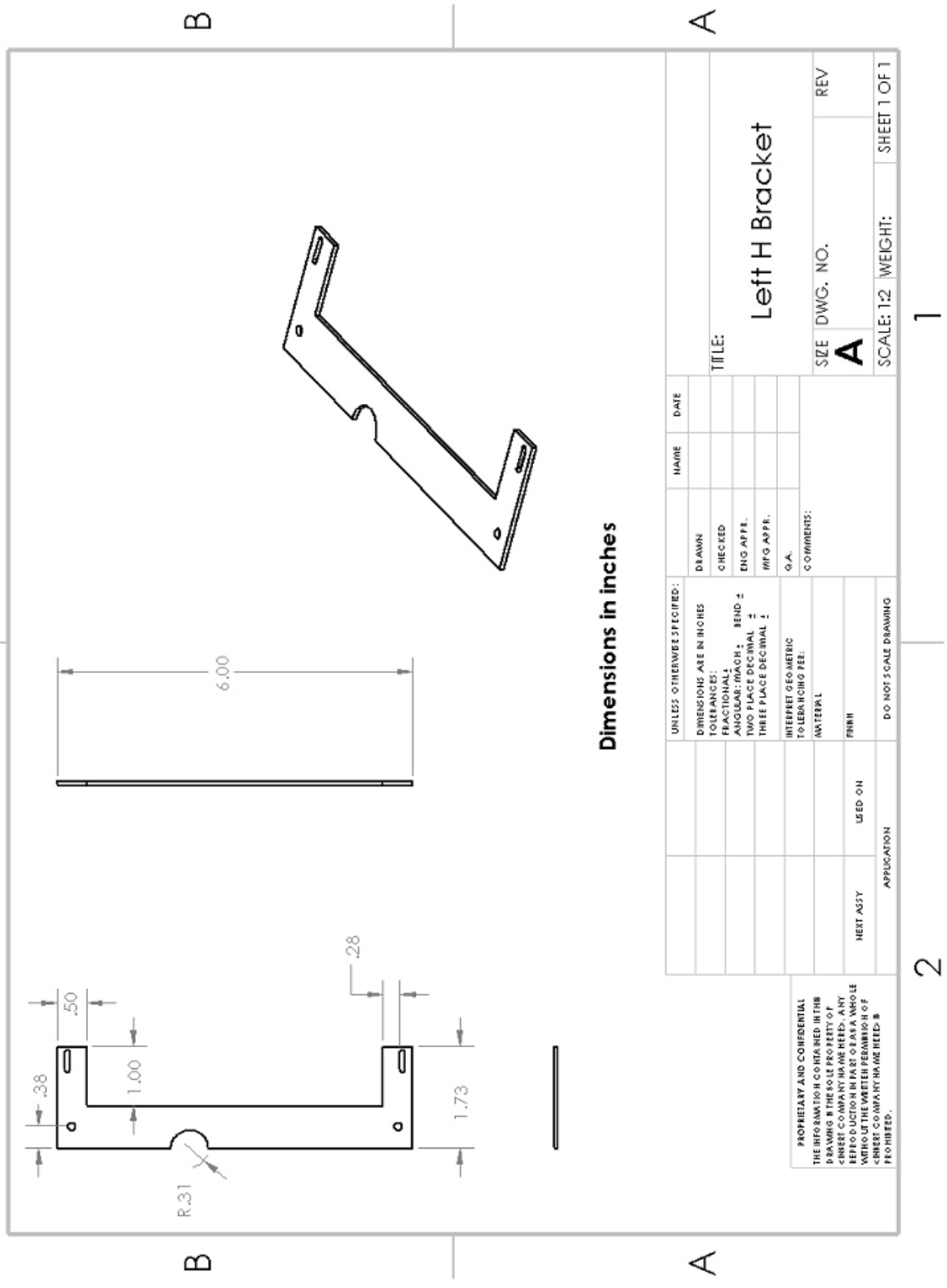

Figure G-10: Furnace Insert – Upper H Bracket Drawing

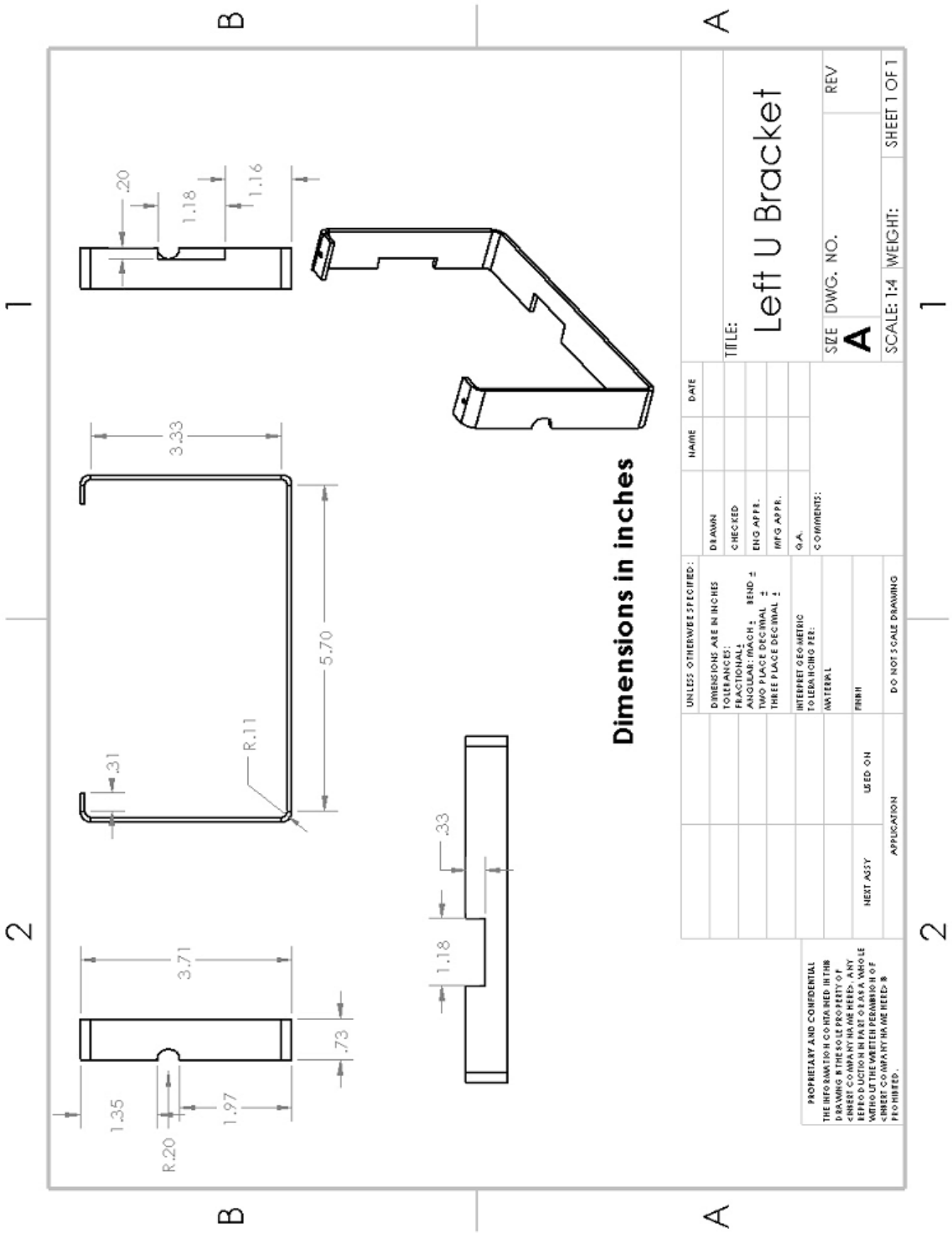

Figure G-11: Furnace Insert – Lower U Bracket Drawing

References

[1] W. G. Fahrenholtz, E. J. Wuchina, W. E. Lee, and Y. Zhou, *Ultra-High Temperature Ceramics: Materials for Extreme Environment Applications*. 2014.

[2] W. D. Callister, "Materials science and engineering: An introduction (2nd edition)," *Mater. Des.*, 1991, doi: 10.1016/0261-3069(91)90101-9.

[3] Dowling, Norman, E, *Mechanical Behavior of Materials*. Upper Saddle River, NJ: Prentice Hall, Inc., 1999.

[4] W. D. Kingery, "Introduction to Ceramics," *J. Electrochem. Soc.*, 2006, doi: 10.1149/1.2133296.

[5] A. P. Mouritz, *Introduction to aerospace materials*. 2012.

[6] A. Paul, J. Binner, and B. Vaidhyanathan, "UHTC Composites for Hypersonic Applications," in *Ultra-High Temperature Ceramics: Materials for Extreme Environment Applications*, 2014.

[7] D. W. Richerson, *Modern Ceramic Engineering*. 2005.

[8] N. S. Jacobson and E. J. Opila, *Oxidation and Corrosion of Non-oxide Ceramics*, no. April 2019. 2016.

[9] B. H. Duff, "Effect of Oxidation on the Strength of Silicon Nitride," *Explic.*, vol. 39, no. 1, pp. 3–4, 1980, doi: 10.1080/00144940.1980.11483398.

[10] G. ERVIN, "Oxidation Behavior of Silicon Carbide," *J. Am. Ceram. Soc.*, vol. 41, no. 9, pp. 347–352, 1958, doi: 10.1111/j.1151-2916.1958.tb12932.x.

[11] T. Mah *et al.*, "Thermal stability of SiC fibres (Nicalon®)," *J. Mater. Sci.*, vol. 19, no. 4, pp. 1191–1201, 1984, doi: 10.1007/BF01120029.

[12] A. G. Evans and R. W. Davidge, "The strength and oxidation of reaction-sintered silicon nitride," *J. Mater. Sci.*, vol. 5, no. 4, pp. 314–325, 1970, doi: 10.1007/BF02397783.

[13] J. J. Sha, T. Hinoki, and A. Kohyama, "Microstructure and mechanical properties of Hi-Nicalon^{TM} Type S fibers annealed and crept in various oxygen partial pressures," *Mater. Charact.*, 2009, doi: 10.1016/j.matchar.2009.01.017.

[14] N. S. Jacobson, E. J. Opila, and K. N. Lee, "Oxidation and corrosion of ceramics and ceramic matrix composites," *Curr. Opin. Solid State Mater. Sci.*, 2001, doi: 10.1016/S1359-0286(01)00009-2.

[15] K. L. More, P. F. Tortorelli, M. K. Ferber, and J. R. Keiser, "Observations of Accelerated Silicon Carbide Recession by Oxidation at High Water-Vapor Pressures," *J. Am. Ceram.*

Soc., vol. 83, no. 1, pp. 211–13, 2000, doi: 10.1111/j.1151-2916.2000.tb01172.x.

[16] E. J. Opila, "Oxidation Kinetics of Chemically Vapor-Deposited Silicon Carbide in Wet Oxygen," *J. Am. Ceram. Soc.*, vol. 77, no. 3, pp. 730–736, 1994, doi: 10.1111/j.1151-2916.1994.tb05357.x.

[17] L. U. J. T. Ogbuji, "A Pervasive Mode of Oxidative Degradation in a SiC-SiC Composite," *J. Am. Ceram. Soc.*, vol. 81, no. 11, pp. 2777–2784, 2005, doi: 10.1111/j.1151-2916.1998.tb02696.x.

[18] J. Roy, S. Chandra, S. Das, and S. Maitra, "Oxidation behaviour of silicon carbide - A review," *Rev. Adv. Mater. Sci.*, vol. 38, no. 1, pp. 29–39, 2014.

[19] A. R. L. Francisco, *Environmental Effects on Non-oxide Ceramics*, vol. 53, no. 9. 2013.

[20] R. C. Breneman, "Phase Changes in Silica and Their Impact on Mechanical Properties in 3-D Printed Investment Casting Molds," *Univ. Michigan*, 2014, [Online]. Available: http://www.engineeringvillage.com/blog/document.url?mid=cpx_M6a43a7f315025149454M7d9310178163171&database=cpx.

[21] M. B. Ruggles-Wrenn, T. Yeleser, G. E. Fair, and J. B. Davis, "Effects of steam environment on creep behavior of Nextel ™ 610/monazite/alumina composite at 1,100°C," *Appl. Compos. Mater.*, vol. 16, no. 6, pp. 379–392, 2009, doi: 10.1007/s10443-009-9105-7.

[22] M. B. Ruggles-Wrenn, P. Koutsoukos, and S. S. Baek, "Effects of environment on creep behavior of two oxide/oxide ceramic-matrix composites at 1200°C," *J. Mater. Sci.*, vol. 43, no. 20, pp. 6734–6746, 2008, doi: 10.1007/s10853-008-2784-x.

[23] C. J. Armani, M. B. Ruggles-Wrenn, R. S. Hay, and G. E. Fair, "Creep and microstructure of Nextel™ 720 fiber at elevated temperature in air and in steam," *Acta Mater.*, vol. 61, no. 16, pp. 6114–6124, 2013, doi: 10.1016/j.actamat.2013.06.053.

[24] 3M Advanced Materials Division, "3M Nextel Ceramic Fibers and Textiles Technical Reference Guide," St. Paul, MN, 2018. [Online]. Available: www.3m.com/ceramics.

[25] G. S. Corman, "Creep of yttrium aluminium garnet single crystals," *J. Mater. Sci. Lett.*, 1993, doi: 10.1007/BF00609160.

[26] T. Parthasarathy, T. Mah, and K. Keller, "High-Temperature Deformation Behavior of Polycrystalline Yttrium Aluminum Garnet (YAG)," *Ceram. Eng. Sci. Proc.*, vol. 18, no. April, pp. 497–505, 1991.

[27] T. Parthasarathy, T. Mah, and K. Keller, "Creep Mechanism of Polycrystalline YAG," vol. 59, pp. 1756–1759, 1992.

[28] C. J. Armani, M. B. Ruggles-Wrenn, R. S. Hay, G. E. Fair, and K. A. Keller, "Creep of polycrystalline yttrium aluminum garnet (YAG) at elevated temperature in air and in

steam," *Mater. Sci. Eng. A*, vol. 589, pp. 125–131, 2014, doi: 10.1016/j.msea.2013.09.083.

[29] C. Armani, "Creep performance of oxide ceramic fiber materials at elevated temperature in air and in steam," 2011, [Online]. Available: http://oai.dtic.mil/oai/oai?verb=getRecord&metadataPrefix=html&identifier=ADA538514

[30] A. DeGregoria, "Creep and Oxidation of Hafnium Diboride-Based Ultra High Temperature Ceramics At 1500˚C," 2015.

[31] M. Wilkinson, "CREEP PERFORMANCE OF ULTRA HIGH TEMPERATURE CERAMICS FOR AEROSPACE SYSTEMS AT 1400 - 1650˚C," Air Force Institute of Technology, 2019.

[32] "A Brief History of Ceramics and Glass," *The American Ceramic Society*, 2018. https://ceramics.org/about/what-are-engineered-ceramics-and-glass/brief-history-of-ceramics-and-glass (accessed Oct. 21, 2019).

[33] P. B. Vandiver, O. Soffer, B. Klima, and J. Svoboda, "The origins of ceramic technology at Dolni Věstonice, Czechoslovakia," *Science (80-.).*, vol. 246, no. 4933, pp. 1002–1008, 1989, doi: 10.1126/science.246.4933.1002.

[34] F. Riley, *Structural Ceramics: Fundamentals and Case Studies*. New York, NY: Cambridge University Press, 2009.

[35] W. Oldfather, "A Note on the Etymology of the Word Ceramic," *J. Am. Ceram. Soc.*, vol. 3, no. 7, pp. 537–542, 1920.

[36] *Encyclopedia of Chemical Technology: Ceramics, Overview*, vol. 3. .

[37] K. K. Chawla, "Composite materials science and engineering," *Composites*, 2003, doi: 10.1016/0010-4361(89)90346-7.

[38] J. B. Wachtman, W. R. Cannon, and M. J. Matthewson, *Mechanical Properties of Ceramics, Second Editon*. 2009.

[39] W. F. Smith, *Principles of Materials Science and Engineering*, 3rd ed. New York, NY: McGraw Hill, Inc., 1996.

[40] W. F. Smith, *Foundations of Materials Science and Engineering*, 3rd Ed. New York, NY: McGraw Hill, Inc., 2004.

[41] E. C. Subbarao, "Advanced ceramics-an overview," *Sadhana*, vol. 13, no. 1–2, pp. 1–11, 1988, doi: 10.1007/BF02811954.

[42] M. C. Tanzi, S. Fare, and G. Candiani, *Foundations of Biomaterials Engineering*, 1st Ed. Academic Press, 2019.

[43] M. Pfeifer, *Materials Enabled Designs*. New York, NY: Elsevier, Inc., 2009.

[44] R. Riedel and I. W. Chen, *Ceramics Science and Technology*. 2013.

[45] R. B. Heimann, *Classic and Advanced Ceramics: From Fundamentals to Applications*. 2010.

[46] K. H. J. Buschow, R. W. Cahn, M. C. Flemings, B. Ilschner, E. J. Kramer, and S. Mahajan, "Encyclopedia of Materials - Science and Technology, Volumes 1-11," *Elsevier*. 2001.

[47] H. F. Al-Qrimli, A. A. Oshkour, F. B. Ismail, and F. A. Mahdi, *Material design consideration for gear component using functional graded materials*, vol. 6, no. 4. 2015.

[48] B. Lawn, "Fracture of Brittle Solids - second edition," *Sci. Ser.*, 1993, doi: 10.1017/CBO9780511623127.

[49] S. Nair and K. Jakus, *High Temperature Mechanical Behavior of Ceramic Composites*. Newton, MA: Buttersworth-Heinemann, 1995.

[50] M. F. Ashby, *Engineering Materials 2*. 2006.

[51] M. F. Ashby, "Materials selection in mechanical design," *Metall. Ital.*, 1994, doi: 10.1016/b0-08-043152-6/00910-4.

[52] S. J. Acquaviva and S. A. Bortz, *Structural Ceramics and Testing of Brittle Materials*. New York, NY: Gordon and Breach, 1968.

[53] N. M. Alford, J. D. Birchall, and K. Kendall, "Engineering ceramics – the process problem," *Mater. Sci. Technol. (United Kingdom)*, vol. 2, no. 4, pp. 329–336, 1986, doi: 10.1179/mst.1986.2.4.329.

[54] UC Davis Library, "Libretexts: Chemistry," 2019. https://chem.libretexts.org/Bookshelves/Inorganic_Chemistry/Supplemental_Modules_(Inorganic_Chemistry)/Descriptive_Chemistry/Main_Group_Reactions/Compounds/Oxides (accessed Oct. 28, 2019).

[55] F. . Petrucci, R.H.; Harwood, W.S. and Herring, *General Chemistry: principles and modern applications 10th ed*. 2002.

[56] J. G. Speight, *Environmental inorganic chemistry for engineers*. 2017.

[57] H. Over and A. P. Seitsonen, "Oxidation of Metal Surfaces," *Science (80-.).*, vol. 297, no. 5589, pp. 2003–2005, 2002.

[58] A. T. Fromhold and R. G. Fromhold, "Chapter 1 An Overview of Metal Oxidation Theory," *Compr. Chem. Kinet.*, vol. 21, no. C, pp. 1–117, 1984, doi: 10.1016/S0069-8040(08)70006-2.

[59] M. M. Ashby and D. R. H. Jones, *Engineering Materials 1*. 2012.

[60] W. Zhi, Q. Qiang, W. Zhanjun, and S. Guodong, "Effect of oxidation at 1100 °c on the strength of ZrB 2-SiC-graphite ceramics," *J. Alloys Compd.*, vol. 509, no. 24, pp. 6871–6875, 2011, doi: 10.1016/j.jallcom.2011.03.163.

[61] "The science and engineering of microelectronic fabrication," *Choice Rev. Online*, 1996, doi: 10.5860/choice.34-2177.

[62] K. M. Prewo and J. A. Batt, "The oxidative stability of carbon fibre reinforced glass-matrix composites," *J. Mater. Sci.*, vol. 23, no. 2, pp. 523–527, 1988, doi: 10.1007/BF01174679.

[63] D. Swanson and J. Wolfrum, "Time to failure modeling of carbon fiber reinforced polymer composites subject to simultaneous tension and one-sided heat flux," *J. Compos. Mater.*, vol. 52, no. 18, pp. 2503–2514, 2018, doi: 10.1177/0021998317749711.

[64] E. Ryshkewitch and D. Richerson, *Oxide Ceramics*, 1st Ed. Orlando, FL: Academic Press, Inc., 1960.

[65] D. Galusek and K. Ghillanyova, *Ceramics Science and Technology Volume 2: Materials and Properties - Chapter: Ceramic Oxides*. 2010.

[66] F. W. Zok, "Developments in oxide fiber composites," *J. Am. Ceram. Soc.*, vol. 89, no. 11, pp. 3309–3324, 2006, doi: 10.1111/j.1551-2916.2006.01342.x.

[67] N. S. Jacobson and D. L. Myers, "Active oxidation of SiC," *Oxid. Met.*, vol. 75, no. 1–2, pp. 1–25, 2011, doi: 10.1007/s11085-010-9216-4.

[68] H. E. Kim and A. J. Moorhead, "Oxidation behaviour and effects of oxidation on the strength of SiC-whisker reinforced alumina," *J. Mater. Sci.*, vol. 29, no. 6, pp. 1656–1661, 1994, doi: 10.1007/BF00368941.

[69] E. J. Opila, "Variation of the Oxidation Rate of Silicon Carbide with Water-Vapor Pressure," *J. Am. Ceram. Soc.*, vol. 82, no. 3, pp. 625–636, 2004, doi: 10.1111/j.1151-2916.1999.tb01810.x.

[70] E. J. Opila and R. E. Hann, "Paralinear oxidation of CVD SiC in water vapor," *J. Am. Ceram. Soc.*, vol. 80, no. 1, pp. 197–205, 1997, doi: 10.1111/j.1151-2916.1997.tb02810.x.

[71] R. J. Kerans, R. S. Hay, and T. A. Parthasarathy, "Structural ceramic composites," *Curr. Opin. Solid State Mater. Sci.*, vol. 4, no. 5, pp. 445–451, 1999, doi: 10.1016/S1359-0286(99)00046-7.

[72] L. U. Ogbuji, "Degradation of SiC/BN/SiC Composite in the Burner Rig," 2010.

[73] K. L. More *et al.*, "Exposure of ceramics and ceramic matrix composites in simulated and actual combustor environments," *J. Eng. Gas Turbines Power*, vol. 122, no. 2, pp. 212–

218, 2000, doi: 10.1115/1.483197.

[74] Ceramics Working Group, “Oxide ceramics,” *University of Chemistry and Technology, Prague*, 2004. http://old.vscht.cz/sil/keramika/Ceramic_Technology.html (accessed Nov. 12, 2019).

[75] R. Riedel, I. Chen, S. K, and D. Strategies, *Ceramics Science and Technology, Vol. 2*. Weinheim: Wiley VCH, 2010.

[76] K. C. Popat and T. A. Desai, “Alumina,” in *Biomaterials Science: An Introduction to Materials: Third Edition*, 2013.

[77] A. Ruys, “Introduction to alumina ceramics,” in *Alumina Ceramics*, 2019.

[78] R. Stevens, *An Introduction to Zirconia*. Twickenham, Middx: Magnesium Elektron Ltd, 1986.

[79] D. R. Clarke, M. Oechsner, and N. P. Padture, “Thermal-barrier coatings for more efficient gas-turbine engines,” *MRS Bull.*, 2012, doi: 10.1557/mrs.2012.232.

[80] M. A. Shand, *The Chemistry and Technology of Magnesia*. 2006.

[81] J. Winkler, *Titanium Dioxide: Production, Properties, and Effective Usage*, 2nd Ed. Hanover, Germany: Vincentz Network, 2013.

[82] C. F. Klingshirn, “ZnO: Material, physics and applications,” *ChemPhysChem*. 2007, doi: 10.1002/cphc.200700002.

[83] G. S. Corman, “Creep of yttrium aluminium garnet single crystals,” *J. Mater. Sci. Lett.*, vol. 12, no. 6, pp. 379–382, 1993, doi: 10.1007/BF00609160.

[84] H. Garem, J. Rabier, and P. Veyssiere, “Slip systems in gadolinium gallium garnet single crystals,” *J. Mater. Sci.*, 1982, doi: 10.1007/BF00540387.

[85] J. R. Smyth and T. C. Mccormick, “Crystallographic Data for Minerals,” 2013.

[86] S. Geller, “Crystal chemistry of the garnets,” *Zeitschrift fur Krist. - New Cryst. Struct.*, vol. 125, no. 125, pp. 1–47, 1967, doi: 10.1524/zkri.1967.125.125.1.

[87] H. King, “Garnet,” *Geology.com*, 2019. https://geology.com/minerals/garnet.shtml (accessed Oct. 12, 2019).

[88] I. Aronovsky, “A trail of garnet and gold: Sri Lanka to Anglo-Saxon England,” *The Historical Association*, 2017. https://www.history.org.uk/publications/resource/9204/a-trail-of-garnet-and-gold-sri-lanka-to-anglo-sax (accessed Sep. 12, 2019).

[89] G. Menzer, “XX. Die Kristallstruktur der Granate,” *Zeitschrift für Krist. - Cryst. Mater.*, 2014, doi: 10.1524/zkri.1929.69.1.300.

[90] S. Kostić *et al.*, “Study of structural and optical properties of YAG and Nd:YAG single crystals,” *Mater. Res. Bull.*, vol. 63, pp. 80–87, 2015, doi: 10.1016/j.materresbull.2014.11.033.

[91] W. Blumenthal and D. Phillips, “High-temperature deformation of single-crystal yttrium-aluminum garnet (YAG).pdf.” .

[92] J. Y. Pastor, J. LLorca, A. Salazar, P. B. Oliete, I. De Francisco, and J. I. Peña, “Mechanical properties of melt-grown alumina-yttrium aluminum garnet eutectics up to 1900 K,” *J. Am. Ceram. Soc.*, vol. 88, no. 6, pp. 1488–1495, 2005, doi: 10.1111/j.1551-2916.2005.00265.x.

[93] K. Keller, T. Mah, and T. A. Parthasarathy, “Processing and Mechanical Properties of Polycrystalline Y3Al5O12 (Yttrium Aluminum Garnet),” 2008.

[94] H. Nozawa, T. Yanagitam, T. Nishimura, and H. Tanaka, “Mechanical properties of fully dense yttrium aluminum garnet (YAG) ceramics,” *J. Ceram. Soc. Japan*, vol. 116, no. 1353, pp. 649–652, 2008, doi: 10.2109/jcersj2.116.649.

[95] L. N. Satapathy and A. H. Chokshi, “Microstructural development and creep deformation in an alumina-5% yttrium aluminum garnet composite,” *J. Am. Ceram. Soc.*, vol. 88, no. 10, pp. 2848–2854, 2005, doi: 10.1111/j.1551-2916.2005.00307.x.

[96] M. Jiménez-Melendo, H. Haneda, and H. Nozawa, “Ytterbium Cation Diffusion in Yttrium Aluminum Garnet (YAG)-Implications for Creep Mechanisms,” *J. Am. Ceram. Soc.*, vol. 84, no. 10, pp. 2356–2360, 2004, doi: 10.1111/j.1151-2916.2001.tb01014.x.

[97] W. X. Que *et al.*, “Transparent ceramics: Processing, materials and applications,” *Prog. Solid State Chem.*, vol. 41, no. 1–2, pp. 20–54, 2012, doi: 10.1016/j.progsolidstchem.2012.12.002.

[98] V. Lupei and A. Lupei, “Nd:YAG at its 50th anniversary: Still to learn,” *J. Lumin.*, 2016, doi: 10.1016/j.jlumin.2015.04.018.

[99] Red Optronix, “ND:YAG Crystal(Neodimium DopedYttrium Aluminum Garnet),” 2019. http://www.redoptronics.com/Nd-YAG-crystal.html (accessed Nov. 12, 2019).

[100] N. Voinova and G. Berezhkova, “Development of Plastic Deformation in Single Crystals of Y3Al5O12 under Compression,” *Sov. Phys. Crystallogr.*, vol. 30, p. 599, 1985.

[101] R. Xu, W. Pang, and Q. Huo, *Modern Inorganic Synthetic Chemistry*. 2011.

[102] L. Mezeix and D. J. Green, “Comparison of the mechanical properties of single crystal and polycrystalline yttrium aluminum garnet,” *Int. J. Appl. Ceram. Technol.*, vol. 3, no. 2, pp. 166–176, 2006, doi: 10.1111/j.1744-7402.2006.02068.x.

[103] T.-I. Mah and T. A. Parthasarathy, “Effects of Temperature, Environment, and Orientation on the Fracture Toughness of Single-Crystal YAG,” *J. Am. Ceram. Soc.*, 2005, doi:

10.1111/j.1151-2916.1997.tb03185.x.

[104] T. Mah and T. A. Parthasarathy, “Fracture toughness of single crystal YAG,” *Scr. Metall. Mater.*, 1993, doi: 10.1016/0956-716X(93)90486-C.

[105] S. Karato, Z. Wang, and K. Fujino, “High-temperature creep of yttrium-aluminium garnet single crystals,” *J. Mater. Sci.*, 1994, doi: 10.1007/BF00354004.

[106] G. N. Morscher, K. C. Chen, and K. S. Mazdiyasni, “Creep-Resistance of Developmental Polycrystalline Yttrium-Aluminum Garnet Fibers,” 2008.

[107] “High-Temperature Creep of Some Single Crystal Oxides.pdf.” .

[108] Y. Kuwano, K. Suda, N. Ishizawa, and T. Yamada, “Crystal growth and properties of (Lu,Y)3Al5O 12,” *J. Cryst. Growth*, 2004, doi: 10.1016/j.jcrysgro.2003.08.060.

[109] American Elements, “Lutetium Aluminum Garnet,” pp. 1–8.

[110] L. An, A. Ito, and T. Goto, “Effect of sintering temperature on the transparency and mechanical properties of lutetium aluminum garnet fabricated by spark plasma sintering,” *J. Eur. Ceram. Soc.*, vol. 32, no. 12, pp. 3097–3102, 2012, doi: 10.1016/j.jeurceramsoc.2012.04.020.

[111] G. Information, D. Ion, and P. Properties, “Lutetium Aluminum Garnet - LuAG - Lu3Al5O12 | Scientific Materials | Laser Materials Laser Materials Lu 3 Al 5 O 12 » Lutetium Aluminum Garnet Lutetium Aluminum Garnet - LuAG - Lu3Al5O12 | Scientific Materials | Laser Materials Page 2 of 2,” pp. 11–12, 2019.

[112] C. Ma *et al.*, “Spectral and Laser Properties of Yb:LuAG Transparent Ceramics Fabricated by Tape Casting Method,” *J. Am. Ceram. Soc.*, vol. 99, no. 10, pp. 3267–3272, 2016, doi: 10.1111/jace.14322.

[113] Z. J. Kiss and R. J. Pressley, “Crystalline Solid Lasers,” *Proc. IEEE*, 1966, doi: 10.1109/PROC.1966.5112.

[114] J. D. Kuntz, J. J. Roberts, M. Hough, and N. J. Cherepy, “Multiple synthesis routes to transparent ceramic lutetium aluminum garnet,” *Scr. Mater.*, vol. 57, no. 10, pp. 960–963, 2007, doi: 10.1016/j.scriptamat.2007.07.017.

[115] Y. K. Liao, D. Y. Jiang, and J. L. Shi, “Transparent lutetium aluminum garnet sintered from carbonate coprecipitated powders,” *Mater. Lett.*, 2005, doi: 10.1016/j.matlet.2005.07.006.

[116] N. J. Cherepy *et al.*, “Cerium-doped single crystal and transparent ceramic lutetium aluminum garnet scintillators,” *Nucl. Instruments Methods Phys. Res. Sect. A Accel. Spectrometers, Detect. Assoc. Equip.*, 2007, doi: 10.1016/j.nima.2007.04.009.

[117] Y. Shi *et al.*, “Microstructure, optical, and scintillation characteristics of Pr 3+ doped

Lu3Al5O12 optical ceramics," *J. Appl. Phys.*, 2011, doi: 10.1063/1.3530679.

[118] T. Yanagida, A. Yoshikawa, A. Ikesue, K. Kamada, and Y. Yokota, "Basic properties of ceramic Pr:LuAG scintillators," *IEEE Trans. Nucl. Sci.*, 2009, doi: 10.1109/TNS.2009.2026475.

[119] J. Li, J. Xu, Y. Shi, H. Qi, J. Xie, and F. Lei, "Fabrication and microstructure of cerium doped lutetium aluminum garnet (Ce:LuAG) transparent ceramics by solid-state reaction method," *Mater. Res. Bull.*, vol. 55, pp. 161–167, 2014, doi: 10.1016/j.materresbull.2014.04.029.

[120] J. Xu *et al.*, "Investigation of an LuAG:Ce translucent ceramic synthesized via spark plasma sintering: Towards a facile synthetic route, robust thermal performance, and high-power solid state laser lighting," *J. Eur. Ceram. Soc.*, vol. 38, no. 1, pp. 343–347, 2018, doi: 10.1016/j.jeurceramsoc.2017.07.036.

[121] E. Auffray and P. Lecoq, "Heavy Scintillating Crystal Fibers for Calorimetry," Geneva, Switzerland, 2009. [Online]. Available: https://indico.cern.ch/event/52562/contributions/1201338/attachments/970709/1379065/EAuffray_meeting180209.pdf.

[122] W. N. Findley, J. S. Lai, K. Onaran, and R. M. Christensen, "Creep and Relaxation of Nonlinear Viscoelastic Materials With an Introduction to Linear Viscoelasticity," *J. Appl. Mech.*, 1977, doi: 10.1115/1.3424077.

[123] I. Shames and F. Cozzarelli, *Elastic and Inelastic Stress Analysis*. Washington DC: Taylor and Francis, 1997.

[124] P. Phillips, "The slow stretch in indiarubber, glass, and metal wires when subjected to a constant pull ," *London, Edinburgh, Dublin Philos. Mag. J. Sci.*, 1905, doi: 10.1080/14786440509463303.

[125] E. Andrade, "On the Viscous Flow in Metals and Allied Phenomena," *Proc. R. Soc.*, 1910.

[126] J. B. WACHTMAN and I. H. MAXWELL, "Plastic Deformation of Ceramic-Oxide Single Crystals," *J. Am. Ceram. Soc.*, 1954, doi: 10.1111/j.1151-2916.1954.tb14041.x.

[127] J. A. STAVROLAKIS and F. H. NORTON, "Measurement of the Torsion Properties of Alumina and Zirconia at Elevated Temperatures," *J. Am. Ceram. Soc.*, 1950, doi: 10.1111/j.1151-2916.1950.tb12796.x.

[128] R. L. COBLE and W. D. KINGERY, "Effect of Porosity on Physical Properties of Sintered Alumina," *J. Am. Ceram. Soc.*, 1956, doi: 10.1111/j.1151-2916.1956.tb15608.x.

[129] W. Roger Cannon and T. G. Langdon, *Creep of ceramics - Part 1 Mechanical characteristics*, vol. 18, no. 1. 1983.

[130] D. Green, *An Introduction to the mechanical properties of Ceramics*. Cambridge

University Press, 1998.

[131] R. W. Davidge, *Mechanical Behaviour of Ceramics*. Cambridge University Press, 1979.

[132] A. Hynes and R. Doremus, "Theories of creep in ceramics," *Crit. Rev. Solid State Mater. Sci.*, 1996, doi: 10.1080/10408439608241255.

[133] W. R. Cannon and T. G. Langdon, "Creep of ceramics - Part 2 An examination of flow mechanisms," *J. Mater. Sci.*, vol. 23, no. 1, pp. 1–20, 1988, doi: 10.1007/BF01174028.

[134] T. G. LANGDON, "Dependence of Creep Rate on Porosity," *J. Am. Ceram. Soc.*, vol. 55, no. 12, pp. 630–631, 1972, doi: 10.1111/j.1151-2916.1972.tb13458.x.

[135] D. P. H. HASSELMAN, "On the Porosity Dependence of the Elastic Moduli of Polycrystalline Refractory Materials," *J. Am. Ceram. Soc.*, vol. 45, no. 9, pp. 452–453, 1962, doi: 10.1111/j.1151-2916.1962.tb11191.x.

[136] J. McClelland, "A Plastic Flow Model of Hot Pressing," *J. Am. Ceram. Soc.*, vol. 44, no. 10, p. 5260, 1960.

[137] A. H. Chokshi and T. G. Langdon, "Characteristics of creep deformation in ceramics," *Mater. Sci. Technol. (United Kingdom)*, vol. 7, no. 7, pp. 577–584, 1991, doi: 10.1179/mst.1991.7.7.577.

[138] A. G. Atkins, "Deformation-mechanism maps (the plasticity and creep of metals and ceramics)," *J. Mech. Work. Technol.*, 1984, doi: 10.1016/0378-3804(84)90015-9.

[139] S. Kailas, "Material Science: Diffusion," Bangalore, India, 2012.

[140] F. R. N. Nabarro, "Deformation of crystals by the motion of single ions," in *Report of a Conference on the Strength of Solids*, 1948, pp. 75–90.

[141] Y. S. Na and J. H. Lee, "Interpretation of viscous deformation of Zr-based bulk metallic glass alloys based on Nabarro-Herring creep model," *Met. Mater. Int.*, 2006, doi: 10.1007/BF03027466.

[142] C. Herring, "Diffusional viscosity of a polycrystalline solid," *J. Appl. Phys.*, vol. 21, no. 5, pp. 437–445, 1950, doi: 10.1063/1.1699681.

[143] R. L. Coble, "A Model for Boundary Diffusion Controlled Creep in Polycrystalline Materials," *J. Appl. Phys.*, vol. 34, no. 6, pp. 1679–1682, 1963, doi: 10.1063/1.1702656.

[144] J. P. Poirier, "Creep of crystals: high-temperature deformation processes in metals, ceramics and minerals.," *Creep Cryst. high-temperature Deform. Process. Met. Ceram. Miner.*, 1985, doi: 10.1016/0191-8141(86)90116-1.

[145] A. G. Evans and T. G. Langdon, "Structural ceramics," *Progress in Materials Science*. 1976, doi: 10.1016/0079-6425(76)90006-2.

[146] H. Frost and M. F. Ashby, “A Second Report on Deformation Mechanisms Maps,” 1973. doi: 10.1017/CBO9781107415324.004.

[147] E. Arzt, M. Ashby, and R. Verrall, “Interface Controlled Diffusional Creep,” *Acta Met.*, vol. 31, no. 12, pp. 1977–1989, 1989.

[148] A. Hynes and R. Doremus, “Theories of creep in ceramics,” *Crit. Rev. Solid State Mater. Sci.*, vol. 21, no. 2, pp. 129–187, 1996, doi: 10.1080/10408439608241255.

[149] Q. Jin, D. S. Wilkinson, G. C. Weatherly, W. E. Luecke, and S. M. Wiederhorn, “Thickness Alteration of Grain-Boundary Amorphous Films during Creep of a Multiphase Silicon Nitride Ceramic,” *J. Am. Ceram. Soc.*, vol. 84, no. 6, pp. 1296–1300, 2004, doi: 10.1111/j.1151-2916.2001.tb00832.x.

[150] F. Nabarro and H. Villiers, *The Physics of Creep*. London: Taylot and Francis, 1995.

[151] I. M. Lifshitz, “On the theory of diffusion-viscous flow of polycrystalline bodies,” *Sov. Phys. JETP*, 1963.

[152] W. A. Rachinger, “Relative grain translations in the plastic flow of aluminium,” *J. Inst. Met.*, vol. 81, pp. 33–41, 1952.

[153] T. G. Langdon, “Grain boundary sliding as a deformation mechanism during creep,” *Philos. Mag.*, vol. 22, no. 178, pp. 689–700, 1970, doi: 10.1080/14786437008220939.

[154] C. H. Yu, C. W. Huang, C. S. Chen, Y. Gao, and C. H. Hsueh, “A micromechanics study of competing mechanisms for creep fracture of zirconium diboride polycrystals,” *J. Eur. Ceram. Soc.*, 2013, doi: 10.1016/j.jeurceramsoc.2013.03.007.

[155] R. C. Gifkins, “The measurement of grain-boundary sliding in polycrystalline specimens,” *Met. Sci. J.*, 1973, doi: 10.1179/030634573790445389.

[156] F. Wakai, N. Kondo, and Y. Shinoda, “Ceramics superplasticity,” *Current Opinion in Solid State and Materials Science*. 1999, doi: 10.1016/S1359-0286(99)00053-4.

[157] F. Wakai, “Superplasticity of ceramics,” *Ceram. Int.*, 1991, doi: 10.1016/0272-8842(91)90062-5.

[158] F. Wakai and A. Domínguez-Rodríguez, “Grain boundary dynamics in ceramics superplasticity,” in *Nanomaterials*, 2006.

[159] D. Hull and D. J. Bacon, *Introduction to Dislocations*. 2011.

[160] R. . S. Molla, “A study on Manufacturing of Deformed Bar (G 60-400W) at Elite Iron and Steel Industries,” 2018. doi: 10.13140/RG.2.2.24320.33289.

[161] J. Weertman, “Steady-State Creep through Dislocation Climb,” *J. Appl. Phys.*, vol. 28, no. 3, pp. 362–364, 1957, doi: 10.1063/1.1722747.

[162] J. Weertman, “Width of a moving edge dislocation calculated with the Nabarro force law,” *Philos. Mag.*, 1968, doi: 10.1080/14786436808227518.

[163] K. V. Ravi, “On the observation of Bardeen-Herring sources in silicon,” *Metall. Trans.*, 1972, doi: 10.1007/bf02642468.

[164] J. Harper and J. E. Dorn, “Viscous creep of aluminum near its melting temperature,” *Acta Metall.*, vol. 5, no. 11, pp. 654–665, 1957, doi: 10.1016/0001-6160(57)90112-8.

[165] T. G. Langdon, “On the possibility of Harper-Dorn creep in non-metallic crystals,” *Philos. Mag. A Phys. Condens. Matter, Struct. Defects Mech. Prop.*, vol. 47, no. 6, pp. L29–L33, 1983, doi: 10.1080/01418618308243115.

[166] L. Jones and R. Tressler, “The High Temperature Creep Behavior of Oxides and Oxide Fibers,” 1991.

[167] R. M. CANNON, W. H. RHODES, and A. H. HEUER, “Plastic Deformation of Fine-Grained Alumina (Al2O3): I, Interface-Controlled Diffusional Creep,” *J. Am. Ceram. Soc.*, 1980, doi: 10.1111/j.1151-2916.1980.tb10648.x.

[168] D. J. Pysher and R. E. Tressler, “Creep rupture studies of two alumina-based ceramic fibres,” *J. Mater. Sci.*, 1992, doi: 10.1007/BF00543932.

[169] J. Gilman, “Monocrystals in Mechanical Technology,” *ASM Trans. Q.*, vol. 59, pp. 597–629, 1966.

[170] R. C. Folweiler, “Creep behavior of pore-free polycrystalline aluminum oxide,” *J. Appl. Phys.*, vol. 32, no. 5, pp. 773–778, 1961, doi: 10.1063/1.1736104.

[171] S. I. WARSHAW and F. H. NORTON, “Deformation Behavior of Polycrystalline Aluminum Oxide,” *J. Am. Ceram. Soc.*, 1962, doi: 10.1111/j.1151-2916.1962.tb11038.x.

[172] E. M. PASSMORE and T. VASILOS, “Creep of Dense, Pure, Fine-Grained Aluminum Oxide,” *J. Am. Ceram. Soc.*, 1966, doi: 10.1111/j.1151-2916.1966.tb15398.x.

[173] E. M. PASSMORE, R. H. DUFF, and T. VASILOS, “Creep of Dense, Polycrystalline Magnesium Oxide,” *J. Am. Ceram. Soc.*, 1966, doi: 10.1111/j.1151-2916.1966.tb13175.x.

[174] C. W. HEWSON and W. D. KINGERY, “Effect of MgO and MgTiO3 Doping on Diffusion-Controlled Creep of Polycrystalline Aluminum Oxide,” *J. Am. Ceram. Soc.*, 1967, doi: 10.1111/j.1151-2916.1967.tb15087.x.

[175] G. W. HOLLENBERG and R. S. GORDON, “Effect of Oxygen Partial Pressure on the Creep of Polycrystalline Al 2 O 3 Doped with Cr, Fe, or Ti,” *J. Am. Ceram. Soc.*, 1973, doi: 10.1111/j.1151-2916.1973.tb15430.x.

[176] P. A. Lessing and R. S. Gordon, “Creep of polycrystalline alumina, pure and doped with transition metal impurities,” *J. Mater. Sci.*, 1977, doi: 10.1007/BF00552251.

[177] A. H. HEUER, N. J. TIGHE, and R. M. CANNON, “Plastic Deformation of Fine-Grained Alumina (Al2O3): II, Basal Slip and Nonaccommodated Grain-Boundary Sliding,” *J. Am. Ceram. Soc.*, 1980, doi: 10.1111/j.1151-2916.1980.tb10649.x.

[178] W. H. Rhodes, D. J. Sellers, T. Vasilos, A. H. Heuer, R. Duff, and P. Burnett, “Summary Report 3-25-65, AVCO Corp., Navy Contract NOW-65-034-P,” 1965.

[179] T. SUGITA and J. A. PASK, “Creep of Doped Polycrystalline Al2O3,” *J. Am. Ceram. Soc.*, 1970, doi: 10.1111/j.1151-2916.1970.tb15983.x.

[180] P. F. Becher, “Deformation substructure in polycrystalline alumina,” *J. Mater. Sci.*, 1971, doi: 10.1007/PL00020367.

[181] A. MOCELLIN and W. D. KINGERY, “Creep Deformation in MgO-Saturated Large-Grain-Size Al2O3,” *J. Am. Ceram. Soc.*, 1971, doi: 10.1111/j.1151-2916.1971.tb12309.x.

[182] L. D. Hou, S. K. Tiku, H. A. Wang, and F. A. Kröger, “Conductivity and creep in acceptor-dominated polycrystalline Al2O3,” *J. Mater. Sci.*, 1979, doi: 10.1007/BF00551027.

[183] R. A. Penty and D. P. H. Hasselman, “Creep kinetics of high-purity, ultra-fine grain polycrystalline mullite,” *Mater. Res. Bull.*, vol. 7, no. 10, pp. 1117–1123, 1972, doi: 10.1016/0025-5408(72)90164-X.

[184] R. M. Cannon and W. H. RHODES, “Deformation processes in forging ceramics, AVCO Corp. Summary Report,” 1970.

[185] C. O. HULSE and J. A. PASK, “Analysis of Deformation of a Fireclay Refractory,” *J. Am. Ceram. Soc.*, 1966, doi: 10.1111/j.1151-2916.1966.tb13271.x.

[186] B. B. Ghate, “Synthesis and pressure-sintering kinetics of high-purity fine-grain mullite,” Lehigh University, 1972.

[187] J. Rabier, H. Garem, and P. Veyssière, “Transmission electron microscopy determinations of dislocation Burgers vectors in plastically deformed yttrium iron garnet single crystals,” *J. Appl. Phys.*, vol. 47, no. 11, pp. 4755–4758, 1976, doi: 10.1063/1.322532.

[188] J. Rabier, P. Veyssière, and H. Garem, “Dissociation of dislocation with a/2⟨111⟩ Burgers vectors in YIG single crystals deformed at high temperature,” *Philos. Mag. A Phys. Condens. Matter, Struct. Defects Mech. Prop.*, vol. 44, no. 6, pp. 1363–1373, 1981, doi: 10.1080/01418618108235815.

[189] T. Mae, “Creep Behavior of an A1203-Y3Al , 012 Eutectic Composite,” vol. 1638, pp. 1628–1638, 1990.

[190] T. A. Parthasarathy, T. Mah, and K. Keller, “High-Temperature Deformation Behavior of Polycrystalline Yttrium Aluminum Garnet (YAG),” *Proceedings of the 15th Annual Conference on Composites and Advanced Ceramic Materials, Part 2 of 2: Ceramic*

Engineering and Science Proceedings, Volume 12, Issue 9/10. pp. 1767–1773, 2008, doi: 10.1002/9780470313848.ch11.

[191] M. Jain, G. Skandan, and R. Cannon, "A New Class of Creep Resistant Oxide/Oxide Ceramic Matrix Composites," 2007.

[192] T. L. Anderson, "FRACTURE MECHANICS Fundamentals and Applications," *Angew. Chemie Int. Ed.*, 2001, doi: 10.1002/1521-3773(20010316)40:6<9823::AID-ANIE9823>3.3.CO;2-C.

[193] R. P. Wei, *Fracture mechanics: Integration of mechanics, materials science and chemistry*. 2010.

[194] A. International, "Engineered Materials Handbook, Ceramics and Glasses," *Engineered Materials Handbook*. 1991.

[195] S. M. WIEDERHORN, "Influence of Water Vapor on Crack Propagation in Soda-Lime Glass," *J. Am. Ceram. Soc.*, 1967, doi: 10.1111/j.1151-2916.1967.tb15145.x.

[196] H. Cao, "HIGH TEMPERATURE STRESS CORROSION CRACKING IN CERAMICS," *Lawrence Berkeley Natl. Lab.*, no. July, 1985.

[197] K. Oda and T. Yoshio, "Hydrothermal Corrosion of Alumina Ceramics," *J. Am. Ceram. Soc.*, vol. 80, no. 12, pp. 3233–3236, 2005, doi: 10.1111/j.1151-2916.1997.tb03258.x.

[198] M. Fritsch, H. Klemm, M. Herrmann, and B. Schenk, "Corrosion of selected ceramic materials in hot gas environment," *J. Eur. Ceram. Soc.*, vol. 26, no. 16, pp. 3557–3565, 2006, doi: 10.1016/j.jeurceramsoc.2006.01.015.

[199] H. Klemm, M. Fritsch, and B. Schenk, "Corrosion of ceramic materials in hot gas environment," *28th Int. Conf. Adv. Ceram. Compos.*, p. 2011, 2011.

[200] J. J. Kruzic, R. M. Cannon, and R. O. Ritchie, "Effects of moisture on grain-boundary strength, fracture, and fatigue properties of alumina," *J. Am. Ceram. Soc.*, vol. 88, no. 8, pp. 2236–2245, 2005, doi: 10.1111/j.1551-2916.2005.00434.x.

[201] W. BLUMENTHAL and A. G. EVANS, "High-Temperature Failure of Polycrystalline Alumina: II, Creep Crack Growth and Blunting," *J. Am. Ceram. Soc.*, 1984, doi: 10.1111/j.1151-2916.1984.tb19512.x.

[202] W.-P. Tai, T. Watanabe, and N. S. Jacobson, "High-Temperature Stability of Alumina in Argon and Argon/Water-Vapor Environments," *J. Am. Ceram. Soc.*, vol. 82, no. 1, pp. 245–248, 2004, doi: 10.1111/j.1151-2916.1999.tb01754.x.

[203] A. K. Kronenberg, J. Castaing, T. E. Mitchell, and S. H. Kirby, "Hydrogen defects in α-Al2O3 and water weakening of sapphire and alumina ceramics between 600 and 1000°C - I. Infrared characterization of defects," *Acta Mater.*, vol. 48, no. 7, pp. 1481–1494, 2000, doi: 10.1016/S1359-6454(99)00448-6.

[204] J. Castaing, A. K. Kronenberg, S. H. Kirby, and T. E. Mitchell, “Hydrogen defects in α-Al2O3 and water weakening of sapphire and alumina ceramics between 600 and 1000°C - II. Mechanical properties,” *Acta Mater.*, vol. 48, no. 7, pp. 1495–1504, 2000, doi: 10.1016/S1359-6454(99)00449-8.

[205] M. Schmücker, P. Mechnich, S. Zaefferer, and H. Schneider, “Water vapor corrosion of mullite: Single crystals versus polycrystalline ceramics,” *J. Eur. Ceram. Soc.*, vol. 28, no. 2, pp. 425–429, 2008, doi: 10.1016/j.jeurceramsoc.2007.03.013.

[206] Y. Harada, T. Suzuki, K. Hirano, and Y. Waku, “Influence of moisture on ultra-high-temperature tensile creep behavior of in situ single-crystal oxide ceramic alumina/yttrium aluminum garnet eutectic composite,” *J. Am. Ceram. Soc.*, vol. 86, no. 6, pp. 951–958, 2003, doi: 10.1111/j.1151-2916.2003.tb03403.x.

[207] N. Bahlawane, T. Watanabe, Y. Waku, A. Mitani, and N. Nakagawa, “Effect of moisture on the high-temperature stability of unidirectionally solidified Al2O3/YAG eutectic composites,” *J. Am. Ceram. Soc.*, 2000, doi: 10.1111/j.1151-2916.2000.tb01685.x.

[208] Nanocerox Inc., “Nanopowder Analysis – High Purity YAG,” no. November, pp. 1–4, 2020.

[209] G. Teikemeier and D. J. Goldberg, “Skin resurfacing with the Erbium: YAG laser,” *Dermatologic Surg.*, 1997, doi: 10.1111/j.1524-4725.1997.tb00389.x.

[210] S. J. Beecher, J. A. Grant-Jacob, P. Hua, D. P. Shepherd, R. W. Eason, and J. I. Mackenzie, “Laser Performance of Yb-doped-Garnet Thin Films Grown by Pulsed Laser Deposition,” 2016, doi: 10.1364/assl.2016.am3a.3.

[211] J. Xu, J. Liu, L. Yang, J. Liu, and Y. Yang, “ Electroluminescent Y 3 Al 5 O 12 nanofilms fabricated by atomic layer deposition on silicon: using Yb as the luminescent dopant and crystallization impetus ,” *Opt. Express*, 2021, doi: 10.1364/oe.412776.

[212] J. Xu, L. Yang, Z. Ma, Y. Yang, and J. Sun, “Electroluminescent polycrystalline Er-doped Lu3Al5O12 nanofilms fabricated by atomic layer deposition on silicon,” *J. Alloys Compd.*, 2021, doi: 10.1016/j.jallcom.2021.160993.

[213] A. Pirri, G. Toci, B. Patrizi, and M. Vannini, “An overview on yb-doped transparent polycrystalline sesquioxide laser ceramics,” *IEEE J. Sel. Top. Quantum Electron.*, 2018, doi: 10.1109/JSTQE.2018.2799003.

[214] Nanocerox Inc., “Nanopowder Analysis – Lutetium Oxide,” no. October, pp. 2–4, 2020.

[215] M. N. Rahaman, *Sintering of ceramics*. 2007.

[216] R. L. Coble, “Intermediate-stage sintering: Modification and correction of a lattice-diffusion model,” *J. Appl. Phys.*, 1965, doi: 10.1063/1.1714479.

[217] F. Parhami and R. M. McMeeking, “A network model for initial stage sintering,” *Mech.*

Mater., 1998, doi: 10.1016/S0167-6636(97)00034-3.

[218] O. N. R.A. Cirelli, "Encyclopedia of Materials: Science and Technology, 2001," in *Comprehensive Nanoscience and Nanotechnology*, 2019.

[219] N. Fourati, N. Blel, Y. Lattach, N. Ktari, and C. Zerrouki, *Reference Module in Materials Science and Materials Engineering*. 2016.

[220] K. Inoue, "Electric-discharge sintering," 3,241,956, 1966.

[221] R. Danzer, T. Lube, R. Morrell, and P. Supancic, "Mechanical Properties of Ceramics," in *Handbook of Advanced Ceramics: Materials, Applications, Processing, and Properties: Second Edition*, 2013.

[222] S. Grasso, Y. Sakka, and G. Maizza, "Pressure effects on temperature distribution during spark plasma sintering with graphite sample," *Mater. Trans.*, 2009, doi: 10.2320/matertrans.M2009148.

[223] S. Grasso, Y. Sakka, and G. Maizza, "Electric current activated/assisted sintering (ECAS): A review of patents 1906-2008," *Science and Technology of Advanced Materials*. 2009, doi: 10.1088/1468-6996/10/5/053001.

[224] R. Orrù, R. Licheri, A. M. Locci, A. Cincotti, and G. Cao, "Consolidation/synthesis of materials by electric current activated/assisted sintering," *Mater. Sci. Eng. R Reports*, vol. 63, no. 4–6, pp. 127–287, 2009, doi: 10.1016/j.mser.2008.09.003.

[225] M. Qian and F. H. Sam Froes, *Titanium powder metallurgy: Science, technology and applications*. 2015.

[226] *Handbook of Advanced Ceramics*. 2013.

[227] M. Prakasam, F. Balima, S. Cygan, P. Klimczyk, L. Jaworska, and A. Largeteau, "Ultrahigh pressure SPS (HP-SPS) as new syntheses and exploration tool in materials science," in *Spark Plasma Sintering*, 2019.

[228] R. M. Pérez *et al.*, "Improving optical transmission of spark-plasma-sintered yag ceramics: Effect of powder conditioning and post-treatments," *J. Ceram. Sci. Technol.*, 2018, doi: 10.4416/JCST2017-00052.

[229] E. Bódis and Z. Károly, "Fabrication of graded alumina by spark plasma sintering," *Int. J. Adv. Manuf. Technol.*, 2021, doi: 10.1007/s00170-021-07855-0.

[230] S. Benaissa, M. Hamidouche, M. Kolli, and G. Fantozzi, "Optical and mechanical characterization of transparent α-alumina fabricated by spark plasma sintering," *Int. J. Appl. Ceram. Technol.*, 2019, doi: 10.1111/ijac.13109.

[231] B. N. Kim *et al.*, "Low-temperature spark plasma sintering of alumina by using SiC molding set," *J. Ceram. Soc. Japan*, 2016, doi: 10.2109/jcersj2.16082.

[232] J. G. Santanach, A. Weibel, C. Estourns, Q. Yang, C. Laurent, and A. Peigney, “Spark plasma sintering of alumina: Study of parameters, formal sintering analysis and hypotheses on the mechanism(s) involved in densification and grain growth,” *Acta Mater.*, 2011, doi: 10.1016/j.actamat.2010.11.002.

[233] V. Nečina and W. Pabst, “Influence of the heating rate on grain size of alumina ceramics prepared via spark plasma sintering (SPS),” *J. Eur. Ceram. Soc.*, 2020, doi: 10.1016/j.jeurceramsoc.2020.03.057.

[234] M. Vukšić, I. Žmak, L. Ćurković, and A. Kocjan, “Spark plasma sintering of dense alumina ceramics from industrial waste scraps,” *Open Ceram.*, 2021, doi: 10.1016/j.oceram.2021.100076.

[235] D. Pravarthana *et al.*, “Growth and texture of spark plasma sintered Al2O3 ceramics: A combined analysis of X-rays and electron back scatter diffraction,” *J. Appl. Phys.*, 2013, doi: 10.1063/1.4802439.

[236] M. Sokol, S. Kalabukhov, V. Kasiyan, M. P. Dariel, and N. Frage, “Functional Properties of Nd:YAG Polycrystalline Ceramics Processed by High-Pressure Spark Plasma Sintering (HPSPS),” *J. Am. Ceram. Soc.*, 2016, doi: 10.1111/jace.14051.

[237] A. Wagner, B. Ratzker, S. Kalabukhov, E. Galun, M. P. Dariel, and N. Frage, “Photoluminescence of Doped YAG Transparent Ceramics Fabricated by Spark Plasma Sintering,” *Isr. J. Chem.*, 2020, doi: 10.1002/ijch.201900131.

[238] A. Wagner, B. Ratzker, S. Kalabukhov, M. Sokol, and N. Frage, “Residual porosity and optical properties of spark plasma sintered transparent polycrystalline cerium-doped YAG,” *J. Eur. Ceram. Soc.*, 2019, doi: 10.1016/j.jeurceramsoc.2018.11.006.

[239] V. D. Paygin *et al.*, “Spark plasma sintering of transparent YAG:Ce ceramics with LiF flux,” 2021, doi: 10.1088/1742-6596/1989/1/012008.

[240] R. Chaim, “Densification mechanisms in spark plasma sintering of nanocrystalline ceramics,” *Mater. Sci. Eng. A*, 2007, doi: 10.1016/j.msea.2006.07.092.

[241] R. Chaim, R. Marder-Jaeckel, and J. Z. Shen, “Transparent YAG ceramics by surface softening of nanoparticles in spark plasma sintering,” *Mater. Sci. Eng. A*, 2006, doi: 10.1016/j.msea.2006.04.072.

[242] R. Chaim and Z. Shen, “Grain size control by pressure application regime during spark plasma sintering of Nd-YAG nanopowders,” *J. Mater. Sci.*, 2008, doi: 10.1007/s10853-008-2742-7.

[243] S. A. Kumar and J. Senthilselvan, “Fabrication and characterization of spark plasma sintered Ce:LuAG ceramic for scintillation application,” 2016, doi: 10.1063/1.4947937.

[244] J. Pejchal *et al.*, “Luminescence and scintillation properties of Lu3Al5O12 nanoceramics sintered by SPS method,” *Opt. Mater. (Amst).*, 2016, doi: 10.1016/j.optmat.2016.01.024.

[245] V. Babin *et al.*, “Luminescence of undoped LuAG and YAG crystals,” 2005, doi: 10.1002/pssc.200460120.

[246] P. A. Cutler, C. L. Melcher, M. A. Spurrier, P. Szupryczynski, and L. A. Eriksson, “Scintillation non-proportionality of lutetium- and yttrium-based silicates and aluminates,” *IEEE Trans. Nucl. Sci.*, 2009, doi: 10.1109/TNS.2009.2016421.

[247] R. Marder, C. Estournès, G. Chevallier, and R. Chaim, “Spark and plasma in spark plasma sintering of rigid ceramic nanoparticles: A model system of YAG,” *J. Eur. Ceram. Soc.*, 2015, doi: 10.1016/j.jeurceramsoc.2014.08.001.

[248] W. Zeng, W. Qin, C. Gu, H. Sun, Y. Ma, and X. Cao, “Microstructure and properties of pure aluminum prepared by spark plasma sintering,” *Metall. Res. Technol.*, 2019, doi: 10.1051/metal/2018105.

[249] D. Y. Kosyanov *et al.*, “Influence of carbon contamination on transparency of reactive SPSed Nd3+:YAG ceramics,” 2020, doi: 10.1088/1742-6596/1461/1/012187.

[250] U. Täffner, V. Carle, U. Schäfer, and M. J. Hoffmann, “Preparation and Microstructural Analysis of High-Performance Ceramics,” in *Metallography and Microstructures*, 2018.

[251] M. Rahmani, O. Mirzaee, M. Tajally, and M. R. Loghman-Estarki, “Comparison of synthesis and spark plasma sintering of YAG nano particles by variation of pH and precipitator agent,” *Ceram. Int.*, 2018, doi: 10.1016/j.ceramint.2018.07.130.

[252] P. Echlin, *Handbook of Sample Preparation for Scanning Electron Microscopy and X-Ray Microanalysis*. 2009.

[253] J. I. Goldstein *et al.*, “Specimen Preparation of Hard Materials: Metals, Ceramics, Rocks, Minerals, Microelectronic and Packaged Devices, Particles, and Fibers,” in *Scanning Electron Microscopy and X-ray Microanalysis*, 2003.

[254] Appalachian State University, “Archimedes Principle,” 2001. http://www.appstate.edu/~cockmanje/labs/1103/spring/Archimedes.

[255] Micromeritics, “AccuPyc II 1345,” 2020. .

[256] Micromeritics, *AccuPyc 1330 Quick Reference Guide*. 1990.

[257] American Elements, “Yttrium Aluminum Garnet,” 2020. .

[258] Scientific Materials, “Laser Materials: Yttrium Aluminum Garnet.” .

[259] D. N. French, “Grain Boundaries.,” *The National Board of Boiler and Pressure Vessel Inspectors*, 1991. https://www.nationalboard.org/index.aspx?pageID=164&ID=194.

[260] ASTM, “ASTM E112-13: Standard test methods for determining average grain size,” *ASTM Int.*, 2013.

[261] S. Kochawattana *et al.*, “Sintering and grain growth in SiO2 doped Nd:YAG,” *J. Eur. Ceram. Soc.*, 2008, doi: 10.1016/j.jeurceramsoc.2007.12.006.

[262] W. Jia *et al.*, “Densification and luminescence properties of Nd:YAG transparent ceramics,” *Optik (Stuttg).*, 2021, doi: 10.1016/j.ijleo.2020.166161.

[263] W. Jia, Q. Wei, H. Zhang, C. Su, G. Ren, and M. Zhao, “Luminescence Properties of Lu3+doped Nd: YAG Transparent Ceramics,” 2021, doi: 10.1088/1742-6596/1907/1/012010.

[264] A. A. Trofimov, M. R. Marchewka, and L. G. Jacobsohn, “Effects of sintering temperature on the microstructure and luminescence of LuAG:Pr ceramics,” *Radiat. Meas.*, 2019, doi: 10.1016/j.radmeas.2019.01.005.

[265] M. R. Marchewka, M. G. Chapman, H. Qian, and L. G. Jacobsohn, “Investigation of Pr incorporation in LuAG powders and ceramics,” 2016, doi: 10.1109/nssmic.2014.7431191.

[266] A. Yoshida, Y. Kaburagi, and Y. Hishiyama, *Chapter 5 - Scanning Electron Microscopy*. Tsinghua University Press Limited, 2016.

[267] Hardnesstesters.com, “Vickers Hardness Testing.” .

[268] S. N. Naik and S. M. Walley, “The Hall–Petch and inverse Hall–Petch relations and the hardness of nanocrystalline metals,” *Journal of Materials Science*. 2020, doi: 10.1007/s10853-019-04160-w.

[269] Z. C. Cordero, B. E. Knight, and C. A. Schuh, “Six decades of the Hall–Petch effect – a survey of grain-size strengthening studies on pure metals,” *Int. Mater. Rev.*, 2016, doi: 10.1080/09506608.2016.1191808.

[270] H. Ryou *et al.*, “Below the Hall-Petch Limit in Nanocrystalline Ceramics,” *ACS Nano*, 2018, doi: 10.1021/acsnano.7b07380.

[271] Y. C. Huang, C. H. Su, S. K. Wu, and C. Lin, “A study on the hall-petch relationship and grain growth kinetics in FCC-structured high/medium entropy alloys,” *Entropy*, 2019, doi: 10.3390/e21030297.

[272] AMTECO Incorporated, *HRFS High-Temperature Furnace Specifications*. 2020.

[273] F. J. Parker and R. W. Rice, “Correlation between Grain Size and Thermal Expansion for Aluminum Titanate Materials,” *J. Am. Ceram. Soc.*, 1989, doi: 10.1111/j.1151-2916.1989.tb06091.x.

[274] J. A. KUSZYK and R. C. BRADT, “Influence of Grain Size on Effects of Thermal Expansion Anisotropy in MgTi2O5,” *J. Am. Ceram. Soc.*, 1973, doi: 10.1111/j.1151-2916.1973.tb12714.x.

[275] Y. Liu, L. Liu, Z. Wu, J. Li, B. Shen, and W. Hu, “Grain growth and grain size effects on

the thermal expansion properties of an electrodeposited Fe-Ni invar alloy," *Scr. Mater.*, 2010, doi: 10.1016/j.scriptamat.2010.04.006.

[276] K. Lu and M. L. Sui, "Thermal expansion behaviors in nanocrystalline materials with a wide grain size range," *Acta Metall. Mater.*, 1995, doi: 10.1016/0956-7151(95)00035-T.

[277] H. Furuse, R. Yasuhara, and K. Hiraga, "Thermo-optic properties of ceramic YAG at high temperatures," *Opt. Mater. Express*, 2014, doi: 10.1364/ome.4.001794.

[278] M. Sokol, S. Kalabukhov, V. Kasiyan, A. Rothman, M. P. Dariel, and N. Frage, "Mechanical, thermal and optical properties of the SPS-processed polycrystalline Nd:YAG," *Opt. Mater. (Amst).*, 2014, doi: 10.1016/j.optmat.2014.10.030.

[279] D. R. Askeland, "Atom Movement in Materials," in *The Science and Engineering of Materials*, 1996.

[280] L. Alekseeva *et al.*, "Study of the hydrolytic stability of fine-grained ceramics based on Y2.5Nd0.5Al5O12 oxide with a garnet structure under hydrothermal conditions," *Materials (Basel).*, 2021, doi: 10.3390/ma14092152.

[281] W. Jia *et al.*, "Comparative analyses of the influence of tetraethoxysilane additives on the sintering kinetics of Nd:YAG transparent ceramics," *J. Mater. Sci. Mater. Electron.*, 2021, doi: 10.1007/s10854-021-06443-y.

[282] J. Wang and R. Raj, "Estimate of the Activation Energies for Boundary Diffusion from Rate-Controlled Sintering of Pure Alumina, and Alumina Doped with Zirconia or Titania," *J. Am. Ceram. Soc.*, 1990, doi: 10.1111/j.1151-2916.1990.tb05175.x.

[283] E. Arzt, "ON THE INTERFACE REACTION IN DIFFUSIONAL CREEP AND DISCONTINUOUS PRECIPITATION," *Le J. Phys. Colloq.*, 1985, doi: 10.1051/jphyscol:1985467.

[284] A. C. F. Cocks, "Interface reaction controlled creep," *Mech. Mater.*, 1992, doi: 10.1016/0167-6636(92)90044-E.

[285] B. Burton, "Interface reaction controlled diffusional creep: A consideration of grain boundary dislocation climb sources," *Mater. Sci. Eng.*, 1972, doi: 10.1016/0025-5416(72)90060-2.

[286] T. Nakakoji, T. Hiraga, H. Nagao, S. Ito, and M. Kano, "Diffusion Creep and Grain Growth in Forsterite +20 vol% Enstatite Aggregates: 1. High-Resolution Experiments and Their Data Analyses," *J. Geophys. Res. Solid Earth*, 2018, doi: 10.1029/2018JB015818.

[287] A. H. Chokshi, "Diffusion creep in oxide ceramics," *J. Eur. Ceram. Soc.*, vol. 22, no. 14–15, pp. 2469–2478, 2002, doi: 10.1016/S0955-2219(02)00105-X.

[288] M. E. Kassner, *Fundamentals of Creep in Metals and Alloys: Third Edition*. 2015.

[289] I. G. Crossland and B. D. Clay, “Diffusion creep and its inhibition in a stainless steel,” *Acta Metall.*, 1977, doi: 10.1016/0001-6160(77)90180-8.

[290] Ł. Dobrzycki, E. Bulska, D. A. Pawlak, Z. Frukacz, and K. Woźniak, “Structure of YAG crystals doped/substituted with erbium and ytterbium,” *Inorg. Chem.*, 2004, doi: 10.1021/ic049920z.

[291] L. Bonnet, R. Boulesteix, A. Maître, C. Sallé, V. Couderc, and A. Brenier, “Manufacturing issues and optical properties of rare-earth (Y, Lu, Sc, Nd) aluminate garnets composite transparent ceramics,” *Opt. Mater. (Amst).*, vol. 50, pp. 2–10, 2015, doi: 10.1016/j.optmat.2015.04.050.

[292] R. S. Hay, C. J. Armani, M. B. Ruggles-Wrenn, and G. E. Fair, “Creep mechanisms and microstructure evolution of Nextel^{TM} 610 fiber in air and steam,” *J. Eur. Ceram. Soc.*, vol. 34, no. 10, pp. 2413–2426, 2014, doi: 10.1016/j.jeurceramsoc.2014.01.032.

[293] C. J. Armani, M. B. Ruggles-Wrenn, G. E. Fair, and R. S. Hay, “Creep of Nextel^{TM} 610 fiber at 1100°C in air and in steam,” *Int. J. Appl. Ceram. Technol.*, vol. 10, no. 2, pp. 276–284, 2013, doi: 10.1111/j.1744-7402.2012.02831.x.

[294] J. Jaseliunaite and A. Galdikas, “Kinetic modeling of grain boundary diffusion: The influence of grain size and surface processes,” *Materials (Basel).*, 2020, doi: 10.3390/ma13051051.

[295] P. Fielitz, G. Borchardt, M. Schmücker, H. Schneider, and P. Willich, “Measurement of oxygen grain boundary diffusion in mullite ceramics by SIMS depth profiling,” 2003, doi: 10.1016/S0169-4332(02)00641-4.

[296] R. K. Koju and Y. Mishin, “The role of grain boundary diffusion in the solute drag effect,” *Nanomaterials*, 2021, doi: 10.3390/nano11092348.

[297] L. Ruiz and M. J. Readey, “Effect of heat treatment on grain size, phase assemblage, and mechanical properties of 3 mol% Y-TZP,” *J. Am. Ceram. Soc.*, 1996, doi: 10.1111/j.1151-2916.1996.tb08980.x.

[298] J. Li *et al.*, “Influence of heat treatment of powder mixture on the microstructure and optical transmission of Nd:YAG transparent ceramics,” *J. Eur. Ceram. Soc.*, 2014, doi: 10.1016/j.jeurceramsoc.2014.03.004.

[299] A. Ikesue, Y. L. Aung, T. Yoda, S. Nakayama, and T. Kamimura, “Fabrication and laser performance of polycrystal and single crystal Nd:YAG by advanced ceramic processing,” *Opt. Mater. (Amst).*, 2007, doi: 10.1016/j.optmat.2005.12.013.

[300] C. M. KAPADIA and M. H. LEIPOLD, “Interrelation of Pore Size and Grain Size During Grain Growth of Oxides,” *J. Am. Ceram. Soc.*, 1973, doi: 10.1111/j.1151-2916.1973.tb12494.x.

[301] T. G. Langdon, “Grain boundary sliding revisited: Developments in sliding over four

decades," *J. Mater. Sci.*, vol. 41, no. 3, pp. 597–609, 2006, doi: 10.1007/s10853-006-6476-0.